Fully Kinetic Numerical Modeling of a Plasma Thruster

by

James Joseph Szabo, Jr.

B.S., Mechanical Engineering, Cornell University (1991)
M.S., Aeronautics and Astronautics, Stanford University (1992)

Submitted to the Department of Aeronautics and Astronautics
in Partial Fulfillment of the Requirements for the Degree of

Doctor of Philosophy in Aeronautics and Astronautics

at the

Massachusetts Institute of Technology

February 2001

Author .....
Department of Aeronautics and Astronautics
Jan 29, 2001

Certified by .....
Manuel Martinez-Sanchez
Professor, Department of Aeronautics and Astronautics
Thesis Supervisor

Certified by .....
Oleg Batishchev
Research Scientist, Department of Nuclear Engineering

Certified by .....
Kim Molvig
Associate Professor, Department of Nuclear Engineering

Certified by .....
Jaime Peraire
Professor, Department of Aeronautics and Astronautics

Certified by .....
Saul Rappaport
Professor, Department of Physics

Accepted by .....
Wallace Vander Velde
Chairman, Department Graduate Committee

Fully Kinetic Numerical Modeling of a Plasma Thruster

by

James Joseph Szabo, Jr.

Submitted to the Department of Aeronautics and Astronautics
on Jan 29, 2001, in Partial Fulfillment of the
Requirements for the Degree of
Doctor of Philosophy in Aeronautics and Astronautics

Abstract

A Hall effect plasma thruster with conductive acceleration channel walls was numerically modeled using 2D3V Particle-in-Cell (PIC) and Monte-Carlo Collision (MCC) methodologies. Electron, ion, and neutral dynamics were treated kinetically on the electron time scale to study transport, instabilities, and the electron energy distribution function. Axisymmetric R-Z coordinates were used with a non-orthogonal variable mesh to account for important small-scale plasma structures and a complex physical geometry. Electric field and sheath structures were treated self-consistently. Conductive channel walls were allowed to float electrically. The simulation included, via MCC, elastic and inelastic electron-neutral collisions, ion-neutral scattering and charge exchange collisions, and Coulomb collisions. The latter were also treated through a Langevin (stochastic) differential equation for the particle trajectories in velocity space. Ion-electron recombination was modeled at the boundaries, and neutrals were recycled into the flow. The cathode was modeled indirectly by injecting electrons at a rate which preserved quasineutrality. Anomalous diffusion was included through an equivalent scattering frequency. Free space permittivity was increased to allow a coarser grid and longer time-step. A method for changing the ion to electron mass ratio and retrieving physical results was developed and used throughout. Results were compared with theory, experiments. Gradients and anisotropy in electron temperature were observed. Non-Maxwellian electron energy distribution functions were observed. The thruster was numerically redesigned; substantial performance benefits were predicted.

Thesis Supervisor: Manuel Martinez-Sanchez
Title: Professor, Department of Aeronautics and Astronautics

Biographical Note

James Szabo graduated from Louis E. Dieruff High School in Allentown, Pennsylvania in June, 1987. That fall, he entered Cornell University with the aid of an Air Force Reserve Officer Training Corps (ROTC) scholarship. While there, he was elected to the Mechanical Engineering honor society, Pi Tau Sigma, and to the oldest Greek letter social organization, The Kappa Alpha Society. In 1991, he was named a Bachelor of Science with Distinction by the Sibley School of Mechanical and Aerospace Engineering. Szabo next studied at Stanford University, from which he was conferred a Master of Science degree in Aeronautics and Astronautics in 1992. That same year, he entered active duty with the United States Air Force. He served four years at Space and Missile Systems Center, Los Angeles Air Force Base, before separating with the rank of Captain. He arrived at MIT in 1996. He is a member of Sigma Xi and the American Institute of Aeronautics and Astronautics (AIAA). He has authored many papers on electric propulsion.

Acknowledgments

I would first like to thank my advisor, Manuel Martinez Sanchez, for making my tenure at MIT possible. I would next like to thank Oleg Batishchev, whose contributions to the numerical model described herein were invaluable. I would also like to thank Saul Rappaport, Kim Molvig, and Jaime Peraire for their advice and for serving on my thesis committee.

I owe special thanks to AFOSR and to Busek Co. for sponsoring my research. I would especially like to thank Vlad Hruby and Jeff Monheiser. I would also like to thank the scientists at The Aerospace Corporation who introduced me to the field of Space Propulsion, Siegfried Janson, Ron Cohen, and Jim Pollard.

On a more personal note, I would like to thank Debie, Monster, and Belle for putting up with my incessant ramblings about "the code."

Finally, I would like to thank the graduate students with whom I shared an office for several years, Tatsuo Onishi, Paulo Lozano and Darrel Robertson. I wish them all a window and a working air conditioner.

This thesis is dedicated to my late grandfather, Frank Szabo, who said a few sunflower seeds would change the surface of Mars. We shall see.

"We ought then to regard the present state of the universe as the effect of its anterior state and as the cause of the one which is to follow. Given for one instant an intelligence which could comprehend all the forces by which nature is animated and the respective situation of the beings who compose it - an intelligence sufficiently vast to submit these data to analysis - it would embrace in the same formula the movements of the greatest bodies of the universe and those of the lightest atom; for it, nothing would be uncertain and the future, as the past, would be present to its eyes. The human mind offers, in the perfection which it has been able to give to astronomy, a feeble idea of this intelligence. Its discoveries in mechanics and geometry, added to that of universal gravity, have enabled it to comprehend in the same analytical expressions the past and future states of the system of the world. Applying the same method to some other objects of its knowledge, it has succeeded in referring to general laws observed phenomena and in foreseeing those which given circumstances ought to produce. All these efforts in the search for truth tend to lead it back continually to the vast intelligence which we have just mentioned, but from which it will always remain infinitely removed."

-From "A Philosophical Essay on Probabilities" by Pierre Simon, Marquis de Laplace [27]

Contents

List of Figures

List of Tables

Chapter 1

Introduction

This thesis describes the fully kinetic numerical simulation of a 50 Watt Hall thruster. This introductory chapter describes the problem and presents a brief overview of the solution. Chapter 2 covers the theory behind the simulation. Chapter 3 describes many portions of the numerical method in detail. Chapter 4 is about validating the code. Chapter 5 presents and discusses various numerical results, while Chapter 6 concludes the thesis and recommends future work. Following all this is an Appendix.

1.1 Electric Propulsion

Spacecraft require on-orbit propulsion systems for tasks such as station-keeping, orbit rephasing, and orbit transfer. Satellite propulsion systems have typically relied upon chemical rockets, which are limited in exhaust speed by the internal energy stored in their propellant. Even the most advanced cryogenic Hydrogen-Oxygen systems achieve only about 470-sec of specific impulse, I_{sp}, defined as the ratio between exhaust speed, $< v >$, and g_o, the gravitational acceleration of the earth's surface. Recently, satellites have begun to rely upon electric rockets (collectively known as "Electric Propulsion" or E.P.), which bypass the internal energy limit by using an outside energy source to accelerate the propellant. Almost unlimited exhaust speeds can be obtained.

The amount of propellant required for a given velocity increment, M_p, is a function of the satellite mass before the maneuver, M_i, and the specific impulse, according to the rocket equation:

$$M_p = M_i[1 - exp(\frac{-\Delta V}{< v >})]. \tag{1.1}$$

Thus, specific impulse can be regarded as a measure of fuel efficiency. In this sense, high I_{sp} electric thrusters are far more economical than low I_{sp} chemical thrusters. Of course, there is a tradeoff between the thrust of a rocket and the amount of power it draws. Given limited power as supplied by a satellite bus, spacecraft designers sometimes choose high thrust systems over high specific impulse systems.

Electric rockets come in all shapes and sizes. The most commonly used electric rockets may be roughly separated into two groups: Electro-thermal and Electrostatic. Electro-thermal thrusters include resistojets and arcjets. Electrostatic thrusters include ion engines, Hall thrusters, FEEP and colloidal thrusters. Other electric propulsion devices include the Pulsed Plasma Thruster (PPT) and Magnetoplasmadynamic (MPD) thruster. Figure 1-1 shows some standard thruster geometries.

1.2 Hall Thrusters

With higher thrust densities than ion engines and specific impulses between one and two thousand seconds, Hall thrusters are considered ideal for many on-orbit applications including station-keeping, orbit re-phasing, and orbit transfer. Originally developed in the 1960's, the first successful on-orbit test was completed in 1972. For over a decade, Soviet/Russian spacecraft have used Hall thrusters for station-keeping and on-orbit maneuvering. Western interest in Hall thrusters has grown with the commercial satellite business; their high efficiencies promise to increase payload mass fractions and operating lives, thereby increasing profits.

Typical flight tested Hall thrusters operate in the 1-kW power range. However, spacecraft come in different sizes. Some missions are optimized with 1-kW thrusters, while others are optimized with relatively diminutive 50-W thrusters. Hence, a market exists for new Hall thruster designs. Computer simulations are one way to develop and test these new designs, as well as understand old ones.

1.2.1 General Theory

Hall effect plasma thrusters are essentially rockets in which the working fluid is a plasma and the means of acceleration is an electric field. The "acceleration zone" of a Hall thruster is shown in Figure 1-2. This region is usually comprised of two concentric cylinders ("walls")

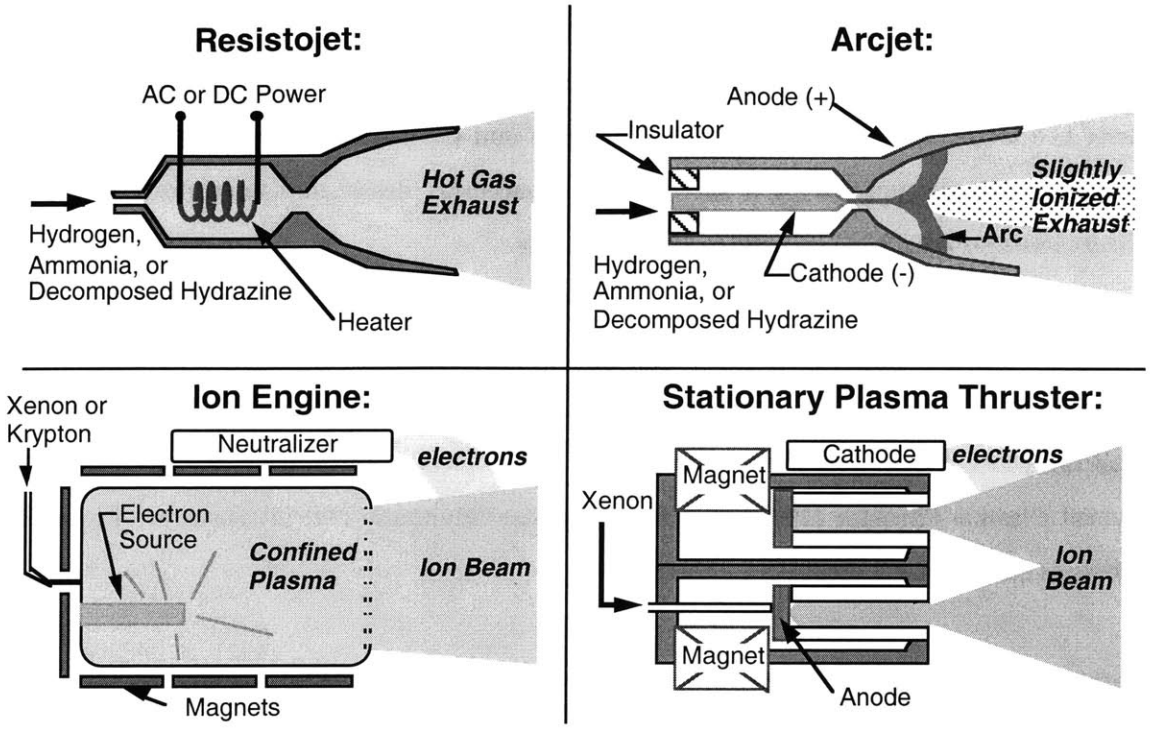

Figure 1-1: *Four types of electric propulsion*: Resistojet, Arcjet, Ion Engine, Hall Thruster (Stationary Plasma Thruster) [37].

which are either metallic (TAL type thrusters) or dielectric (SPT type thrusters). At one end of the annulus sits a highly biased (300 Volts is typical) hollow anode which produces a nominally axial electric field. The other end of the annulus opens to free space. Neutral gas is injected through the anode, ionized through inelastic collisions with electrons, and accelerated out the other end of the annulus by the electric field. An external cathode supplies electrons to neutralize the beam and sustain the discharge. Electrons are impeded in their motion toward the anode by a radial magnetic field. Trapped in cyclotronic motion, they spend most of their time drifting azimuthally due to the Hall effect (which gives these thrusters their name), allowing them time to ionize the neutrals.

The special role of Soviet researchers and engineers in developing Hall thrusters should be acknowledged. They developed much of the theory, they were the first to create efficient engines, and they were the first to fly them on spacecraft. The very names applied to these thrusters, ("Stationary Plasma Thruster" and "Thruster with Anode Layer") were coined in the Soviet Union.

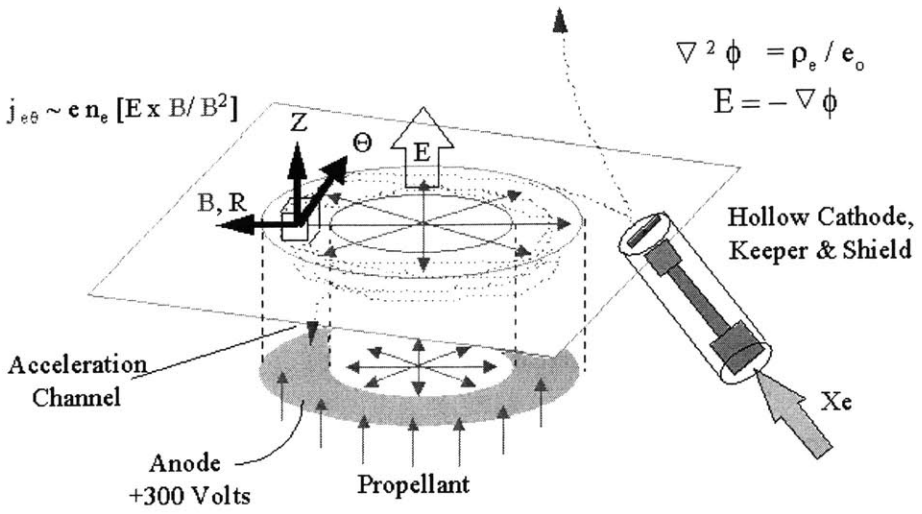

Figure 1-2: *The acceleration zone of a Hall thruster.* Electrons are drawn from the cathode to the highly biased anode. Along the way, they drift azimuthally (the Hall current) and ionize the propellant. Coordinate system used is (r, z, θ).

1.2.2 Types of Hall Thrusters

Most flight Hall thrusters have been "Stationary Plasma Thrusters" (SPT's). In an SPT, the walls of the acceleration channel are made of an insulating (dielectric) material. The length (in the axial direction) of the acceleration channel is usually greater than the width, and the magnetic field is usually structured such that the primary ionization zone is located near the channel exit. The "Thruster with Anode Layer" (TAL) is similar in construction, but the walls of the acceleration channel are conductive. (They are either held at the cathode potential or allowed to float.) In a TAL, the length of the channel is usually short (or even non-existent), and the field is often constructed such that the primary ionization zone abuts the anode, giving these thrusters the name "Anode Layer". It is also possible to extend the acceleration zone of a TAL downstream some distance, although such thrusters are reported to have lower efficiency [12]. In general, TAL's and SPT's offer comparable performance.

SPT's have been successfully modeled at MIT and elsewhere using one and two dimensional Hybrid PIC methods. Such models typically assume the plasma is quasineutral ($n_i \approx n_e$). These models may not be applicable to TAL thrusters. Because metals have much less secondary electron emission than the dielectrics, TAL's lose less heat to the acceleration channel walls than do SPT's, yielding, in general, higher electron temperatures and

more abrupt ionization layers. Equally important is the location of the ionization layer; it is usually, as the name suggests, next to the anode and may be just a few electron cyclotron radii wide (see Section 2.11)[12]. To model such a layer, the numerical model must allow for non-neutrality and non-Maxwellian electron energy distributions. Such a model is the subject of this thesis.

1.3 Statement of Technical Problem

Hall thrusters are, despite years of development, still poorly understood. They are designed based of a set of generalized assumptions regarding the energy in the discharge, the influence of the magnetic field, and methods of electron transport. Unfortunately, measurements of the discharge are hard to obtain and must be interpreted based on the same assumptions. A self-consistent numerical model of the discharge region is needed to validate and refine the assumptions. Were such a model applicable to non-idealized thrusters, it would enable a new generation of thruster designs which address issues such as erosion, beam divergence, and doubly charged ions directly by tailoring the discharge.

1.4 Literature Survey/Brief Summary of Previous Work

Relevant research performed by others includes Hall thruster modeling efforts at MIT and elsewhere, the building of a mini-TAL at MIT, and measurements of the electron energy distribution function (EEDF) taken in France.

To date, most modeling efforts have been too general to resolve features of the discharge such as charge separation, boundary layers, and high frequency oscillations. A fully kinetic simulation of a real thruster is needed.

Hall thruster are nominally axisymmetric in construction, although azimuthal oscillations may play an important role in electron diffusion. Most modeling efforts have been 1 or 2 dimensional. In the latter case, the RZ plane is usually modeled. Hirakawa has also modeled the $R\Theta$ plane [17]. A 3 dimensional model would be ideal, but this is beyond the capabilities of a current workstation.

1.4.1 1-D Modeling

Lentz used a one-dimensional numerical model to accurately predict the operating characteristics and plasma parameters in the acceleration channel of a Japanese Hall thruster [28]. His model uses kinetic conservation equations and the method of characteristics to solve the Boltzmann equation for electron and ion distribution functions. The electron distribution function was assumed to be Maxwellian (the normal distribution).

More recently, Noguchi, Martinez-Sanchez, and Ahedo performed a linear (analytic) 1-D analysis of oscillations in Hall thrusters. This model aids in analyzing low frequency axial oscillation instabilities found in SPT's [32].

2-D Hybrid-PIC Modeling

MIT's "hybrid PIC" SPT simulations rely upon Maxwellian electron distributions, assumed levels of Bohm diffusion, and wall effects based on the local electron temperature [9] [8] [52].

Fife built a 2-D model of the SPT-100 which included detailed wall effects [9] [8] [10]. This "Hybrid Particle-in-Cell" (Hybrid PIC) simulation treats ions and neutrals as particles, and electrons as a fluid. It assumes a Maxwellian Electron Energy Distribution Function (EEDF) centered about some electron temperature, T_e, which is assumed to be constant along any given magnetic streamline. This model successfully predicts overall Stationary Plasma Thruster performance. It also predicts experimentally observed ionization oscillations to within a factor of ≈ 2 in frequency. This success relies upon Bohm diffusion of electrons and associated adjustable coefficients.

A modified version of Fife's Hybrid-PIC numerical model was used to simulate the Busek BHT-200-X2 SPT type Hall thruster (The author's previous research, [52]). Predicted performance agreed well with experimental measurements when Bohm diffusion coefficients of $\approx .25 - .3$ times the classical Bohm coefficient $(1/16B)$ were used. High frequency oscillations and electron transport were found to be sensitive to wall boundary conditions. Correction factors to predict and account for doubly charged ions (XeIII) were introduced. The predicted XeIII fraction was about half that measured in the laboratory for similar thrusters. Fife modified the SPT-100 code to account directly for XeIII, but achieved a similar result. It was supposed that the assumed isotropic and Maxwellian electron energy distribution was incorrect.

2D Full PIC Modeling

To correctly model the thin ionization layer present in a TAL, a numerical simulation should not require quasineutrality or an isotropic Maxwellian Electron Energy Distribution Function (EEDF). Instead, the simulation should allow the EEDF to evolve. To predict the correct rate of electron transport, the simulation should include mechanisms for both classical and anomalous diffusion. A full PIC simulation fulfills these requirements.

The PIC/Monte-Carlo/DSMC Hall thruster simulations performed by Hirakawa are the most relevant to the simulation we construct [16][17] [15]. Hirakawa studied transport and charge separation. Most significantly, she modeled the effects of azimuthal electric field on electron transport The following should also be noted:

- The geometry was not that of a real thruster.
- An artificial mass ratio was assumed.
- No ion-neutral collisions were modeled.
- Hirakawa pre-simulated neutrals using DSMC and applied a 1-D density gradient due to ionization of the form $n_n/n_{n,o} = exp(\frac{z}{L} ln(1 - \eta_u))$, where $n_{n,o}$ is the density in the case of no ionization, and η_u is propellant utilization.
- Charged particles re-combined at surfaces, but neutrals were not re-introduced into the flow.

The EEDF in Hirakawa's simulation started out Maxwellian, but a non-Maxwellian was allowed to develop as elastic and inelastic (excitation, ionization) collisions with neutrals and ions were accounted for.

At MIT, Beidler developed a 2D3V PIC model of an Argon Hall thruster [3]. This model used an idealized geometry, idealized cross sections, a uniform mesh, and imposed a constant potential at the downstream boundary. The cathode current was limited by the equation $I_c = I_a$. This simulation implemented many concepts essential for modeling a real Hall thruster.

1.4.2 Measurements of the EEDF

Measurements of the EEDF in SPT type Hall thrusters show multiple populations of electrons and gradients in temperature along magnetic streamlines. Interpreting most data,

however, requires knowledge of the EEDF.

Guerrini, et.al. have measured the plasma inside SPT's by inserting probes through the channel wall [13]. The second derivative of probe data was then used to estimate the EEDF under the assumption that the EEDF is isotropic. They found a single population of electrons near the anode and at the exit plan. In between, they found three different populations (0-20, 20-35, and 35-55 eV) of electrons. These populations were affected by voltage and flow rate. Three higher energy populations were found near the (insulating) walls everywhere.

Emission spectroscopy shows the presence of XeIII, but electron density and temperature measurements are needed to interpret the data. Knowledge of the EEDF will help further.

1.4.3 The mini-TAL

The thruster chosen for this simulation is the miniaturized 50-Watt TAL thruster (Hall effect plasma thruster with conductive acceleration channel walls) built at MIT by Khayms and shown in Figure 1-3. This thruster has been tested in the laboratory [25]. Design characteristics of the mini-TAL are shown in Table 1.1, along with a summary of actual performance measurements. Experimental performance date collected by Khayms are plot-

	Design	Actual
Anode Current(A)	.17	.20
Anode Power(W)	50	60
Thrust (mN)	2.2	.86
I_{sp} (sec)	1600	670
Efficiency	.32	.048

Table 1.1: The design performance of the mini-TAL is presented in the left column. The design mass flow rate was .13 mg/s. Actual performance linearly interpolated to the same mass flow rate is presented in the right column. Propellant: Xenon; Diameter: 4.8 mm; B-field: .5 T; Mass flow rate: .13 mg/s; Anode Potential: 300 V.

ted in Figure 5-1 [25]. (Note: These results differ from those reported in [51], which were preliminary). The actual variables measured were thrust, anode current, and mass flow rate. The thrust efficiency is calculated from the thrust, T, anode current, I_d , and mass flow rate, $\dot{m}_n$;

$$\eta_{th} = \frac{T^2}{2\dot{m}_n I_d V_d}. \tag{1.2}$$

The utilization efficiency is calculated assuming all of the ions exiting the system have kinetic energies equal to the anode potential. That is,

$$\eta_u = \frac{\dot{m}_i}{\dot{m}_n} = \frac{T/v_i}{\dot{m}_n}, \tag{1.3}$$

where $v_i = \sqrt{\frac{2(\Phi-\Phi_o)}{m_i}}$ and $(\Phi - \Phi_o) = V_d = 300V$.

The thrust efficiency of this thruster is quite low due to leakage of electrons to the cathode. This suggests a magnetic field that is too weak or improperly aligned. Khayms states "with a certain degree of confidence" that the permanent magnets experienced only minimal damage due to heating [25]. Therefore, he concludes, heating of the center pole is the most likely cause: Improper cooling may lead to high temperatures at which the magnetic permeability of iron sharply approaches zero. Such a reduction in permeability would increase fringing of the magnetic field inside the channel, possibly changing field strength or allowing some field lines to cross directly to the anode, en effect "short circuiting" the discharge.

A mean free path analysis indicates that both electron-neutral and Coulomb scattering should be important to this thruster's operation, and that the length L of the simulation region will be about 150 nominal Debye lengths.

1.5 Thesis Topic

The subject of this thesis is a PIC/Monte-Carlo numerical simulation of a Hall effect plasma thruster with conductive acceleration channel walls. All particles are treated kinetically; none are pre-simulated. Because the Debye length in this thruster is large in comparison to geometrical scale lengths, the simulation can be run on an ordinary workstation. The simulation includes elastic and inelastic (exciting and ionizing) electron-neutral scattering collisions. It also includes electron-electron and electron-ion collisions, as well as ion-electron recombination at the boundaries. Other interesting kinetic effects such as charge exchange collisions and ion-neutral scattering are also included.

Both an artificial mass ratio and an artificial permittivity are assumed. Other modifications to the physical parameters are introduced in order to retrieve physical results despite the modified mass ratio (see 2.6.2). The magnetic field is pre-computed, while the electric

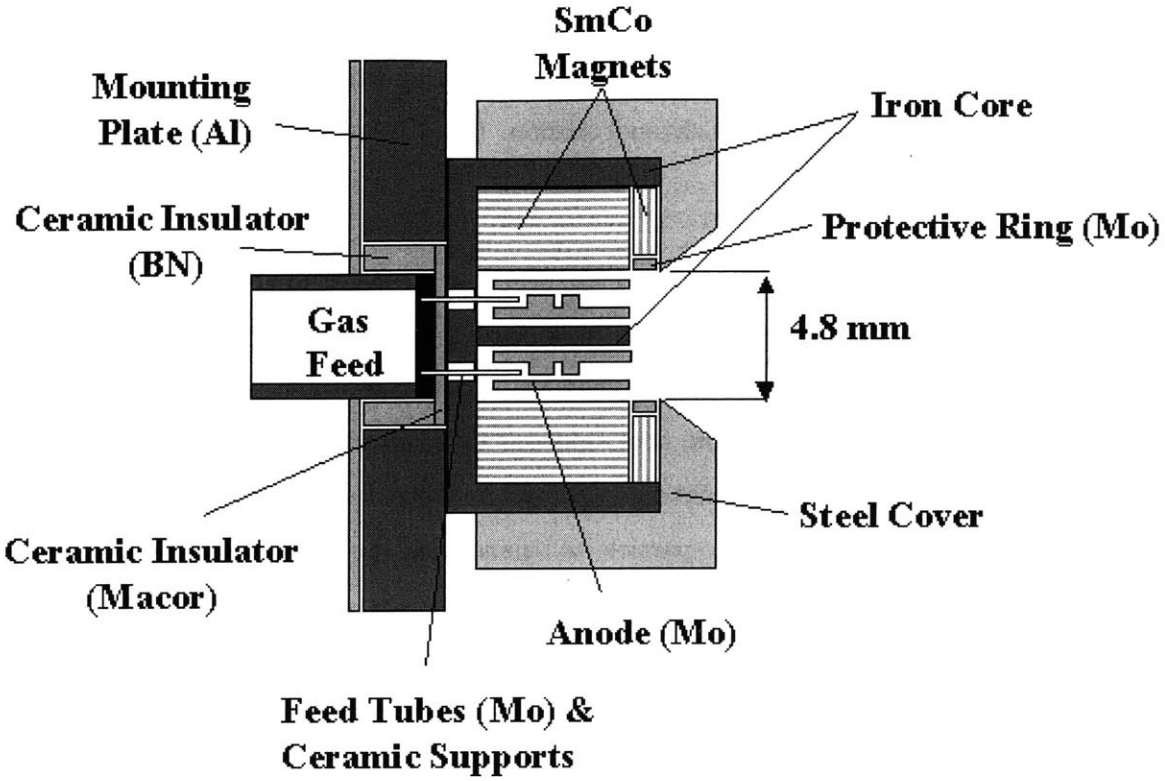

Figure 1-3: *Diagram of Khayms mini-TAL.*

field and sheath structures are computed self-consistently using a finite difference method. The simulation proceeds on the electron time-scale to capture high frequency dynamics and the EEDF.

Objectives of Research

Specific goals of the simulation include:

- Predict performance of a real thruster.
- Predict particle moments such as electron temperature and density.
- Predict the electron energy distribution function.
- Examine methods of electron transport.
- Examine oscillations.
- Predict particle moments.
- Create a design tool.

In short, we wish to understand the plasma in a microscopic sense. This will help engineers predict and design around oscillations, electro-magnetic emissions, efficiency loss mechanisms, plume divergence and channel erosion. It will also aid in spectroscopy.

1.6 Methodology

The first formal step in solving the thesis problem was to devise and write a 2D-3V PIC algorithm to handle the charged particle dynamics, and embed a Monte-Carlo algorithm to handle heavy particle dynamics. The next step was to adapt the algorithm to the specific thruster, and to account for all possible relevant effects such as: electric potential boundary conditions; cathode emission; heavy particle collisions with the walls; scattering collisions; ionization collisions; multiply charged ions; Coulomb collisions; excitation collisions; charge exchange collisions; Bohm diffusion; azimuthal waves; and secondary electron emission. (The last two effects are not modeled in the simulation). These steps were described in papers, along with preliminary results [50] [51]. The final phase of the research was to validate the results through parametric studies and comparison with experimental measurements.

1.7 Summary of Theory (Chapter 2)

To simulate the mini-TAL, we use a fully kinetic model which includes both Maxwell's equations and collision terms.

1.7.1 Dimensions

Hall thrusters are nominally axisymmetric. Therefore, an axisymmetric numerical model should be sufficient to reproduce most features observed in the laboratory. Here, we model two dimensions in space, the R (radial) and Z (axial) directions (See Figures 1-2 and 3-21 for visualization). To track the particles, we model three dimensions in velocity: R, Z, and Θ, the azimuthal direction. However, particles are not permitted to move out of the R-Z plane; they are moved in three dimensions at each time-step, but their final positions are always "folded back" into the R-Z plane. For these reasons, we term this a 2D3V simulation.

1.7.2 Equations and Units

The unit systems used in this thesis are discussed in Section 2.5. Maxwell's equations may be normalized using the natural units shown in Table 1.2. This enables easy interpretation of results. The normalized unit system is derived in Section 2.5.2. In this system, the unit of distance is the nominal Debye length, the unit of time is the nominal inverse plasma frequency, the unit of potential is the nominal electron temperature in eV, and so on. Nominal values are estimated at program initialization. For the cases presented, the nominal temperature was $T_e = 50$ eV. Other nominal values can be read from Table 1.4.

	units	base
charge	[q]	e
mass	[m]	m_e
temperature	[T]	T_e
distance	[x]	λ_D
time	[t]	ω_{pe}^{-1}
velocity	[v]	$v_{th,e}/\sqrt{2}$
electric field	[E]	$[v]\sqrt{4\pi n_e m_e}$
magnetic field	[B]	$c\sqrt{4\pi n_e m_e}$

Table 1.2: Normalization Constants. Note that $[v] = \frac{[x]}{[t]}$, $[E] = \frac{[v][m]}{[t][q]}$, and $[B] = \frac{[c][m]}{[t][q]}$. T_e and n_e are pre-computed nominal estimates. System is based on CGS units.

1.7.3 Mean Free Path Analysis

A mean free path analysis is presented in Section 2.8. Particles gain and lose energy and momentum during elastic and inelastic collisions with other particles. A mean free path analysis helps decide which collisions to include in the simulation, and which to ignore. Table 1.3 lists the types of collisions we considered and those we included.

The reaction rate between two species can be expressed as a function of their densities (n_1, n_2), relative velocities (v_{12}), and a cross section Q_{12};

$$R_{12} = n_1 n_2 v_{12} Q_{12}. \tag{1.4}$$

The mean free path of a particle of species 1 interacting with a background of species 2 is

$$\lambda_{12} = \frac{1}{Q_{12} n_2} \tag{1.5}$$

Type	Included
Electron-Neutral Elastic Scattering	X
Electron-Neutral Ionization	X
Electron-Neutral Excitation	X
Electron-Electron Coulomb	X
Electron-Ion Coulomb	X
Ion-Neutral Charge Exchange	X
Ion-Neutral Scattering	X
Ion-Ion Coulomb	
Neutral-Ion Scattering	X
Neutral-Neutral Scattering	
Electron-Ion bulk recombination	
Electron-Ion wall recombination	X

Table 1.3: Types of collisions in a Hall thruster. Based on the mean free path analysis, only certain types of collisions are included in the simulation. Table reappears as 2.11.

where Q_{12} is the cross section for the interaction. Electron-neutral scattering cross sections gathered from the literature are presented in Figure 2-7. Third and Fourth order polynomial fits to the data are used in the code. These are shown by solid lines in Figure 2-7

Some of the expected mean free paths are listed in Table 1.4. The large Knudsen number ($Kn = \lambda_{mfp}/L$ where L is an expected path length) for heavy-heavy particle interactions justifies the collisionless approximation. Electrons are magnetized (trapped on magnetic streamlines) which extends their path lengths such that each is expected to undergo many collisions. Indeed, the thruster wouldn't work otherwise. Coulomb collisions should only be important for low energy electrons. Charge-exchange collisions are included; they are of special interest to plume modeling and erosion studies. Ion-Neutral elastic scattering is also included since the cross section is similar. Neutral-neutral scattering is ignored; the effect should be minor, and doing otherwise would require using a more computationally expensive Direct Simulation Monte Carlo (DSMC) methodology.

1.7.4 Diffusion

Diffusion is discussed in Section 2.10. Possible mechanisms for electron transport toward the anode include classical diffusion, Coulomb scattering, wall effects such as secondary electron emission, azimuthal plasma waves, and $\vec{E} \times \vec{B}$ drift associated with the Θ fields of azimuthal plasma waves. Since the walls of the acceleration channel are metallic, we ignore secondary emission (thought to play an important role in SPT electron transport). Furthermore, since

Parameter	Symbol		
Electron Temperature (eV)	$[T_e]$	30	50
Mass Flow Rate (mg/s)	$\dot{m}_N$	.13	.13
Neutral Injection Temp (eV)	T_n	.1	.1
Magnetic Field	B	5000	5000
Ion Sonic Speed	v_{si}	5e5	6e5
Elec Mean Thermal Vel.	$\bar{c_e}$	3.7e8	4.7e8
Plume area	s_p	.10	-
Neutral Density	$n_{n,o}$	7e14	-
Plasma Density	$[n_{e,o}]$	1e13	9e12
Debye Length	λ_d	.0012	.0018
Characteristic Length	L	.24	.24
	L/λ_D	199	135
Electron Gyro Radius (mm)	r_{ce}	.0037	.0048
Ion Gyro Radius	r_{ci}	1.3	1.7
e-n scattering mfp	λ_{en}	.66	.66
i-n charge exchange mfp	$\lambda_{cex,i}$	.25	.26
n-i charge exchange mfp	$\lambda_{cex,n}$	.69	.73
i-n scattering mfp	λ_{in}	.83	1.1
n-i scattering mfp	λ_{ni}	2.3	3.0
n-n scattering mfp	λ_{nn}	.30	.30
e-e Coulomb mfp	λ_{ee}	95	320
e-i Coulomb mfp	λ_{ei}	130	450
Electron Plasma Freq.	ω_{pe}	1.9e11	1.7e11
Elec Cyclotron Freq.	ω_{ce}	8.8e10	-
Ion Cyclotron Freq.	ω_{ci}	3.7e5	-
Neutral Transit Time (ω_{pe}^{-1})	τ	2.1e6	1.8e6

Table 1.4: Mean free paths for various collision processes along with estimates of various lengths, velocities, and frequencies in the channel of the mini-TAL. All units CGS unless otherwise noted. Numbers assume physical free space permittivity. Neutral transit time $L/ < v_n >_z$ in terms of (ω_{pe}^{-1}) drops by a factor of 10 with ϵ_o increase of 100x. Neutral transit time is further decreased by adopting an artificial mass ratio. Similar table reappears as 2.12.

Parameter	Symbol	x-Factor
plasma frequency	ω_{pe}	$1/\gamma$
Debye length	λ_D	γ
time	[t]	γ
distance	[x]	γ
velocity	[v]	1

Table 1.5: Effect on reference values of increasing permittivity by a factor of γ^2.

the model is axisymmetric, azimuthal wave effects are not considered. However, anomalous Bohm type electron diffusion is included through an equivalent scattering frequency. This effect may be turned on or off through a numerical switch in the header file.

1.7.5 Speeding up Heavy Particles

Methods to accelerate convergence of the simulation are discussed in Section 2.6. To capture electron dynamics, we need a time-step on the order of the inverse plasma time. Unfortunately, neutral particles at the real mass ratio will require millions of such time-steps to cross the simulation region. (The number of time-steps required is the "characteristic time" in Table 1.4, which assumes $T_n \sim .1$ eV.). We cannot track billions of particles for millions of time-steps. To allocate resources more efficiently we do the following:

- We use super-particles (groups of $\sim 10^6$ particles) in lieu of tracking individual particles.
- We decrease the heavy particle mass such that $M/m_e \sim 100$. This speeds up heavy particles.
- We increase the free-space permittivity constant ($\epsilon_o' = \epsilon_o \gamma^2$). This increases the Debye length, allowing a coarser grid, and slows plasma oscillations, allowing a longer time-step. Effects on some nominal parameters are shown in Table 1.5.

To preserve densities and mean-free-paths when heavy particles travel too fast, the factor $f < 1$ is introduced. This is defined by the following:

$$\frac{M'}{M} = f\,;\; \frac{v_n'}{v_n} = \sqrt{\frac{1}{f}}. \tag{1.6}$$

The neutral density n_n at the anode exit is preserved by scaling back the mass flow rate. Since $\dot{m} = Mn_n v_n A$, holding n_n constant requires

$$\frac{\dot{m}'}{\dot{m}} = \frac{M'v_n'}{Mv_n} = \sqrt{f}. \tag{1.7}$$

Relative rates of electron and ion transport are nominally preserved by scaling collision cross sections according to

$$\frac{Q_t'}{Q_t} = \sqrt{\frac{1}{f}}. \tag{1.8}$$

This is equivalent to increasing the scattering frequency. As discussed fully in Chapter 2, this increases the electrical conductivity of the plasma perpendicular to the magnetic field in proportion to the increase in ion velocity (due to its artificial mass) across the magnetic field, thus preserving internal scales such as the width of the ionization region. Mass flow rate, thrust, and I_{sp} must be re-scaled at the thruster exit in order to plot the performance.

1.8 Summary of Numerical Method (Chapter 3)

This section introduces the numerical method which is described fully in Chapter 3. The simulation combines Particle-in-Cell and Monte Carlo methodologies [50]. All particles are treated kinetically; their trajectories are followed as they move within a computational grid. All particles move on the same time-scale. Charged particles experience electric and magnetic forces according to Maxwell's equations. Electrons also experience electron-neutral and Coulomb collisional forces. Neutrals are subject only to Newton's laws, except when they encounter boundaries. Ion-neutral scattering and charge exchange collisions are included. Other heavy particle collisions are ignored; mean free paths justify a collisionless approximation. Recombination of electrons and ions at the boundaries is modeled, and neutrals are re-introduced into the flow. However, bulk recombination is ignored.

The simulation region is shown in Figure 1-4. The methodology is visualized in Figure 1-5. In words, the basic structure of the code is as follows:

```
Pre-commutate B-field, grid, neutral plume
Call "pic"
- Initialize variables
- Load particles from previous run
Iterate in time XX time-steps
- Calculate charge distribution
```

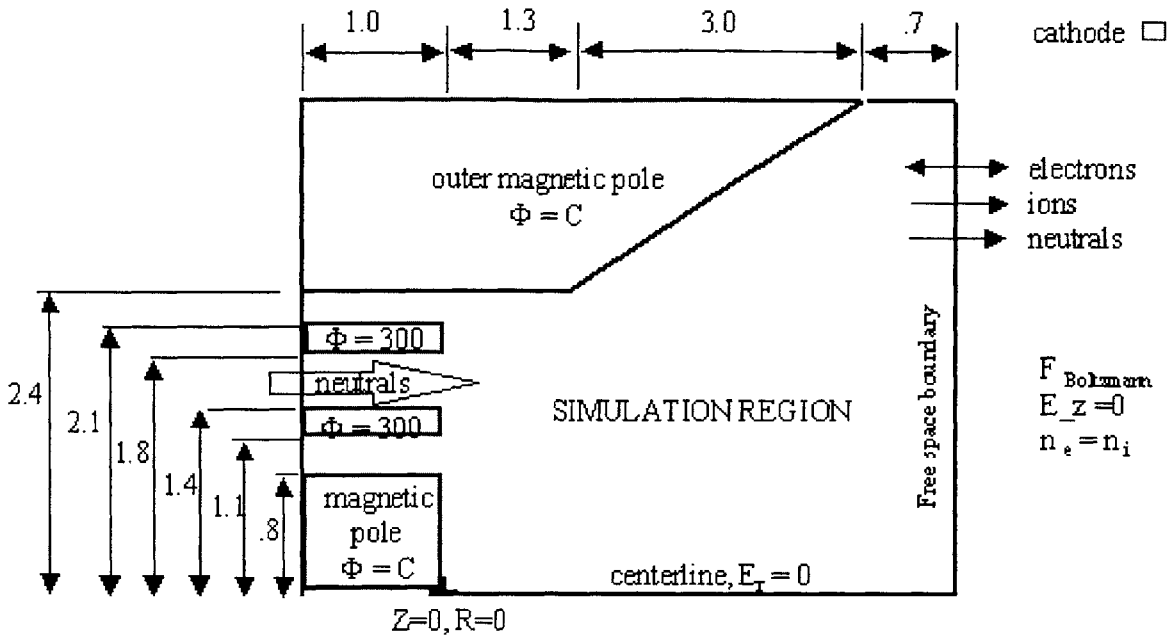

Figure 1-4: *The simulation region.* Preliminary versions of the simulation modeled the anode boundary as a flat wall [51]. The simulation region was later expanded to encompass the complex anode and inner magnetic pole boundaries. In contrast, early versions of the simulation placed the cathode on the free space boundary, while later versions assume it is beyond the domain of simulation. Dimensions are in millimeters.

```
- Solve Poisson eqn. for electric potential
- Calculate E-field
- Move neutrals, ions, and electrons v*dt
  -- apply fields
  -- boundary conditions/particle losses
  -- statistics:  scatter, ionize, excite
  -- create new particles
Post-process data
```

1.8.1 New Features

This simulation differs significantly from previous full PIC Hall thruster simulations. Unique features include the following:

- The geometry is that of a real thruster, for which some experimental data is available.
- The numerical grid is non-orthogonal.
- A novel method for accelerating classical diffusion and retrieving physical results is implemented.

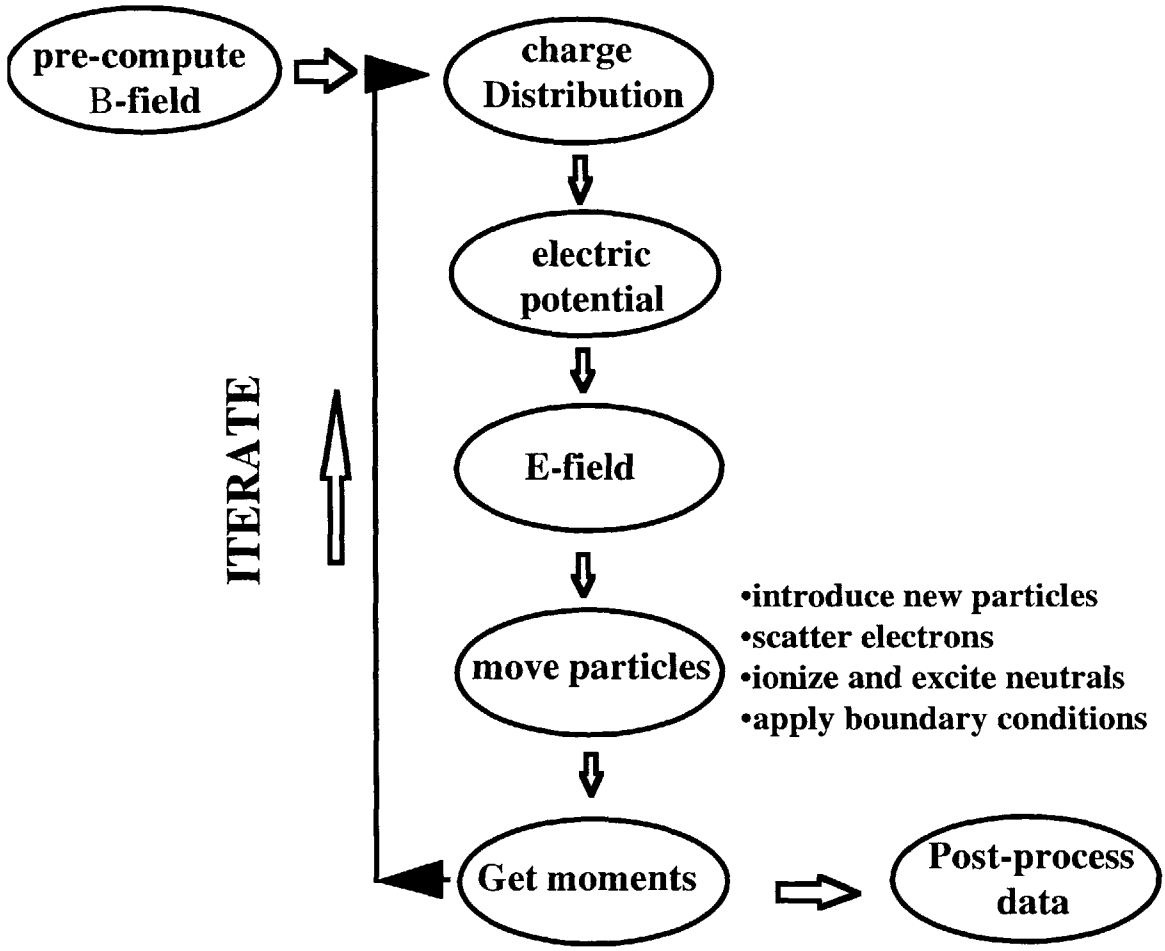

Figure 1-5: *The PIC Monte-Carlo methodology.*

- The free space permittivity constant is changed to exaggerate sheaths and accelerate the simulation.
- Anomalous diffusion is included via an equivalent scattering frequency.
- Ion-neutral charge exchange and scattering collisions are modeled.
- The wall potential is allowed to float. It is computed self-consistently.
- Cathode electrons are injected at the rate required to preserve quasineutrality at the free-space (plume) boundary.
- Coulomb collisions are modeled as a diffusion process in velocity space.

An important (but not entirely unique) feature of this simulation that all particles are simulated on the same time-scale. Neutral self-collisions are lost, but the result is more self-consistent. Beidler did this, but Hirakawa pre-simulated neutrals using DSMC. Like Beidler and Hirakawa, we use an artificial mass ratio and neglect multiply charged ions.

1.8.2 Running the Code

We begin the simulation by allowing a plume of neutrals to expand from the anode with a long time-step until we approach a steady state. Next we introduce a background plasma which "ignites" the neutrals. A high density plasma develops in the near anode region and the ions accelerate toward the free-space boundary under the influence of the electric potential. Electrons diffuse from the cathode to the anode, elastically and inelastically interacting with other particles to determine the EEDF. Quantities such as anode current, thrust, and ionization rate are saved at each time step.

1.8.3 Grid

The numerical scheme requires a grid fine enough to resolve a Debye length, λ_d. [5]. For the mini-TAL, such a grid would require about 800 x 500 nodes. To make the problem more tractable, we artificially increase ϵ_o by a factor of γ^2, thereby increasing λ_d by γ. This allows us to use a much coarser grid. If $\gamma = 10$, an 87 x 49 grid yields approximately a Debye length of resolution.

1.8.4 Time-Step

The stability of typical PIC schemes requires a time-step on the order of the inverse of the plasma frequency. This means $\approx 10^{-8}$ seconds for the ions, and $\approx 10^{-11}$ seconds for the electrons. The time-step also needs to be short enough to resolve electron cyclotronic motions. We increase the time-step an order of magnitude by adopting an artificial ϵ_o.

1.8.5 Magnetic Field

The magnetic field is discussed in Section 3.13. The magnetic circuit in the thruster was designed by Dexter Magnetics, who provided a mapping of the field. This field was bilinearly interpolated to our numerical grid. The near-anode field is shown in Figure 1-6.

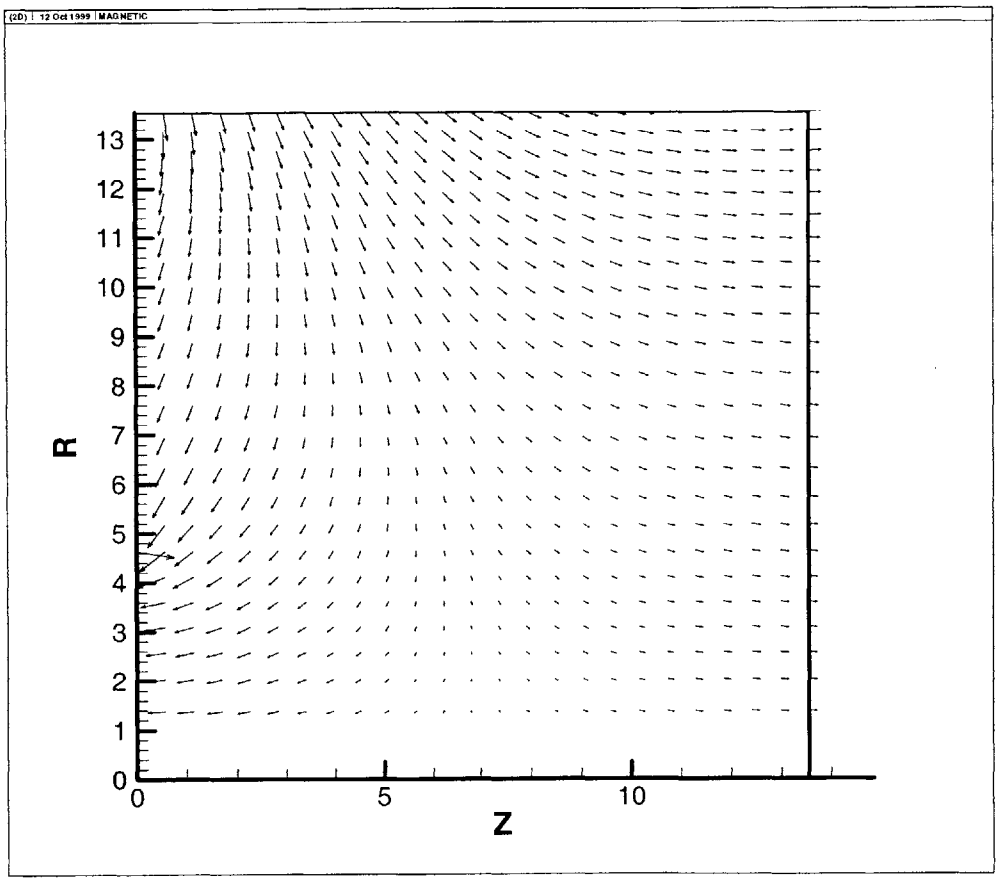

Figure 1-6: *The magnetic field of the thruster in the near anode region.* The anode begins at $Z = 0$. The centerline is at $R = 0$. The outer magnetic pole begins at the top of the shown region. The field mapping from Dexter continues beyond left, right, and top boundaries. The axes are in nominal Debye lengths, after accounting for $\epsilon_o' = \gamma^2 \epsilon_o$. Nominal field strength is 5000 Gauss (0.5 Tesla).

1.8.6 Initial Distributions and Particle Injection

As discussed in Section 3.19, initial Maxwellian particle distributions are achieved by using the rejection method for position, and the Box-Muller transformation for velocity [7]. A half-Maxwellian is assumed for neutrals entering the system at the anode and cathode electrons entering the system at the free space boundary. Neutrals are given an initial temperature of .1-eV, while cathode electrons are given a temperature of between 0.2-eV and 2.5-eV, depending on where they enter the simulation region. Low energy secondary electrons are created in the center of the plasma through ionization events. Likewise, neutrals are created at the walls through ion-electron recombination.

1.8.7 Interpolation and Computational Coordinates

Interpolation is discussed in Section 3.8. All positions in the computational domain are assigned two sets of coordinates: Real coordinates, corresponding to the location in Z-R space, and computational coordinates, which are integers at the nodes. Bilinear interpolation (weighting by areas in computational coordinates) is used to map real coordinates to computational coordinates, and vice versa, as per Ref. [45]. It is also used to weight particles to the grid nodes, where the field equations are solved, and to weight the fields back to the particles.

1.8.8 Calculating the Electric Potential and Field

The method of solving for the electric potential is presented in Section 3.12. The electric potential is re-calculated each time-step using finite differences and the integral form of Gauss's Law (CGS): $\oint \nabla\phi \cdot ds = 4\pi \int e(n_i - n_e)\, dv = 4\pi Q$. The left hand side represents the flux of electric field across a cell boundary, while Q is the charge contained within that boundary. This equation is solved iteratively using successive over-relaxation (SOR). At each iteration, the potential ϕ^{t+1} is calculated from the potential at iteration t according to

$$\phi_{k,j}^{t+1} = \phi_{k,j}^{t} + \omega\left(\phi_{k,j}^{t+.5} - \phi_{k,j}^{t}\right) \tag{1.9}$$

where $\phi_{kj}^{t+.5}$ is determined by the potential at the surrounding nodes according to Gauss's Law. To estimate $\phi_{kj}^{t+.5}$, we use a 9 point scheme which accommodates both Cartesian and

non-Cartesian (e.g.elliptic) grids:

$$\phi_{k,j}^{t+.5} = \frac{C}{N+S+E+W} \tag{1.10}$$

where

$$\begin{aligned} C = 4\pi Q_{k,j} &+ N\phi_{k,j+1} + S\phi_{k,j-1} + E\phi_{k+1,j} + W\phi_{k-1,j} \\ &+\acute{N}\tfrac{1}{4}(\phi_{k+1,j} + \phi_{k+1,j+1} - \phi_{k-1,j} - \phi_{k-1,j+1}) \\ &+\acute{S}\tfrac{1}{4}(\phi_{k+1,j} + \phi_{k+1,j-1} - \phi_{k-1,j} - \phi_{k-1,j-1}) \\ &+\acute{E}\tfrac{1}{4}(\phi_{k+1,j+1} + \phi_{k,j+1} - \phi_{k+1,j-1} - \phi_{k,j-1}) \\ &+\acute{W}\tfrac{1}{4}(\phi_{k-1,j+1} + \phi_{k,j+1} - \phi_{k-1,j-1} - \phi_{k,j-1}). \end{aligned} \tag{1.11}$$

The constants N,S,E,W and $\acute{N}$,$\acute{S}$,$\acute{E}$,and $\acute{W}$ incorporate both areas and derivatives. Convergence is determined by the difference between zero and the largest value of the quantity Δ_{kj}, defined by

$$\Delta_{kj} = -C + \phi_{k,j}^{t+1}(N+S+E+W). \tag{1.12}$$

Machine level precision is achieved in less than a thousand iterations ($t \sim 800$ is sufficient for a 50×80 grid). Once the potential is determined, the electric field $\vec{E} = -\nabla\phi$ is calculated using finite differences. The field is then interpolated to the particles.

1.8.9 Moving the Particles

The leapfrog method of Boris is used to time-step the particles forward [5]. This involves separating the Lorentz force into electric and magnetic components. This method can be shown to produce less than one percent error in angle of rotation for $\omega_c \Delta t < .35$ [5]. As particles are stepped forward in real coordinates, they are also tracked in computational (grid) coordinates, ξ and η.

1.8.10 Boundary Conditions

Boundary conditions for particle impact are discussed both in Section 2.12 and in Section 3.18. When particles encounter boundaries, they may be collected, destroyed, or re-emitted.

Anode

All electrons which hit the anode boundary are destroyed. Ions which hit are partially accommodated; they are neutralized and re-emitted in a random direction at half their initial energies. Neutrals which hit are fully accommodated; they are re-emitted according to a half Maxwellian at the wall temperature.

Conductive Walls

At conductive walls, electrons are destroyed, ions are neutralized and partially accommodated, and neutrals are fully accommodated. No secondary emission is assumed. The center pole and the outer wall are electrically connected; at any time-step, they have a common floating potential determined by the net charge collected and a pre-computed capacitance.

Insulators and Gaps

The gaps between the anode and floating walls may be modeled as insulators, magnetic boundaries, or perfect reflectors. At insulators, particles are accommodated as at the conducting walls, but charge accumulates locally. The sheath is then determined through Poisson's equation by the electric potential solver (a stand-alone function), which takes into account the charge collected at the wall. At magnetic boundaries, electrons are reflected according to their kinetic energy and magnetic moment; if they have sufficient energy to reach the conducting walls, they are destroyed. Otherwise they are reflected. Purely reflecting boundaries are self explanatory.

Cathode

The cathode is not modeled explicitly in this simulation. Instead, electrons which originated at the cathode are injected through the free space boundary.

Free Space

At the free space boundaries, all particles are deleted. Electrons are re-introduced at a rate which preserves local charge neutrality. This rate is determined by integrating in space along the free space boundary to find the net charge (along the entire boundary) at each

iteration. If the net charge is positive, an equivalent number of electrons are introduced. If the net charge is negative, no electrons are introduced.

Centerline

Any particle which encounters the centerline is specularly reflected. This is an extremely rare event; it only occurs for particles with zero angular momentum.

1.8.11 Inter-particle Collisions

The numerical method associated with particle-particle collisions is discussed in Section 3.2, which describes the Monte Carlo Collision methodology, and Section 3.15, which describes changes in energy and momentum.

Electron-Neutral Collisions

The dynamics of electron-neutral scattering collisions are discussed in Section 3.15. Electron-neutral scattering is handled during the electron loop. For each electron at each time-step, the total scattering cross section is found, which yields an expected collision frequency. This frequency, the length of the time-step, and a random number are then used to determine whether a scattering event takes place. If so, cross sections for excitation, ionization, and elastic scattering are compared to determine what type of event occurs. In all cases, the electron is scattered isotropically. If the collision is inelastic, energy is subtracted from the electrons. In the case of ionization, ions and secondary electrons are created at the primary electron's location. Positions of ionization events are recorded and neutrals are deleted accordingly when they are moved.

Ion-Neutral Collisions

Ion-neutral charge exchange and scattering collisions are handled using a similar Monte Carlo methodology.

Coulomb Collisions

Coulomb collisions are discussed in Section 3.16 of the thesis. They are handled using either a Monte Carlo approach discussed in Section 3.15.4, or a diffusive approach discussed in

Section 3.16.3. The latter approach uses the Langevin equation [2]. The nonlinear Landau Coulomb collision term contains both a dynamical friction force component, $\vec{F}^{\alpha/\beta}$, and a component of diffusion tensor, $\overleftrightarrow{D}^{\alpha/\beta}$, which is caused by Coulomb interaction of α with species β. Both $\vec{F}^{\alpha/\beta}$ and $\overleftrightarrow{D}^{\alpha/\beta}$ are given in terms of Rosenbluth potentials. In effect, each particle collides with the whole ensemble as represented by the Rosenbluth potentials.

1.8.12 Particle Moments

The positions and velocities of the particles are tracked in any PIC scheme. The EEDF and particle moments such as density, mean velocity, and temperature can be extracted at any time-step. Section 3.10 presents the method for doing so. Moments are tallied at each grid point. The EEDF is tallied at several internal points and along magnetic streamlines. Time averaging provides smooth curves for analysis.

1.9 Facilities

The simulation was performed alternately on a 64 bit SGI Octane workstation

```
CPUs:  2 175MHz MIPS R10000(IP30)
Main Memory:  256 MB
Operating System:  IRIX64 Release 6.5
```

and on a PC which is over twice as fast.

```
CPU: AMD 850MHz Athlon
Main Memory:  512 MB
Operating System:  Windows 2000
```

With 20K plasma particles of each species and a simplified anode geometry (a flat wall), the PC accomplishes about $\approx 80K$ time-steps (iterations) in 35 hours. In Section 2.7, we show that this is equivalent to the neutral transit time from the anode to the free space boundary assuming $M/m = 96$, $\gamma = 10$, and $\omega_{pe}\Delta t = .1$. With a more realistic anode geometry and $50K$ particles of each species, the simulation achieves $\approx 30K$ time-steps per day. The time to reach a "converged" solution on a 50 x 80 grid ($\gamma = 10$) with $\sim 50K$ super-particles of each species and an artificial mass ratio thus ranges from several days at $M/m = 96$ to more than a week at $M/m = 960$. Using $\gamma = 5$, which is more physical, requires more CPU

time per iteration; the simulation then runs about four times slower. The computational restrictions are frustrating, but the machines we use will soon be superannuated.

Contour and vector plots of results were created using Tecplot^{TM}. Additional plots were generated using Matlab^{TM}.

1.9.1 Future Requirements

Using a real mass ratio and ϵ_o would require much longer convergence times and, hence, a more powerful computer. Alternately, convergence times might be decreased running electrons and heavy particles at separate time-steps, or holding heavy particles still while allowing electrons to equilibrate.

1.10 Summary of Code Validation (Chapter 4)

Chapter 4 describes the tests performed to validate the code. The accuracy of the potential solver was tested on a function which is periodic in z and r. The leapfrog algorithm was tested by tracking single particles with electric field only, magnetic field only, and a combination of the two. Cyclotron motion and ExB drift were successfully observed to high levels of accuracy. A cold plasma was created and oscillations at the plasma frequency were observed. Momentum conservation, energy conservation, and numerical heating were observed by creating an initial thermal distribution, closing the boundaries such that no particles could escape, and letting the plasma oscillate, assuming specular reflection at all boundaries. Energy conservation of single particles was tested by tracking the energies and positions in time of a few chosen electrons as the simulation ran, with the electric potential fixed in time, and with the electric potential allowed to oscillate. Similar tests showed magnetic bottling and conservation of magnetic moment. The general methodology of Maxwellian particle injection, the initial particle distribution, and the methodology for finding the EEDF and other moments were tested simultaneously by analyzing the initial EEDF. Parametric tests were performed to assure that effects of capacitance, mass ratio, artificial permittivity, and inclusion or exclusion of various collisions were understood. The ultimate test was a comparison of predicted results with experimental results.

1.11 Summary of Results and Conclusions (Chapters 5 and 6)

Results of the simulation are presented and discussed in Chapter 5. Results are summarized in Chapter 6, which also includes recommendations for improving and extending the simulation. New numerical results include the following:

- The magnetic field of the mini-TAL was designed incorrectly.
- The mini-TAL was re-designed numerically; thrust efficiency increased by about ninety percent.
- The mini-TAL's published propellant utilization was corrected.
- The electron distribution is non-isotropic; it is best represented by a two-temperatures, one each for directions parallel ($T_{\|}$) and perpendicular ($T_{\perp}$)to $\vec{B}$.
- The model predicts non-Maxwellian electron populations in the perpendicular direction near the anode (see Figure 5-17).

Other interesting numerical results include the following:

- Numerical and experimental results are similar. The simulation over-predicts Thrust and I_{sp} by about thirty percent.
- Performance increased with mass flow rate.
- Ionization oscillations were observed at higher mass flow rates.
- The plasma extends to the interior of the hollow anode under certain conditions.
- The simulation predicts gradients in electron temperature along magnetic streamlines.
- Oscillations in plasma density were observed.
- Anomalous diffusion increased performance by ten percent.
- Coulomb collisions changed performance slightly.
- Langevin Coulomb changed the electron temperature and distribution.

In conclusion, we showed that the full-PIC Monte-Carlo method is a viable alternative for investigating small scale plasma flows in a Hall thruster.

Chapter 2

Theory

Hall effect plasma thrusters are essentially rockets in which the working fluid is a plasma and the means of acceleration is an electric field. The plasma acceleration region is usually comprised of two concentric cylinders which are either metallic (TAL type thrusters) or dielectric (SPT type thrusters). At one end of the annulus sits a highly biased (300 Volts is typical) hollow anode which produces an axial electric field. The other end of the annulus opens to free space. Neutral gas is injected through the anode, electron impact ionized, and accelerated out the other end of the annulus by the E field. An external cathode supplies electrons to neutralize the beam and sustain the discharge. Electrons are impeded in their motion toward the anode by a radial magnetic field. Trapped in cyclotronic motion, they spend most of their time drifting azimuthally due to the Hall effect (which gives these thrusters their name), allowing them time to ionize the neutrals. They arrive at the anode primarily through diffusion.

2.1 Dimensions of Simulation

Figure 2-1 shows both the mini-TAL and the simulation region used to model it. To simplify the problem numerically, our model neglects gradients in density and field in the azimuthal (Θ) direction. Since Hall thrusters are nominally axisymmetric, our model should nevertheless reproduce most features observed in the laboratory.

This model does not ignore all movement in the azimuthal direction. Particle velocities are tracked in three dimensions: R, Z, and Θ. (The coordinate ordering is (r, z, θ).) Furthermore, at each time-step, particle positions are stepped forward in all three directions.

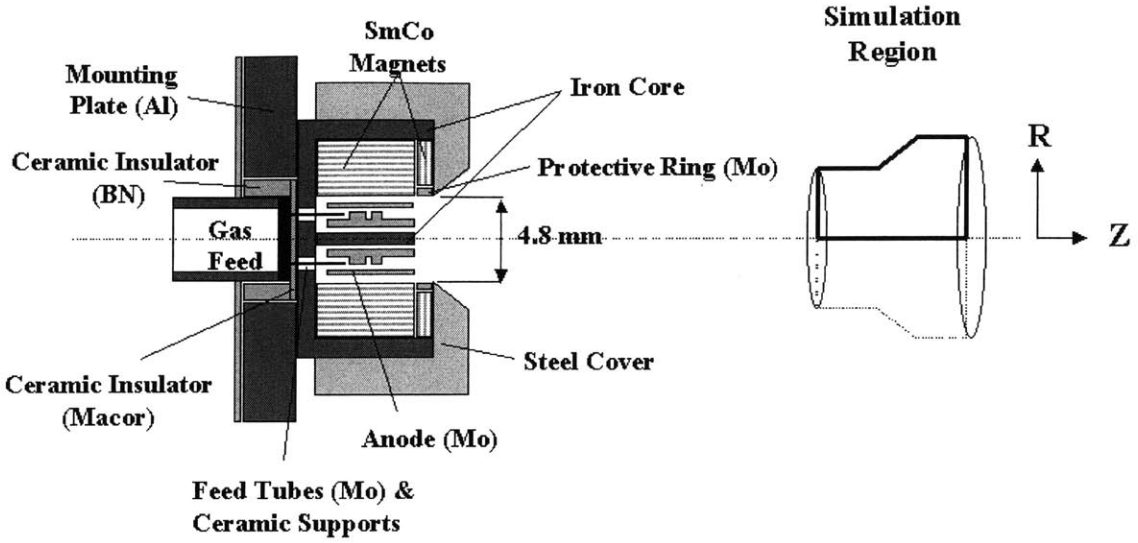

Figure 2-1: *The mini-TAL and an outline of the simulation region.* The left side of the simulation region lies upstream from the anode exit. Thrust is in the Z (axial) direction, while the magnetic field is nominally in the R (radial) direction.

However, only the radial and axial components of position are maintained; the azimuthal component of position is discarded. For this reason, we term this a 2D3V simulation. Such simulations are sometimes called $2\frac{1}{2}$ D. For a full description of the "particle pusher", see Section 3.14.

2.2 Simulation Region

The relationship between the thruster and the space vehicle is shown in Figure 2-2. The larger control volume encompasses the entire spacecraft. The smaller control volume delineates the boundary of the simulation region. (The thruster shown is only representative; the biased anode sits inside the floating body of the thruster.) The circuit shown was used to develop boundary conditions for our simulation. In a steady state, the net current leaving the control volume around the space vehicle is zero. The anode is biased some discharge voltage above spacecraft ground (which floats relative to infinity). The cathode is normally held at spacecraft ground potential. In a TAL, the metallic channel walls are often held at cathode potential. Here, we let them float as per the mini-TAL. We insert a numerical capacitor of $1 \times 10^{-10} F$ in between the walls and spacecraft ground to limit oscillations due to variations in wall potential. The calculated capacitance of the thruster body modeled as

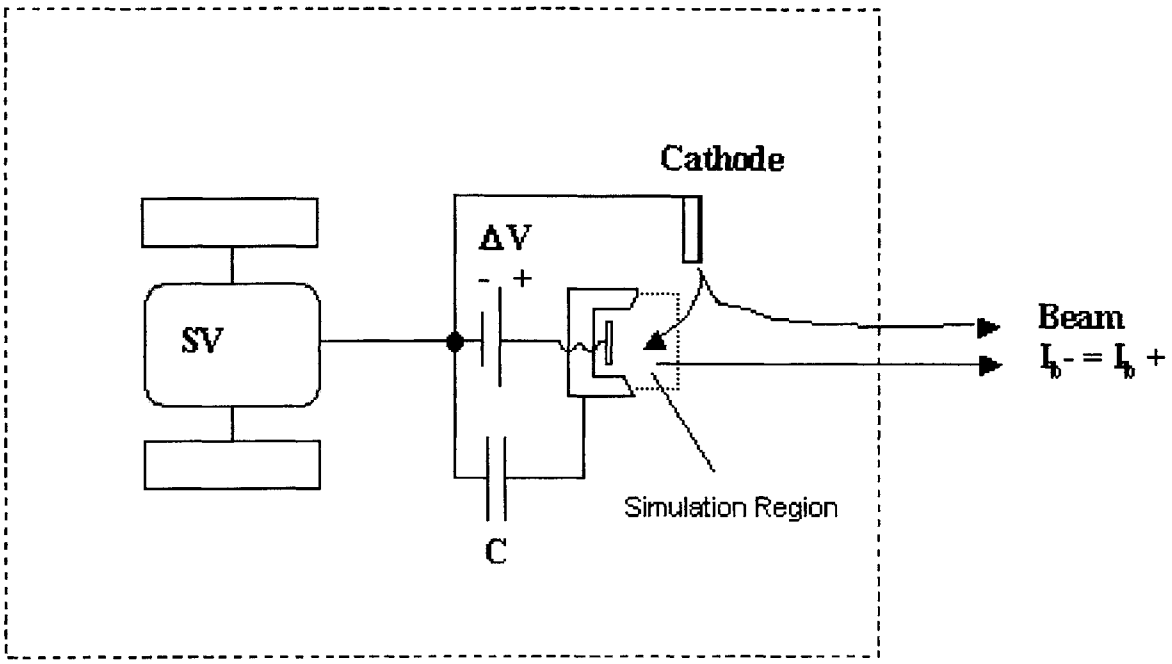

Figure 2-2: *Circuit diagram of spacecraft and thruster.* The larger region encompassing the entire spacecraft was used to generate boundary conditions for the smaller region, which is actually simulated. The thruster shown is only representative; the biased anode sits inside the floating body of the thruster.

an isolated body in free space is about two orders of magnitude smaller.

Any full PIC simulation is computationally intensive. Our simulation is especially cumbersome because we track oscillations at the electron plasma frequency; we need to solve Poisson's equation on a grid with spatial resolution of a Debye length. To maximize resources, we want the simulation region to be as small as possible.

It is possible to simulate the cathode and plume directly, but this requires a control volume large enough to allow electron transport to occur naturally. Such a control volume is computationally cumbersome. To save resources, we use a smaller, CPU saving control volume and simulate the cathode indirectly. Hence, Figure 2-2 shows the cathode outside the simulation region (the smaller control volume). Details of the region modeled explicitly are shown in Figure 2-3. It would be inappropriate to model the cathode directly by placing it inside this smaller simulation region. It would be too close to the thruster body, and electron transport would be skewed.

The assumption that the plasma is quasineutral ($n_e = n_i$) is valid when λ_d is much smaller than other scale lengths of interest. Oh's plume model [33] assumes quasi-neutrality

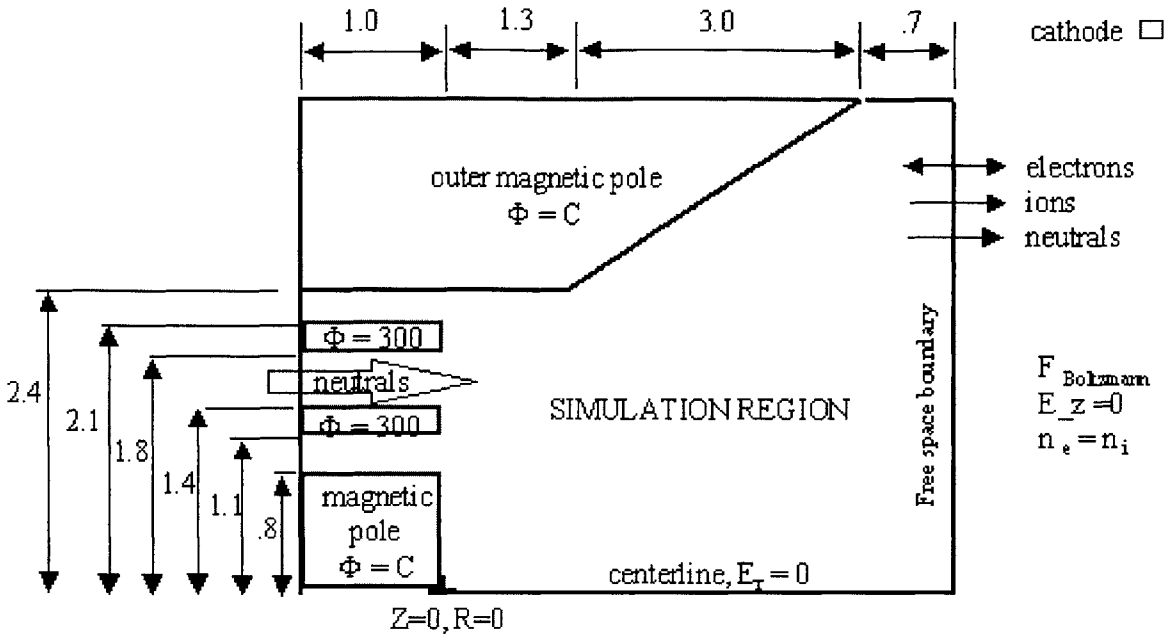

Figure 2-3: *The simulation region.* Dimensions are in millimeters.

and constant electron temperature ($T_e = 2eV$), in which case the Boltzmann relation, $n_e = n_{e,o}exp(\frac{e\phi}{KT})$, may be applied to predict the electric potential, ϕ. Fife's SPT thruster model [10] uses these same assumptions, but only applies them along magnetic streamlines. In this simulation, we model sheaths self-consistently, only assuming quasi-neutrality at the downstream boundaries of the simulation region. This assumption is the basis for a "bang-bang" electron injection control system; we inject electrons at the free space (simulation region to plume) boundary at the rate required to preserve quasineutrality, $n_e \approx n_i$. An alternative option is to use the steady state relation $I_d = I_c$ to determine the electron current across the free space boundary. In Chapter 4, we show that this "steady state" condition is flawed.

Following Oh and Fife, the potential at the free space boundary of our simulation may be calculated from the Boltzmann relation. Alternately, it may be assumed to be constant ($\Phi = 0$), or it may be calculated from Poisson's equation by assuming $E_z = 0$. This last condition is assumed to produce results presented in Chapter 5. The upper right corner of the simulation region is assumed to be at cathode potential, $0V$.

I_a^+	anode ion current
I_a^-	anode electron current
I_d	discharge (net anode) current
I_c	cathode electron current
I_i	ionization current
$I_{b.r.}$	loss to bulk recombination
I_w^+	ion loss to wall recombination
I_w^-	electron loss to wall recombination
I_b^+	beam ion current
I_b^-	beam electron current
I_{cd}	electron current from cathode to the discharge
I_{cb}	electron current from cathode to the beam

Table 2.1: Symbology used for current balance. A (+) attached to a current means ions, while a (-) means electrons. For example, I_b^+ is the beam ion current.

2.3 Current Balance

A simplified current balance is visualized in Figure 2-4, where the symbology of Table 2.1 applies. In electrical engineering, current is normally taken to be positive in the direction of ion motion and negative in the direction of electron motion. For clarity, however, Figure 2-4 shows current to be in the direction of motion for both ions and electrons. Free space, anode, and cathode boundary conditions are inter-related.

The discharge current is the sum of the anode electron and ion currents:

$$I_d = I_a^+ - I_a^-. \tag{2.1}$$

The current from the cathode both compensates the beam and sustains the discharge. This may be written

$$I_c = I_{cd} + I_{cb}, \tag{2.2}$$

where I_{cd} is the cathode current which goes to the discharge, and I_{cb} is the cathode current to the beam. If the ions in the beam are fully charge compensated by electrons, then

$$|I_b^+| = |I_{cb} + I_{az}| = |I_b^-|. \tag{2.3}$$

In other words, the beam is compensated by a combination of cathode electrons and electrons which diffuse outward from the acceleration zone through the free space boundary,

I_{az}.

Ion conservation leads to the next equation. Ions are produced through electron-neutral impact ionization. They are lost to the beam, and through recombination at the anode, walls, and in the main body of the discharge (bulk recombination);

$$I_i = I_b^+ + I_a^+ + I_w^+ + I_{b.r}^+ = I_b^+ + I_{losses}^+. \tag{2.4}$$

This equation says the beam current is equal to the ionization current minus losses. In a steady state, $|I_{losses}^+| = |I_{losses}^-|$. Of course, $|I_i^+| = |I_i^-|$.

Electron conservation leads to the last key equation. In a steady state, the electron current leaving the computational domain at the anode, free space boundary, and through recombination must equal the electron current being introduced through ionization and through the cathode;

$$I_a^- + I_{az} + I_w^- = I_i + I_{cd}. \tag{2.5}$$

We have assumed that $I_{b.r}^+ = I_{b.r}^- = 0$. Note that double ion production ionization (Xe^{2+})is accounted for automatically.

By substituting I_i from Equation 2.4 into Equation 2.5, assuming $I_w^+ = I_w^-$, and $I_{b.r} = 0$, one obtains the equation

$$I_a^+ - I_a^- = -I_b^+ - I_{cd} + I_{az}. \tag{2.6}$$

This equation says the magnitude of the net anode current into the anode is equal to the magnitude of the ion beam current plus the cathode current required to sustain the discharge minus those electrons which diffuse through the free space boundary. Thus, in a steady state,

$$I_d = -I_c. \tag{2.7}$$

The net current into the anode is equal to the electron flux out of the cathode. In fact, this is the usual mode of operation for a Hall thruster. Exceptions occur at startup or at other transients.

Note that the net current across the free space boundary is equal to the cathode/anode current.

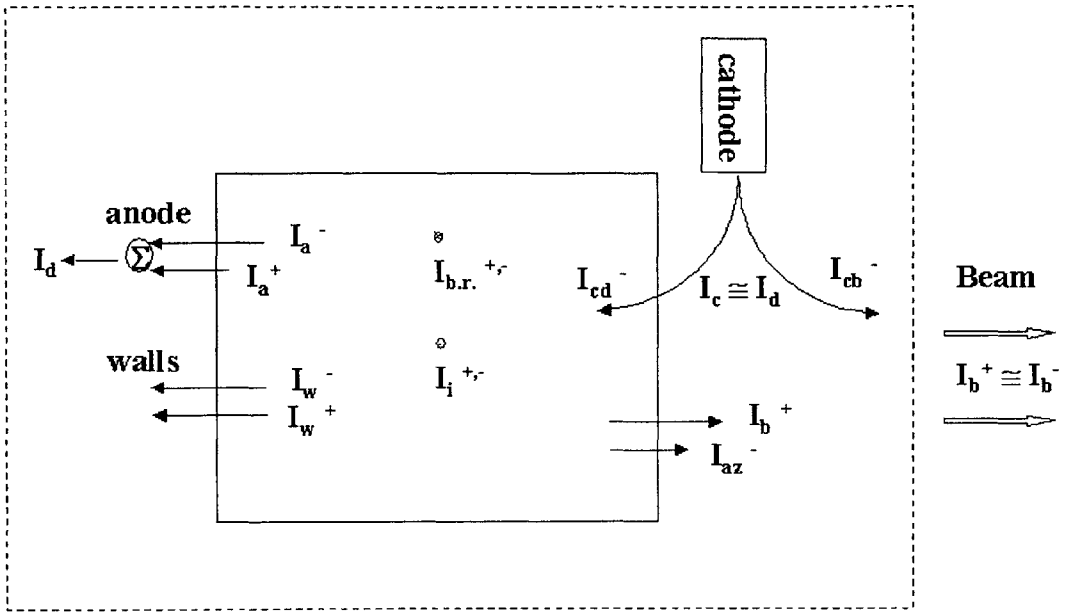

Figure 2-4: *Steady state current balance in a Hall thruster.* During startups and transients, I_c does not equal I_a exactly. The net beam current leaving the spacecraft depends on external factors such as the overall charge balance between the spacecraft and surrounding space. For both electron and ions, current is shown to be in direction of net particle motion.

2.3.1 Numerical Implementation

Electrons must be replenished through the free space boundary to produce I_{cd}. But at what rate should they be created? Let us consider two options. First, we consider controlling the cathode current according to the steady state conditions $I_c = I_d$. Then we consider letting the cathode current be determined by the beam quasineutrality assumption. In both cases, we simulate I_{cd}, that portion of the cathode current which enters the discharge, but implicitly assume I_{cb} goes to the beam somewhere downstream, outside of the simulation region.

Our first option is to require that the cathode and anode currents exactly balance as in a steady state: $I_c = I_d$. This allows us to determine I_{cd}, the electron flux at the free space boundary. Henceforth, this will be called the "steady state current control method of electron injection". Numerically, we subtract from I_c the beam ion current, I_b^+, and add the number of electrons which diffuses outward across the free space boundary, I_{az}, to determine the number of electrons to be created along the free space boundary:

$$I_{cd} = I_c + I_{az} - I_b^+. \tag{2.8}$$

This method was used to generate results presented in Reference [51]. The problem with this method is that at startup the charge distribution is unbalanced. Furthermore, transients and wall losses further complicate the charge balance. Unless there are no oscillations and we have exactly guessed the net charge at the beginning of the simulation, the result is a plasma which is not always quasi-neutral near the free space boundary. In fact, we shown in Chapter 4 that the entire simulation is unbalanced.

Our second option is more natural: We calculate I_{cd} from the assumption that $n_e \approx n_i$ along the boundary and then post calculate I_c. Henceforth, this shall be called "the quasi-neutral electron injection method". This approach appears to be more effective. It is implemented as follows: At each iteration, we find the net charge in the volumes along the boundary, $Q = \Sigma_i q_i = \int \rho_e dV$. If $Q > 0$, we inject Q electrons, locating them by using ρ_e as a distribution function. If $Q < 0$, we inject no electrons. This control system results in a charge distribution at the free space boundary which is quasi-neutral, the state in the plume. The cathode current is then a result of the state inside the simulation region,

$$I_c = I_b^+ + I_{cd} - I_{az} \sim I_b^+ + I_{cd}, \tag{2.9}$$

where the last expression refers to the fact that I_{az} is usually small.

More details of the electron injection methods are found in Section 3.20.

2.4 Performance Variables

The total power required to sustain the discharge can be written

$$P = P_{discharge} + P_{cathode} + P_{magnets}. \tag{2.10}$$

The discharge voltage, V_d, is typically applied between the anode and cathode, the cathode being at spacecraft ground (which is itself sometimes floating). Hall thrusters are typically operated at constant V_d. Thus, the discharge power used by the thruster is determined primarily by the net current (electrons minus ions) entering the anode, a.k.a. the discharge current, I_d:

$$P_{discharge} = P_d = V_d I_d. \tag{2.11}$$

Discharge current varies with anode potential, mass flow rate, magnetic field strength and shape, and many other factors.

The mini-TAL can use either a thermionic or hollow cathode. Depending on the cathode chosen, $P_{cathode}$ can vary, but an appropriately sized hollow cathode should require less than 10 percent of the discharge power.

Since the mini-TAL uses permanent magnets, the power drawn by the magnets is zero, i.e. $P_{magnets} = 0$.

A typical measure of efficiency is the "thrust efficiency", η_t, defined by

$$\eta_t = \frac{T^2}{2\dot{m}P_d}. \tag{2.12}$$

This figure of merit compares the amount of kinetic energy in the beam to the amount of energy required to sustain the discharge, considering only the anode. Factors influencing the thrust efficiency include the propellant utilization, beam divergence, location of the main region of ionization, and losses due to recombination. The overall efficiency of the thruster would use P instead of P_d.

The thrust is equal to the mass flow rate times the mean exit velocity,

$$T = \dot{m} < v >= \dot{m}_{i,b} < v_i > + \dot{m}_{n,b} < v_n > \approx \dot{m}_{i,b} < v_i >, \tag{2.13}$$

where $\dot{m}_{i,b}$ is the ion mass flow to the beam, $< v_i >$ is the mean axial velocity of ions entering the beam, and so on. (Thrust predictions presented in Chapters 4 and 5 factor in both neutral and ion thrust). The specific impulse of the thruster is equal to the mean exit velocity divided by the gravity at the earth's surface, $I_{sp} =< v > /g$. This takes into account total thrust and total mass flow rate.

Since $T \approx \dot{m}_{i,b} < v_i >$, the thrust efficiency may be rewritten

$$\eta_t = \frac{\dot{m}_{i,b}^2 \frac{1}{2} < v_i >^2}{\dot{m}_n I_d V_d} = \frac{\dot{m}_{i,b}}{\dot{m}_n} \frac{I_b^+}{I_d} \frac{M}{e} \frac{\frac{1}{2} < v_i >^2}{V_d}, \tag{2.14}$$

where M is the mass of a Xenon ion, V_d is the discharge voltage, I_d is the discharge current, e is the charge of a singly charged Xenon ion, and $\dot{m} = \dot{m}_n$ is the mass flow rate of neutrals into the thruster. This last expression for thrust efficiency may be rewritten as the product

of three other efficiencies;

$$\eta_t = \eta_e \eta_a \eta_u. \tag{2.15}$$

These are the propellant utilization efficiency, η_u, the acceleration efficiency, η_a, and the electrical efficiency, η_e. The electrical efficiency is the ratio of ion beam current to electron discharge current,

$$\eta_e = \frac{I_b}{I_d}. \tag{2.16}$$

This accounts for the electrons required to sustain the discharge. Ideally, this figure will be close to unity. The acceleration efficiency is a measure of the mean kinetic energy of the ions entering the beam;

$$\eta_a = \frac{M < v_i >^2}{2eV_d}. \tag{2.17}$$

If all ions were created at the anode, then the acceleration efficiency would be one; all the ions would see the maximum potential drop possible and hence have an energy of eV_d when they leave the system. (Khayms used this assumption when calculating the efficiency of his thruster [25].) The propellant utilization is a measure of the efficiency with which neutrals are converted to beam ions;

$$\eta_u = \frac{\dot{m}_{i,b}}{\dot{m}_n}, \tag{2.18}$$

where $\dot{m}_{i,b}$ is the ion mass flow rate at the exit plane of the thruster (to the beam), and $\dot{m}_n$ is the neutral mass flow rate at the anode. Propellant utilization may, in turn, be expressed as the the product of the ionization efficiency, η_i, and what we will call the "beam efficiency", η_b;

$$\eta_u = \eta_i \eta_b. \tag{2.19}$$

The ionization efficiency is the efficiency with which neutrals are converted to ions;

$$\eta_i = \frac{\dot{m}_{i,created}}{\dot{m}_n}. \tag{2.20}$$

The beam efficiency is the fraction of ions created which actually enter the beam;

$$\eta_b = \frac{\dot{m}_{i,b}}{\dot{m}_{i,created}}. \tag{2.21}$$

Factors which go into the beam efficiency include recombination at the walls and in the

body of the plasma. Only recombination at the walls is modeled in this simulation. Note that a neutral produced thus can be re-ionized in our simulation. This is one of the major differences between this simulation and the simulations of Hirakawa [16][17] [15].

2.5 Maxwell's Equations

Only MKS and English units are commonly used in Aerospace Engineering. Plasma physicists, however, frequently use CGS units. The normalized unit system we derive and use in the simulation is based upon CGS equations and constants. For reference, Maxwell's equations in MKS units are provided in the appendix.

2.5.1 Maxwell's Equations in CGS Units

The acceleration channel of the mini-TAL is only .48 cm in diameter. Thus, CGS units seem more natural than MKS units. In the CGS system, $\epsilon_o = 1$ and $\mu_o = 1$. Charge is measured in statcoulombs, voltage in statvolts, mass in grams. (See Table 2.2).

	symbol	value	units
permittivity	ϵ_o	1	-
permeability	μ_o	1	-
light speed	c	2.9979e10	cm/s
electron mass	m_e	9.1094e-28	gm
proton mass	M_p	1.6726e-24	gm
Xe neutral mass	M_n	2.18e-22	gm
electron charge	e	4.8032e-10	statcoulomb
Boltzmann constant	k_b	1.3807e-16	erg/Kelvin

Table 2.2: CGS Units: ϵ_o is the permittivity of free space, μ_o is the permeability of free space, m_e is the mass of an electron, M_p is the mass of a proton, M_n is the mass of a Xenon neutral, e is the charge of one electron, and k_b is Boltzmann's constant.

Maxwell's equations are thus written as follows:

$$\nabla \times \vec{E} = -\frac{\partial \vec{B}}{\partial t}\frac{1}{c}; \tag{2.22}$$

$$\nabla \times \vec{H} = \frac{\partial \vec{E}}{\partial t} + \vec{J} + \vec{J}_{ext}; \tag{2.23}$$

$$\nabla \cdot \vec{E} = 4\pi(\rho_e + \rho_{e,ext}); \tag{2.24}$$

$$\nabla \cdot \vec{B} = 0. \tag{2.25}$$

The Lorentz force completes the unit system;

$$F = q(\vec{E} + \frac{v \times \vec{B}}{c}). \tag{2.26}$$

Integrating Gauss's Law and letting $e(n_i - n_e) = \rho_e$ and $\int \rho_e \, dv = Q$ we get

$$\int \nabla \cdot \vec{E} \, dv = 4\pi \int e(n_i - n_e) \, dv. \tag{2.27}$$

and

$$\oint \vec{E} \cdot ds = 4\pi Q, \tag{2.28}$$

where Q is enclosed charge, and ds is an element of surface area. Thus, the flux of electric field across the surface of a volume is a function of the charge within the volume. Gauss's law thus leads to a method of solving for the electric potential. First we break the computational space into many tiny volumes, each of which contains a number of charged particles. Given boundary conditions and the charge distribution, we can then solve for the electric potential, defined by $\vec{E} = -\nabla\phi$. Since area is measured in cm^2 and charge in statcoulombs, the units of electric field are seen to be statcoulombs/cm^2.

2.5.2 Normalized Unit System

Let us now derive a normalized system of units. This unit system is based on scales appropriate for the plasma, such as the Debye length and plasma frequency, and makes it easy to interpret results of the simulation.

First, let the fundamental unit of mass be the electron mass, $[m] = m_e$. Electron super particles will have mass $\hat{m} = [m] = 1$, while ion super particles will have mass $\hat{M} = \frac{M_{ze}}{m_e}$, and neutral super particles will be some integer multiple larger. Next, let $[q] = e$ be the fundamental unit of charge. Electrons will have charge $\hat{q} = -1$, while ions will have charge $\hat{q} = Z$, where $Z = 1$ in most cases. Furthermore, let the size of electron and ion super particles be $[size]$: Each electron super particle with $\hat{m} = 1$ will actually represent $[size]$ electrons. As already mentioned, neutrals may be some integer multiple larger, such that the overall uncharged super-particle count is similar to the charged super-particle count. Now, let the unit of distance be the nominal Debye length, $[x] = \lambda_D = (k[T]/4\pi[n_e]e^2)^{\frac{1}{2}}$,

and the unit of time be the nominal inverse plasma frequency, $[t] = \omega_{pe}^{-1} = (4\pi[n_e]e^2/m_e)^{-\frac{1}{2}}$. Both λ_D and ω_{pe}^{-1} are based upon nominal values for electron temperature, $[T]$, and density, $[n_e]$. The unit of electric potential is the nominal electron temperature, $[T]$, in electron volts. If we use $[m]$,$[q]$, $[size]$, $[x]$ and $[t]$ to normalize the electric and magnetic fields, $\vec{E}$ and $\vec{B}$, then we can solve for particle motions entirely within the normalized unit system. If we have estimated the nominal temperature and density correctly, most quantities will be of order one. In the normalized unit system, the Lorentz force equation may be written

$$\frac{d\vec{\hat{v}}}{d\hat{t}}\frac{[v]}{[t]} = \frac{\hat{q}[q]}{\hat{m}[m]}(\vec{\hat{E}}[E] + \frac{\vec{\hat{v}}[v] \times \vec{\hat{B}}[B]}{\hat{c}[c]}). \tag{2.29}$$

The electric part may be rewritten as

$$\frac{d\vec{\hat{v}}[v]}{d\hat{t}[t]} = \frac{\hat{q}\vec{\hat{E}}}{\hat{m}}\frac{[q][E]}{[m]}, \tag{2.30}$$

or

$$\vec{\hat{E}}[E] = \frac{d\vec{\hat{v}}}{d\hat{t}}\frac{\hat{m}}{\hat{q}}\frac{[v][m]}{[t][q]}. \tag{2.31}$$

Since $[v] = [x]/[t] = \lambda_D\omega_{pe} = v_{th}/\sqrt{2} = \sqrt{K[T]/m_e}$, the units for electric field are

$$[E] = \frac{[v][m]}{[t][q]} = (4\pi n_e m_e)^{\frac{1}{2}}\frac{v_{th}}{\sqrt{2}} = \frac{[\Phi]}{[x]}. \tag{2.32}$$

Physically, [E] is the voltage drop across a nominal Debye length [x] given as a fraction of the nominal electron temperature in eV. Note that $[\Phi] = [T]$ (both are in terms of eV). In terms of Debye lengths, we find

$$[E] = 4\pi e n_e \lambda_D. \tag{2.33}$$

We also find

$$[E]\lambda_D = \frac{K[T_e]}{e}, \tag{2.34}$$

so $[E]$ is the field due to thermal voltage across one Debye length. To transform from normalized units to CGS units, we simply multiply by [E]:

$$\vec{E} = \vec{\hat{E}}[E]. \tag{2.35}$$

We use the same principle to arrive at units for B:

$$\frac{d\vec{\hat{v}}}{d\hat{t}}\frac{[v]}{[t]} = \frac{\hat{q}[q]}{\hat{m}[m]}(\frac{\vec{\hat{v}}[v]\times\vec{\hat{B}}[B]}{\hat{c}[c]}); \tag{2.36}$$

$$[B] = \frac{[m][c]}{[t][q]} = (4\pi n_e m_e)^{\frac{1}{2}}c. \tag{2.37}$$

The unit [B] is such that the gyro radius at velocity $[v] = \sqrt{K[T]/m_e}$ is the nominal Debye length, $[x] = \lambda_D$. To apply the $\vec{v}\times\vec{B}$ rotation when we are given $\vec{B}$ in CGS units, we need only divide by [B] to arrive at $\vec{\hat{B}}$;

$$\vec{\hat{B}} = \vec{B}\frac{1}{[B]}. \tag{2.38}$$

Some equations in this system differ from standard CGS equations; we cannot always simply transpose $\vec{\hat{E}}$ for $\vec{E}$ and so on. In CGS units, Gauss's Law is written

$$\oint E\cdot ds = 4\pi Q, \tag{2.39}$$

where Q is the charge contained within the control volume defined by the boundary $\oint ds$. Let $\hat{N}_i$ and $\hat{N}_e$ be the number of ion and electron super-particles in the control volume. The total charge in the volume is then $Q = \hat{Q}[q] = (\hat{N}_i - \hat{N}_e)[size][e]$, where $\hat{Q}$ is the number of real particles $N_i - N_e$ of charge $[q] = e$ in the volume. Thus we may write

$$\oint \hat{E}\cdot d\hat{s}\,[E]\,[x]^2 = 4\pi\hat{Q}[size][q], \tag{2.40}$$

which goes to

$$\oint \hat{E}\cdot d\hat{s}\,[n_e\lambda_D^3] = (\hat{N}_i - \hat{N}_e)[size]. \tag{2.41}$$

(Strictly speaking, $\hat{Q}$ should be an integer. However, when using the Particle-In-Cell method, the total charge $\hat{Q}$ inside a given control volume is determined by weighting each particle of charge 1 or -1 to four separate grid nodes; $\hat{Q}$ will be a floating point number.) Finally we write

$$\oint \hat{E}\cdot d\hat{s} = (\hat{N}_i - \hat{N}_e)\frac{[size]}{[n_e\lambda_D^3]}. \tag{2.42}$$

The quantity $\hat{n}_{e,o} = [n_e\lambda_D^3]/[size]$ is the nominal super-particle number per Debye cube (λ_D^{-3}). Therefore, before solving Gauss's Law for $\vec{E}$ (and Φ) using only normalized units, we multiply the charge by $[size]/[n_e\lambda_D^3]$.

name	units	base
charge	[q]	e
mass	[m]	m_e
temperature	[T]	T_e
distance	[x]	λ_D
time	[t]	ω_{pe}^{-1}
velocity	[v]=[x]/[t]	$v_{th,e}/\sqrt{2}$
electric potential	[Φ]	T_{eV}
electric field	[E]=[Φ]/[x]	$\sqrt{4\pi n_e m_e}[v]$
magnetic field	[B]	$\sqrt{4\pi n_e m_e}c$

Table 2.3: Normalization Constants. Note that $[v] = \frac{[x]}{[t]}$, $[E] = \frac{[v][m]}{[t][q]}$, and $[B] = \frac{[c][m]}{[t][q]}$

The constants used to normalize the equations are summarized in 2.3. The unit system can be easily expanded to include other equations. Consider, for instance, the electric field due to a super-particle point charge: $\vec{E} = \hat{q}/r^2$ in CGS units. In normalized units, we would write

$$\vec{\hat{E}} = \frac{\hat{q}}{\hat{r}^2}\frac{[size][q]}{[x]^2[E]}, \tag{2.43}$$

or

$$\vec{\hat{E}} = \frac{\hat{q}}{\hat{r}^2}\frac{[size]}{[4\pi n_e \lambda_D^3]}. \tag{2.44}$$

The 4π appears in the denominator because there is no 4π in the numerator of the original equation.

As stated above, the actual simulation is written in normalized units. For clarity, however, the majority of the theory section of this thesis will use either CGS or SI units.

Useful Results

The normalized unit system simplifies many calculations. In this system, temperature, energy, and electric potential are given in terms of the nominal temperature, $[\Phi] = [T]$, where it is most useful to express temperature in electron volts. If $[T] = T_e = 25eV$, then a kinetic energy of $\hat{\epsilon} = 1/2|\hat{v}|^2 = 1[T]$ translates to 25 eV. The local thermal velocity is given in terms of local temperature, $\hat{v}_{th}^2 = 2\hat{T}$. The local Debye length (in units of $[x]$) is given by

$$\lambda_D = \sqrt{\hat{T}_e}\sqrt{\frac{\hat{n_{e,o}}}{\hat{n_e}}}, \tag{2.45}$$

where $\hat{n}_e$ is the normalized plasma super-particle density, $\hat{n}_{e,o}$ is the nominal normalized plasma super-particle density, and $\hat{T}$ is the normalized temperature. Similarly, the local plasma frequency is given (in units of $[t]^{-1}$) by

$$\hat{\omega_{pe}} = \sqrt{\frac{\hat{n_e}}{\hat{n_{e,o}}}}. \tag{2.46}$$

This last result is useful when choosing a time-step; we need Δt short enough for stability across the entire grid. Also, Hockney has shown that we need $\omega_{pe}\Delta t < .5H/\lambda_D$ across the grid to minimize stochastic (numerical) heating, where H is the local spacing of the grid nodes [19]. It is easy to show that this requirement reduces to $\Delta\hat{t}_{kj} < .5\hat{H}/\sqrt{\hat{T}_e}$ in normalized units, where the subscripts indicate that this must be true across the entire grid. This will be discussed more fully in Chapter 3.

name	symbol	units
temperature	$\hat{T}_e$	[T]
energy	$\hat{\epsilon}$	[T]
potential	$\hat{\phi}$	[T]
plasma frequency	$\hat{\omega}_{pe}$	$1/[t]$
Debye length	$\hat{\lambda_D}$	[x]

Table 2.4: Normalized units for various quantities of interest.

In CGS units, $\omega_{ce} = \frac{eB}{m_e c}$. Thus, in normalized units, $\hat{\omega}_{ce}\frac{1}{[t]} = \frac{\hat{e}\hat{B}}{\hat{m}}\frac{[q][B]}{[m]c}$. However, [B] was defined to be $[B] = \frac{[c][m]}{[t][q]}$. Therefore, in normalized units,

$$\begin{aligned} \hat{\omega}_{ce} &= \hat{B}, \\ \hat{\omega}_{ci} &= \frac{\hat{B}}{\hat{M}_i}. \end{aligned} \tag{2.47}$$

This is, perhaps, the most useful result.

2.6 Simulation Requirements

In order to define the model, we must answer some basic questions:

- What is the time scale of the simulation?
- How many grid cells will we need?

	SPT-100	mini-TAL
Propellant	Xenon	Xenon
Diameter (mm)	100	4.8
Magnetic Field (T)	.02	.5
Mass Flow Rate (mg/sec)	5.3	.13
Anode Potential (V)	300	300
Anode Power (W)	1350	50
Thrust (mN)	83	2.2
I_{sp} (sec)	1600	1700
Efficiency	.48	.32

Table 2.5: Empirical performance of the SPT-100 and design performance of the mini-TAL.

- How many particles will we need?
- How can we accelerate the simulation?

These questions are considered in the following sections.

2.6.1 Basic Length and Time Scales

The subject of this simulation is Khayms mini-TAL Hall thruster, which is shown in Figures 1-3 and 2-1. The design performance is shown in Table 2.5 [26], where data from the well known SPT-100 are shown for comparison. The mini-TAL is, by comparison, a diminutive device.

We now estimate the basic length and time scales which shape the nature of the simulation. These are collected in Table 2.6. The nominal flow velocity of ions in the ionization region is estimated to equal the acoustic speed, $v_{si} = \sqrt{k_b T_e / M_n}$. Choosing the plume area, s_p, to be the total area of the anode, and an appropriate utilization efficiency, ϵ_u, the plasma density in the throat, $n_{e,o} \sim n_{i,o}$ is estimated to be

$$n_{e,o} = \frac{\epsilon_u \dot{m}}{M_n v_i s_p}. \tag{2.48}$$

The nominal density of neutrals at the anode exit, $n_{n,o}$, is estimated from the inner exit area of the anode, s_a, the temperature of the anode, $T_{anode} = T_n$, and the mass flow rate through the anode, $\dot{m}$,

$$n_{n,o} = \frac{2\dot{m}}{M_n \bar{c}_n s_a}. \tag{2.49}$$

Here, $\bar{c}_n/2$ is the mean flow speed to the right of a half-Maxwellian entering the simulation

region at the anode exit plane, and $\bar{c} = v_{th,n}\sqrt{\frac{4}{\pi}}$. is the mean neutral thermal speed. The "neutral transit time" τ is the time it will take the average neutral to move a distance L, equivalent to the radius of the outer acceleration channel wall: $\tau = L/(\bar{c}_n/2)$. Typical electron temperatures are on the order of 50-eV, while anode temperatures are closer to 0.1-eV. Thus, the neutral density at the anode exit is estimated to be more than 50 times the plasma density.

The electron density allows us to calculate (in CGS units) the plasma frequency, $\omega_{pe} = \sqrt{\frac{4\pi n_e e^2}{m_e}}$, and the Debye length, $\lambda_D = \sqrt{\frac{kT}{4\pi n_e e^2}}$. Important length scales include the electron cyclotron radius, $r_{ce} = \frac{m_e v_{th,e} c}{eB}$, the ion cyclotron radius, $r_{ci} = \frac{M v_i c}{eB}$, and collision mean-free-paths.

Parameter	Symbol	Nominal		Code
Electron Temperature (eV)	$T_e = [T]$	30	50	50
Neutral Injection Temp. (eV)	T_n	.1	-	-
Magnetic Field (Gauss)	B	5000	-	-
Utilization Efficiency	ϵ_u	.9	-	-
Permittivity Factor	γ^2	1	1	100
Permittivity (F/m)	ϵ_o	8.85e-12	8.85e-12	8.85e-10
Anode exit area (cm^2)	s_a	.04	-	-
Plume area (cm^2)	s_p	.10	-	-
Neutral Density (cm^{-3})	$n_{n,o}$	6.9e14	-	-
Neutral Velocity to right (cm/s)	$\bar{c}_n/2$	22e4	-	
Ion Sonic Speed (cm/s)	v_{si}	4.7e5	6.1e5	-
Plasma Density (cm^{-3})	$n_{e,o} = [n_e]$	1.1e13	8.8e12	-
Debye Length (cm)	$\lambda_d = [X]$	.0012	.0018	.018
Characteristic Length (cm)	L	.24	-	-
Characteristic Length [x]	$\hat{L}$	199	135	13.5
Elec Mean Thermal Vel. (cm/s)	$\bar{c}_e$	3.7e8	4.7e8	-
Electron Gyro Radius (cm)	r_{ce}	3.7e-3	4.8e-3	-
Ion Gyro Radius (cm)	r_{ci}	1.3	1.7	-
Electron Plasma Freq.(sec^{-1})	$\omega_{pe} = 1/[t]$	1.9e11	1.7e11	1.7e10
Elec Cyclotron Freq. (sec^{-1})	ω_{ce}	8.8e10	-	-
Ion Cyclotron Freq.(sec^{-1})	ω_{ci}	3.7e5	-	-
Neutral Transit Time (ω_{pe}^{-1})	τ	2.1e6	1.8e6	1.8e5

Table 2.6: Estimates of various lengths, velocities, and frequencies in the channel of the mini-TAL assuming a real mass ratio. All units CGS unless otherwise noted. Right column accounts for artificial permittivity (See next section). Neutral transit time $L/ < v_n >_z$ in terms of (ω_{pe}^{-1}) drops by a factor of 10 with ϵ_o increase of 100x. Neutral transit time is further decreased by adopting an artificial mass ratio. These values assume $\dot{m}_n = .13mg/s$.

2.6.2 Simplifying and Accelerating the Simulation

The PIC method can be used to predict the electron energy distribution function and the true state of the plasma. At first glance, however, the computational requirements seem daunting.

- Particle densities inside the simulation region are on the order of 10^{13} per cubic centimeter or greater. Tracking billions and billions of particles is impractical, to say the least.
- The PIC method requires a time-step on the order of the inverse plasma frequency. But with $\omega_{pe} \approx 10^{11}$, it would take millions of iterations for neutrals of physical mass to cross the simulation region. Convergence would be maddeningly slow.
- The PIC method requires a grid with node spacing of about a Debye length. Nominal density and temperature estimates suggest that $400,000$ grid nodes (a 500×800 grid) or more may be required. The memory and CPU time required to process such a grid would be phenomenal.

Clearly, we cannot track billions of particles for millions of time-steps on a grid containing hundreds of thousands of nodes. To use the PIC method, we must simplify and accelerate the simulation. Ways to do this include to following:

- Use super-particles in lieu of tracking individual particles.
- Change the mass ratio M_n/m_e to speed up heavy particles.
- Alter the free space permittivity constant to reduce the grid density.

Some of these changes affect densities and mean free paths. To preserve such aspects of the simulation, we must also change the mass flow rate and collision cross sections.

The effects of introducing un-physical constants into the system must be understood, and the results of the simulation interpreted.

Super-particles

The first simplification is the use of super-particles, i.e. groups of $\sim 10^6$ particles. This standard practice conserves memory and CPU time.

To determine the size of a nominal super-particle, we first choose a target number of neutral super-particles, TARGET, which depends on the number of grid cells in the simulation, and the degree of error we are willing to accept. Given the finite number of particles, N, at any grid cell, non-physical density fluctuations on the order of order of $1/\sqrt{N}$ can occur. What N is required for "good" statistics? Results presented in Chapter 4 suggest that counts of $N \approx 20$ per cell in the ionization zone produce similar results to counts of $N \approx 40$ per cell. However, results presented in Chapter 5 show that it is difficult to observe modes of oscillations with $N \approx 20$. We should also note that statistics will be worst near the axis of the thruster, where the cell volumes are smallest.

This still leaves us with a problem: The neutral density is much higher than the plasma density. If neutral and plasma super-particles are the same size, the simulation will be swamped with neutrals. To solve this problem, we let neutral super-particles be some integral number s times larger than plasma super-particles. We term this the "statistical weight" of the super-particle. Neutrals are introduced at the anode with, for example, statistical weight $s = s_o = 50$, while ions and electrons always have weight $s = 1$. As a neutral undergoes ionization events, s decreases until $s = 0$ and the particle disappears. By varying s_o, we can easily find a value which results is similar numbers of neutrals, ions, and electrons.

Given $TARGET$, s_o, and the total volume of the simulation region, V_{tot}, we calculate the [size] of each super-particle of statistical weight $s = 1$;

$$[size] = \frac{n_{n,o} V_{tot}}{s_o \times TARGET}. \tag{2.50}$$

Thus, each super-particle in our simulation represents $s \times [size]$ particles.

Artificial Mass Ratio

The stability of typical PIC schemes requires a time-step on the order of the inverse of the plasma frequency. This means $\approx 10^{-8}$ seconds for the ions, and $\approx 10^{-11}$ seconds for the electrons. Unfortunately, Xenon atoms are about 240 thousand times as massive as electrons. Thus, the velocities of an electron and ion of the same kinetic energy differ by a factor of $\sqrt{240e3} \approx 500$. Furthermore, neutrals in the simulation have lower thermal energy than electrons; they are slower still.

If we use the correct physical values for neutral temperature, T_n, and mass, M_n, it will take neutrals on the order of a million or more plasma times to cross the simulation region from the anode to the exit plane. Ions are more energetic than neutrals, but they are still much slower than electrons. Hence, if we assume correct mass ratios and temperatures and run heavy and light particles at the same time-step, the simulation will take a very long time to converge. We will not be able to use an ordinary workstation.

Our modus vivendi is to speed up heavy particles by an order of magnitude by introducing a variable artificial mass ratio. One such factor is $M/M' = 2500$, which means that heavy particles are 2500 times lighter than they should be. Instead of $M/m \approx 240,000$, this yields $M/m \approx 96$. Heavy particles now move 50 times faster. The characteristic time to reach a converged solution thus drops by a factor of 50; the transit time $\tau \approx 2 \times 10^6$ shown in Table 2.6 drops to about $40,000$. Such a solution would take about 400 thousand iterations (at $\omega_{pe}\Delta t \approx .1$) to achieve. This is not impossible, although it would take a very long time on a PC.

Changing the mass ratio is a common trick of plasma physics, where $M/m = 100$ is often employed. However, we must take care to preserve the physics of the problem. Quantities such as the mass flow rate and collision cross sections have to be altered in order to conserve densities and mean free paths. Also, an artificial mass ratio may also change the floating potential of the metallic acceleration chamber walls, which could in turn change the EEDF. These issues are considered in Section 2.6.3.

Artificial Permittivity

To speed up the simulation several additional orders of magnitude, we alter the physics of the universe. We increase the free space permittivity constant ϵ_o by a factor γ^2:

$$\epsilon_o{}' = \epsilon_o \gamma^2. \tag{2.51}$$

The benefits of using an "artificial permittivity" are twofold. First, sheaths are thicker, allowing us to use a coarser grid. Second, plasma dynamics are slower, allowing us to use a longer time-step.

Implementing the artificial permittivity is rather simple. One simply inserts γ when calculating the nominal Debye length and plasma frequency, and $\frac{1}{\gamma}$ when calculating [B]

and [E]. Poisson's equation in normalized units remains $\partial^2\hat{\phi}/\partial\hat{x}^2 = -(\hat{n}_i - \hat{n}_e)/\hat{n}_{e,o}$, but $[x]$ is longer by a factor of γ. The end result is that $E = \hat{E}[E]$ is smaller for a given charge imbalance. Since the permittivity does not appear in the Lorentz force equation, the leapfrog scheme does not have to be modified. As shown in Table 2.7, increasing ϵ_o by a factor of γ^2 increases sheath thicknesses by a factor of γ and decreases the plasma frequency by a factor of $1/\gamma$. Also shown in Table 2.7 is the effect of γ on $[v]$, $[E]$, and $[B]$.

Since grid spacing scales off the Debye length, the artificial permittivity enables us to reduce the number of grid cells required to model the domain of interest by a factor of γ^2. We may also reduce the number of super-particles in the simulation by γ^2 while retaining identical statistics (per cell). Both reductions save memory and CPU time. Furthermore, since the required time-step scales off the plasma frequency, the physical time-step can be increased by up to a factor of γ, speeding convergence.

Parameter	Symbol	x-Factor
plasma frequency	ω_{pe}	$1/\gamma$
Debye length	λ_D	γ
time	[t]	γ
distance	[x]	γ
velocity	[v]	1
electric field	[E]	$1/\gamma$
magnetic field	[B]	$1/\gamma$

Table 2.7: Effect on reference values of increasing permittivity by a factor of γ^2.

However, this benefits of this trick are limited. First, the time-step must remain short enough to resolve electron gyro motion. Unless we alter the strength of the magnetic field, this limits us to $\gamma^2 \approx 100$. Also, the Debye length must remain a small quantity with respect to overall thruster dimensions. If sheaths become too large, they can interfere with the discharge. Similarly, excessive charge imbalance may occur, altering the efficiency with which neutrals are ionized.

2.6.3 Modified Estimates of Plasma Parameters

In Table 2.6 we presented some estimates of basic plasma parameters. Now, let us take into account the use of un-physical constants. We begin with the artificial heavy particle mass ratio,

$$\frac{M'}{M} = f < 1, \tag{2.52}$$

where M is the physical mass of a Xenon neutral, and M' is the mass used in the simulation. The factor f will be less then one. From the neutral and electron temperatures, T_n and $[T_e]$, in Kelvin, we estimate the neutral and electron thermal speeds which are, respectively,

$$v_{th,n} = \sqrt{\frac{2KT_n}{M_n}} \sim \sqrt{\frac{1}{M_n}} \tag{2.53}$$

and

$$v_{th,e} = \sqrt{\frac{2KT_e}{m_e}}. \tag{2.54}$$

Thus, neutrals are accelerated by the factor

$$\frac{v_n'}{v_n} = \sqrt{\frac{1}{f}}. \tag{2.55}$$

The nominal flow velocity of ions in the region where they first appear is estimated to equal the ion acoustic speed;

$$v_i = \sqrt{\frac{KT_e}{M_n}}. \tag{2.56}$$

Thus, ions are also accelerated by the factor

$$\frac{v_i'}{v_i} = \sqrt{\frac{1}{f}}. \tag{2.57}$$

The acceleration factor of $1/\sqrt{f}$ is why we introduced the artificial mass ratio.

Nominal Densities and Mass Flow Rate

Choosing an appropriate plume area s_p, and utilization efficiency ,ϵ_u, we estimate the plasma density in the throat to be

$$n_{e,o} = \frac{\epsilon_u \dot{m}}{M_n v_i s_p} \sim \frac{1}{\sqrt{M_n}}. \tag{2.58}$$

Similarly, we estimate the nominal density of neutrals at the anode exit from the area of the anode, s_a, the temperature of the anode, $T_{anode} = T_n$, and the mass flow rate through the anode, $\dot{m}$,

$$n_{n,o}' = \frac{\dot{m}}{M_n < v >_z s_a} = \frac{2\dot{m}}{M_n \bar{c} s_a} \sim \frac{1}{\sqrt{M_n}}. \tag{2.59}$$

Here, $< v >_z = \bar{c}/2$ is the mean flow speed to the right of a half-Maxwellian entering the simulation region at the anode exit plane, and $\bar{c}$ is the mean neutral thermal speed,

$$\bar{c} = \sqrt{\frac{8KT_n}{\pi M_n}}. \tag{2.60}$$

Thus, if we run the thruster at the actual mass flow rate, but use $M_n' = fM$, then both neutral and plasma densities will be too HIGH. The number of particles introduced per time-step, $dn/dt = \dot{m}/M$, has a greater effect on the neutral number density then the increased velocity. To preserve $n_{n,o}$ in the anode exit region, i.e. to keep

$$\frac{n_{n,o}'}{n_{n,o}} = \frac{\dot{m}'}{\dot{m}} \frac{M v_n}{M' v_n'} = 1, \tag{2.61}$$

the required mass flow rate must be scaled by

$$\frac{\dot{m}'}{\dot{m}} = \sqrt{\frac{M'}{M}} = \sqrt{f}. \tag{2.62}$$

Nominal Plasma Frequency and Debye Length

The plasma density allows us to estimate basic plasma parameters such as the plasma frequency, ω_{pe},

$$\omega_{pe} = \sqrt{\frac{4\pi n_{e,o} e^2}{m_e}} \sim \frac{1}{\sqrt{\epsilon_o} M_n^{1/4}}, \tag{2.63}$$

and the Debye length,

$$\lambda_d = \sqrt{\frac{KT_e}{4\pi n_e e^2}} \sim \sqrt{\epsilon_o} M_n^{1/4}. \tag{2.64}$$

The scaling effect due to ϵ_o is why we introduced the artificial permittivity. The M_n factors on the right disappear after $\dot{m}$ is scaled as $\sqrt{M_n}$, such that n_e is preserved.

Cyclotron Radii and Frequencies

Other important length scales include the electron and ion gyro frequencies and radii, which are

$$r_{ce} = \frac{m_e v_{th,e} c}{eB}, \tag{2.65}$$

$$r_{ci} = \frac{M v_i c}{eB} \sim \sqrt{M}, \tag{2.66}$$

$$\omega_{ce} = \frac{eB}{mc}, \tag{2.67}$$

and

$$\omega_{ci} = \frac{eB}{Mc} \sim \frac{1}{M}. \tag{2.68}$$

The electron cyclotron radius and frequency will be unaffected by changes in heavy particle mass or by changes in ϵ_o. The same cannot be said for the ion cyclotron radius and frequency. For instance, as the ion mass decreases, so does the ion gyro radius ($r_{ci} \sim \sqrt{M}$). As M approaches m, this becomes a problem. To preserve r_{ci} and ω_{ci} at their physical values (with $M/m \sim 240,000$), the magnitude of the magnetic field which the ions see, B', should be reduced by the factor $\sqrt{f}$,

$$B' = \sqrt{f}B \tag{2.69}$$

such that

$$\frac{r'}{r} = \frac{M'v'}{eB'}\frac{eB}{Mv} = \sqrt{f}\frac{B}{B'} = 1. \tag{2.70}$$

No factor is applied to B for the electrons.

Mean Free Paths

A mean free path analysis is presented in Section 2.8. There, we show that collision mean free paths may be estimated according to the formula

$$\lambda_{12} = \frac{v_1}{\nu_{12}}. \tag{2.71}$$

Here, λ_{12} is the mean free path of a particle of species one in a background of species 2, $\nu_{12} = n_2 v_{12} Q_{12}$ is the frequency with which particle 1 interacts with species 2, v_{12} is the relative velocity of the two species, and Q_{12} is the cross section for this interaction. Since $\nu_n \approx n_e v_e Q$, and $\nu_e \approx n_n v_e Q$, the mean free path for neutrals traveling in the z direction is

$$\lambda_{n,z} = \frac{v_{n,z}}{\nu_n} = \frac{v_{n,z}}{n_e v_e Q}, \tag{2.72}$$

while the mean free path for electrons is

$$\lambda_e = \frac{v_e}{\nu_e} = \frac{1}{n_n Q}. \tag{2.73}$$

Changing M alters the mean free path analysis. If we adjust $\dot{m}$ to preserve the neutral density at the anode exit, then λ_e should be the same. However, $\lambda_{n,z}$ is proportional to $v_{n,z}$. If we do nothing else, than either the ionization zone will stretch out, or a lower fraction of neutrals overall will be ionized. In Section 2.11 we estimate the extent of the ionization zone, finding that $v_{n,z}$ is not (at least directly) a factor. This result makes our latter postulate more likely.

In either case, the solution is to preserve $\lambda_{n,z}$ by increasing the ionization cross section Q by a factor of $\sqrt{\frac{1}{f}}$. The electron mean free path will decrease, but as long as electrons remain magnetized, results should not change much.

Conductivity

What about the overall conductivity of the plasma? If ions move too fast, then the ratio of ion to electron conductivity is proportionally too large. The solution follows from above. If we scatter each time we ionize, and also increase the total *scattering* cross section as above, then the electron mean free path will decrease by the factor $\sqrt{f}$. If the Hall parameter is large ($\beta = \omega_c/nu >> 1$, see Section 2.10), then the bulk electron velocity across the magnetic field should increase as

$$< v_e >_\perp \sim D_\perp \sim \nu_e \sim \frac{1}{\sqrt{f}}. \tag{2.74}$$

Thus, the conductivity in the direction normal to the magnetic field will increase at the rate required to (nominally) preserve the ratio of ion to electron current normal to $\vec{B}$.

This makes sense from an energy point of view. Neutrals are entering the ionization zone faster than they should be. Thus, the thruster is dissipating energy into ionization faster. Electron transport must be increased to deliver energy to the ionization zone at the same proportional rate. This is accomplished by increase overall scattering cross sections (to get the electrons to the acceleration zone quicker) and inelastic scattering cross sections (to deposit energy in the zone quicker).

2.6.4 Recovery of Physical Solution

By altering the mass flow rate and collision cross sections, we may preserve neutral, plasma, and ion densities. The cross section factors are shown in Table 2.8. Also, by altering collision

cross sections, we may locate energy losses as they would be located in the real thruster, i.e. we can preserve the features of the acceleration and ionization zone(s).

M/M'	M'/m	${v_n}'/v_n$	Q'/Q
1	239,000	1	1
250	960	16	16
2500	96	50	50
10,000	24	100	100

Table 2.8: Artificial mass ratios used in the numerical simulation. M is the physical neutral mass. M' is the numerical neutral mass. The ratios M'/m, ${v_n}'/v_n$, and Q'/Q are approximate. The last ratio is applied to preserve heavy particle mean free paths.

Once the simulation has converged, we can extrapolate backward to recover performance parameters such as thrust and specific impulse. The kinetic energy of any given ion depends on the potential field through which it travels according to

$$K.E. = \Delta\Phi = \int \frac{d\phi}{dl} dl = \int \vec{E} \cdot dl. \tag{2.75}$$

If the bulk field properties are the same or similar, then the kinetic energy of any given ion in the flow should be about the same at point (z,r) no matter what M is. Therefore, by multiplying all final (computational) ion velocities by $\sqrt{f}$, we should be able to recover the "real" ion velocity distribution, e.g.

$$\frac{v_{i,z}}{I'_{i,z}} = \frac{I_{sp}}{I'_{sp}} = \sqrt{f}. \tag{2.76}$$

Since $\frac{v'_i}{v_i} = \sqrt{\frac{1}{f}}$ and $\frac{\dot{m}'}{\dot{m}} = \sqrt{\frac{M'}{M}} = \sqrt{f}$, the ratio of computational to "real" thrust is

$$\frac{T'}{T} = \frac{\dot{m}' v'_i}{\dot{m} v_i} = 1. \tag{2.77}$$

The thrust predicted by the code will be the same with or without the artificial mass ratio! Since we preserve densities, the current density in the perpendicular direction $j_z = e\dot{n} = en_e v_z$ will scale with the velocity. As before, multiplication by $\sqrt{f}$ returns the "real" value,

$$(\frac{j}{j'})_z = \frac{n v_z}{n' v'_z} \approx \sqrt{f}. \tag{2.78}$$

Here, we note that the azimuthal or Hall current should not be re-scaled at the end of the simulation. It should not change with M. For further discussion, see Section 5.3.6.

This simple method of recovery assumes the bulk properties $(n_n, n_e, T_e, ...)$ of the discharge remain invariant when an artificial mass ratio is introduced. In practice, this is not exactly true. For instance, the wall potential varies with the artificial mass ratio. They can have an effect on plasma density, as will be discussed in Chapter 4. The recovery can therefore only be considered approximate. The best way to get the "real" physical performance and particle moments is to use physical values for M_n and ϵ_o. Therefore, we make the constants as close to physical as possible, given the computational power available.

2.6.5 Limits of Artificial Mass Approximation

In Section 2.10, we show that the coefficient for classical diffusion of electrons in a weakly ionized but magnetized plasma can be written:

$$D_\perp \approx \frac{KT}{m}\frac{\nu}{\nu^2+\omega_c^2}. \tag{2.79}$$

The ratio $\beta = \omega/\nu$ can be used to describe the degree of magnetization in a plasma. It is called the "Hall Parameter." If $\beta^2 >> 1$, the preceding expression is well approximated by

$$D_\perp \approx \frac{KT}{m}\frac{\nu}{\omega_c^2}. \tag{2.80}$$

This expression provides the rationale for increasing Q to increase electron transport perpendicular to $\vec{B}$ (as previously described). However, the expression is not always valid. Figure 2-5 shows its limits. The approximate expression for $D_\perp$ is only valid above $\beta \approx 2-3$. Below this range, $D_\perp$ does not increase linearly with collision frequency. In fact, collisions may hinder diffusion if $\beta < 1$. Even at $\beta = 2$, the "approximate" and "exact" diffusion coefficients differ by twenty percent.

We only want to increase the collision frequency within the range of validity of the approximate expression $D_\perp \sim \nu$. That is, we want to keep the computational β greater than 2, at a minimum. In the acceleration channel of the mini-TAL, the physical value for β is typically between 100 and 200. Therefore, we should not increase the collision frequency by more than a factor of 50. This limits us to $M_n/M_n' = 2500$, or $M_n/m_e \approx 96$. Even at this mass, the approximations used to scale the simulation break down and the results can

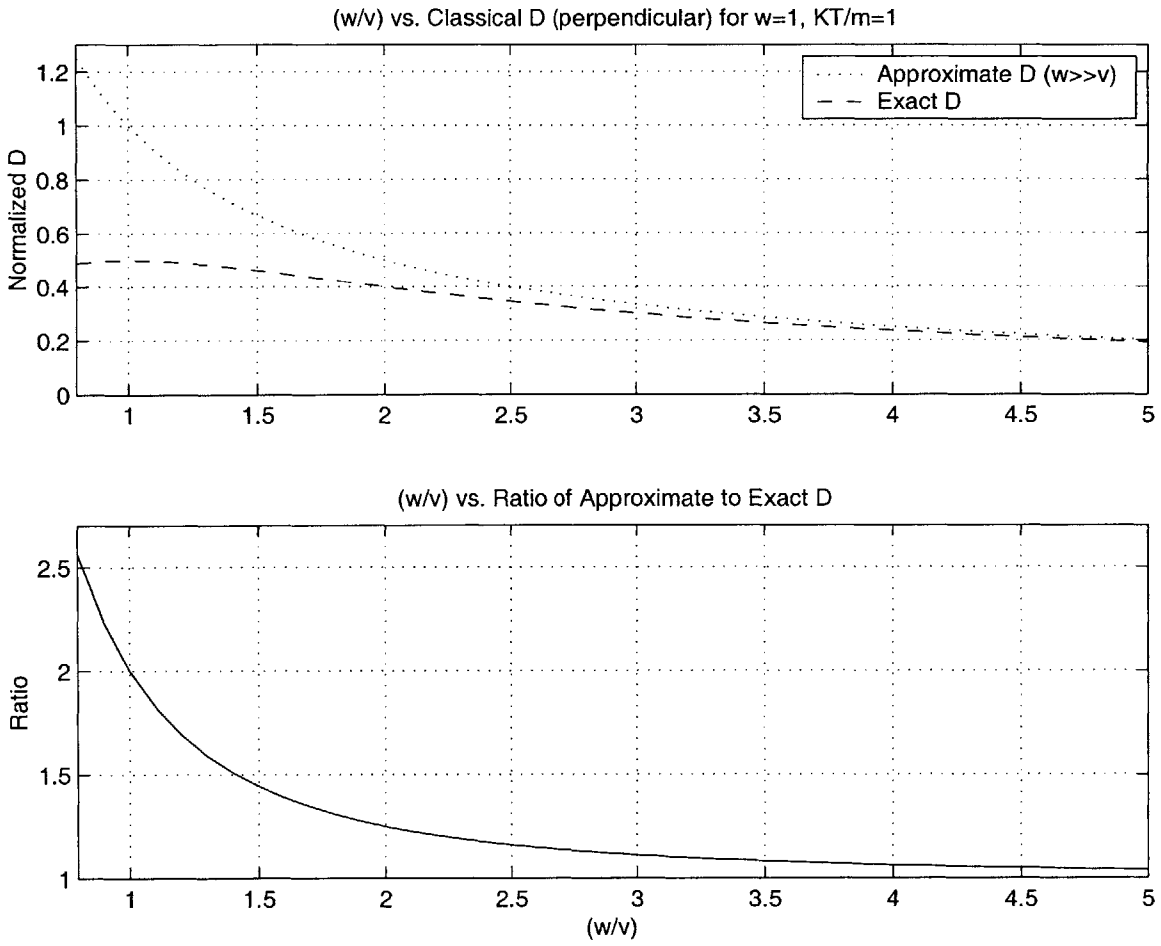

Figure 2-5: *Limits of the approximation* $D_\perp \sim \nu$.

only be considered approximate. (In Chapter 5, we show that $\beta \approx 2-3$ at the anode exit even with $M_n/m_e \approx 96$!). A better choice is $M_n/M_n' = 250$, or $M_n/m_e \approx 960$.

2.7 Characteristic Times for Convergence

How long will the simulation take to converge? In Section 2.6 we defined the "neutral transit time, τ, to be the time it will take the average neutral to move a distance L, equivalent to the radius of the outer acceleration channel wall. If $L = L_o = .24cm$ and $< v >_z = 21,600cm/s$, then $\tau \approx 1.1 \times 10^{-5}$ sec. At a nominal plasma frequency of $\omega_{pe} = 1.8 \times 10^{11}$ ($n_{e,o} = 8.8 \times 10^{1}2$ cm^{-3}, $T_e = 30eV$), the neutral transit time is $2 \times 10^6 \omega_{pe}^{-1}$. Therefore, if $\omega_{pe}\Delta t = .1$ and $\gamma = 10$, it will take a typical neutral of physical mass $M/m = 240,000$ about $\tau = 2 \times 10^6$ time-steps to move the distance L_o.

To see what this means for convergence, we define three additional lengths: $L_1 = .5$ cm; $L_2 = .13$cm; $L_3 = .05$ cm. These are, respectively, the distance from the end of the anode to the right hand (free space) boundary, the distance from the end of the anode to the point where the channel diverges, and the approximate width of the ionization layer. The last, L_3, was derived in Section 2.11. For each of these lengths, we can define a transit time. These times are shown in Table 2.9. The neutral temperature was assumed to be $.1eV$. Transit times and characteristic lengths are summarized in Figure 2-6.

➢ **Neutrals (units are $1/\omega_p$ at physical permittivity)**

	L	real	M/m=960	M/m=96
T1	0.5	4166667	263523	83333
T2	0.13	1083333	68516	21667
T3	0.05	416667	26352	8333

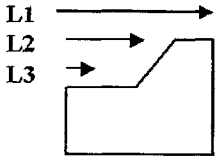

➢ **Ions**

	L	real	M/m=960	M/m=96
T1	0.5	104167	6588	2083
T2	0.13	27083	1713	542
T3	0.05	10417	659	208

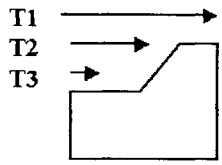

Figure 2-6: *Approximate transit times and characteristic lengths* for the mini-TAL in units of $1/\omega_{pe}$ at physical permittivity.

Ions typically have directed energies of about 150 eV by the time they reach the free

space boundary. If we assume that ions move 40 times as fast as neutrals, we arrive at the ion transit times shown in Table 2.10.

	L (cm)	M/m=240,000 $1/\sqrt{f}=1$	$M/m=960$ $1/\sqrt{f}=15.8$	$M/m=96$ $1/\sqrt{f}=50$
τ_o	.24	2,000,000	130,000	40,000
τ_1	.5	4,200,000	260,000	83,000
τ_2	.13	1,100,000	69,000	22,000
τ_3	.05	420,000	26,000	8,300

Table 2.9: Neutral transit times. $M'/M = f$. Times are in iterations assuming $T_e = 30$eV, $\gamma = 10$, $\dot{m} = .1mg/s$, $\omega_{pe}\Delta t = .1$.

	L (cm)	M/m=240,000 $1/\sqrt{f}=1$	$M/m=960$ $1/\sqrt{f}=15.8$	$M/m=96$ $1/\sqrt{f}=50$
τ_o	.24	50,000	3,200	1000
τ_1	.5	100,000	6,600	2100
τ_2	.13	27,000	1,700	540
τ_3	.05	10,000	660	210

Table 2.10: Ion transit times. $M'/M = f$. Times are in iterations assuming $T_e = 30$eV, $\gamma = 10$, $\dot{m} = .1mg/s$, $\omega_{pe}\Delta t = .1$.

With regard to the time-scales in Tables 2.9 and 2.10 we note the following.

- For both $M/m = 96$ and $M/m = 960$, τ_2 and τ_3 are well within the limits of our computational resources.
- If $M/m = 96$ and $\gamma = 10$, eighty thousand iterations (τ_1) are required to see the complete flow of neutrals from the end of the anode to the free space boundary. With fifty to a hundred thousand plasma particles, a fast PC (for the turn of the Millennium) can do thirty thousand iterations of our code (with $\gamma = 10$) in a day. Therefore, such time-scales can be simulated in 2-3 days.
- If $M/m = 960$, two hundred and sixty thousand iterations (τ_1) are required to see the complete flow. This is impractically long.
- Ion time-scales are very short compared to neutral time-scales. If neutrals were not simulated directly, we could conceivably use mass ratios such as $M/m = 10,000$ or even $M/m = 100,000$.

- The time-step is often shorter than $\omega_{pe}\Delta t = .1$. More typical is $\omega_{pe}\Delta t = .07$.

The time-scales τ_1, τ_2 and τ_3 provide estimates for how long it will take aspects of the simulation to reach a state of quasi-convergence. In practical terms, the neutral time-scale τ_1 is so long that results presented in Chapter 5 for $M/m = 960$ do not show the correct neutral flow at the free space boundary. The simulations are never "fully converged." However, these simulations are run for periods of time longer than τ_2 and τ_3, which means that neutrals in the discharge itself are re-distributed in accordance with the electron and ion fluxes. Furthermore, time-scales for ions and (by association) electrons are so much shorter that performance predictions obtained at the free-space boundary should be fairly accurate, even for $M/m = 960$.

2.8 Mean Free Path Analysis

Particles gain and lose energy and momentum during elastic and inelastic collisions with other particles. A mean free path analysis helps decide which collisions to include in the simulation, and which to ignore. Table 2.11 lists the types of collisions we considered and those we actually included. Based on the analysis described below, we model electron-neutral elastic and inelastic scattering collisions, electron-electron and electron-ion Coulomb collisions, and ion-neutral charge exchange and scattering collisions. We also include recombination at the walls.

Type	Included
Electron-Neutral Elastic Scattering	X
Electron-Neutral Ionization	X
Electron-Neutral Excitation	X
Electron-Electron Coulomb	X
Electron-Ion Coulomb	X
Ion-Neutral Charge Exchange	X
Ion-Neutral Scattering	X
Ion-Ion Coulomb	
Neutral-Ion Scattering	X
Neutral-Neutral Scattering	
Electron-Ion bulk recombination	
Electron-Ion wall recombination	X

Table 2.11: Types of collisions in a Hall thruster. Based on the mean free path analysis, only certain types of collisions are included in the simulation.

2.8.1 Collisions and Mean Free Paths

The reaction rate between two species can be expressed as a function of their densities (n_1, n_2), relative velocities (v_{12}), and a cross section Q_{12};

$$R_{12} = n_1 n_2 v_{12} Q_{12}. \tag{2.81}$$

Thus, the frequency with which a typical particle of species 1 interacts with background species 2 is

$$\nu_{12} = \frac{R_{12}}{n_1} = n_2 v_{12} Q_{12}. \tag{2.82}$$

Let the mean distance a particle of species 1 travels in the laboratory frame between interactions with species 2 be called the mean free path, λ_{12}.

If $v_1 >> v_2$, then $v_{12} \approx v_1$ such that

$$\lambda_{12} = \frac{v_1}{\nu_{12}} \approx \frac{v_1}{n_2 v_1 Q_{12}} = \frac{1}{Q_{12} n_2}. \tag{2.83}$$

If the velocities of the species are comparable $(v_1 \approx v_2)$, then

$$\lambda_{12} \approx \frac{1}{Q_{12} n_2}. \tag{2.84}$$

If $v_2 >> v_1$, then $v_{12} \approx v_2$ such that

$$\lambda_{12} = \frac{v_1}{\nu_{12}} \approx \frac{v_1}{n_2 v_2 Q_{12}}. \tag{2.85}$$

The Knudsen number is a measure of the degree of rarefaction of a gas. It is the ratio of mean free path to some characteristic length, $Kn = \lambda_{mfp}/L$. The Navier-Stokes equations are traditionally held to be valid for $Kn < 0.1$. This can be misleading if L is chosen poorly. L should be the scale length for macroscopic gradients [4], e.g. $L = \frac{\rho}{\partial \rho / \partial x}$. If the locally defined Knudsen number is greater than .1, then the error in the Navier-Stokes equations is significant. If $Kn > .2$, the molecular model must be used in place of the continuum model. In the limit $Kn = 0$, the Navier-Stokes equations reduce to the inviscid Euler equations. In the limit $Kn \to \infty$, the collisionless Boltzmann equation applies.

We assume that a collision event with a mean free path on the order of the path length a particle can expect to see before exiting the simulation can be ignored without significantly

affecting the results of the simulation. At higher energies, electron-ion Coulomb collisions may fall into this category. More frequent events such as electron-neutral scattering must always be modeled.

2.8.2 Electron-Neutral Scattering

The total cross section for all electron-neutral scattering events is the sum of the cross sections for elastic scattering, q_s, excitation, q_e, and ionization, q_i. The last two represent inelastic scattering. Thus,

$$Q_t = q_s + q_e + q_i \tag{2.86}$$

Scattering cross sections gathered from the literature are presented in Figure 2-7. Third and Fourth order polynomial fits to the data are used in the code. These are shown by solid lines in Figure 2-7.

The total cross sections for electron neutral scattering, Q_t, is about $1-4\times10^{-15}cm^2$ for most energies of interest. Since the neutral density exiting the anode is around $5\times10^{14}cm^{-3}$, the mean free path for electron-neutral scattering is on the order of 1-cm. This is larger than the characteristic size of the simulation region in the R-Z plane. Electrons are, however, magnetized: They spiral around the magnetic field lines, and drift around the axis of the thruster (the azimuthal $\vec{E}x\vec{B}$ drift which gives the Hall thruster it's name) such that the total path length of an electron traveling from the cathode to the anode is much longer then the scattering mean free path. Indeed, it must be so for the thruster to operate efficiently. Ions are produced through inelastic scattering, the cross section for which represents just a portion of the total scattering cross section. Thus, the model must consider electron-neutral scattering collisions. As we shall see, cross sections for elastic scattering, ionization, and neutral excitation are all comparable, hence all three effects must be included.

Total Scattering Cross Section

Early measurements of Q_t were performed by Ramsauer [38], Ramsauer and Kollath [39], and others. Pronounced minima near 1-eV were discovered by Ramsauer, and independently by Townsend and Bailey [30]. The Ramsauer-Townsend Effect required quantum theory to be explained. Ramsauer's apparatus did not distinguish between elastic and inelastic scattering. Hence, his measurements represent elastic scattering only up to the first

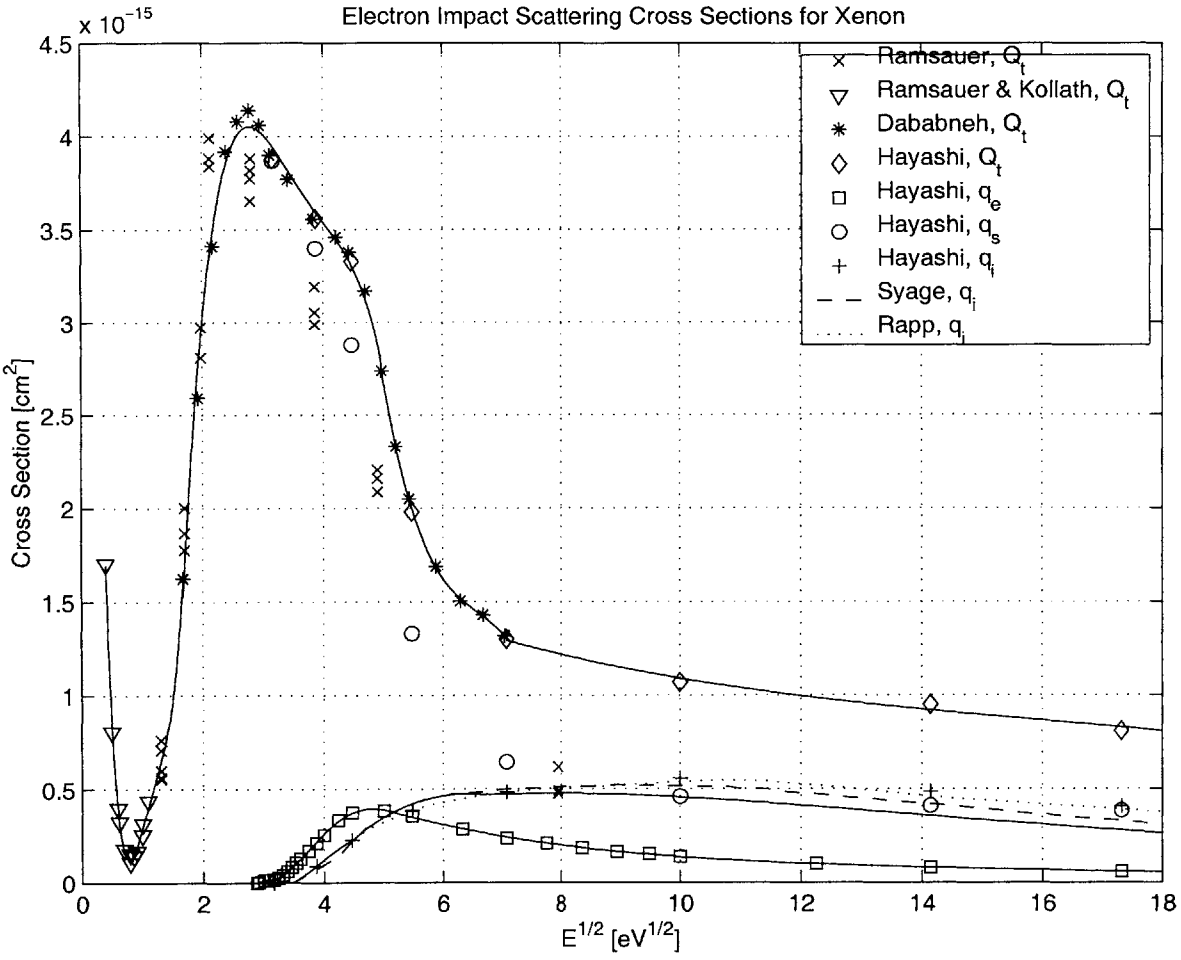

Figure 2-7: *Electron-neutral scattering cross sections.* Shown is experimental data from Ramsauer [38] , Ramsauer and Kollath [39], Dababneh (Phys. Rev. A, 22, 1872-77, 1980.), Syage [49], Rapp and Englander-Golden [41], along with cross sections determined by Hayashi [14]. The solid lines are polynomial curve fits to the total scattering, first order ionization, and neutral excitation cross sections which are used in the simulation. The curve fits are found in the Appendix, Section B.

excitation energy of 8.32-eV. To obtain a curve fit $Q_t(E)$, we use Ramsauer's measurements of Q_t up to about 3-eV, above which we use more recent measurements by Dababneh (Phys. Rev. A, 22, 1872-77, 1980.) (The Ramsauer data points were obtained using a ruler and the original data points graphed in references [38] and [39].) Above 50-eV, we use values of Q_t compiled by Hayashi [14], who states that this quantity is now known to within an error of about 5 percent. Data from all these sources is shown in Figure 2-7.

Ionization Cross Sections

Rapp and Englander-Golden have measured total cross sections for Xenon ionization [41]. Hayashi has also recommended values of q_i [14]. These data are shown directly in Figure 2-7. Syage has measured electron-impact cross sections for multiple ionization of Xenon [49]. In Figure 2-7, we show the sum of the first five ionization cross sections from Syage, also labeled q_i. To obtain the shown curve fit for single ionization from neutrals, $q_{i,1+}(E)$, we used Rapp and Englander-Golden's data below 20-eV, and Syage's data above 20-eV. Curve fits to cross sections for higher order ionization ($q_{i,2+}(E)$, $q_{i,3+}(E)$...) were obtained using Syage's data. Note that the total ionization cross section is noticeably larger than $q_{i,1+}(E)$; small but significant populations of multiply charged ions are observed in Hall thrusters.

Total Excitation Cross Section

After selecting recommended values of elastic momentum transfer cross sections and ionization cross sections, Hayashi determined from Townsend ionization coefficients the total excitation cross section, q_e, from threshold to 100-eV. He then connected the result with high energy values obtained from theory [14]. Hayashi also summed q_e with q_i and with recommended values of elastic scattering cross section, q_t, and showed that the total (with roughly estimated errors) was within the error bars of Q_t. Hayashi's recommended values of q_e, q_i, and q_s are shown in Figure 2-7. Hayashi's tabulated q_e is used to obtain the curve fit, $q_e(E)$.

Polynomial Fits

In practice, we use the polynomial curve $Q_t(E)$ to determine whether or not a scattering event takes place, and then use the relative magnitudes of $Q_t(E)$, $q_i(E)$, and $q_e(E)$ along

with a random number to determine what kind of an event takes place. The polynomial fit for $Q_t(E)$ where the relative energy E is given in eV is given by the following:

- $E \leq .1592$, $Q = 1.699 \times 10^{-15}$
- $E \leq 2.8$ eV, $Q_t = 1.0 \times 10^{-13} \times (0.07588072747894 \times E^2 - 0.34475940259139 \times E \times \sqrt{E} + 0.58473840309059 \times E - 0.42726069455393 \times \sqrt{E} + 0.11430271021684)\ cm^2$
- $E \leq 24.7$ eV , $Q_t = 1.0 \times 10^{-13} \times (-0.00199145459640 \times E^2 + 0.02974653588357 \times E \times \sqrt{E} - 0.16550787909579 \times E + 0.40171310068942 \times \sqrt{E} - 0.31727871240879)\ cm^2$
- $E \leq 50$ eV, $Q_t = 1.0 \times 10^{-13} \times (-0.00217736834537 \times E \times \sqrt{E} + 0.04302155076778 \times E - 0.28567311384223 \times \sqrt{E} + 0.65180228051047)\ cm^2$
- $E \leq 500$eV, $Q_t = 1.0 \times 10^{-14} \times (-0.00002249610521 \times E \times \sqrt{E} + 0.00109930275788 \times E - 0.02071463195923 \times \sqrt{E} + 0.22876772390428)\ cm^2$
- $E > 500$ eV, $Q_t = 6.4 \times 10^{-16}\ cm^2$

Functions (written in C) generating the polynomial curve fits for Q_t, q_e, and q_i are found in the Appendix, Section B.

Temperature Averaged Cross Sections

If the electron distribution is isotropic and Maxwellian at temperature T_{ev}, then one can integrate across the distribution to find equivalent electron-neutral scattering cross sections as a function of T;

$$Q(T) = \int Q(e) f(e) de. \tag{2.87}$$

If we let both energy and temperature be in units of electron volts, we find

$$f(e) = \frac{dN/N}{de} = \frac{2}{\sqrt{\pi}} \sqrt{\frac{e}{T^3}} exp(\frac{-e}{T}). \tag{2.88}$$

The integration can be performed numerically. At each temperature T, we sum across 3000 energy bins of uniform width $\Delta e_i = 20 \times T/3000$ such that we capture all the electrons out to 20 times the temperature;

$$Q(T) = \Sigma_i Q_i(e_i) f(e_i, T) \Delta e_i. \tag{2.89}$$

For each energy bin of width Δe_i centered about e_i, we obtain $Q(e_i)$ from the polynomial fits already discussed. The results of this integration are shown in Figure 2-8. The total scattering cross section was assumed to be constant below $\approx .16eV$, the lowest data point.

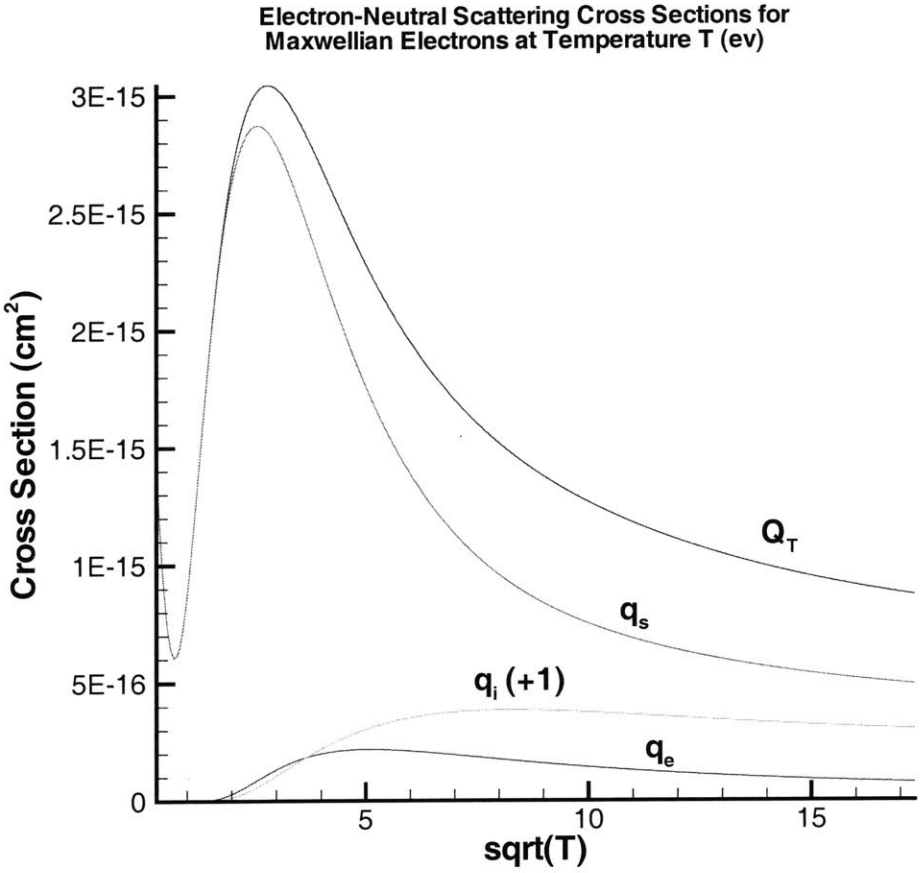

Figure 2-8: *Electron-neutral scattering cross sections as a function of electron temperature.* Starting with a Maxwellian electron distribution at temperature T, we numerically integrated to find $Q(T) = \int Q(e)f(e)de$ Shown (in order of nominal size) are total scattering, elastic scattering, first order ionization, and neutral excitation cross sections.

Multiply Charged Ions

The results presented in Chapters 4 and 5 were obtained modeling only singly charged Xenon ions. However, multiply charged ion populations on the order of five to ten percent have been reported in Hall thruster plumes. Multiply charged ions can easily be added to the model to produce more realistic results. In fact, the code was written with this addition in mind. In Chapter 6 (Conclusions) we recommend adding multiply charged ions to the mix.

Multiple Excitation States

Only one level of excitation was included in the model, 8.32 eV. However, the cross section used is the *total* excitation cross section, q_e, as calculated by Hayashi [14]. This means electron energy losses to excitation are (if Hayashi's q_e values are correct) underestimated. In Chapter 6 (Conclusions) we recommend modifying the method to account for higher excitation energies.

No metastable neutral excitation states were included in the model.

2.8.3 Ion-Neutral Collisions

Both ion-neutral charge exchange and elastic scattering collisions were considered. The former type appear to be more prevalent.

For ions interacting with a background of neutrals, we compare mean free paths to the expected ion path length, i.e. the distance from where ions enter the simulation region to where they exit. For neutrals interacting with a background of ions, we compare mean free paths to the expected neutral path length.

Because ions are only weakly magnetized (they escape the acceleration region without spiraling around the field lines) their expected path length is on the order of the grid dimensions, about 5-mm from end to end. Neutrals are unmagnetized. Hence, their expected path length is also around 5-mm.

Ion-Neutral Charge Exchange Collisions

First, we consider resonant charge exchange between neutrals and singly charged xenon (charge exchange collisions). In one of these collisions, a neutral and an ion exchange an electron. The neutral becomes an ion, and the ion becomes a neutral. Oh [33] and Samanta Roy [43] used the charge exchange cross section calculated by Rapp and Francis [40],

$$Q_{cex} = (k_1 \, ln(c_r) + k_2)^2 \times 10^{-16} \; cm^2, \tag{2.90}$$

where $k_1 = -.8821$, $k_2 = 15.1262$, and c_r is in m/s. This formula was used in our simulation. For comparison, we consider the results of Sakabe and Izawa [42], who used quantum theory to calculate cross sections, compared with experimental results, and tabulated their estimates. Cross sections from both sources are shown in Figure 2-9, which shows that

$Q_{cex} \approx 5 \times 10^{-15} cm^2$ for ion energies of interest (10-300 eV). This is about 3 times the size of the electron-neutral total scattering cross section, to be considered next.

The plasma density in the channel is on the order of $n_e \approx 10^{13} cm^{-3}$ Since neutrals are much slower than ions, let $c_r = v_{s,i} = v_i$, the ion sonic speed at the plasma temperature. At $T_e = 30eV$ we then obtain $Q_{cex} = 5.9 \times 10^{-15} cm^2$. Thus, at $T_i = .1eV$ the mean free path for a neutral between charge exchange events is about

$$\lambda_{cex,n} \approx \frac{v_n}{Q_{cex} n_i v_i} \approx .69cm. \tag{2.91}$$

The neutral density inside the anode near the exit is about $n_{n,o} \approx 7 \times 10^{-14} cm^{-3}$. In this region, the mean free path for an ion between events is about

$$\lambda_{cex,i} \approx \frac{1}{Q_{cex} n_n} \approx .25cm. \tag{2.92}$$

However, the neutral density drops by an order of magnitude, within the first millimeter from the anode exit. This will increase $\lambda_{cex,i}$ proportionally.

Both mean free paths are similar to the expected path lengths of 5-mm. Hence, charge exchange collisions should affect thruster performance. Furthermore, charge exchange electrons are a topic of interest in the field of Hall thruster plume modeling. Hence, charge exchange collisions are included in in the simulation. However, this option may be switched off to save computational time.

Ion-Neutral Elastic Scattering

Let the cross section for ion-neutral elastic scattering interactions be [33]

$$Q_{in} = \frac{8.28072 \times 10^{-10}}{c_r} cm^2, \tag{2.93}$$

where c_r is the relative speed between species 1 and species 2 in cm/s. (Note: The cross section assumed by Lentz [28], $Q = 2.145 \times 10^{-14} cm^2$, is an order of magnitude too large.) Since neutrals are much slower then neutrals, let $c_r = v_{s,i} = v_i$, the ion sonic speed at the plasma temperature. At $T_e = 30eV$ we obtain $Q_{in} = 1.8 \times 10^{-15} cm^2$. With $T_n = .1eV$ we then obtain

$$\lambda_{n,i} \approx \frac{v_n}{n_i Q_{in} v_i} = \frac{1}{Q_{cex} n_n} \approx 2.3cm. \tag{2.94}$$

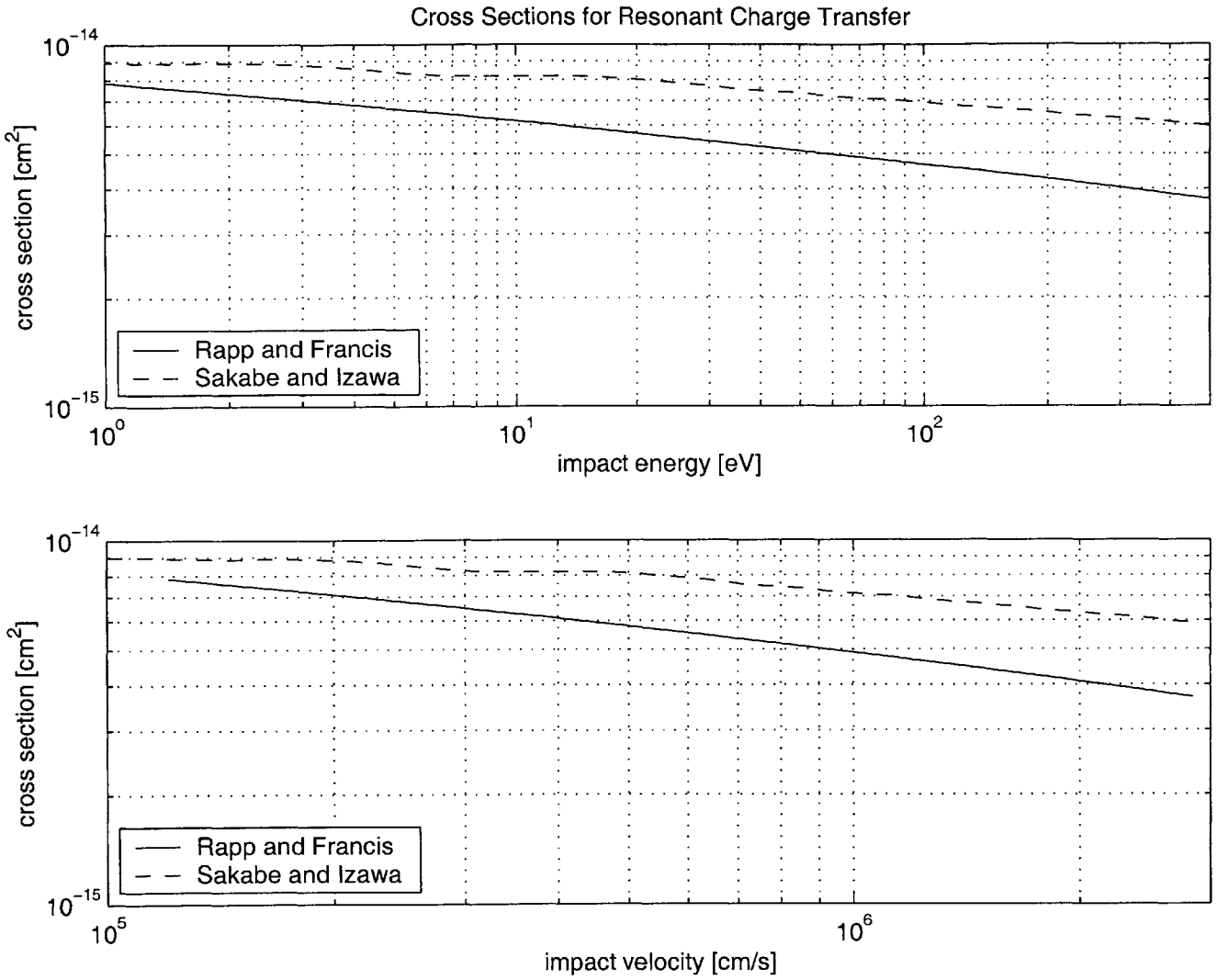

Figure 2-9: *Resonant charge transfer (charge exchange) cross sections* from Rapp and Francis , and Sakabe and Izawa In the energy range of interest, the two methods differ by a factor of 1-2. Neither is a perfect fit to the data.

The neutral density inside the anode near the exit is about $n_{n,o} \approx 7 \times 10^{-14} cm^{-3}$. Thus, in this region,

$$\lambda_{i,n} \approx \frac{v_i}{n_n Q_{in} v_i} = \frac{1}{Q_{cex} n_n} \approx .83cm. \tag{2.95}$$

Farther from the anode exit, the neutral density drops by an order of magnitude, which will increase $\lambda_{i,n}$ accordingly.

The mean free paths for both species are again on the order of the dimensions of the thruster, meaning $Kn \approx 1$. They are $3-4$ times the mean free paths for resonant charge exchange. Hence, these interactions may not be important. A Hard Sphere model of these collisions has been included in the simulation, but this option can be switched off to save computational time.

2.8.4 Neutral-Neutral Scattering

Next we consider neutral-neutral scattering. Let the cross section for neutral-neutral scattering interactions be [33]

$$Q_{nn} = 2.117 \times 10^{-14} c_r^{-.24} cm^2, \tag{2.96}$$

where c_r is in m/s. At $T = .1eV$, we obtain $Q_{nn} \approx 4.9 \times 10^{-15} cm^2$ The neutral density inside the anode near the exit is about $n_{n,o} \approx 7 \times 10^{-14} cm^{-3}$. Here, the mean free path for neutrals interacting with each other is about

$$\lambda_{n,n} \approx \frac{1}{n_{n,o} Q_{nn}} = .3cm. \tag{2.97}$$

What are the relevant Knudsen numbers? The inner diameter of the anode is about $L = .04$ cm. Outside the anode, we find (numerically) that $n_{n,o}$ drops by an order of magnitude within $L = \frac{\rho}{\partial \rho / \partial x} \approx .05$ cm. Using these scale lengths, we find $Kn = 7.5$ inside the anode $Kn = 6$ at the anode exit, and $Kn \approx 60$ a distance L from the anode (where the density is an order of magnitude less). Since neutral flow inside the anode is not the topic of this thesis, we ignore neutral-neutral collisions.

2.8.5 Coulomb Collisions

Let us now estimate the cross sections for charged particle collisions.

Electron-Ion Coulomb Collisions

The Rutherford differential cross section for Coulomb scattering is

$$I(\varsigma, v_{12}) = \frac{(b_o/2)^2}{sin^4(\varsigma/2)}, \tag{2.98}$$

where ς is the scattering angle, and

$$b_o = \frac{Ze^2}{4\pi\epsilon_o m_{12} v_{12}^2} \tag{2.99}$$

is the impact parameter. This is the perpendicular distance of the pre-scattered particle trajectory from (a parallel line through the center of) the target particle for ninety degree scattering. Note that $b_o = A/2E$, where $A = Ze^2/4\pi\epsilon_o$ and $E = 1/2m_{12}v_{12}^2$ is the relative energy of the two particles. The reduced mass $m_{12} = m_1 m_2/(m_1+m_2) \approx m_e$ for electron-ion collisions and $m_{12} = m_e/2$ for electron-electron collisions.

The total scattering cross section is found by integrating over $d\Omega$. Assuming azimuthal symmetry,

$$Q_{12}(v_{12}) = \int_{4\pi} I(\varsigma, v_{12}) d\Omega = 2\pi \int_0^{\pi} I(\varsigma, v_{12}) sin(\varsigma) d\varsigma. \tag{2.100}$$

When considering Coulomb collisions, the momentum transfer cross section,

$$Q_{12}^m(v_{12}) = \int_{4\pi} (1 - cos(\varsigma)) I(\varsigma, v_{12}) d\Omega \tag{2.101}$$

is frequently used. Note that if the differential scattering cross section is not a function of deflection angle, ς, then $Q_{12}^m = Q_{12}$. For the Coulomb potential [31],

$$Q_{12}^m(v_{12}) = 2\pi \int_{\varsigma_m}^{2\pi} (1 - cos(\varsigma) I(\varsigma, v_{12}) sin(\varsigma) d\varsigma, \tag{2.102}$$

where ς_m is a minimum angle below which one assumes no scattering and the potential is assumed to cut off at the Debye length. The momentum transfer cross section for a single electron scattering off singly charged Xenon at relative energy E is thus

$$Q_{ei}^m = 4\pi b_o^2 ln[1 + (\frac{\lambda_D}{b_o})^2]^{1/2} \approx \frac{6.5 \times 10^{-14}}{E^2} ln\Lambda \, cm^2. \tag{2.103}$$

The term $ln\Lambda$ is the Coulomb logarithm.

The *energy averaged* cross section for charged particle momentum transfer in a Maxwellian distributed, singly ionized species is about [31]

$$\bar{Q}_{ei}^{m} = \bar{Q}_{ee}^{m} = 6\pi \bar{b}_o^2 \, ln\Lambda = \frac{4.34 \times 10^{-14} ln\Lambda}{T_{eV}^2} \, cm^2, \tag{2.104}$$

where $\bar{b}_o = e^2/(12\pi\epsilon_o KT)$ is the *average* impact parameter. In the mini-TAL, $ln\Lambda \approx 15$. Thus, $\bar{Q}_{ei}^{m} \approx 6.5 \times 10^{-13} T_{eV}^{-2} cm^2$. The inverse dependence on T_e^2 is important; at low energies, $\bar{Q}_{ei}^{m} >> Q_{in}$. At 5-eV, $\bar{Q}_{ei}^{m} \approx 2.6 \times 10^{-14} \, cm^2$, which is still ten times larger than the neutral scattering cross section. The cross sections don't near parity until about 25-eV. (Note that this does not mean $\nu_{ei} = \nu_{en}$ at 25-eV. The ion density is much less than the neutral density!).

The cross section Q_{ei} must be larger than the atomic cross section, $\pi r^2 \approx 3.66 \times 10^{-16} cm^2$ (the atomic radius of Xenon is $r \approx 1.08 \times 10^{-8}$ cm, or 1.08 Angstroms). Also, the cross section should not be less than Q_{en}, the electron-neutral scattering cross section.

The mean ion velocity is much greater than the mean neutral velocity such that the ion density is between one and two orders of magnitude less than the neutral density. Still, at low E, the Coulomb cross section is so large that the mean free path is small. Electrons created at the cathode have energies of only .2 eV, and secondary electrons created during ionization events may have similarly low energies. For such electrons, Coulomb collisions are important.

It is possible to model electron-ion Coulomb collisions using a standard Monte Carlo Collision (MCC) approach described in Section 3.15.4. This model treats both electron-ion and electron-electron collisions as binary, large angle scattering events.

This is not a physical picture of what happens. Due to the $\frac{1}{r^2}$ nature of the interaction force, most collisions are relatively low angle. Furthermore, most electrons are, at any time, scattering of many other charged particles (this is the origin of the Coulomb logarithm). To capture collisional relaxation to equilibrium, it is more appropriate to model electron-ion collisions as a diffusion process in velocity space. One such model is described in Section 3.16. It is based on the Fokker-Planck equation. Some results obtained using this model are presented in Chapter 5.

However, if the fact that collisions are not binary is ignored and the cut-off collision integral (to λ_D) is used, then the answer for *momentum transfer* between species should be

the same as that obtained by using the Fokker-Planck equation [47]!

Electron-Electron Coulomb Collisions

The cross section for electron-electron collisions should be of the same order as the cross section for ion-electron collisions; these collisions should also be included in the simulation. An MCC model of electron-electron collisions was implemented (see Section 3.15.4). However, the MCC method should not really be applied in situations where self-collisions are important or where collisions have a substantial impact on the distribution function of the other species [33]. Such is the case with electron-electron Coulomb collisions. Electron-electron collisions are more appropriately modeled as a diffusion process in velocity space. One such model is described in Section 3.16. Some results obtained using this model are presented in Chapter 5.

2.8.6 Bulk Recombination

The bulk three-body electron recombination rate can be written

$$\frac{dn_e}{dt} = -\alpha n_e n_i, \tag{2.105}$$

where α is a macroscopic recombination rate [10] [31]. According to Mitchner and Kruger [31], α can be approximated in MKS units using the formula

$$\alpha = 1.09 \times 10^{-20} n_e T^{-9/2} \, [\frac{m^3}{s}], \tag{2.106}$$

which was derived by Hinnov and Hirschberg. Mitchner and Kruger state that this formula has been shown to agree with experimental measurements for temperatures less than 3000 K.

Sheppard has developed a model for recombination at temperatures on the order of several electron Volts [46]. For Argon, Sheppard's recombination coefficient is about an order of magnitude less than that produced by the Hinnov and Hirschberg formula at $T_e = .5$ eV, and one to two orders of magnitude less at $T_e > 1$ eV. At these temperatures (which are appropriate for the mini-TAL), Sheppard's own predictions matched experimental results far better than the Hinnov and Hirschberg formula. Since Xenon is a noble gas similar to Argon,

it seems logical that Hinnov and Hirschberg's formula also over-predicts recombination for Xenon by at least an order of magnitude.

Given $T = 3000K$ and $n_e \approx n_i = 1 \times 10^{19} m^{-3}$, the bulk recombination rate (using the Hinnov and Hirschberg formula) is $\frac{dn_e}{dt} = 2.46 \times 10^{15} cm^{-3} s^{-1}$. Let us compare this to a characteristic ionization rate. Given $\dot{m} = .13mg/s$, the ion mass flow rate is $\dot{N}_i \approx \dot{N}_n = 5.9 \times 10^{17}$ particles/second. Given a characteristic volume of $V = \pi r^2 L \approx \pi L^3 = .043cm^3$, we find $\frac{dn_i}{dt} = \dot{N}_i / V = 1.4 \times 10^{19} cm^{-3} s^{-1}$. Since the ionization rate is much larger than the recombination rate, we can ignore recombination. Sheppards results further reinforce this decision.

2.8.7 Summary of Mean Free Paths

Table 2.12 shows some of the relevant mean free paths along with estimated plasma densities and temperatures used to calculate them. Mean free paths for Coulomb collisions are from Mitchner and Kruger [31] and assume Maxwellian electron populations at T_e. These are included in the simulation because of their importance to low energy electrons. Ion neutral scattering and charge exchange mean free paths use an ion velocity of v_{si} to calculate $Q_{cex}(v)$, using Oh's approximations [33]. The cross section for electron neutral scattering assumed in this table was a constant $Q_t = 2.2 \times 10^{-15} cm^2$.

2.9 Simple Orbit Theory

A charged particle is subject to forces by electric and magnetic fields according to the Lorentz Force,

$$F = q(\vec{E} + \vec{v} \times \vec{B}), \tag{2.107}$$

where $\vec{v}$ is the particle's velocity at any given time. Note that the $\vec{v} \times \vec{B}$ force always acts perpendicular to the magnetic field, causing charged particles to gyrate about lines of force. If the field is mono-directional and invariant, then this gyration is stable and the guiding center cannot move in the direction perpendicular to $\vec{B}$. This is not, however, the situation in a Hall thruster, wherein the field varies in both magnitude and direction. In the parallel direction, particles motion is only affected by gradients in $\vec{B}$.

The non-periodic effect of electric field and magnetic field gradients can be summarized as follows[54]:

Parameter	Symbol		
Electron Temperature	$[T_e]$	30	50
Neutral Injection Temp.	T_n	.1	.1
Magnetic Field	B	5000	5000
Ion Sonic Speed	v_{si}	5e5	6e5
Elec Mean Thermal Vel.	$\bar{c_e}$	3.7e8	4.7e8
Plume area	s_p	.10	-
Neutral Density	$n_{n,o}$	7e14	-
Plasma Density	$[n_{e,o}]$	1e13	9e12
Debye Length	λ_d	.0012	.0018
Characteristic Length	L	.24	.24
	L/λ_D	199	135
Electron Gyro Radius	r_{ce}	.0037	.0048
Ion Gyro Radius	r_{ci}	1.3	1.7
e-n scattering mfp	λ_{en}	.66	.66
i-n charge exchange mfp	$\lambda_{cex,i}$	.25	.26
n-i charge exchange mfp	$\lambda_{cex,n}$	.69	.73
i-n scattering mfp	λ_{in}	.83	1.1
n-i scattering mfp	λ_{ni}	2.3	3.0
n-n scattering mfp	λ_{nn}	.30	.30
e-e Coulomb mfp	λ_{ee}	95	320
e-i Coulomb mfp	λ_{ei}	130	450
Electron Plasma Freq.	ω_{pe}	1.9e11	1.7e11
Elec Cyclotron Freq.	ω_{ce}	8.8e10	-
Ion Cyclotron Freq.	ω_{ci}	3.7e5	-
Neutral Transit Time	τ	2.1e6	1.8e6

Table 2.12: Mean free paths for various collision processes along with estimates of various lengths, velocities, and frequencies in the channel of the mini-TAL. L is the radius of the acceleration zone. All units CGS except T_e and T_n, which are in eV. Numbers assume physical free space permittivity, $\dot{m}_n$ = .13 mg/s, $v_n = \sqrt{2KT/m\pi}$, $n_n = \dot{m}/m_n A v_n$. Neutral transit time, $\tau = L/ < v_n >_z$, drops by a factor of 10 with ϵ_o change of 100x.

- The magnetic dipole moment, $\mu = \frac{1}{2}mv_\perp^2/B$, is an adiabatic invariant, meaning that it is nearly constant when the field experienced by the particle changes little during an orbit.

- The guiding center moves along the magnetic field subject to the acceleration $m\dot{v}_{||} = (eE_{||} + F_{||}) - \mu\partial|B|/\partial x_{||}$, where $x_{||}$ is some distance along the field line.

- The guiding center drifts across the magnetic field with various well known drift velocities.

2.9.1 Hall Thruster Geometry

A very simple model of the magnetic field in a Hall thruster is shown in Figure 2-10. The z direction in this figure corresponds to the axial direction. Here, $\vec{B} = B_o/r\,\vec{i}_r$, where $\vec{r}$ is a vector drawn from the axis. In Cartesian coordinates, the magnetic field is $\vec{B} = B_o(\frac{x}{x^2+y^2}\,\vec{i}_x + \frac{y}{x^2+y^2}\,\vec{i}_y)$. Such a field satisfies the divergence criterion, $\vec{\nabla}\cdot\vec{B} = 0$, although it is clearly non-physical at r=0.

The gradient of this field is important. In Cartesian coordinates, four terms exist, $\frac{\partial B_x}{\partial x}$, $\frac{\partial B_x}{\partial y}$, $\frac{\partial B_y}{\partial x}$, and $\frac{\partial B_y}{\partial y}$. In cylindrical coordinates, only one term exists, $\frac{\partial B_r}{\partial r}$, which is parallel to $\vec{B}$. This gradient results in the "magnetic mirror" effect.

2.9.2 Motion of a Charged Particle

Let us consider the motion of a single electron under the influence of such a field. Let the electron be located at $\vec{r} = x\vec{i}_x + y\vec{i}_y$ (see Figure 2-10).

In the absence of an electric field, the force on a particle will be

$$\dot{\vec{v}} = -\omega_o \begin{vmatrix} 0 & 0 & \frac{-y}{x^2+y^2} \\ 0 & 0 & \frac{x}{x^2+y^2} \\ \frac{y}{x^2+y^2} & \frac{-x}{x^2+y^2} & 0 \end{vmatrix} \vec{v}, \tag{2.108}$$

where $\omega_o = eB_o/m_e$. The equations of motion are not simple; there are forces in three directions. What, then, can we expect to see?

To predict the particle's motion, let us use the standard method of considering first the zeroeth, then the first order movements. If the particle starts at $y = 0$, then $\vec{B} = B_x\vec{i}_x$. Off axis, there is a much smaller component of field in the y direction. To zeroeth order,

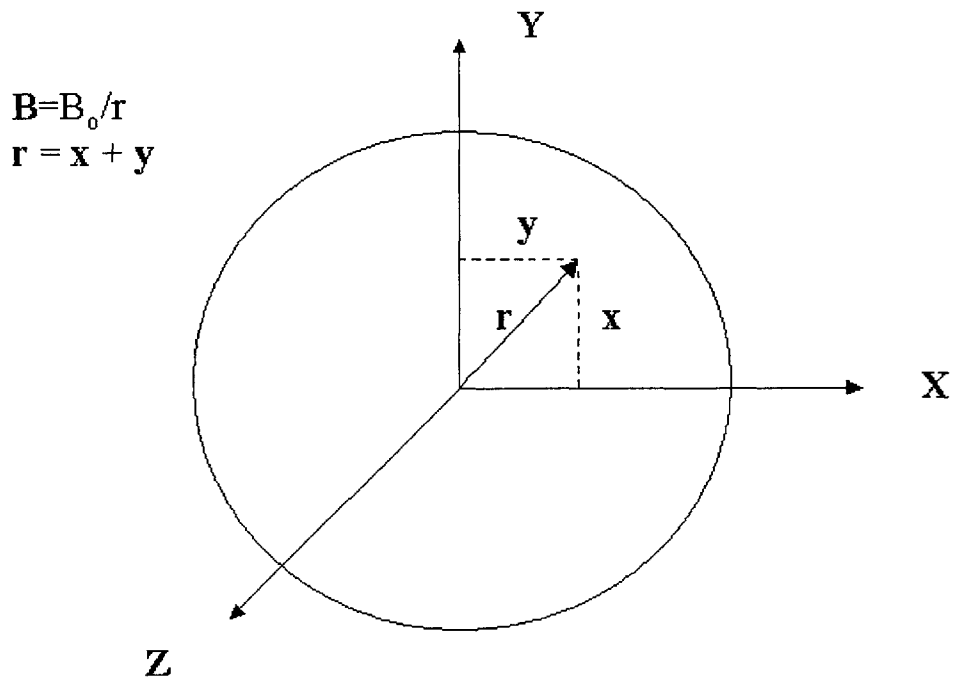

Figure 2-10: *Simplified version of the magnetic field in a Hall thruster,* $\vec{B} = B_o/r\vec{i}_r$.

$\vec{v} \times \vec{B} = B_x v_z \vec{i}_y - B_x v_y \vec{i}_z$. This results in the usual cyclotron motion. Adding the y component of magnetic field, we have $\vec{v} \times \vec{B} = -B_y v_z \vec{i}_x + B_x v_z \vec{i}_y + (B_y v_x - B_x v_y)\vec{i}_z$. However, the term $B_y v_x$ is very small. The significant new force term is $F_x = (e/m)B_y v_z \vec{i}_x$. This represents a motion in the nominal parallel direction. Note that the $B_y v_z$ always has the same sign. This means the motion does not average out over a gyration. Instead, the guiding center moves outward along the field line.

If we place an electron in this field with no kinetic energy in the parallel direction, then the electron will gyrate about the field line with $\vec{\omega} = \omega_c \vec{i}_r$. However, the electron is not stable in the parallel direction. The particle is driven outward by the force due to the gradient of the field in the parallel direction, $\partial|B|/\partial r < 0$ (this is really the same force we just discussed). The resulting motion outward along $\vec{B}$ toward the region of lower $|B|$ is entirely natural. It occurs because both energy and magnetic dipole moment are conserved. It is often called the "magnetic mirror" effect.

The addition of electric fields changes the picture. Electric fields (or any other force) perpendicular to the magnetic field will produce guiding center drifts in the θ direction.

2.10 Electron Transport in a Hall Thruster

In a Hall thruster, transport parallel to the magnetic field is driven by the electric field, diffusion, and gradients in the magnetic field. Transport perpendicular to the magnetic field comes from diffusion, wall effects such as secondary emission, $\vec{E} \times \vec{B}$ drift due to the E_θ in azimuthal waves, and diamagnetic drift due to density gradients in the azimuthal direction. All of these mechanisms will be discussed in the following sections.

2.10.1 Secondary Emission and Wall Effects

In an SPT, secondary electron emission at dielectric surfaces is thought to play an important role in electron transport. In a TAL, where the acceleration channel is metallic, secondary emission effects are thought to be less important. The secondary electron yield from metals is much less than the yield from insulators; in metals, the maximum of the yield rarely exceeds 1, while insulators may show values up to 10 or more [44]. Since this effect is thought to be small, we ignore it. Secondary emission is not modeled in this simulation.

2.10.2 Classical Diffusion and Guiding Center Drifts

In this section of the thesis, we present a simple theory for electron transport applicable to the TAL thruster. We start with an un-magnetized plasma, then move on to a magnetized plasma, and end with a discussion of anomalous diffusion.

Conservation Equations: Unmagnetized Plasma

Electron transport may be described through the momentum equation. Assuming collisions are isotropic and excluding the magnetic field, the momentum equation may be written

$$mn\frac{d\vec{v}}{dt} = \pm en\vec{E} - \vec{\nabla}p - mn\nu\vec{v}. \tag{2.109}$$

Here, $\vec{v}$ is the bulk velocity, $p = nKT$ is the pressure, ν is the collision frequency, and $\frac{d\vec{v}}{dt}$ is the convective derivative, which may be ignored if $\vec{v}$ is small (or ν is sufficiently large). This leaves the equation

$$\vec{v} = \pm\frac{e}{m\nu}\vec{E} - \frac{KT}{m\nu}\frac{\nabla n}{n}. \tag{2.110}$$

Here, $\mu = \frac{e}{m\nu}$ is termed the mobility and $D = \frac{KT}{m\nu}$ is the diffusion coefficient. The flux Γ can thus be written,

$$\vec{\Gamma} = n\vec{v} = \pm\mu n\vec{E} - D\nabla n. \tag{2.111}$$

The first term is transport due to the electric field; μ is, essentially, the conductivity of the plasma. The second term is just diffusion. If $\vec{E} = 0$ or the species is uncharged, this transport equation reduces to

$$\vec{\Gamma} = -D\nabla n, \tag{2.112}$$

which is just Fick's law. This describes transport due to gradients in pressure and is a statement of a fundamental thermodynamic concept, that the system wants to come to equilibrium.

Meaning of the Diffusion Coefficient

Einstein was the first to mathematically explain the diffusion flux caused by Brownian motion [11]. In his solution, he says the mean square displacement of a particle along x due to random fluctuations (as by collisions) after time τ is given by

$$< (\Delta x)^2 >= 2D_x\tau, \tag{2.113}$$

where D_x is the diffusion coefficient. Inverted, this equation says

$$D_x = \frac{1}{2\tau} < (\Delta x)^2 > . \tag{2.114}$$

For isotropic diffusion in d dimensions ($D_x = D_y = D_z$), $< (\Delta r)^2 >= d < (\Delta x)^2 >$ such that

$$< (\Delta r)^2 >= 2dD_x\tau \tag{2.115}$$

and

$$D_x = \frac{1}{2d\tau} < (\Delta r)^2 > . \tag{2.116}$$

Electron Collision Frequency

In a Hall thruster, electron collisional transport arises from encounters with neutrals, ions, and other electrons. The total electron collision frequency may be written

$$\nu_e = \nu_{en} + \nu_{ei} + \nu_{ee}. \tag{2.117}$$

The electron-neutral collision frequency ν_{en} is determined by cross sections, Q_{en}, for collisions with neutrals, the neutral background density, and the electron velocity according to $\nu_{en} \approx n_n v_e Q_{en}$. The electron-ion collision frequency is determined by $\nu_{ei} \approx n_i v_e Q_{ei}^m$, where some caution must be used in estimating the momentum transfer cross section Q_{ei}^m (see Section 2.8.5). If $n_e Q_{ei} >> n_n Q_{en}$, and $\nu_{ee} \sim \nu_{ei}$, then $\nu_e \approx \nu_{ei} + \nu_{ee}$. This is true in a fully ionized gas, but can also be true in a gas with a low ionization fraction but low temperature such that Q_{ei} is large.

Most Hall thruster analyses assume the opposite case, that $\nu_e \approx \nu_{en}$ [10] [12]. This may be appropriate for a Maxwellian plasma with temperatures from 5 to 20 eV. However, our simulation contains low energy electrons for which the Coulomb cross section is very large. Such electrons are, for instance, produced through ionization. Thus, we include these collisions.

Conservation Equations: Magnetized Plasma

We now consider a magnetized plasma[6]. Since $\vec{B}$ does not effect motion in the parallel direction, the parallel flux can be written

$$\vec{\Gamma}_{||} = \pm \mu n \vec{E}_{||} - D \nabla_{||} n. \tag{2.118}$$

In the perpendicular direction, however, electrons are impeded by the magnetic field. A different momentum equation is required. Letting temperature and collisions again be isotropic, the perpendicular fluid equation of motion may be written

$$mn \frac{d\vec{v}_\perp}{dt} = \pm en(\vec{E}_\perp + \vec{v}_\perp \times \vec{B}) - KT\vec{\nabla} n - mn\nu\vec{v}, \tag{2.119}$$

where

$$\vec{v_\perp} = \vec{v}_x + \vec{v}_y. \tag{2.120}$$

Ignoring the convective derivative, separating into x and y components, utilizing the definitions of μ and D, and letting $\beta = \omega_c/\nu$, one finds,

$$\begin{aligned} v_x(1+\beta^2) &= \pm\mu E_x - \tfrac{D}{n}\tfrac{\partial n}{\partial x} + \beta^2 \tfrac{E_y}{B} \mp \beta^2 \tfrac{KT}{eB}\tfrac{1}{n}\tfrac{\partial n}{\partial y} \\ v_y(1+\beta^2) &= \pm\mu E_y - \tfrac{D}{n}\tfrac{\partial n}{\partial y} - \beta^2 \tfrac{E_x}{B} \pm \beta^2 \tfrac{KT}{eB}\tfrac{1}{n}\tfrac{\partial n}{\partial x}. \end{aligned} \tag{2.121}$$

More generally, this may be written

$$\vec{v}_\perp = \pm\mu_\perp \vec{E} - D_\perp \frac{\vec{\nabla} n}{n} + \frac{\vec{v}_E + \vec{v}_D}{1 + 1/\beta^2}, \tag{2.122}$$

where

$$\mu_\perp = \frac{\mu}{1+\beta^2}\,;\; D_\perp = \frac{D}{1+\beta^2}. \tag{2.123}$$

The "Hall parameter", β, determines the "magnetization" of the plasma. Without collisions, β goes to infinity and $\mu_\perp$ and $D_\perp$ go to zero. In this case, all transport comes from the guiding center drifts, $\vec{v}_E$ and $\vec{v}_D$.

2.10.3 Perpendicular Transport due to Guiding Center Drifts

The terms $\vec{v}_E$ and $\vec{v}_D$ in Equation 2.122 are, respectively, the $\vec{E}\times\vec{B}$ drift and the diamagnetic drift. Let us assume a field geometry similar to that found in a Hall thruster, $\vec{B} = B_r$, where the coordinate system is (r, z, θ). Let x correspond to z, and y correspond to θ, such that $\vec{v}_\perp = \vec{v}_z + \vec{v}_\theta$. Then, the velocity terms resulting from these terms may be written,

$$\vec{v}_z = \frac{\beta^2}{1+\beta^2}\left(\vec{E}_\theta B - \frac{KT}{eB}\frac{1}{n}\frac{dn}{r d\theta}\right) \tag{2.124}$$

and

$$\vec{v}_\theta = \frac{\beta^2}{1+\beta^2}\left(-\vec{E}_z B + \frac{KT}{eB}\frac{1}{n}\frac{dn}{dz}\right). \tag{2.125}$$

The first equation shows drift in the axial direction. If variations in θ are not modeled, then $\vec{v}_z = 0$. The second equation shows drift in the azimuthal direction. The first term of the second equation yield the Hall current, $j_\theta = -neE_z/B$. Thrusters with "closed electron drift" are called "Hall" thrusters. This is why.

Note that if β^2 is large, then collisions do not affect the drift velocities. Also, note that the diamagnetic drift is proportional to KT/eB. This is also the form of "Bohm" diffusion,

discussed in Section 2.10.5.

2.10.4 The Meaning of Mobility and Diffusion

Without collisions ($\beta = \infty$), the first two terms in Equation 2.122 go to zero. Without guiding center drifts ($\vec{v}_E = \vec{v}_D = 0$), the particles would be trapped on the magnetic field lines. With collisions, the particles migrate across $\vec{B}$ to the wall along the density gradients in a random walk process; the guiding centers move in collisions and the particles diffuse in the direction opposite ∇n.

If $\beta >> 1$, the mobility and diffusion coefficients are well represented by

$$\mu_\perp = \mu\frac{\nu^2}{\omega_c^2} = \frac{\mu}{\beta^2} \quad D_\perp = D\frac{\nu^2}{\omega_c^2} = \frac{D}{\beta^2} \tag{2.126}$$

In this case, transport across $\vec{B}$ is proportional to the electron collision frequency, ν_e. The step length is the magnitude of the Larmor radius. When the magnetic field is increased, the Larmor radius decreases and the flux decreases, too. When $\beta << 1$, the magnetic field has little effect on transport, which can be described by Equation 2.111.

Note that for $\nu << \omega_{ce}$, $D_\perp = \nu\frac{KT}{m\omega_{ce}^2}$. If we let $v_\perp^2 = 2KT/m$, this reduces to $D_\perp = \frac{1}{2}\nu v_\perp^2/\omega_{ce}^2$. In the next section, we obtain the same result through a simple model.

Simple Model of Diffusion across $\vec{B}$

In a magnetic field, the effect of a random scattering event (as from a collision) is to move the center of gyration in a random direction through a vector distance $\vec{\delta r}$ such that $0 < |\delta r| < 2r_{ce}$, where $r_{ce} = v_\perp/\omega_{ce}$ is the gyro radius. On average, for a 90 degree collisions, $\Delta r^2 = (\Delta x)^2 + (\Delta y >^2 = 2r_{ce}^2$. (See Figure 2-11).

Let the collision frequency be ν. If τ is time, the mean square distance diffused after $N = \nu\tau$ steps is then

$$< |\Delta r|^2 >= N|\delta r|^2 = N2r_{ce}^2 = 2\nu\tau\frac{v_\perp^2}{\omega_{ce}^2}. \tag{2.127}$$

For 2D diffusion ($d = 2$) in the plane perpendicular to the magnetic field, $D_x = D_\perp = 1/4\tau < (\Delta r)^2 >$ such that

$$D_\perp = \frac{1}{2}\nu\frac{v_\perp^2}{\omega_{ce}^2}. \tag{2.128}$$

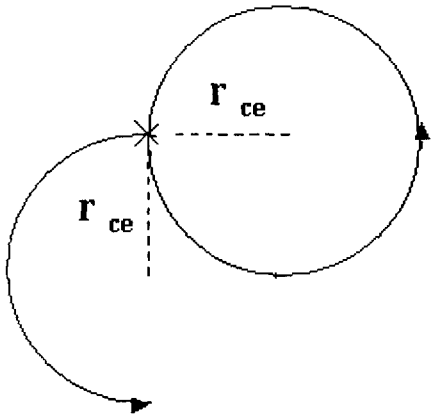

Figure 2-11: *A ninety degree electron-neutral collision*, for which $\Delta r^2 = (\Delta x)^2 + (\Delta y >^2 = 2r_{ce}^2$.

2.10.5 Anomalous Diffusion

Observed levels of electron transport in SPT type Hall thrusters are not explained by classical electron-neutral diffusion and mobility alone. To explain reality, theorists have turned to "anomalous" sources of transport. In the SPT, one possible mechanism for anomalous transport is secondary electron emission due to electron and ion impacts with the walls. However, this mechanism should not be important to TAL thrusters, which have metallic walls. For more discussion of secondary emission, see Section 2.12.5. Other sources of "anomalous" transport applicable to all types of Hall thrusters are the guiding center drifts discussed in Section 2.10.3. Anomalous is in quotations because there is really nothing anomalous about these mechanisms.

Bohm Diffusion

Laboratory plasmas often show diffusion rates not explained by classical diffusion. In nuclear reactor experiments, Bohm and others observed that $D_\perp$ usually has a $\frac{1}{B}$ dependence. Bohm introduced the following semi-empirical relation to describe the observed diffusion:

$$D_B = D_\perp = \frac{1}{16}\frac{KT_e}{eB} = \frac{1}{16}\frac{T_{ev}}{B}[\frac{m^2}{s}]. \tag{2.129}$$

The last result comes from $KT/e = T_{ev}$, which is only true in MKS units. Anomalous diffusion following this form is often termed "Bohm Diffusion." The factor of 1/16 is only approximate and may vary by several factors of 2. If we take $v_{th}^2 = 2KT/m$, then

$$D_B = D_\perp = \frac{1}{32}\frac{v_{th}^2}{\omega_{ce}}. \tag{2.130}$$

Wall effects, convective ExB convective cells, and oscillating electric fields resulting from unstable plasma waves have been proposed to explain Bohm diffusion [6].

If both anomalous Bohm diffusion and classical diffusion are present, what is their relative magnitude? The classical result for a weakly ionized gas in a magnetic field is $D_\perp = \frac{KT}{m}\frac{\nu}{\omega_{ce}^2}$, while $D_B = \frac{1}{16}\frac{KT}{m}\frac{1}{\omega_{ce}}$ such that

$$\frac{D_\perp}{D_B} \approx \frac{\nu_{en}}{\omega_{ce}} \times 16. \tag{2.131}$$

If $\nu_{en} = n_n v_e Q_{en}$ and $v_e \approx \sqrt{\frac{8KT}{\pi m}}$, then (in MKS units)

$$\frac{D_\perp}{D_B} \approx \frac{n_n\sqrt{T_{ev}}Q_{en}}{B}\sqrt{\frac{m}{e}} \times 26. \tag{2.132}$$

Aside from constants,

$$\frac{D_\perp}{D_B} \sim \frac{n_n\sqrt{T_e}}{B}, \tag{2.133}$$

where we note that Q_{en} is a weak function of temperature and is approximately $2.2 \times 10^{-19}m^2$ for temperatures of interest. In regions where the magnetic field is strongest, classical diffusion is expected to provide less diffusion proportionally than in areas where the field is weakest. What range of n_n, T_e, and B are required in order for these terms to be comparable? In the anode region of the TAL thruster, $n_n \approx 7 \times 10^{20}m^{-3}$, $\sqrt{T_{ev}} \approx 5$, $B \approx .5$ Tesla and $Q_{en} \approx 2.2 \times 10^{-19}m^2$. Also, in Hall thrusters, D_B seems to be better approximated using the coefficient 1/64 than with 1/16 (see next section). Therefore, $D_\perp/D_B \approx 2/5$. If Bohm diffusion is present in this region, then it should be comparable to classical diffusion. Both classical and anomalous diffusion (if present) should contribute significantly to electron transport!

2.10.6 Coulomb Collisions and Electron Transport

As stated earlier, this simulation models electrons at all ranges of energy, at some of which the cross sections for electron-ion and electron-electron collisions are orders of magnitude larger then the cross section for electron-neutral collisions (the cross sections are estimated in Section 2.8.5).

Coulomb collisions are not expected to produce much bulk transport precisely because they occur at low energies, i.e. low electron velocities. However, some transport will result. Furthermore, Coulomb collisions will influence the electron energy distribution function; they produce transport in *velocity* space. Therefore, the simulation must include them.

Coulomb collisions are modeled using both a standard Monte Carlo Collision (MCC) approach described in Section 3.15.4 and a diffusive model described in Section 3.16. Results obtained using both models are presented in Chapter 5.

2.11 The Extent of the Ionization Layer

Grishin and Leskov present a simple method for estimating the extent of the anode layer. Let τ be the time of flight of the average electron through the anode layer of thickness L,

$$\tau \approx \frac{L}{< v_e >_\perp}. \tag{2.134}$$

If the plasma is magnetized, then the mobility is determined by the classical formula, such that

$$\tau \approx \frac{L}{\mu_\perp E} \approx \frac{L^2}{\mu_\perp \Delta\phi}, \tag{2.135}$$

where $\Delta\phi$ is the potential difference across the layer. If the steady state rate of electron drift from the layer is equal to the ionization rate, then $\tau\nu_i \approx 1$, where ν_i is the ionization rate. Thus,

$$L^2 = \frac{\mu_\perp \Delta\phi}{\nu_i} = \frac{m\Delta\phi}{eB^2}(\frac{\nu_e}{\nu_i})^2. \tag{2.136}$$

We can rationalize this through the scale length R_L, defined by

$$R_L \approx \sqrt{\frac{e\Delta\phi}{m}}\frac{1}{\omega_{ce}}. \tag{2.137}$$

In terms of R_L, the extent of the layer is

$$L \approx R_L \sqrt{\frac{\nu_e}{\nu_i}}. \tag{2.138}$$

Note that R_L takes the form of the electron Larmor radius, but is determined by half the potential difference across the anode layer; it is higher than the average Larmor radius of the electrons in the simulation by a factor of $R_L / < r_L > \approx \sqrt{\Delta\phi / 2T}$. Also note that this result is not a function of $< v_n >_z$.

Let us now step away from Grishin and Leskov. Figure 2-8 shows temperature averaged cross sections for electron-neutral scattering. If the temperature of the electrons in the anode layer is about 25 eV, this figure says the total scattering frequency is about ten times the ionization frequency, meaning that L should be about twice R_L. Also, $R_L / \bar{r}_L \approx \sqrt{300/50} \approx 2.5$. Thus, Equation 2.138 says the anode layer should be 5-10 electron cyclotron radii wide. Since the electron cyclotron radius is about .005 cm (see Table 2.12), the width of the ionization zone is on the order of .05 cm.

In an anode layer thruster, diffusion is thought to be determined primarily through electron neutral collisions. In this case, ν_e is well represented by the total electron neutral collision frequency. In an SPT type thruster, which has dielectric walls, diffusion is thought to be increased by wall effects, increasing the electron mobility. In this case, ν_e may be thought of as an effective collision frequency. As this effective frequency increases, so should the extent of the ionization layer. Let us make Equation 2.138 more general:

$$L = R_L \sqrt{\frac{\omega_c}{\nu_i \beta}}. \tag{2.139}$$

We have introduced the Hall parameter, β. Anomalous diffusion may be taken into account by modifying β. Note that Equation 2.139 does not change if both ν_e and ν_i are multiplied by the same constant $1/\sqrt{f}$. This means that the method for increasing electron transport described in Section 2.6.2 should not change the length of the acceleration zone.

2.12 Boundary Conditions for Particle Impact

Following is a brief discussion of the rationale behind the boundary conditions applied in this simulation. For more discussion of the numerical method, See Section 3.18.

Many details of gas-surface interactions are still unknown, but models which reproduce the important features have been developed. Common solutions divide particle reflection from solid surfaces into two classes: specular and diffuse. Figure 2-12 illustrates the difference. A given interaction may be described by one of these classes, or a combination of both [35].

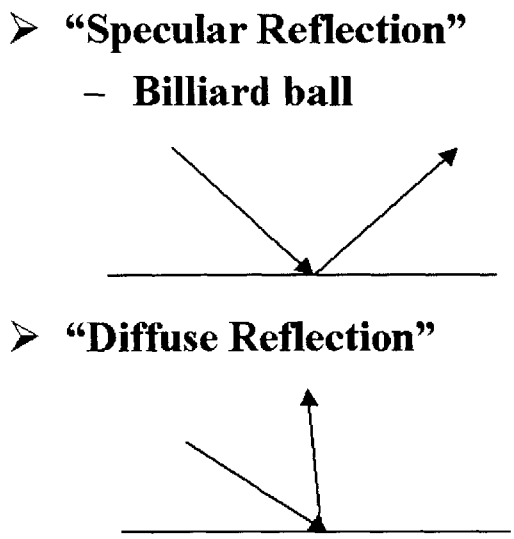

Figure 2-12: *Reflection off boundaries is specular or diffuse.*

2.12.1 Specular Reflection

In specular reflection, a particle bounces off a surface like a billiard ball, but without loss of energy. The normal component of momentum is reversed, and the tangential component is unchanged. This is intended to model an interaction with a perfectly smooth (frictionless) surface. It may also be used to model a symmetry plane.

2.12.2 Diffuse Reflection

In diffuse reflection, the impinging particle is re-emitted without regard to its thermal state. Thus, a high speed particle gives up a portion of its energy to the surface. In full thermal and momentum accommodation, the outgoing velocity may be assigned according to a half-range Maxwellian at the surface temperature. An "accommodation coefficient" may be defined in terms of the incident and reflected energy fluxes, q_i and q_r, and the energy

carried away in diffuse reflection at the wall temperature, q_w;

$$a_c = \frac{q_i - q_r}{q_i - q_w}. \tag{2.140}$$

A coefficient of $a_c = 0$ implies specular reflection, while $q_c = 1$ implies diffuse reflection.

According to Bird, experiments with "engineering" surfaces in contact with gases at normal temperatures indicate that the reflection process approximates diffuse reflection with complete thermal accommodation [4]. Bird also states the diffuse assumption must be "critically reviewed" if the surface is a smooth metal which has been out-gassed through exposure to high vacuum and high temperatures, or if the translational energy of the molecules relative to the surface is more than several electron volts.

Oh built a hybrid PIC model of a Hall thruster plume. In doing so, he assumed semi-specular reflection of neutrals at surfaces, stating that the their temperatures were unknown [33]. This means he retained the magnitude of the neutral velocity (no accommodation of energy), but scattered the direction (full accommodation of momentum).

Piekos used DSMC methods to model micro-mechanical devices, which often contain surfaces cut along silicon crystal planes [35]. Such surfaces have accommodation coefficients less than one. Piekos used a random number generator to describe the accommodation coefficient; if the random number was less than a_c, then reflection was specular, and if greater, then reflection was diffuse.

2.12.3 Application to mini-TAL

The mini-TAL contains out-gassed metal surfaces exposed to high temperatures. However, ion bombardment will sputter the surfaces, leaving them microscopically rough. Thus, low velocity particles should scatter diffusely.

Neutrals

Neutrals rarely impact with more than 1 eV of energy. Therefore, we assume full accommodation in both energy ($a_c = 1$) and momentum. Numerically, all neutrals which impact are re-emitted according to a half-Maxwellian at the wall temperature, assumed to be 700 Kelvin. A thermal model would yield a better estimate of wall temperature.

Note: Charge exchange neutrals are *not* low velocity, but they are uncommon. In

Chapter 6, "Conclusions," we recommend modifying the boundary conditions to allow for partial accommodation of high energy neutrals. Accommodation coefficients less than one could be simulated by using random numbers as per the method of Piekos [35].

Ions

In contrast to most neutrals, ions may impact the wall with tens or even hundreds of electron volts of energy. Plasma fusion modeling experience indicates that the ions give up, on average, about half their kinetic energy to the wall [1]. (During recombination, the wall gives up energy as electrons are extracted from the lattice, but also receives kinetic energy and energy liberated during recombination. See the next section for further discussion.)

Numerically, an ion which impacts disappears and a neutral is created with one half of the ions initial kinetic energy, but in a random direction. The particle is thus partially accommodated ($a_c = .5$) in energy, and fully accommodated in momentum. This may be likened to the method of Oh.

2.12.4 Energy Loss to Walls

As stated above, energy is liberated when particles collide with surfaces of the thruster. This heat flux is of interest to engineers. The wall receives half the ion kinetic energy flux, $\dot{q}_i$ (recall, $a_c \approx 0.5$). The wall also receives, for each impacting ion, an additional $E_i = 12.1$ eV (in the case of singly charged Xenon), liberated during recombination. However, the neutralizing electron must be extracted from the lattice at an energy cost equal to the work function, $e\phi$. So, the net is $e(V_i - \phi)$ per ion. To this, we must add the entire electron kinetic energy flux, $\dot{q}_e$; electrons are entirely absorbed when they impact. Secondary electron emission, which would give back some of this energy, is not currently modeled. Neutrals also give up energy to the walls, but this energy will not be statistically significant unless the neutral gas temperature is much higher than the wall temperature, which is not assumed to be the case in this thruster. Thus we may write

$$\dot{Q}_{wall} \approx \int \frac{1}{2}\,\dot{q}_i + (E_i - e\phi)\,\dot{n}_i + \dot{q}_e\,ds, \tag{2.141}$$

where $\dot{Q}_{wall}$ is total energy flux to the wall (the power absorbed by the wall), $E_i = 12.1eV$ is the first ionization energy of Xenon, and $\dot{n}_i$ is the number flux of ions to the wall. In

addition, metastable atoms or ions also deliver their excitation energy. However, we do not keep track of these.

Work Functions

Measurements of electron work functions of the elements vary, depending on the source. The body of the mini-TAL is made of Mo and steel. For Mo, the Handbook of Chemistry and Physics [20] lists photoelectric work functions of 4.15 and 4.34 eV, for an average value of $< \phi > \approx 4.25$ eV. For Fe, the same source lists photoelectric work functions of 3.91, 3.92, 4.72, and 4.77 eV, for an average value of $< \phi > \approx 4.33$ eV. Based on the degree of variation in measurements, it seems reasonable to assume a value of $< \phi > = 4.3$ eV for both.

2.12.5 Secondary Electron Emission

Secondary electron emission due to electron and ion impact with the anode and thruster body is ignored in the numerical model; we assume that secondary emission from ion impact is insignificant, and that secondary electrons from electron impact do not have enough energy to overcome the sheath and make their way into the plasma. However, inclusion of secondary emission would make the simulation more physically realistic. Here, we discuss some types of secondary emission which could be included.

Secondary Electron Yield due to Electron Impact

The secondary electron yield δ due to electron impact is defined as the ratio between the total number of emitted electrons and the total number of primary electrons. Values of the peak secondary electron yield for Mo and Fe are taken from McDaniel [30] and reproduced in Table 2.13. At very low and very high energies few secondary electrons are ejected, but the yield is larger at intermediate energies and may exceed unity there. At low primary energies the energy of many secondary electrons is less than the work function at the surface; they cannot escape. At high energies, most secondary electrons are produced deep within the target; they loose so much energy in collisions with other electrons before reaching the surface that they cannot escape either. In general, insulators have extremely high yields. This happens because of quantum effects which keep electrons from dissipating their energy in collisions with other electrons as they work their way toward the surface [30]. McDaniel

reports maximum yields as high as $\delta_{max} = 24$, for NaBr, and as low as $\delta_{max} = 1.5$ for Al_2O_3 and $\delta_{max} = 2.4$ for SiO_2 (Quartz).

Since secondary yields due to electron impact are, for high energy electrons, on the order of $\delta = 1$, this phenomenon may be quantitatively significant and could be included to generate a more realistic sheath model. (A more detailed analysis must be conducted to determine the yield below E_{p+}.) Elastic backscattering could also be included. A model for the energy distribution of secondary electrons would be required. According to McDaniel, for primary energies between 20 and 1000 eV, the energy distribution of the "true" secondary electrons (those within the range 0-50 eV) is almost independent of the primary energy and has a common shape. The maximum for metals generally lies between 1.4 and 2.2 eV. The curve drops off with energy, but is still 25 percent of its peak value at 25 eV. *A large fraction of secondary electrons produced at the wall might escape the sheath.* Secondary electrons produced at the anode, however, seem likely to fall straight back.

Symbol	δ_{max}	E_{p0}	E_{p+}	E_{p-}
Fe	1.3	400	120	1400
Mo	1.25	375	150	1300

Table 2.13: Values of the peak secondary electron yields δ_{max} and the primary electron energies E_{p0} at which they occur for different metals. Electron energies E_{p+} and E_{p-} at which the yield equals unity are also included. These values are reproduced from McDaniel [30], who reproduced them from another source.

Secondary Electron Yield due to Ion Impact

Secondary electron yield for ion impact results from a phenomenon called potential ejection. This involves electronic interaction between the incoming ion and the conduction electrons of the metal while the ion is a few Angstroms from the surface. The discussion here is condensed from McDaniel [30], who, in turn, cites the work of H. D. Hagstrum (references in McDaniel). Hagstrum collected data on electron yield versus bombarding energy for Xe^+ on atomically clean Mo. The data is presented in terms of γ_i, the secondary electron yield per primary electron. At energies between 0 and 1000 eV, the yield for Xe^+ on Mo is about $\gamma_i = .02$, while the yield for Xe^+ on W is about $\gamma_i = .015$. Significantly, the yields are nearly independent of the kinetic energy of the ions! For Xe^{2+} in the range $0 < E_p < 400$ eV, γ_i varies between .3 per ion (near $E = 0$) and .2 per ion (near $E = 400$).

Since only Xe^+ is currently modeled, for which $\gamma_i \approx .02$, emission of secondary electrons due to ion impact is quantitatively insignificant and can be ignored. However, if the simulation is expanded such that multiply charged Xenon is modeled, for which $\gamma_i \approx .25$, then ion impact should be included. A model for the energy distribution of the secondary electrons would again be required.

2.13 Wall Potential and Sheath Formation

Over most of the simulation region, the sheath near the wall is calculated self-consistently by the potential solver and particle moving algorithm. The potential of the conducting wall is determined by the amount of charge collected and a pre-determined capacitance. (The potential at an insulator may be computed in a similar fashion by simply collecting the charge along the boundary.) An analytic model is only used to apply boundary conditions for the potential on the portion of the simulation boundary parallel to and most distal from the centerline (in the upper right hand corner). An alternative would be to apply the condition $E_r = 0$ at that boundary.

2.13.1 Insulators, Conductors, and Capacitance

The macroscopic aspects of the response of material bodies to electric fields can be described by dividing the bodies into two classes, insulators and conductors. A conductor is a substance inside which there is no electric field and no polarization, in static situations. An insulator is a substance in which the polarization at each point is some function of the electric field at the same point. Of course, these two classes are limiting cases; in between there is a whole range of bodies with finite conductivity.

In a perfect conductor, in an electrostatic situation, all parts of the conductor will be at the same potential, since the field inside it is zero. For zero current only, if there are outside distributions of charge and polarization that would tend to cause different parts of the conductor to be at different potentials, the electrons in the conductor will move until the potential produced by them combines with the externally produced potential to give zero field and a constant potential throughout the conductor [23]. In general, this requires non-uniform distribution of charge over the surface. In dealing with conductors, the charge is usually treated as a surface charge. Thus, the net charge maintained on a surface may

be written

$$Q_s = \int q_s ds. \tag{2.142}$$

The term capacitance may be used in several different ways, but it always refers to a charge that will produce a unit potential. If a conductor is not isolated, its potential is influenced by any outside charges or polarization in its neighborhood. However, if a conductor is isolated, its potential is determined by its own charge only. In the case of an isolated sphere of radius R, the capacitance is given by

$$C = 4\pi\epsilon_o R. \tag{2.143}$$

Thus, the surface potential of a sphere holding charge Q_s may be written

$$\Phi_s = \frac{Q_s}{C}. \tag{2.144}$$

In the case of mutual capacitance (e.g. an electrical capacitor), two conductors are essentially isolated from the outside. In this case, the capacitance is the charge on one conductor divided by the difference in potential, when the two conductors have equal and opposite charges [23].

2.13.2 Wall Potential

In the simulation, the potential of the conducting wall at time t with respect to spacecraft ground, $\phi_w(t)$, is determined by the amount of charge held by the wall and the capacitance of the wall;

$$\phi_w(t) = \frac{Q(t)}{C}. \tag{2.145}$$

(This approach is electrostatic; we assume charges in the wall re-arrange themselves instantaneously at each time-step.) The charge in the wall starts at zero at the beginning of the simulation, but changes over time according to the net charged particle flux into the wall;

$$Q_{wall}(t) = e \int \int (\dot{\Gamma}_i - \dot{\Gamma}_e)\, ds\, dt. \tag{2.146}$$

The potential of the wall eventually comes to a state of quasi-equilibrium with the plasma. In this state, $\Gamma_e \approx \Gamma_i$ such that ϕ_w oscillates about some mean, $< \phi_w >$, which is constant

over time.

We used the program Maxwell^{TM} to estimate the capacitance, C, of the thruster body. This involved entering the geometry of the entire thruster body and assuming that the thruster was isolated from its surroundings. Maxwell predicted that $C \approx 1.62 \times 10^{-12}$ Farads (Coulombs/Volt). This is equivalent to the capacitance of a sphere of radius $R \approx$ 14.5 mm. The Maxwell estimate seems reasonable, since the outer radius of the main thruster body is 9.7 mm. To increase stability, we actually use a larger capacitance, e.g. $C = 1 \times 10^{-10} F$. This is equivalent to placing an additional capacitor between the floating body of the thruster and the spacecraft. In Chapter 4, we show that the choice of C (within reason) does not change $< \phi_w >$ or overall thruster performance if the quasineutral method of electron injection is applied.

Implementing the wall potential is numerically simple. We merely track the net charge which has impacted the wall, $\hat{Q}$. Each electron which impacts contributes charge $\Delta\hat{Q} = -1$, while each ion contributes charge $\Delta\hat{Q} = +1$ (or $\Delta Q = +Z$, if multiply charged Xenon is included). No secondary electron emission is modeled. Then, in normalized units,

$$\hat{\phi_w} = \frac{\hat{Q} \times e \times [size]}{C[T_{ev}]}, \tag{2.147}$$

where C is in Farads, $[size]$ is the size of a super-particle, $e = 1.6 \times 10^{-19}$ Coulombs, and $\hat{\phi}$ is some multiple of $[T_{ev}]$.

Chapter 3

The Numerical Method

This simulation employs the Particle-In-Cell (PIC) and Monte Carlo Collision (MCC) methodologies to simulate a collisional plasma [50]. All particles are treated kinetically; their trajectories are followed as they move within a computational grid. Charged particles experience electric and magnetic forces according to Maxwell's equations. Electrons also experience electron-neutral and Coulomb collisional forces. Various other collision processes are also modeled. The simulation is nominally explicit (as opposed to implicit), meaning that most quantities which affect the motion of a given particle are sampled from the previous time-step.

3.1 The Particle-In-Cell Methodology

The Particle-In-Cell (PIC) methodology is used to apply forces to particles. The general concept is illustrated in Figure 3-1. In essence, the forces experienced by charged particles can be modeled via a grid. Forces are calculated at the grid nodes and interpolated to the particles which reside within. Particles are shielded from other particles beyond the Debye length, λ_D; this determines the grid spacing.

Figure 3-2 is a generic flow chart of the method. First, particles are weighted to a computational grid at time t to determine the charge density and other particle moments. Next, the electric potential and field are calculated on the grid. Then, both electric and (pre-computed) magnetic fields are weighted back to the particles, which are time-stepped forward to $t+1$ according to a leapfrog scheme. Then, the cycle begins again. Convergence of the simulation is determined by the rate at which parameters of interest change.

This methodology did not spring full grown from the head of Zeus. It is a well known method in plasma physics. Entire books are devoted to the subject. One of the best known is Reference [5].

Many PIC schemes are possible. Our modus operandi is nominally momentum conserving. The computational grid is structured and non-Cartesian. The coordinates on this grid are mapped to a set of Cartesian computational coordinates according to the method of Reference [45]. Particles are interpolated to nodes according to area weighting in computational coordinates. Forces are weighted back according to the same scheme. Other interpolation schemes are possible. Each has advantages and disadvantages.

3.2 The Monte Carlo Methdology

Systems wherein a time dependent random variable exists are called stochastic. Our thruster is one such system. Collisions in this simulation are considered Markov processes. This means that the conditional probability of a collision occurring is determined by knowledge of the most recent condition only, e.g. the probability of an electron colliding with the neutral background at time t is determined by the electron velocity $v(t)$ and the background density $n_n(r, z, t-1)$. The neutral density at time $t-2$ is not relevant. Brownian motion as derived by Einstein is a Markov process.

Large angle, stochastic, Markov collisions may be modeled with a Monte Carlo methodology. The basic idea of the Monte Carlo method is as follows:

- For each particle of species α, the probability of a collision in Δt with species β is computed; $p_{\alpha,\beta} = fn(n_\beta, v_{\alpha,\beta}, Q(v_{\alpha,\beta}))$.
- The probability $p_{\alpha,\beta}$ is then compared to a random number ξ to determine whether an event takes place.
- If an event occurs, the momentum of the primary particle changes discontinuously by some (vector) amount which must also be determined randomly.

The result is diffusion not unlike that due to Brownian motion.

Many Monte Carlo methods are possible. Those relevant to this discussion are the Monte Carlo Collision (MCC) method, and the Direct Simulation Monte Carlo (DSMC) method. The MCC method assumes that the test particle is traveling at much higher

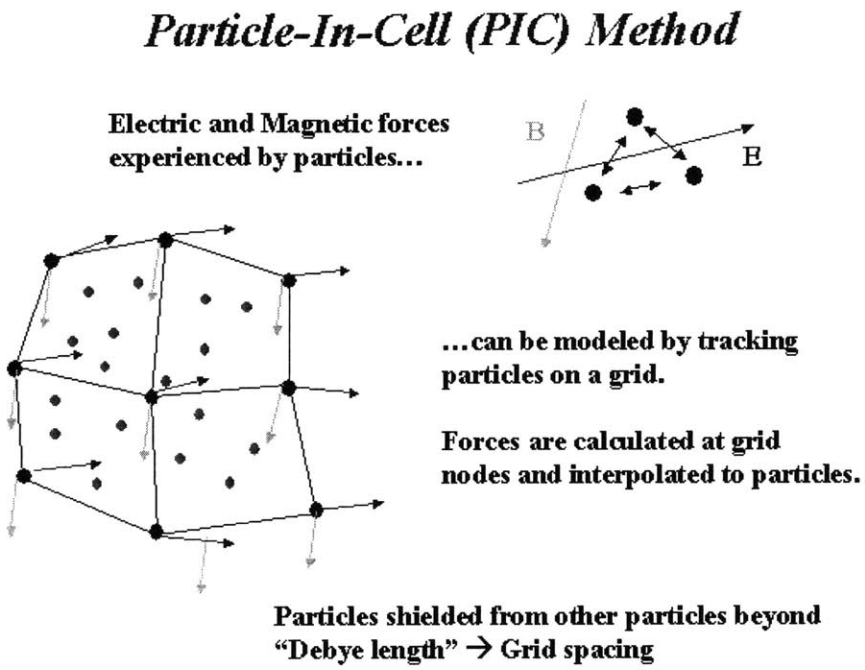

Figure 3-1: *The general concept underlying Particle-In-Cell(PIC) simulations.*

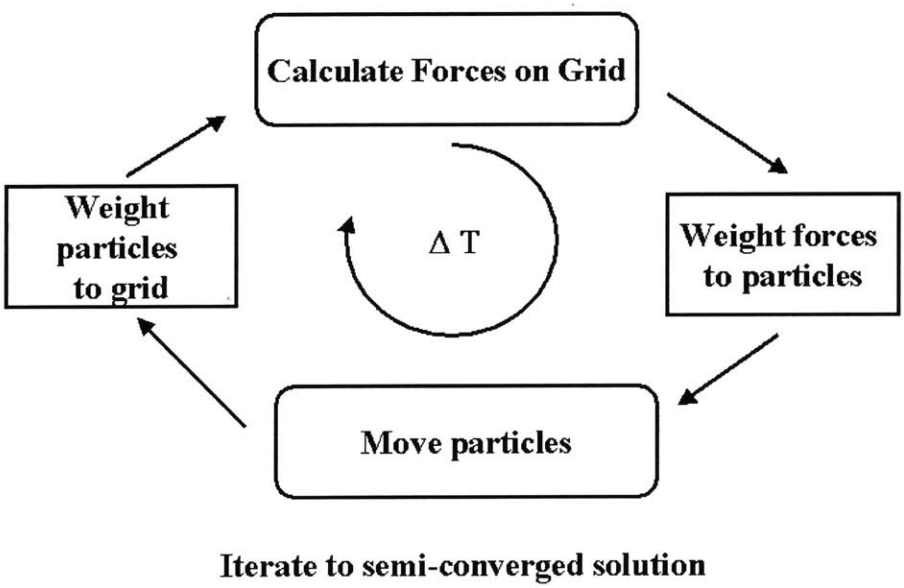

Figure 3-2: *Flow chart of the PIC method.*

velocity than the background species. Thus, the test particle scatters of the background. The DSMC method chooses two particles and collides them explicitly. This is required to model self-collisions (e.g. neutral-neutral collisions) where the collisions significantly affect the background distribution. Note that the terminology is not well defined; Bird seems to apply the term DSMC to MCC as well [4].

In this simulation, electron diffusion across magnetic field lines occurs primarily through a series of large angle collisions. Since electrons are much faster than neutrals, the MCC method is appropriate for electron-neutral scattering. The MCC method may also be used for ion-neutral scattering. We also use MCC to model electron-ion and electron-electron scattering, although the latter especially could be better modeled using DSMC. There is, however, a alternative approach to Coulomb collisions which is based on the Langevin equation, described in the next section.

3.3 The Langevin Equation

When Langevin re-derived Brownian motion, he introduced a form of equation now bearing his name [11]. A Langevin equation, in its simple form, has a steady and a stochastic term. A simple example is

$$\frac{dx}{dt} = a(x,t) + b(x,t)\xi(t) \tag{3.1}$$

where $\xi(t)$ is a rapidly fluctuating random term having the properties $< \xi(t) >= 0$ and $< \xi(t)\xi(t') >= 0$, $t \neq t'$ (there is no correlation between times). The random term is essentially white noise. A form of the Langevin equation is used to model the diffusion in velocity space due to Coulomb collisions (see Section 3.16).

3.4 Code and Data Structure

The simulation is written in C. The general methodology is visualized in Figure 3-3. The basic structure of the code is as follows:

- Pre-computation:
  - Calculate time-invariant magnetic field
  - Make Grid
- Call "pic"

- Initialize variables
- Calculate normalization constants based on nominal conditions
- Load grid and normalize
- Assign boundary materials
- Load particles
- Get moments of initial distribution (density, bulk velocity, temperature)
- Interpolate magnetic field to grid
- Iterate
  * Calculate charge distribution and other particle moments
  * Solve Poisson equation for electric potential
  * Calculate electric field
  * Save intermediate data (periodic)
  * Neutral loop
    · create neutral stream at anode
    · delete neutrals ionized
    · add momentum and energy from ion-neutral collisions
    · move particles
    · apply boundary conditions
    · sweep up excess particles (periodic)
  * Ion loop
    · make charge exchange ions and neutrals (MCC)
    · scatter ions off neutrals (MCC)
    · move particles
    · apply boundary conditions
    · create neutrals due to wall recombination
    · collect charge at walls
  * Electron loop
    · apply electron-neutral MCC collisions
    · apply Coulomb collisions
    · apply Bohm collisions (if applicable)
    · move particles
    · apply boundary conditions
    · collect charge at walls
    · create new ions and electrons
  * Sum kinetic and potential energies
- Post-process data
- Save data
- Clear variables

• Post-process data

- Performance

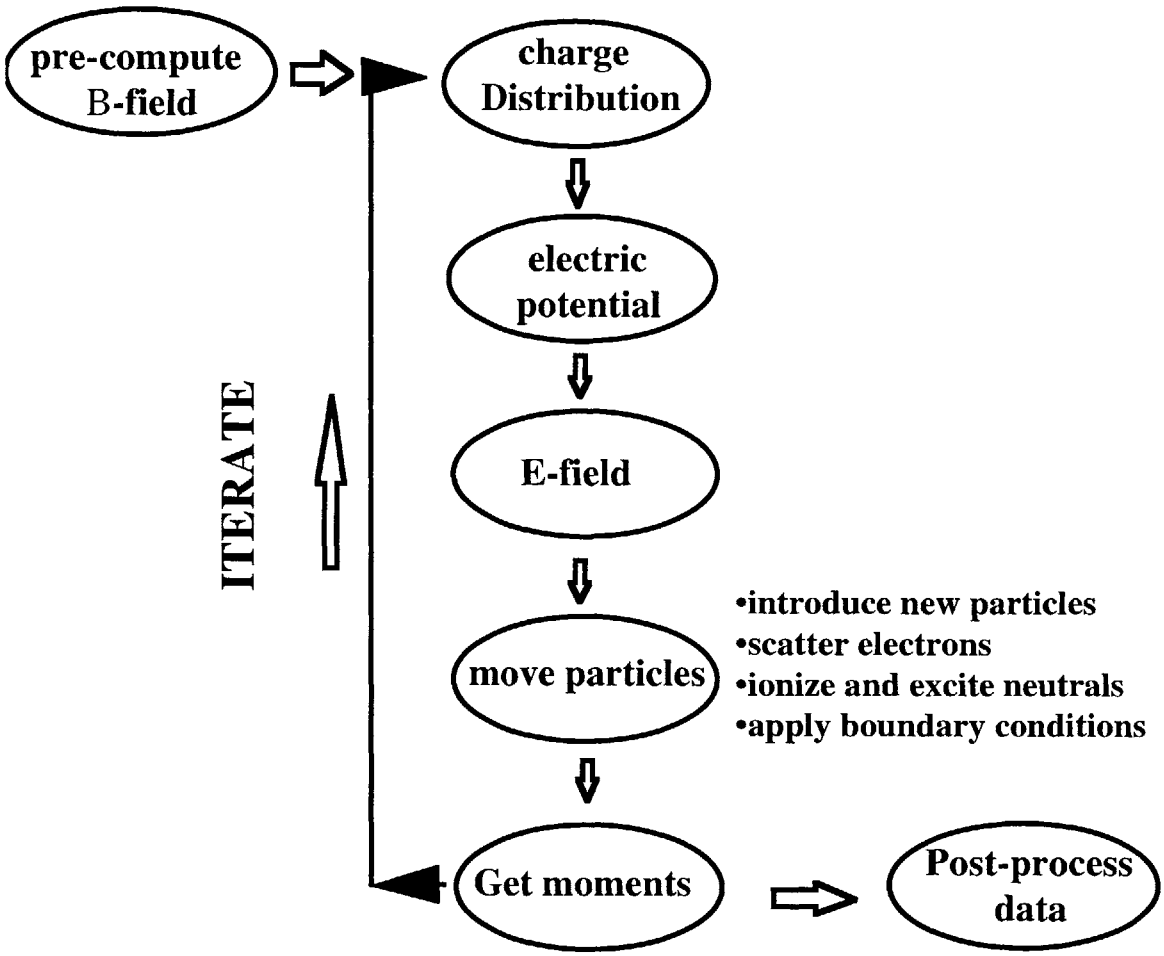

Figure 3-3: *The full PIC MCC methodology.* Particles are weighted to a grid on which the electric potential and field are calculated. Forces are then weighted back to the particles. Most collisions are treated using the Monte Carlo method.

- Moments
- EEDF

Each species of particle (electrons, ions, neutrals) is stored in a separate linked list. Using linked lists allows flexibility. Particles may be added to or subtracted from the lists at almost any time. Memory is allocated dynamically, eliminating the memory overhead associated with an array. The size of a list can grow to the limits of the machine's memory. Drawbacks to using linked lists may include performance issues associated with trading memory in an out of the CPU cache [33]. Also, access to the middle of the list is limited, but this is generally not a problem since we work on one particle at a time. In fact, the code could be re-written to run on multiple processors at once. This is called "multi-threading."

Each structure in the linked list represents a single particle. The structure looks like this:

```
struct charged_particle {
  double r;              /* radial position */
  double z;      /* axial position */
  struct vectorjj v;  /* velocity (v.r, v.z, v.theta) */
  float mass;        /* normalized mass; 1 or M/m */
  short charge;  /* normalized charge; 0, 1, or -1
  short size;            /* statistical weight of particle; 1,2,...10 */
  short fate;  /* used for manipulating particles */
  short tag;  /* used to track individual particles */
  double xi;             /* computational coordinate, nominally axial */
  double eta;  /* computational coordinate, nominally radial */
  double p00;            /* interpolation fractions to the 4 corners of */
  double p11;            /* the cell where a given particle is located  */
  double p01;
  double p10;
  struct charged_particle *next;  /* memory location of next in list */
};
```

The structure contains the particle's position (z, r) , velocity (v_r, v_z, v_θ), mass (1 or M/m_e), charge (0,1,or -1), statistical weight or size (1-50), computational coordinates on the grid (xi,eta), and weighting constants to the four corner nodes of the cell in which the particle resides $(P_{00}, P_{11}, P_{01}, P_{10})$. The structure also contains room for tags (fate, tag) which can be use to track, for instance, whether a particle was created through charge exchange or whether it was created at the wall. The last entry is the memory location of the next particle in the list. The list is accessed by storing the memory location of the first particle as a static variable and then following the trail to the next particle until the end of the list is reached.

3.5 Initializing the Simulation

Before the simulation begins, we stipulate the mass flow rate, $\dot{m}$, the nominal neutral temperature, T_n, the nominal plasma temperature, T_e, the nominal number of particles we wish to follow in the simulation, TARGET, and the initial statistical weight of each neutral super-particle, s_o.

At initialization, the simulation estimates the nominal neutral and plasma densities. The method is described in Chapter 2. The neutral density, TARGET, and s_o yield $[size]$, the number of particles each super-particle of statistical weight $s = 1$ represents. The nominal plasma density and frequency are then calculated, yielding the normalization constants [x],[t],[E],[B], etc. Then the grid is loaded and converted to normalized units, old particle data is loaded, and the pre-computed magnetic field is loaded and converted to normalized units.

Output from the code as it initializes is found in Appendix A.

3.5.1 Important Note on Units

Unless otherwise noted, the nominal temperature used in scaling figures presented in this chapter was $[T_e] = 50$ eV, the nominal mass flow rate was $\dot{m} = .13mg/s$, the nominal plasma density was $[n_e] = 9 \times 10^{12} cm^{-3}$, and the free space permittivity constant was 100 times higher than physical. Thus the nominal Debye length for most figures is $[x] = .018cm$, while the nominal time-step is $[t] = 5.9 \times 10^{-11}$ sec. Bear in mind that the nominal $[x]$ and $[t]$ are 10 times larger than their expected physical values. Furthermore, values such as $[x]$ are only scales; the local Debye length λ_D may be smaller or larger than $[x]$.

3.6 Time-Step

The time-step Δt of the PIC scheme must be short enough to resolve all frequencies of interest. For stability and accuracy, we must resolve both the plasma frequency, $\omega_{pe} \sim 2 \times 10^{+10} sec^{-1}$ (after accounting for artificial permittivity) and the electron cyclotron frequency, $\omega_{ce} = 1.4\times \sim 10^{11} sec^{-1}$. It is not enough to resolve the nominal plasma frequency; we must resolve the local plasma frequency across the entire grid.

3.6.1 Leapfrog Stability Criterion

The leapfrog method used for particle pushing has error, with the error vanishing as $(\Delta t)^2$. When applied to a simple harmonic oscillator of radian frequency ω, there is no amplitude error for $\omega\Delta t \leq 2$ [5]. However, for $\omega\Delta t > 2$ the explicit finite difference approximation to Newton's laws of motions is unstable [19]. The time-step must, therefore, satisfy this leapfrog stability criterion:

$$\omega\Delta t < 2. \tag{3.2}$$

The phase advance for one step is given by [5]:

$$\omega_o\Delta t + \frac{1}{24}(\omega_o\Delta t)^3 + h.o.t. \tag{3.3}$$

For reasonably accurate integration of electron orbits, a time-step significantly less than $\omega\Delta t = 2$ is required, e.g. $\omega\Delta t = .7$. According to Birdsall, a choice of $\omega\Delta t \leq .3$ is required to accurately observe oscillations or waves for some tens of cycles.

3.6.2 Gyro Frequency Criterion

The B-field magnitude varies with position. Inside the center pole, the field strength is as high as 19300 Gauss (1.9 T). Let the field here be B_{max}. Over most of the simulation region, the magnitude is between 1500 and 3500 Gauss ($.08 < B/B_{max} < .18$). Near the poles, the field rises to about to about $5000 - 8500$ Gauss ($.26 < B/B_{max} < .44$) and even higher on the last line of nodes.

Corresponding to B_{max} there is a gyro frequency, ω_{max}. By satisfying the leapfrog stability criterion $\omega_{max}\Delta t < 2$, we ensure that $\omega_{ce}\Delta t < .36$ over much of the interior, which limits errors in rotation to about 1 percent (see Section 3.14). Near the center pole, $\omega_{ce}\Delta t$ is as much as 1, and errors can be ten percent. However, this only happens at the boundary; if electrons reach here, they will probably be destroyed anyway.

Hockney points out that electron drift should still be determined accurately with large time-steps, e.g. 9 per gyro motion or $\omega_{ce}\Delta t < .67$ [19].

3.6.3 Plasma Frequency Criterion

To resolve the plasma frequency across the entire grid, the leapfrog stability criterion requires $\omega_{pe}\Delta t < 2$ at each node. The required time-step at each iteration therefore depends upon the highest plasma frequency ω_{pe} in the simulation region. The local plasma frequency is (in normalized units)

$$\hat{\omega}_{pe} = \sqrt{\frac{\hat{n}_e}{\hat{n}_{e,o}}}, \tag{3.4}$$

where $\hat{n}_e$ is the local density and $\hat{n}_{e,o}$ is the nominal density. Allowing at least 2π steps per oscillation, and using the normalized unit system, we require $\Delta\hat{t} < \sqrt{\hat{n}_{e,o}/\hat{n}_e}$ everywhere. For more accurate integration, we require $\Delta\hat{t} < .3\sqrt{\hat{n}_{e,o}/\hat{n}_e}$ everywhere. This criterion is less stringent than the criterion imposed by the requirement to resolve the cyclotron frequency. After changing ϵ_o, the nominal plasma frequency is $\omega_{pe} \sim 2 \times 10^{-10} sec^{-1}$, which is actually 4-5 times slower than the nominal gyro frequency. This means the time-step is still (usually) limited by the gyro frequency; we lose half the speed we gained by increasing ϵ_o. On the other hand, we have better resolution of the plasma oscillations and can use coarser grids.

3.6.4 Numerical Heating Criterion

Another consideration when choosing Δt is stochastic (numerical) heating, as arises due to arithmetic rounding, the size of the time-step, the finite-differencing of the equations, and the use of super-particles. Hockney and others have quantified this heating for Charge-In-Cell systems like our own [19]. Hockney defines an optimum path to minimize heating;

$$(\omega_{pe}\Delta t)_{opt} = min[\frac{H}{2\lambda_D}, 1] \tag{3.5}$$

where H is the grid spacing. Again, this criterion must be applied across the entire grid. Recalling that $[v] = \lambda_D\omega_{pe} = v_{th}/\sqrt{2}$, the first term on the right hand side simplifies to

$$\frac{1}{2}\frac{H}{\lambda_D}\frac{1}{\omega_{pe}} = \frac{H}{v_{th}\sqrt{2}}. \tag{3.6}$$

Thus, the numerical heating criterion says that the grid spacing should be fine enough to resolve the motion of a typical particle at the local thermal speed. In normalized units we

may write

$$\Delta\hat{t} < min[\frac{\hat{H}}{2\sqrt{\hat{T}}}, \frac{\hat{n}_{e,o}}{\hat{n}_e}] \tag{3.7}$$

where $\hat{H}$ is the local grid spacing in nominal Debye lengths and $\hat{T}$ is the local temperature in normalized units ($T = \hat{T}[T]$). To apply this new criterion, we compute the electron temperature across the grid at each time-step. In practice, we again find that resolving the gyro frequency is usually the more stringent criterion.

3.7 Grid

A grid is required to perform computational plasma physics over a finite domain. Grid spacing should be fine enough to resolve a Debye length, in order to measure the charge density and thus calculate the electric field [5].

3.7.1 Elliptic Grid Generator

The location of the grid points determines a transformation between computational space and physical space. This transformation can sometimes introduce numerical errors. So called "grid metrics" can be used to measure the acceptability of a grid. One way to achieve reasonable grid metrics is by using an elliptic grid generator.

Numerous references discuss elliptic grid generation. Here we apply the method of Steger and Sorenson [48] as modified by [22] and [21]. First, we specify the locations of the boundary nodes (Neumann boundary conditions). Next, we generate an algebraic grid. Finally, we pass the node distribution iteratively through a set of elliptic equations until appropriate error criteria are met.

In computational fluids, orthogonality is often imposed at the grid boundaries. The method of [48] was applied to achieve approximate orthogonality at the centerline and on the top boundaries of all grids used in this simulation. In addition, all grids used to produce results presented in Chapters 4 and 5 are exactly orthogonal at the left hand boundary ($r_k = r_{k+1}$) and at the right boundary ($r_k = r_{k-1}$).

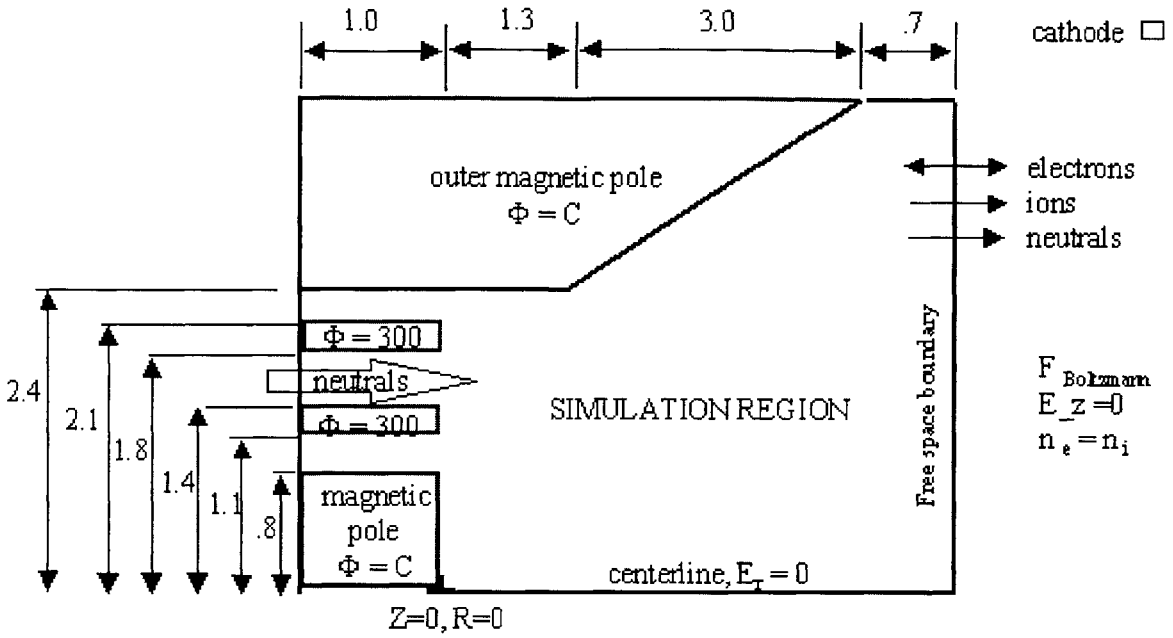

Figure 3-4: *Details of the simulation region.* Preliminary versions of the simulation modeled the anode boundary as a flat wall at $z = 0$ [51]. The simulation region was later expanded to encompass the complex anode and inner magnetic pole boundaries. Dimensions are in millimeters.

3.7.2 Grids Used in Simulation

Details of the simulation region are shown in Figure 3-4. Two of the grids used to model this region are shown in Figures 3-5 and 3-7.

Flat Anode Boundary Grid

Preliminary research focused on a simplified simulation region, characterized by a flat anode boundary. A typical grid for this simplified geometry is shown in Figure 3-5. The anode is flush with the left hand side at $z = 0$. This grid required making some approximations at parts of the left hand boundary through which particles should flow. For instance, electrons were destroyed and ions were neutralized at the center of the anode, in effect making it a continuous slab. Gaps between the anode and floating walls were modeled as magnetic boundaries (conservation of energy and magnetic dipole moment were used to determine whether a particle would reach the wall or be returned, see Section 3.18.7). A grid like this was used to produce the results reported in Reference [51].

Grid nodes on the left hand side were spaced uniformly. At simulation initialization, we found the node nearest to each physical feature in the thruster and made that node's

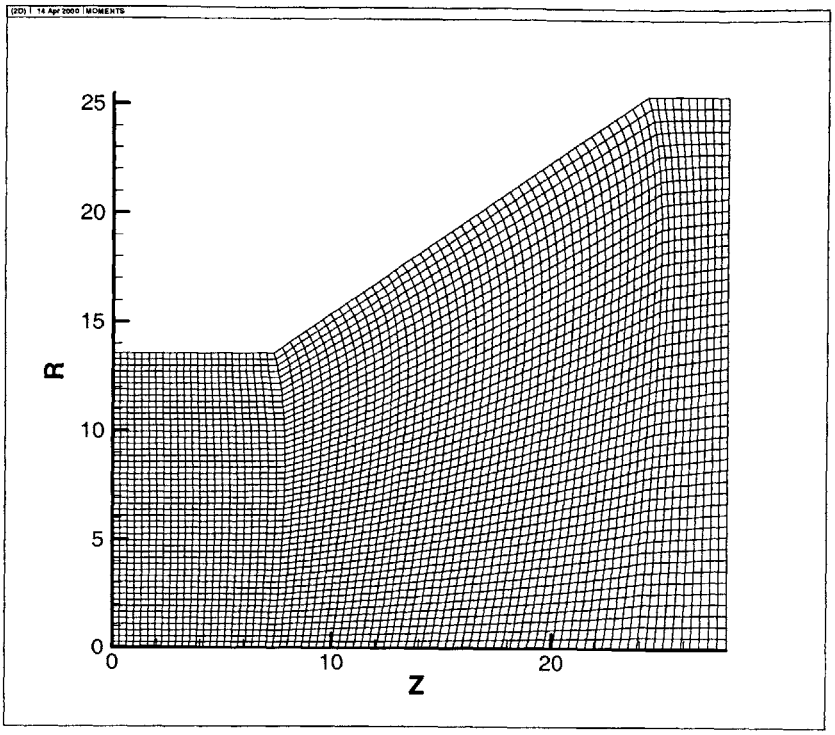

Figure 3-5: *The flat boundary* 80×50 *computational grid.*

location the location of the feature in the simulation. For instance, if node (0,19) was the closest node to the corner of the center pole, the location of the node became the location of the corner. Consequently, some features were slightly misplaced.

Complex Anode Boundary Grid

Because many plasma particles were impacting the left hand boundary at places other than the anode, the simulation region was expanded to become more physically realistic. The grid shown in Figure 3-7 extends 1 mm to the left of the anode exit, encompassing parts of both the hollow anode and center pole. Plasma can now form inside the anode, and magnetic boundaries are no longer required. The boundaries of the grid are further clarified in Figure 3-6. Grids of this type are used to produce all results in Chapters 4 and 5 of this thesis.

Physically, the anode continues beyond $z = -.1$ mm. However, this grid seems to be sufficiently large. Almost no plasma reaches the left hand boundary, either inside or outside of the anode. Inside the anode, backscattered neutrals do reach the left hand boundary. This boundary was assumed to be part of the anode, i.e. neutrals are accommodated at the anode temperature. Outside the anode, almost no particles of any species reach the left

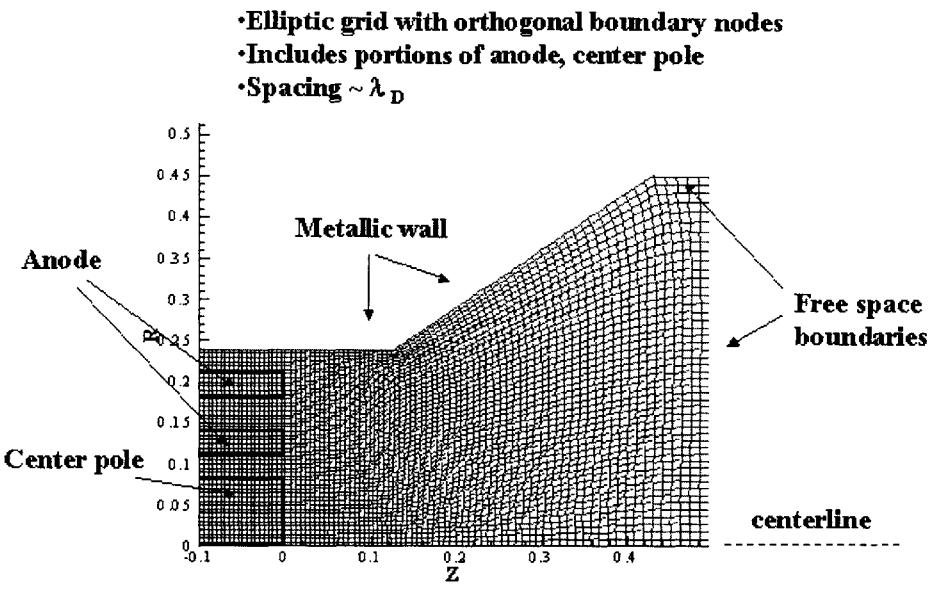

Figure 3-6: *The computational grid annotated with boundary features.*

hand boundary. For simplicity, these regions were modeled as pure reflectors. No magnetic boundaries were assumed.

This grid's left hand boundary nodes are determined by the physical geometry of the thruster. This means the node distribution is slightly non-uniform, but features are never misplaced.

3.7.3 Node Density

In order to achieve a Debye length of resolution using physical permittivity (ϵ_o), the grid should be on the order of 800×500. However, if $\epsilon_o' = epsilon_o\gamma^2$ where $\gamma^2 = 10$, then a 87×49 grid yields about a Debye length of resolution.

The node density is greatest near the anode, where we expect the Debye length to be shortest. The node density is least near the free space boundary at large radii, where we expect the Debye length to be longest.

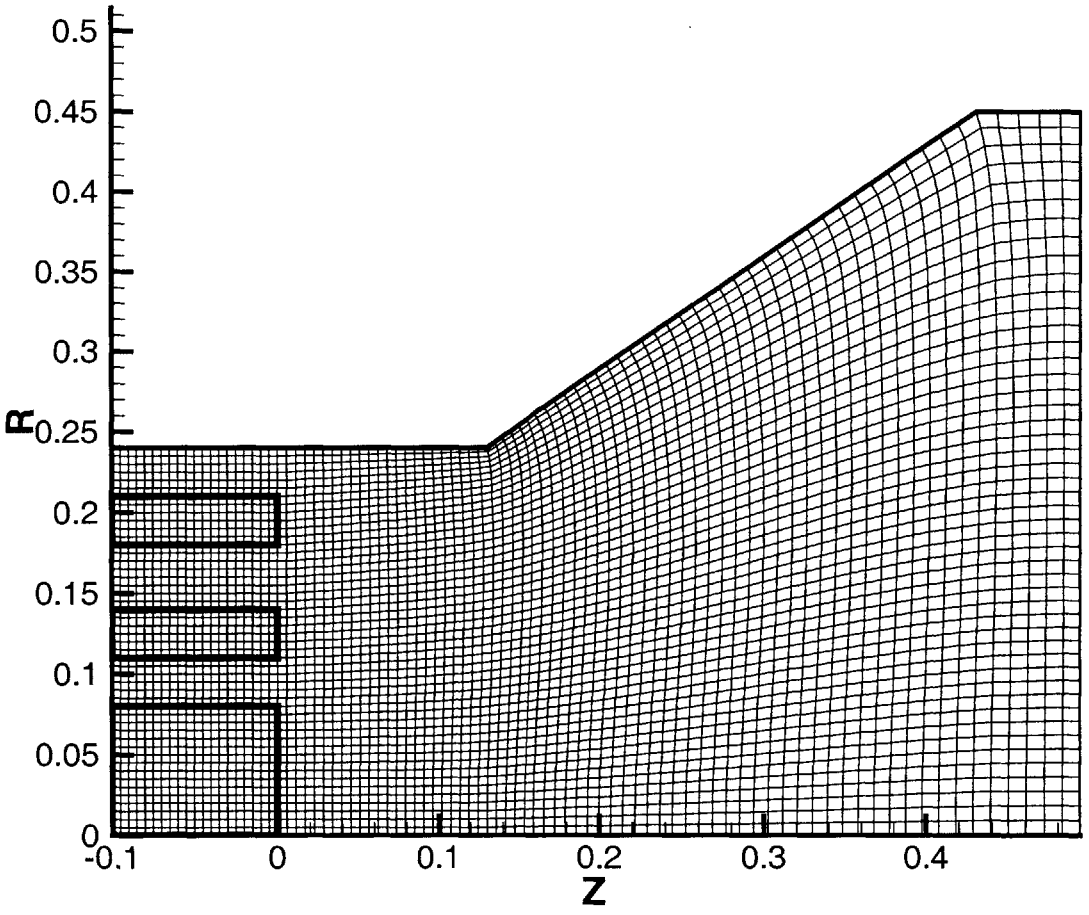

Figure 3-7: *The complex boundary* 87×49 *computational grid.* Portions of the anode and center pole are located inside the grid.

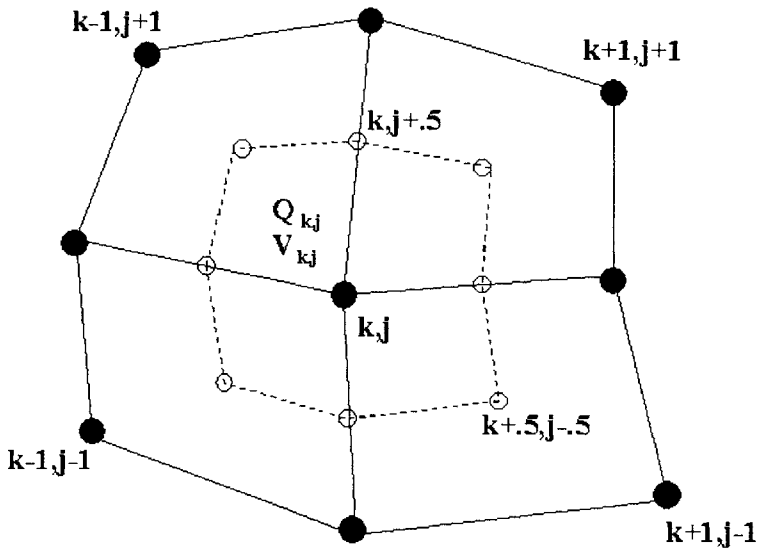

Figure 3-8: *Illustration of the grid cell associated with node (k,j).* The volume of cell (k,j) is the volume of the eight sided polygon defined by computational coordinates $(k \pm .5, j \pm .5)$, $(k, j \pm .5)$,and $(k \pm .5, j)$ rotated about $r = 0$.

Criticism

This simulation attempts to achieve the desired resolution everywhere at all times by making the grid fine. A better solution might be to use an irregular grid, e.g. Delauney triangles. Although this would require fundamentally re-writing large portions of the code, it would enable abrupt transitions in grid fineness, which might speed up the simulation. A further evolution would be to regenerate the grid at each time-step according to areas of interest; as the local densities and Debye lengths evolved, the grid would follow.

3.7.4 Geometry of a Grid Cell

Each grid node (k,j) defines an integration cell (a finite volume). The cross section of this cell (at any θ) is an 8 sided polygon defined by the computational coordinates $(k \pm .5, j \pm .5)$, $(k, j \pm .5)$,and $(k \pm .5, j)$. This polygon is illustrated in Figure 3-8.

The volume of the cell is obtained by rotating the polygon about $r = 0$; $V_{k,j} = \int dV = \int dzrdrd\theta$, where θ goes from 0 to 2π. $V_{k,j}$ is calculated by judiciously applying the formula for volume of a right circular cone (see Figure 3-9).

Each boundary line represents a surface. These surfaces are conic sections. The surface area of such a conic section is easily computed; the outside area of a right circular cone of radii r_1 and r_2 and height h is $|s| = \pi(r_1 + r_2)l = 2\pi\bar{r}l$ where $l = \sqrt{(r_1 - r_2)^2 + h^2}$

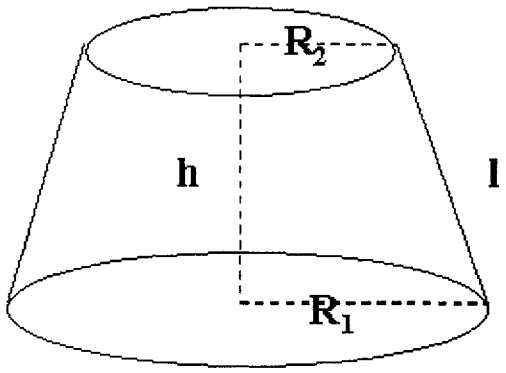

$$V = 1/3\ \pi\, h\, (R_1^2 + R_2^2 + R_1 R_2)$$
$$S = \pi\, (R_1 + R_2)\, l$$

Figure 3-9: *The volume and surface area of the frustum of a right circular cone.*

(see Figure 3-9). The projection along the r-axis is $2\pi\bar{r}h$, the projection along the z-axis is $2\pi\bar{r}(r_2 - r_1)$, and the projection along the azimuthal axis is the area of the trapezoid, $\bar{r}h$.

3.8 Interpolation

The computational grid has $N_z \times N_r$ nodes. Each node has a set of integer valued coordinates, (k, j), where $0 \leq j < N_z - 1$ and $0 \leq j < N_r - 1$. For instance, the lower left corner has coordinates $(k, j) = (0, 0)$. Each node also has a set of real coordinates, (z, r), which represent the node's location in Z-R space. (Numerical Note: The simulation is written in the C programming language, which begins array indices at 0. For instance, the first element of array A containing 3 elements is A[0]. The last element is A[2].)

All particles travel within the outer boundaries of the grid. Each time a particle moves, its location on the grid is re-assessed. Therefore, each particle may be assigned a set of real coordinates and a set of computational coordinates; $(z, r) \rightarrow (\xi, \eta)$. The computational coordinates of a particle are comprised of the indices of the lower left corner of the cell in which the particle resides, (k,j), plus some fractional amounts α_1 and α_2;

$$\xi = k + \alpha_1; \eta = j + \alpha_2. \tag{3.8}$$

On a Cartesian grid, α_1 and α_2 may be determined by linear interpolation. On a non-Cartesian grid, a mapping must be constructed. This mapping will be discussed in the next

sections. The method is taken from Reference [45].

3.8.1 The Interpolation Concept

Let us first consider an arbitrary quadrilateral, denoted by the computational coordinates of its "South-West" corner, (k,j). The functional value f at any location $(\xi, \eta) = (k+\alpha_1, j+\alpha_2)$ within the cell can always be expressed as the sum of the weighted functional values at the four corners, (k,j), (k,j+1), (k+1,j), (k+1,j+1) according to

$$f = p_{k,j} f_{k,j} + p_{k+1,j+1} f_{k+1,j+1} + p_{k,j+1} f_{k,j+1} + p_{k+1,j} f_{k+1,j}, \tag{3.9}$$

where $p_{k,j} + p_{k+1,j+1} + p_{k,j+1} + p_{k+1,j} = 1$. This is illustrated in Figure 3-10. This concept

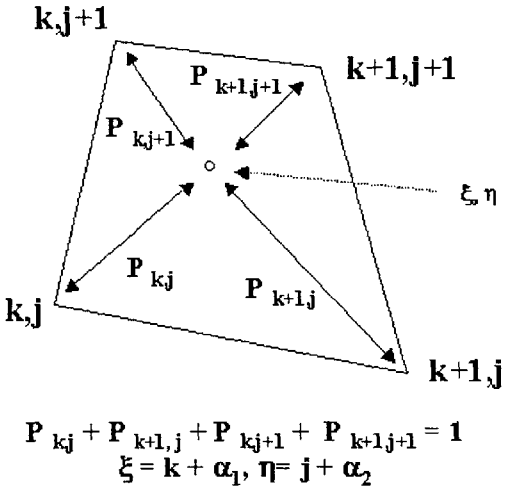

Figure 3-10: *The interpolation method illustrated.* Each particle is weighted to four grid nodes, shown here as the corners of a quadrilateral.

is completely general. Calculating the weighting coefficients is not. We assume the weights may be expressed in the forms

$$p_{k,j} = (1 - \alpha_1)(1 - \alpha_2), \tag{3.10}$$

$$p_{k+1,j+1} = \alpha_1 \alpha_2, \tag{3.11}$$

$$p_{k,j+1} = (1 - \alpha_1)\alpha_2, \tag{3.12}$$

and

$$p_{k+1,j} = (1 - \alpha_2)\alpha_1, \tag{3.13}$$

where $0 \leq \alpha_1 < 1$ and $0 \leq \alpha_2 < 1$ are the computational coordinates within cell (k, j). Thus, the interpolation method amounts to area weighting in the computational coordinate system. But how are α_1 and α_2 determined?

3.8.2 Square

Given a particle located with a simple square cell, α_1 and α_2 may be determined through linear interpolation;

$$\alpha_1 = \frac{z - z_{0,0}}{z_{1,0} - z_{0,0}}; \tag{3.14}$$

$$\alpha_2 = \frac{r - r_{0,0}}{r_{0,1} - r_{0,0}}. \tag{3.15}$$

Here, we let $k = j = 0$ for clarity. In this case, Equation 3.9 amounts to area weighting in real space. For the square, area weighting has the property that bi-linear functions (i.e. those of the form $f = az+br+czr+d$) are approximated exactly in [0,1]x[1,0] (see Reference [45]).

3.8.3 Arbitrary Quadrilateral

For an arbitrary quadrilateral, α_1 and α_2 are not so easily determined. We must find a function f which assigns α_1,α_2 ϵ [0,1] to every point (z,r) in (k,j) such that for all linear functions,

$$f(z,r) = az + br + c = p_{k,j}f_{k,j} + p_{k+1,j+1}f_{k+1,j+1} + p_{k,j+1}f_{k,j+1} + p_{k+1,j}f_{k+1,j}. \tag{3.16}$$

Restriction to linear functions is required; arbitrary bilinear function cannot be approximated exactly [45].

The most basic function to map is the location of a particle;

$$\begin{aligned} z &= z_{0,0}(1 - \alpha_1)(1 - \alpha_2) + z_{1,1}\alpha_1\alpha_2 + z_{0,1}(1 - \alpha_1)\alpha_2 + z_{1,0}\alpha_1(1 - \alpha_2); \\ r &= r_{0,0}(1 - \alpha_1)(1 - \alpha_2) + r_{1,1}\alpha_1\alpha_2 + r_{0,1}(1 - \alpha_1)\alpha_2 + r_{1,0}\alpha_1(1 - \alpha_2) \end{aligned} \tag{3.17}$$

This may be rewritten;

$$\begin{aligned} z - z_{0,0} &= \alpha_1\alpha_2(z_{0,0} - z_{1,0} + z_{1,1} - z_{0,1}) + \alpha_1(z_{1,0} - z_{0,0}) + \alpha_2(z_{0,1} - z_{0,0}); \\ r - r_{0,0} &= \alpha_1\alpha_2(r_{0,0} - r_{1,0} + r_{1,1} - r_{0,1}) + \alpha_1(r_{1,0} - r_{0,0}) + \alpha_2(r_{0,1} - r_{0,0}). \end{aligned} \tag{3.18}$$

The equations may be solved for α_1 and α_2 (see Reference [45]). First the system is transformed. Then, it is solved for α_1 and α_2. If we multiply through by the transformation matrix

$$\overleftrightarrow{A} = \begin{vmatrix} z_{1,0} - z_{0,0} & z_{0,1} - z_{0,0} \\ r_{1,0} - r_{0,0} & r_{0,1} - r_{0,0} \end{vmatrix}^{-1} = \begin{vmatrix} A_{00} & A_{10} \\ A_{01} & A_{11} \end{vmatrix}, \tag{3.19}$$

then we arrive at the following system of equations:

$$\alpha_1\alpha_2(\Delta z_{11s} - 1) + \alpha_1 = \Delta z_s \tag{3.20}$$

$$\alpha_1\alpha_2(\Delta r_{11s} - 1) + \alpha_2 = \Delta z_s \tag{3.21}$$

where

$$\begin{bmatrix} \Delta z_{11s} \\ \Delta r_{11s} \end{bmatrix} = \overleftrightarrow{A} \begin{bmatrix} \Delta z_{11} \\ \Delta r_{11} \end{bmatrix} = \overleftrightarrow{A} \begin{bmatrix} z_{1,1} - z_{0,0} \\ r_{1,1} - r_{0,0} \end{bmatrix} \tag{3.22}$$

and

$$\begin{bmatrix} \Delta z_s \\ \Delta r_s \end{bmatrix} = \overleftrightarrow{A} \begin{bmatrix} \Delta z \\ \Delta r \end{bmatrix} = \overleftrightarrow{A} \begin{bmatrix} z - z_{0,0} \\ r - r_{0,0} \end{bmatrix}. \tag{3.23}$$

We can easily solve for α_1 in terms of α_2

$$\alpha_1 = \frac{\Delta z_s}{1 + \alpha_2(\Delta z_{11s} - 1)}. \tag{3.24}$$

We can then write a quadratic equation for α_2;

$$\alpha_2^2(\Delta z_{11s} - 1) + \alpha_2[1 + \Delta z_s(\Delta r_{11s} - 1) - \Delta r_s(\Delta z_{11s} - 1)] - \Delta r_s = 0. \tag{3.25}$$

This quadratic equation may be solved for α_2:

$$\begin{aligned} \alpha_2 &= \frac{\Delta r_s}{(1 + \Delta z_s(\Delta r_{11} - 1))} & \Delta z_{11s} &= 1.0 \\ \alpha_2 &= \frac{-p + \sqrt{p^2 + q}}{(\Delta z_{11s} - 1)} & \Delta z_{11s} &\neq 1.0 \end{aligned} \tag{3.26}$$

where

$$p = 0.5\,[1 + \Delta z_s(\Delta r_{11s} - 1) - \Delta r_s(\Delta z_{11s} - 1)]$$
$$q = \Delta r_s(\Delta z_{11s} - 1). \tag{3.27}$$

The coefficient α_1 is then determined by Equation 3.24.

3.8.4 Computational Implementation

Each time a particle is moved, its computational coordinates must be re-evaluated. However, the quantities $\overleftrightarrow{A}$, Δz_{11s}, and Δr_{11s} may be pre-computed for each grid cell. Once we know which cell (k,j) the particle is in, we need only compute Δz_s, Δr_s, p and q to arrive at α_1 and α_2, and hence the new computational coordinates $(k + \alpha_1, j + \alpha_2)$. Immediately, the weighting coefficients may be calculated and saved in memory along with the particle. This saves CPU time.

3.8.5 Accuracy of the Interpolation Scheme

The interpolation scheme used is exact for functions linear in real space i.e those of the form $f(z,r) = a + b(z - z_o) + c(r - r_o)$. It is only approximate for higher order models. This is an unfortunate consequence of using an irregular mesh.

3.9 Creating Particle Distributions

To initialize the simulation, the interior of the control volume may be "seeded" with neutrals, ions, and electrons. Similar seeding occurs when particles are introduced into the simulation region across a series of cells. These particles are usually distributed according to a Maxwellian. Uniform, Maxwellian particle distributions may be created by using the rejection method for position, and the Box-Muller transformation for velocity [7].

3.9.1 Creating a Distribution in Space

A nearly uniform distribution in space is achieved by using the rejection method. First the volume of each grid cell as a fraction of the total volume is calculated. This represents a distribution:

$$f(k,j) = \frac{V_{k,j}}{V_{total}}\,;\ \Sigma_{k,j} f = 1. \tag{3.28}$$

Next, we draw a box around the distribution; the "top of the box" is at the largest cell fraction, f_{max}. Then, a position on the computational grid is chosen randomly;

$$\begin{aligned} k &= (N_z - 1)\, R(0 \rightarrow 1); \\ j &= (N_r - 1)\, R(0 \rightarrow 1). \end{aligned} \tag{3.29}$$

A third random number determines whether position (k,j) is accepted or rejected. If $p = f_{max} * R(0 \rightarrow 1)$ falls under the distribution, $(p < f(k,j))$ then the point is accepted. If the number is above the distribution $(p > f(k,j))$ then the point is rejected. The resulting density distribution is nearly uniform.

3.9.2 Maxwellian Velocity Distribution

Particles are typically created according to a Maxwellian velocity distribution function,

$$\hat{f}_m(v) = (\frac{m_e}{2\pi K T_e})^{\frac{3}{2}} \exp - \frac{m([v_x - < v_x >]^2 + [v_y - < v_y >]^2 + [v_z - < v_z >]^2)}{2KT_e}. \tag{3.30}$$

If we define $v_{th} = \sqrt{\frac{2k_b T}{M}}$, then this may be rewritten

$$\hat{f}_m(v) = \pi^{-\frac{3}{2}} v_{th}^{-3} \exp - \frac{([v_x - < v_x >]^2 + [v_y - < v_y >]^2 + [v_z - < v_z >]^2)}{v_{th}^2}, \tag{3.31}$$

where

$$\int_{-\infty}^{\infty} \hat{f}_m \, d^3v = 1, \tag{3.32}$$

which can also be written

$$\int_{-\infty}^{\infty} \int_{-\infty}^{\infty} \int_{-\infty}^{\infty} \hat{f}_z \hat{f}_r \hat{f}_\theta \, dv_r \, dv_z \, dv_\theta = 1. \tag{3.33}$$

Each of the three integrals contained therein equals $\sqrt{\pi} v_{th}$.

Note that in the normalized coordinate system, $[v] = \sqrt{\frac{T_e K}{m_e}}$, such that for electrons, $\vec{v}_{th} = \sqrt{2}[v]$ and for ions and other particles, $\vec{v}_{th} = \sqrt{2}\sqrt{\frac{T m_e}{T_e M}}[v]$. Furthermore, since the ion sonic velocity $v_s = \sqrt{\frac{T_e K}{M_i}}$, then in normalized coordinates, $\hat{v}_s = \sqrt{\frac{m_e}{M_i}}$.

The average velocity in any direction can be easily computed for a general distribution by

$$< v_z >= \int_{-\infty}^{\infty} v_z \hat{f}_z dv_z. \tag{3.34}$$

If we consider only a Maxwellian velocity in the positive direction, then the average speed in the z direction is

$$< |v_z| >= \int_0^\infty 2\frac{v_z}{\sqrt{\pi}v_{th}} \exp(-\frac{v_z^2}{v_{th}^2})dv_z = \frac{v_{th}}{\sqrt{\pi}}. \tag{3.35}$$

If we have a two sided distribution and a boundary normal to the Z direction, then the flux across the boundary in each direction can be easily computed from

$$\dot{m} = mn\bar{v}A = m\frac{1}{2}n\frac{v_{th}}{\sqrt{\pi}}A. \tag{3.36}$$

This says $\dot{n} = \frac{n\bar{c}}{4}$, where $\bar{c} = \sqrt{\frac{8kT}{\pi m}}$ is the average speed of the particles in the equilibrium distribution. Notice that $\bar{c}$ is twice the one sided mean velocity: $\bar{c} = 2 < |v_z| >$.

If the distribution is one sided, then

$$\dot{m} = mn\frac{v_{th}}{\sqrt{\pi}}A, \tag{3.37}$$

which is equivalent to $\dot{n} = \frac{n\bar{c}}{2}$.

3.9.3 Creating a Maxwellian Distribution in Velocity

The Box-Muller method (1958) for generating random deviates with a normal (Gaussian) distribution may be applied to create a Maxwellian distribution. This transformation is based on the 2-D cumulative distribution function for the speed, $|v|$, [5],

$$F(\vec{v}) = \frac{\int_0^{v_x}\int_0^{v_y} \exp(-v^2/v_t^2)dv_x dv_y}{\int_0^{\infty}\int_0^{\infty} \exp(-v^2/v_t^2)dv_x dv_y} = 1 - \exp(-v^2/v_t^2). \tag{3.38}$$

In Equation 3.38, $v^2 = v_x^2 + v_y^2$ and $v_t = \frac{2KT}{m}$. To obtain the speeds, $F(\vec{v})$ is set equal to a set on uniformly distributed random numbers varying from 0 to 1;

$$R(0 \rightarrow 1) = F(\vec{v}). \tag{3.39}$$

Such random numbers can be easily created using functions known as "random number generators." Noting the equivalence of $R(0 \rightarrow 1)$ and $1 - R(0 \rightarrow 1)$, one may invert Equation

3.38 and take the square root to obtain

$$|v| = v_t\sqrt{-ln(R(0 \rightarrow 1))}. \tag{3.40}$$

This is the magnitude of a 2-D Gaussian distributed velocity vector. Once $|v|$ is determined, the following may be used to used to extract any two components of velocity along axes normal to each other:

$$\begin{aligned} \Theta &= 2\pi R(0 \rightarrow 1); \\ v_1 &= |v|sin(\Theta); \\ v_2 &= |v|cos(\Theta). \end{aligned} \tag{3.41}$$

This method may be applied over and over to generate a cornucopia of Gaussian distributed velocities, e.g. v_3, v_4, v_5, ... However, we only need three at once for any given particle. Therefore, we apply Equation 3.38 twice and let $v_r = v_1$, $v_z = v_2$, $v_\theta = v_3$, saving v_4 for the next particle which must be assigned a velocity according to a Maxwellian at v_{th}.

3.10 Moments of a Particle Distribution

For each species, we desire to compute the density, momentum, and temperature as a function of position. In addition, we wish to calculate the electron energy distribution function along different magnetic streamlines.

Particle moments are found by scrolling through the particles and weighting them to the grid. Recall from Section 3.4 that each particle is represented by a data structure which includes the position in real space $(\hat{z}, \hat{r})$, the position in computational space, (ξ, η), the velocity $(\hat{v}_z, \hat{v}_r, \hat{v}_\theta)$, the mass ($\hat{m} = 1$ of $m_i = M/m_e$), the charge ($\hat{q} = 0, 1, -1$), the statistical weight or size ($\hat{s} = 1 - 50$), and weighting constants to the four corners of the cell in which the particle resides, $(P_{00}, P_{11}, P_{01}, P_{10})$.

The total number of particles represented by a single super-particle is

$$N_i = \hat{s}_i[size], \tag{3.42}$$

where $[size]$ is the number of particles represented by a super-particle of statistical weight

$s = 1$. Thus, the physical mass of a given superparticle is determined by

$$M_i = \hat{m}_i \hat{s}_i [size] m_e, \tag{3.43}$$

where m_e is the mass of a single electron.

3.10.1 Mass Density

If there are C super-particles of a particular species in the simulation, the total number of super-particles of that species weighted to grid node (k, j) is simply $C_{k,j} = \Sigma_{i=1}^{C} p_{i,k,j}$. Here $p_{i,k,j}$ is the weight of particle i to node (k,j). Recall that each particle is weighted to four (and only four) separate grid nodes according to the following (see Figure 3-10):

$$\begin{aligned} p_{k,j} &= (1-\alpha_1)(1-\alpha_2); \\ p_{k+1,j+1} &= \alpha_1 \alpha_2; \\ p_{k,j+1} &= (1-\alpha_1)\alpha_2; \\ p_{k+1,j} &= (1-\alpha_2)\alpha_1. \end{aligned} \tag{3.44}$$

For an non-Cartesian grid, α_1 and α_2 are determined through Equations 3.24 and 3.26. The sum of all $C_{k,j}$ is the total number of super-particles,

$$C = \Sigma_{k=0}^{N_z - 1} \Sigma_{j=0}^{N_r - 1} C_{k,j}, \tag{3.45}$$

where N_z is the number of grid nodes in the ξ or nominal Z direction, and N_r is the number of grid nodes in the η or nominal R direction. A more useful measure than C is the total number of particles size $s = 1$ this represents, N, determined by

$$N_{k,j} = \Sigma_{i=1}^{C} s_i p_{i,k,j}. \tag{3.46}$$

All electrons have charge $\hat{q}_e = -1$. If all ions have charge $\hat{q} = 1$, the total charge distribution is simply

$$Q_{k,j} = (N_i - N_e)_{k,j}, \tag{3.47}$$

where the index i in this last equation refers to ions. If multiply charged ions are accounted

for, the charge distribution for each species must be tallied separately, e.g.

$$Q_{k,j} = \Sigma_{i=1}^{C} \hat{q}_i s_i p_{i,k,j}. \tag{3.48}$$

The charge distribution, $Q_{k,j}$, is used to solve Gauss's Law equation for the electric potential.

The number density (number of particles per volume) is just

$$n_{k,j} = \frac{N_{k,j}}{V_{k,j}}, \tag{3.49}$$

where $V_{k,j}$ is the three dimensional volume associated with node (k, j). Number densities are used to determine reaction rates between different species.

The mass density is found by multiplying by the mass of the species, which is the same for all particles of that species,

$$\rho_{k,j} = m n_{k,j}. \tag{3.50}$$

The total mass, M, of all super-particles of a particular species in the system can be easily extracted from the particle moments;

$$M = \Sigma_{k=0}^{N_z-1} \Sigma_{j=0}^{N_r-1} \rho_{k,j} V_{k,j}. \tag{3.51}$$

3.10.2 Velocity and Momentum

Let the absolute velocity of a particle be $\vec{v} = (u, v, w) = (\hat{v}_z, \hat{v}_r, \hat{v}_\theta)$. For each species, the bulk velocity at node (k, j) is simply the average velocity of all the particles which are weighted to that node:

$$< \vec{v}_{k,j} > = \frac{\sum_{i=1}^{C} s_i p_{k,j} \vec{v}_i}{N_{k,j}} \tag{3.52}$$

The factor s_i is included to account for super-particles of different statistical weights. The flux density is then $n_{k,j} < \vec{v}_{k,j} >$. The relative velocity of a super-particle of species β with respect to its bulk velocity may then be denoted $(U, V, W)_\beta = (u - < u >, v - < v >, w - < w >)_\beta$. Relative velocities determine the temperature of the species.

3.10.3 Energy

The kinetic energy of a particle is

$$e = \frac{m}{2}(u^2 + v^2 + w^2) = \frac{m}{2}[(U+ < u >)^2 + (V+ < v >)^2 + (W+ < w >)^2]. \quad (3.53)$$

The mean energy of the flow may thus be written

$$< e >= \frac{m}{2}(< (U+ < u >)^2 > + < (V+ < v >)^2 > + < (W+ < w >)^2 >). \quad (3.54)$$

Since $< U >=< V >=< W >= 0$, this may be re-written

$$< e >= \frac{m}{2}(< U^2 > + < V^2 > + < W^2 >) + \frac{m}{2}(< u >^2 + < v >^2 + < w >^2). \quad (3.55)$$

The mean energy of the flow is thus a combination of thermal energy and drift energy,

$$< e >= \frac{m < c^2 >}{2} + \frac{m}{2}q_o^2, \quad (3.56)$$

where q_o is the bulk speed of the fluid, and $< c^2 >=< U^2 > + < V^2 > + < W^2 >$ is the mean square relative speed. The thermal energy defines the temperature according to

$$\frac{1}{2}m < c^2 > = \frac{3}{2}KT. \quad (3.57)$$

Temperature may be defined along different directions. For instance, in (r, z, θ) coordinates one may write:

$$\frac{1}{2}m < U^2 > = \frac{1}{2}KT_z; \quad (3.58)$$

$$\frac{1}{2}m < V^2 > = \frac{1}{2}KT_r; \quad (3.59)$$

$$\frac{1}{2}m < W^2 > = \frac{1}{2}KT_\theta. \quad (3.60)$$

To extract T_z from the particle positions and velocities, we need only find $< U^2 >$ from $< e >_z$ and $< u >^2$.

In a magnetized plasma, we may find different temperatures in the directions parallel

and perpendicular to the magnetic field. Let us define $T_{||}$ and $T_{\perp}$ as follows:

$$\frac{1}{2}KT_{||} = \frac{1}{2}m < c_{||}^2 >; \tag{3.61}$$

$$\frac{2}{2}KT_{\perp} = \frac{1}{2}m < c_{\perp}^2 >. \tag{3.62}$$

By transforming coordinates, we are able to extract $T_{||}$ and $T_{\perp}$ from the flow:

$$T_{||} = \frac{m}{K} < c_{||}^2 >= \frac{m}{K} < (v_{||} - < v_{||} >)^2 >= \hat{m}(< \hat{v}_{||}^2 > - < \hat{v}_{||} >^2)[T]; \tag{3.63}$$

$$T_{\perp} = \frac{m}{2K} < c_{\perp}^2 >= \frac{m}{2K} < (v_{\perp} - < v_{\perp} >)^2 >= \frac{\hat{m}}{2}(< \hat{v}_{\perp}^2 > - < \hat{v}_{\perp} >^2)[T], \tag{3.64}$$

Here, $[T]$ is the nominal temperature. Parallel temperature is obtained by projecting the velocity in the (R,Z) plane onto the magnetic field, which is assumed to have no azimuthal component, to obtain $< c_{||}^2 >$. The perpendicular temperature is then obtained easily through the relation

$$< c_{\perp}^2 >=< c^2 > - < c_{||}^2 > . \tag{3.65}$$

Alternately, the perpendicular velocity vector in the (R,Z) plane may be computed and added to the azimuthal velocity vector to get the total perpendicular velocity vector, and $< c_{\perp}^2 >$ may then be computed.

Expressions for temperature may be written in normalized units. For example,

$$T = \frac{\hat{m} < \hat{c}^2 >}{3K}[m][v]^2. \tag{3.66}$$

Noting that [v]= $\lambda_d \omega_{pe} = \sqrt{\frac{KT_e}{m_e}}$ and [m][v]$^2 = K[T]$, this reduces to

$$T = \frac{\hat{m} < \hat{c}^2 >}{3}[T], \tag{3.67}$$

where $[T]$ is the nominal electron temperature, $\hat{m} = 1$ for electrons, and $\hat{m} = M_{xe}/m_e$ for neutrals and ions.

The pressure may be defined by [37]

$$P = \frac{1}{3}nm < c^2 > . \tag{3.68}$$

Substituting $< c^2 >= \frac{3KT}{m}$, we find this is just the universal gas law, $P = nKT$.

3.10.4 Numerical Implementation of Particle Moments

Moments for a particular species are extracted by scrolling through the list of super-particles and weighting them to the grid. To find the temperature, for instance, one must perform the following steps:

- Find the total mass weighted to each node.
- Find the total flux and energy at each node.
- Divide through to get $< v >$ and $< e >$
- Calculate $< c^2 >$
- Multiply by a constant to get the temperature

Many particle moments are found at each time-step.

3.11 The Numerical Electron Energy Distribution Function

Fife's Hybrid PIC simulation assumed the electron energy distribution was Maxwellian. We can test whether this is true in our kinetic model by constructing distribution functions from numerical data, specifically particle velocities. Numerical distributions can be collected at individual points, or they can be collected along entire streamlines. To do the latter, we break the magnetic stream function, ψ, into bands. (The function ψ is defined in Section 3.13.4.) By interpolating ψ to the electrons, we may categorize them by band (i.e. by streamline). We can create as many bands as we like, with the understanding that statistics on each band get worse as the number of bands increases and the particle count per band decreases.

For each electron, we find the relative speeds c^2, $c_{||}^2$, and $c_{\perp}^2 = c^2 - c_{||}^2$. However, instead of averaging these energies, we allocate them to locally normalized energy bins according to $\epsilon' = \epsilon/T_e$, where $\epsilon = 1/2 m_e c^2$. We let each bin be $0.1\epsilon/T_e$ wide. We then divide by the total number of particles on each streamline to achieve, for each streamline, $g(\epsilon') = dN/d(\epsilon')$. If the function $g(\epsilon', \vec{x})$ varies only through the scale factor $T_e(\vec{x})$, i.e. if all $g(\epsilon)$ have the same shape, then this procedure should recover that shape.

3.11.1 Theoretical Distributions

We compare the numerical distribution function with the theoretical energy distribution for an isotropic Maxwellian at T, and for a two-dimensional Maxwellian at $T_\perp$ and $T_{||}$. We start with the three dimensional isotropic Maxwellian velocity distribution

$$\hat{f}(v) = \frac{(dN)/N}{dv_r dv_z dv_\theta} = (\frac{m_e}{2\pi K T_e})^{\frac{3}{2}} \exp(-\frac{m(v_x^2 + v_y^2 + v_z^2)}{2KT_e}) \tag{3.69}$$

where

$$\int_{-\infty}^{\infty}\int_{-\infty}^{\infty}\int_{-\infty}^{\infty} \hat{f}_z \hat{f}_r \hat{f}_\theta \, dv_r \, dv_z \, dv_\theta = 1. \tag{3.70}$$

Let us construct $g(\epsilon')$. We begin with the speed distribution, $g(c)$:

$$dN/N = 4\pi(\frac{m_e}{2\pi KT})^{\frac{3}{2}} c^2 \exp(-\frac{mc^2}{2KT})dc; \tag{3.71}$$

$$c^2 = v_r^2 + v_z^2 + v_\theta^2; \tag{3.72}$$

$$g(c) = \frac{dN/N}{dc}\,; \int_0^\infty g(c)dc = 1. \tag{3.73}$$

Next, we define ϵ and ϵ':

$$\epsilon = \frac{1}{2}mc^2\,;\; d\epsilon = mcdc; \tag{3.74}$$

$$\epsilon' = \frac{\epsilon}{T}\,;\; d\epsilon' = \frac{d\epsilon}{T}. \tag{3.75}$$

One can easily show that

$$g(\epsilon') = \frac{dF}{d\epsilon'} = \frac{2}{\sqrt{\pi}}\sqrt{\epsilon'}exp(-\epsilon') \tag{3.76}$$

and

$$\int_0^\infty g(\epsilon')d\epsilon' = 1. \tag{3.77}$$

This function peaks at $\epsilon' = 1/2$. If the distribution is Maxwellian in 3-D, this is what we find by collecting the electrons into energy bins according to $1/2mc^2/T$, as described previously.

Next we consider only the direction parallel to the magnetic field. By projecting particle and bulk velocities on to the local magnetic field lines, we get $v_{||}$ for each electron. As before,

we construct an energy distribution function, starting with the velocity distribution

$$f(v_{||}) = dF/dv_{||} = (\frac{m_e}{2\pi KT_{||}})^{\frac{1}{2}} \exp(-\frac{mv_{||}^2}{2KT_{||}}) \tag{3.78}$$

where

$$\frac{1}{2}KT_{||} = \int_{-\infty}^{\infty} \frac{1}{1} mv_{||}^2 f(v_{||}) dv_{||} \tag{3.79}$$

and

$$\int_{-\infty}^{\infty} f(v_{||}) dv_{||} = 1. \tag{3.80}$$

Letting $c_{||}^2 = v_{||}^2$, $\epsilon_{||} = 1/2mc_{||}^2$, and $\epsilon'_{||} = \epsilon_{||}/T_{||}$, we find

$$g(\epsilon'_{||}) = \frac{dF}{d\epsilon'_{||}} = \frac{1}{\sqrt{\pi\epsilon'_{||}}} exp(-\epsilon'_{||}) \tag{3.81}$$

where

$$\int_0^{\infty} g(\epsilon'_{||}) d\epsilon'_{||} = 1. \tag{3.82}$$

The final function we need is an energy distribution for the perpendicular direction. As before, we start with a velocity distribution,

$$f(v_{\perp}) = dF/dv_{\perp} = 2\pi(\frac{m_e}{2\pi KT_{\perp}}) \exp(-\frac{mv_{\perp}^2}{2KT_{\perp}}) \tag{3.83}$$

where

$$KT_{\perp} = \int_{-\infty}^{\infty} \int_{-\infty}^{\infty} mv_{\perp}^2 f(v_{\perp}) d^2 v_{\perp} \tag{3.84}$$

and

$$\int_{-\infty}^{\infty} \int_{-\infty}^{\infty} f(v_{\perp}) d^2 v_{\perp} = 1. \tag{3.85}$$

Letting $c_{\perp}^2 = v_{\perp}^2$, $\epsilon_{\perp} = 1/2mc_{\perp}^2$, and $\epsilon'_{\perp} = \epsilon_{\perp}/T_{\perp}$, we find

$$g(\epsilon'_{\perp}) = \frac{dF}{d\epsilon'_{\perp}} = exp(-\epsilon'_{\perp}) \tag{3.86}$$

where

$$\int_0^{\infty} g(\epsilon'_{\perp}) d\epsilon'_{\perp} = 1. \tag{3.87}$$

3.11.2 Testing the Algorithm on a Numerical Distribution

To test the algorithm, we generate a Maxwellian velocity distribution of particles and compare it to $g(\epsilon')$, $g(\epsilon'_{\|})$, and $g(\epsilon'_{\perp})$. The ψ bands used in this section are shown in Figure 3-15 The results are shown in Figures 3-11, 3-12, 3-13, and 3-14. (The method for producing the Maxwellian distribution is discussed elsewhere.) Overall particle count N varies by band; the rougher curves were constructed from fewer particles. Particle count in the four bands shown is listed in Table 3.1.

ψ band	particle count
2-3	2,195
4-5	10,179
7-8	49,537
8-9	79,346

Table 3.1: Particle count in the four bands of ψ used to analyze the EEDF in this section.

The isotropic distribution is compared to the initial distribution in Figure 3-11. This parallel distribution is compared to the initial distribution in Figure 3-12. The perpendicular distribution is compared to the initial distribution in Figures 3-13 and 3-14. Figures 3-11 through 3-14 indicate that the initial distribution is indeed Maxwellian. The figures also show that the function for determining $g(\epsilon')$ works well when considering both an isotropic (T) and anisotropic ($T_{\perp}, T_{\|}$) distribution. The function can therefore be used to analyze the actual distribution function in the plasma as the solution converges. The figures also place bounds on the degree of roughness expected with particle count; fewer particles means more roughness, which is important when analyzing results.

3.12 Calculating the Electric Potential and Field

The electric potential, Φ, can be found using finite differences or finite elements. We choose finite differences. However, instead of solving Poisson's Equation (the usual approach), we solve an integral form of Gauss's Law.

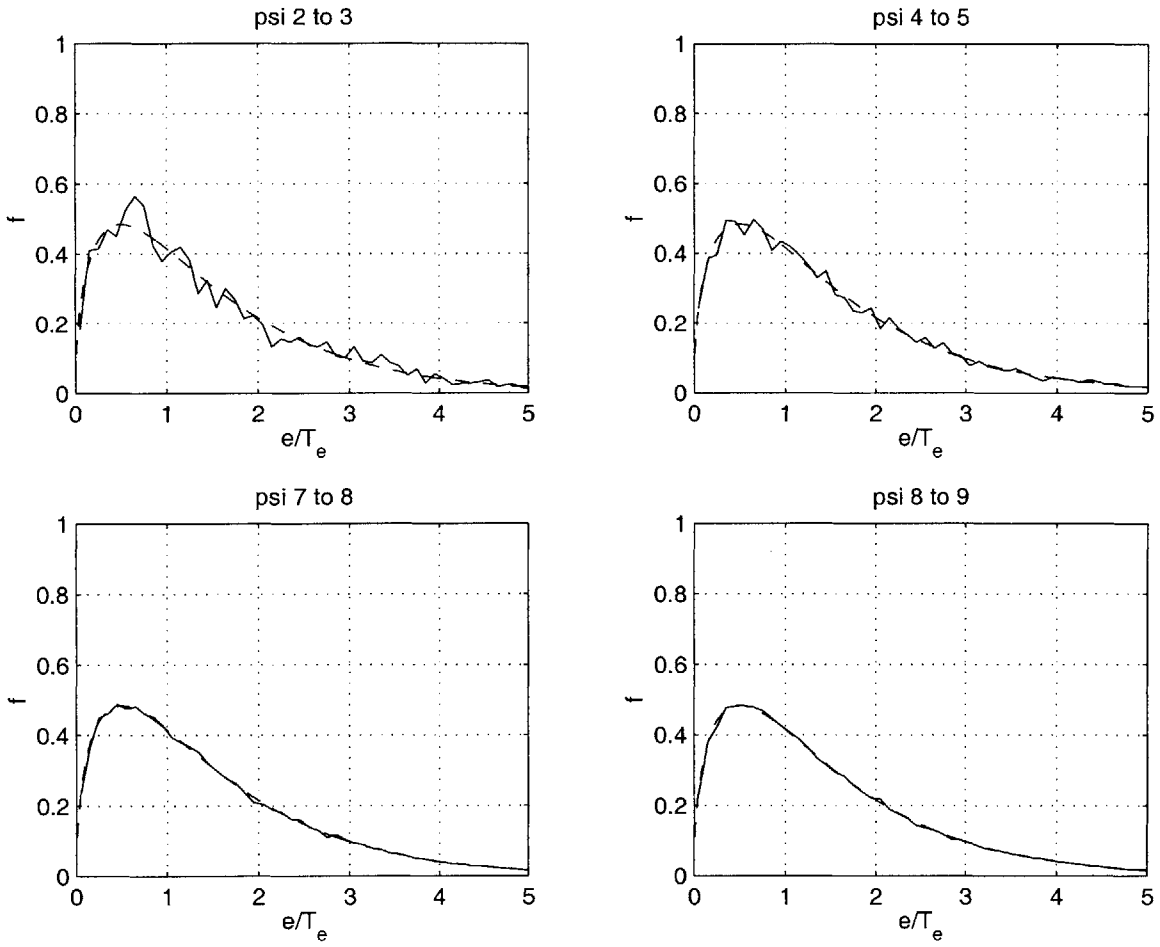

Figure 3-11: *Initial isotropic energy distribution* of 300,000 electrons along different magnetic streamlines compared with $g(\epsilon')$, the dashed line. Roughness is indicative of particle count on each streamline. Particle count is listed in Table 3.1.

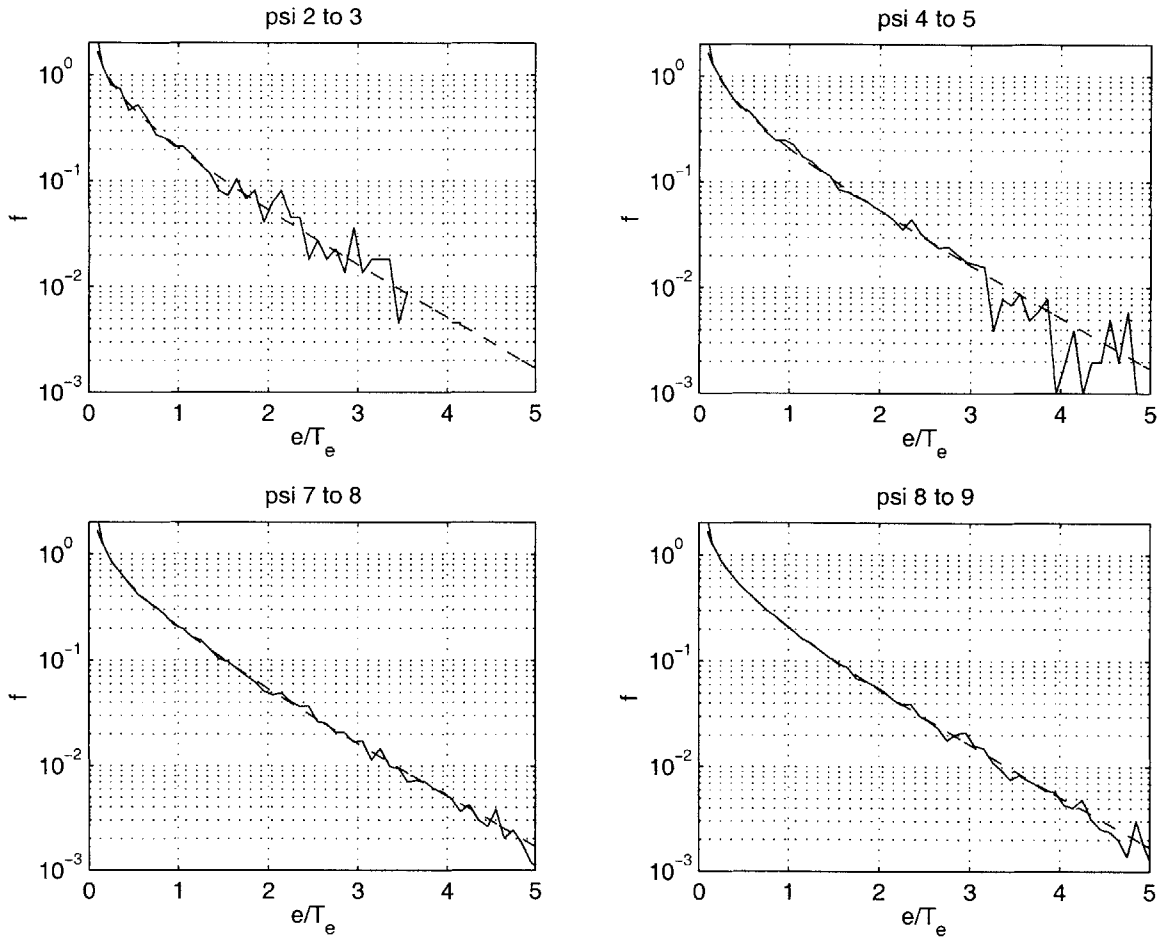

Figure 3-12: *Initial parallel* $\|$ *energy distribution* of 300,000 electrons along different magnetic streamlines compared with $g(\epsilon'_{\|})$, the dashed line. Semi-logarithmic plot. Particle count is listed in Table 3.1.

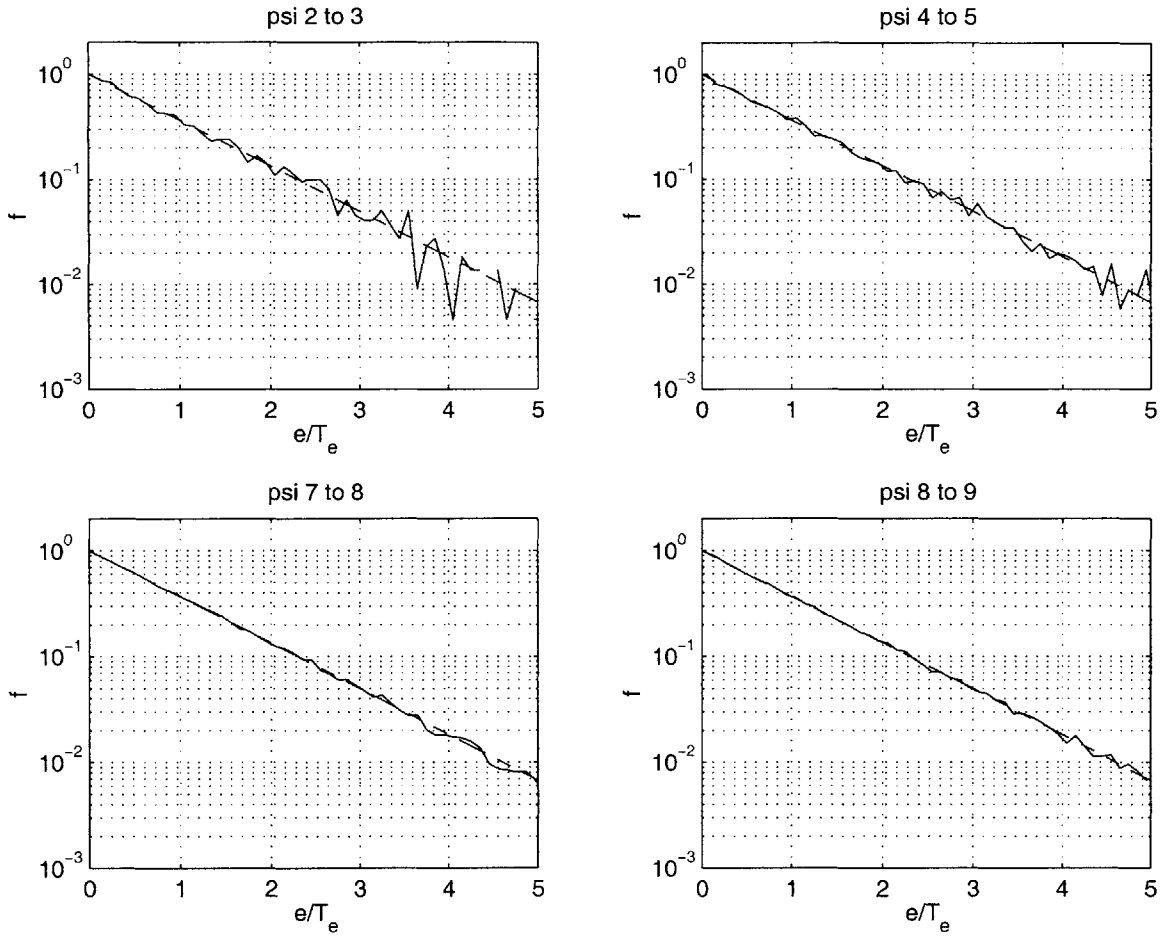

Figure 3-13: *Initial perpendicular* $\perp$ *energy distribution* of 300,000 electrons along different magnetic streamlines compared with $g(\epsilon'_\perp)$, the dashed line. Semi-logarithmic plot. Particle count is listed in Table 3.1.

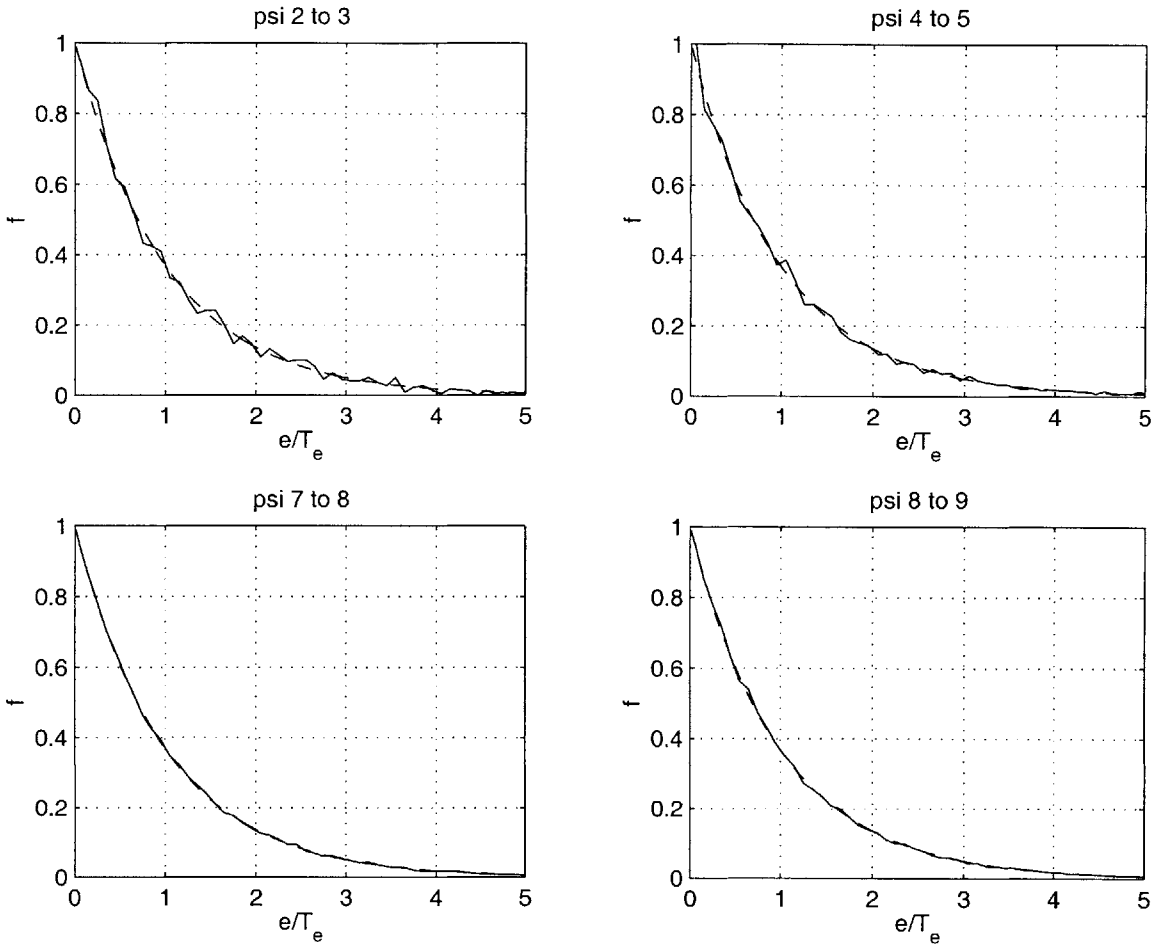

Figure 3-14: *Initial perpendicular* $\perp$ *energy distribution* of 300,000 electrons along different magnetic streamlines compared with $g(\epsilon'_\perp)$, the dashed line. Particle count is listed in Table 3.1.

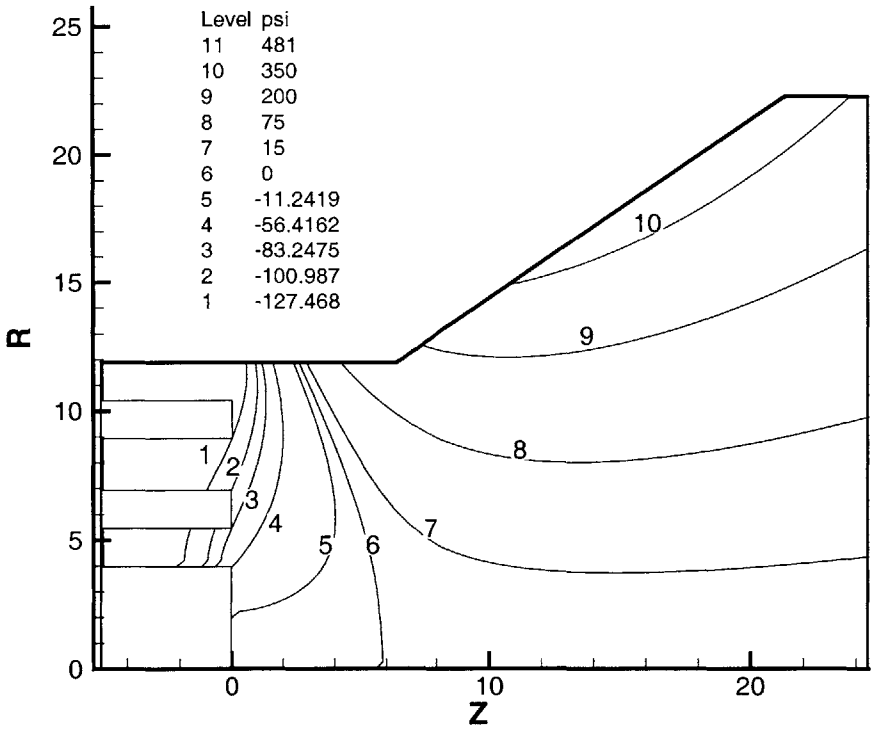

Figure 3-15: *Values of magnetic potential used to define the EEDF of the initial distribution.* The band between contours 1 and 2 reaches the anode interior. The bands between contours 2 and 5 define the main ionization zone. Contours 2 and 3 define the region of highest T_e, while contours 3 and 5 define the region of highest n_e near the anode. Normalized units with $\gamma = 10$, $\dot{m} = .1mg/s$, and $[T] = 50$ eV are assumed.

3.12.1 Method 1: Poisson's Equation

A usual way to find ϕ is to discretize Poisson's equation, which is derived by combining the electrostatic approximation, $\vec{E} = -\nabla\Phi$, with Gauss's Law, $\nabla \cdot \vec{E} = \frac{e}{\epsilon_o}(n_i - n_e)$:

$$\nabla^2\phi = -\frac{1}{\epsilon_o}(\rho_i - \rho_e). \tag{3.88}$$

In two dimensional cylindrical coordinates, considering only the r-z cross section, we have

$$\nabla^2\phi = \frac{1}{r}\frac{\partial}{\partial r}(r\frac{\partial\phi}{\partial r}) + \frac{\partial^2\phi}{\partial z^2}. \tag{3.89}$$

The partial derivatives on the right hand side of this equation can be expressed in terms of computational grid coordinates ξ and η;

$$\frac{\partial\phi}{\partial r} = \frac{\partial\phi}{\partial\xi}\frac{\partial\xi}{\partial r} + \frac{\partial\phi}{\partial\eta}\frac{\partial\eta}{\partial r}, \tag{3.90}$$

$$\frac{\partial\phi}{\partial z} = \frac{\partial\phi}{\partial\xi}\frac{\partial\xi}{\partial z} + \frac{\partial\phi}{\partial\eta}\frac{\partial\eta}{\partial z}, \tag{3.91}$$

and so on for the second derivatives. The functions ξ_z, ξ_r, η_z, and η_r are functions of the grid geometry which may be pre-computed. Since

$$d\xi = \frac{\partial\xi}{\partial x}dx + \frac{\partial\xi}{\partial y}dy, \tag{3.92}$$

$$d\eta = \frac{\partial\eta}{\partial x}dx + \frac{\partial\eta}{\partial y}dy, \tag{3.93}$$

$$dx = \frac{\partial x}{\partial\xi}d\xi + \frac{\partial x}{\partial\eta}d\eta, \tag{3.94}$$

and

$$dy = \frac{\partial y}{\partial\xi}d\xi + \frac{\partial y}{\partial\eta}d\eta, \tag{3.95}$$

we know that

$$\begin{vmatrix} \xi_x & \xi_y \\ \eta_x & \eta_y \end{vmatrix} = \begin{vmatrix} x_\xi & x_\eta \\ y_\xi & y_\eta \end{vmatrix}^{-1} = \frac{1}{x_\xi y_\eta - y_\xi x_\eta}\begin{vmatrix} y_\eta & -x_\eta \\ -y_\xi & x_\xi \end{vmatrix} \tag{3.96}$$

and so forth (see, for instance, Ref. [19]). Thus, we can thus fully discretize Poisson's equation and solve it using one of many numerical methods.

3.12.2 Method 2: Gauss's Law

An alternate approach to finding ϕ is based on the integral form of Gauss's Law. This is the method used in the code. A more basic form of this method is described in Ref. [5]. We start by integrating $\nabla \cdot \vec{E}$ over a control volume,

$$\int \nabla \cdot \vec{E}\, dv = \frac{1}{\epsilon_o} \int \rho_e\, dv. \tag{3.97}$$

This is equivalent to

$$\oint \vec{E} \cdot ds = \frac{1}{\epsilon_o} Q. \tag{3.98}$$

In CGS units, $\oint \vec{E} \cdot ds = 4\pi Q$. The left hand side represents the flux of electric field across a cell boundary and the right hand side is the charge contained within that boundary. As before, the electric field is defined by the potential

$$\vec{E} = -\nabla \Phi = -\frac{\partial \phi}{\partial z} i_z - \frac{\partial \phi}{\partial r} i_r - \frac{1}{r} \frac{\partial \phi}{\partial \theta} i_\theta \tag{3.99}$$

where we assume $\frac{\partial}{\partial \theta} = 0$. This equation may be rewritten using the first order approximations

$$\frac{\partial \phi}{\partial r} = \frac{\partial \phi}{\partial \xi} \frac{\partial \xi}{\partial r} + \frac{\partial \phi}{\partial \eta} \frac{\partial \eta}{\partial r} \tag{3.100}$$

and

$$\frac{\partial \phi}{\partial z} = \frac{\partial \phi}{\partial \xi} \frac{\partial \xi}{\partial z} + \frac{\partial \phi}{\partial \eta} \frac{\partial \eta}{\partial z}. \tag{3.101}$$

Again, we pre-compute ξ_z, ξ_r, η_z, and η_r across the grid. Given a computational grid, boundary conditions and a charge distribution, equation (3.98) can be iteratively solved for the electric potential distribution across the entire computational domain. When "successive over-relaxation" (SOR) is used, machine level precision is achieved in approximately 10^3 iterations.

A test function may be used to test the accuracy of the potential solver. We used a cosine function. We found that a five point scheme reproduced the function accurately

when the grid was Cartesian. However, five points were inadequate when the grid was non-Cartesian. A nine point scheme was found to be more accurate. The method will be discussed forthwith.

3.12.3 Geometry of the Integral Method

In the schemes discussed here, the quadrilateral defined by the points $(k \pm .5, j \pm .5)$ is used to calculate surface fluxes in lieu of the polygon discussed previously(compare Figures 3-8 and 3-16). The quadrilateral and the polygon produce extremely similar results.

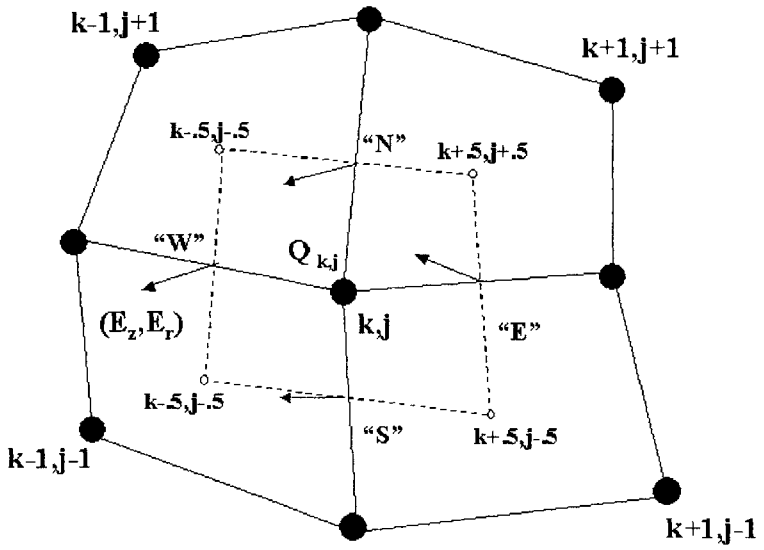

Figure 3-16: *Illustration of the Gauss's Law scheme at interior node (k,j).* The electric field $\vec{E}$ across the "N", "S", "E", and "W" boundaries is determined by ϕ at the central and surrounding nodes. The potential at node (k,j) is estimated from the $\vec{E}$, the boundary areas, and the charge $Q_{k,j}$.

The assumption of azimuthal symmetry allows us to perform computations in only two dimensions. This means the two dimensional grid is actually a cross section of the three dimensional whole. This is illustrated in Figure 3-17. Each particle in the simulation therefore represents a ring of charge.

The charge inside a given integration cell, $Q_{k,j}$, is assumed to be the total charge interpolated to cell (k,j). If we used simple Nearest Grid Point (NGP) weighting, then all the particles would lie inside the polygon surrounding cell (k,j). However, we use bi-linear interpolation. This means some of the particles interpolated to (k,j) actually lie outside the polygon. For instance, ninety five percent of particle close to node (k-1,j-1) in Figure 3-16

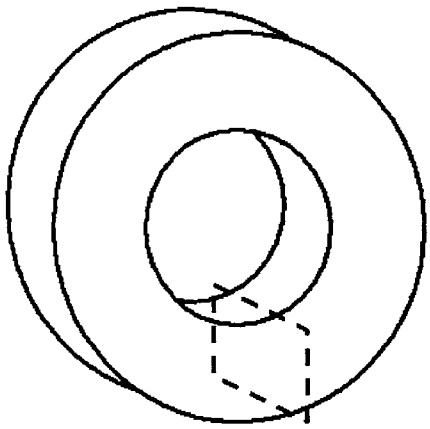

Figure 3-17: *A 2-D cross section in which particle moments and forces are calculated and the 3-D annular region it represents.*

may be weighted to (k-1,j-1), but the other five percent is split between the other three nodes.

We denote each cell surface by the two nodes it splits, e.g. the surface between nodes (k,j) and (k,j+1) is denoted by $s_{k,j+.5}$. Surface $s_{k,j+.5}$ is also called the "North" surface, $s_{k,j-.5}$ is the "South" surface, surface $s_{k+.5,j}$ is the "East" surface, and surface $s_{k-.5,j}$ is the "West" surface. These directions refer to the computational proximity of the surface relative to the central grid point. Each surface of the quadrilateral in Figure 3-16 is equivalent to two surfaces of the polygon in Figure 3-8 the North surface is properly composed of the "North Northeast" surface in the upper right quadrant and the "North Northwest" surface in the upper left quadrant.

If we take the normal $\vec{n} = \frac{\nabla s}{|\nabla s|}$ to a surface, then $\vec{s} = |s|\vec{n}$. The projection of a surface along any line $\hat{f}$ is $\hat{f} \cdot \vec{s}$.

Five Point Scheme (Cartesian Grid)

A five point scheme uses information at(k+1,j),(k-1,j), (k,j+1), and (k,j-1) to update the potential at (k,j). The terms ξ_z, ξ_r, η_z, and η_r across the North, South, East, and West surfaces are pre-computed.

In the simplest approximation, we use only the two nodes separated by a surface to calculate the flux across that surface. For example, in the North ($+\eta$ direction), the flux is

calculated using nodes (k,j) and (k,j+1). We assume $\frac{\partial \phi}{\partial \xi} = 0$ across that face. (We will add this missing "cross term" later.) We then use a first order approximation to calculate the electric field:

$$\vec{E} = -(\phi_{k,j+1} - \phi_{k,j})\frac{\partial \eta}{\partial z}\vec{i}_z - (\phi_{k,j+1} - \phi_{k,j})\frac{\partial \eta}{\partial r}\vec{i}_r = (\phi_{k,j} - \phi_{k,j+1})(\bar{\eta_z}\vec{i}_z + \bar{\eta_r}\vec{i}_r). \quad (3.102)$$

Here, we have averaged the dielectric constant and the grid constants straddling the face:

$$\begin{aligned} \bar{\eta_z} &= \tfrac{1}{2}(\eta_z)_{k,j} + \tfrac{1}{2}(\eta_z)_{k,j+1}; \\ \bar{\eta_r} &= \tfrac{1}{2}(\eta_r)_{k,j} + \tfrac{1}{2}(\eta_r)_{k,j+1}; \\ \bar{\epsilon_o} &= \tfrac{1}{2}(\epsilon_o)_{k,j} + \tfrac{1}{2}(\epsilon_o)_{k,j+1}. \end{aligned} \quad (3.103)$$

The dielectric constant may vary if, for example, the grid extends into a wall. However, the mini-TAL simulation requires solving Poisson's equation only in the plasma such that ϵ_o is constant everywhere. Now, let $\hat{\vec{n}}$ be the unit normal vector to any given surface, taken such that it always points out of the control volume. In this notation, on the North face,

$$\int \bar{\epsilon_o}\vec{E} \cdot ds = (\phi_{k,j+1} - \phi_{k,j})(\bar{\eta_z}\vec{i}_z + \bar{\eta_r}\vec{i}_r) \cdot (A_N \vec{n}_N)\bar{\epsilon_o}. \quad (3.104)$$

All terms in this expression are invariant with time except for ϕ. Hence, they can be pre-computed and grouped together:

$$\int \bar{\epsilon_o}\vec{E} \cdot ds = (\phi_{k,j+1} - \phi_{k,j})N; \quad (3.105)$$

$$N = \left|(\bar{\eta_z}\vec{i}_z + \bar{\eta_r}\vec{i}_r) \cdot (A_N \vec{n}_N)\bar{\epsilon_o}\right| = \left|(\bar{\eta_z}\vec{i}_z + \bar{\eta_r}\vec{i}_r) \cdot (A_{nne}\vec{n}_{nne} + A_{nnw}\vec{n}_{nnw})\bar{\epsilon_o}\right|. \quad (3.106)$$

We have defined the coefficients to be positive. This last expression shows the approximate equivalence of the 8 sided polygon and the quadrilateral, where, A_N and $\vec{n}_N$ are evaluated using only the North-East and North-West points.

Equation (3.98) thus reduces at each node to the following expression for the potential:

$$\phi_{k,j} = \frac{1}{N + S + E + W}(\phi_{k,j+1}\,N + \phi_{k,j-1}\,S + \phi_{k+1,j}\,E + \phi_{k-1,j}\,W + q_{k,j}). \quad (3.107)$$

Here, $q_{k,j}$ is the charge located inside the volume, i.e. at node (k,j).

Relaxation

Successive over-relaxation (SOR) may be applied to solve equation 3.107 for the electric potential at each node across the grid. In the predictor step, we find $\phi_{k,j}^{t+.5}$ according to

$$\phi_{k,j}^{t+.5} = \frac{1}{N+S+E+W}(\phi_{k,j+1}^{t} N + \phi_{k,j-1}^{t+.5} S + \phi_{k+1,j}^{t} E + \phi_{k-1,j}^{t+.5} W + q_{k,j}) \qquad (3.108)$$

where the superscripts are appropriate for a forward sweep. Relaxation takes place in the corrector step,

$$\phi_{k,j}^{t+1} = \phi_{k,j}^{t} + \omega\,(\phi_{k,j}^{t+.5} - \phi_{k,j}^{t}), \qquad (3.109)$$

where the relaxation factor ω controls the convergence (or divergence) of the solution. Convergence is determined by re-arranging equation 3.108 as follows:

$$RHS_{k,j} = -(N\phi_{k,j+1} + S\phi_{k,j-1} + E\phi_{k+1,j} + W\phi_{k-1,j} + q) + \phi_{k,j}(N+S+E+W). \quad (3.110)$$

The solution is considered converged when the right-hand-side at all nodes is nearly zero to nearly machine level accuracy, $0(10^{-12})$. Why go this far? To eliminate one more source of uncertainty.

On a 49×87 mesh, SOR with $\omega = 1.96$ yields a nearly converged solution in ≈ 800 iterations. Initial error growth can theoretically be mitigated by using Chebyshev acceleration [20], which introduces a variable ω. However, we did not use this. We did find that values closer to the "optimal" relation coefficient [19] of $\omega = 2/(1+\sqrt{1-\rho_j^2})$ where $\rho_j = .5[cos(\pi/N_z) + cos(\pi/N_r)]$ can yield convergence in only ≈ 400 iterations.

Nine Point Scheme (Non-Cartesian Grid)

The previously described five point scheme works well on a Cartesian grid, but works poorly on a non-Cartesian grid. We need to consider the "cross terms"; we must consider $\frac{\partial \phi}{\partial \xi}$ when considering the $+\eta$ face, and so on. To correct this fault, we may calculate the other component of flux using the same five points. However, this modification is inadequate; the solution still takes on aspects of the computational grid. Using a nine point scheme to calculate $\frac{\partial \phi}{\partial \xi}$ and $\frac{\partial \phi}{\partial \eta}$ on all faces is more accurate.

The simplest nine point scheme is just an extension of the original 5 point scheme. It uses all nine points illustrated in Figure 3-16. Data from the "Northeast", "Northwest",

"Southeast" and "Southwest" corners is used to estimate the cross-flux across the boundaries. If we consider the $+\eta$ boundary, we may write

$$-E_r = \frac{\partial \phi}{\partial r} = \frac{\partial \phi}{\partial \xi}\frac{\partial \xi}{\partial r} + \frac{\partial \phi}{\partial \eta}\frac{\partial \eta}{\partial r} \tag{3.111}$$

and

$$-E_z = \frac{\partial \phi}{\partial z} = \frac{\partial \phi}{\partial \xi}\frac{\partial \xi}{\partial z} + \frac{\partial \phi}{\partial \eta}\frac{\partial \eta}{\partial z}. \tag{3.112}$$

The η derivatives are calculated as before:

$$\frac{\partial \phi}{\partial \eta}\frac{\partial \eta}{\partial r} = (\phi_{k,j+1} - \phi_{k,j})\bar{\eta_r}; \tag{3.113}$$

$$\frac{\partial \phi}{\partial \eta}\frac{\partial \eta}{\partial z} = (\phi_{k,j+1} - \phi_{k,j})\bar{\eta_z}. \tag{3.114}$$

The ξ derivatives are calculated by averaging values from the corners:

$$\frac{\partial \phi}{\partial \xi}\frac{\partial \xi}{\partial r} = \frac{1}{2}\frac{\phi_{k+1,j+1} - \phi_{k-1,j+1}}{2}(\frac{d\xi}{dr})_{k,j+1} + \frac{1}{2}\frac{\phi_{k+1,j} - \phi_{k-1,j}}{2}(\frac{d\xi}{dr})_{k,j}; \tag{3.115}$$

$$\frac{\partial \phi}{\partial \xi}\frac{\partial \xi}{\partial z} = \frac{1}{2}\frac{\phi_{k+1,j+1} - \phi_{k-1,j+1}}{2}(\frac{d\xi}{dz})_{k,j+1} + \frac{1}{2}\frac{\phi_{k+1,j} - \phi_{k-1,j}}{2}(\frac{d\xi}{dz})_{k,j}. \tag{3.116}$$

As before,

$$\vec{E} \cdot \vec{A} = E_z n_z A + E_r n_r A \tag{3.117}$$

where $\hat{\vec{n}} = n_z i_z + n_r i_r$ defines the direction normal to a face and always points outward. We can simplify even more by taking the average $\frac{\partial \eta}{\partial z}$ and $\frac{\partial \eta}{\partial r}$ and the average $\frac{\partial \phi}{\partial \eta}$. In fact, this approximation makes almost no difference to the final solution. Following though, the flux over the whole cell $\sum \vec{E} \cdot A = \frac{\rho}{\epsilon_o}$ can be approximated as the following:

$$\phi_{k,j}^{t+.5} = \frac{C}{N + S + E + W}; \tag{3.118}$$

$$\begin{aligned} C = {} & N\phi_{k,j+1} + S\phi_{k,j-1} + E\phi_{k+1,j} + W\phi_{k-1,j} + q_{k,j} \\ & \acute{N}\tfrac{1}{4}(\phi_{k+1,j} + \phi_{k+1,j+1} - \phi_{k-1,j} - \phi_{k-1,j+1}) + \\ & \acute{S}\tfrac{1}{4}(\phi_{k+1,j} + \phi_{k+1,j-1} - \phi_{k-1,j} - \phi_{k-1,j-1}) + \\ & \acute{E}\tfrac{1}{4}(\phi_{k+1,j+1} + \phi_{k,j+1} - \phi_{k+1,j-1} - \phi_{k,j-1}) + \\ & \acute{W}\tfrac{1}{4}(\phi_{k-1,j+1} + \phi_{k,j+1} - \phi_{k-1,j-1} - \phi_{k,j-1}); \end{aligned} \tag{3.119}$$

$$\phi_{k,j}^{t+1} = \phi_{k,j}^{t} + \omega\,(\phi_{k,j}^{t+.5} - \phi_{k,j}^{t}); \tag{3.120}$$

$$RHS = -C + \phi_{k,j}^{t+1}(N + S + E + W). \tag{3.121}$$

We pre-compute the following integration constants:

$$\begin{aligned} E &= \left|(\bar{\xi_z}\vec{i_z} + \bar{\xi_r}\vec{i_r})_E \cdot \vec{n}_E A_E\right|; \\ W &= \left|(\bar{\xi_z}\vec{i_z} + \bar{\xi_r}\vec{i_r})_W \cdot \vec{n}_W A_W\right|; \\ N &= \left|(\bar{\eta_z}\vec{i_z} + \bar{\eta_r}\vec{i_r})_N \cdot \vec{n}_N A_N\right|; \\ S &= \left|(\bar{\eta_z}\vec{i_z} + \bar{\eta_r}\vec{i_r})_S \cdot \vec{n}_S A_S\right|; \end{aligned} \tag{3.122}$$

$$\acute{E} = 0.5\left[(\frac{\partial \eta}{\partial z}_{k} + \frac{\partial \eta}{\partial z}_{k+1})\vec{i_z} + (\frac{\partial \eta}{\partial r}_{k} + \frac{\partial \eta}{\partial r}_{k+1})\vec{i_r}\right] \cdot \vec{n}_E A_E; \tag{3.123}$$

$$\acute{W} = 0.5\left[(\frac{\partial \eta}{\partial z}_{k} + \frac{\partial \eta}{\partial z}_{k-1})\vec{i_z} + (\frac{\partial \eta}{\partial r}_{k} + \frac{\partial \eta}{\partial r}_{k-1})\vec{i_r}\right] \cdot \vec{n}_W A_W; \tag{3.124}$$

$$\acute{N} = 0.5\left[(\frac{\partial \xi}{\partial z}_{j} + \frac{\partial \xi}{\partial z}_{j+1})\vec{i_z} + (\frac{\partial \xi}{\partial r}_{j} + \frac{\partial \xi}{\partial r}_{j+1})\vec{i_r}\right] \cdot \vec{n}_N A_N; \tag{3.125}$$

$$\acute{S} = 0.5\left[(\frac{\partial \xi}{\partial z}_{j} + \frac{\partial \xi}{\partial z}_{j-1})\vec{i_z} + (\frac{\partial \xi}{\partial r}_{j} + \frac{\partial \xi}{\partial r}_{j-1})\vec{i_r}\right] \cdot \vec{n}_S A_S. \tag{3.126}$$

Refinements Not Used

Taking the 9 point scheme one step further, we might consider each face of the 8 sided polygon separately. This means considering two normal vectors and surface areas for each side ($+\eta$,$-\eta$,$+\xi$,$-\xi$) of the polygon. The dot products may be pre-computed and saved as before. However, this is needless detail; it was found to make little if any difference to the solution.

3.12.4 Testing the Potential Solver

We tested the accuracy of the potential solver by using an analytic function. This test is discussed in Chapter 4. We also tracked the convergence of the solution. This is also discussed in Chapter 4.

3.12.5 The Electric Field

Once the potential, $\phi(z,r)$, is determined, the elcctric field at the grid nodes is calculated from

$$\vec{E} = -\nabla\Phi = -(\frac{\partial\phi}{\partial\eta}\frac{\partial\eta}{\partial z} + \frac{\partial\phi}{\partial\xi}\frac{\partial\xi}{\partial z})\,\vec{i}_z - (\frac{\partial\phi}{\partial\eta}\frac{\partial\eta}{\partial r} + \frac{\partial\phi}{\partial\xi}\frac{\partial\xi}{\partial r})\,\vec{i}_r \tag{3.127}$$

where the factors $\frac{\partial\eta}{\partial z}$, $\frac{\partial\xi}{\partial z}$ $\frac{\partial\eta}{\partial r}$ and $\frac{\partial\xi}{\partial r}$ are pre-computed.

3.13 Magnetic Field

The magnetic circuit of the mini-TAL was originally designed by Dexter Magnetics. Dexter provided us with mappings of the field, $\vec{B}(z,r)$, and magnetic potential, $\phi_B(z,r)$. These mappings were calculated with a commercial simulation package and delivered on a Cartesian grid.

Prior to any plasma computations, Dexter's field is mapped to the (plasma) computational grid, allowing us to use identical interpolation constants to weight $\vec{B}$ and $\vec{E}$ to the particles. The magnitude of the field after interpolation is shown in Figure 3-18.

A magneto-static solution is assumed; the magnetic field is assumed to be invariant. Magnetic fields induced by currents in the plasma are ignored, as is degradation due to heating of the magnetic poles. We show in Section 5.3.6 that the former assumption is valid. The latter assumption should be re-examined if work on the mini-TAL is continued.

3.13.1 Solving for $\vec{B}$ on Computational Grid

With appropriate boundary conditions, we could use Gauss's Law to find the magnetic potential directly on the computational grid. Let $\vec{B} = \nabla\phi_B$ where ϕ_B is the magnetic potential. Since $\nabla\cdot\vec{B} = 0$, one can write for each grid cell

$$\int \nabla\phi\cdot ds = 0 \tag{3.128}$$

where ds is the area of a cell wall. This equation says the magnetic flux across the boundaries is conserved. It is identical to the equation used to solve for the electric potential, except that the charge inside the cell is set to zero. We can, therefore, use the electric potential solver described elsewhere to calculate ϕ_B and $\vec{B}$.

We formulated simple boundary conditions and tested this method, comparing the

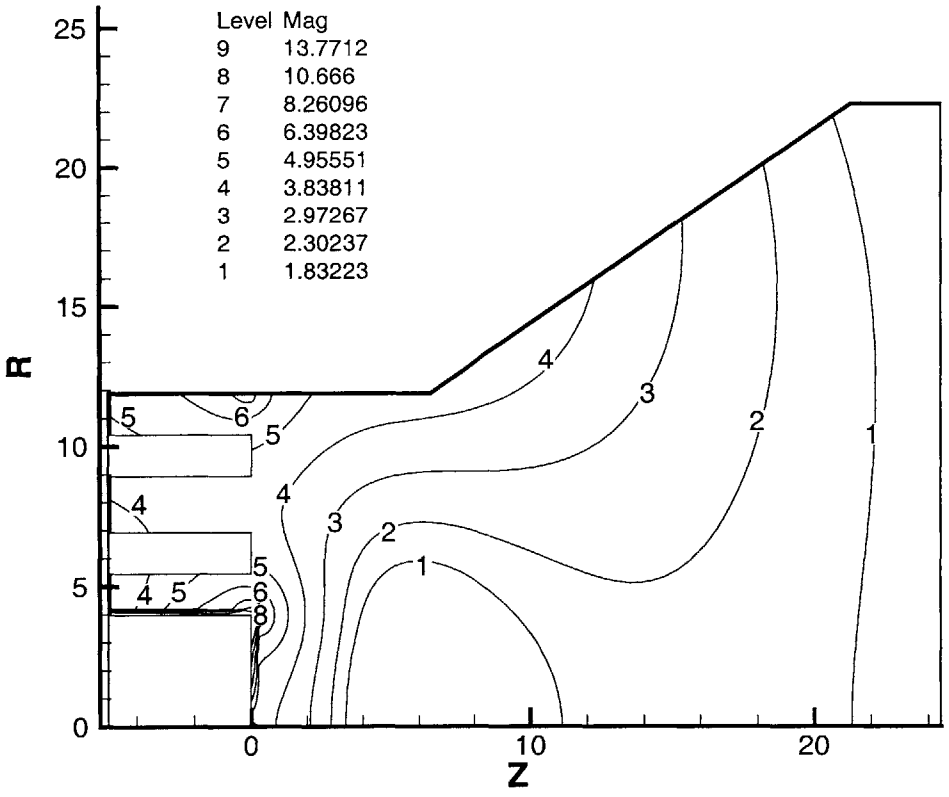

Figure 3-18: *Contour plot of the magnetic field strength in normalized units*; $\hat{B} = \omega_c \, rad/[t]$ where $[t] = 1/\omega_p$, and ω_p is the nominal plasma frequency. Here, $\gamma = 10$ and $\dot{m} = .1$ mg/s such that $1[B] = 835$ Gauss. Field strength in front of the anode is thus about 3300 Gauss.

results with Dexter's mapping. At the right and left boundaries, we specified no flux ($\frac{d\phi_B}{dz} = 0$). At the axis, we required $\frac{d\phi_B}{dr} = 0$. On the outer magnetic pole, we specified $\phi_B = 1.0$, and on the inner pole we specified $\phi_B = 0.0$. We then solved for ϕ_B across the domain, and took the gradient to arrive at $\vec{B}$. Finally, we specified a control point and a field strength at that control point, and used that to normalize the field.

The resulting field was similar to Dexter's near the anode, but dissimilar near the boundaries, Evidently, the boundary conditions were too simplistic for the grid. An accurate solution would require a larger grid or more detailed boundary conditions.

3.13.2 Solving for $\vec{B}$ using other Algorithms

Fife's hybrid PIC methodology requires pre-calculating ϕ_B on a large Cartesian grid and then interpolating to a much smaller, non-orthogonal grid used to model the plasma [9]. This is just a more accurate extension of the methodology already described. Unfortunately, the algorithm as presently constructed does not account for material properties of the permanent magnets used in Khayms' thruster.

Fortunately, commercial packages which account for material properties such as permanent magnets already exist (e.g. $Maxwell^{TM}$). Dexter Magnetics used such a package in designing the magnetic circuit of the mini-TAL. To model the mini-TAL, we obtained the field from Dexter on a Cartesian grid.

3.13.3 Interpolation of Magnetic Field

The magnetic field is interpolated from the Cartesian grid to the computational grid using a bilinear (area weighted) function. Let the four corners of a Cartesian grid cell be (z,r), (z+δz, r), (z, r + δr), (z+δz,r +δ r), and let the location of a computational node somewhere within the Cartesian cell be (z+$\delta z'$, r+$\delta r'$) such that $0 \leq \delta'_z < \delta z$ and $0 \leq \delta'_r < \delta r$. Next, define $\alpha_1 = \delta z'/\delta z$ and $\alpha_2 = \delta r'/\delta r$. The values of B_z and B_r at the four Cartesian grid nodes may then be weighted to the computational grid node as per Equation 3.9:

$$B(\vec{z}, r) = \sum p\vec{B}; \tag{3.129}$$

$$p_{(z,r)} = (1 - \alpha_1)(1 - \alpha_2); \tag{3.130}$$

$$p_{(z+\delta z,r)} = \alpha_1\alpha_2; \tag{3.131}$$

$$p_{z,r+\delta r} = (1-\alpha_1)\alpha_2; \tag{3.132}$$

$$p_{(z+\delta z,r)} = (1-\alpha_2)\alpha_1. \tag{3.133}$$

This is bilinear interpolation in the real domain, as opposed to bilinear interpolation in the computational domain.

3.13.4 Magnetic Streamlines

In a magnetized plasma, electrons are trapped on magnetic streamlines. Flux between the streamlines results largely from diffusion, both classical and anomalous. We wish to analyze the electron energy distribution function along different streamlines. The magnetic stream function makes this possible. Since $\nabla \cdot \vec{B} = 0$, it is possible (as per Fife, [10]) to define a magnetic stream function ψ, the gradient of which is everywhere orthogonal to $\vec{B}$:

$$\frac{\partial \psi}{\partial z} = rB_r; \tag{3.134}$$

$$\frac{\partial \psi}{\partial r} = -rB_z. \tag{3.135}$$

This scalar function is constant along any given magnetic streamline. We may interpolate ψ to the electrons and thus swiftly categorize them for analysis. (Note that ψ is not the conventionally defined magnetic stream function $\vec{A}$, given by $\vec{B} = \nabla \times \vec{A}$. This cross product results in $\frac{\partial r A_\theta}{\partial z} = -rB_r$ and $\frac{\partial r A_\theta}{\partial r} = rB_z$. Thus, $\psi = -rA_\theta$.)

To construct $\psi_{k,j}$, we set $\psi = 0$ at the lower left corner of the grid; this level is arbitrary. Since $B_r = 0$ along the axis, $\psi = 0$ along the axis. Thus, to find ψ in the interior we need only integrate in the r direction. On a Cartesian grid, we let $\psi_{k,j+1} = \psi_{k,j} + (r_{k,j+1} - r_{k,j})\frac{\partial \psi}{\partial r}_{k,j}$. On the non-Cartesian grid, we integrate along η according to

$$\frac{\partial \psi}{\partial \eta} = \frac{\partial \psi}{\partial r}\frac{\partial r}{\partial \eta} + \frac{\partial \psi}{\partial z}\frac{\partial z}{\partial \eta} \tag{3.136}$$

where

$$\frac{\partial r}{\partial \eta} = r_{k,j+1} - r_{k,j} \tag{3.137}$$

and

$$\frac{\partial z}{\partial \eta} = z_{k,j+1} - z_{k,j}. \tag{3.138}$$

This simple method provides us with a stream function good enough for diagnostics. Values of ψ which results from $\gamma = 10$ and $\dot{m} = .1$ mg/s are shown in Figures 3-19 and 3-20. The streamlines in Figure 3-19 are equally spaced in ψ.

Streamlines equally spaced in ψ are shown in Figure 3-19. Streamlines in the near-anode region are shown in Figure 3-20.

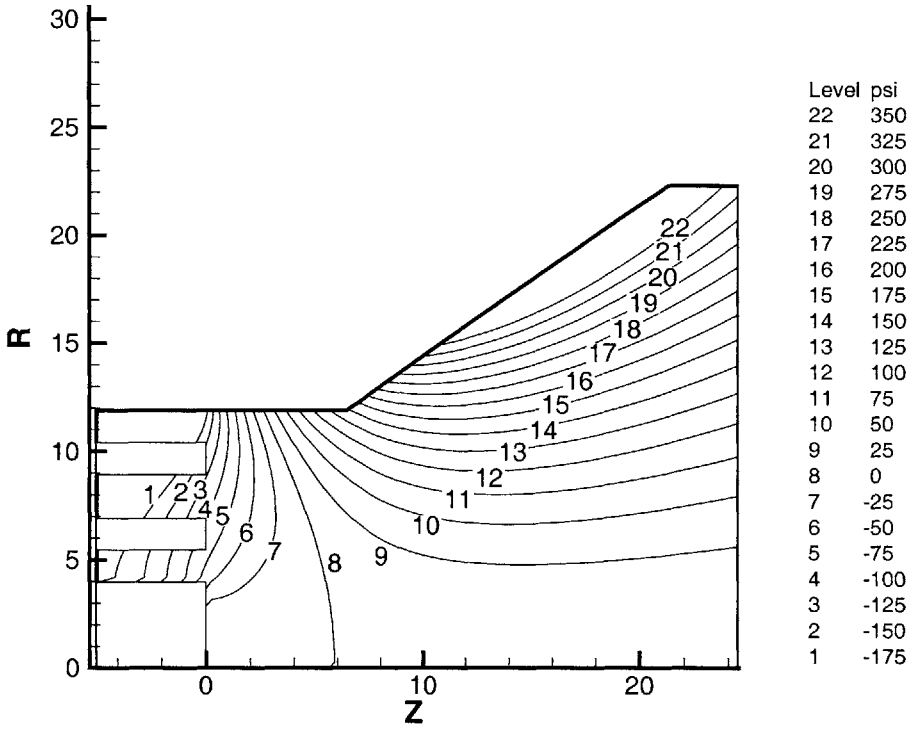

Figure 3-19: *Contour plot of the magnetic stream function, ψ.* Contours of ψ are streamlines of the magnetic field. Contours are equally spaced in ψ.

3.13.5 Divergence of $\vec{B}$

The divergence of the Dexter Magnetics magnetic field was tested. This test is described in Chapter 4.

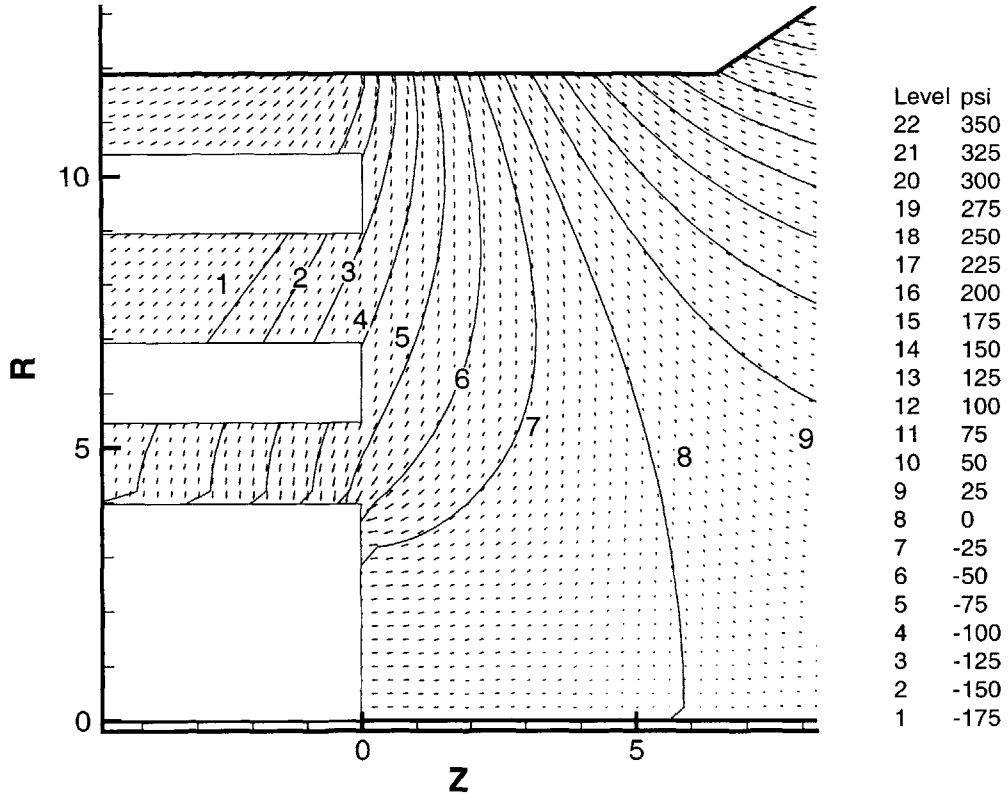

Figure 3-20: *Vector plot of the magnetic field in the near anode region overlaid by contour plot of the magnetic stream function, ψ.* The field is nominally radial near the anode, but diverges further to the right. Nominal field strength is 5000 Gauss (0.5 Tesla).

3.14 Moving the Particles

Particles are moved according to the standard leapfrog method described in Birdsall [5]. The two first order differential equations to be integrated separately for each particle are

$$m\frac{d\vec{v}}{dt} = \vec{F} \tag{3.139}$$

and

$$\frac{d\vec{x}}{dt} = \vec{v} \tag{3.140}$$

where $\vec{F}$ is the force to be applied. The force is, excepting collisions, the Lorenz force. The leapfrog method replaces these with two finite difference equations:

$$\begin{aligned} m\tfrac{v_{t+1}-v_t}{dt} &= \vec{F}_t; \\ \tfrac{x_{t+1}-x_t}{dt} &= \vec{v}_{t+1}. \end{aligned} \tag{3.141}$$

After moving a particle in real space, we transform coordinates (the system is cylindrical), and move the particle in computational space. Both additions will be discussed below.

3.14.1 Accuracy of the Leapfrog Method

The leapfrog method has error, with the error vanishing as $\Delta t \to 0$ [5]. When applied to a simple harmonic oscillator of radian frequency ω_o, there is no amplitude error for $\omega_o \Delta t \leq 2$ (the leapfrog stability criterion previously discussed) and the phase advance for one step is given by

$$\omega_o \Delta t + \frac{1}{24}(\omega_o \Delta t)^3 + h.o.t. \tag{3.142}$$

These error terms dictate a choice of $\omega_o \Delta t \leq .3$ to accurately observe oscillations or waves for some tens of cycles [5].

3.14.2 Position and Velocity Offset

In the leapfrog method, velocity and position are offset by a half time step. This is why it is called a leapfrog method. The computer advances $\vec{v}_t$ to $\vec{v}_{t+1}$ and $\vec{x}_t$ to $\vec{x}_{t+1}$ even though both were not known at the same time.

If we simply create a particle at position $\vec{x}$ with velocity $\vec{v}$, then small offset errors will

occur. In this simulation, these are assumed to be ignorable. However, we recommend in Chapter 6 that these offset errors be accounted for in the future.

3.14.3 Determination of Newton-Lorentz Force

The force which each charged particle sees is the Lorentz force

$$\frac{d\vec{\hat{v}}}{d\hat{t}}\frac{[v]}{[t]} = \frac{\hat{q}[q]}{\hat{m}[m]}(\vec{\hat{E}}[E] + \frac{\vec{\hat{v}}[v] \times \vec{\hat{B}}[B]}{\hat{c}[c]}) \tag{3.143}$$

or

$$\vec{\hat{F}} = \hat{q}(\vec{\hat{E}} + \vec{\hat{v}} \times \vec{\hat{B}}). \tag{3.144}$$

The force at each particle's position is obtained by interpolating from the four nodes surrounding the particle:

$$\vec{\hat{E}} = p_{k,j}\vec{\hat{E}}_{k,j} + p_{k+1,j+1}\vec{\hat{E}}_{k+1,j+1} + p_{k,j+1}\vec{\hat{E}}_{k,j+1} + p_{k+1,j}\vec{\hat{E}}_{k+1,j}; \tag{3.145}$$

$$\vec{\hat{B}} = p_{k,j}\vec{\hat{B}}_{k,j} + p_{k+1,j+1}\vec{\hat{B}}_{k+1,j+1} + p_{k,j+1}\vec{\hat{B}}_{k,j+1} + p_{k+1,j}\vec{\hat{B}}_{k+1,j}. \tag{3.146}$$

Let us dispense now with the "hats"; it is understood that all quantities are normalized. For any locally orthogonal 3-D coordinate system, the cross products are carried out the same, i.e.

$$\vec{v} \times \vec{B} = \begin{vmatrix} i_r & i_z & i_\theta \\ v_r & v_z & v_\theta \\ B_r & B_z & B_\theta \end{vmatrix}. \tag{3.147}$$

When $B_\theta = 0$, $B_r \neq 0$, $B_z \neq 0$, this results in forces and velocities in all three directions.

The scale of this simulation is such that the magnetic field bends ion trajectories only slightly. Electrons, on the other hand, are caught in cyclotronic motion.

Particles are also subject to random collisional forces implemented through Monte Carlo schemes. Collisions are discussed in Section 3.15 and elsewhere.

3.14.4 Three Dimensional $\vec{v} \times \vec{B}$ Integrator

The method of Boris [5] is used to integrate (time-step charged particle velocities forward according to) the Lorentz force. This method applies the electric and magnetic fields serially;

the particle takes half a time-step in velocity space applying only the electric field, then a full time-step applying only the magnetic field, and finally another half time-step applying to the electric field. The details are described below.

First, one half of the electric field is applied according to

$$\vec{v}^{-} = \vec{v} + K\vec{E}, \tag{3.148}$$

where $\vec{v}$ is the velocity at time t and

$$K = \frac{\hat{q}}{\hat{m}}\frac{\Delta\hat{t}}{2}. \tag{3.149}$$

In normalized units, $\hat{m}_e = 1$, $\hat{M} = M/m_e$, and $\hat{q} = \pm 1$. The full vector formulation is

$$\begin{vmatrix} v_r^- \\ v_z^- \\ v_\theta^- \end{vmatrix} = \begin{vmatrix} v_r + KE_r \\ v_z + KE_z \\ v_\theta \end{vmatrix}. \tag{3.150}$$

Next, a full time-step of rotation about $\vec{B}$ is applied. This step is based on the relation

$$\vec{c} = \vec{v}^{-} + K\vec{v}^{-} \times \vec{B} = \vec{v}^{+} - K\vec{v}^{+} \times \vec{B}, \tag{3.151}$$

where $\vec{v}^{+}$ is the velocity after the full time-step of rotation about $\vec{B}$. Equation 3.151 must be solved for $\vec{v}^{+}$. When $B_\theta = 0$, the solution is

$$\vec{v}^{+} = \begin{vmatrix} v_r^+ \\ v_z^+ \\ v_\theta^+ \end{vmatrix} = \begin{vmatrix} c_r - KB_z v_\theta^+ \\ c_z + KB_r v_\theta^+ \\ (c_\theta + KB_z c_r - KB_r c_z)/(1 + K^2B_z^2 + K^2B_r^2) \end{vmatrix}. \tag{3.152}$$

This completes the magnetic rotation. Finally, the second half of the electric field is applied according to

$$\vec{v}' = \vec{v}^{+} + K\vec{E}. \tag{3.153}$$

The full vector formulation is

$$\begin{vmatrix} v'_r \\ v'_z \\ v'_\theta \end{vmatrix} = \begin{vmatrix} v_r^+ + KE_r \\ v_z^+ + KE_z \\ v_\theta^+ \end{vmatrix}. \tag{3.154}$$

This is the final particle velocity at time t+1 in the old coordinate system. Next, we step the particle forward in space and rotate the coordinate system.

3.14.5 Error in Method of Boris

The angle of rotation through which an electron moves should be close to $\omega_c \Delta t = qB\Delta t/m$. Birdsall [5] shows that the Boris method produces a rotation through angle

$$\Theta = \omega_c \Delta t[1 - \frac{(\omega_c \Delta t)^2}{12} + ...]. \tag{3.155}$$

Thus, the error in Θ is less than one percent for $\omega_c \Delta t < .35$, and 2-7 percent for $.5 < \omega_c \Delta t < .9$.

3.14.6 Moving Particles and Transforming Coordinates

The leapfrog method now calls for position to be stepped forward. The coordinate system is cylindrical. Let the positions at time t and t+1 be given by, respectively,

$$\vec{r}_t = r_t \vec{i}_{r,t} + z_t \vec{i}_{z,t} \tag{3.156}$$

and

$$\vec{r}_{t+1} = (r_t + v_r \Delta t)\vec{i}_{r,t} + (v_\theta \Delta t)\vec{i}_{\theta,t} + (z_t + \vec{v}_z \Delta t)\vec{i}_{z,t} = x\vec{i}_{r,t} + y\vec{i}_{\theta,t} + (z_t + \vec{v}_z \Delta t)\vec{i}_{z,t}. \tag{3.157}$$

In all cases $\vec{i}_{z,t} = \vec{i}_{z,t+1}$ such that $\Delta z = v'_z \Delta t$. However, if there is a component of velocity in the θ direction, the coordinate system rotates about $\vec{i}_z$, i.e. $\vec{i}_{r,t} \neq \vec{i}_{r,t+1}$ and $\vec{i}_{\theta,t} \neq \vec{i}_{\theta,t+1}$.

The radial position after the move is the hypotenuse of the right triangle shown in Figure 3-21 such that

$$\vec{r}_{t+1} = \sqrt{x^2 + y^2}\, \vec{i}_{r,t+1} + 0\, \vec{i}_{\theta,t+1} + (z_t + \vec{v}_z \Delta t)\, \vec{i}_{z,t+1}. \tag{3.158}$$

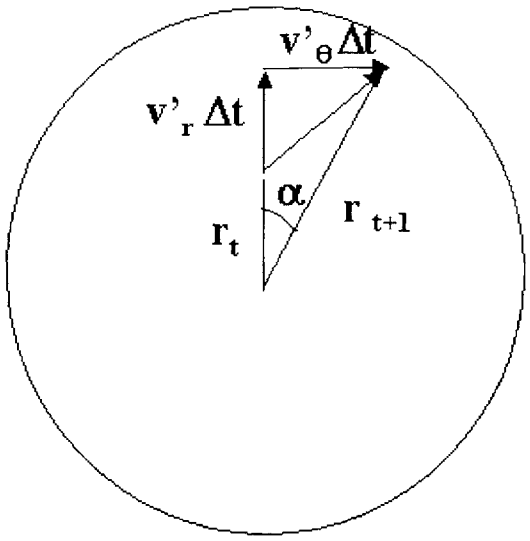

Figure 3-21: *Transformation of coordinates* when particle moves in the azimuthal direction.

Thus, the net radial displacement of a particle is

$$\Delta r = r_{t+1} - r_t. \tag{3.159}$$

Once $\vec{r}_{t+1}$ is determined, the velocity must be transformed to the new coordinate system. Let the angle of rotation in the θ direction be equal to α. Then if $r_{t+1} = 0$, $cos(\alpha) = 1$ and $sin(\alpha) = 0$. If $r_{t+1} \neq 0$, then $cos(\alpha) = x/r_{t+1}$ and $sin(\alpha) = y/r_{t+1}$.. Finally, we arrive at the new velocity of the particle:

$$\vec{v}_{t+1} = \begin{vmatrix} cos(\alpha)v'_r + sin(\alpha)v'_\theta \\ v'_z \\ -sin(\alpha)v'_r + cos(\alpha)v'_\theta \end{vmatrix}. \tag{3.160}$$

Note that it is not necessary to call trigonometric functions to find $cos(\alpha) = x/r_{t+1}$, and $sin(\alpha) = y/r_{t+1}$.

Numerical Simplification

To first order in Δt, $\Delta r = v_r{}'\Delta t$. To second order, after expanding, $\Delta r = v_r{}'\Delta t + \frac{1}{2}\frac{(v_\theta{}')^2}{r_t}\Delta t^2$. This may speed computation. Also, v_r and v_θ in Equation 3.160, could be replaced by the first order expansions

$$v_{r,t+1} = v_r{}' + \frac{(v_\theta{}')^2}{r_t}\Delta t - \frac{3}{2}\frac{(v_\theta{}')^2 v_r{}'}{r_t^2}\Delta t^2 \tag{3.161}$$

and

$$v_{\theta,t+1} = v'_\theta - \frac{v_r{}' v_\theta{}'}{r_t}\Delta t + \frac{v_\theta{}'}{r_t^2}[(v_r{}')^2 - \frac{(v_\theta{}')^2}{2}]\Delta t^2. \tag{3.162}$$

This less accurate expansion requires more mathematical calls, but eliminates the square root call.

3.14.7 Particle Tracking in Computational Coordinates

As a particle is stepped forward in real coordinates, it is also tracked in computational coordinates. First, its new computational coordinates are estimated as follows:

$$\xi = \xi_o + \frac{\partial \xi}{\partial z}\Delta z + \frac{\partial \xi}{\partial r}\Delta r; \tag{3.163}$$

$$\eta = \eta_o + \frac{\partial \eta}{\partial z}\Delta z + \frac{\partial \eta}{\partial r}\Delta r. \tag{3.164}$$

The coefficients ξ_z, ξ_r, η_z, and η_r may be interpolated from the nearest grid nodes. Then, we verify the estimate. A special function does this each time a particle is moved. First, the function checks to see if the particle it is actually inside the cell it's supposed to be in, $(k, j) = (int(\xi), int(\eta))$. If the particle is not found, a search is performed, starting with cell (k, j) and spiraling outward. If a boundary cell is checked, then a separate function is called which checks whether the particle trajectory crossed the boundary or boundaries in that cell. What happens after that depends on the type of particle being simulated, and the boundary conditions. Particle-boundary "collisions" are discussed more in Section 3.18.

Each time a particle moves, it must be re-weighted to the grid. This means that the weighting constants to the four corner nodes of the cell in which the particle resides, P_{00} P_{01} P_{10}, and P_{11}, must be recalculated. As shown in Section 3.4, these values are included in the particle data structure, Thus, they must be calculated only once per position.

Numerical Test of Magnetic Part of Lorentz Equation

This section describes tests performed to make sure the $\vec{v} \times \vec{B}$ was able to correctly track an electron. Unless otherwise noted, the tests were performed on a cylindrical simulation region while developing the code.

The magnetic part of the Lorentz Equation is a step in the rotation of the velocity vector about a magnetic field line. We test the accuracy of the solver by taking the magnetic field to be entirely in the theta direction, $\vec{B} = B_\theta = 1.0$. This allows us to see the circular motion of the electron. For this case, we set $\vec{E} = 0$ everywhere. Because $\hat{B} = 1$ and $\omega_{ce} = \hat{B}$, the unit of time $\hat{t} = \omega_{pe}^{-1} = \omega_c e^{-1}$. The unit of time is, in effect, the inverse gyro frequency such that the electron should perform one gyration every $2\pi\hat{t}$.

We place one electron in the center of the domain, giving it velocity $\vec{v} = v_z = 1.0$. Then we step the electron position forward by 150 time-steps, at $\Delta\hat{t} = .25$. Figure 3-22 shows a trace of the particle position and the associated fast Fourier transform, which shows a frequency of gyration $\nu = .04$. Thus, the period $1/\nu = 25\Delta\hat{t} = 6.25\hat{t}$, which is quite close to $2\pi = 6.28$.

We also check that the Larmor radius, $r_L = \frac{v_\perp}{\omega_{ce}}$ is correct. This should be 1.0. The trace shows a difference from max to min of 1.0077, where the error is easily attributable to step size, since each step is about 4 percent of the radius.

Figure 3-23 shows the first twenty time-steps of this trace. The electron starts at the square and ends at the star. In the (r, z, θ) coordinate system, $\hat{\vec{B}} = 1.0 i_\theta$ points into the page, such that an electron should rotate clockwise. This is observed.

With the electric field solver turned on, and boundary conditions of $\Phi = 0$ on the outer edges, and $E_r = 0$ at the centerline, the electron experiences a slight electric field. This is because the electron digs a potential well of fixed depth. By forcing the potential to zero at three sides, the gradient of Φ must be greater at one side or the other. A test particle half way between the ends of the test computational cylinder indeed experiences no electric field in the z direction, as can easily be checked. But a particle slightly off center experiences a small E_z. The measured period does not change, although the maximum deviation in the Z direction is now 1.0147, and the maximum deviation in the R direction is now 1.0071. A numerical trace shows the very slight oblongation (see Figure 3-24).

Turning the field solver back off, we test whether the solver works if the B-field is

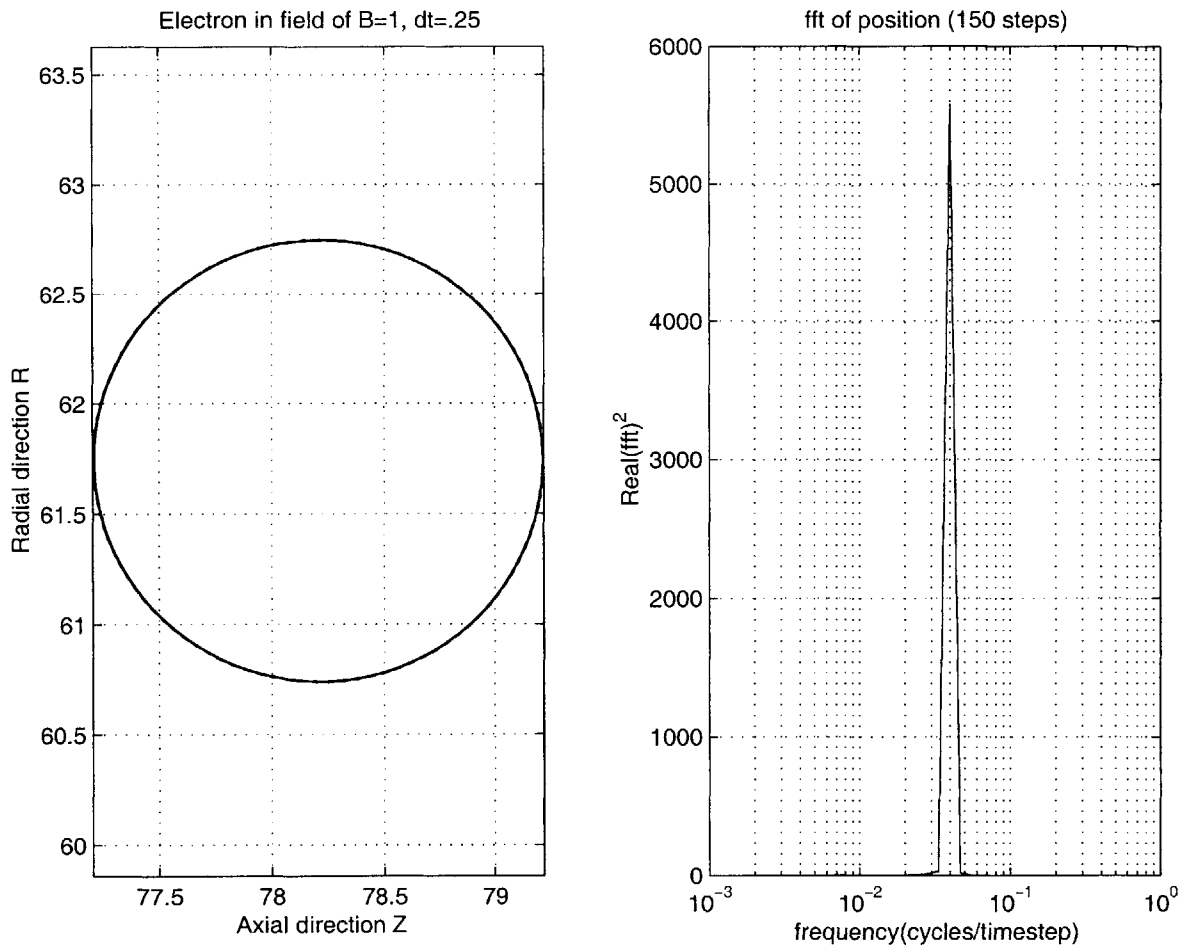

Figure 3-22: *Electron trace with no field solver.* $\hat{B} = 1\vec{i}_\theta$. Period is $1/.04 * .25\hat{t} \approx 2\pi\hat{t}$.

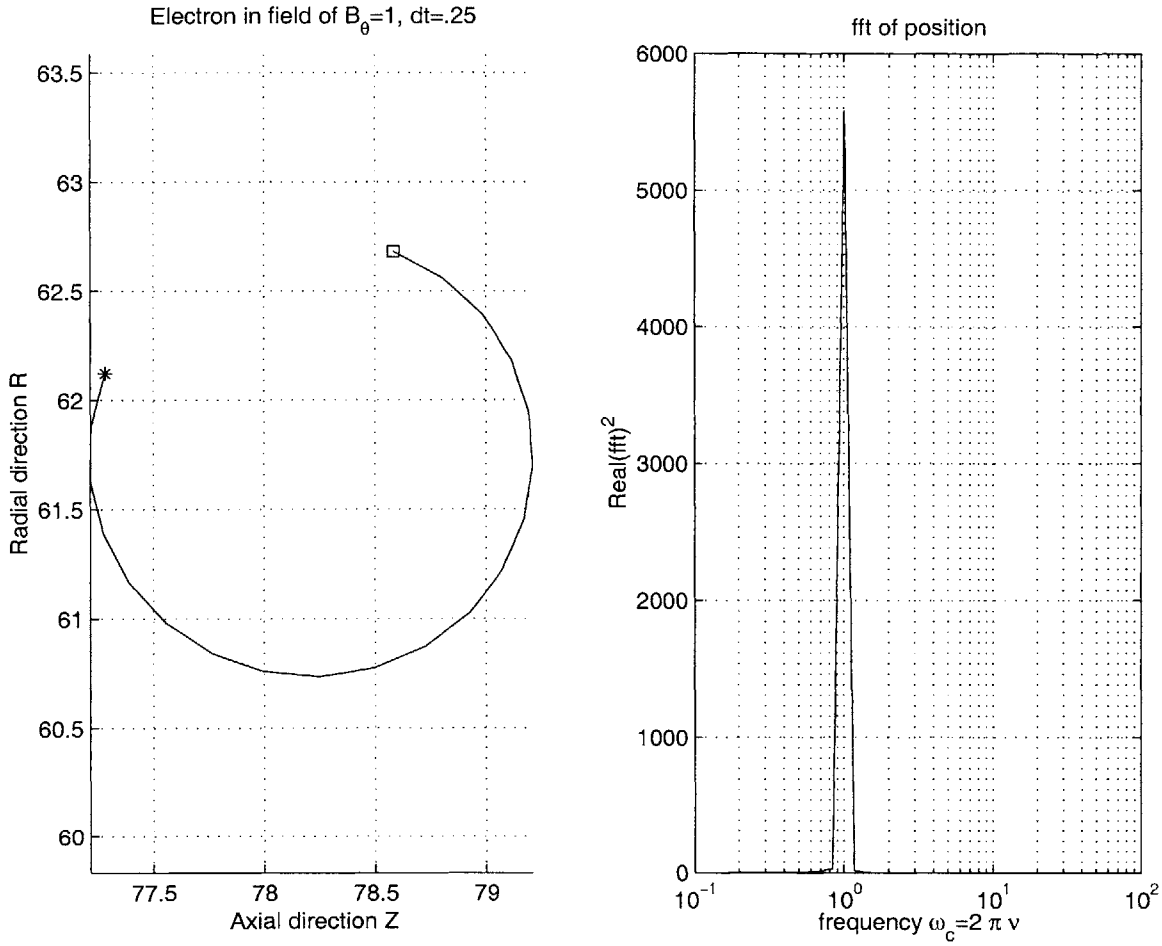

Figure 3-23: *Electron trace with no field solver.* Shown are 20 time-steps at $\Delta\hat{t} = .25$ where $\hat{\vec{B}} = 1.0\vec{i}_\theta$. Since $\hat{q} = -1$ and $\hat{m} = 1$, the frequency of rotation is $\omega_c = 1.0$. B-field is into the page. Square is the beginning of trace. Star is the end. Electron rotates clockwise, as expected.

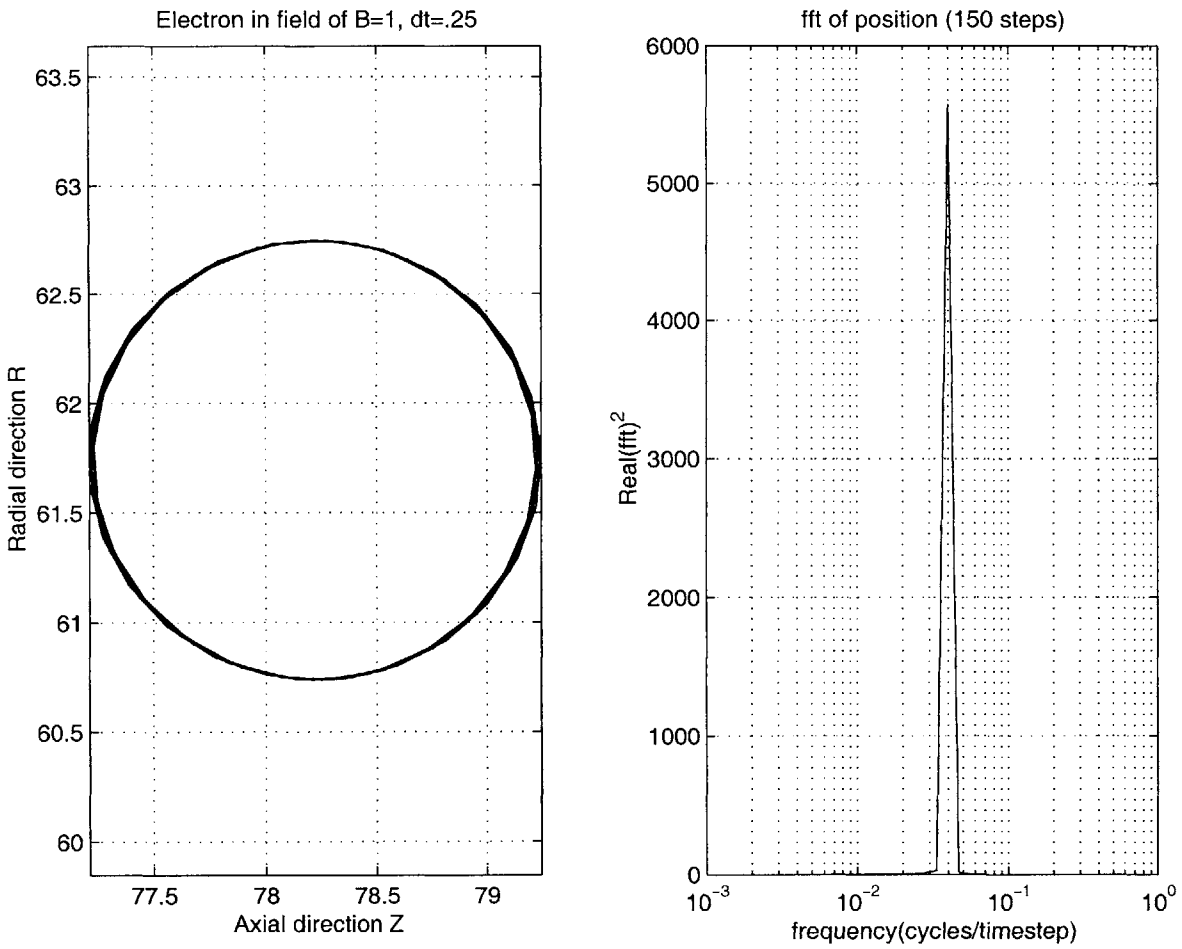

Figure 3-24: *Electron trace with field solver.* $\hat{B} = \vec{i_\theta}$. Period is $1/.04 * .25\hat{t} \approx 2\pi\hat{t}$.

oriented along the R axis. First, we turn off the coordinate transformation; the geometry is, in effect, that of a linear Hall thruster. With $\vec{v} = v_z$, we should, and indeed we do, see a horizontal line as the particle cycles around the field line. Again, we observe a period of 25 time-steps. (See Figure 3-25).

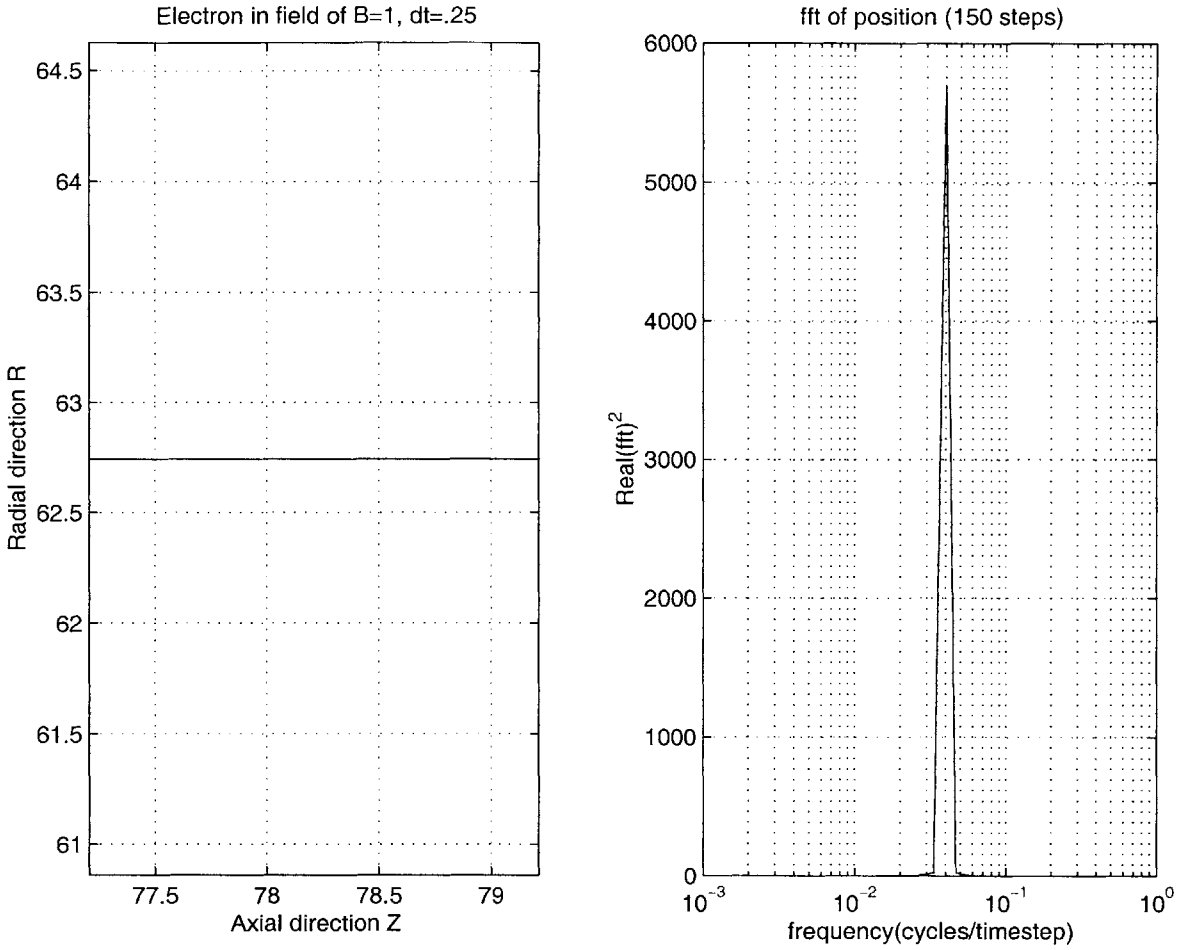

Figure 3-25: *Electron trace with field in R direction. No coordinate transformation.* $\hat{B} = 1\vec{i}_r$. Period is $1/.04 * .25\hat{t} \approx 2\pi\hat{t}$. Situation corresponds to a linear Hall thruster.

If the coordinate transformation is turned on but the field remains in the radial direction, then the field must be modified to produce zero divergence. Figure 3-26 shows a particle trace obtained using the field $\vec{B} = B_o/r$, which satisfies $\vec{\nabla} \cdot \vec{B} = 0$. The particle begins with zero parallel energy, but is accelerated outward. This behavior is expected. As discussed in Section 2.9, a parallel gradient in field strength produces a parallel force. This is often called the "magnetic mirror" effect. Both kinetic energy and magnetic dipole moment are conserved, showing the accuracy of the $\vec{v} \times \vec{B}$ integrator. This figure was acquired using the actual simulation (not the cylinder). The time-step used is rather long, reflected in the

jaggedness of the curve.

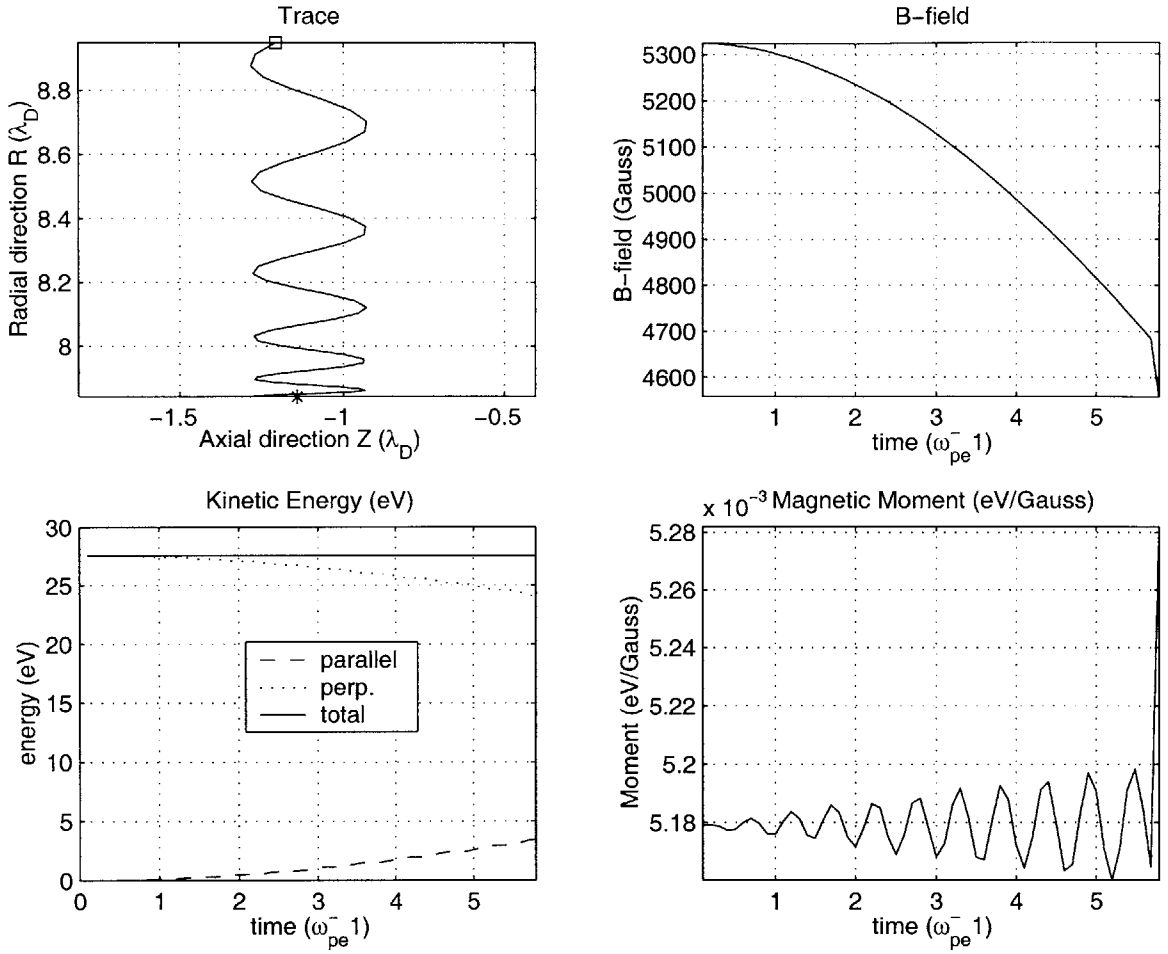

Figure 3-26: *Magnetic mirror effect.* Electron trace with field in R direction. Coordinate transformation turned on. $\hat{B} = B_o/\vec{ri}_r$. Particle is accelerated along $\|$ gradient toward region of lower $|B|$. Kinetic energy and magnetic dipole moment are conserved.

Putting the field entirely in the z direction yields predictable results; the electron rotates around $\vec{B}$ (see Figure 3-27). In this case, the magnetic field is isotropic, so there is no net drift to the outside, even though the coordinate effect is turned on.

Next, we want to test for the guiding center's ExB drift,

$$\vec{v}_{E\times B} = \frac{\vec{E}\times\vec{B}}{B^2}. \tag{3.165}$$

We let $\vec{E} = E_r = 3.0$, and $\vec{B} = B_\theta = 5.0$, and start with an electron initially at rest. The trace is shown in Figure 3-28. The code shows $\Delta z = 22.4950$ over 150 time-steps. (Since the cyclotron radius is small compared to the drift distance, we simply take the difference

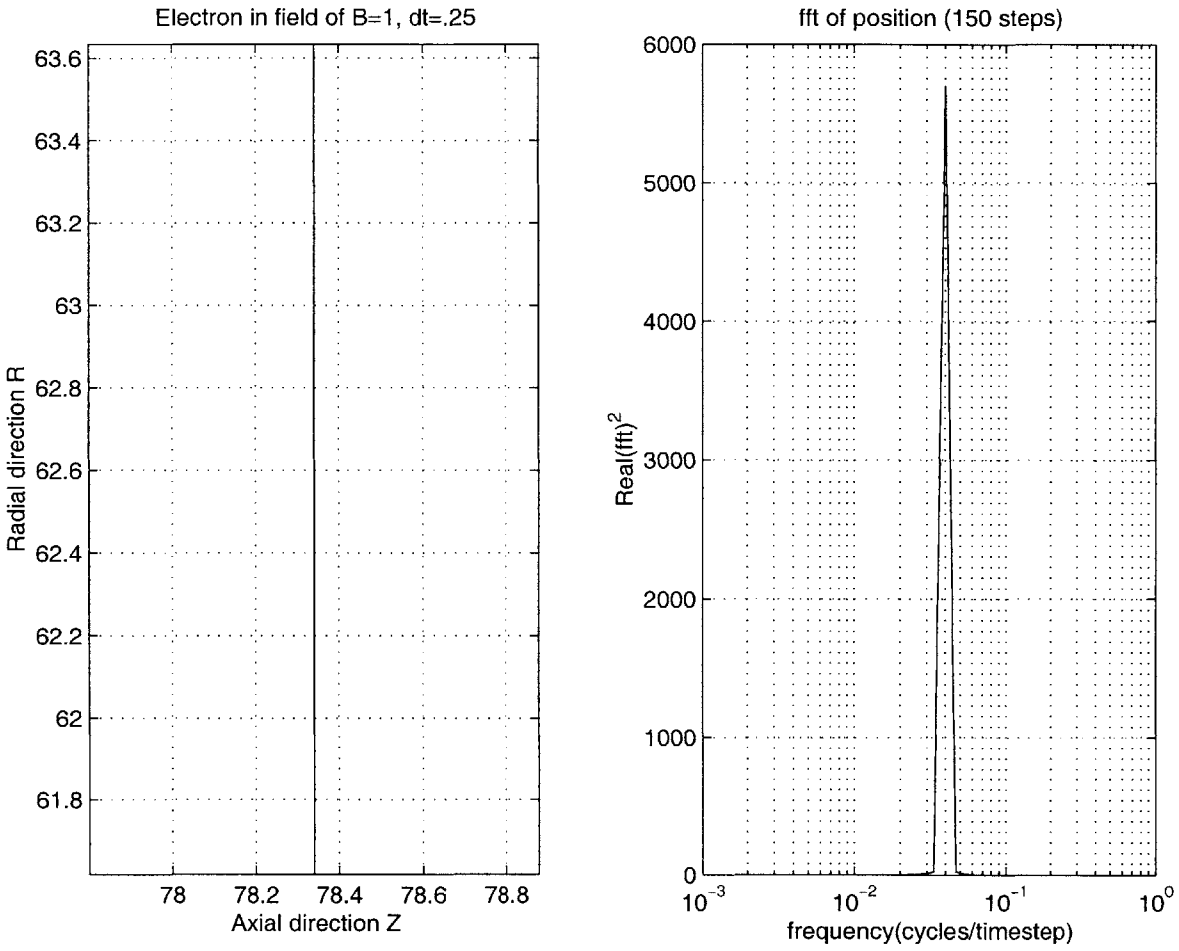

Figure 3-27: *Electron trace with field in Z direction.* $\hat{B} = 1\vec{i}_z$. Period is $1/.04 * .25\hat{t} \approx 2\pi\hat{t}$

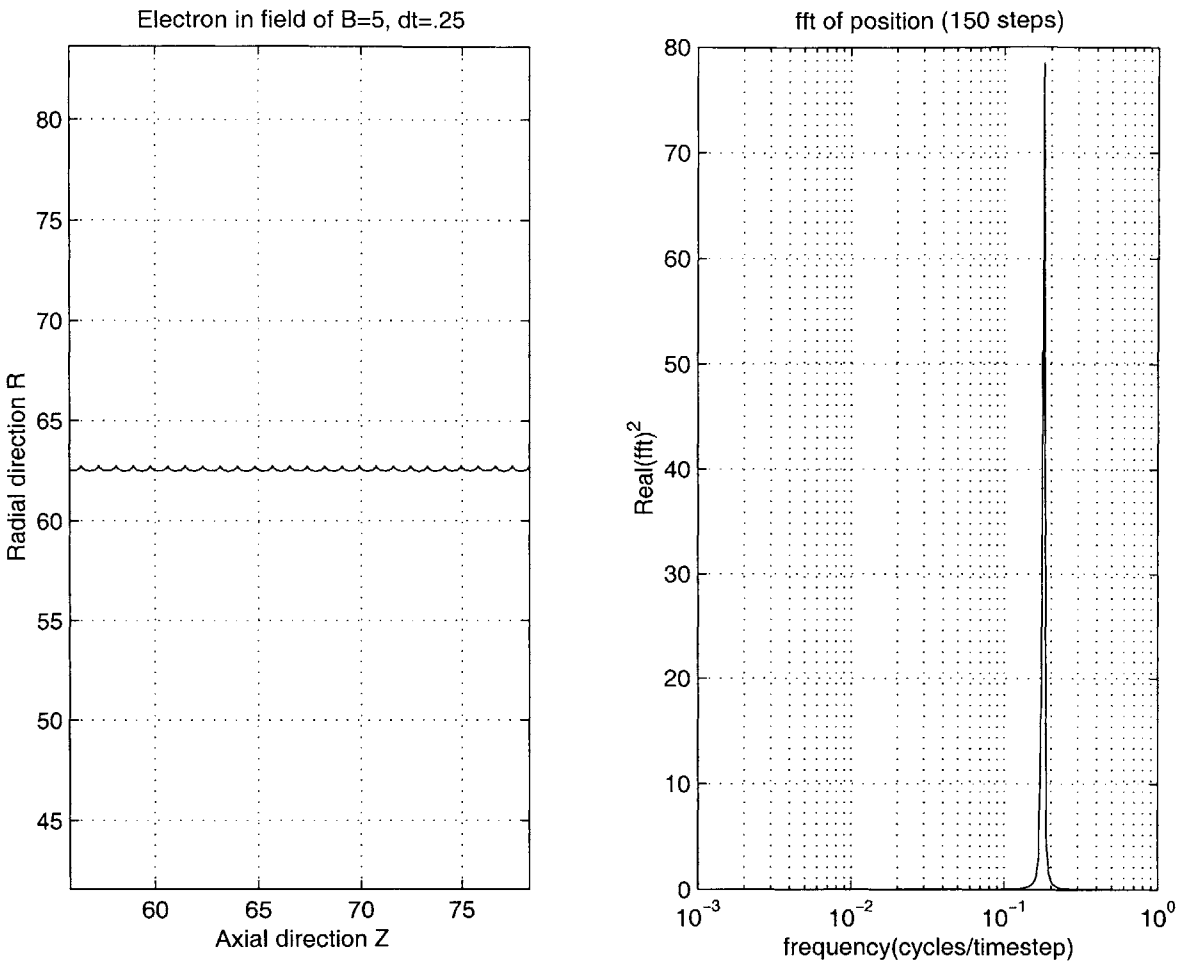

Figure 3-28: *Electron $\vec{E} \times \vec{B}$ drift.* $\hat{B} = 5\vec{i}_\theta$. Period is $1/.18 * .25\hat{t} \sim 2\pi/5\hat{t}$

between the maximum and minimum z). Thus, $\vec{v} \approx 22.4950/(150 * .25)i_z = .5999i_z$. In theory, the drift should be $\vec{v}_{E\times B} = 0.6i_z$. This seems to confirm the drift. A Fast Fourier Transform of the motion in the radial direction shows a period of 5.6 time-steps, or about 5 times the original cyclotron frequency, as expected. Greater accuracy is expected with a smaller time step.

3.14.8 Magnetic Dipole Moment

Magnetic bottling and conservation of magnetic dipole moment were demonstrated in a series of tests similar to the leapfrog tests just described. Please see Chapter 4 for a description of these tests.

3.15 Particle-Particle Collisions

Electron-neutral elastic scattering, excitation, and ionization collisions, and ion-neutral scattering and charge exchange collisions are treated using a Monte Carlo methodology. Cross section for these events are presented in Section 2.8. Numerical functions for extracting the cross Sections are listed in Appendix, B.

3.15.1 Electron-Neutral Collisions

Given an electron of velocity $\hat{\vec{v}}$ and a slow neutral background of density $\hat{n}_n[size]$, the frequency with which one electron scatters off the neutrals is

$$\nu = \hat{v}\hat{Q}_t\hat{n}_n[size] \tag{3.166}$$

where $\hat{Q}_t$ is calculated at the electron velocity.

Each time we move an electron, we calculate the probability of at least one scattering event happening in that time-step, $p = 1 - e^{-\Delta t\nu}$ [34] [3]. We compare this to a random number. If $R(0 \rightarrow 1) < p$, an event occurs. In this case, we compare another random number to the cross sections for elastic scattering, excitation, and ionization to determine which type of event occurs.

This commonly used method is based on the exponential decay law. Let ν be the collision frequency and λ_{mfp} be the mean free path. If N identical electrons are present in a box at time t, and each electron which undergoes a collision is "taken out of the box", then the probability per unit time for the collision of an electron is $\nu = -\frac{(dN/dt)}{N}$, or equivalently, $1/\lambda_{mfp} = -\frac{(dN/dx)}{N}$. Thus, $N(t) = N_o e^{-\Delta t\nu}$, and the probability that the electron will not undergo any collisions in time dt (or in distance dx)is $p = e^{-\Delta t\nu}$. The probability that it will is $p = 1 - e^{-\Delta t\nu}$.

If an event occurs, in all cases, the primary electron is reflected in a random direction. This is a variation of the Hard Sphere (VHS) model of DSMC collisions. The difference is that DSMC involves choosing two particles and colliding them explicitly. Momentum is transferred from/to both particles. Here, electrons are scattered of a background species at a bulk velocity; momentum is transferred to electrons, but not to neutrals. It would be easy, however, to factor in bulk momentum transfer; we do it for ion-neutral collision. Also, it would be easy to allow for non-isotropic scattering; we would simply have to find the new

random direction according to a non-isotropic distribution.

If the collision is inelastic, additional steps must be taken. If the event is an excitation collision, the primary electron loses energy. If the event is an ionization collision, four things happen: A secondary electron is created; energy is subtracted from the primary electron; an ion is created; and mass is subtracted from the neutrals.

The Hard Sphere Collision Model

The Hard Sphere model of a two particle collision is illustrated in Figure 3-29. Let $\vec{c}_r$ be the relative velocity vector between two particles in the center of mass frame before they collide, and let $\vec{c}_r^*$ be the relative velocity vector after they collide. In the Hard Sphere model, the force acts only when and where the particles hit each other; the particles bounce off each other like billiard balls. Scattering from such a process is isotropic in the center of mass frame of reference. During the collision, the magnitude of the relative velocity is conserved: $c_r = c_r{}^*$. However, all directions are equally likely for $\vec{c}_r^*$ [4].

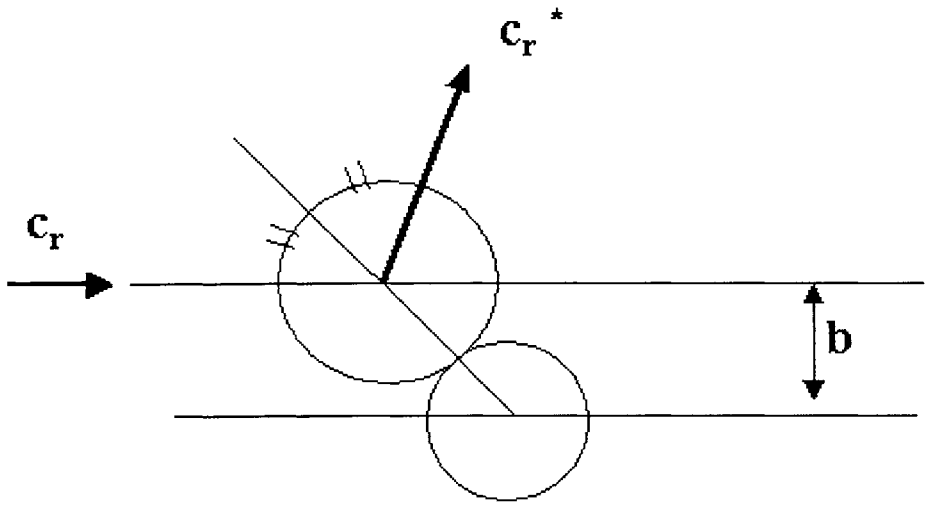

Figure 3-29: *Illustration of hard sphere collision.* The relative velocity before the collision is c_r. The relative velocity after the collision is c_r^*. Scattering from hard sphere molecules is isotropic in the center of mass frame of reference [4].

Elastic Scattering

For elastic electron-neutral collisions, we assume that the neutrals are infinitely heavy. Hence, $\vec{c}_r = \vec{v}_e$ and $|v_e| = |v_e|^*$. The electron retains its initial speed (and energy), but is

scattered isotropically in direction. Momentum is not conserved; momentum transferred to the neutrals is ignored. Energy is not conserved either; there is a recoil energy transferred on the order of $2m_e/M$ times that of the electron.

These collisions produce electron transport across $\vec{B}$.

Inelastic Scattering: Excitation

All Xenon excitation is assumed to occur at 8.32 eV, the first excitation energy. If an excitation event occurs, the primary electron loses 8.32 eV of energy and is scattered isotropically in direction. The total cross section for excitation is used to determine the frequency of these events, but only the first excitation is modeled. Thus, energy losses are underestimated in the simulation. A better model (recommended as future work in Chapter 5) would take into account different energy levels; such a model could be obtained by summing cross sections for various energy levels and making one or several "effective" excitation levels.

The neutrals are assumed to immediately radiate. Hence, no effects on the neutrals are directly modeled.

Inelastic Scattering: Ionization

If an ionization event occurs, the primary electron is scattered isotropically in direction. The electron also loses energy, but the amount must be determined.

Only $e + Xe \rightarrow 2e + Xe^{1+}$ ionization events are modeled (although inclusion of higher order ions would not be difficult). Since the first ionization energy of unexcited Xenon is $12.1eV$, each primary electron must lose at least $12.1eV$ of kinetic energy ($E_p < E_{p,o} - 12.1\,eV$). However, a secondary electron is also produced; this also carries away some energy. We use a probability distribution to find the primary and secondary electron energies. This will be described in the next section.

At the end of each electron loop, ions and secondary electron are created at the primary electrons' locations. Initial ion velocities are the neutral background velocity. Locations of all ionization events are tallied according to the Nearest Grid Point (NGP) in computational space such that we arrive at $\Delta N_n(z,r)$ due to ionization after each time-step. Neutrals are deleted accordingly during the neutral loop.

Secondary Electron Emission During Ionization

When an electron ionizes a neutral, a secondary electron is created. The differential cross-section for ionization by an electron of primary energy E_p with emission of a secondary electron of energy E_s is taken to be of the form

$$\sigma(E_p, E_s) = \sigma(E_p)C(E_p)f(E_s); \int_0^\infty \sigma(E_p, E_s)dE_s = \sigma(E_p) \tag{3.167}$$

where $\sigma(E_p)$ is the total ionization cross section for all E_s,

$$C(E_p) = \frac{1}{E_j tan^{-1}[(E_p - I)/2E_j]}, \tag{3.168}$$

and

$$f(E_s) = \frac{1}{1 + (E_s/E_j)^2}. \tag{3.169}$$

Here, $I = 12.1$ is the ionization energy for Xe^{1+} and $E_j = 8.7$. This function is taken from Opal, et. al. [35], who state it is in fact a poor fit for Xenon due to unaccounted for excitation lines. We justify its use by stating that excitation is accounted for elsewhere.

In practice, we randomly choose a secondary emission energy: $E_s = R(0 \rightarrow 1) \times (E_p - I)$. We then use the rejection method to determine if this energy is acceptable. (Let $R2 = R(0 \rightarrow 1)$. If $R2 < f(E_s)$, then E_s is accepted.) Finally, the energy of the primary is computed exactly; $E_p = E_{p,o} - E_s - 12.1eV$. For higher order ionization, we can either extend this method, or simply create the secondary electrons at the mean neutral flow velocity – zero energy, essentially.

Deletion of Neutrals

At the end of each electron iteration loop, ions and secondary electrons are created, and the positions of all ionization event are tallied. Therefore, we know the number of neutrals size $s = 1$ which need to be deleted in each control volume on the grid. Let this quantity be $\Delta N_n(k, j)$. This is just the mass to be deleted. It is an integer quantity. This is not the number of super-particles which must be deleted, unless $s = 1$ for all neutral super-particles. (Recall that neutral super-particles are an integral factor s times larger than charged particles. This is the statistical weight discussed in Section 3.10 which keeps the number of charged particles and neutrals roughly equivalent. Ions and electrons are always

$s = 1$.) We also know the number of neutrals size $s = 1$ in each grid volume, $N_n(k,j)$. This is just the total mass. As before, this is not the number of super-particles in the control volume. If 2 electrons experienced ionization events in cell (5,6) during the previous electron loop, then $\Delta N_n(5,6) = 2$ and two units of mass ($2s$) must be deleted. As we move the neutrals, we calculate for each a probability of ionization, $p_i = s_i \Delta N_n(k,j)/N_n(k,j)$, and compare it to a random number to determine whether it will experience a loss of mass. If so and $s_i > 1$, then $s_i \rightarrow s_i - 1$, while if $s_i = 1$, the super-particle is deleted.

The quantity $\Delta N_n(k,j)$ is maintained as a static variable (it is not automatically re-initialized at the end of each neutral loop) such that the number of events is conserved. Hence, if the neutral mass deleted on a given time-step is less than $\Delta N_n(k,j)$, the remainder is maintained for the next time-step. Thus, mass is conserved overall.

This CPU sparing NGP method is easy to implement.

3.15.2 Ion-Neutral Charge Exchange Collisions

Given an ion of velocity $\hat{\vec{v}}$ and a neutral background of super-particle density $\hat{n}_n[size]$ moving at bulk velocity $\hat{\vec{v_n}}$, the frequency with which one ion exchanges charge with the neutrals is

$$\hat{\nu}_{cex} = \hat{c}_r \hat{Q}_{cex}(\hat{c}_r) \hat{n}_n[size] \tag{3.170}$$

where the relative speed is

$$c_r = |\vec{v}_i - < \vec{v_n} > |. \tag{3.171}$$

As per Equation 2.90, the cross section is taken to be $Q_{cex} = (k_1\, ln(c_r) + k_2)^2 \times 10^{-16}\ cm^2$. In addition, we take into account that heavy particles are moving too fast by a factor of $\sqrt{1/f}$, which means the cross section should be taken at speed $c\sqrt{f}$. Thus, the equation is modified to

$$\hat{\nu}_{cex} = \hat{c}_r \hat{Q}_{cex}(\hat{c}_r \sqrt{f}) \hat{n}_n[size], \tag{3.172}$$

where the additional factors of $\sqrt{f}$ for velocity and $\sqrt{1/f}$ for cross section cancel out.

Each time we move an ion, we calculate the probability of a charge exchange event happening in that time-step: $p = 1 - e^{-\Delta \hat{t} \hat{\nu}_{cex}}$. We compare this to a random number. If $R(0 \rightarrow 1) < p$, an event occurs. In that case, an ion with the neutral bulk velocity is created at the original ion's location. The original ion loses its charge, is removed from the

list of ions, and is added to the list of neutrals. Since ion and neutral time-steps may be unequal by a factor of 10, there is a slight loss of accuracy with regard to position. The locations of these charge exchange events are tabulated according to the nearest grid node in computational space. The next time the neutrals are moved, some will be deleted just as they are for ionization events (see "Deletion of Neutrals", above).

Note that this is a secondary effect which may be "turned off" to speed up the simulation.

3.15.3 Ion-Neutral Scattering Collisions

Ion-neutral scattering collisions are treated as a variant of the Hard Sphere(HS) model. Ions are treated during the ion loop. First, we find the relative velocity of the ions to the background neutral bulk velocity, $\vec{c_r} = |\vec{v_i} - < \vec{v_n} > |\sqrt{f}$. The variable $\sqrt{f}$ accounts for the fact that all heavy particles are moving a factor of $1/\sqrt{f}$ too fast. As before, we use c_r along with a cross section $Q_{in}(c_r)$ and a random number to determine whether an event takes place. (Since we model both ion neutral scattering and charge exchange collisions, we lump the collisions together as we did with electron-neutral scattering collisions. That is, $Q_{tot} = Q_{in} + Q_{cex}$, and so on.)

When a collision occurs, the magnitude of the relative velocity is conserved ($|c_r|^* = |c_r|$), but the direction in the center of mass frame is determined randomly. Thus, the ion leaves along a relative velocity vector drawn from an isotropic distribution. The amount of momentum ($\Delta\vec{p} = M(\vec{v_o} - \vec{v_f})$) and energy ($\Delta E = .5M(v_o^2 - v_f^2)$) lost to the neutrals is tallied and applied to the neutrals during the neutral loop.

Rather than picking one neutral randomly, we act upon all neutrals in the cell where the ion-neutral collision took place (using NGP weighting). We conserve both momentum and energy. First we calculate the change in bulk velocity required to conserve momentum,

$$\Delta < \vec{v_n} >_{kj} = \Delta\vec{p}_{kj}/M_{kj}. \tag{3.173}$$

Again, $\Delta\vec{p}_{kj}$ is the net momentum lost by the ions, which is to be gained by the neutrals. This velocity change is applied to all neutral super-particles in the cell according to

$$< \vec{v_n} >'_{kj} = < \vec{v_n} >_{kj} + \Delta < \vec{v_n} >_{kj} . \tag{3.174}$$

The bulk energy of the neutrals is determined by

$$E_{bulk} = \frac{1}{2} M < v >^2, \tag{3.175}$$

where M is the total mass of all particles at (k,j). Thus, Equation 3.174 changes the bulk energy of the neutrals from $E_{bulk,o}$ to $E_{bulk,f}$, but the internal energy stays the same. Let us calculate the change in internal energy required to conserve energy. To conserve energy overall, we balance the internal and bulk energies before and after the "collision";

$$E_{bulk,f} + E_{internal,f} = E_{bulk,o} + E_{internal,o} + \Delta E. \tag{3.176}$$

Again, ΔE is the kinetic energy lost by the ion in its collision with the cloud of neutrals. The internal kinetic energy of the i particles in cell (k,j) is just

$$E_{internal} = \frac{1}{2} \Sigma_i M_i (v_i - < v >)^2, \tag{3.177}$$

where M_i is the mass of a single particle, and where $\vec{v_i} - < \vec{v} >$ is the relative velocity. Equation 3.176 is balanced by multiplying all the neutral relative velocities by a scaling factor α. For each of the i particles in cell (k,j), we let

$$\vec{v} = < \vec{v_n} >'_{kj} + \alpha(\vec{v} - < \vec{v_n} >_{kj}), \tag{3.178}$$

where

$$\alpha^2 = \frac{E_{bulk,o} + E_{internal,o} + \Delta E - E_{bulk,f}}{E_{internal,o}}. \tag{3.179}$$

This increases the internal energy of the neutrals, but has no effect on the neutral bulk velocity. Thus, both energy and momentum are conserved overall.

3.15.4 Monte Carlo Coulomb Collisions

In Section 2.8.5 we stated that electron-ion and electron-electron Coulomb collisions should be modeled. In Section 3.16.3 we present a diffusive model for these collisions which was an extension of the Langevin equation. However, this diffusive model is complicated and computationally intensive. Before the diffusive model was completed, a much simpler Monte Carlo Coulomb Collision (MCCC) model was implemented. This model was used to produce

all results in Chapter 4 and many in Chapter 5.

In the MCCC model, the local collision frequency is estimated and compared with a random number to determine whether an electron experiences a collision. When a collision occurs, it is treated as a discrete, isotropic, large angle scattering event. Such "hard sphere" collisions are described in Section 3.15.1. We assume that no momentum is transferred to the ions in these collisions; they are characterized by random jumps in electron momentum.

At first glance, the method may seem to be invalid. After all, most Coulomb collisions are small angle and involve many particles at once. However, if the fact that collisions are not actually binary is ignored and the cut-off collision integral (to λ_D) is used, then the answer for momentum transfer between electrons and ions should actually be the same as that obtained by using the Fokker-Planck equation [48]. Unfortunately, the method is less valid for like-particle interactions, and collisional relaxation to equilibrium is not correctly represented.

Two versions of the MCCC model were used to produce results presented in this thesis. Most of the results in this thesis were generated by Version 1.0. Its most obvious flaws were corrected in Version 2.0. Results from Version 2.0 are discussed in Chapter 5.

MCCC Model Version 1.0

In Version 1.0 of the MCCC model, the collision frequency is estimated according to

$$\nu_{ei} = n_i Q_{ei}^m |v_e| \; ; \; \nu_{ee} = n_e \bar{Q}_{ee}^m |v_e|, \tag{3.180}$$

where $|v_e|$ is the absolute speed of the electron. For electron-ion collisions, the momentum transfer cross section, was defined (see Section 2.8.5) to be

$$Q_{ei}^m = 4\pi b_o^2 = \frac{6.5 \times 10^{-14}}{E_{eV}^2}, cm^2. \tag{3.181}$$

Here, $E = 1/2 m_{12} v_{12}^2 \approx 1/2 m_e v_e^2$ and b_o is the impact parameter for electron-ion interactions. The minimum cross section Q_{ei}^m was assumed to be the atomic cross section, $\pi r^2 \approx 3.66 \times 10^{-16} cm^2$. Furthermore, if $Q_{ei}^m < Q_{en}$, then Q_{en} was used. The energy

averaged momentum transfer cross section for electron-electron collisions was defined to be,

$$\bar{Q}_{ee}^{m} = 9\pi \bar{b}_o^2 = \frac{6.5 \times 10^{-14}}{T_{eV}^2}, cm^2. \tag{3.182}$$

There is an error in this equation; the coefficient should be 6π!

Note that ν_{ee} is often calculated assuming that $|v_e| = \bar{c}_e = \sqrt{8KT/\pi m_e}$. Thus, $|v_e|$ is replaced by a temperature. However, we prefer to use individual electron velocities.

There are two obvious mistakes in this model:

- The energy averaged momentum cross section Q_{ee}^{m} is a factor of three halves too large. The coefficient should be 6π.
- Both equations omit the Coulomb logarithm, $ln\Lambda$. There was on purpose. For particles of average speed, the fractional contribution from large-angle collisions is of order $1/ln\Lambda$ [32]. We tried to restrict the model to *large angle* collisions by setting $ln\Lambda = 1$. Thus, we essentially ignored the effects of small angle collisions.

These errors were corrected in MCCC Model Version 2.0.

MCCC Model Version 2.0

The second MCCC model corrects the most obvious flaws of the first model. In this model, the collision frequency is again estimated according to

$$\nu_{ei} = n_i Q_{ei}^{m} |v_e| \; ; \; \nu_{ee} = n_e \bar{Q}_{ee}^{m} |v_e|, \tag{3.183}$$

where $|v_e|$ is again the absolute speed of the electron. However, we now account for all particles out to the Debye length by inserting the Coulomb logarithm. For electron-ion collisions, we use (see Section 2.8.5),

$$Q_{ei}^{m} = 4\pi b_o^2 ln\Lambda = \frac{6.5 \times 10^{-14}}{E_{eV}^2} ln\Lambda \, cm^2. \tag{3.184}$$

The minimum cross section Q_{ei}^{m} is still assumed to be the atomic cross section, $\pi r^2 \approx 3.66 \times 10^{-16} cm^2$. Furthermore, if $Q_{ei}^{m} < Q_{en}$, then Q_{en} is used. For electron-electron

collisions, we add the Coulomb logarithm and correct the coefficient, such that

$$\bar{Q}_{ee}^{m} = 6\pi \bar{b}_o^2 \, ln\Lambda = \frac{4.34 \times 10^{-14} ln\Lambda}{T_{eV}^2} \, cm^2. \tag{3.185}$$

Although this model should produce nearly correct electron momentum transport, it is still imperfect. It will not predict the correct energy distribution relaxation rates, and should not really be used at all for electron-electron collisions. Fortunately, Coulomb collisions are only significant for low energy electrons.

3.16 Diffusive Model of Coulomb Collisions

At any given instant of time, an electron will typically be scattering off many other charged particles. Thus, it is inappropriate physically (though convenient numerically) to treat Coulomb scattering as a sequence of Monte Carlo collisions [30]. It is more correct to represent Coulomb scattering as a diffusion process in velocity space. We developed and implemented a method which does this. The method is similar to that described in Ref. [2].

3.16.1 The Boltzmann Equation

Evolution of the plasma species is determined by coupled ion and electron kinetic equations for the time dependent, 3D distribution function $f_\alpha(t, \vec{r}, \vec{v})$. Ignoring source and sink terms, one may write the Boltzmann equation

$$\frac{\partial f_\alpha}{\partial t} + \vec{v} \cdot \nabla f_\alpha + \frac{\vec{F}}{m} \cdot \frac{\partial f_\alpha}{\partial \vec{v}} = C_\alpha^c \tag{3.186}$$

where $C_\alpha^c = (\frac{\partial f_\alpha}{\partial t})^c$ is the non-linear collision term. For electrons, the collision term formally has three components, i.e.

$$(\frac{\partial f}{\partial t})^c = (\frac{\partial f}{\partial t})_{en} + (\frac{\partial f}{\partial t})_{ei} + (\frac{\partial f}{\partial t})_{ee}. \tag{3.187}$$

A more thorough discussion of the Boltzmann equation is found in the Appendix, Section C.

3.16.2 The Fokker-Planck Equation

The Fokker-Planck equation describes the change in f_α produced by the small, overlapping, and almost continuous encounters of electrons diffusing in velocity space [48]. For the continuous distribution function f_α defined as the probability of finding dn particles in the $d\vec{v}$ element of phase space,

$$dn = f(\vec{v}, t)d\vec{v} \tag{3.188}$$

the Fokker-Planck evolution equation (Trubnikov's form [56], summation on repeated indices) is written

$$(\frac{\partial f_\alpha}{\partial t})_f = -\frac{\partial}{\partial v_i}(f_\alpha \frac{F_i}{m_\alpha} - \frac{\partial f_\alpha}{\partial v_k} D_{ik}). \tag{3.189}$$

The dynamical friction vector, $\vec{F}^{\alpha/\beta}$, and diffusion tensor, $\overleftrightarrow{D}^{\alpha/\beta}$, may be given in terms of Rosenbluth potentials, φ_β and ψ_β, which describe the distribution of background species β:

$$F_i = L^{\alpha/\beta} \frac{m_\alpha^2}{m_\beta} \frac{\partial \varphi_\beta}{\partial v_i} \; ; \; D_{ik} = L^{\alpha/\beta} \frac{\partial^2 \psi_\beta}{\partial v_i \partial v_k}. \tag{3.190}$$

Here $L^{\alpha/\beta} = (4\pi q_\alpha q_\beta / m_\alpha)^2 ln\Lambda$ (CGS units), where ln Λ is the Coulomb logarithm. (In MKS units, $L^{\alpha/\beta} = (q_\alpha q_\beta / \epsilon_o m_\alpha)^2 ln\Lambda$). The Rosenbluth potentials simplify calculations. They obey Poisson's equation according to

$$\nabla_v^2 \varphi^\beta = f^\beta \; ; \; \nabla_v^2 \psi^\beta = \varphi^\beta. \tag{3.191}$$

(Note: In Plasma Physics texts, one sometimes finds the convention $\nabla^2 = \nabla \cdot \nabla = \Delta$. For the sake of clarity, we avoid this notation.) In terms of Rosenbluth potentials, the complete Coulomb collision operator is written

$$C_\alpha^c = -\sum_{\beta=e,i} L^{\alpha/\beta} \frac{\partial}{\partial v_i} (\frac{m_\alpha}{m_\beta} f_\alpha \frac{\partial \varphi_\beta}{\partial v_i} - \frac{\partial}{\partial v_k} f_\alpha \frac{\partial^2 \psi_\beta}{\partial v_i \partial v_k}). \tag{3.192}$$

This equation describes the change in distribution of species α due to collisions with the whole ensemble of species β as represented by the Rosenbluth potentials, φ_β and ψ_β.

3.16.3 Langevin Formulation

Given an arbitrary function of $x(t)$: $f[x(t)]$, one can use Ito's formula to write an equivalent stochastic differential equation which the function will obey [12]. This is called a Langevin equation. For a more general discussion of Langevin equations, see Section 3.3

Applying Ito's formula to the Fokker-Planck equation, one obtains the form

$$\frac{dv_i}{dt} = A_i + \sum B_{ij}\,\xi_j \tag{3.193}$$

which is equivalent to first order. This Langevin equation can be used to describe the collisional Fokker-Planck step. Here ξ is a δ-correlated random vector with zero mean value,

$$< \xi_i(t) >= 0, \;\; < \xi_i(t)\xi_j(t') >= \delta_{ij}\delta(t-t'), \tag{3.194}$$

where δ_{ij} is the Kronecker delta, and $< ... >$ implies ensemble average [2].

The functions $A_i = fn(t, \vec{r}, \vec{v})$ and $B_{ij} = fn(t, \vec{r}, \vec{v})$ represent the net probabilistic effect of many small angle scattering events off the background ensemble as represented by φ^β and ψ^β. Computation of A_i and B_{ij} is discussed in the next sections.

3.16.4 Normalized Units

The Fokker-Planck equation may be simplified through normalization. Let $x_j = v_j/v_T^\beta$ where $v_T^\beta = \sqrt{2KT_\beta/m_\beta}$. Also let, $\lambda = m_\alpha/m_\beta$ (for self collisions, $\lambda = 1$). Furthermore, note that $f_\beta = dn_\beta/dv$. The collisional Fokker-Planck term can then be normalized by the factor (CGS units)

$$[t] = \frac{[v_T^\beta]^3}{n_\beta L^{\alpha/\beta}} = \frac{\sqrt{2(kT_\beta)^3 m_\alpha}}{ln\Lambda 8\pi^2 e_\alpha^2 e_\beta^2 n_\beta}\lambda^{3/2}. \tag{3.195}$$

For illustrative purposes, we first consider a 1V (spherical) solution which assumes an isotropic background Maxwellian distribution. Here, $x = \sqrt{v_x^2 + v_y^2 + v_z^2}/v_T^\beta$. In this case, the normalized collision term can be written

$$\frac{\partial f^\alpha}{\partial t} = \frac{1}{x^2}\frac{\partial}{\partial x}x^2[\lambda\frac{\partial \varphi^\beta}{\partial x}f^\alpha - \frac{\partial^2\psi^\beta}{\partial x^2}\frac{\partial f^\alpha}{\partial x}]. \tag{3.196}$$

One can show that the equivalent stochastic Ito-Langevin equation is [1]

$$\frac{\partial x}{\partial t} = -\lambda\frac{\partial \varphi}{\partial x} - \frac{2}{x}\frac{\partial^2 \psi}{\partial x^2} + \frac{\partial^3 \psi}{\partial x^3} + \sqrt{2\frac{\partial^2 \psi}{\partial x^2}}\zeta. \tag{3.197}$$

Equation 3.197 describes the change in modulus x of a particle of species α which occurs per normalized time $\hat{t} = t/[t]$ due to Coulomb collisions with species β. The first three terms represent friction, (A_i in Equation 3.193), while the last term represents diffusion, (B_{ij} in Equation 3.193). The factor ζ is a random number distributed according to

$$\zeta = cos(2\pi R[0,1])\sqrt{-2ln(R[0,1])}. \tag{3.198}$$

Equation 3.197 describes the change in modulus in one dimension, assuming that the change happens isotropically. The derivatives φ', ψ'', and ψ''' are listed in the next section. The 3-D formulation actually used is found in Section 3.16.6.

3.16.5 Isotropic Maxwellian Distribution

For an isotropic Maxwellian distribution $f_\beta(t, \vec{r}, \vec{v})$ at temperature $T_\beta(t, \vec{r})$ and density $n_\beta(t, \vec{r})$, the Rosenbluth potentials may be written [56]

$$\varphi(x)_\beta = -\frac{erf(x)}{4\pi x} n_\beta; \tag{3.199}$$

$$\psi(x)_\beta = \frac{-1}{16\pi}[(2x + \frac{1}{x})erf(x) + erf'(x)]n_\beta. \tag{3.200}$$

Here $x = v_j/v_T^\beta$, and $v_T^\beta = \sqrt{2KT_\beta/m_\beta}$ (as before). The normalized Rosenbluth potential are obtained by dividing through by n_β. Useful derivatives of the normalized potentials include the following:

$$\varphi'(x) = \frac{1}{16\pi}[4\mu]; \tag{3.201}$$

$$\psi'(x) = \frac{1}{16\pi}[\mu - 2erf(x)]; \tag{3.202}$$

$$\psi''(x) = \frac{1}{16\pi}[\frac{-2}{x}\mu]; \tag{3.203}$$

$$\psi'''(x) = \frac{1}{16\pi}[\frac{6}{x^2}\mu - \frac{4}{x}erf'(x)]. \tag{3.204}$$

We have used the following functions to simplify:

$$erf'(x) = \frac{2}{\sqrt{\pi}} e^{-x^2}; \tag{3.205}$$

$$erf''(x) = -2x\, erf'(x); \tag{3.206}$$

$$\mu(x) = -\frac{\partial}{\partial x}\frac{erf(x)}{x} = \frac{erf(x) - x\, erf'(x)}{x^2}; \tag{3.207}$$

$$\mu'(x) = 2erf'(x) - \frac{2}{x}\mu. \tag{3.208}$$

The functions $g(x) = \mu(x)/2$ and $erf(x) - g(x)$ are shown in Figure 3-30.

The energy distribution resulting from application of the Langevin equation to electron-electron and/or electron-ion collisions may be compared with the energy distribution for a Maxwellian at T,

$$\frac{dN/N}{d < x^2 >} = g(\epsilon) = \frac{2}{\sqrt{\pi}}\sqrt{\epsilon}\, e^{-\epsilon}. \tag{3.209}$$

Here $x^2 = \epsilon = \frac{1}{2}m < c^2 > /T$. It is perhaps worth noting that

$$\mu(x^2) = \frac{2}{\sqrt{\pi}} \int_o^{x^2} \sqrt{\epsilon}\, e^{-\epsilon}\, d\epsilon \tag{3.210}$$

is the so called "Maxwell Integral" [56]. This is the integral over a sphere of finite radius of the Maxwellian distribution normalized to unity. The integral may be expressed in terms of the error function and the function defined earlier, $\mu(x)$;

$$\mu(x^2) = erf(x) - xerf'(x) = x^2\mu(x) \tag{3.211}$$

where

$$erf(x) = \frac{2}{\sqrt{\pi}} \int_o^x e^{-y^2} dy. \tag{3.212}$$

3.16.6 Three Dimensional Form

The simulation implements Coulomb scattering in three dimensions. Both diffusion and friction act along the relative velocity vector $\vec{v_r} = \vec{v}^{\alpha} - < \vec{v}^{\beta} >= \vec{v}_{||}$. Thus, in time-step $\tau = \Delta t/[t]$, the parallel velocity increment due to collisions can be expressed

$$\Delta v_{||} = \frac{< (\Delta v_{||}) >}{\Delta t}\tau + \zeta_1 \sqrt{\frac{< (\Delta v_{||})^2 >}{\Delta t}\tau}, \tag{3.213}$$

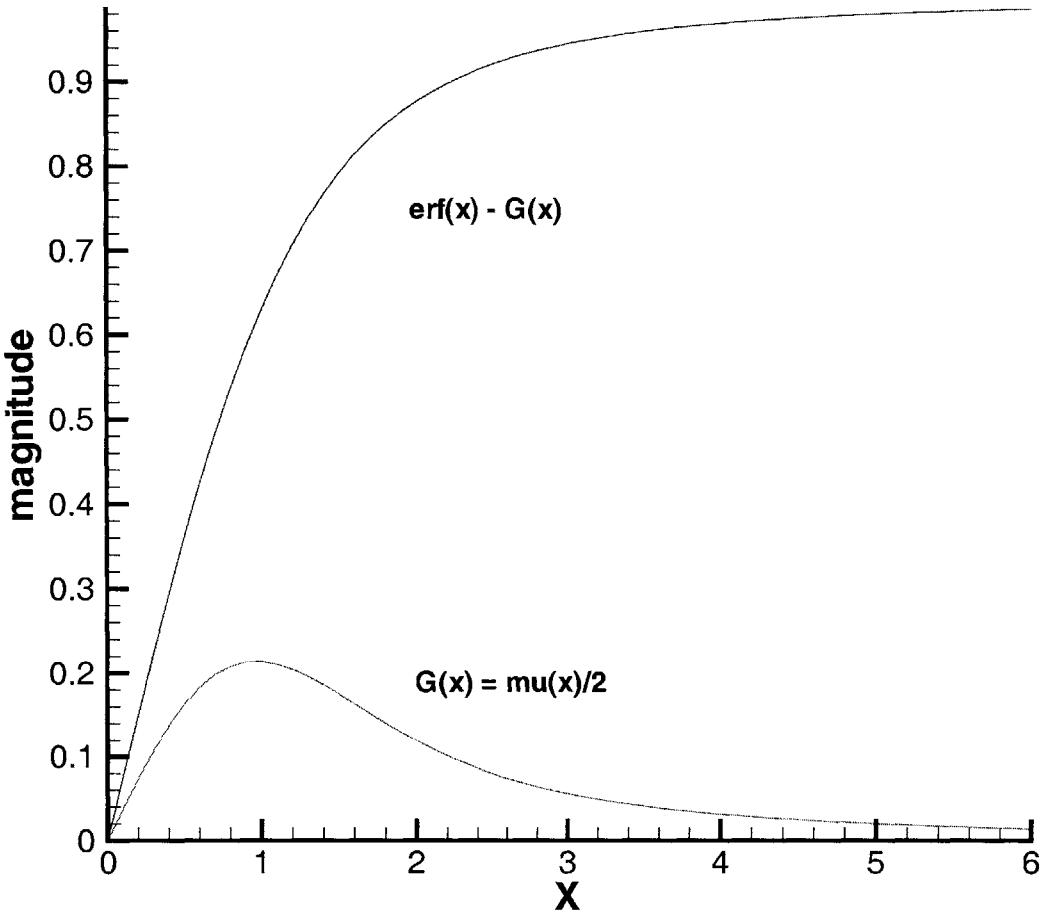

Figure 3-30: *The functions* $g(x) = \mu(x)/2$ *and* $erf(x) - g(x)$. These are used to determine the diffusion coefficients.

where ζ_1 is a random number. Only diffusion acts perpendicular to $\vec{v_r}$ such that

$$\Delta v_\perp = \zeta_2 \sqrt{\frac{< (\Delta v_\perp)^2 >}{\Delta t}} \tau. \tag{3.214}$$

The mean square velocity shifts can be written as diffusion coefficients:

$$D_x = \frac{1}{2} \frac{< (\Delta v_x)^2 >}{\Delta t}; \tag{3.215}$$

$$D_y = \frac{1}{2} \frac{< (\Delta v_y)^2 >}{\Delta t}; \tag{3.216}$$

$$D_z = \frac{1}{2} \frac{< (\Delta v_z)^2 >}{\Delta t}. \tag{3.217}$$

Here, x is the direction of particle motion ($D_x = D_{||}$), and directions y and z are the perpendiculars ($D_y = D_z = D_\perp$) which define an orthogonal set of axes. Thus, $< (\Delta v)^2_\perp >=< (\Delta v_y)^2 > + < (\Delta v_z)^2 >$. For such an orthogonal system, Trubnikov shows that [56]

$$< (\Delta v_x)^2 >= -2\psi''(x); \tag{3.218}$$

$$< (\Delta v_y)^2 >=< (\Delta v_z)^2 >= -2\frac{\psi'(x)}{x}; \tag{3.219}$$

where

$$x = \frac{|v_{||}|}{v_T^\beta}. \tag{3.220}$$

Using the functions described in Section 3.16.5 for an isotropic Maxwellian, we find

$$D_{||} = -\psi''(x) = \frac{1}{8\pi} \frac{\mu(x)}{x}; \tag{3.221}$$

$$D_\perp = -\frac{\psi'(x)}{x} = \frac{1}{16\pi} \frac{2erf(x) - \mu(x)}{x}. \tag{3.222}$$

What about friction? The mean rate of change of momentum of a test particle of species α in a field of species β may be written,

$$< p_\alpha >= -m_\alpha (1 + \lambda) L^{\alpha/\beta} \vec{\nabla} \varphi_\beta. \tag{3.223}$$

Thus, the dynamical friction coefficient ($A =< \Delta v_{||} > /\Delta t$) may (in normalized units) be written

$$A = -(1+\lambda)\frac{\mu(x)}{4\pi}. \tag{3.224}$$

For a complete derivation, see Trubnikov [56]. Note that if the field particles are all at rest and infinitely heavy, the *dynamical* friction goes to zero, but the mean rate of momentum exchanged does not. There is still friction.

3.16.7 Defining Coordinate Axes

To apply the 3-D diffusion coefficients, we define a unique set of orthogonal coordinate axes at each iteration. The parallel direction, $\vec{i}_x$, is along the relative velocity vector;

$$\vec{i}_x = \frac{\vec{v}_r}{|v_r|}. \tag{3.225}$$

The perpendicular axes, $\vec{i}_y$ and $\vec{i}_z$, are found by first defining any vector $\vec{i}_1 \neq \vec{i}_x$. The functions,

$$\vec{i}_y = \frac{\vec{i}_1 \times \vec{i}_x}{|\vec{i}_1 \times \vec{i}_x|} \tag{3.226}$$

and

$$\vec{i}_z = \frac{\vec{i}_x \times \vec{i}_y}{|\vec{i}_x \times \vec{i}_y|} \tag{3.227}$$

then complete the orthogonal set of axes.

3.16.8 Implementation

Since $D_x = D_{||}$, and $D_y = D_z = D_\perp$, the velocity shift due to Coulomb diffusion along the parallel direction in time τ may be implemented as:

$$\Delta v_x = A\tau + \zeta_1\sqrt{2D_{||}\tau} \tag{3.228}$$

where

$$\zeta_1 = cos(2\pi R[0,1])\sqrt{-2ln(R[0,1])}. \tag{3.229}$$

In the perpendicular direction the modulus and direction are found separately by

$$\Delta v_\perp = 2\zeta_2\sqrt{D_\perp\tau}, \tag{3.230}$$

$$\zeta_2 = cos(2\pi R[0,1])\sqrt{-2ln(R[0,1])}, \tag{3.231}$$

and

$$\zeta_3 = 2\pi R[0,1]. \tag{3.232}$$

Thus,

$$\Delta v_y = cos(\zeta_3)|\Delta v_\perp| \tag{3.233}$$

and

$$\Delta v_z = sin(\zeta_3)|\Delta v_\perp|. \tag{3.234}$$

Finally, $\Delta\vec{v}_x = \Delta v_x\vec{i}_x$, $\Delta\vec{v}_y = \Delta v_y\vec{i}_y$, and $\Delta\vec{v}_z = \Delta v_z\vec{i}_z$.

3.16.9 Testing

To test the algorithm, we inject a single electron and perturb it 10^8 times at $dt \approx .01$. At each time-step, we record the energy of the electron and use that energy to build a distribution, which should be Maxwellian. The resulting energy distribution is compared to $g(\epsilon)$ in Figure 3-31. The numerical energy distribution underestimates the peak slightly, but is otherwise a good fit.

3.16.10 Domain of Integration

Over which ensemble of species β should we integrate to determine T^β?

Manheimer, et. al. [30] integrate along magnetic field lines, reasoning that the time scale for electron motion perpendicular to the field lines is much greater than that for motion parallel to the field lines. They show quantitatively that that the electron distribution can often be treated as isotropic, even when $T_{||}/T_\perp = 2$. For multiple distributions, e.g. multiple humped background distributions, they note that the friction and diffusion coefficients can be calculated as vector or tensor sums of contributions from several distributions displaced from each other in velocity space.

In our simulation, we do not assign one T^β to an entire magnetic streamline. Along streamlines, magnetic bottling and electrostatic (sheath) effects limit where electrons can go. Furthermore, gradients in electron and ion temperature exist. *Not all electrons will see the same ensemble.* Therefore, we assume the electrons interact with an isotropic, Maxwellian background distribution determined by the *local* moments of density, n_β, energy, T_β, and

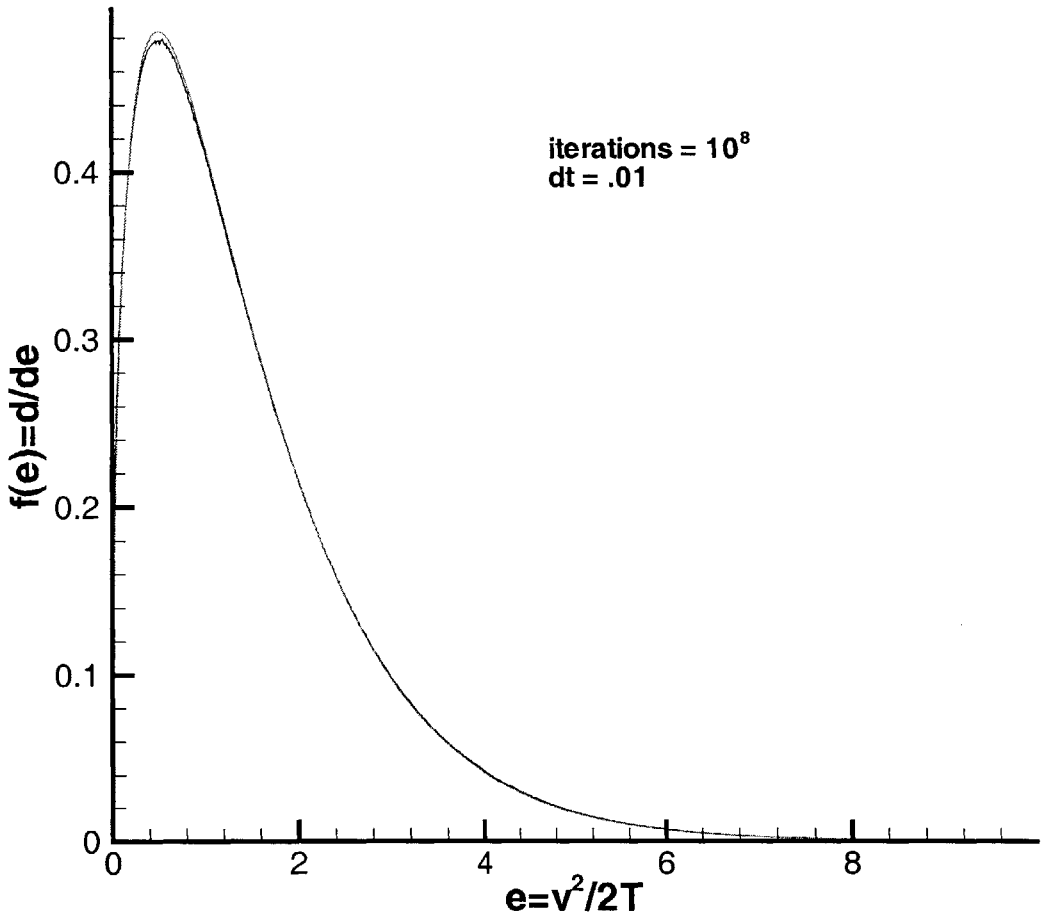

Figure 3-31: *Energy distribution of a single electron for electron self diffusion.* A single electron is injected and perturbed one hundred million times at a time-step of $\tau = .01$. This distribution is a representation of how often the electron has each value of energy. The resulting energy distribution is compared to $g(\epsilon)$.

momentum, v_β. This is easier numerically, and more correct physically; an real electron interacts with other charged particles in its immediate vicinity (within a Debye length). Manheimer's results provide some justification for assuming species β is Maxwellian.

3.16.11 Numerical Notes

- The diffusive method is required to capture relaxation to an isotropic distribution function. However, the much simpler MCC method described in Section 3.15.4, should capture the correct rate of momentum transfer. It should produce nearly the right amount of transport.

- If artificial mass ratios are used, this affects the relative velocity vector. For instance, if species α is electrons and species β is ions, then $\vec{v}_r = \vec{v}_\alpha - \sqrt{f} < \vec{v}_\beta >$, where $f = M'/M$.

- The normalization constant [t] must be increased by 1/f to account for the decreased lifetime of electrons.

- Assuming species β is Maxwellian is not a very good assumption for ions, where $T_z \approx 40 - 60$ eV, $T_r \approx 1 - 5$ eV and $T_\theta \approx .01$ ev, numerically.

- In practice, we apply no force if $|x_{||} + \Delta x_{||}| < .01$.

- If the argument is very small ($x \approx .001$), our function can produce $D_\perp < 0$. This error seems to come from a curve fit we use for $erf(x)$. If this numerical error arises, we set $D_\perp = 0$.

3.17 Anomalous Diffusion

Anomalous Bohm type diffusion is included in the numerical model. The rationale for this was discussed in Section 2.10.

3.17.1 Past Numerical Modeling of Anomalous Electron Transport

Fife found that Bohm diffusion was required to explain the electron transport observed in an SPT [10]. His simulation included both secondary emission at the walls and classical diffusion resulting from electron-neutral collisions, but cross field transport due to classical

scattering (and wall effects?) was only 70 percent of the total [10]. Bohm diffusion was required to make up the difference between the simulated discharge current and the measured discharge current.

When modeling a Busek thruster using Fife's Hybrid PIC code, we discovered that Fife had been using a cross section for electron neutral collisions which was approximately an order of magnitude too high. After fixing the error, Bohm diffusion dominated [53]. We furthermore found that Bohm diffusion using the coefficient $D_B = \frac{1}{16}\frac{KT_e}{eB}$ produced too much diffusion. A value closer to $D_B \sim \frac{1}{64}\frac{KT_e}{eB}$ was required to match the numerical predictions of the Hybrid PIC code with the experimentally measured performance [53].

Hirakawa attempted to explain the anomalous diffusion observed in a Hall thruster by modeling azimuthal waves [18]. First she performed a 2D simulation in the $r\theta$ plane. Then she applied the observed electric field oscillations to a 2D simulation in the rz plain, resulting in flux levels comparable to Bohm diffusion. But are such azimuthal waves present in a TAL thruster? And if so, are they present everywhere between the cathode and the anode, or only far from the anode?

3.17.2 Present Numerical Modeling of Anomalous Transport

Since we are not sure whether or not "anomalous" diffusion is an important mechanism for electron transport in the mini-TAL, we account for it using a method which may be turned on or off at our discretion, allowing us to run parametric tests. Our method is to scatter the electrons randomly according to a "Bohm frequency", ν_B. To derive this frequency, we equate our general result for $D_\perp$ with $D_B \sim \frac{1}{16}\frac{KT_e}{eB}$, which results in the relation

$$D_\perp = \frac{1}{2}\nu\frac{v_\perp^2}{\omega_{ce}^2} = \frac{1}{32}\frac{v_{th}^2}{\omega_{ce}}. \tag{3.235}$$

Letting $v_\perp = v_{th}$, we find $\nu_B = 1/16\,\omega_{ce}$. This means that the effective Hall parameter, $\beta = \nu_B/\omega_{ce}$, is limited to less than 16. Since $\omega_{ce} = 2\pi\nu_{ce}$, $\nu_B/\nu_{ce} \approx 1/3$. In other words, each electron scatters approximately once every three gyro rotations.

If we use $D_B \sim \frac{1}{64}\frac{KT_e}{eB}$, we simply decrease ν_B proportionally. In this case, the effective Hall parameter β is limited to 64. This is numerically friendlier than the previous case ($\beta \approx 16$) for reasons which will shortly be clear.

Once the Bohm collision frequency is implemented, the electron scattering rate is deter-

mined by

$$\nu_e' = \nu_e + \nu_B. \tag{3.236}$$

If we model Bohm scattering, we must include the scaling factor $f = M'/M < 1$ to account for artificial mass ratios:

$$\nu_B' = \nu_B/\sqrt{f}. \tag{3.237}$$

This changes the effective Hall parameter according to

$$\beta' = \beta/\sqrt{f}. \tag{3.238}$$

We must take care to ensure that β' does not drop below 2 (so that the electrons remain magnetized). When Bohm shattering is implemented, this requires us to use mass ratios on the order of $M_n/m_e \approx 960$. If only Bohm scattering is modeled (no classical scattering), this results in $\beta' \approx 4$. In practice, the addition of classical scattering decreases β' further, but it should be above $\beta' = 2$ everywhere. Mass ratios on the order of $M_n/m_e \approx 96$ are only marginally acceptable as β' can be less than 2, while lower mass ratios are really out of the question.

3.18 Particle-Boundary Collisions

In this simulation, particles are specularly reflected off some boundaries (a billiard ball without any English), and diffusely reflected off others (the normal and/or tangential components change). Figure 2-12 illustrates the difference. The rationale behind these boundary conditions was discussed in Chapter Two.

To actually implement a particle/boundary collision, we first calculate precisely where and when a particle impacts the boundary. Then we assign the particle a new velocity, which depends on the species of the particle and the boundary being encountered. Finally, we step the particle away from the boundary according to the new velocity.

3.18.1 Calculating the Impact Point and Time

To minimize artificial electron transport, one should calculate the particle/boundary intersection point precisely. This is also important when testing the simulation for energy and momentum conservation.

Each time a particle moves, its new position in three dimensions in space is determined. This position is then transformed back to the R-Z plane (See Figure 3-21). If the transformed position of the particle is found to be either outside the domain of the simulation or inside a solid piece such as the anode, then we determine exactly where and when the particle intersected the boundary. The particle is then reflected from that point. At some boundaries, such as the free space boundary, the particle may be destroyed. At other boundaries, the energy the particle gives up is tallied.

Vertical (Radial) Boundary

If the boundary is vertical, the intersection point is simply the intersection of the line defining the boundary with the line determined by the starting and ending points of the particle. The time τ to intersection is determined by displacement along the Z axis, along which motion is unaffected by the coordinate transformation. Let z be the position of the particle and Z be the position of the boundary. Then, $\tau = \Delta t(Z - z_o)/(z_f - z_o)$. Once τ is determined, the particle undergoes two motions. First, it moves τ to the boundary, where it interacts with the surface. Then it steps $\Delta t - \tau$ away from the boundary with its new velocity.

Horizontal (Axial) Boundary

If the boundary is horizontal (parallel with the centerline) or sloped, then determining the intersection point is a three dimensional problem: We must find the intersection of the trajectory, $\vec{v}\Delta t$, with a three dimensional surface defining the boundary. Let (r', z') be the position at which the particle intersects the boundary. Furthermore, let r_o be the initial radial position, and let τ be the time to intersection. If the boundary is parallel with the centerline at radius R, then $r' = R$, but we don't know either z' or τ. However, we do know that $(r')^2 = R^2 = (r_o + v_r\tau)^2 + (v_\theta\tau)^2$ (see Figure 3-21). We can thus determine τ from the quadratic equation. It is

$$\tau = \frac{-b \pm \sqrt{b^2 - 4ac}}{2a} \tag{3.239}$$

where $a = v_r^2 + v_\theta^2$, $b = r_o v_r 2$, and $c = r_o^2 - R^2$. The (+) solution is for $R > r_o$, while the (−) solution is for $R < r_o$. The parameter a is never equal to zero because a particle with $v_r = v_\theta = 0$ will never cross a horizontal boundary. Finally, we step the particle forward

τ, at which point the particle hits the boundary: $(r', z') = (R, z_o + v_z\tau)$. After the new velocity is determined, we then compute the new trajectory and step the particle forward an additional $\Delta t - \tau$.

Sloped Boundary

Finally, we consider the non-vertical boundary with slope $s \neq 0$. Here, r' is also undetermined. To find τ, we first calculate $r_{z,o}$, the radial position of the boundary corresponding to z_o: If you draw a line radially outward from (r_o, z_o), then $(r_{z,o}, z_o)$ is the point where you hit the boundary. The intersection point of the particle may then be written

$$\begin{aligned} r' &= r_{z,o} + s(z' - z_o); \\ z' &= z_o + v_z\tau. \end{aligned} \tag{3.240}$$

As before, we solve the quadratic equation to find τ:

$$\begin{aligned} \tau &= (-b + \sqrt{b^2 - 4ac})/2a; \\ a &= v_r^2 + v_\theta^2 - s^2 v_z^2; \\ b &= 2(r_o v_r - v_z s r_{z,o}); \\ c &= r_o^2 - r_{z,o}^2. \end{aligned} \tag{3.241}$$

If $a = 0$, $\tau = -c/b$, and if $c = 0$, $\tau = -b/a$. This (+) solution is the only one we need consider for the given simulation region. As before, we move the particle τ and $\Delta t - \tau$ in two steps, the first with the old velocity, and the second with the new velocity.

3.18.2 Neutral Impact

Neutral-boundary impacts fall into three categories:

- At the free space boundary, neutrals are deleted.
- At the centerline, neutrals are specularly reflected.
- At all other surfaces, neutrals are diffusely reflected according to a half-Maxwellian at the surface temperature, taken to be .1 eV at the anode, and 700K at the constant potential walls. These values could be changed easily to test the effect of wall temperature on performance.

3.18.3 Ion Impact

Ion-boundary impacts are as follows:

- At the free space boundary, ions are deleted from the simulation. A count of the flux is maintained.
- At the centerline, ions are specularly reflected.
- At the anode, ions lose their charge and are re-emitted as neutrals. Their charge helps determine the anode current. The velocity magnitude after impact is determined by the assumption that ions give up 50 percent of their energy to the walls. The velocity direction is randomized.
- At the constant potential walls, ions lose their charge and are re-emitted as neutrals. The charge is collected to help determine the wall potential. The velocity magnitude after impact is determined by the assumption that ions give up 50 percent of their energy to the walls. The velocity direction is randomized.
- At insulators (when modeled), ions lose their charge and are re-emitted as neutrals. The charge is collected to help determine the sheath. The velocity magnitude after impact is determined by the assumption that ions give up 50 percent of their energy to the walls. The velocity direction is randomized.
- At the cathode (when modeled directly), ions are neutralized and the cathode emits one less electron.

3.18.4 Electron Impact

Unlike heavy particles, electrons do not bounce when they impact most boundaries. They are simply destroyed. Electron-boundary impacts are as follows:

- At the free space boundary, all electrons are allowed to pass out of the domain. A count of the flux is maintained.
- At the centerline, electrons are specularly reflected.
- At the anode, electrons are destroyed.
- At the walls, electrons are destroyed and charge is collected to help determine the wall potential.
- At insulators (when modeled), charge is collected to help determine the sheath.
- At the cathode (when modeled directly) charge is collected and re-emitted.

3.18.5 Energy Flux

As discussed in Section 2.12.4, particles give up energy to the walls. This energy is tallied at each time-step which, in theory, enables a thermal model to be created.

3.18.6 Thrust and Isp

The thrust and specific impulse of the thruster is determined by keeping track of the particles which leave the simulation through the free space boundary. If the boundary potential where an ion exits the simulation is not equal to zero, the velocity in the axial direction is adjusted to account for the additional energy gain (or loss) expected before the particle reaches free space. The additional ΔV is considered when predicting the thrust and Isp.

3.18.7 Magnetic Boundary

Before fully modeling the anode region, the left hand boundary of the simulation region was flat [52]. Particles which intersected the left hand boundary between the center pole and the anode were turned around if their energy was such that they were magnetically bottled. We termed this a "magnetic boundary."

A magnetic boundary is easily implemented. Essentially, we determine if the particle has enough kinetic energy to make it to the center pole. If it doesn't, then we reflect it. If it does, then we delete it and add it's charge to the wall.

How do we do this? First, we compute the charged particle's energy, KE, and magnetic moment, $\mu = KE_{\perp}/|B|$. (Both energy and magnetic moment must be conserved.) Next, we compute the change in electric potential between the current location and the wall: $\Delta\phi = \phi - \phi_{wall}$. Then we estimate the KE which the particle would have at the wall, after accounting for the change in potential

$$KE' = KE - \Delta\phi. \tag{3.242}$$

If $KE' < 0$, then the particle is electro-statically confined; absent energy adding mechanisms as through, for instance, oscillations, the particle could never reach the wall. Next, we estimate the magnetic field strength at the wall. Between the anode and the center pole or

outer pole (in the region of interest), we say $\partial B_z/\partial z \approx 0$ such that, at the wall,

$$B'_r = B_r \frac{r}{r'}; B'_z = B_z. \tag{3.243}$$

Finally, we estimate $KE'_{||}$ at the wall given that we must conserve Magnetic moment ($\mu = \mu'$),

$$KE'_{\perp} = \mu'|B'| = \mu|B'|; KE_{||} = KE - KE_{\perp}. \tag{3.244}$$

If $KE'_{||} > KE'$, then there is not enough kinetic energy to both reach the wall and conserve the magnetic moment: The particle is confined by the magnetic field.

3.19 Particle Injection

Particles are routinely injected into the simulation along the boundaries. The rejection method is used to locate injected particles in space. The Box-Muller transformation (see Section 3.9.3) is used to locate injected particles in velocity space.

3.19.1 Neutral Injection

A stream of neutrals is created at the anode. Neutral positions are determined by the rejection method such that the time averaged density of the stream at the entrance point is constant. Neutral velocities are determined by assuming a half Maxwellian distribution about the anode temperature, taken to be $.1eV$. Neutrals introduced through recombination at the walls are also given a half Maxwellian velocity distribution, but at a different temperature.

Number of Neutrals

The number of neutrals created per time-step at the anode, N, is a function of the mass flow rate according to

$$\frac{dN}{dt} = \frac{\dot{m}}{m_n * s_o[size]}. \tag{3.245}$$

Here, $[size]$ is the number of particles a super-particle of size $s = 1$ represents, and $s_o = 50$ is (usually) the initial statistical weight of a neutral. These particles are created according to a half-range Maxwellian [4]. That is, the R and Θ velocities are calculated according

to the standard Box-Muller transformation, while the Z velocity of the created particles is distributed according to

$$v_z = v_{th}\sqrt{-ln(R(0 \rightarrow 1))}. \tag{3.246}$$

An alternate method to achieve the same injection rate is to create Maxwellian particles according to the frequency with which they cross an imaginary plane; we can use the rejection method and the distribution function for flux as a function of velocity. This is equivalent to having a constant density reservoir of particles to the left of the anode boundary and entering them as they collide with the wall.

Culling the Neutral Population

Before charged particles are introduced into the system, the simulation is run for a thousand or so iterations at $\delta\hat{t} = 25$ (or some large number) such that a neutral plume is created. This plume is culled by assuming a utilization efficiency of $\eta_u \approx 0.9$ to create an initial distribution.

Assume neutrals are ionized at a rate $R = dn_n/dt \approx n_n n_i Q v_e$. Then,

$$\frac{dn_n}{dx} = \frac{dn_n}{dt}\frac{dt}{dx} = \frac{n_n n_i Q v_e}{v_n}. \tag{3.247}$$

The mean free path for neutrals being ionized (where $n_e = n_i$) is just $\lambda = v_n/n_i v_e Q$ such that

$$\frac{dn_n}{n_n} = \frac{dx}{\lambda}. \tag{3.248}$$

Integrating with the very crude assumption that λ is constant, we obtain

$$ln(\frac{n_n}{n_{n,o}}) = \frac{x - x_o}{\lambda}. \tag{3.249}$$

If we assume that some fraction η_u of the neutrals has been ionized (utilized) by position $x - x_o = L$, then

$$ln(\frac{n_n}{n_{n,o}}) = ln(1 - \eta_u) = \frac{L}{\lambda}. \tag{3.250}$$

In general,

$$\frac{n_n}{n_{n,o}} = exp[ln(1 - \eta_u)\frac{x - x_o}{L}] = (1 - \eta_u)^{(\frac{x-x_o}{L})}. \tag{3.251}$$

This equation was used by Hirakawa to estimate the neutral population in her simulation[18].

The approximation is too simple because the plasma density is not constant in the acceleration zone. However, we can use this approximation to cull the neutral population before we introduce plasma into the simulation, thereby speeding up convergence.

3.19.2 Electron Injection

Cathode electrons introduced at the free space boundary are introduced according to a half or full Maxwellian, depending on whether bulk velocity is assumed. The temperature of these electrons is between .2 eV and 2.5 eV. A complete discussion of cathode electron injection will follow in the next section.

Electrons are also created in the center of the plasma through ionization events. This has been previously discussed.

3.20 Modeling the Cathode

Cathode electrons must be re-introduced into the simulation region. Rather than simulating a cathode directly, we introduce these electrons at the free space boundary. This allows a smaller simulation region. To do this, two basic questions must be answered:

- How much charge should be introduced at the downstream boundary each iteration?
- Exactly where should this charge be placed?

As discussed in Chapter 2, we can either control the number of cathode electrons introduced as per a steady state, starting from $I_c = I_a$, or we can introduce electrons along the free space boundary at a rate sufficient to neutralize the plasma along the boundary. Simulations documented in References [51] and [52] assumed the former. Final results presented in the thesis assume the latter.

In both cases, charges were allocated by creating a distribution proportional to the charge density along the boundary. The difference between the two boundary conditions just discussed is the number of charges introduced each iteration.

3.20.1 Steady State Injection

The amount of charge to introduce may be determined through a steady state current balance, as described in detail in 2.3, According to this balance, we may determine the

current from the anode/cathode current, the ion beam current, and the electrons which pass through the free space boundary. Recall first that in a steady state the cathode current, I_c, is equal to the discharge current, I_d, such that

$$I_c = I_d. \tag{3.252}$$

Recall also that some portion of the cathode current, I_{cb}, goes to compensate the beam ions, while the rest, I_{cd}, enters the discharge, such that

$$I_c = I_{cb} + I_{cd}. \tag{3.253}$$

Assuming that no net charge leaves the thruster (i.e. we only allow as many electrons as ions to leave the simulation),

$$I_b^+ = I_b^- = I_{cb} + I_{az}, \tag{3.254}$$

where I_{az} is the electron current that passes from inside the simulation region out the free space boundary. Thus we can estimate I_{cd} as

$$I_{cd} = I_c - I_b^+ + I_{az}. \tag{3.255}$$

This is the amount of charge which is introduced at any iteration when the steady state method of electron injection is applied. Note that the net current crossing the boundary is the cathode current, which is equal to the discharge current,

$$I_{cd} - I_{az} + I_b^+ = I_c = I_d. \tag{3.256}$$

We now know the amount of charge to be introduced at the downstream boundary at each iteration, $dN_e/dt = I_{cd}$. But where should these charges be introduced? Since we have ions leaving as well as electrons coming in, the current density $j = en_e(v_i - v_e)$. The net current across the boundary goes according to $I = \int j dA \approx \sum j_i A_i$, where the sum is over the free space boundary, each node of which has an area associated with it. Locally we may write

$$j_{cd} = j - j_b^+ + j_{az}. \tag{3.257}$$

Instead of applying Ohm's Law directly, we allocate the charges according to the quasineutral assumption. If the plasma is quasineutral on the other side of the free space boundary, then n_e should equal n_i along the boundary. To make this as true as possible, given I_{cd}, we use the charge imbalance $Q(i) = N_i(i) - N_e(i)$ as a distribution function in space; $p(i) \sim Q(i)$. The rejection method can then be used to place electrons along the boundary according to the distribution $p(i)$. In short, the incoming electrons are placed where they best balance the ions. This method is extended in the next section, which uses the quasineutrality condition to determine I_{cd}, as well.

3.20.2 Quasineutral Injection

During transients, the steady state method of electron injection is inadequate. Net charge may be stored in the body's capacitance such that $I_d \neq I_c$. As discussed in Chapter 4 (see Section 4.3.2), this results in a region along the free space boundary which is either ion rich or electron rich, whereas a real plasma bordering the plume should be quasineutral. Fortunately, quasineutrality may be achieved if we determine I_{cd} by ρ_e along the free-space boundary.

Essentially, we determine I_{cd} through a "bang-bang" control system. At each iteration, we sum along the free-space boundary to find the total net charge, Q_{fs};

$$Q_{fs} = \Sigma_{i=1}^{j}[N_i(i) - N_e(i)] \tag{3.258}$$

Here, each i represents one of j boundary cells to be summed across. If $Q_{fs} > 0$, then we introduce $\approx Q_{fs}$ cathode electrons (the number must be an integer) such that Q_{fs} goes to zero. If $Q_{fs} < 0$, we introduce nothing. As before, we use the charge imbalance $Q(i) = N_i(i) - N_e(i)$ as a distribution function in space; $p(i) \sim Q(i)/Q_{fs}$. Then we use random numbers to place the electrons according to the distribution function. The cathode current is then post-calculated and saved.

This method results in a plasma which is indeed quasineutral along the boundary. Furthermore, the cathode current is found to approximate the anode current over time, the desired steady state result. The quasineutral boundary conditions are further validated in Chapter 4, where we alter the capacitance of the thruster body but obtain the same basic numerical results. The same cannot be said for the current-controlled boundary conditions.

3.20.3 Energy of New Electrons

We assume electrons enter the simulation region with internal energy according to $T_e \leq 2.5eV$. The internal energy with which electrons are created will be dwarfed by the kinetic energy they gain from the electric field once within the simulation region. First, recall that the energy of an electron flow has both bunk and internal components, $e = .5m_e < v >^2 + .5m_e(v - < v >)^2$. The first quantity is the bulk energy, while the second is the thermal energy, $\frac{3}{2}T_{ev}$. If the magnitude of the local potential is less than the cathode temperature (taken to be .2 eV), then the electrons are introduced according to a half-Maxwellian at the cathode temperature with no bulk velocity ($< v >= 0$). If $.2eV < \phi < \frac{2}{3} \times 2.5eV$ then a half-Maxwellian at $T = \frac{2}{3}\phi$ is assumed. Again, $< v >= 0$. In $\phi > \frac{2}{3} \times 2.5eV$, then electrons are given a full Maxwellian thermal distribution at $T_e = 2.5eV$, and a bulk velocity along $\vec{B}$ according to $.5m < v >^2 = \phi - \frac{3}{2} \times 2.5$. Thus, their average energy equals ϕ.

3.21 Limiting Neutral Counts

The background density of neutrals in the acceleration channel is at least an order of magnitude greater than the plasma density. For this reason, neutrals created at the anode are given a master size (statistical weight) of, for example, $s = s_o = 50$. Although the statistical weight of each neutral super-particle decreases as it passes through the ionization region and mass is deleted, the average value of s is much greater than one. However, neutrals are also created through ion recombination at the walls, and these begin with statistical weight $s = 1$. Over long periods of time, these low mass neutrals can build up in the system, which is undesirable from a computational standpoint.

In his Hybrid PIC code, Fife solved this problem by creating only large super-particles at the walls according to the ion flux [10].

Here, we take a different approach. Each SWEEP neutral iterations, the code scrubs the neutrals, looking for low mass particles. (The number SWEEP is specified in a header file. Typically, SWEEP is 1000). In areas of good statistics, (high particle count, typically taken to be 50 or more particles per cell), it combines each Y super-particles with weight $s = 1$ into two super-particle of weight $s \approx Y/2$. The new statistical weights, s_1 and s_2, may be different, depending on whether Y is odd or even. Normally, we limit Y to a maximum of 10. In areas of poor statistics (areas of low density, taken to be $N < 50$), small super-particles

are not combined.

The center of mass is conserved by placing the center of mass of the two new particles at the original center of mass. Momentum is conserved by conserving the center of mass velocity, measured in the laboratory frame. Energy is conserved by giving both particles a relative velocity with respect to the center of mass. Angular momentum is conserved by separating the particles by some distance Δr, measured in the radial direction. The algorithm was tested to ensure that energy and momentum are indeed conserved.

By tagging certain species of particles, e.g. charge exchange neutrals, we avoid combining them with other particles. Thus, at any iteration, we can isolate and examine only the extant neutrals due to charge exchange.

Chapter 4

Code Validation

The topic of this thesis is the numerical simulation of a 50 W TAL thruster. A standard Leapfrog scheme was used to move all species of particles. A Particle-In-Cell (PIC) methodology was used to apply electrostatic and magnetic forces to the particles. A Monte Carlo Collision (MCC) methodology was used to model most collisions. The methods themselves are only tangentially in question; others have shown them to be effective plasma simulation tools. However, each piece of code must be tested and the simulation as a whole must be validated; it must represent a TAL thruster and not some other imaginary device.

Validation tests described here are categorized. Part level tests involve the smallest pieces of the code. Component level tests involve much larger pieces of the code and general concepts. System level tests show that the code as a whole produces realistic and consistent results.

4.1 Part Level Tests

The most fundamental pieces of code should be tested first. Such pieces include the random number generators, the potential solver, the gradient and divergence functions, the leapfrog method of particle pushing, and the magnetic field.

4.1.1 Random Numbers

Random numbers are often required in Monte Carlo simulations. These are usually produced by functions known as random number generators. Several of these functions were tested. The first of these, ran0(), is merely the machine's random number generator. The

second and third, ran1() and ran2(), are taken from "Numerical Recipes in C" [8], which recommends ran1() for most purposes.

First, we must show that these functions produce numbers between 0 and 1 with a mean of .5. After calling the functions 10^8 times we found: $< ran0() >= 0.499986$, $< ran1() >= 0.500005$, and $< ran2() >= 0.500035$. The function ran1() returned the average closest to 1/2. Hence, we use this function most often. This test also showed that ran0() on the SGI workstation sometimes produces both zero and 1. This limits the usefulness of ran0(). (The SGI function drand48() is equivalent to ran0() and never produced zero or 1, but is incompatible with the PC.)

Random number generators are supposed to produce uncorrelated numbers. This is tested by choosing three random numbers in sequence according to

$$\begin{aligned} \zeta_1 &= \sqrt{2}cos[2\pi ran1()], \\ \zeta_2 &= \sqrt{2}cos[2\pi ran1()], \\ \zeta_3 &= \sqrt{2}cos[2\pi ran1()]. \end{aligned} \tag{4.1}$$

If this is done many times, the following mean values should be obtained:

$$\begin{aligned} < \zeta_1 >=< \zeta_2 >=< \zeta_3 >= 0; \\ < \zeta_1^2 >=< \zeta_2^2 >=< \zeta_3^2 >= 1; \\ < \zeta_1\zeta_2 >=< \zeta_1\zeta_3 >=< \zeta_2\zeta_3 >= 0. \end{aligned} \tag{4.2}$$

After 10^7 iterations, the following results were obtained:

$$\begin{array}{lll} < \zeta_1 >= -.00037 & < \zeta_2 >= -.00017 & < \zeta_3 >= -.00083; \\ < \zeta_1^2 >= .99981 & < \zeta_2^2 >= 1.00017 & < \zeta_3^2 >= 1.00037; \\ < \zeta_1\zeta_2 >= .00029 & < \zeta_1\zeta_3 >= .0000532 & < \zeta_2\zeta_3 >= .00049. \end{array} \tag{4.3}$$

4.1.2 Potential Solver

The electric potential at each time-step is related to the charge density by Poisson's equation in cylindrical coordinates,

$$\nabla^2\phi = \frac{1}{r}\frac{\partial}{\partial r}(r\frac{\partial\phi}{\partial r}) + \frac{\partial^2\phi}{\partial z^2} = -\frac{1}{\epsilon_o}(\rho_i - \rho_e). \tag{4.4}$$

To find Φ numerically, we use a finite difference method based on Gauss's Law which works backward from the charge distribution, $Q(z,r)$, determined by interpolating all of the super-particles in the simulation to the grid nodes.

Analytic Function

The potential solver was tested using the periodic function $F(z,r)$:

$$F = C_z cos(\frac{n_1 \pi z}{L_z}) + C_r cos(\frac{n_2 \pi r}{L_r}) + C; \tag{4.5}$$

$$\vec{\nabla} F = -C_z sin(\frac{n_1 \pi z}{L_z})(\frac{n_1 \pi}{L_z}) i_z - C_r sin(\frac{n_2 \pi r}{L_r})(\frac{n_2 \pi}{L_r}) i_r; \tag{4.6}$$

$$\vec{\nabla} \cdot \vec{\nabla} F = -C_z cos(\frac{n_1 \pi z}{L_z})(\frac{n_1 \pi}{L_z})^2 - C_r cos(\frac{n_2 \pi r}{L_r})(\frac{n_2 \pi}{L_r})^2 - C_r sin(\frac{n_2 \pi r}{L_r})(\frac{n_2 \pi}{L_r}) \frac{1}{r}. \tag{4.7}$$

$F(z,r)$ is plotted in Figure 4-2. The number of maxima and minima in each direction is controlled by varying n_1 and n_2 or, equivalently, by varying scale lengths L_z and L_r. The magnitude is controlled by varying C_z, C_r, and C.

Method

The electric potential solver works backward from the charge distribution, $Q(z,r)$ to find $\Phi(z,r)$. Let $\Phi = F$. If the potential solver works correctly, it should be possible to numerically reproduce the analytic potential, $F(z,r)$ from the analytic charge density, $\rho_e(z,r) = -\nabla^2 F(z,r)$

First, the charge distribution on the grid, $Q_{k,j}$, is estimated by multiplying the analytic charge density at each grid node by its surrounding volume: $Q_{k,j} \approx V_{k,j} \rho_{k,j}$. (This is inexact, but exact integration is cumbersome when the grid is non-Cartesian). Next, the potential solver is called using $Q(\xi, \eta)$ as input. Dirichlet conditions ($\Phi = F$) are applied at the boundaries. Finally, the resulting numerical potential, Φ, is compared to the analytic function, F.

Comparison of Results

To compare the analytic and numerical potentials, the difference between them is normalized by the maximum of the analytic function: $\Delta = (\Phi - F)/F_{max}$. The result is shown in Figure 4-2, where the 87×49 grid shown in Figure 4-1 was used. The potential solver reproduces

the analytic potential almost everywhere to within one percent. Larger errors occur where the grid is highly non-orthogonal or has less resolution. Smaller errors occur when a more slowly varying function is chosen. The potential is resolved sufficiently to capture most features of interest in the simulation, although numerical heating as a result of errors is still an issue.

Sidenotes

The potential solver was tested on grids of different regularity and fineness. Some conclusions were drawn from these tests:

- The method for obtaining the charge distribution from the charge density was found to be adequate. On a Cartesian grid, the results obtained by using an exact charge distribution ($Q_{k,j} = \int \rho_{k,j} dv$) were compared to the results obtained using an inexact charge distribution ($Q_{k,j} = \rho_{k,j} V_{k,j}$). The difference was everywhere small.
- Grid fineness and, equivalently, sharpness of features to be captured were found to be important.
- In most cases, the nine-point scheme achieved similar accuracy on both Cartesian and non-Cartesian grids. Highly non-orthogonal regions could, however, result in errors of several percent.

Convergence

The convergence of the potential solver is tracked by looking at the largest value of $RHS_{k,j}$ (as per Equation 3.110), where

$$RHS_{k,j} = -(N\phi_{k,j+1} + S\phi_{k,j-1} + E\phi_{k+1,j} + W\phi_{k-1,j} + Q) + \phi_{k,j}(N + S + E + W). \quad (4.8)$$

The logarithm of this value decreases linearly with the number of iterations until machine level accuracy is achieved at approximately 800 iterations. Convergence of the potential solver is shown in 4-3, where the test function F was assumed with $n_r = n_z = 5$.

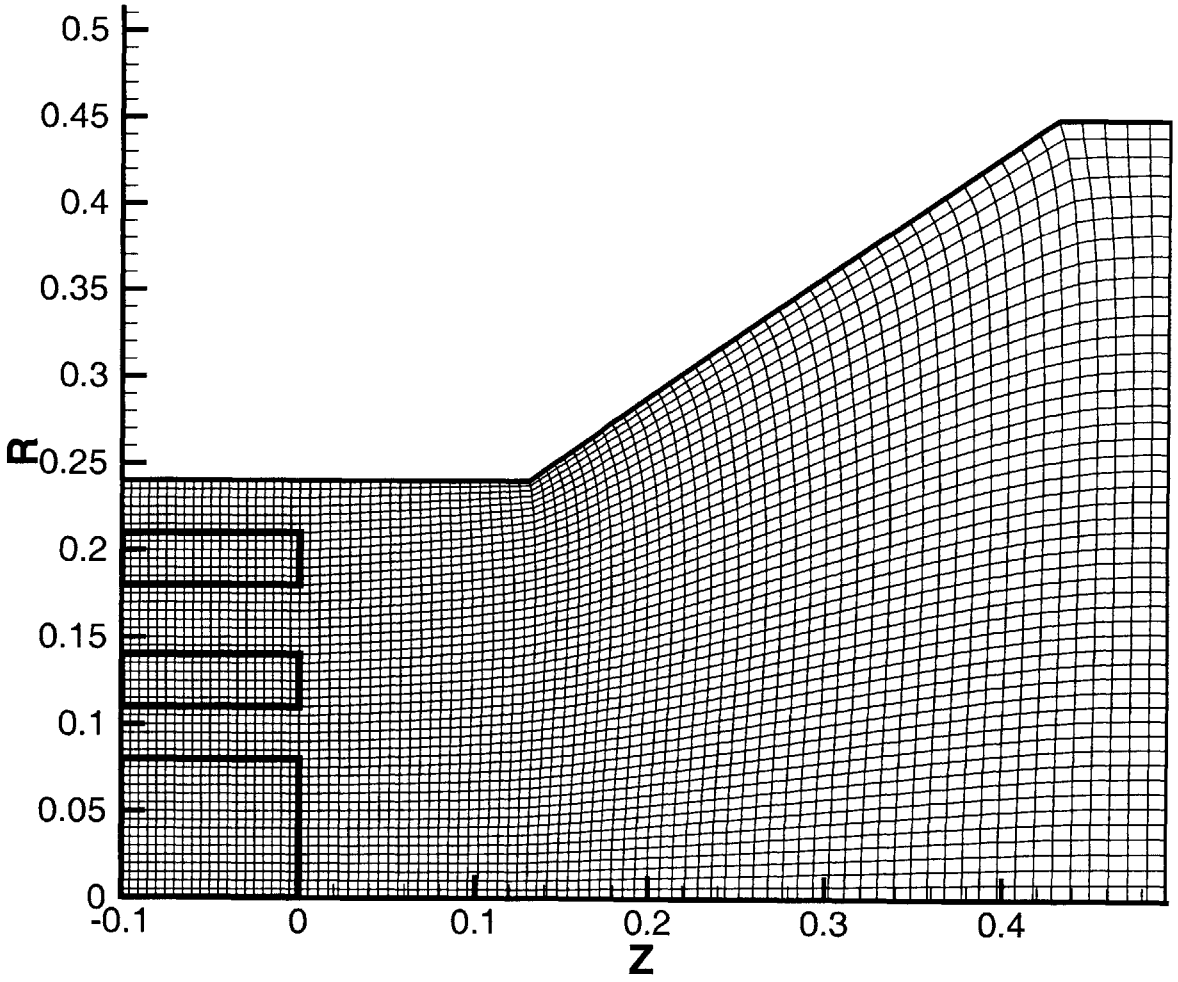

Figure 4-1: *The 87 x 49 grid used to test the potential, gradient and divergence functions.* The anode and center pole are outlined; these were "invisible" for the potential, gradient, divergence, and potential solver tests. The grid is Cartesian to the left of the anode exit and nominally elliptic elsewhere. Axes are in centimeters.

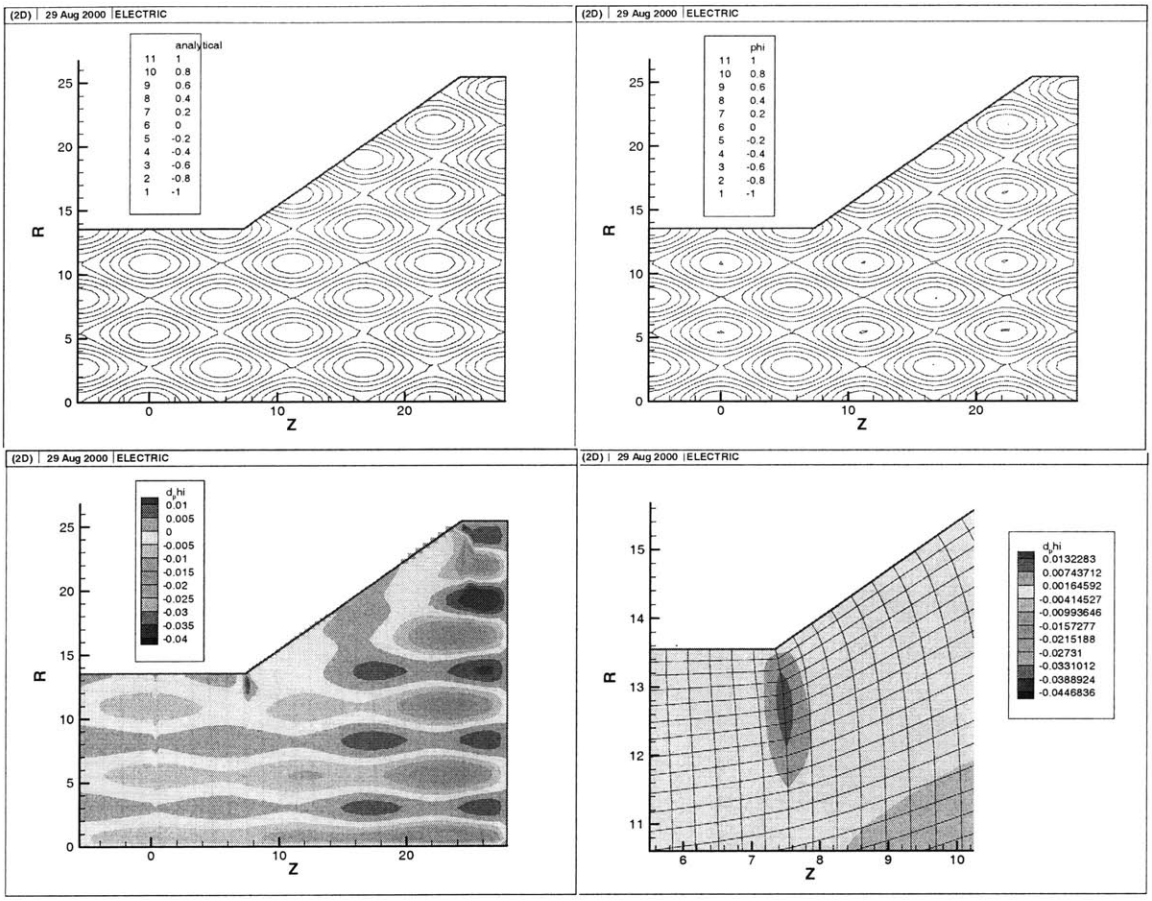

Figure 4-2: *Test of* Φ *solver for an* 87×49 *grid.* Upper left: Analytic potential. Upper right: Numerically calculated potential. Lower left: Normalized difference. Lower right: Details of normalized difference showing that errors arise where grid is highly non-regular. Axes are in normalized units.

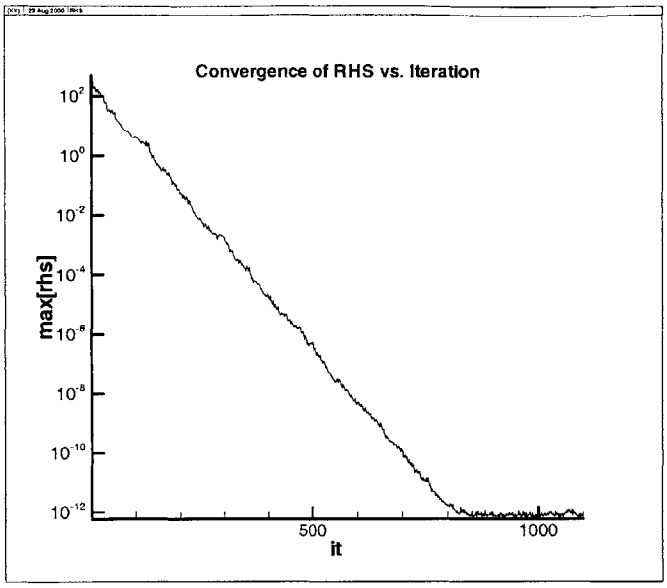

Figure 4-3: *Convergence of the Potential Solution on 80 x 50 grid.* The solution is reached in $\approx$ 800 iterations.

4.1.3 Gradient and Divergence

The numerical gradient and divergence functions were tested using the analytic function $F(z,r)$ described in section 4.1.2. Variables in F were $n_z = n_r = 5$, with $c_r = c_z = .5$, $l_r \approx 13.6$, and $l_z \approx 27.9$. The grid used is shown in Figure 4-1.

Gradient

To test the gradient function, $-\vec{E} = \vec{\nabla}F$ was computed numerically and compared to the analytic solution. Errors in the negative gradient are shown in Figure 4-4. Errors were normalized by the maximum magnitudes of the analytic E_z and E_r, e.g. $\Delta E_z = (E_{z,o} - E_z)/max(E_{z,o})$ where $E_{z,o} = -\nabla_z F$ is the analytic function. Most errors are in $\vec{E}$ are small, but some as large as 10 or 20 percent are found on the boundaries.

Divergence

To test the divergence function, $\vec{\nabla} \cdot \vec{\nabla}F$ was computed numerically (starting from the analytic $\vec{\nabla}F$) and compared to the analytic solution. Errors are again normalized by the analytic expression and plotted in Figure 4-4. Errors in divergence are less than 1 percent over much of the domain, rising to 2-4 percent in some areas near the right hand boundary.

Discussion

The most obvious source of error is grid spacing; The grid captures E_z better than E_r because $\delta z \approx \delta r$, but $l_z \approx 2l_r$. Another source of error is finite differencing on the non-Cartesian grid; the Cartesian portion of the grid (to the left of the anode exit) reproduces the function better than the non-Cartesian portion. Another source of error is forward and backward differencing at the boundaries.

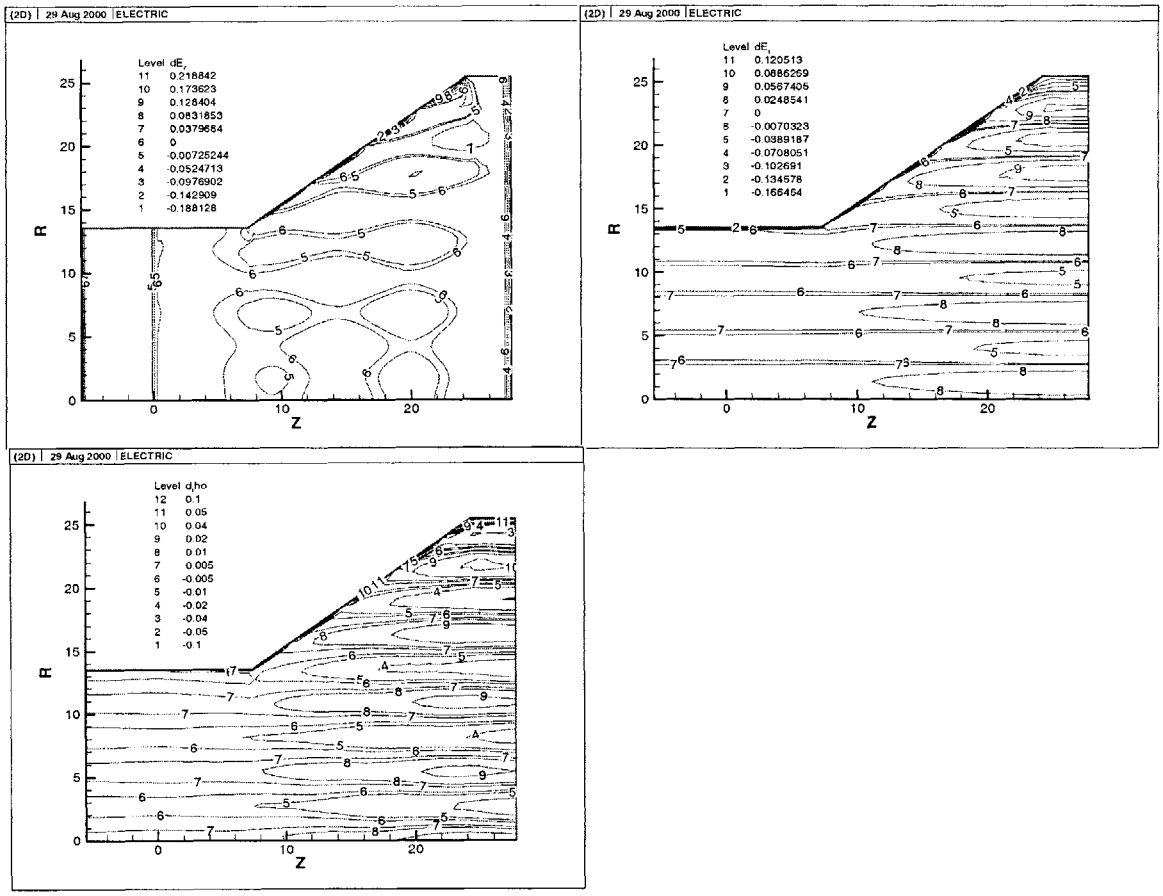

Figure 4-4: *Gradient and divergence tests on an* 87×49 *grid.* Upper left: Difference in E_z: $(E_{z,o} - E_z)/max(E_z)$. Error is less than 1 percent over most of domain, jumps to $\approx$ 20 percent at the right hand boundary. Upper right: Difference in E_r. Error of ≈ 5 percent is common. Lower left: Error in divergence of analytically obtained $\vec{\nabla} F$. Most errors are less than 2 percent. Axes are in normalized units assuming $\dot{m} = .13$ mg/s.

4.1.4 Leapfrog Method

The leapfrog algorithm was tested as it was developed. To summarize results presented in Chapter 3, the algorithm was tested by tracking single particles with electric field only, magnetic field only, and a combination of the two. Cyclotron motion and ExB drift were successfully observed to high levels of accuracy.

Gyro Motion

The magnetic part of the Lorentz Equation is a rotation of the velocity vector about a magnetic field line. The accuracy of the particle pusher was tested by taking the magnetic field to be entirely along the different axes. In one such test, the B-field was in one test taken be entirely in the θ direction. One electron was placed in the center of the domain, given an initial velocity $\vec{v} = v_z = 1.0$, and stepped forward time-steps. The resulting position trace was plotted in Matlab, and a fast Fourier transform performed to confirm the result. Figure 4-5 shows that the particle cycles back on itself 6 times without appreciable error.

$\vec{E} \times \vec{B}$ Drift

A different test verifies guiding center ExB drift, $\vec{v}_{E\times B} = \vec{E} \times \vec{B}/B^2$, Starting with the conditions $\vec{E} = E_r = 3.0$, and $\vec{B} = B_{theta} = 5.0$, an electron was placed in the center of the domain with zero initial velocity and stepped forward in time as before. The expected drift velocity of $\vec{v}_{E\times B} = 0.6i_z$ was successfully reproduced (Figure 4-6).

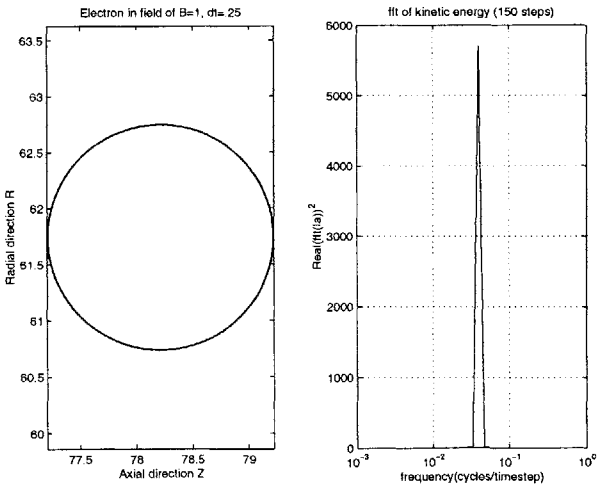

Figure 4-5: *Cyclotron motion of a single electron.* In normalized units, $\omega_{ce} = \hat{B}$ and $\omega_{ci} = \frac{\hat{B}}{\hat{M}_i}$

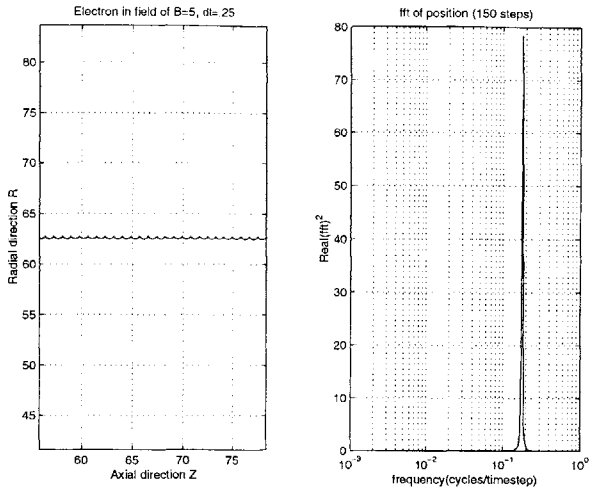

Figure 4-6: *ExB drift of a single electron.*

4.1.5 Divergence of Magnetic Field ($\vec{\nabla} \cdot \vec{B}$)

The magnetic field solution provided by Dexter Magnetics was tested to ensure that $\vec{\nabla} \cdot \vec{B} = 0$ everywhere. The previously validated function was used. Figure 4-7 shows $\vec{\nabla} \cdot \hat{B}$ in normalized units in the region next to the center pole. Clearly, $\vec{\nabla} \cdot \hat{B} \neq 0$ at the corner. However, $\vec{\nabla} \cdot \hat{B} \approx 0$ at interior points. The source of error is unknown. It seems too large to have arisen in the divergence function, or in interpolation from the Cartesian grid on which the field was provided. However, the field is several thousand Gauss near the corner. The error may be a result of poor resolution.

In fact, the field shown has been modified slightly to reduce the divergence. Before modification the divergence was 60 and -30 at the nodes just to the left and right of the corner. To reduce this, the field at the corner was made the average of the field at the four surrounding nodes. A similar modification was made to the field at the upper boundary.

A more accurate B field is desirable, as the divergence of B drives magnetic bottling. However, since $\vec{\nabla} \cdot \vec{B} \approx 0$ at all interior nodes, the field is judged to be adequate for this simulation. Component level tests showing magnetic bottling and conservation of magnetic moment validate this judgment.

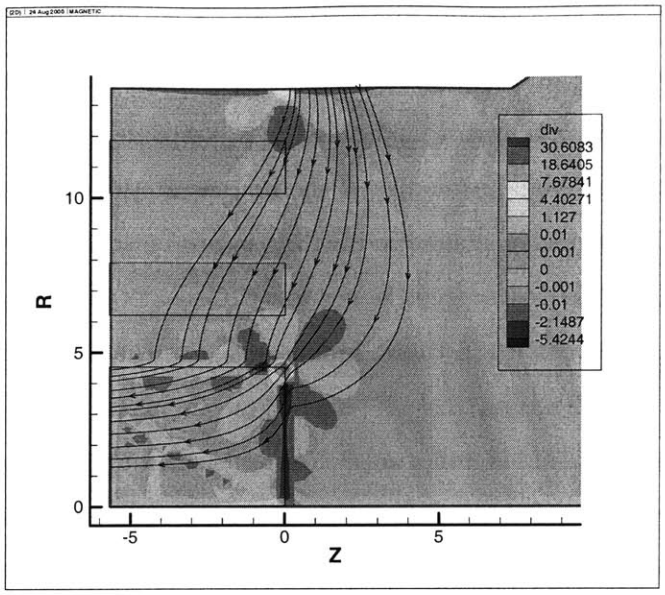

Figure 4-7: *Divergence of the magnetic field (80×50 grid) after modifying B at corner node.* Units are normalized. Also shown are magnetic streamlines, the spacing of which has not special significance.

4.2 Component Level Tests

Component level tests involve large pieces of code and, more broadly, basic plasma concepts. Typically, one aspect of the model is examined while another is idealized. Tests are required to show that magnetic moment is conserved by particles, that mass is conserved in the simulation, that plasma oscillations can be reproduced, that numerical heating is tolerable, and that the diffusive Coulomb collision algorithm drives electrons toward a Maxwellian.

4.2.1 Magnetic Bottling

To zeroeth order along a given streamline, the magnetic Dipole moment, $\mu_\perp = \frac{1}{2}\frac{u_\perp^2}{B}$, is conserved. In the absence of outside forces such as due to an electric field or collisions, the kinetic energy of this particle,

$$KE = \frac{1}{2}mu_\perp^2 + \frac{1}{2}mu_\parallel^2, \tag{4.9}$$

must also be conserved. Thus, for a charged particle of given kinetic energy, there is, along any magnetic streamline, a critical value of B beyond which the charged particle is trapped, or "bottled." At this B, all of the particle's kinetic energy must be in the $\perp$ direction in

order to conserve μ. At the critical value, $u'_{||} = 0$ and the particle must either stop it's motion in the $||$ direction, or turn around and return to an area of low B. To the next order, a particle bouncing in a mirror field undergoes jumps in μ which may be regarded as the result of resonances of high harmonics of the bounce motion and the gyro motion [54].

If $\vec{B}$ is constructed correctly, magnetic bottling is produced naturally, through application of the Lorentz Force, $dV/dt = e/m(E + v \times \vec{B})$. Consider the case where $\vec{E}$=0 and an electron has some initial velocity in three dimensions. Let the direction of the field at the guiding center be the Z direction, $\vec{B} = B_z$, such that the particle gyrates about $\vec{B}_z$ in the $R\Theta$ plane. If the magnetic field is uniform ($\vec{B}$ constant), no magnetic bottling should occur. If the magnetic field varies, $\partial\vec{B}/\partial z \neq 0$, bottling should occur. But it won't the way the magnetic field has been specified; we must have zero divergence. In cylindrical coordinates:

$$\frac{1}{r}\frac{\partial}{\partial r}(rB_r) + \frac{\partial B_z}{\partial z} = 0 \tag{4.10}$$

Because $\partial B_z/\partial z \neq 0$, there must exist some B_r or B_θ. The assumption that $B_r = B_\theta = 0$ is invalid physically! It is these other components of magnetic field which result in bottling.

To show that this occurs, an electron was tracked in the bulk of the plasma, setting $\vec{E} = 0$ and $\phi = C$ (some constant). The resulting trace is shown in Figures 4-8. Bottling is observed and magnetic moment is conserved, justifying use of the given magnetic field in the simulation. Other tests showing this "magnetic mirror" effect are described in Section 3.14.

4.2.2 Conservation of Mass

To test mass conservation, neutrals of size $s_o = 25$ are injected at the base of the anode and allowed to expand to the free space boundary at $\Delta\hat{t} = 30$. Neutrals which pass through the free space boundary are logged, along with their momentum. The neutral mass flow rate and thrust are then plotted verses time. Figure 4-9 shows that, for $M/m = 96$ and $\gamma = 10$, the number of super-particles tops out after between 30-40K nominal plasma times, and that mass is conserved. Significantly, the neutral mass flow through the free space boundary is only about 80 percent of the final expected flow after 15K nominal plasma times, which would take 150,000 iterations to simulate using the typical time-step of $\omega_{pe}\Delta t = .1$. In Section 2.7, we said that a "typical" neutral would cross the simulation

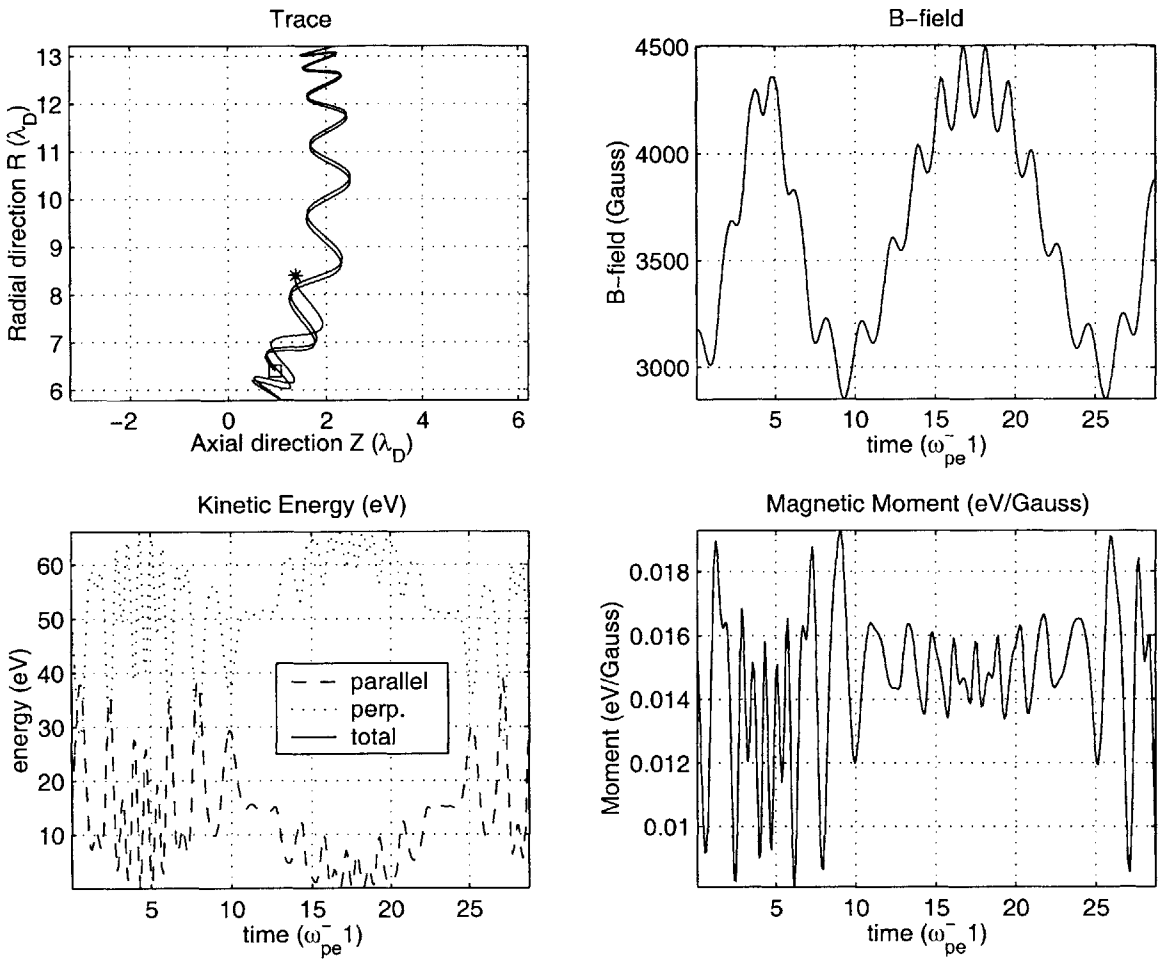

Figure 4-8: *Magnetic bottling of a single electron.* Upper Left: Trace of an electron in the near anode region with $\phi = C$. Particle begins at (*), ends at square. Upper Right: Magnetic field strength seen by the electron. Lower left: Kinetic and potential energy of the electron. Energy is conserved almost perfectly (sum of kinetic and potential is on top of the upper boundary; it is invisible in the plot). Lower Right: Magnetic moment of the electron, showing conservation. Line of symmetry is observed at time $\approx 17 - 18$. Units are in nominal λ_D and ω_p for the chosen mass flow rate.

region in $\tau_1 = 83,000$ iterations at $M/m = 96$, $\gamma = 10$, and $\omega_{pe}\Delta t = .1$. That result was, in some sense, over-idealized. Even at $M/m = 96$, the simulation must progress for several hundred thousand time-steps to achieve a completely converged result!

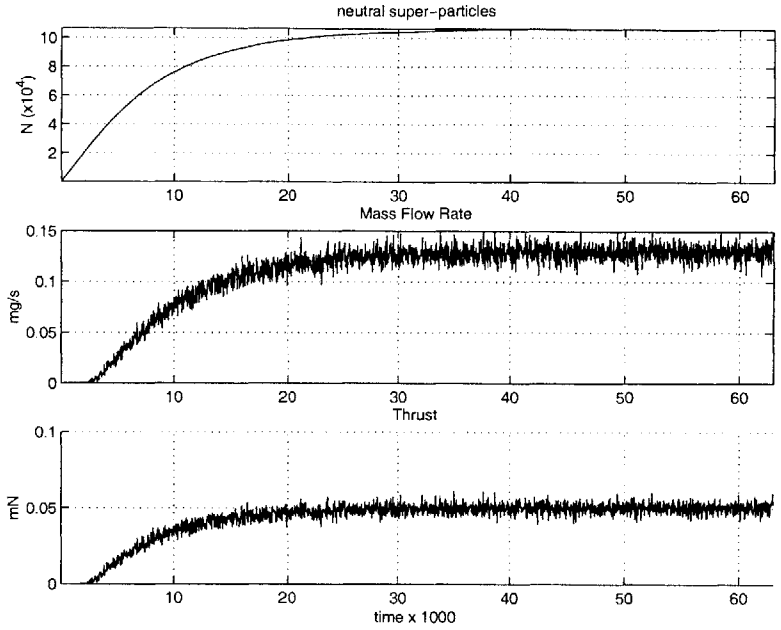

Figure 4-9: *Mass conservation in neutral flow.* Neutrals are injected at the base of the anode at $T = .1$ eV, $\dot{m} = .13$ mg/s and allowed to expand freely toward the free space boundary. For this plot, $M/m \approx 96$ and $\gamma = 10$. The top plot shows the total number of neutral super-particles of size 25 entering the system, the middle plot shows the mass flow rate of neutrals exiting the system, and the lower plot shows the momentum flux in the z direction exiting the system, i.e. the thrust. It takes $\approx 30K$ nominal plasma times for the neutral mass flows entering and exiting the system to equalize.

To accelerate the convergence, we start out with the free stream solution and then cull the neutral population according to $n_n/n_{n,o} = exp(\frac{z}{L}ln(1-\eta_u))$, where $n_{n,o}$ is the free stream density (See Figure 4-10), η_u is the propellant utilization, and L is a scale length. In practice, $L = .65mm$ is a good choice.

4.2.3 Boundary Reflection

As the particle pusher was being constructed, it was tested for momentum conservation, angular momentum conservation, and energy conservation. To minimize wall effects, the exact boundary intersection point and time was calculated as discussed in Section 3.18, and boundary reflection was assumed to be specular (perfectly reflecting). When exact boundary conditions were not implemented, angular momentum and energy were not conserved.

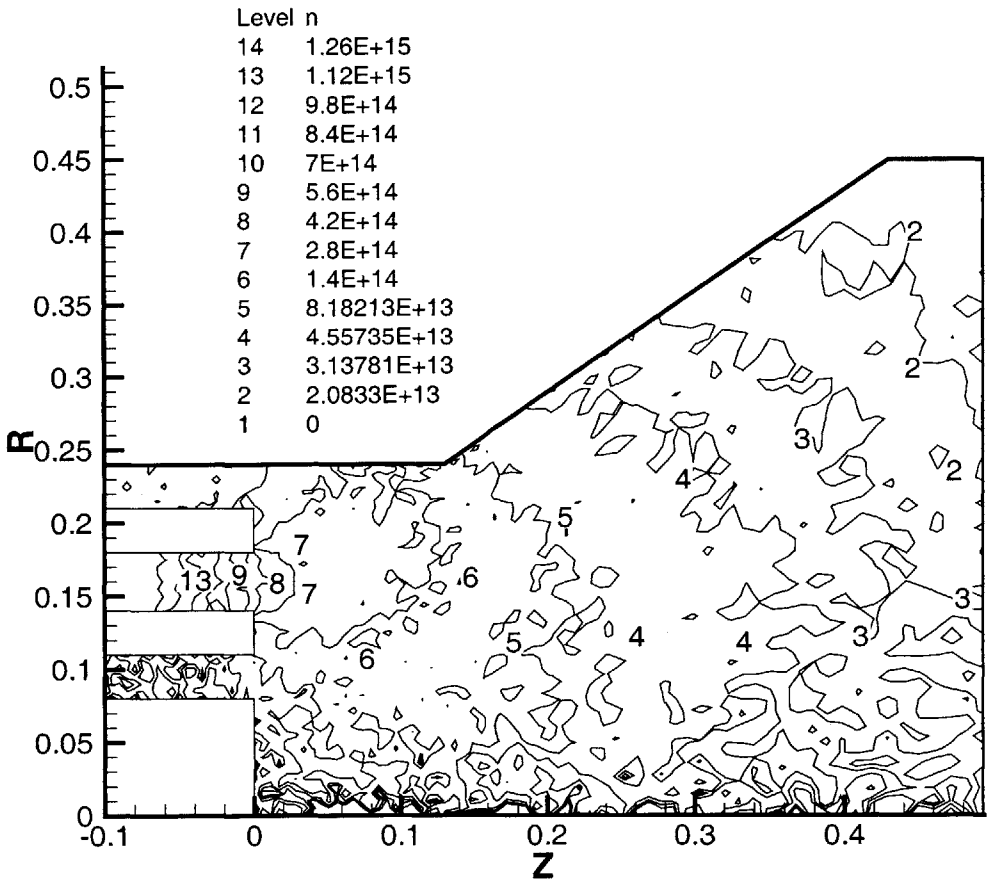

Figure 4-10: *A contour plot of neutral density,* $n_{n,o}$ after free expansion for $\approx 33K$ nominal plasma times (1100 iterations at $\Delta\hat{t} = 30$). Axes are in cm, while density is per cubic centimeter. Grid is 89×49. Values are cell average. Axes are in centimeters.

In the final version of the simulation, most boundary reflection is diffuse such that energy and angular momentum are not conserved anyway. But intersection points are still calculated exactly in order to minimize any artificial electron transport along the wall.

4.2.4 Plasma Oscillations

The simulation solves Poisson's equation to find the electric field. Hence, oscillations at the plasma frequency should be visible. A component level test was performed to verify this.

First, a plasma distribution was created such that $\rho_e(z,r)$ was exactly zero. Seventy five thousand zero energy electrons were distributed throughout the simulation region using the rejection method to achieve a nearly uniform density. A zero energy ion was created on top of each electron such that the charge at each node summed to exactly zero.

Next, the simulation was perturbed by displacing all the electrons in a certain cell by $\Delta\xi = .5$ such that the simulation had potential energy, but no kinetic energy.

Then, the electrons were time-stepped forward. Electric potential and field were re-calculated each time-step. For this test, ions were assumed to have infinite mass (they were not allowed to move), and electrons were specularly reflected off all boundaries. After each time-step, the kinetic and electric (potential) energy densities were calculated. These should oscillate at twice the plasma frequency. The expected oscillation period, τ, is easily computed from $\omega_{pe} = 2\pi\nu_{pe} = fn(\sqrt{n_{e,o}})$. The period for a complete cycle is $\tau_{pe} = 2\pi/\omega_{pe} = 2\pi[t]$. The period we should observe in energy is one half this, $\tau = \pi[t]$. Of course, if the density is not nominal, the frequency will be different.

In MKS units, the energy of an electric field per unit volume is given by the formula $\varepsilon = \frac{1}{2}\epsilon_o E^2\ (J/m^3)$. In CGS units, the formula reads $\varepsilon = \frac{1}{8\pi}E^2\ (erg/cm^3)$. Numerically, we calculate the total energy of the field (the potential energy) according to

$$E.F. = \int \varepsilon dV = \frac{\gamma^2}{8\pi}\sum_{k=0}^{N_z-1}\sum_{j=0}^{N_r-1}(\hat{E}_z^2 + \hat{E}_r^2)\hat{V}_{k,j}[E]^2[x]^3\ (ergs) \tag{4.11}$$

where N_z and N_r are the number of nodes in the ξ and η directions, and [E] and [x] relate normalized units to CGS units. Note that the artificial permittivity, $\epsilon_o' = \epsilon_o \times \gamma^2$ must be taken into account. To convert to electron volts, we divide by 1.6×10^{-12}. The kinetic

energy, $K.E.$, is just

$$K.E. = \sum_{i=1}^{N} \frac{1}{2} \hat{v}^2[T]\, eV. \tag{4.12}$$

The kinetic and potential energies are plotted in Figure 4-11. The electron density in this case was approximately 1×10^{12} per cubic centimeter, a factor of 6.7 less than the "nominal" density. Thus we should see oscillations with period $\tau \approx \pi\sqrt{6.7} = 8.1$. This is observed, validatin;

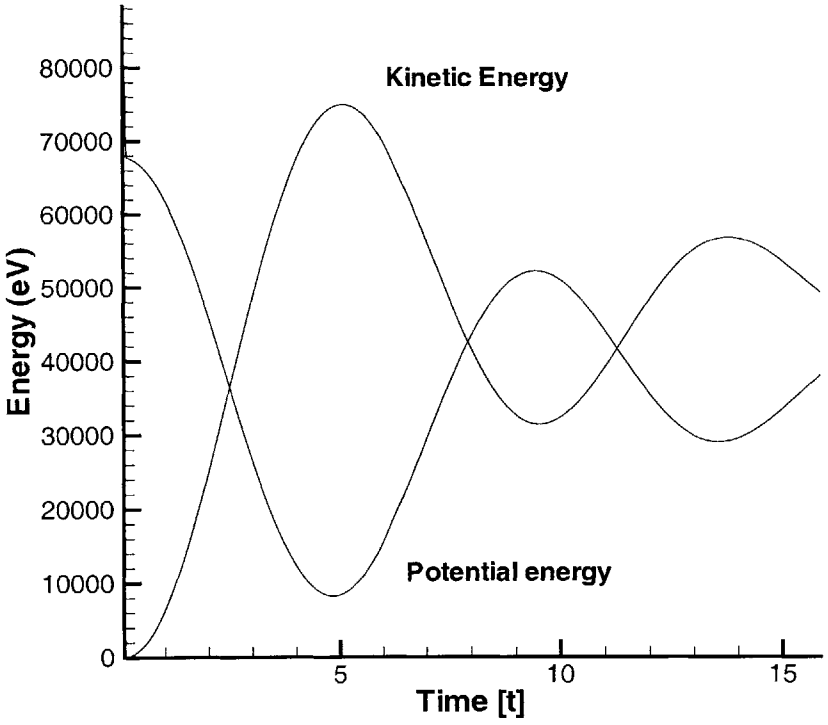

Figure 4-11: *Plasma Oscillations observed starting with a cold plasma.*

4.2.5 Heating Time

Some non-physical, stochastic heating of the plasma is expected to occur. Such heating is present in all computer models, to some extent, and cannot be entirely eliminated. It arises from arithmetic rounding, the size of the time-step, the finite-differencing of the equations, and the use of super-particles. Hockney and others have quantified this heating for "Cloud-In-Cell" systems such as ours [19]. (Note: The term "Cloud-In-Cell" (CIC) refers to the method by which charge is assigned to the mesh. NGP is another possible method.)

Non-physical heating may be observed by creating an initial thermal distribution with

$N_e = N_i$, closing the boundaries such that no particles can escape, and letting the plasma oscillate. This is merely an extension of the oscillation test previously described. If the simulation is allowed to continue for a long period of time, the energy of the plasma is observed to rise steadily, even if all boundary reflection is specular.

For a system with approximately 100 thousand particles of each species, particle flow through the system (a different case), and no energy sinks, we observed heating on the order of that described in Hockney for CIC systems; The electron temperature doubles every five to ten thousand iterations.

Sources of heating may be varied, but they are clearly related to the potential solver. With the potential solver turned off and boundary conditions specular, the simulation conserves energy almost perfectly. Some other observations follow:

- Time-step matters. Therefore, the optimum time-step criterion developed by Hockney and described in Chapter 3 was used [19].
- Transient charge imbalances may be a factor. The mean charge summed over all the nodes was observed to fluctuate from positive to negative and back, although the mean was of magnitude 10^{-13}, which is nearly zero to machine precision.
- Tests on Cartesian and non-Cartesian grids showed similar heating rates.
- Increasing particle count (from 100K to 200K) did not seem to affect the energy rise.
- Boundary conditions were most significant. Constant potential boundaries reduced the heating by approximately one half. In contrast, using second order derivatives for electric field and grid constants at the boundaries actually tended to increase the heating.
- Interpolation method was relevant. Different methods of interpolation resulted in slightly different heating rates.

To test the sensitivity of the heating rate to the interpolation scheme, a volume based scheme as described by Oh [33] was implemented on an orthogonal grid. Only slightly less heating resulted. When a $T_e = 15eV$ plasma was simulated on a 25x25 grid (with irregular spacing in the r direction to increase statistics near the axis) along with a common set of boundary conditions and 200K particles, the volume weighting was observed to result in

an average electron energy of $T_e = 16.28$ after 500 iterations (at a time-step of 0.2) vs. $T_e = 16.30$ with "normal" weighting. Using a purely Cartesian grid with normal weighting also resulted in $T_e = 16.30$. For these three simulations, $\phi = 0$ was assumed along the upper and left hand boundaries, while $E_n = 0$ was assumed along the right hand and centerline boundaries.

Over time, numerical heating can become a problem. But how long are electrons actually in the system before they are destroyed? Let us assume that the mean lifetime of the electrons is similar to the mean lifetime of the ions, which, in turn, depends on the mass ratio and the time-step chosen. In Chapter 2 (Section 2.7) we found that the transit time for a typical ion to pass from the anode to the free space boundary with $M/m = 960$ and $\gamma = 10$ was about $\tau_1 = 6,600$ iterations. This assumed $\omega_{pe}\Delta t = .1$. Let us assume the mean lifetime of an electron is τ_1. This is time enough for the electron temperature to double. We also found that the transit time between the anode and the point where the channel diverges was about $\tau_2 = 1700$ iterations. This is the region where the electron temperature begins to rise. The transit time for the discharge itself was just $\tau_3 = 660$ iterations.

Since the electron temperature over most of the simulation region is only a few eV, the electron lifetimes are such that heating should not be a problem which threatens numerical divergence in any way. Even without energy sinks (ionization, excitation, recombination), the temperature rise should be limited to a few eV. Still, numerical heating creates uncertainty in the results. Specifically, stochastic errors would tend to make the electron energy distribution not only more thermally energetic, but also more isotropic and Maxwellian.

More advanced grid weighting schemes have been shown to decrease numerical heating by orders of magnitude [19]. In Chapter 6, we recommend that such weighting be considered if the code is developed further.

4.2.6 Diffusive Coulomb Collision Algorithm

The diffusive Coulomb collision algorithm was tested by moving a single electron many times subject to the random forces determined by a pre-defined background density and temperature. Over time, the distribution of particle energies became nearly Maxwellian at T. This test was described in Chapter 2. The effects of adding diffusive Coulomb collisions to the simulation are discussed in Chapter 5.

4.3 System Level Tests

System level tests involve the complete simulation. Typically, these tests are parametric and address several concepts at once. Results must be consistent above all. Tests in this category involve electron injection, wall capacitance, electric potential boundary conditions, particle count, artificial mass ratio, and artificial permittivity.

4.3.1 Performance Plots

Many thruster performance variables are computed and saved at each time-step to a file called "perf.dat" (perf stands for performance). In order of appearance, these variables are:

- Iteration.
- Number of electron super-particles.
- Number of ion super-particles.
- Number of neutral super-particles.
- Simulation time (normalized units).
- Electron/Ion time-step (seconds).
- Cathode electron current, $I_c^- = I_{cd}^- + I_b^- I_{az}^-$ (Amps).
- Net anode current, $I_a = I_a^+ + I_a^-$ (Amps).
- Ion beam current, I_b^+ (Amps).
- Ionization current, I_i (Amps).
- Ion thrust (mN).
- Neutral thrust, T (mN).
- $\dot{m}_i$ at free space boundary (mg/sec).
- $\dot{m}_n$ at free space boundary (mg/sec).
- Specific impulse, $I_{sp} = T/\dot{m}_o g$ (seconds), based on nominal mass flow rate.
- Wall potential, ϕ_w (Volts).
- Average electron kinetic energy $\times 2/3$, (eV).
- Average ion kinetic energy $\times 2/3$, (eV).
- Energy loss to the center pole, (eV).
- Neutral density at control point, n_n (cm^{-3}).

- Ion density at control point, n_i (cm^{-3}).
- Total neutral mass in system (mg).
- Total ion mass in system (mg).
- Electron density at control point, n_e (cm^{-3}).

These variables are plotted and used to validate the simulation. All variables are time averaged using a sample size of 100 to eliminate noise and make plots more readable. This reduces the original number of data-points by a factor of 100. The time averaged data set is created by a separate program called "process.c", which saves the reduced data set into a separate file, e.g. "perf.dat" $\rightarrow$ "perfb.dat". The variables are plotted in an (almost) standard format. In most plots, the specific impulse is based on the thrust at time t and the nominal mass flow rate, e.g. .1 mg/sec. In some figures (e.g. Figure 4-22), the specific impulse based on the instantaneous flow rate is also shown.

When the simulation is run, the time-step is usually constant when $\gamma = 10$, but usually varies from time-step to time-step when $\gamma = 5$ as a result of minimum heating criteria discussed in Chapter 3.

4.3.2 Electron Injection, Wall Capacitance, and Free Space Potential

Electrons are destroyed and injected (re-introduced) into the simulation at each iteration along the free space boundary. Two methods for injecting electrons were developed. The first method assumed that the cathode and discharge currents were identical at each and every time-step. The second method forced the plasma to be quasineutral near the boundary by injecting (or withholding) however many electrons were needed. These two methods were tested parametrically. They were judged on criteria related to the capacitance and floating potential of the acceleration channel walls and thruster body. These tests were conducted with a simulation containing electron-neutral elastic scattering, exciting, and ionizing collisions, ion-neutral scattering and charge exchange collisions, and MCC Coulomb collisions.

Parametric Test Criteria for Electron Injection: A "Gedanken" Experiment

In conventional TAL thrusters, the walls of the acceleration channel are often held at cathode ground. In the mini-TAL, however, the walls and body of the thruster are nominally

floating at a common potential. To signify this, the mini-TAL body is shown connected to a capacitor in the space vehicle circuit diagram (Figure 2-2). The capacitance of the thruster body modeled as an isolated body in free space was estimated to be about $1.6 \times 10^{-12} F$. The capacitance of a thruster attached to a spacecraft will, of course, be different. The following questions must be answered:

- What capacitance should be assumed in the numerical model?
- How may the capacitance change numerical results?

To help answer these questions, we perform a thought experiment.

First, let the walls of the thruster have infinite capacitance, $C \rightarrow \infty$. In this case, the wall potential will never change, no matter how much charge the wall absorbs. Now, let C be much larger than the physical value, but less than infinity. In this case, electron and ion fluxes to the walls determine the floating potential, ϕ_w, which should oscillate very little about the mean value, $< \phi_w >$. This mean value may be estimated through the simple sheath theory described in section 4.3.3 . Finally, let C decrease toward the physical value. As the wall and plasma equilibrate, oscillations in ϕ_w appear, but $< \phi_w >$ should stay the same; sheath theory says $< \phi_w >$ is not a function of plasma density. As long as oscillations are much smaller than the overall potential drop, performance should not change much, if at all. The thought experiment thus yields two criteria for testing boundary conditions. First, $< \phi_w >$ should not vary with C. Second, performance should not change much (if at all) with C.

Steady State Injection

Results inconsistent with the thought experiment result from using the steady state current condition ($I_c = I_d$) to inject electrons at the free space boundary. Capacitance is found to strongly influence $< \phi_w >$ and overall thruster performance.

The different conditions tested are summarized in Table 4.1. The first test listed assumed mass ratio $M_n/m_e \approx 24$, the free space permittivity factor $\gamma = 10$, and wall capacitance $C = 1.6 \times 10^{-12} * 10$. The electric potential boundary condition $\phi = 0$ was imposed at the right hand free space boundary. This test resulted in a wall potential of $< \phi_w > \approx 60V$. Performance estimates for this case are shown in Figure 4-13. The next two tests varied the mass ratio, but held C constant. The floating potential changed, but in a pattern largely

Topic	M/m	ϕ_{rhs}	C	$< \phi_w >$	Figure
Mass Ratio	24	$\phi = 0$	$1.6 \times 10^{-11} F$	≈ 60 V	4-13
Mass Ratio	96	$\phi = 0$	$1.6 \times 10^{-11} F$	≈ 47 V	4-13
Mass Ratio	960	$\phi = 0$	$1.6 \times 10^{-11} F$	≈ 37 V	-
Capacitance	24	$\phi = 0$	$1.6 \times 10^{-10} F$	≈ 18 V	-

Table 4.1: Overview of tests used to invalidate steady state method of electron injection. Nominal physical capacitance of thruster body in free space is $1.6 \times 10^{-12} F$.

consistent with sheath theory (see discussion in Section 4.3.3). The last test reverted to $M_n/m_e \approx 24$, but assumed $C = 1.6 \times 10^{-12} * 100$. This resulted in a wall potential of $< \phi_w > \approx 18V$. This is not consistent with the Gedanken experiment. Furthermore, various measures of performance changed by ten percent or more. These results are also inconsistent.

What happened? The "steady state" method for injecting electrons along the free space boundary is flawed. Unless the steady state particle count is known ahead of time (e.g. 50K ions, 60K electrons) the system is charge unbalanced. Typically, the simulation is starved for electrons, which is reflected in the high potential of the floating thruster body. Examination of particle moments provides further confirmation; the plasma is not always quasineutral near the free space boundary.

Note: Performance results obtained for the steady state and quasineutral cathode boundary conditions (presented in the next subsection) are not exactly comparable due to some small, miscellaneous enhancements to the code only implemented for the latter.

Quasineutral Injection

Results far more consistent with the thought experiment are obtained when cathode electrons are injected at the rate required to maintain quasineutrality along the free space boundary. This is the "quasineutral" electron injection method discussed in Chapters 2 and 3.

The tests performed to validate the quasineutral electron injection method are summarized in Table 4.2. To begin, the simulation was run with capacitance $C = 1 \times 10^{-10} F$, again letting $M_n/m_e \approx 24$ and $\gamma = 10$ (Figure 4-17). As before, the electric potential at the right hand boundary was frozen at zero, and the potential drop between the constant potential wall at ϕ_w and the upper right hand corner at $\phi = 0$ V was linear (this is the top free space

Topic	M/m	ϕ_{rhs}	C	$< \phi_w >$	Figure
Electron Injection	24	$\phi = 0$	$1 \times 10^{-10} F$	$\approx .5$ V	4-17
Boundary Conditions	24	$\phi = 0$	$1 \times 10^{-10} F$	$\approx .5$ V	4-18
Capacitance	24	$E_z = 0$	$1 \times 10^{-10} F$	≈ 2 V	4-19
Capacitance	24	$E_z = 0$	$2 \times 10^{-11} F$	≈ 2 V	4-20

Table 4.2: Overview of capacitance and boundary condition tests performed to validate the quasineutral method of electron injection. Nominal physical capacitance of thruster body in free space is $1.6 \times 10^{-12} F$. The first test assumed a linear drop in potential from the wall at the upper right hand boundary. All other tests used a sheath equation to determine the potential at this boundary. The second, third, and fourth tests all began from the dataset generated by the first set.

electric potential boundary condition). Thus, the set of conditions imposed was in every sense identical to the set previously imposed, except that the capacitance was different and cathode electrons were injected differently. But the results from this one change were striking: Figure 4-17 shows that wall potential dropped to ≈ 0 and performance shifted dramatically.

The next three tests listed in Table 4.2 are variations on the first test. All three began with the particle distribution saved at the end of the first test, but all three calculated the upper right hand boundary potential according to the equation for a sheath, assuming that $\phi = 0$ at the upper right corner. The first of these tests assumed $C = 1 \times 10^{-10} F$ with $\phi = 0$ at the right hand side. The result, shown in Figure 4-18, is performance almost identical to that that already shown in Figure 4-17. The electric potential boundary conditions along the upper free space boundary do not seem to be important to the overall solution. The next test assumed $C = 1 \times 10^{-10} F$ with $E_z = 0$ at the right hand side (Figure 4-19). The wall potential changed by couple eV, but performance was almost the same. This verifies that we can use the boundary condition $E_z = 0$. The final test assumed $C = 2 \times 10^{-11} F$ with $E_z = 0$ at the right hand side (Figure 4-20). This test shows the effects of changing the capacitance. Four observations follow from a comparison of Figures 4-19 and 4-20.

- The magnitude of oscillations in ϕ_w is ≈ 5 times greater in Figure 4-20 than in Figure 4-19. This is the same factor by which capacitance changed.

- The frequency of oscillations in ϕ_w is one and a half to two times greater in Figure 4-20 than in Figure 4-19.

- $< \phi_w >$ differs by less than a Volt.
- Thruster performance differs by only a few percent.

The first result means that the number of particles absorbed by the wall per cycle is nearly the same, no matter the capacitance. This suggests that the magnitude of fluctuations in plasma density is not a strong function of the wall potential; the fluctuations originate in the plasma itself. The second result indicates a feedback mechanism with the discharge. The third result ($< \phi_w >$ is unchanged) is expected from the thought experiment. The fourth result, also consistent with the thought experiment, confirms that wall oscillations on this scale are not a strong determinant of thruster performance.

Results

Based on the tests described above, the quasineutral method of electron injection and the electric potential condition $E_z = 0$ at the right hand free space boundary were base-lined. The latter condition was modified slightly after these tests were performed; the simulation was found to diverge under certain transient conditions. The requirement $\phi \geq 0$ at the right hand free space boundary was found to eliminate the problem.

4.3.3 Validation Tests with $I_c = I_a$

The steady state method of electron injection was developed first. It was later invalidated, but not before many parametric tests were performed. Not all of these tests must be discarded. Many yield useful information. These tests are described in the following subsections.

Mass Ratio

The mass of a Xenon neutral is 2.18×10^{-22} gm, while the mass of an electron is 9.11×10^{-28} gm. Thus, the physical mass ratio $M/m_e \approx 239,000$. To accelerate convergence, we changed the mass ratio by a factor $M/M' = 1/f$. This means that heavy particles move $v_n'/v_n = \sqrt{M/M'} = \sqrt{1/f}$ faster than they should.

To preserve ion and neutral mean free paths, the mass flow rate was scaled by $\dot{m}'/\dot{m} = \sqrt{f}$, cross sections were increased by $Q'/Q = \sqrt{1/f}$, and output was rescaled. If the

simulation is at all linear, the original physical solution should be recovered. This assumption can be tested parametrically. If we can show that the solutions obtained from $1/f = 10,000$ and $1/f = 2500$ are the same, then, by induction, the solutions for $1/f = 10000, 2500, 625, 100, ...1$ should all be the same, or similar.

The first option is to change the mass ratio, begin at $t = 0$, run the simulation until it is converged, and then compare it to a previously converged solution which assumed a different mass ratio. However, for this previously converged solution, we already have a time history and a complete list of particles and their current positions. This enables a quicker method: If we change the mass ratio, re-load all the particles, and then re-scale the mass flow rate and all of the heavy particle velocities according to the new mass ratio, then the particle densities should stay the same and the solution should continue smoothly, producing very similar particle moments. This amounts to re-scaling the simulation "on the fly." It enables us to change the mass ratio at will.

Neutral Test of Mass Ratio

Figure 4-12 demonstrates re-scaling on the fly for neutrals. Here we modeled the neutral flow with two different mass ratios. The simulation was run for 1000 iterations at $\Delta t = 30$ with $M_n/M_n' = 10,000$ and the results were saved. The mass ratio was then reset to $M_n/M_n' = 2500$, the particles were re-loaded, velocities were re-scaled by $v'/v = \sqrt{2500/10000} = .5$ and the simulation was run for another 2000 iterations. (All this is automated; all we do is change the mass ratio in the header file). Results were re-scaled before saving. The transition appears smooth. Comparison with Figure 4-9 shows that the neutral flow at $M_n/M_n' = 10000$ converges in half as many iterations as it does at $M_n/M_n' = 2500$.

M/M'	$M'/m = f$	$v_n'/v_n = \sqrt{1/f}$	Q'/Q
1	239,000	1	1
250	960	16	16
2500	96	50	50
10,000	24	100	100

Table 4.3: Artificial mass ratios used in the numerical simulation. M is the physical neutral mass. M' is the numerical neutral mass. The ratios M'/m, v_n'/v_n, and Q'/Q are approximate. The last ratio is applied to preserve mean free paths.

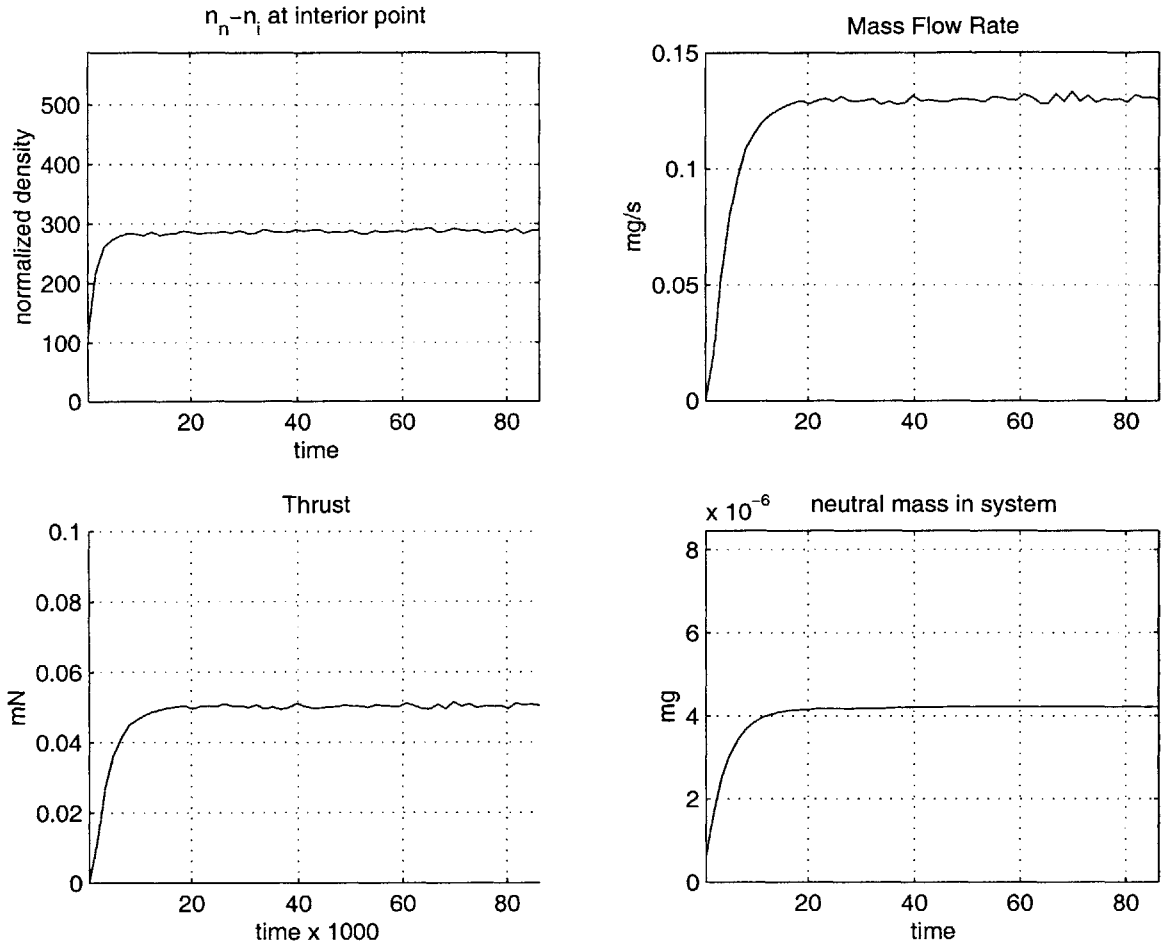

Figure 4-12: *Neutral flow with changing mass ratio.* Transition from $M_n/M_n' = 10000$ to $M_n/M_n' = 2500$ occurs at $t = 30,000$. Upper left: The normalized density at an interior point (sum of super-particles*size where size=25). Upper right: Mass flow through free space boundary. Lower left: Thrust from neutrals only. Lower right: Total mass in system. Time is in nominal plasma times with $[T_e] = 50$, $\dot{m} = .13$ mg/s, $\gamma^2 = 100$.

Plasma Test of Mass Ratio

Using an artificial mass ratio with a plasma is more difficult. The following points are important:

- It is best to keep Q'/Q as small as possible. If the plasma becomes too collisional, the electron flux across the field lines is no longer proportional to ν_{en}.
- The ion flux into the wall changes with M_n/M_n', affecting the wall potential.
- The period of heavy particle ionization (predator prey) oscillations changes with M_n/M_n'

Let us compare two solutions at $\dot{m} = .1mg/s$, setting our nominal temperature to $[T_e] = 50eV$ and the wall capacitance to $C = 1.6 \times 10^{-11}$ F. The anode potential is set to 300V. Charge exchange, excitation, ionization, and Monte Carlo Coulomb collisions are included. For both solutions, we assume a free space permittivity factor of $\gamma = 10$. The grid is similar to that shown in Figure 4-1.

First we expand the neutrals for 2000 time-steps at $M_n/M_n' = 10,000$ and $\delta t = 30$. Next, we introduce the background plasma (still at $M_n/M_n' = 10,000$) and run to a "converged" solution. This run is shown in Figure 4-13. At first, the wall potential fluctuates by tens of electron volts, but it then settles down to about 60 eV. After $\hat{t} = 13440.3$ (171,696 iterations), the simulation was stopped at declared converged. However, the figure shows that a semi-converged solution was actually reached by $\hat{t} = 3000$. After that point, the neutral flow evened out, but performance parameters only changed a little. Many neutrals of statistics weight $s = 1$ were produced at the beginning of the run as ions impacted the floating walls, and it takes time for these to work their way out of the system. But these small neutrals do not seem to effect performance very much. Next, we switch to $M_n/M_n' = 2500$, restart the simulation at $\hat{t} = 13440.3$, and allow the simulation to once again converge. After some fluctuations, performance predictions again even out. The new performance is also shown in Figure 4-13. The frequency of long period oscillations drops by a factor of 2, which means that $\nu \sim 1/\sqrt{M_n}$. (This is consistent with the expected frequency for "predator prey" oscillations, $2\pi\nu = \frac{1}{L}\sqrt{v_n v_i}$). The wall potential drops by $15eV$, which is largely consistent with sheath theory. This potential drop will be discussed more in the next section.

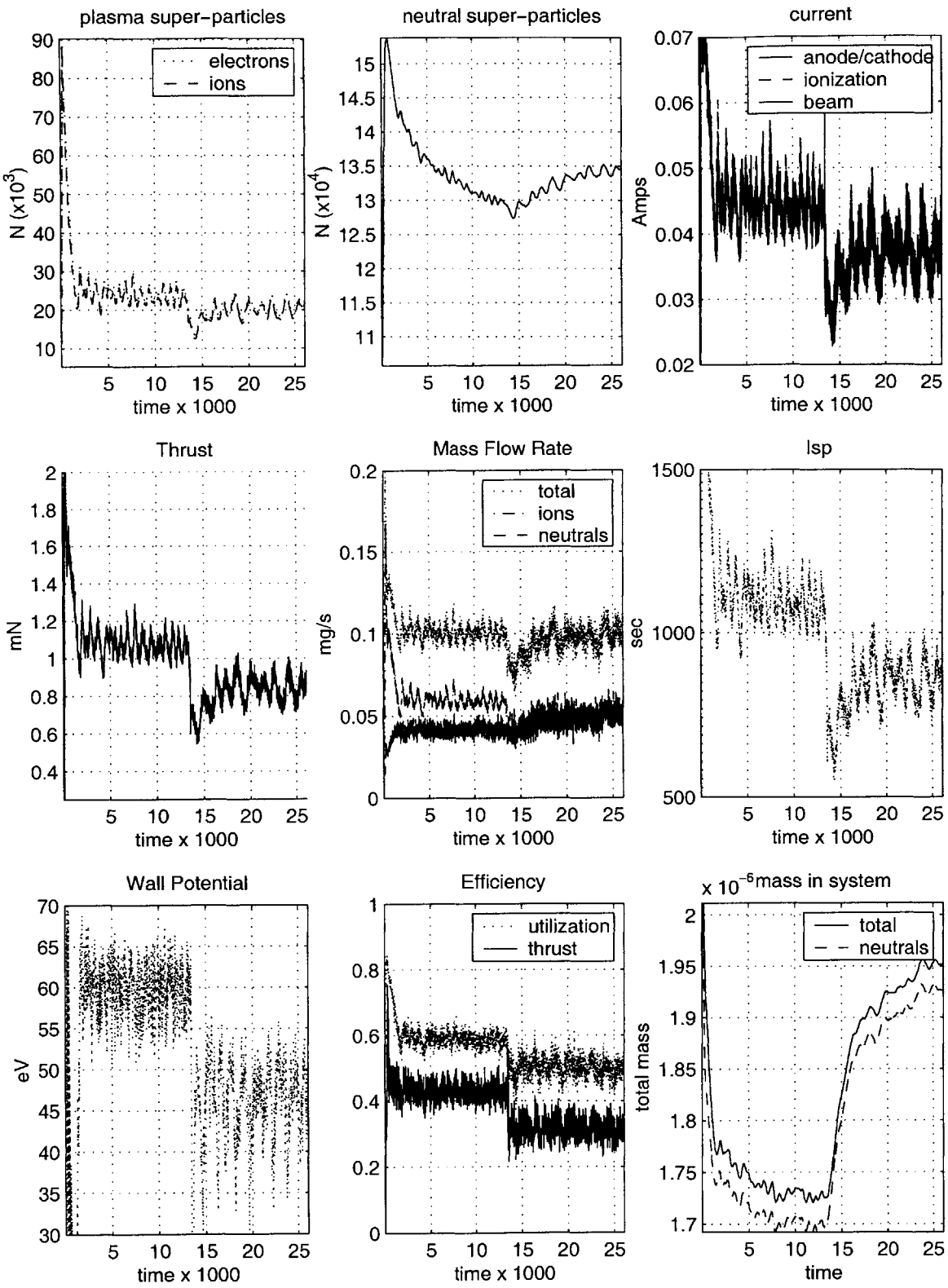

Figure 4-13: *Performance predictions for* $M_n/m_e \approx 24$ *transitioning to* $M_n/m_e \approx 96$ *at* $\hat{t} \approx 13,000$. Ion and neutral mass flow rates are nearly equal; the curves are on top of each other. Levels shown are 100 time-step averages. Capacitance has been increased by factor of 10 to limit oscillations. *Steady state electron injection used.*

Theoretical Wall Potential and Mass Ratio

The wall potential may be estimated using conventional sheath theory. A sheath is expected to form around a floating conductor placed in the middle of a uniform plasma. The conductor as a whole should acquire a negative net charge, and hence have a negative surface potential with respect to the ambient plasma potential. This potential is derived below.

Let ϕ_s be the plasma potential at the edge of the sheath, ϕ_w be the potential at the wall, and $\Delta\phi = \phi - \phi_s$ be the potential difference somewhere in between. Let n_s be the quasineutral plasma density at the sheath edge. If the electrons are Maxwellian, then the electron density between the sheath edge and the wall is determined by the Boltzmann relation,

$$n(x) = n_s e^{e\Delta\phi/KT}. \tag{4.13}$$

Let ions enter the sheath region at $T_i = 0$ but with some bulk velocity $v_{i,o}$. They gain energy from the potential difference according to

$$v_i(x)^2 = v_{i,o}^2 + \frac{2e\Delta\phi}{M_i}. \tag{4.14}$$

By continuity, $\Gamma_i = n_s v_{i,o} = n_i(x)v_i(x)$. Poisson's equation inside the sheath is therefore written

$$\epsilon_o \frac{d^2\phi}{dx^2} = e(n_e - n_i) = en_s[e^{e\Delta\phi/KT} - (1 - \frac{2e\Delta\phi}{mv_{i,o}^2})^{-1/2}]. \tag{4.15}$$

This is the well known nonlinear equation of a plane sheath, which has an admissible solution only if $M^2 > 1$, where $M = v_{i,o}/V_a$ is the mach number of the ions entering the sheath region. This means that ions must enter the sheath region with a velocity greater than or equal to the acoustic speed, $V_a = \sqrt{KT_e/M}$ [6]. In turn, this requires a pre-sheath of some sort.

The thickness of the sheath can be estimated. The sheath (not including the pre-sheath) is on the scale of λ_D. There is also a region essentially free of electrons next to the wall. The thickness of this region may be estimated with the Child-Langmuir Law [6].

Now, let n_s be the ion density where $M = 1$. Furthermore, assume quasineutrality in the pre-sheath ($n_e \approx n_i$). Continuity says the ion flux $\Gamma_i(x)$ is constant inside the sheath.

Thus, the ion flux into the wall is the flux into the sheath;

$$\Gamma_i = n_s V_a = n_s \sqrt{KT/M_i}. \tag{4.16}$$

Assuming the electrons are Maxwellian, the electron flux at the wall is

$$\Gamma_e = \frac{n_s \bar{c_e}}{4} e^{e\Delta\phi/KT} \tag{4.17}$$

where $\bar{c_e} = \sqrt{8KT/\pi m_e}$. Here, $\Delta\phi = \phi_w - \phi_s$, where ϕ_s is the plasma potential at the sheath edge and ϕ_w is the floating wall potential. In a steady state, the electron flux to the wall $\Gamma_e = \Gamma_i$. Thus we may write

$$\Delta\phi = \phi_w - \phi_s = \frac{KT}{e} ln \sqrt{2\pi m_e/M_i}. \tag{4.18}$$

If the ambient potential $\phi_s = 0$, then $\phi_w < 0$, as expected.

In this classical formulation, Γ_i is a function only of the electron temperature. If the plasma temperature remains constant, then Γ_i (and consequently Γ_e) should change only in proportion to $\sqrt{1/M_n}$. Since Γ_i is not a function of ϕ_w, ion flux to the wall should occur at the correct physical rate regardless of the wall potential. The wall potential ϕ_w will change to ensure $\Gamma_i = \Gamma_e$, but this should not greatly affect the plasma properties beyond the sheath, except that sheath thickness does increase as $\lambda_D (e\Delta\phi/kT_e)^{3/4}$, as follows from Child-Langmuir.

The theoretical value of ϕ_w as a function of mass ratio M/m is plotted in Figure 4-14 for $T = 10eV$ with $\phi_s = \phi_a = 80eV$, which are values obtained by fitting the curve to the numerical data points. (These values are consistent with a visual inspection of particle moments near the point of nozzle divergence.) The potential increases as the ratio M/m decreases. The slope is a function of the electron temperature. The function moves left or right depending on the ambient potential, but nowhere exceeds the ambient potential. Also plotted in Figure 4-14 are data points from the simulation for various mass ratios, where the steady state electron injection method was used. Following the curve to the real mass ratio, a wall potential of about 10 Volts is predicted.

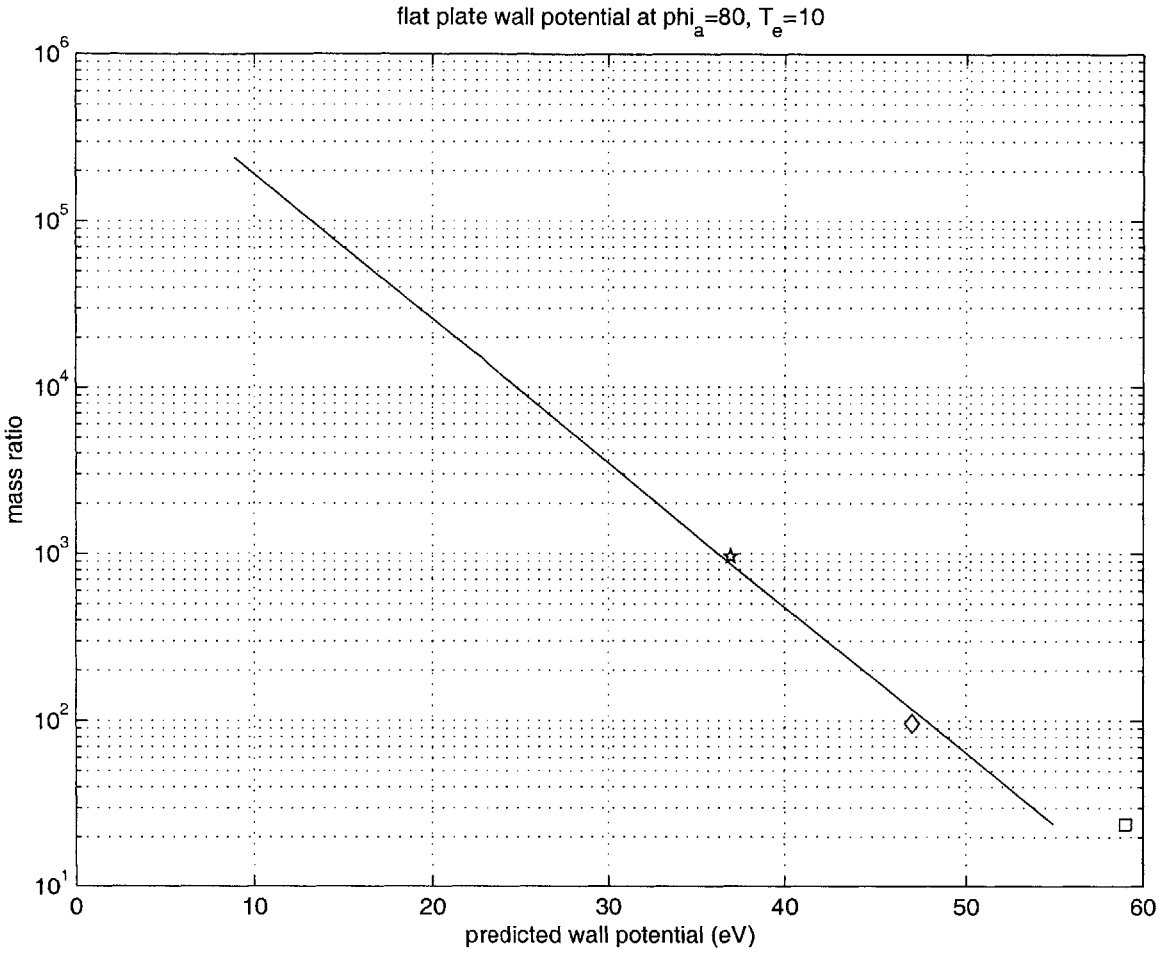

Figure 4-14: *Wall potential assuming steady state electron injection method.* The predicted wall potential when the ambient plasma potential is 80 eV and the temperature is 10 eV. These values were obtained by fitting the curve to the numerical data points. With the very heavy real ion mass (mass ratio $M/m = 239,000$), the wall becomes very negative (over 70 eV) with respect to the plasma in order to stop most electrons, since ion arrivals are infrequent. As ion mass increases, smaller potential differences are required. Numerical operating points are marked with a square and diamond.

Numerical Wall Potential and Mass Ratio

The theoretical solution does not fit the numerically observed data points exactly. As neutral mass is decreased, the wall potential should increase. This is observed, but not at the rate expected if ambient plasma properties are constant. Examination of particle moments shows that the plasma density changes, but even so, the wall potential is not supposed to be a function of the density. What is going on?

One cause seems obvious: The steady state electron injection method is invalid. The simulation region is starved for electrons. This explains why the ambient potential to fit the curve is 80 V when the free space boundary so close to parts of the floating wall is at ≈ 0 V.

Of course, some variation from theory is expected, even with correct boundary conditions. The thruster is not a flat plate.

A more subtle error source may be the artificial permittivity. The preceding theory assumes that sheaths are small. They form as a result of the processes inside the plasma, but they interact with the primary discharge only on the periphery. However, the free space permittivity was altered to speed up the simulation. Increasing ϵ_o by γ^2 increases sheath thicknesses by a factor of $\gamma = \sqrt{\epsilon_o'/\epsilon_o}$. With $\gamma = 10$, the sheath at the wall (which is several λ_D) begins extending into the plume. The magnitude of the potential drop across the sheath may too strongly influence the discharge. This effect can be quantified somewhat through parametric tests of the artificial permittivity.

Particle Count

The statistical accuracy of the simulation is expected to increase according to the square root of particle count per cell. Ideally, we want thousands of super-particles per cell, resulting in millions of super-particles total. This is numerically infeasible; to produce results in a matter of a few days, we can run the simulation with just 20 thousand particles and time average the results to produce smooth curves. Such results have just been presented. But do we have enough super-particles to trust the results? To find out, we doubled the number of super-particles and compared the results.

Figure 4-15 shows that time averaged performance does not change much, if at all, when particle count is doubled. This figure may be compared with the left portions of Figure 4-13.

The time averaged wall potential appears to decrease by a little over a volt ($\phi \approx 58.4$). The noise in the simulation is reduced, which means that some of the high frequency fluctuations we see are just numerical.

Permittivity

Since the steady state method of electron injection fails to satisfy the criteria outlined in the previously described thought experiment, little value is gained from testing the permittivity assumption under these conditions. The artificial permittivity assumption is instead tested with the quasineutral method of electron injection.

Summary of "Steady State" Results

Tests obtained using the steady state method of electron injection at the free space boundary showed that particle counts of $\approx 25K$ and $\approx 50K$ (with $\gamma = 10$) produced similar results. Furthermore, variation of the wall potential with mass ratio was largely explainable. However, performance predictions in an absolute sense were invalidated when wall capacitance was found to have undue influence. The boundary conditions had to be re-formulated.

4.3.4 Validation Tests with Quasineutral Method of Electron Injection

The quasineutral method of cathode electron injection along the free space boundary produced results more consistent with experiment. Table 4.4 lists some of the parametric validation tests performed using this method. All of the tests listed assumed Monte Carlo Coulomb collisions. This assumption will be re-examined in the next Chapter. All solutions compared in this section assume $\dot{m} = .1mg/s$, a nominal temperature of $[T_e] = 50eV$ and an anode potential of 300V.

The wall potential for the first, third, and fourth cases in Table 4.4 is plotted against the theoretical temperature in Figure 4-16. The wall potential plot differs strongly from that shown in Figure 4-14, which assumed $I_c = I_d$. In the earlier case, the simulation region was "starved" for electrons, resulting is a wall which floated artificially high. Here, the wall floats near 0 V and variation is almost logarithmically linear. The curve was fit by inspection.

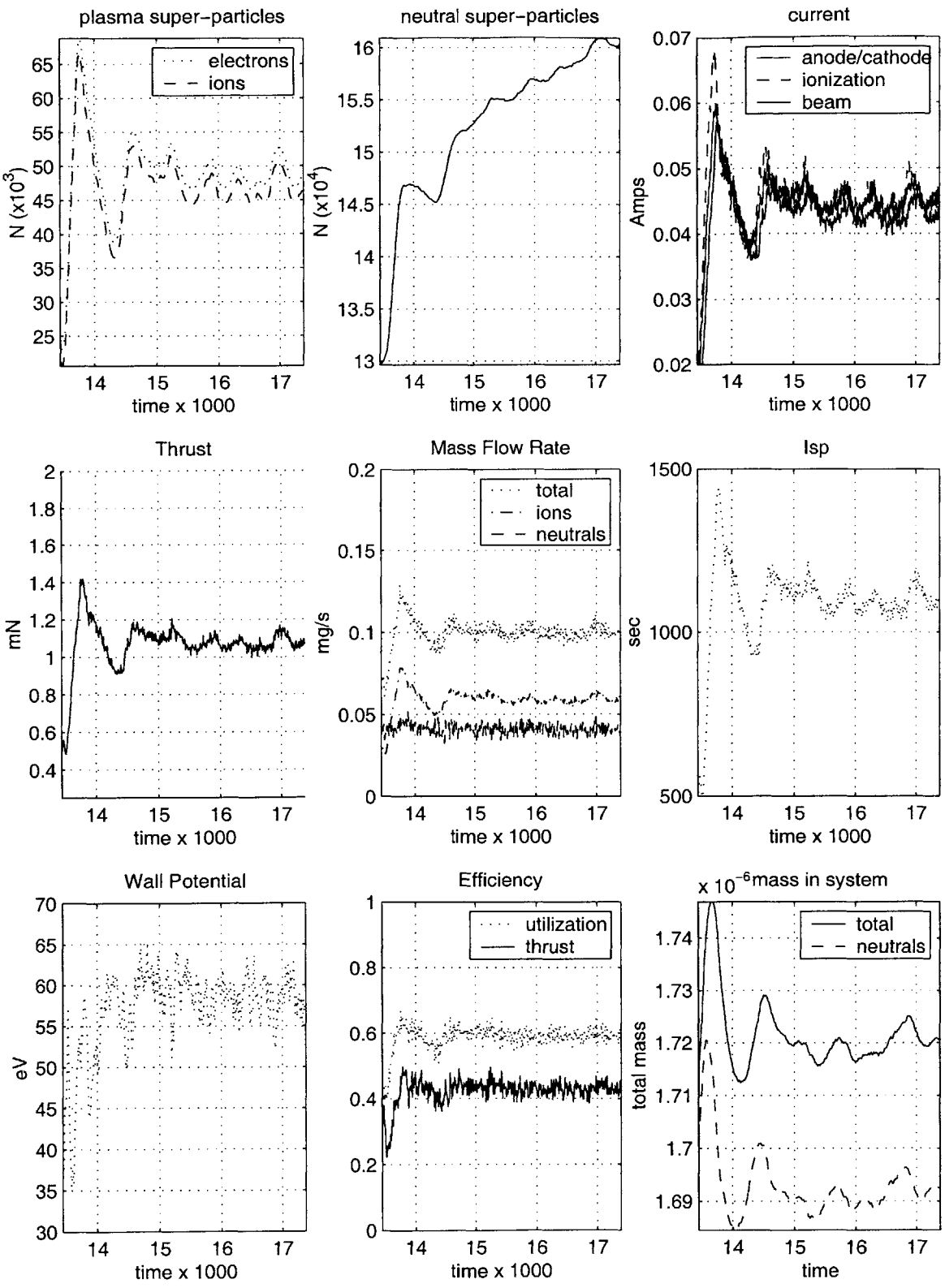

Figure 4-15: *Performance predictions for $M_n/m_e \approx 24$ with approximately 50K plasma particles.* Particle size was halved at $\hat{t} \approx 13,000$, allowing twice as many plasma particles to accumulate. Levels shown are 100 time-step averages. *Steady state electron injection used.*

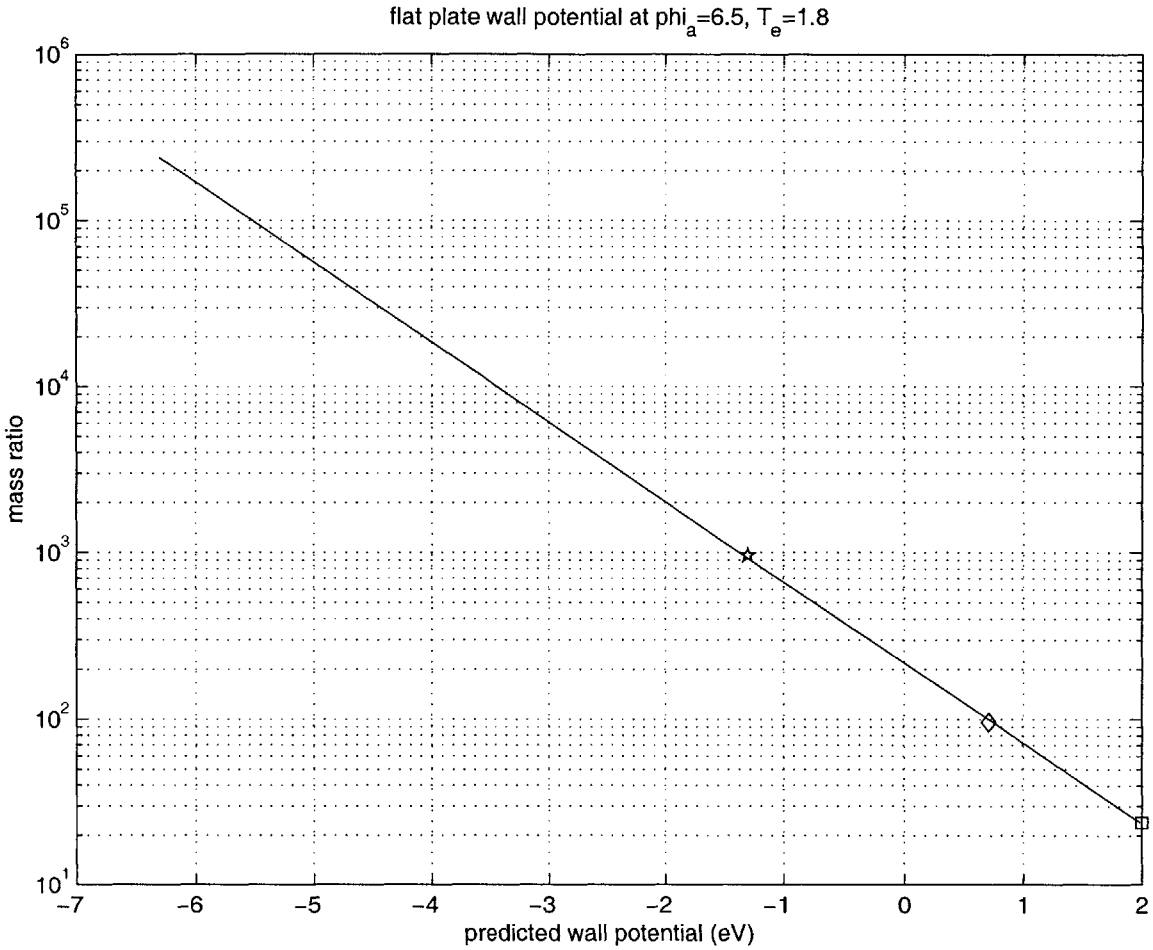

Figure 4-16: *Wall potential assuming quasineutral electron injection.* Numerical and predicted wall potential vs. mass ratio ($< \phi_w >$ vs. M/m) with $\gamma = 10$, MCC Coulomb collisions, Capacitance and boundary conditions held constant. Numerically observed operating points are marked individually with a star, a square, and a diamond. The slope and intercept of the theoretical curve were determined by fitting the line to the numerical data points (by inspection). Numerical data points are spaced linearly in log space as predicted by theory.

Topic	M/m	γ	ϕ_{rhs}	C	$< \phi_w >$	Figure
Boundary Conditions	24	10	$\phi = 0$	$1 \times 10^{-10} F$	$\approx .5$ V	4-18
Capacitance	24	10	$E_z = 0$	$1 \times 10^{-10} F$	≈ 2 V	4-19
Capacitance	24	10	$E_z = 0$	$2 \times 10^{-11} F$	≈ 2 V	4-20
Mass Ratio	96	10	$E_z = 0$	$1 \times 10^{-10} F$	$\approx .7$ V	4-21
Mass Ratio	960	10	$E_z = 0$	$1 \times 10^{-10} F$	$\approx$ -1.3 V	4-22
Permittivity	96	5	$E_z = 0$	$1 \times 10^{-10} F$	≈ 2 V	4-23
Permittivity	960	5	$E_z = 0$	$1 \times 10^{-10} F$	$\approx X$ V	N/A

Table 4.4: Parametric tests used to validate final version of simulation. Quasineutral boundary conditions are assumed. Changing wall capacitance made vary little difference in wall potential or overall performance. Effects due to mass ratio and permittivity were more marked. The last test was not performed due to computational limitations.

Parametric Test of Permittivity

For numerical reason, the free space permittivity constant was increased by a factor of γ^2. This decreased the plasma frequency by a factor of $1/\gamma$ and increased the Debye length by a factor of γ We argued that the performance would not change much. This assumption is tested parametrically. If we can show that the solutions for $\epsilon_o = 8.854e-10\,F/m$ ($\gamma = 10$) and $\epsilon_o = 2.21e-10\,F/m$ ($\gamma = 5$) are very similar, then, by induction, they should also be very similar to the solution for $\epsilon_o = 8.854e-12\,F/m$, which is the physical permittivity.

The first solution of interest is that already presented for $M_n/m_e \approx 96$ with $\gamma = 10$ (Figure 4-21). The second solution of interest is that already presented for $M_n/m_e \approx 960$ with $\gamma = 10$ (Figure 4-22). The new solution assumes $M_n/m_e \approx 96$, but uses $\gamma = 5$ (Figure 4-23). To generate this solution, the simulation was started anew assuming neutrals only and then uniformly seeded with 5000 plasma particles of each species. Because $\gamma = 5$, the nominal plasma frequency and Debye length change by a factor of 2 with respect to simulations conducted with $\gamma = 10$. Particle moments show less charge inequality. Even so, sheaths are still a factor of $\gamma = 5$ too large.

A comparison between Figures 4-23 and 4-21 (both $M/m = 96$) is discouraging. Performance seems to change too much. More encouraging is the comparison between Figures 4-23 ($M/m = 96, \gamma = 5$) and 4-22 ($M/m = 960, \gamma = 10$). These are the two most physical cases simulated. Neither solution is completely converged simply because the simulations are very slow. However, these figures show similar performance. Thus, there is a convergence of solutions when the numerical assumptions are made more physical. Furthermore, the trend is toward Khayms experimental performance measurements. We compare numerical

and experimental measurements more in Chapter 5.

Unfortunately, the more physical solutions are computationally cumbersome. The simulation which assumes $M_n/m_e = 96$ and $\gamma = 5$ takes over a week to converge! There are two main reasons for this. The primary reason the $\gamma = 5$ solution is so slow is that the grid must be refined to include four times as many mesh points as it contains when $\gamma = 10$. This means the Poisson solver runs four times slower. This also means four times as many plasma particles are required to maintain the same level of statistics per grid cell. To save CPU time, only twice as many particles were used in the $\gamma = 5$ case. In Section 4.3.3, we showed that this should not change the predicted performance much. Unfortunately, this change is not enough to make the simulation converge in less than a week. The secondary reason the simulation takes so long to converge is time-step. With $\gamma = 10$, the time-step is (usually) driven by the need to resolve gyro motions everywhere. Hence, it is the same almost every iteration. However, when $\gamma = 5$, the time-step is often determined by the Δt criteria for resolving the plasma frequency and/or minimizing numerical heating. It is on average shorter, and it usually varies from iteration to iteration. The number of time-steps required to reach a converged solution increases, by an additional factor of ≈ 1.5.

Why does the performance change with γ? The simple answer is the particle distribution in space is different. When $\gamma = 10$, there is far more charge separation than with $\gamma = 5$. As long as charge separation is local, then oscillations should average out such that time averaged densities are the same. But this does not happen near the anode because there is an applied potential difference, a component of which is along $\vec{B}$. If $\gamma = 10$, the electrons tend to bunch up near the anode; the field resulting from charge separation is not enough to hold the electrons where the ions are. Naturally, the potential gradient across the anode layer is affected by the charge density. If there are more ions in the middle of the discharge than electrons, the potential there is higher than it would be if the plasma were neutral. Ions produced there would be accelerated to greater energies and the performance would increase. Of course, the full answer is far more complicated.

4.3.5 Charge Imbalance and the Plasma Approximation

In our simulation we solve Poisson's equation, inherently assuming that $n_e \neq n_i$. However, in a plasma, it is often possible to assume $n_e = n_i$ ("quasineutrality") and $\vec{\nabla} \cdot E \neq 0$ at the same time. This is called the "plasma approximation" and is used in deriving the fluid

equation of motion [6]. How close to quasineutrality should our simulation come? Let's look at a 1-D version of Poisson's equation,

$$\frac{\partial^2 \phi}{\partial x^2} = \frac{ne}{\epsilon_o}. \tag{4.19}$$

In 1 dimension,

$$\frac{dE_x}{dx} = \frac{-ne}{\epsilon_o} \tag{4.20}$$

and

$$E_x \approx \frac{-ne}{\epsilon_o}(x - x_o). \tag{4.21}$$

A simple way to derive the Debye length is to equate the work (the energy) required for a particle to go a distance x ,

$$W = \int_0^d E_x e dx = \frac{-ne^2}{\epsilon_o}\frac{d^2}{2}, \tag{4.22}$$

with the internal energy of the plasma $W = \frac{1}{2}KT$. This is an easy way to derive the Debye length, $d = \lambda_D = \sqrt{\epsilon_o KT/ne^2}$. But now imagine there is an external energy source in the form of a potential difference $\Delta\Phi$, and imagine that this potential difference drops off in a scale length comparable to the Debye length. We see such a situation in the near-anode region of the mini-TAL when we modify ϵ_o. Let us call the resulting characteristic length the anode length, λ_a. If $W = \Delta\Phi$, then $d = \lambda_a = \sqrt{\epsilon_o 2\Delta\Phi/ne^2}$ such that $\lambda_a/\lambda_D = \sqrt{2\Delta\Phi/T_e v}$. What this means is that in the presence of a strong externally imposed potential (e.g $\Delta\Phi > T_{ev}$), a significant charge imbalance on the scale of n_e can exist in a region of the scale length λ_a. In the near anode region of our thruster, the external potential difference across a few λ_D is ≈ 100 V. Thus, we may see a charge imbalance of $\approx en_e$ on the scale of several λ_D. The gradient $d\Phi/dx$ is determined, in the absence of charge inequalities, by the external geometry. If we assume λ_a is fixed, then the allowed charge density, $q = e(n_i - n_e)$, is proportional to ϵ_o.

In our simulation, we sometimes use an ϵ_o which is 100 times larger than the physical value. In this case, the anode supported charge inequality is 100 times too large! Because ϵ_o is so large, the internal potential differences created by the charge imbalance are not great enough to produce quasineutrality on a scale comparable to the anode exit. When a physical ϵ_o is used, then the anode potential and internal temperature should support much

smaller charge imbalances. Thus, if γ is small (but > 1), the artificial ϵ_o can be viewed as exaggerating the existing features of the plasma. If γ becomes too large, the particle moments change too much to give a reasonable picture of the plasma.

4.3.6 Grid Density

The grid should be fine enough to resolve a Debye length. To test this assumption, we simply analyze the final (or time averaged) moments of the electron (or ion) distribution. For each cell, we let $\delta \approx \sqrt{(\delta z)^2 + (\delta r)^2}$, where $(\delta z)^2 = (\partial z/\partial \xi)^2 + (\partial z/\partial \eta)^2$ and $(\delta r)^2 = (\partial r/\partial \xi)^2 + (\partial r/\partial \eta)^2$. We divide the normalized, local Debye length by δ to determine whether we have enough resolution, R, defined by

$$R = \frac{\lambda_D}{\delta}. \tag{4.23}$$

Instantaneous electron particle moments with $\gamma = 10$ show a resolution as low as $R = .64$ near the axis close to the exit plane. However, outside of the "mach cone" near the axis, the resolution is much better, generally greater than $R = .8$. Along the axes, the resolution will be on the order of one. That is, since $\delta \approx \sqrt{2}\delta_z$, we see that

$$R_z = \frac{\lambda_D}{\delta_z} \approx 1, \tag{4.24}$$

even near the axis. It would not hurt, however, to use a finer grid.

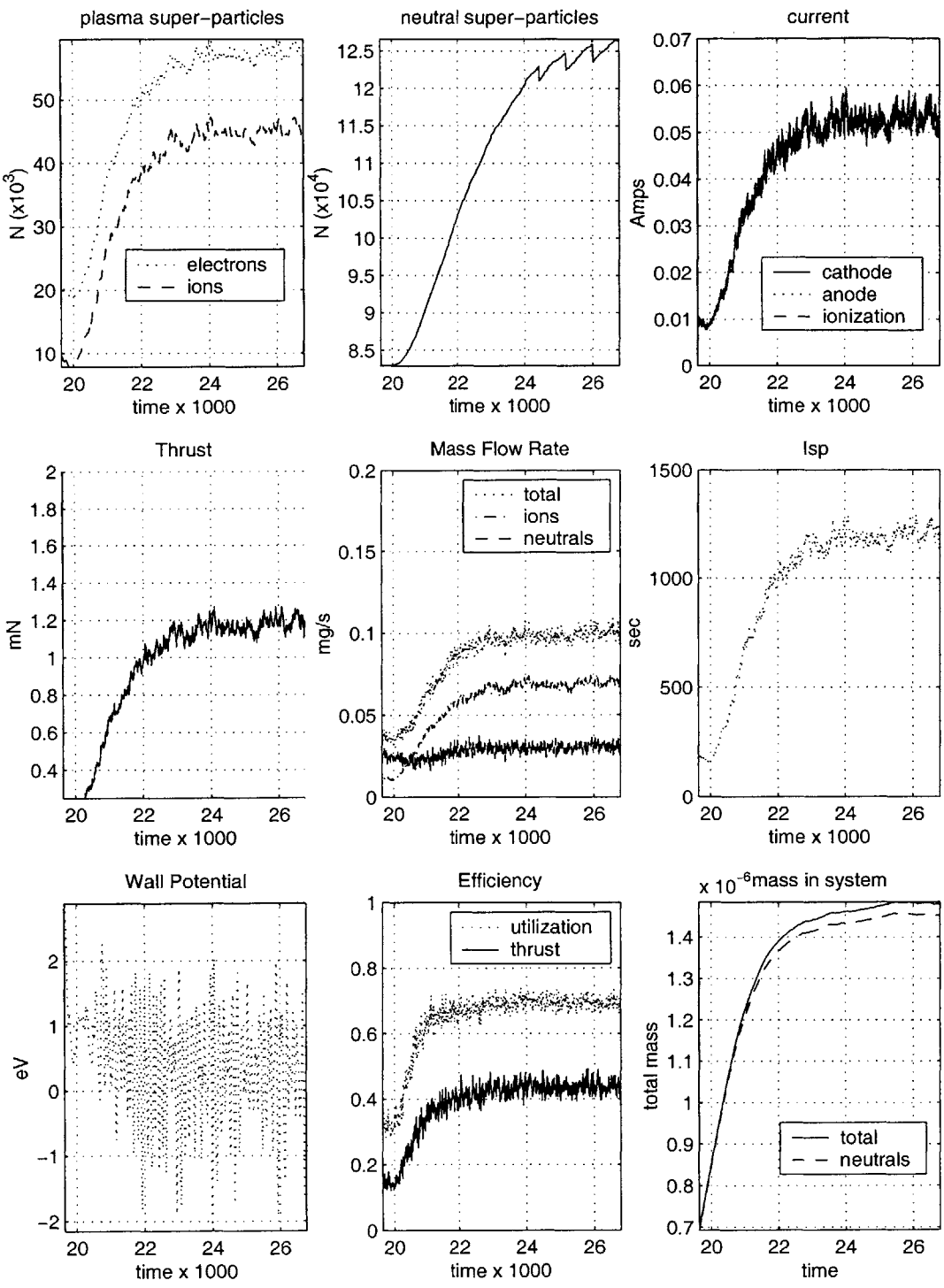

Figure 4-17: *Electron injection test.* Performance for $\gamma = 10$, $M/m \approx 24$, $s_o = 50$, $C = 1 \times 10^{-10}$. Quasineutral cathode electron injection assumed. MCC Coulomb collisions only. $\phi = 0$ *at RHS.* This solution precedes those in Figures 4-20,4-19, and 4-18. *Test assumes linear drop in* ϕ *from* ϕ_w *to* 0 *V on upper right boundary.*

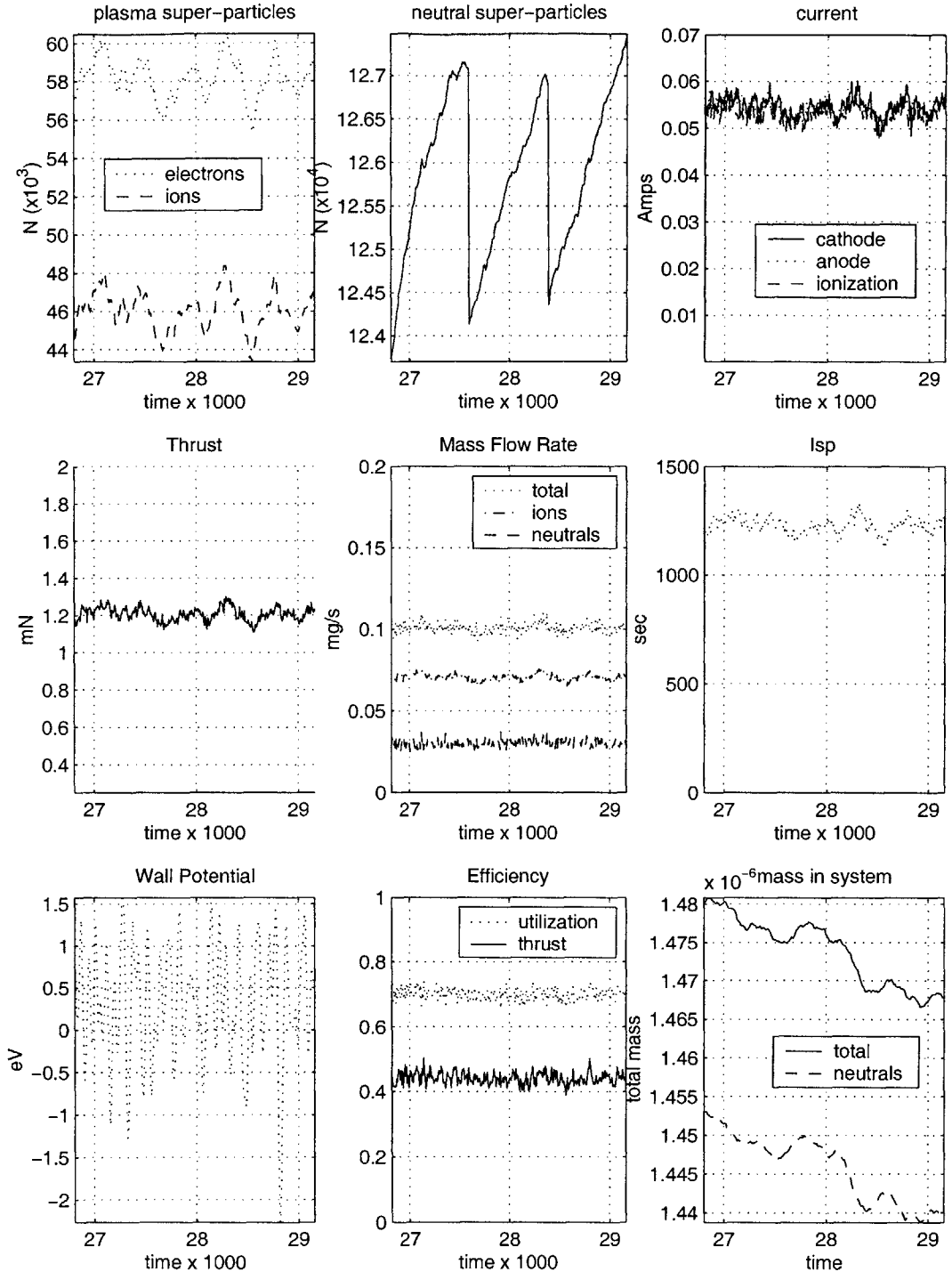

Figure 4-18: *Boundary condition test.* Performance for $\gamma = 10$, $M/m \approx 24$, $s_o = 50$, $C = 1 \times 10^{-10}$. Quasineutral cathode electron injection assumed. MCC Coulomb collisions only. Starts from the solution shown in Figure 4-17. $\phi = 0$ *at RHS. Sheath calculated explicitly on upper right boundary.*

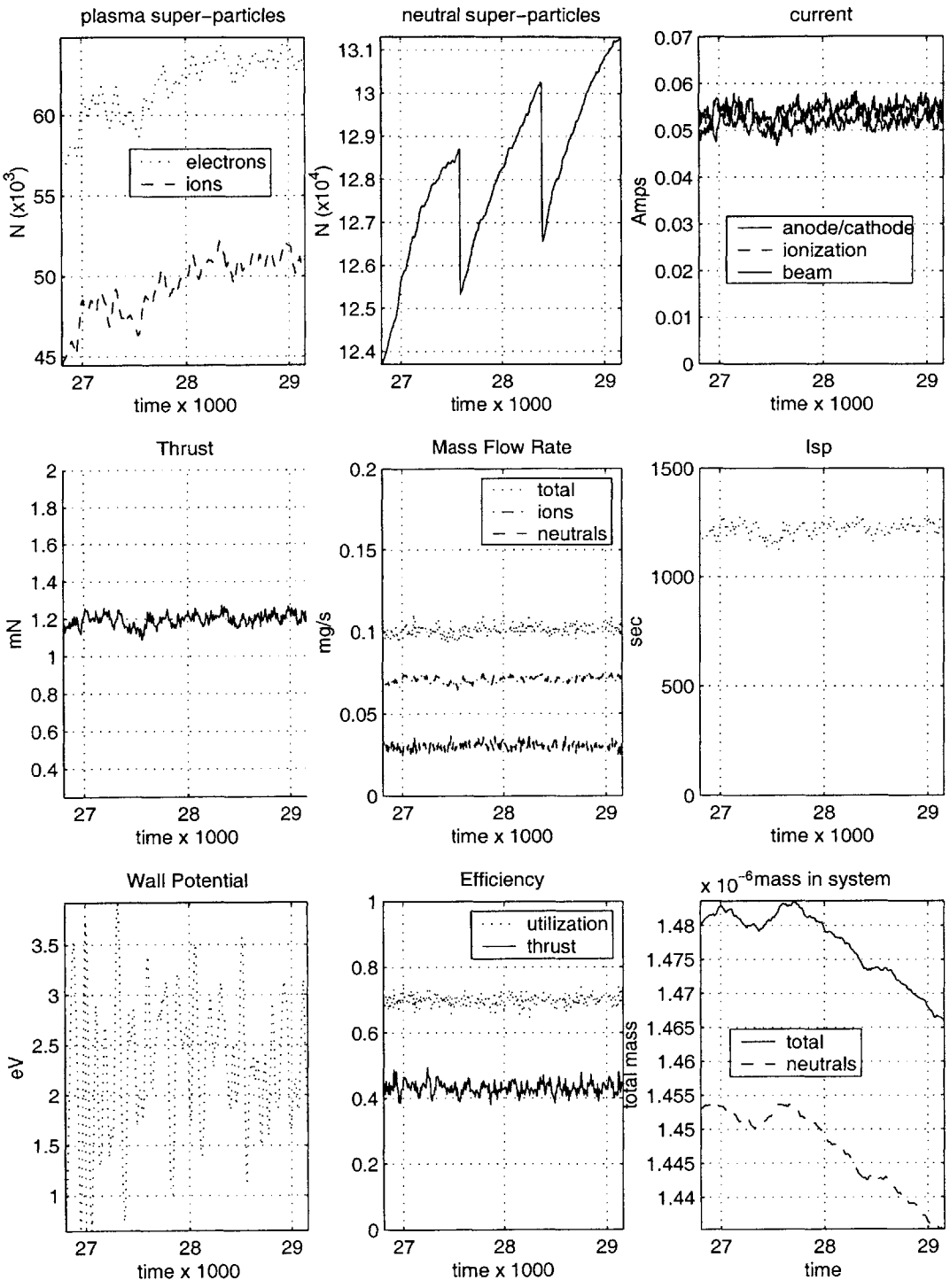

Figure 4-19: *Boundary condition test.* Performance for $\gamma = 10$, $M/m \approx 24$, $s_o = 50$, $C = 1 \times 10^{-10}$. Quasineutral cathode electron injection assumed. MCC Coulomb collisions only.. Starts from the solution shown in Figure 4-17. $E_z = 0$ *at RHS. Sheath calculated explicitly on upper right boundary.*

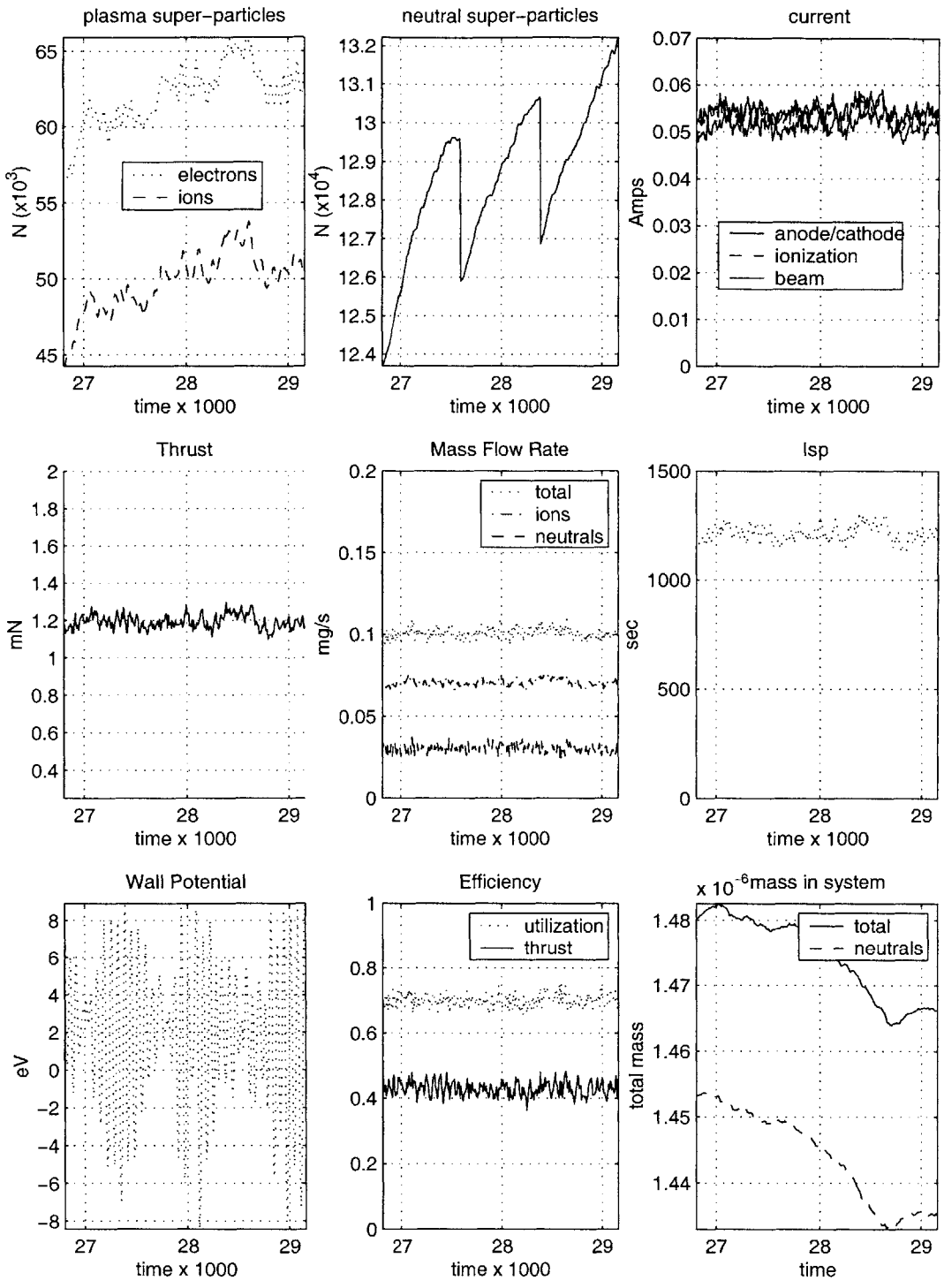

Figure 4-20: *Capacitance test.* Performance for $\gamma = 10$, $M/m \approx 24$, $s_o = 50$, $C = 2 \times 10^{-11}$. Quasineutral cathode electron injection assumed. MCC Coulomb collisions only. Starts from the solution shown in Figure 4-17. $E_z = 0$ *at RHS. Sheath calculated explicitly on upper right boundary.*

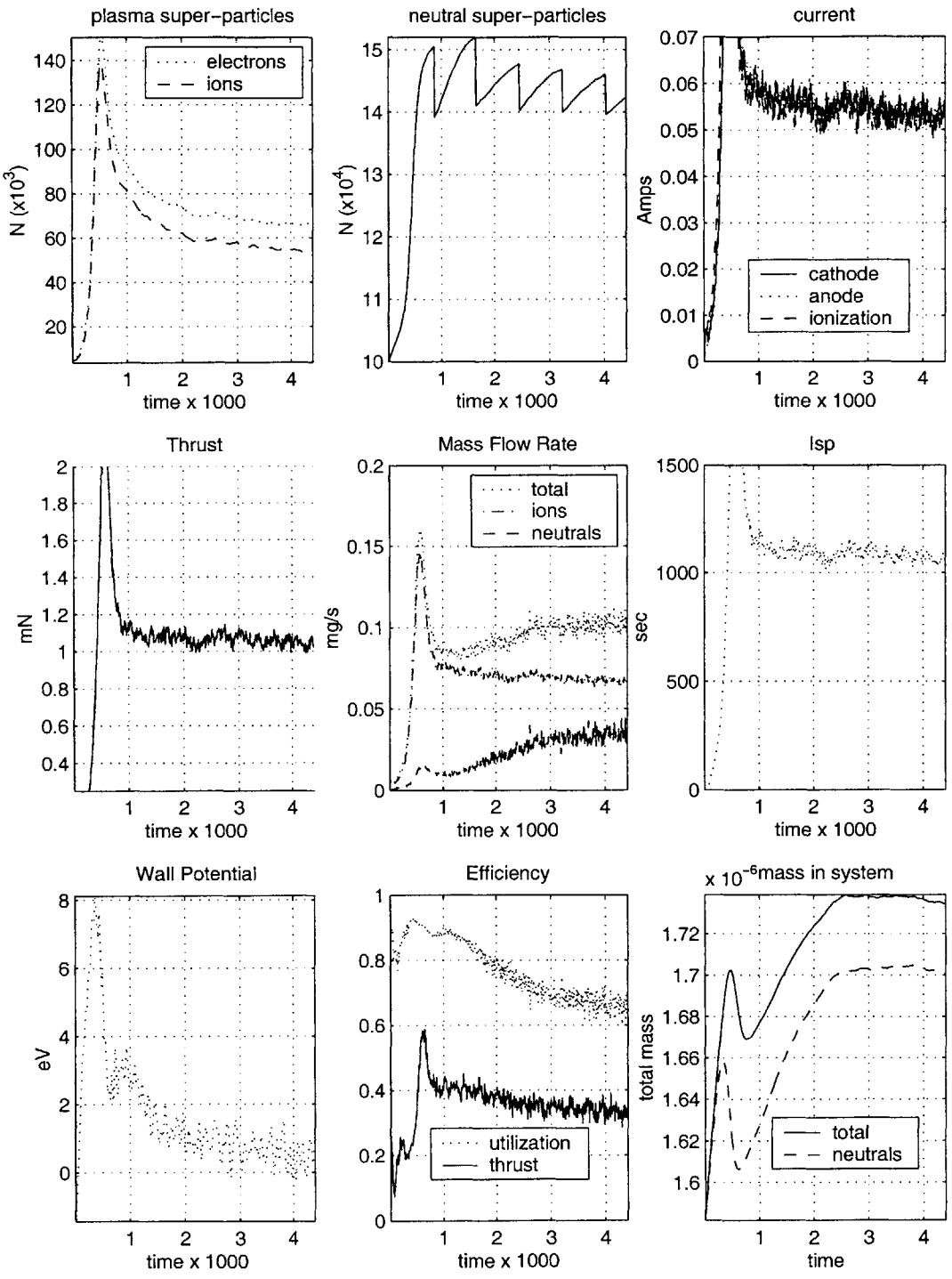

Figure 4-21: *Mass ratio test.* Performance for $M/m \approx 96$, $\gamma = 10$, $s_o = 50$, $C = 1 \times 10^{-10}$. Quasineutral cathode electron injection assumed. MCC Coulomb collisions only. $E_z = 0$ at RHS. Sheath calculated explicitly on upper right boundary.

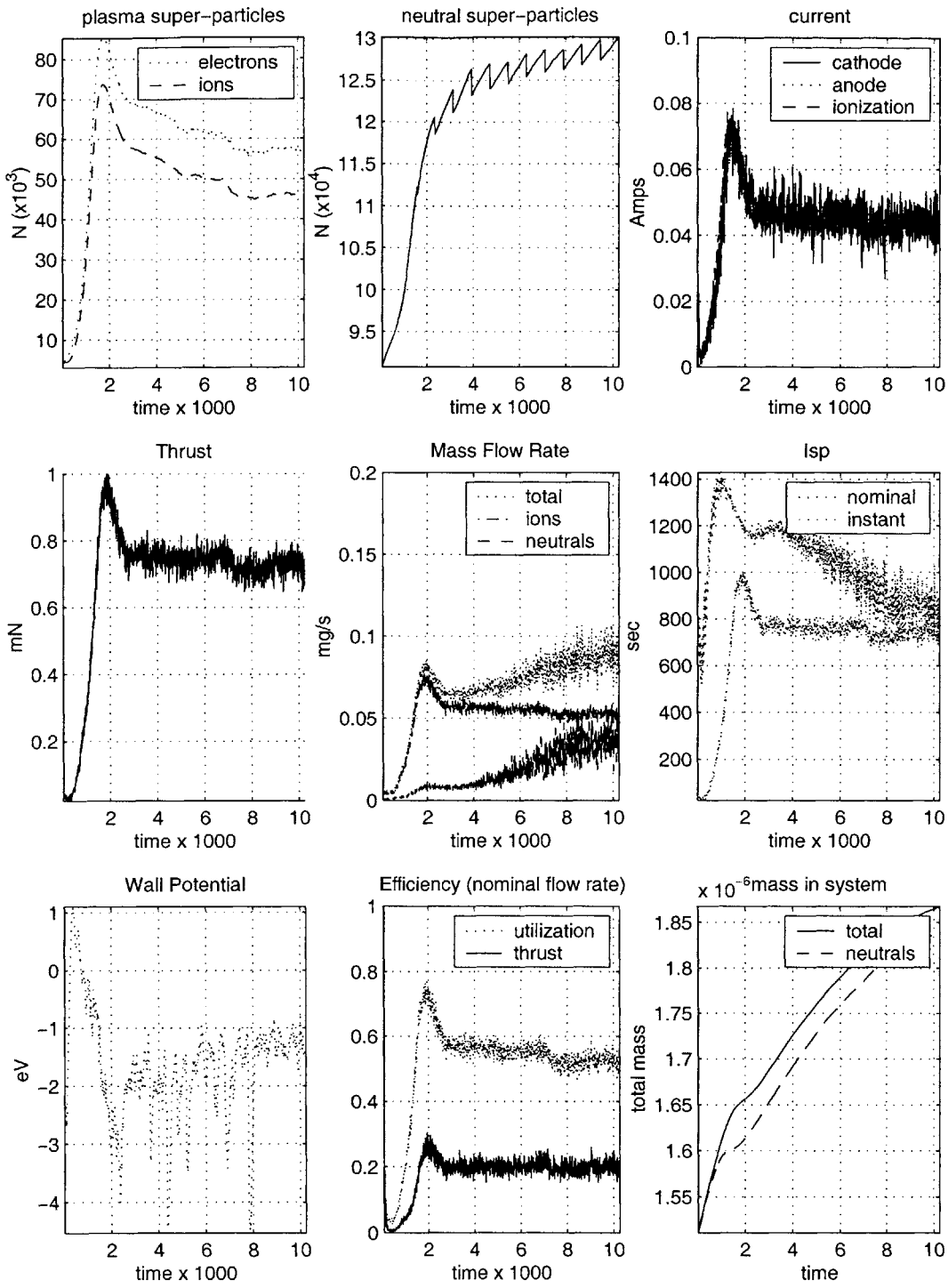

Figure 4-22: *Mass ratio test.* Performance for $M/m \approx 960$, $\gamma = 10$, $s_o = 50$, $C = 1 \times 10^{-10}$. Quasineutral cathode electron injection assumed. MCC Coulomb collisions only. $E_z = 0$ at RHS. Sheath calculated explicitly on upper right boundary. Solution is not fully converged. This graph differs from the others presented in this chapter in that the middle right plot also shows the instantaneous I_{sp} (the upper curve) which based on mass flow through free space boundary. Unlike other plots in this chapter (but like all plots in the next), efficiencies η_u and η_t are based on nominal mass flow rate, not instantaneous flow rate at the right hand boundary.

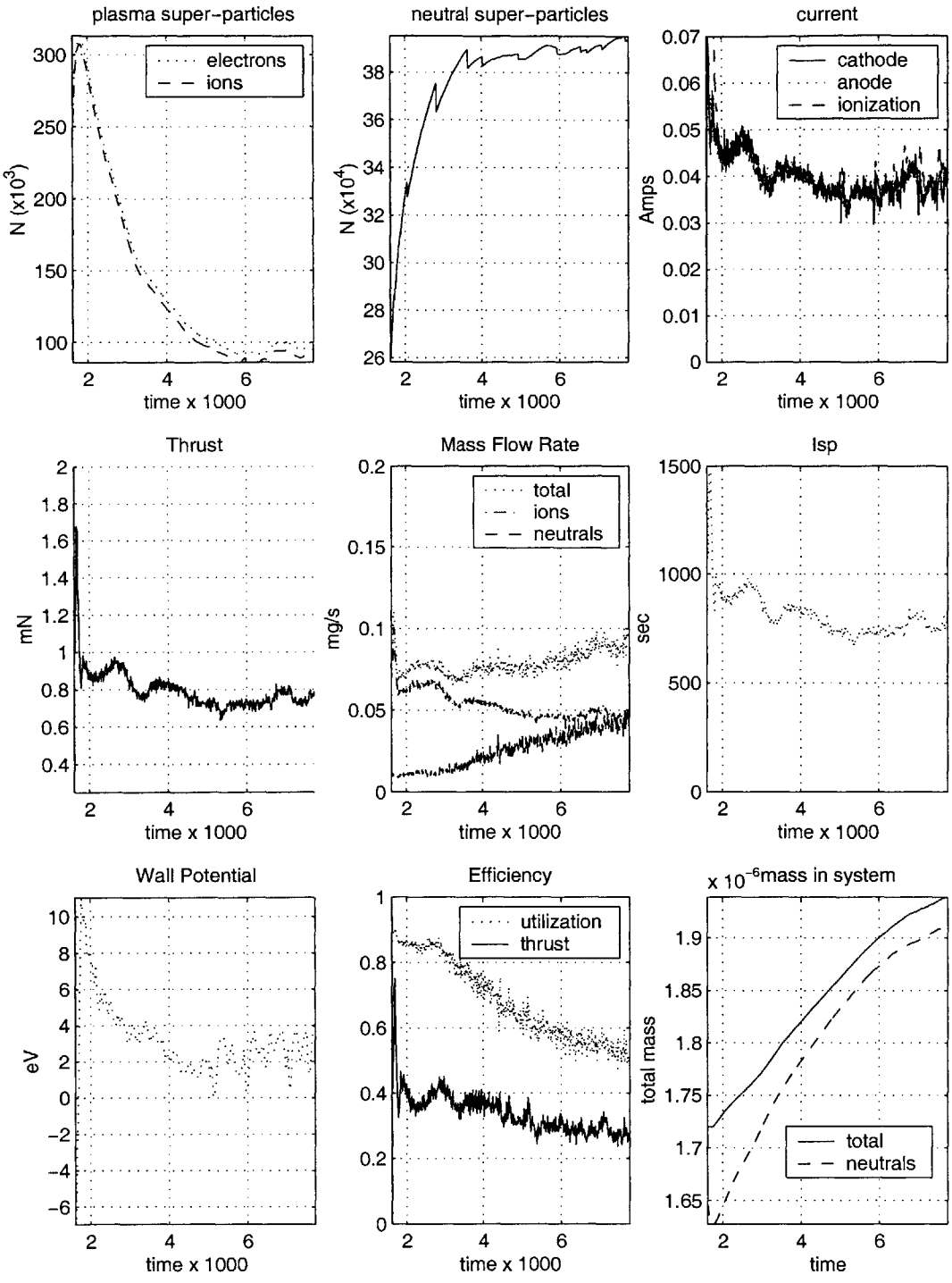

Figure 4-23: *Permittivity Test.* Performance for $\gamma = 5$, $M/m = 96$, $s_o = 50$, $C = 1 \times 10^{-10}$. Particle count doubled. Quasineutral cathode electron injection assumed. MCC Coulomb collisions only. $E_z = 0$ at RHS. Sheath calculated explicitly on upper right boundary. Results show performance similar to shown in Figure 4-22. Solution is not fully converged.

Chapter 5

Results and Discussion

This thesis describes the numerical simulation of a 50 Watt Hall thruster. The final version of the code assumes $E_z = 0$ at the right hand free space boundary and that cathode electrons are injected at the rate required to preserve quasi-neutrality. It includes electron-neutral elastic scattering, exciting, and ionizing collisions, as well as ion-neutral charge exchange and scattering collisions, all of which are implemented through Monte Carlo schemes. The code also includes electron-electron and electron-ion Coulomb collisions, which were implemented through both a Monte Carlo scheme and a diffusive scheme rooted in the Fokker-Planck equation. Numerical artifices employed to speed up the simulation include super-particles, artificial mass ratios, and an artificial free space permittivity constant. Collision cross sections are changed to preserve internal scales across artificial mass ratios. Because the simulation is non-linear, these numerical artifices are visible in particle moments such as n_e and T_e. However, parametric tests showed performance differences which are small.

This 2D-3V, fully kinetic, electron time-scale simulation can be used to predict the overall performance of the mini-TAL. However, 2D hybrid-PIC models, 1-D models, and even analytic models can also predict performance. The real strength of our simulation method is that it is fundamentally kinetic. This enables direct studies of the following:

- The electron energy distribution function.
- Plasma oscillations.
- Electron transport.

- Coulomb collisions.

Results pertaining to each of these areas will be discussed.

5.1 Normalization Constants

To predict the performance of the mini-TAL, the most physical cases allowable given computational constraints (see Section 2.7) are used. These are ($M_n/m_e \approx 96$, $\gamma = 5$) and ($M_n/m_e \approx 960$, $\gamma = 10$). Normalization constants for these cases (and all cases) are calculated at the beginning of each run. The following is an edited data stream from the ($M_n/m_e \approx 96$, $\gamma = 5$) case. Some quantities appear twice, once in CGS units, and once in normalized units.

```
Running PIC.C, Version 1.0, 2000
Anode Potential: 300-V
Tev (nominal) of neutrals: 0.1-eV
Tev (nominal) of electrons: 50-eV
neutral velocity to right: 0.00205725-X/T (Debye lengths/w_pe^-1)
nominal ion acoustic speed: 3.03044e+007-cm/s (assumes artificial mass)
nominal ion acoustic speed: 0.10219-X/T
nominal electron thermal velocity: 4.19309e+008-cm/sec
nominal electron thermal velocity: 1.41395-X/T
Nominal neutral density:  5.27464e+014 cm^-3
Nominal plasma density:  6.77565e+012 cm^-3
Nominal Debye length: 0.0100972 cm
Nominal plasma frequency: 2.93695e+010 sec^-1
Nominal gyro frequency: 1.40706e+011 rad/sec
Nominal gyro frequency: 4.79091 rad/T
Nominal gyro radius: 0.00298003 cm
Units of charge:  1 Q = 4.8032e-010 emu
Units of mass:  1 M = 9.1094e-028 gm
Units of distance:  1 X = 0.0100972 cm
Units of time:  1 T = 3.4049e-011 sec
Units of velocity:  1 V = 2.9655e+008 cm/sec
Units of B-field:  1 B = 1669.83 gauss
Units of E-field:  1 E = 16.5062 statvolts/cm (statcoul/cm^2)
Units of Potential: 1 Phi = 0.166667 statvolts = 50 volts
```

A more extensive data stream is found in the Appendix.

Numerical notes: The nominal magnetic field strength used to create the data stream is near the center pole; it is much higher here than elsewhere. Also, the acoustic speed appears high because ions are only about 100 times more massive than electrons.

5.2 Thruster Performance

Numerical and experimental performance can be compared. Khayms tested the mini-TAL at mass flow rates of $.1005mg/s$, .1676 mg/s, and .2146 mg/s. The code was validated at a mass flow rate of $.1mg/s$. This is close enough to $.1005mg/s$ that the results may be compared directly. The second flow rate, .1676 mg/s, was also simulated exactly. The third flow rate was not simulated. *Unless otherwise noted, all tests described in this chapter assume that* $\dot{m} = .1mg/s$.

Many thruster performance variables are computed and saved at each time-step. Chapter 4 showed a convergence of these variables toward the solutions shown in Figures 4-23 ($M/m \approx 96, \gamma = 5$) and 4-22 ($M/m \approx 960, \gamma = 10$). Note that these solutions include Monte Carlo Coulomb Collisions (MCCC V1), but do not include anomalous diffusion. The effects of changing these assumptions will be discussed later in this chapter. These cases represent the practical limit of the simulation on a PC; they take about a week to generate. A more realistic case to run would be with $M/m \approx 960$ and $\gamma = 5$ with more particles. However, this case would take about a month to converge on our computers.

5.2.1 Experimental Performance

Experimental performance as reported by Khayms [25] is graphed in Figure 5-1. This performance may be re-analyzed using results from the numerical simulations graphed in Figures 4-23 and 4-22. Original and re-analyzed experimental performance at is compared to numerical performance at the lowest flow rate in Table 5.1. Numerical performance was obtained by averaging over the last 10,000 time-steps of the numerical runs (this is $\approx$ 1000 nominal plasma times). The simulation over-predicts most performance parameters by about twenty five percent.

5.2.2 Thrust and Exhaust Velocity

Khayms measured thrust on a stand inside a vacuum tank. He then calculated specific impulse from the equation

$$I_{sp} = \frac{T}{\dot{m}g} \tag{5.1}$$

where $\dot{m}$ is the nominal mass flow rate of neutrals entering the system. In the numerical simulation, thrust is obtained by summing the momentum loss due to particles passing

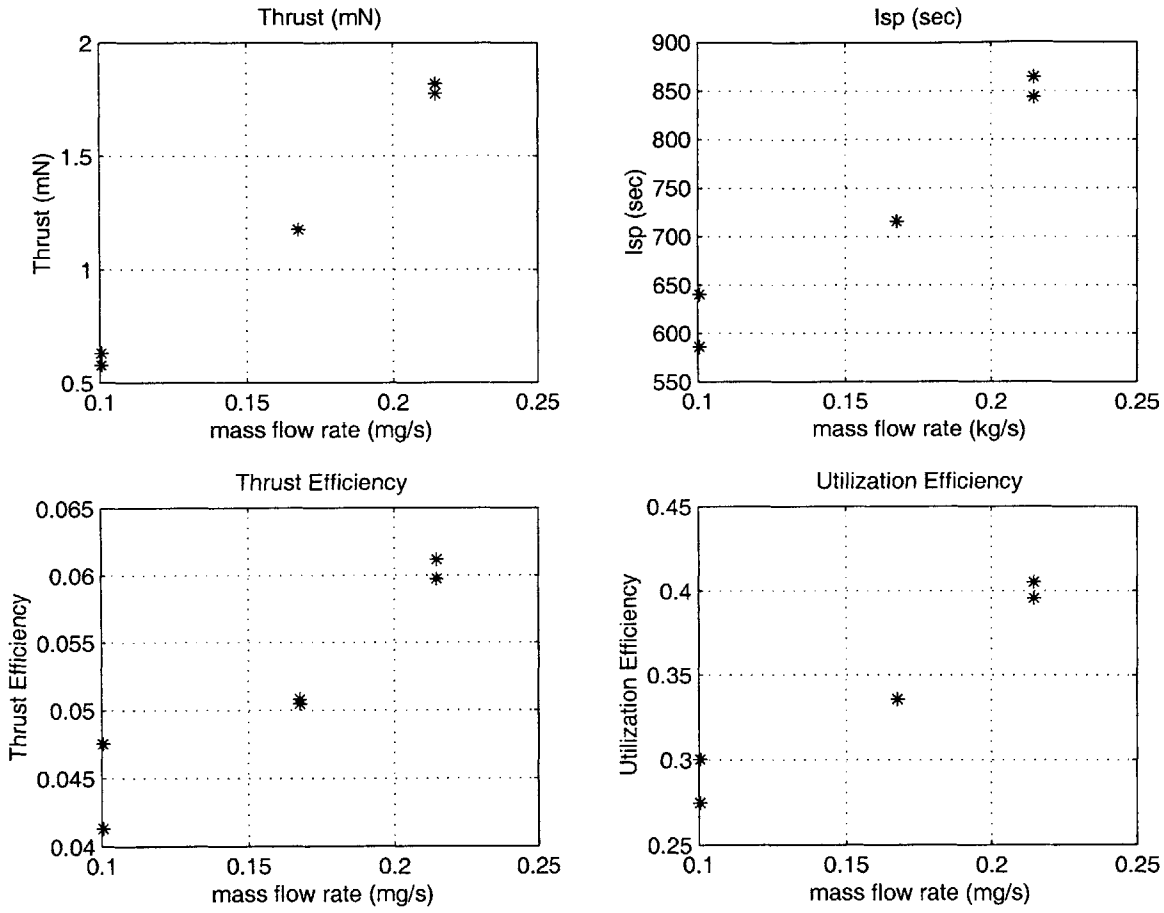

Figure 5-1: *Performance of the mini-TAL at 300 Volts as reported by Khayms* [25]. The performance improves with mass flow rate.

	Khayms	PIC/MCC	PIC/MCC	Modified Khayms
Figure	5-1	4-23	4-22	
$\dot{m}$ (mg/s)	.1005	.1	.1	.1005
M/m	240,000	96	960	240,000
γ	1	5	10	1
Thrust (mN)	.6	.76	.73	.6
I_{sp} (sec)	612	776	745	612
η_a	1.0	.47	.37	.42
η_u	.29	.48	.53	.44
η_t	.05	.25	.20	.05

Table 5.1: Comparison of performance measured by Khayms in laboratory tests and numerical performance predicted by full PIC MCC code under conditions outlined previously. MCC V1 Coulomb collisions assumed. Mass flow rate is $.1mg/s$. Values are approximate. Acceleration efficiency = η_a. Utilization efficiency=η_u. Thrust efficiency = η_t.

through the free space boundary, and specific impulse is again calculated by $I_{sp} = T/\dot{m}g$. The simulation over-predicts thrust and I_{sp} by about twenty five percent.

Note that there are two components to thrust: Ion thrust and neutral thrust. If the simulation has not been run long enough for the neutral flow to converge, then the total thrust and I_{sp} will be incorrectly predicted. Of course, the neutral thrust predicted by the simulation is less than ten percent of the total thrust, so the error is not large.

5.2.3 Acceleration Efficiency

The acceleration efficiency, η_a, was defined to be the ratio of the mean kinetic energy in the axial direction of ions entering the beam, $< \epsilon_i >$, to the potential difference, $\Delta\phi = 300V$. In analyzing data, Khayms assumed the acceleration efficiency was one ($< \epsilon_i >= 300eV$, $< v_i >_z = 20,980\ m/s$). This means the beam is mono-energetic ($T_i = 0$), and all ions are produced at the anode potential. Numerically, however, we find $< \epsilon_i >$ is closer to $\eta_a = .42$ (see Table 5.1). This means the beam does not originate at $\phi = 300$ V, which affects the calculated propellant utilization efficiency, η_u. Furthermore, the simulation predicts that $T_i \approx 60$ eV in the axial direction where most ions pass through the free space boundary. The beam is far from mono-energetic. This is of interest to the field of plume-modeling.

In Section 5.9.2 we discuss a design error in the magnetic circuit. This error resulted in a magnetic field which is not parallel to the anode at $z = 0$. As a result, the discharge is "short circuited" by about 150 Volts. This explains some of the disparity between the numerically observed $< \epsilon_i >$ and 300 V.

5.2.4 Utilization Efficiency

To calculate utilization efficiency, η_u, Khayms assumed that all ions exit with $300eV$ of energy in the axial direction, i.e. $n_a = 1.0$. The utilization efficiency at neutral mass flow rate $\dot{m} = .1mg/s$ was then calculated;

$$\eta_u = \frac{T}{\dot{m} < v_i >_z} = \frac{.6 \times 10^{-3}N}{.1 \times 10^{-6}kg/s \times 20,980m/s} \approx .29. \tag{5.2}$$

This utilization efficiency is only 50 percent of that predicted numerically. However, we can use the numerical η_a to correct Khayms calculated propellant utilization; if $\eta_a = .42$, then

$$\eta_u = \frac{T}{\dot{m} < v_i >_z \sqrt{\eta_a}} = \frac{.6 \times 10^{-3} N}{.1 \times 10^{-6} kg/s \times 20,980 m/s \sqrt{.42}} \approx .44. \tag{5.3}$$

This is about eighty percent of the utilization predicted by the simulation.

5.2.5 Thrust Efficiency

Khayms measured thrust efficiency is much lower than he predicted, and much lower than the simulation predicts. Khayms blames this on the magnetic field which, he hypothesizes, was degraded by heating of the center iron pole piece [25]. He measured the field after the tests and found that the magnitude had not changed much. Therefore, he concluded, "fringing" or changes in the shape of the magnetic field were to blame. The new shape theoretically increased leakage of electrons across the field, increasing the anode current.

Let us estimate how large changes in shape and magnitude would have to be to explain the anomalously high discharge current of the mini-TAL in actual operation. As a simple approximation, assume all electron diffusion happens through classical diffusion such that $< v_e >_z \sim \nu_{en}/\omega_c^2$. If ion moments are constant, but magnetic field is halved, then ω_c drops by a factor of 2 and $< v_e >_z$ increases by a factor of 4. Thus, to increase I_d by a factor of 6 (as suggested by Table 5.1), a reduction in magnetic field strength of only factor $\sqrt{6} \approx 2.5$ is required. Such a reduction certainly seems possible. A decreased magnitude may also explain the difference between experimental and predicted utilization. If the field weakens when the poles heat up, then electron density and ion production in front of the anode exit may decrease.

Changes in shape may also contribute to poor thrust efficiency. If the magnetic field lines near the anode shift toward the axial direction, then a portion of the discharge can be short circuited. We validate this theory theory in Section 5.9.2 by re-designing the anode such that the magnetic field is more parallel to the anode face. Numerical thrust efficiency increases by ninety percent!

In Section 5.6.2, we show that including anomalous diffusion only changes performance by about 10 percent. This is not enough to explain the discrepancy between Khayms measured discharge current and the numerical discharge current.

5.2.6 Variation with Mass Flow Rate

Both numerical and experimental performance improve with mass flow rate. Table 5.1 compared experimental and numerical performance at the mass flow rate $\dot{m} = .1mg/s$; the code was found to over-predict thrust and specific impulse by about twenty five percent. Table 5.2 compares experimental and numerical performance for $\dot{m} = .1676mg/s$, where the numerical assumptions were $M/m \approx 96$ and $\gamma = 5$. Numerical values were obtained by averaging over the last 10,000 time-steps of the run shown in Figure 5-2. At this flow rate, the code over-predicts thrust and specific impulse by about thirty three percent. The simulation has had time for the discharge to develop; most final values should be similar. As before, Khayms utilization efficiency, η_u was modified using the numerical value of η_a to bring it more in line with numerical predictions.

Most notable about Figure 5-2 is perhaps the presence of ionization oscillations (see Section 5.2.8). These happen when the electrons do not have enough energy to ionize all the neutrals. They are not present at $\dot{m} = .1mg/s$ when proper boundary conditions (i.e. quasi-neutral electron injection) are imposed.

	Khayms	PIC/MCC	Modified Khayms
$\dot{m}$ (mg/s)	.1676	.1676	.1676
M/m	240,000	96	240,000
γ	1	5	1
Thrust (mN)	1.2	1.6	1.2
I_{sp} (sec)	717	960	717
$< \epsilon_i >$(eV)	300	171	171
η_a	1.0	.57	.57
η_u	.33	.55	.44
η_t	.05	.35	.05

Table 5.2: *Performance at* $\dot{m} = .17$ *mg/s.* Comparison of performance measured by Khayms in laboratory tests and numerical performance predicted by full PIC code under conditions outlined previously. MCC V1 Coulomb collisions assumed. Values are approximate.

5.2.7 Startup Transients

Transients in density, temperature, and other particle moments exist whenever something significant changes in the simulation. The quasi-neutral method of electron injection allows the simulation to come to equilibrium. If the simulation starts somewhere far out of equilibrium, the adjustments may be abrupt. Figure 5-3 shows the ionization current, the ion

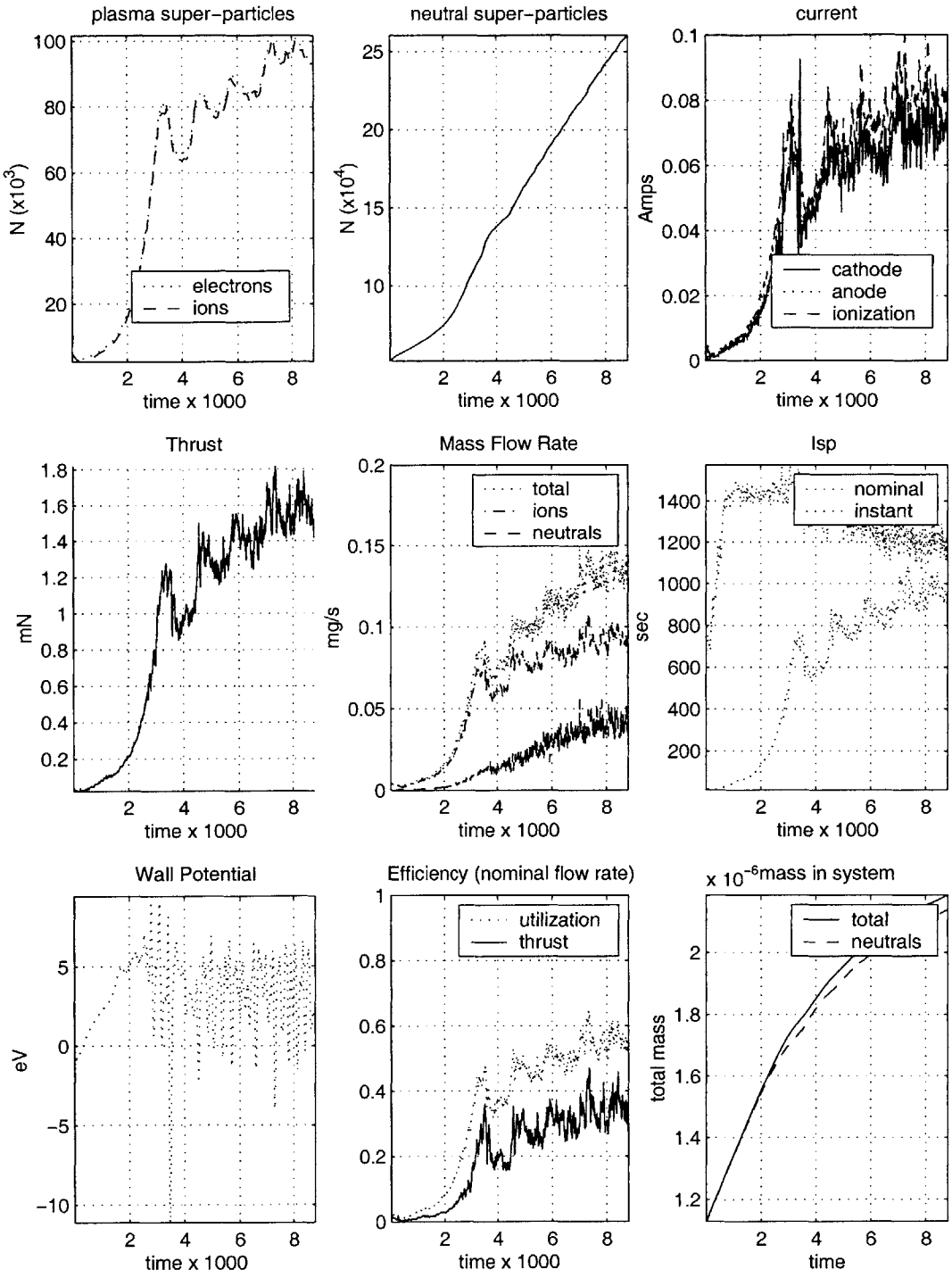

Figure 5-2: *Mass flow rate test, $\dot{m} = .1676$ mg/s.* Performance for $\gamma = 5$, $M_n/M_n' = 2500$, $s_o = 50$, $C = 1 \times 10^{-10}$. Quasineutral cathode electron injection assumed. MCCC Coulomb collisions only. $E_z = 0$ at RHS. Sheath calculated explicitly on upper right boundary. Results may be compared to Figure 4-23, which showed estimated performance for $\dot{m} = .1$ mg/s. Solution is not fully converged.

beam current, the net (ion plus electron) anode current, and the cathode electron current as the simulation comes to equilibrium. This is a most unusual case in that a converged solution for $\dot{m} = .1mg/s$ was the starting point for a new run at $\dot{m} = .1676mg/s$. The original particle distribution was used, but all particle weights changed abruptly.

Let us step through the plots. The first plot shows that ionization current increased dramatically a short time after the mass flow was changed. Why? With $\dot{m} = .1676$, each super-particle now represented ≈ 1.7 times as many particles as it had before. The ionization rate increased dramatically. The middle left plot shows the resultant deluge of electrons hitting the anode. The time difference between when the electrons are produced and when they leave the simulation region is about 2000 of the units used to define τ_3, the time-scale for ion transits, in Chapter 2 ($\delta\hat{t} = 350$ with $\gamma = 5$ goes to about $\delta\hat{t} = 1750$ with $\gamma = 1$). The upper right plot shows the ions exiting through the free space boundary. The middle right plot shows the cathode attempting to compensate. Some explanation is required. The cathode current is here taken to be the sum of the ions which exit through the free space boundary plus the electrons created at the free space boundary minus the electrons which exit through the free space boundary. Using the symbols defined in Chapter 2,

$$I_c^- = I_{cd}^- + I_b^+ - I_{az}^-. \tag{5.4}$$

As the ions approach the right hand side, the net charge along the boundary becomes more and more positive, and the quasi-neutral injection function compensates by creating many electrons. However, the ions soon pass out of the simulation, leaving behind an excess of negative charge. The negative charge and the boundary condition $E_z = 0$ causes the electric potential to drop. However, the electric potential at the right hand boundary is artificially limited to $\phi \geq 0$. *Without this limit, a large electron population can cause the potential to diverge toward negative infinity.* The potential limiter give the excess electron a chance to pass out of the simulation. The cycle continues until the simulation comes to a state of quasi-equilibrium where electrons are almost continuously created at the free space boundary.

The plot of $I_c - I_a$ (lower left) shows that the anode and cathode currents are approximately equal in a steady state. The large jumps show the simulation coming to equilibrium. The control system is robust.

The plot of $I_c - I_b$ shows the sum of the electron current created at the free space boundary minus the electron current exiting through the free space boundary. The sum dips negative for a period, signifying that more electrons were leaving than were being created.

5.2.8 Ionization Oscillations

Figure 5-4 shows the simulation shown in Figure 5-2 ($\dot{m} = .1676$) coming to equilibrium. In this figure, the simulation was started from $t = 0$. The long time-period oscillations evident in Figures 5-2 and 5-4 (which we have already remarked upon) may be influenced by the boundary conditions, but the frequency corresponds well to the expected ionization ("predator-prey") oscillation, expected to occur at a frequency of

$$\omega = 2\pi\nu = \frac{1}{L}\sqrt{V_i V_n}, \tag{5.5}$$

where V_i is the characteristic ion velocity in the acceleration zone, V_n is the characteristic neutral velocity in the zone, and L is the width of the ionization zone [8]. Visual inspection of particle moments corresponding to Figure 5-2 indicate that $V_i \approx .22$, $V_n \approx .007$, and the width of the ionization zone is about $L = 8$. Thus, a period of about $\tau = 1/\nu = 1280$ should be observed. This is almost exactly the period seen in Figures 5-2 and 5-4, suggesting that the current oscillations are physically induced. This view is further re-enforced by the fact that, when boundary conditions are correctly formulated, these oscillations only appear at the higher mass flow rate. At higher flow rates, there is not always enough energy to ionize all the neutrals. For still more discussion of the ionization oscillation, please see Section 5.5.

5.2.9 Ion Losses to Walls

Figure 5-4 allows us to estimate the fraction of ions lost to the walls. Let us use the peak of the second oscillation, for which $I_i \approx .082$ Amps and $I_b \approx .065$ Amps. The fraction of ions lost to the wall at this flow rate is thus $(I_i - I_b)/I_b \approx 25 - 30 percent.$

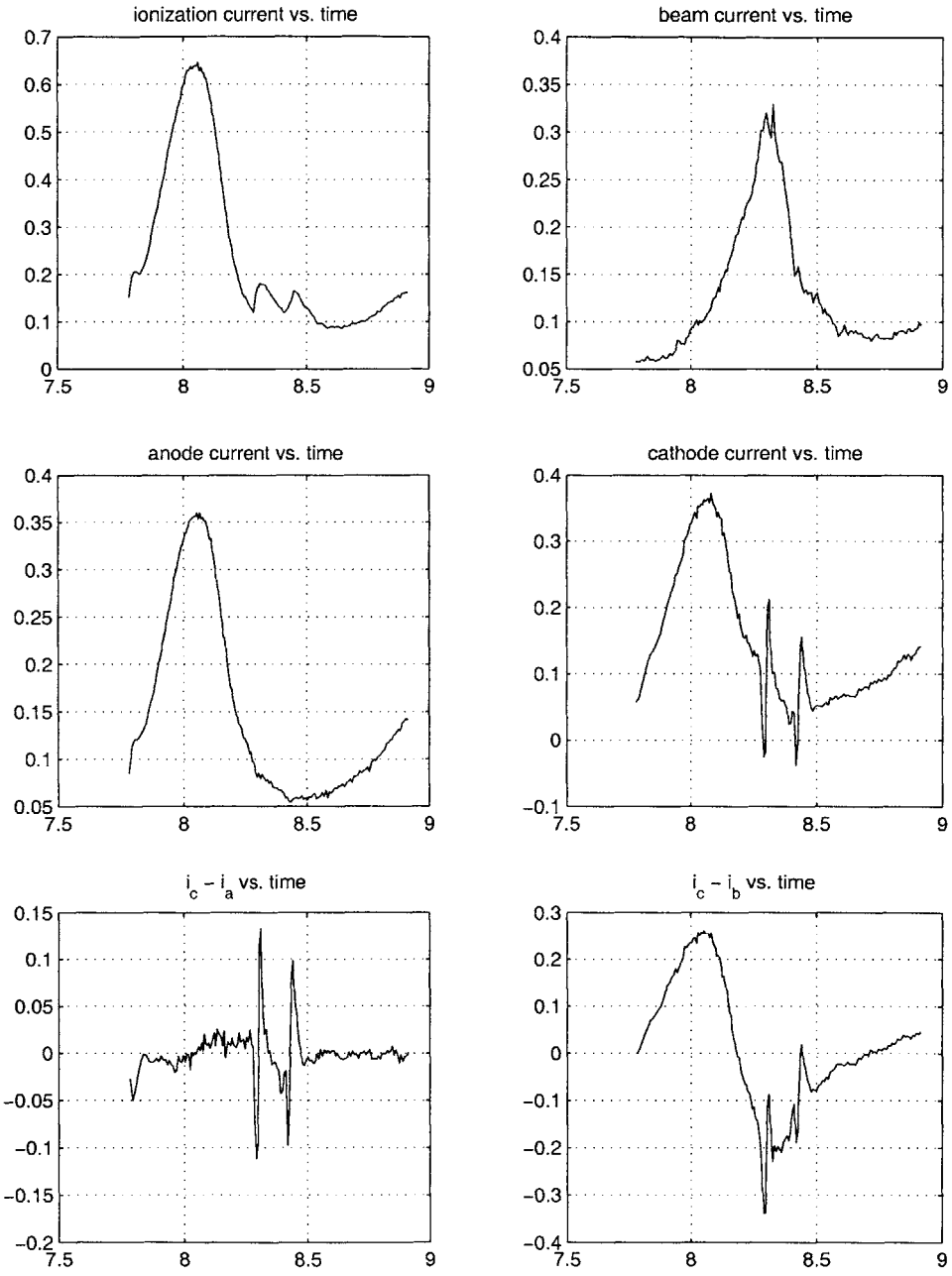

Figure 5-3: *The simulation coming to equilibrium after mass ratio was changed.*

5.2.10 Electrical Efficiency

Figure 5-4 also allows us to estimate the electrical efficiency, $\eta_e = I_b/I_d$. The amount of electrons from the cathode flowing into the system is on average (by the plot of $I_c - I_b$) about .05 Amps. The same number can be obtained by comparing the plots of I_b and I_a. Thus, η_e is (numerically, at least) above ninety percent. Experimentally, however, this number is much lower, which explains why the measured and predicted thrust efficiencies are so far off.

5.3 Particle Moments

Particle moments from the more physical cases modeled are of special interest. Here we look at the case $M/m \approx 96$ with $\gamma = 5$. Other pertinent parameters are: $E_z = 0$ at right hand boundary, quasi-neutral electron injection, $\dot{m} = .1mg/s$, MCC Version 1.0 Coulomb collisions, no anomalous diffusion.

5.3.1 Electric Potential

The time averaged electric potential is shown in Figure 5-5. Most of the potential drop occurs close to the anode. The walls float near $\phi = 0$. The upper right corner of the simulation region is fixed at $\phi = 0$, but the potential along the rest of the boundary is determined by the boundary condition $E_z = 0$, and by the local charge density.

5.3.2 Number Density

The time averaged number density of ions and electrons in units of cm^{-3} is given in Figure 5-6. Values are close to the nominal values used to normalize our equations. Plasma density inside the anode exit is lower than this when more physical mass ratios are used, e.g. $M/m \approx 960$. See, for instance, Figure 5-31, which plots n_i for $M/m \approx 960$ with $\gamma = 10$ and anomalous diffusion. Unfortunately, the case assuming both $M/m \approx 960$ and $\gamma = 5$ is too slow to run on a current PC in less than several weeks.

5.3.3 Charge Density

The time averaged normalized charge density, $q = (n_i - n_e)/n_{e,o}$, is shown in Figures 5-7 and 5-8. The charge density is nearly zero over the bulk of the simulation region, showing

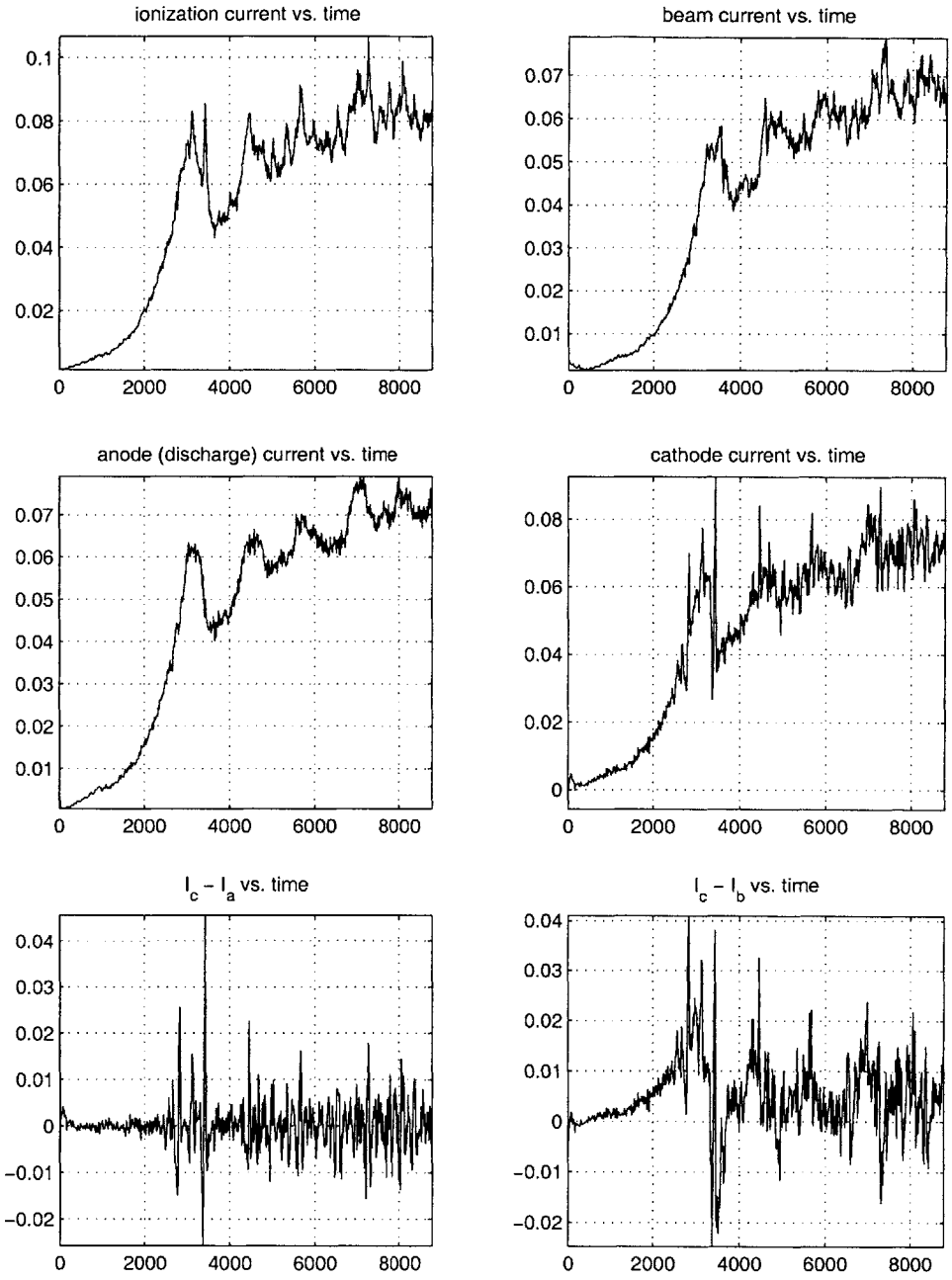

Figure 5-4: *The simulation coming to equilibrium from* $t = 0$ *at* $\dot{m} = .1676$ *mg/s.*

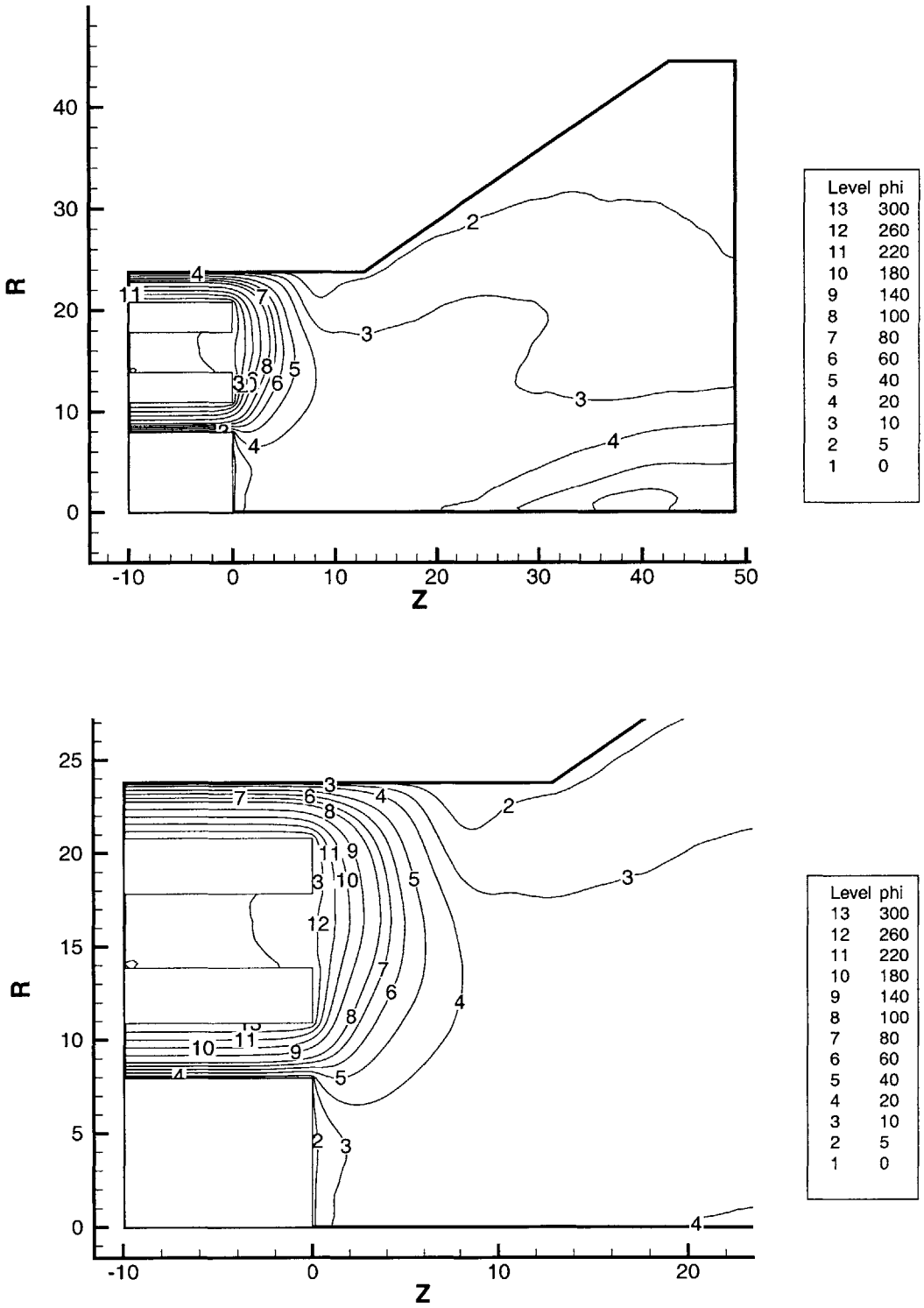

Figure 5-5: *The electric potential* for $M/m \approx 96$, $\gamma = 5$ at $\dot{m} = .1mg/s$.

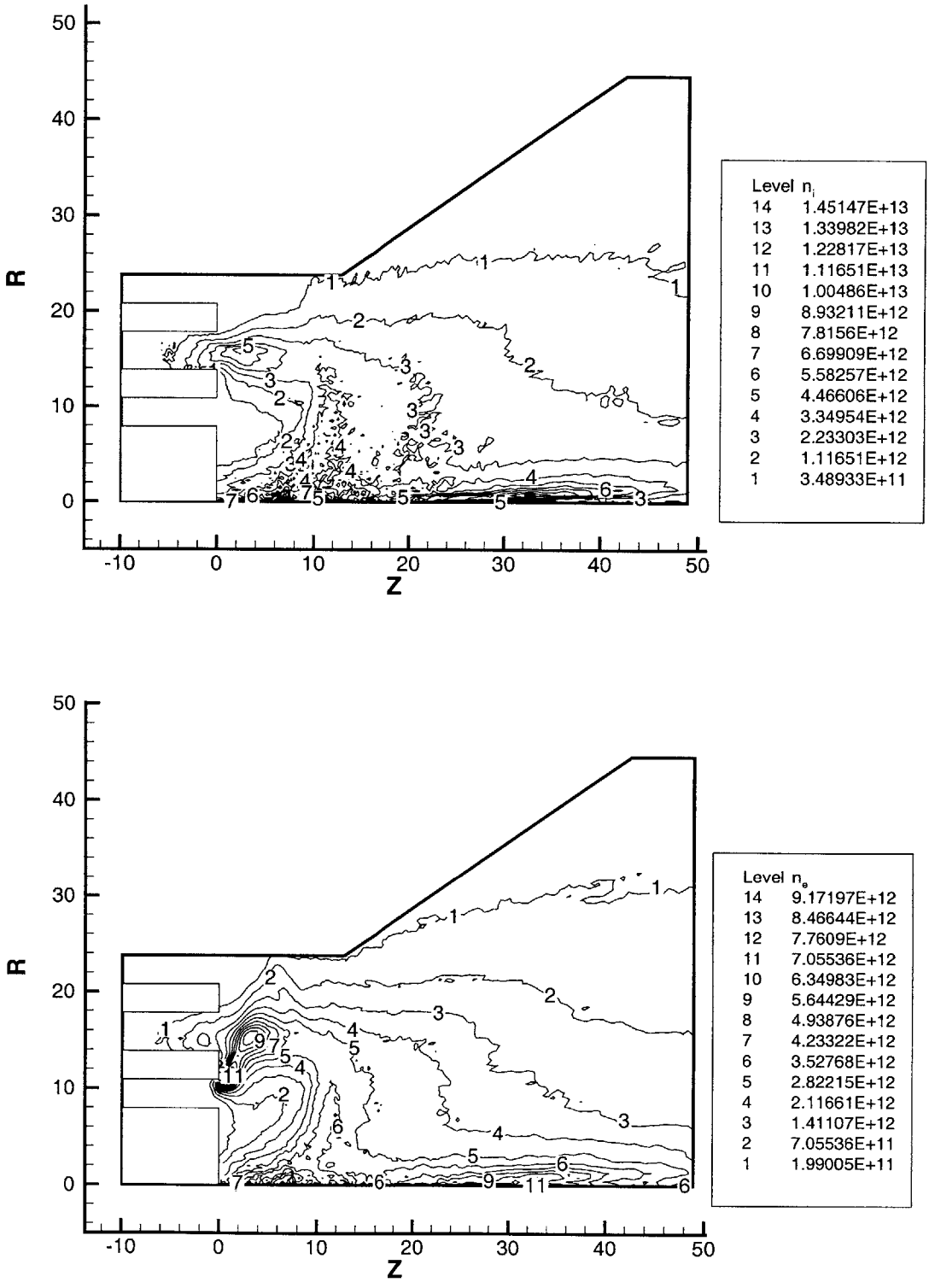

Figure 5-6: *Top*: Ion density n_i. *Bottom*: electron density, n_e.

the success of the quasi-neutral cathode electron injection methodology. Near the anode, geometrically determined potential drops overwhelm plasma induced potentials, resulting in significant (and largely spurious) charge separation.

In general, it should be possible to create a quasi-neutral ionization layer downstream from the anode by selecting an appropriate magnetic field profile [12]. In the mini-TAL, however, the anode layer is so close to the positive electrodes that the plasma cannot be quasi-neutral.

5.3.4 Temperature

Figures 5-9 and 5-10 show the time averaged electron temperature, assumed to be isotropic. The first of these plots also contains magnetic streamlines. The temperature is roughly constant along $\vec{B}$ near the middle of these streamlines. However, gradients in temperature occur along the streamlines. Wall losses do not explain this, as they would tend to act on all electrons on a given streamline equally. Another possibility is that diffusion across the field is accelerated so much to compensate for the artificial neutral mass ratio, M'/M, that energy added near the center of the anode does not have time to make it to the edges. But this seems unlikely, as strong gradients occur no matter what mass ratio is assumed. Potential gradients are the most likely source.

The electron temperature is high near the anode, as expected. However, another region of high electron temperature occurs near the axis near the free space boundary. This is due to the injection of electrons with $T_e = 2.5$ eV, but bulk energies near the plasma potential at the central portion of the free space boundary. This feature is much less extreme in some other cases which were run.

The anisotropy of the electron temperature is shown in Figure 5-11. Factors influencing the ratio $T_{\|}/T_{\perp}$ include magnetic bottling, electric potential gradients, wall losses, scattering frequencies, and diffusion rates. Bottling tends to force parallel energy into the perpendicular direction. Potential gradients channel energy into the electrons preferentially. For instance, the electric field near the anode acts largely perpendicular to $\vec{B}$, "pumping" the parallel electron temperature. Likewise, the electric field near the free-space boundary acts largely parallel to $\vec{B}$, pumping parallel energy. Wall losses act preferentially along $\vec{B}$, since parallel energy is required to overcome sheaths. The temperature becomes more isotropic and thermal through scattering, both elastic and inelastic, which happens at dif-

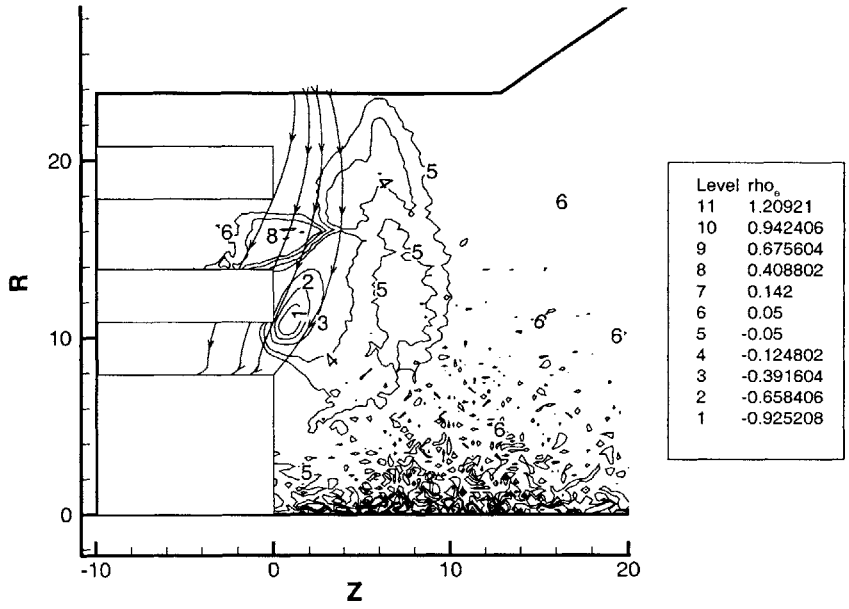

Figure 5-7: *Normalized charge density*: $q = (n_i - n_e)/n_{e,o}$. Shown is the anode region, where geometrically determined potential drops overwhelm internal potentials. Shown also are several magnetic streamlines.

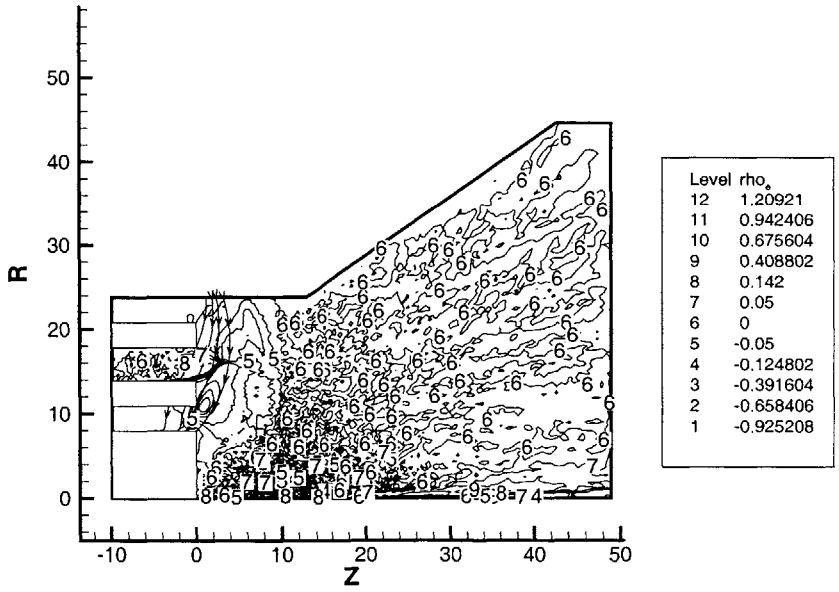

Figure 5-8: *Normalized charge density*, $q = (n_i - n_e)/n_{e,o}$, where $n_{e,o} = 6.78 \times 10^{12} cm^{-3}$. Shown is the overall simulation region. The charge density is nearly zero over the bulk of the simulation region, showing the success of the quasi-neutral cathode electron injection methodology. Shown also are several magnetic streamlines.

ferent rates for $T_\perp$ and $T_\parallel$. Temperature mixing also occurs through diffusion (classical, Bohm, Coulomb) and through oscillations. This is really a very complicated issue.

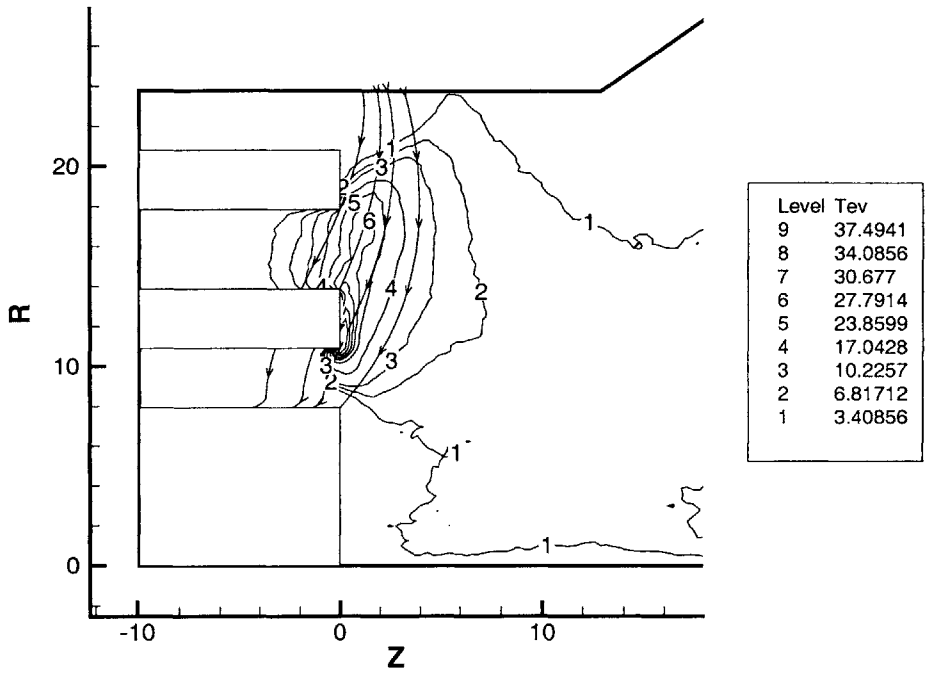

Figure 5-9: *Electron temperature near the anode.* Shown also are several magnetic streamlines.

5.3.5 Ion Temperature and Flux

The ion temperature measures the thermal spread of ions from their bulk velocity. In the azimuthal direction, the temperature is very small, less than 1 eV. In the radial direction, it is just a few eV. In the axial direction, however, the ion temperature is large, typically ≈ 60 eV, as shown in the top part of Figure 5-12. The large temperature just downstream from the anode means that ions are produced in a zone which is approximately forty to sixty volts wide. The thermal spread of ions at the exit plane is a valuable parameter since it is one of the required inputs for numerical thruster plume models.

Another valuable parameter is the flux into the wall as a function of position. The bottom part of Figure 5-12 is a vector plot of the ion flux, $\hat{n}_i\vec{v}$ at a portion of the wall. This parameter can be scaled to physical units, averaged over time and used to predict the erosion rate of the wall material. This is an important design consideration for Hall

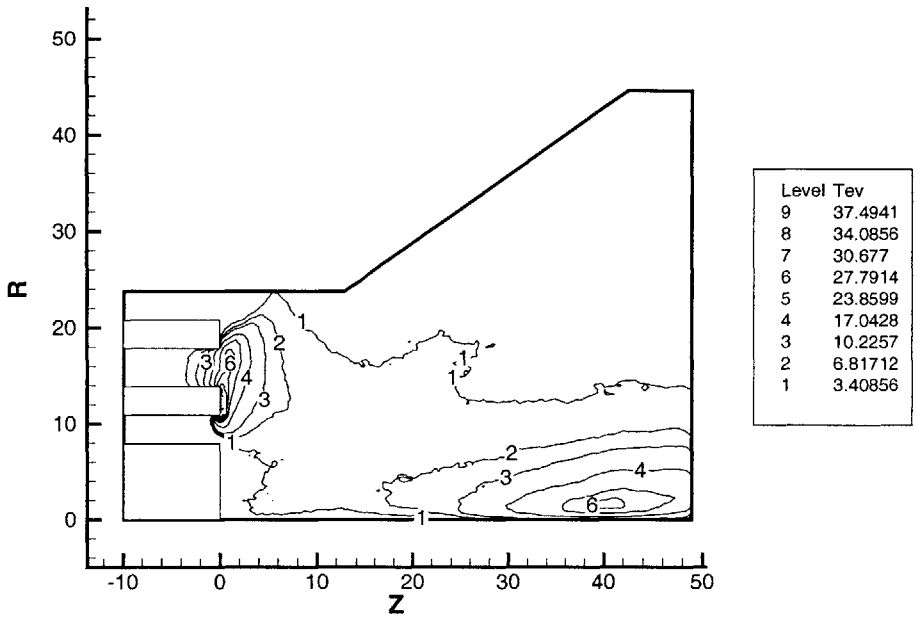

Figure 5-10: *Electron temperature across the entire simulation region.*

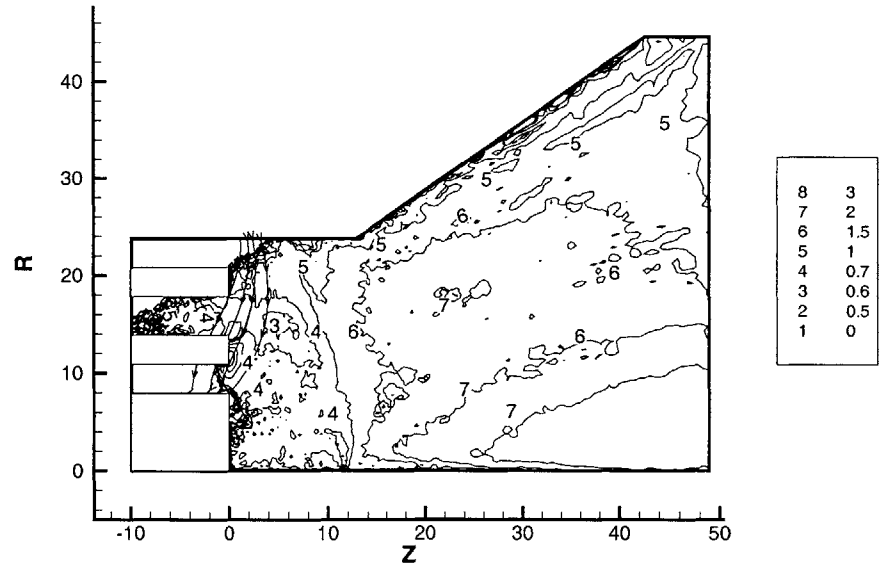

Figure 5-11: *Anisotropy in the time averaged electron temperature across the entire simulation region.* Shown is the ratio $T_{\|}/T_{\perp}$. Shown also are several magnetic streamlines.

thrusters.

5.3.6 Electron Current and Induced Magnetic Field

The electron current density can be post-calculated using the formula $\vec{j} = en_e\vec{v}$ and rescaled to rational units. Figure 5-13 shows the electron current in Amps per square centimeter predicted by the simulation. To generate this figure, all numerical values were post-multiplied by the factor $\sqrt{M_n'/M_n}$. However, it is incorrect to do so for the azimuthal current, j_θ. The azimuthal Hall current, given by $j_\theta = -neE_z/B \times \beta^2/(1+\beta^2)$ (see Section 2.10.3) is nearly invariant with respect to the Hall parameter. If β^2 is sufficiently large, $j_\theta \approx -neE_z/B$. Thus, the simulation predicts something very close to the "physical" j_θ all the time. When determining the "physical" j_θ from the computational j_θ, one should *not* multiply by $\sqrt{M_n'/M_n}$.

The Biot-Savart Law provides a convenient means of estimating the magnetic field which would result from a given current density. In MKS units, the magnetic field strength as a function of distance would be

$$B_{ind} = \frac{\mu_o i}{2\pi r}. \tag{5.6}$$

From the figure, the Hall current near the anode is about 3 Amps per square centimeter over an area of about $.1 \times .1$ cm, yielding a current of $i_\theta \approx .03$ Amps. However, this value is a factor of $\sqrt{M_n'/M_n} = 50$ too low (see above explanation). The correct current is $i_\theta \approx 1.5$ Amps. With $\mu_o = 1.26 \times 10^{-6} H/m$, the Biot-Savart Law predicts an induced field strength of about 30 Gauss at $r = .1mm$, which is about equivalent to the nominal Debye length.

The importance of the induced field is commonly described by the magnetic Reynolds number, R_B. This can be loosely interpreted as

$$R_B \approx \frac{\Delta B}{B_o}, \tag{5.7}$$

where ΔB is the induced field and B_o is the nominal field. If $R_B << 1$, the induced field can reasonably be neglected. If $R_B >> 1$, it will dominate [24]. In our case, $B_o \approx 3000$ Gauss and $R_B \approx .01$. Thus, we are justified in ignoring the induced field.

Note that under Khayms' "ideal scaling" ($i \sim L$, $r \sim L$ and so on) B_{ind} is scale-invariant. On the other hand, the applied B-field scales as $B_o \sim 1/L$, and so

$$\frac{B_{ind}}{B_o} \sim L. \tag{5.8}$$

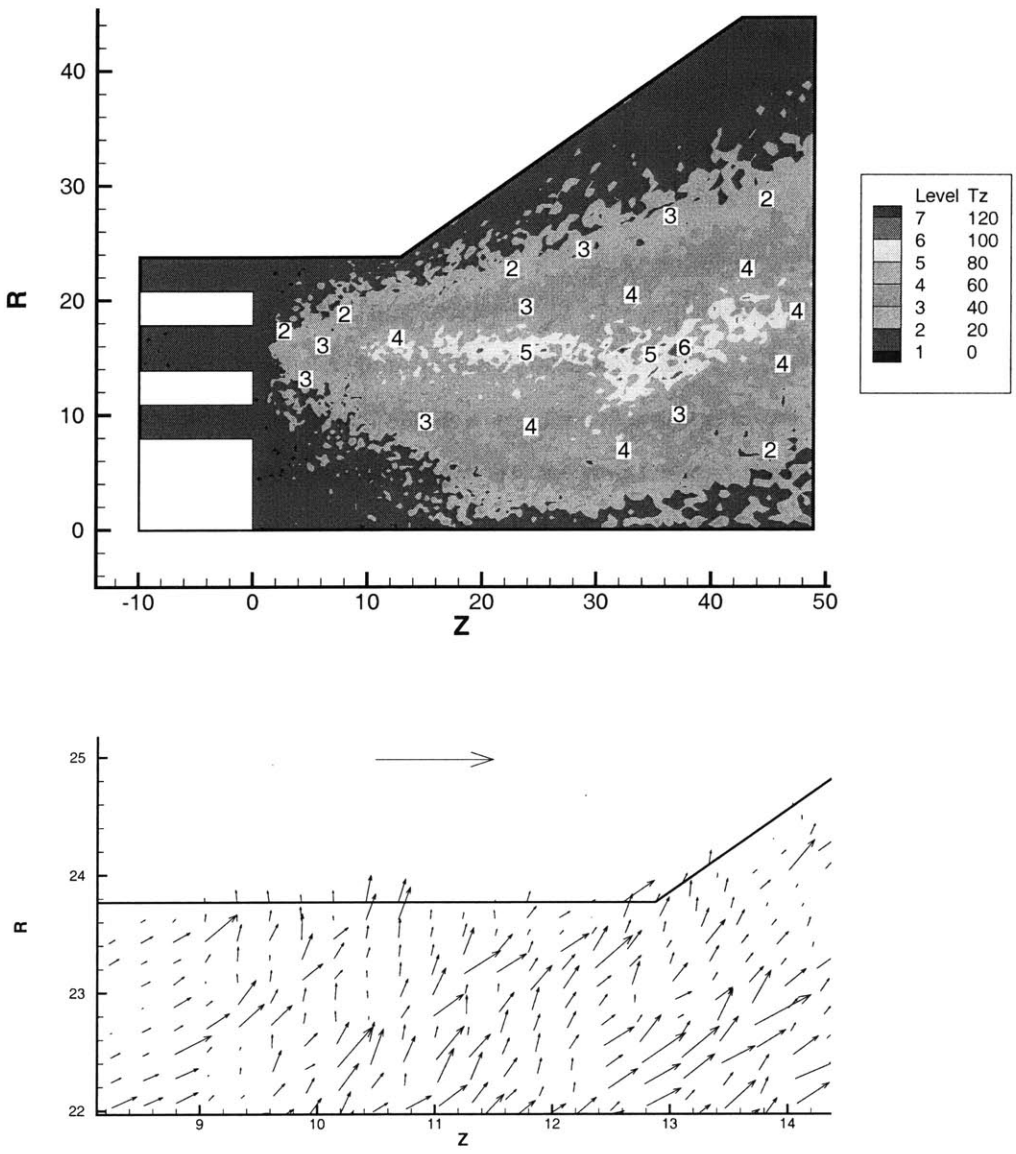

Figure 5-12: *Top*: The ion temperature in the axial direction, $T_{i,z}$ eV, which shows the spread in potential across which ions are produced. The temperature in the radial and azimuthal directions is much smaller. *Bottom*: The flux into the wall in the channel of the thruster. Scale vector is length .1, in normalized units. Both plots are instantaneous; they are not time averaged.

This explains the small effect seen here, but also says that the induced magnetic field will be more important at higher power.

5.3.7 Hall Parameter

The Hall parameter $\beta = \omega_c/\nu_e$ is a measure of the degree to which the electrons are magnetized. To increase electron mobility perpendicular to the magnetic field, the cross sections for electron neutral scattering are increased by a factor $Q'/Q = 1/\sqrt{f}$ where $f < 1$. For $M_n/M_n' = 2500$ ($M_n/m_e \approx 96$), $1/\sqrt{f} = 50$. Is β in this case enough to justify the assumption that electron conductivity perpendicular to the field is proportional to ν_e? For this to be true, the modified Hall parameter $\beta' = \beta\sqrt{f}$ should be at least 2 or 3. To estimate β and β', the following relations were used:

$$\nu_{en} \approx n_n c Q(c^2); c = < |v_e| > = \sqrt{\frac{8KT_e}{\pi m}}. \tag{5.9}$$

The electron temperature was averaged over a period of one hundred time-steps (See Figure 5-15). The neutral density used was the instantaneous density at the end the one hundred time-steps. From T_e, c was calculated and used to find the collision cross section $Q(c^2)$ (which was not averaged over the Maxwellian). The resulting first order approximation to β' for $M/m \approx 96$, and $\gamma = 10$ is shown in Figure 5-14. Inside the anode, $\beta' < 2$. Outside the anode, $\beta' > 2$. Thus, inside the anode, the assumption that conductivity is nearly proportional to ν_{en} breaks down. Here, the Hall parameter increases primarily because the neutral density is very high.

Note, however, that this case assumed $M/m \approx 96$ and $\gamma = 10$, for which some plasma makes its way into the anode. But the electron density in the anode is lower when $\gamma = 5$. In that case, the problem is diminished. Furthermore, when $M/m \approx 960$, there is not a problem in any case, as the plasma density in the anode is even lower. Later in this chapter we present more accurate estimates of the hall parameter obtained by counting actual scattering events.

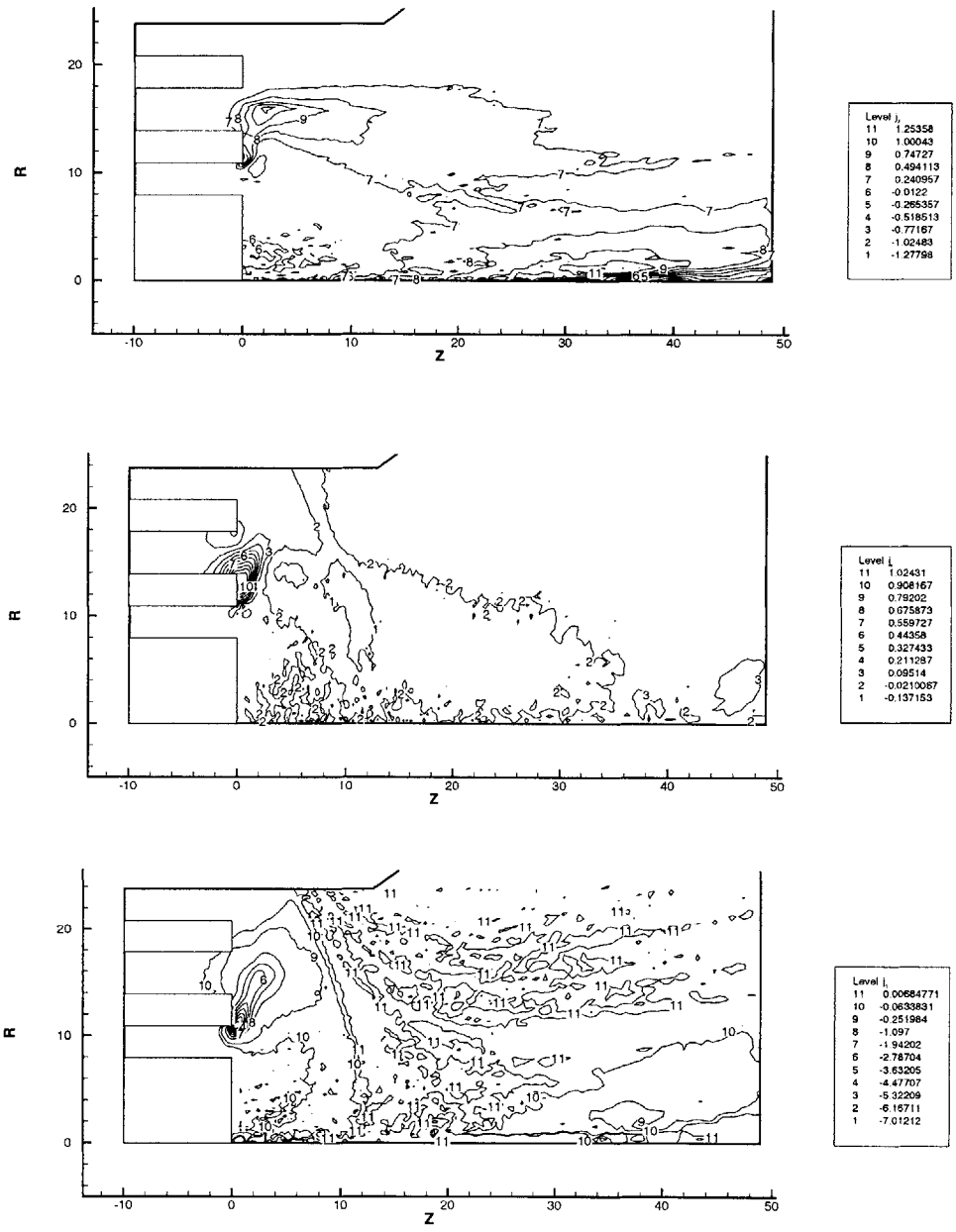

Figure 5-13: *The electron current density,* $\vec{j} = en_e\vec{v}$, in units of Amps per square centimeter. Top: j_z. Middle: j_r. Bottom: $j_\theta \times .02$; j_θ is the Hall current.

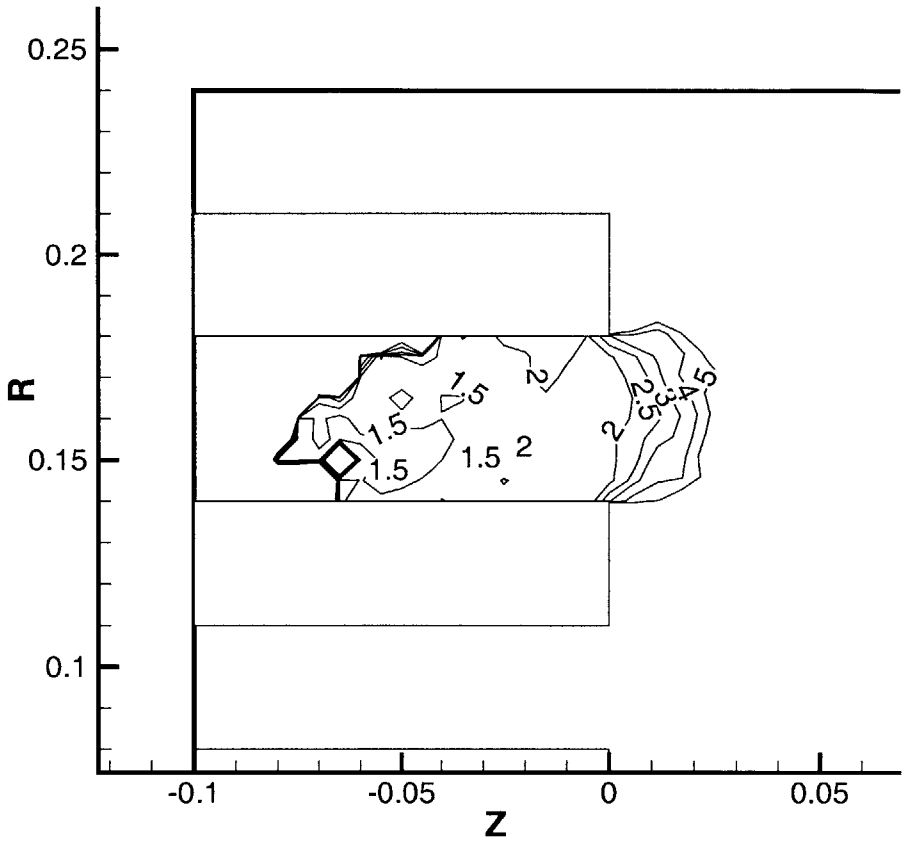

Figure 5-14: *A first order approximation of the modified Hall parameter β' in the anode region of the thruster.* $< T_e >$ was averaged over 100 time-steps with $M_n/m_e \approx 96$, $\gamma = 10$, MCC V1 Coulomb collisions. Electron density tapers to zero within the anode leading to poor statistics.

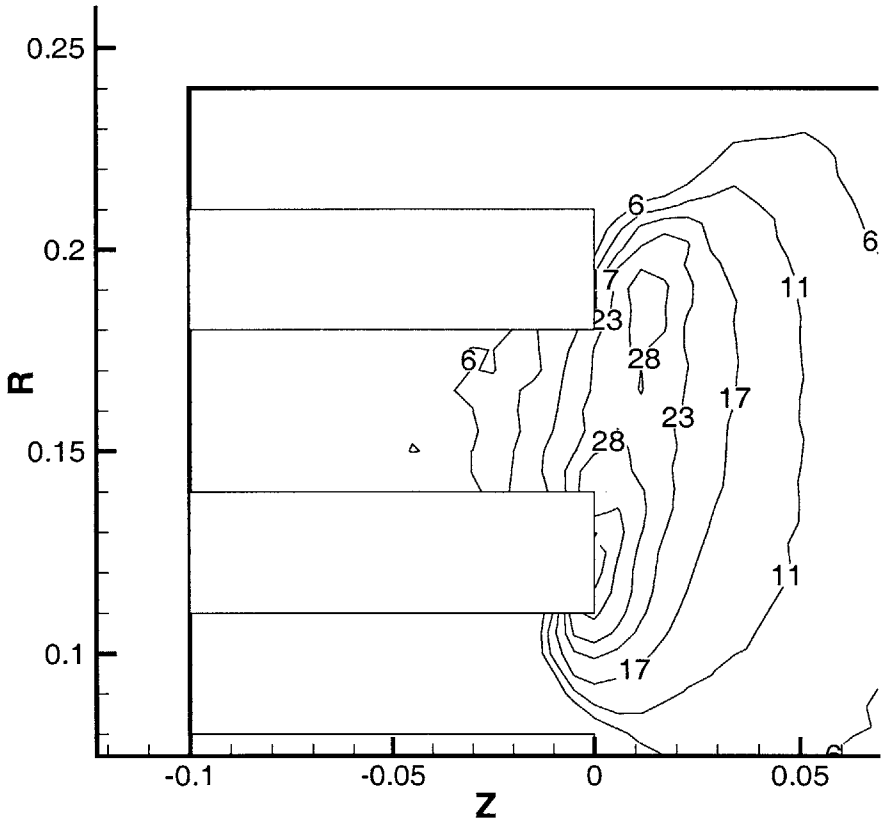

Figure 5-15: *The electron temperature in electron volts in the anode region of the thruster.* One hundred simulation time-steps were used to get $< T_e >$. Results are time averaged assuming $M_n/m_e \approx 96$, $\gamma = 10$, MCCC Coulomb collisions.

5.4 Electron Energy Distribution Function

In this section, we analyze the normalized distributions electron distribution functions, $g(\epsilon')$, $g(\epsilon'_{||})$, and $g(\epsilon'_{\perp})$, which were described in Section 3.11 The distributions are time averaged from the case $M_n/m_e \approx 96$ and $\gamma = 5$. Other pertinent parameters are: MCC V1 Coulomb collisions, $E_z = 0$ at right hand boundary, quasi-neutral electron injection, $\dot{m} = .1mg/s$, no anomalous diffusion.

5.4.1 EEDF by Magnetic Stream Function

The magnetic stream function used for analysis is shown in Figure 5-19. The bands near the anode are defined by physical features at the exit plane of the anode. The second band of ψ is the region of highest T_e, while the third band is the region of highest n_e near the anode. The distribution functions shown in Figures 5-16, 5-17, and 5-18. are averaged over 1000 time-steps. Statistics are worst in the first band. To generate the numerical distributions, the energy of each electron in a given band of ψ was normalized by the local temperature as interpolated from the grid and tabulated. Thus, the plots are the shape of the distribution as if it were constant everywhere with respect to the local T. Figure 5-16 shows a roughly Maxwellian distribution at T_e, but Figures 5-17 and 5-18 show that the distribution near the anode is better described two temperatures, $T_\perp$ and $T_{||}$. The parallel distribution seems to be quite Maxwellian, but the perpendicular distribution seems to be non-Maxwellian. Since the electric field is in the perpendicular direction, this may reflect gyro energy which does not have time to thermalize.

5.4.2 EEDF by Point

Points inside the acceleration zone used for analysis are listed in 5.3. The first point is on the exit plane of the anode. The second point is in the ψ band of maximum T_e. The third point is in the region of greatest n_e near the anode. The remaining points are spaced evenly in computational coordinates to past the point in the channel where the outer wall diverges.

The time averaged distributions $f(e_z, e_r, e_\theta, z, r)$ for four points centered (in the radial direction) approximately on the anode exit are shown in Figures 5-20, 5-21, and 5-22. (Since the time-step was allowed to vary, the plots are actually iteration averaged.) Only distributions at the first four points are plotted. The time (iteration) averaged temperature

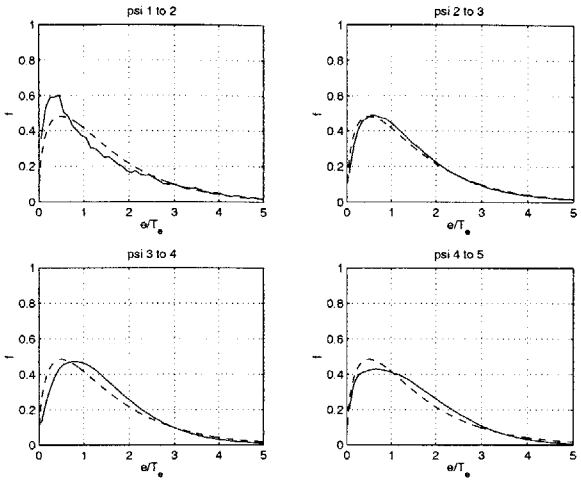

Figure 5-16: $g(\epsilon')$ for streamlines.

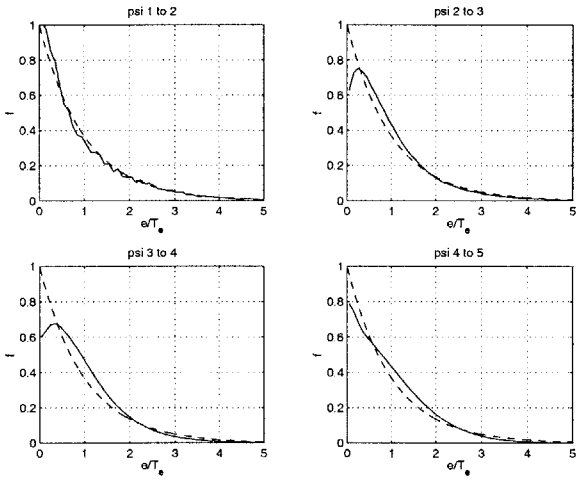

Figure 5-17: $g(\epsilon'_{\perp})$ for streamlines.

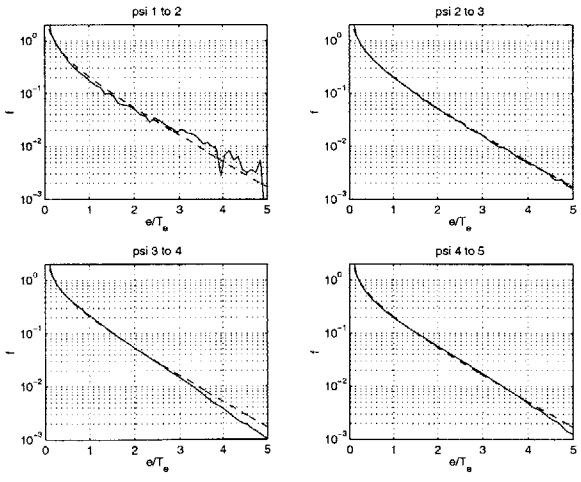

Figure 5-18: $g(\epsilon'_{||})$ for streamlines.

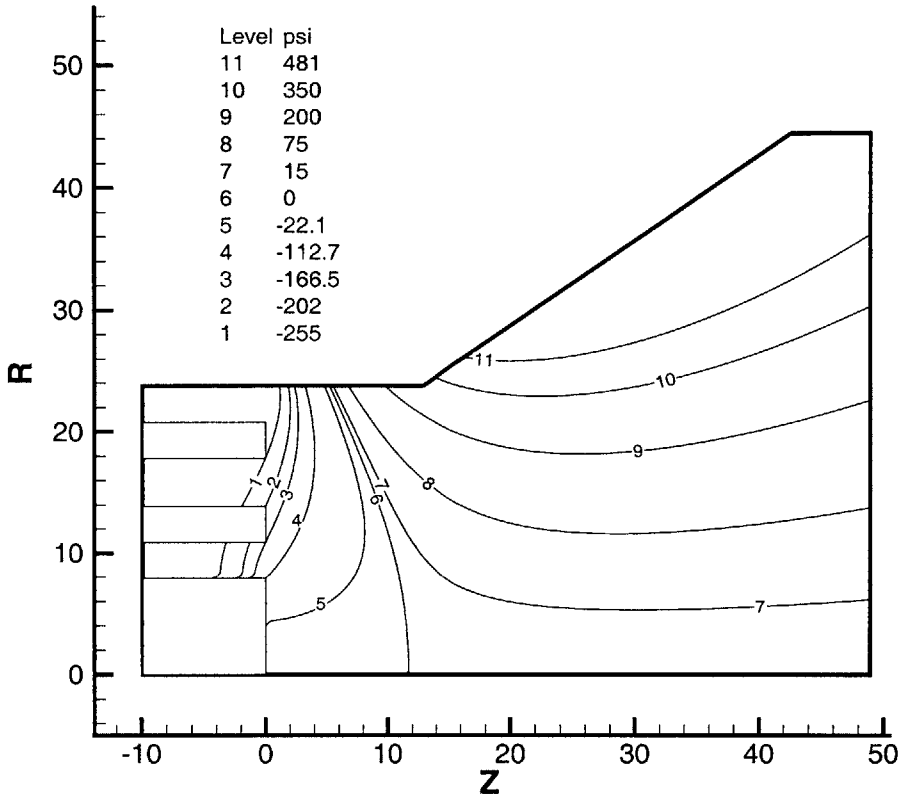

Figure 5-19: *Values of magnetic potential used to define the EEDF.* The band between contours 1 and 2 reaches the anode interior. The bands between contours 2 and 5 define the main ionization zone. Contours 2 and 3 define the region of highest T_e, while contours 3 and 5 define the region of highest n_e near the anode. Normalized units with $\gamma = 5$, $\dot{m} = .1mg/s$, and $[T] = 50$ eV are assumed.

point	(ξ, η)	$(\hat{z}, \hat{r})$
1	(40, 65)	(0 , 15.8459)
2	(46, 65)	(1.66097 , 15.9521)
3	(52, 65)	(3.32714 , 16.0804)
4	(58, 65)	(4.99776 , 16.2118)
5	(64, 65)	(6.67616 , 16.355)
6	(70, 65)	(8.36679 , 16.5199)
7	(76, 65)	(10.0758 , 16.7184)
8	(82, 65)	(11.8119 , 16.9673)
9	(88, 65)	(13.5878 , 17.2992)
10	(94, 65)	(15.4209 , 17.7664)

Table 5.3: Locations of points used for analyzing the EEDF. Each point is located on top of a grid node with computational coordinates (ξ, η). The lower left corner of the grid has computational coordinates $(\xi, \eta) = (0, 0)$. Each grid node has location $(\hat{z}, \hat{r})$ in real space, where normalized units with $\gamma = 5$, $\dot{m} = .1mg/s$, and $[T] = 50$ eV are assumed.

at each of the four points is listed in Table 5.4.

point	(ξ, η)	T	$T_{\|}$	$T_{\perp}$
1	(40, 65)	23.9	15.5	28.1
2	(46, 65)	26.2	16.5	31.1
3	(52, 65)	16.1	11.5	18.4
4	(58, 65)	9.7	6.7	11.2

Table 5.4: Time (iteration) averaged electron temperatures at each of the points used to create the distributions shown in Figures 5-20, 5-21, and 5-22.

Although a smaller sample size leads to coarser plots, the figures show the same trends described in the previous section. This means that the electron distribution on the edges is not significantly warping the plots of $f(e_z, e_r, e_\theta, \psi)$.

5.4.3 General Comments on the EEDF

In Section 5.8 we show that the non-Maxwellian shape of the distribution function in the perpendicular direction is still observed when $M/m = 960$ and $\gamma = 10$, and also when no Coulomb collisions are modeled. However, the shape is more Maxwellian when Langevin Coulomb collisions are modeled.

In general, there are many factors driving the distribution toward a Maxwellian. In addition to Coulomb collisions, there are inelastic collision with other electrons, and also many types of oscillations, some of which are only statistical. The latter can be minimized through high particle counts, but can never, as a matter of practicality, be eliminated. An energy conserving algorithm should probably be used if efforts to estimate the distribution function continue. We have but lit a candle in the Stygian gloom which surrounds this topic.

5.5 Plasma Oscillations

Since the simulation proceeds along the electron time-scale, it should capture both high and low frequency plasma oscillations. Some of these oscillations may be observed by applying the fast Fourier transform (FFT) to internal density data at various grid points, i.e. $n_e(z, r, t)$, $n_i(z, r, t)$, and $n_n(z, r, t)$. Other oscillations may be observed through the discharge current, I_d.

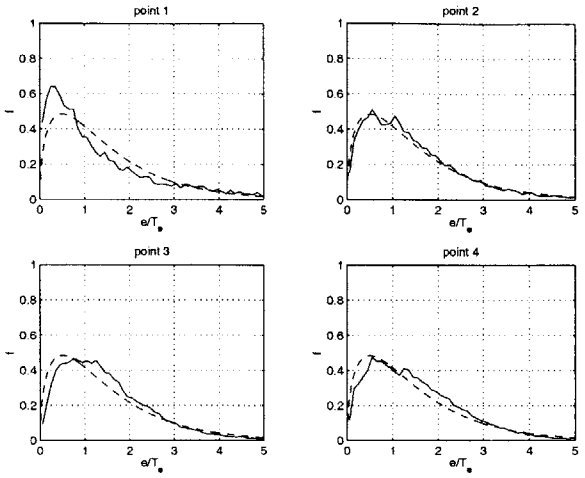

Figure 5-20: $g(\epsilon')$ for points. See Table 5.4 for corresponding temperatures.

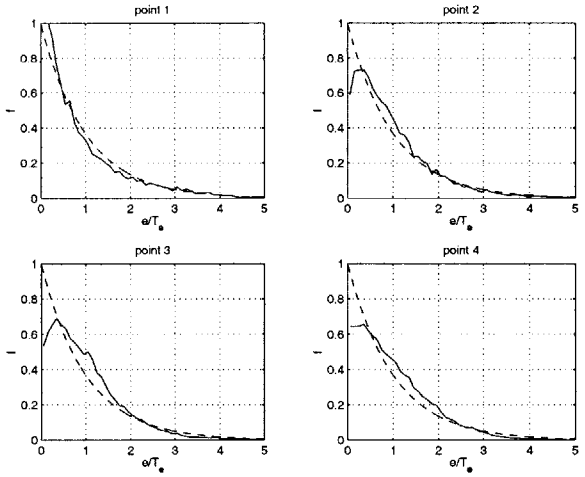

Figure 5-21: $g(\epsilon'_{\perp})$ for points. See Table 5.4 for corresponding temperatures.

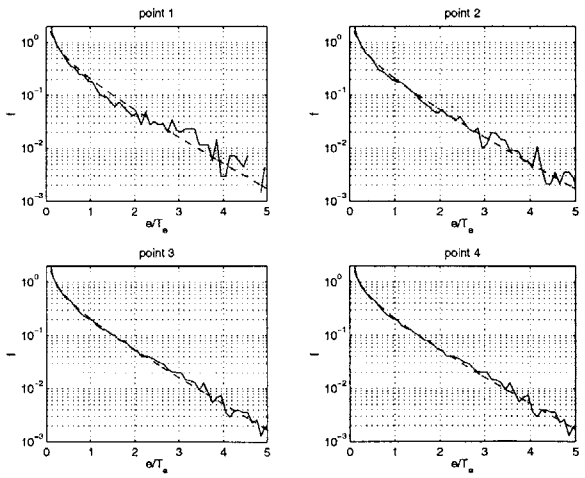

Figure 5-22: $g(\epsilon'_{||})$ for points. See Table 5.4 for corresponding temperatures.

5.5.1 Theoretical Modes of Oscillation

Some well known oscillations are listed in Table 5.5. All oscillations listed are electrostatic.

Species	Orientation	Frequency	Name
Electron	$\vec{K}\|\|\vec{B}$	$\omega^2 = \omega_p^2 + \frac{3}{2}K^2 v_{th}^2$	Plasma
Electron	$\vec{K}\perp\vec{B}$	$\omega_h^2 = \omega_p^2 + \omega_c^2$	Upper hybrid
Ion	$\vec{K}\|\|\vec{B}$	$\Omega_a^2 = K^2[\frac{\gamma K T_e + \gamma K T_i}{M}]$	Acoustic
Ion	$\vec{K}\perp\vec{B}$	$\Omega^2 = \Omega_c^2 + K^2 V_s^2$	Cyclotron
Ion	$\vec{K}\perp\vec{B}$	$\frac{1}{\Omega_l^2} = \frac{1}{\omega_c \Omega_c} + \frac{1}{\Omega_p^2}$	Lower hybrid
Ion	$\vec{K}\perp\vec{B}$	$\Omega_i = \frac{\sqrt{V_n V_i}}{L}$	Ionization

Table 5.5: Some well known electrostatic oscillations, from Reference [6]. Capital letters indicate ion frequency, e.g. Ω_c is the ion cyclotron frequency.

If evident, electron plasma waves should be parallel to the $\vec{B}$, while upper hybrid waves should be perpendicular to $\vec{B}$. The ionization oscillation is usually visible in the discharge current and is typical for Hall thrusters [8]. It is a density fluctuation which is nominally perpendicular to $\vec{B}$. Electromagnetic electron waves (0,X,R,L) and ion waves (Alfven, Magnetosonic) will not occur in this simulation because the magnetic field is assumed to be static.

In the next section, we will look for modes of oscillation in a numerical data-set showing n_e, n_i, and n_n at a single grid node,$(\xi, \eta) = (50, 65)$, over the course of 1000 time-steps. To predict what frequencies should be seen, the average values of n_e, n_i, and n_n were used. The average electron density was $n_e \approx 5.7 \times 10^{12}$, while the average ion density was $n_i \approx 6.4 \times 10^{12}$. Other values used to predict frequencies were $< T_e > \approx 19.5$ eV, $T_i \approx 10.8$ eV, and $|B| \approx 3136$ Gauss. (The ion temperature was not time averaged). The nominal plasma density for this case was $n_{e,o} = 6.77 \times 10^{12}$ particles per cm^3. Because the density is not nominal, the local plasma frequency in terms of nominal units should be ($K = 0$)

$$\omega_p = \sqrt{n_e / n_{e,o}} = \sqrt{5.7/6.77} \approx .92. \tag{5.10}$$

Other frequencies follow. The ion plasma and lower hybrid frequencies assume $n =< n_i >= 6.4 \times 10^{12}\ cm^{-3}$. The ion acoustic frequencies use $T_{i,r} = .95$ eV and assume that waves must be resonating to be seen. To estimate frequencies, several wave numbers ($K = 2\pi/\lambda$) were estimated using the condition $n\lambda = 4R$, where R is the inner radius of the thruster channel,

$\approx$ .24 cm. (The ion temperature is highly non-isotropic; the temperature in the axial direction is $T_{i,z} = 31$ eV.) The time averaged electric potential at this point is $< \phi >= 142$ V. In this simulation, $|B|$ is decreased for ions such that the physical ion cyclotron frequency and radius should be observed. Thus, Ω_c may be hard to detect numerically. The ionization frequency assumes $V_{i,z} = .155$ (instant at end of run), $V_{n,z} = .0059$ (instant at end of run), and $L = 5$.

Species	Orientation	Frequency	Name
Electron	$\vec{K} \| \vec{B}$	$\omega_p = .92$	Plasma
Electron	$\vec{K} \perp \vec{B}$	$\omega_h = 2.1$	Upper hybrid
Ion	$\vec{K} \| \vec{B}$	$\Omega_p = .099$	Plasma
Ion	$\vec{K} \| \vec{B}$ $(\lambda = R)$	$\Omega_a = .0018$	Acoustic
Ion	$\vec{K} \| \vec{B}$ $(\lambda = R/5)$	$\Omega_a = .0089$	Acoustic
Ion	$\vec{K} \perp \vec{B}$	$\Omega_c = 7.8 \times 10^{-6}$	Cyclotron
Ion	$\vec{K} \perp \vec{B}$	$\Omega_l = .0038$	Lower hybrid
Ion	$\vec{K} \perp \vec{B}$	$\Omega_i = .0060$	Ionization

Table 5.6: Predicted electrostatic oscillation frequencies at node $(\xi, \eta) = (50, 65)$. These frequencies are defined in 5.5. Ion plasma and lower hybrid frequencies assume $n =< n_i >= 6.4 \times 10^{12}\ cm^{-3}$. Electron frequencies assume $n =< n_e >= 5.7 \times 10^{12}\ cm^{-3}$. Averages obtained over 1000 iterations. Also, $T_{i,r} = .95$ is used to predict V_s for acoustic waves.

5.5.2 Numerical Oscillations

Figures 5-23, 5-25, 5-24, and 5-27, show oscillations in n_n, n_i, and n_e at grid node$(\xi, \eta) = (50, 65)$, which is ten nodes in front of the middle of the anode exit. The first three plots come from a single run of the simulation for 1000 uniform time-steps with $\gamma = 5$, $M/m = 96$. There are about 25 electron super-particles per grid node in this area. In the plots shown, 20 charged super-particles corresponds to a density of about 3.9×10^{12}, and vice versa. Over the entire simulation region, the number of particles per cell varies. A more typical number is 15. Inside sheaths, the count is quite a bit less. (The same particle count would yield four times as many particles per cell were it applied with $\gamma = 10$). The last plot (of ion density, Figure 5-27) comes from a much longer period solution where time-step was allowed to vary. The time period covered immediately preceded the time period shown in the other three plots.

Figure 5-23 contains three plots which show, in order from the top, n_n, n_i, and n_e vs.

time. All show higher frequency oscillations than expected. Reasons for this may include:

- Too few super-particles
- A superposition of many waves

The first reason seems most likely. Let's look at the middle plot, n_i vs. time. Between $\hat{t} = 5$ and $\hat{t} = 20$, there are four peaks, translating to a frequency of $\omega \approx 1.7$. However, this frequency is too high for most ion oscillations. Very short wavelength acoustic oscillations could produce these fluctuations, but this source seems unlikely. Ionization events in the cell are also not responsible for the fluctuations; an ionization event would look like a step function. It seems most likely that the peaks in density are due to ion transits in a sparsely populated cell. Most peaks seem to have amplitudes between 10 and 20 percent of the total density. Ions here move at a mean velocity of about $< V_i >_) z \approx .155[x]/[t]$ (about 63 eV of energy), and each cell here is about $.28[x]$ wide. A node sees a particle (through interpolation) as it passes through 2 cell distances. Thus, if individual transits could be seen, they would have a characteristic time of $\tau = \Delta z / < V_i >_z \approx .56/.155 = 3.6$. This translates to a frequency of about $\omega = 1.7$, the same frequency we observe. Let us call this the "ion transit frequency", $\Omega_t = 1.7$, where the capital letter signifies that it originates with the ions. If this explanation is correct, then a higher particle count should diminish the noise. Similar reasoning explains the oscillations in the neutral density plot. There are, in this region, nearly a thousand neutrals per cell, which is why most oscillations are much smaller in amplitude. Since some neutrals are much larger than others, larger amplitude changes are possible, too. Neutrals here travel much slower than ions, explaining the width of the peaks. Electron noise can be explained, too. The time averaged $T_{||}$ is about 14.3 eV which means that the electrons move (parallel to $\vec{B}$) about three to four times faster than the previously discussed ions. Noise should have similar amplitude, but a frequency three to four times higher. This is about what we see.

To see oscillations underneath the noise, we filter the data using a simple algorithm: The density at time t is the average density in the period $t \pm \Delta t$,

$$n_e(t) = mean[n_e(t - \Delta t) : n_e(t + \Delta t)]. \tag{5.11}$$

This suppresses some of the spikes in the data. The filters at the beginning and end of the

run are one sided. For instance, near the end of a period lasting t_f, we use

$$n_e(t) = mean[n_e(t - \Delta t) : n_e(t_f)]. \tag{5.12}$$

This filter is most valid for constant time-step. The data is produced in terms of nominal plasma frequency ($w_{p,o} = 1/[T]$).

To be effective, the filter should average over many passage times. This makes the filter marginal when used to detect low frequency ion oscillations.

5.5.3 Electron Density Oscillations

Using only electron density with a filter of $\Delta t = 5$ time-steps (each measurement is the mean of 11), broad peaks close to $.6 - .9[\omega_p]$ (peaking at .9) and $1.1 - 1.2[\omega_p]$ are observed (see Figure 5-24). A smaller peak near $\omega \approx 1.5$ is also observed; perhaps this is correlated with the ion transit frequency, $\omega = 1.7$. The frequency at $\omega = .9$ seems to correspond to the plasma frequency; the peak in the FFT is weak, but the actual plot looks fairly sinusoidal. A filter of $\Delta t = 10$ time-steps seems to draw out an additional frequency band near $2 < \omega < 3$ (see Figure 5-25).

To see oscillations more clearly, the function $q = n_i - n_e$ was constructed and plotted in Figure 5-26. A filter level of 10 was applied after the vector q was constructed. The peak near $\omega = .9$ (the plasma frequency) is now stronger, which is a positive development. There are also additional peaks at $\omega = .7$ and, again, in the range $2 < \omega < 3$. The small peak at $\omega = 2.1$ corresponds to the upper hybrid frequency (predicted to be a 2.1), but this may just be serendipity.

5.5.4 Ion Density Oscillations

Ion waves may also be analyzed. Some ion waves are visible in the Fast Fourier Transform of Figure 5-27, which seems to show a peak in the range $.01 < \omega < .02$. This is too low to be the ion plasma frequency ($\Omega_p \approx .1$) or transit time oscillation, but too high to be anything else but a short wavelength ($R/\lambda > 6$) acoustic wave or noise. There is a broad, low frequency band near $.005 \leq \Omega \leq .0064$. These could be the ionization oscillation ($\Omega_i = .006$) or, again, an acoustic wave. The former assumption is not entirely improbable since the point chosen is very close to the point of greatest ion density near the anode. Ionization happens

here. There also seem to be weak peaks at $\Omega \approx .02$, $\Omega \approx .035$, and $\Omega \approx .05$ and still weaker peaks at $\Omega = .06$ and $\Omega = .07$. These could again be short wavelength acoustic waves, but the peaks are so small it is very hard to draw any conclusions. Of course, a higher particle count would help the analysis; noise is a problem.

In Section 5.2.8, we discussed the ionization oscillations which are clearly seen at $\dot{m} = .1676mg/s$. We did not see these at $\dot{m} = .1mg/s$ when the quasi-neutral injection method was used. However, they were observed at $\dot{m} = .1mg/s$ when the steady state ($I_c = I_d$) electron injection method was used. See, for instance, Figure 4-13. For this case, the wall potential is observed to oscillate along with the low frequency ionization oscillations. However, both Γ_i and Γ_e are proportional to n such that only a short period oscillation should be seen. The wall potential $< \phi_w >$ should not track the density on the time-scale of the ionization oscillation. This is another demonstration of the invalidity of the steady state boundary conditions. The plasma far from the wall is not quasi-neutral, and so the sheath does not behave as expected.

5.6 Diffusion

Mechanisms for diffusion in a Hall thruster include plasma oscillations, inter-particle collisions, and particle-boundary collisions. Electron diffusion resulting from scattering is termed "Classical." Diffusion resulting from other effects is often called "Anomalous" or "Bohm" diffusion.

5.6.1 Classical Diffusion

The theory behind classical diffusion was discussed in Chapter 2. Here we observe classical diffusion directly. Figure 5-28 shows a single electron diffusing across the magnetic field. This figure was obtained from the full simulation with $M_n/m_e = 960$ and $\gamma = 10$ (specifically, the beginning of the run shown in Figure 4-22). The particle is initially trapped on one field line, but then undergoes a collisions which kicks it to a different field line. Kinetic energy increases as the particle moves to the left, toward higher potential. (The anode is located at position z=0). Oscillations in energy occur as the particle spirals about a field line nominally perpendicular to a strong E field. Magnetic moment on each line is nominally conserved.

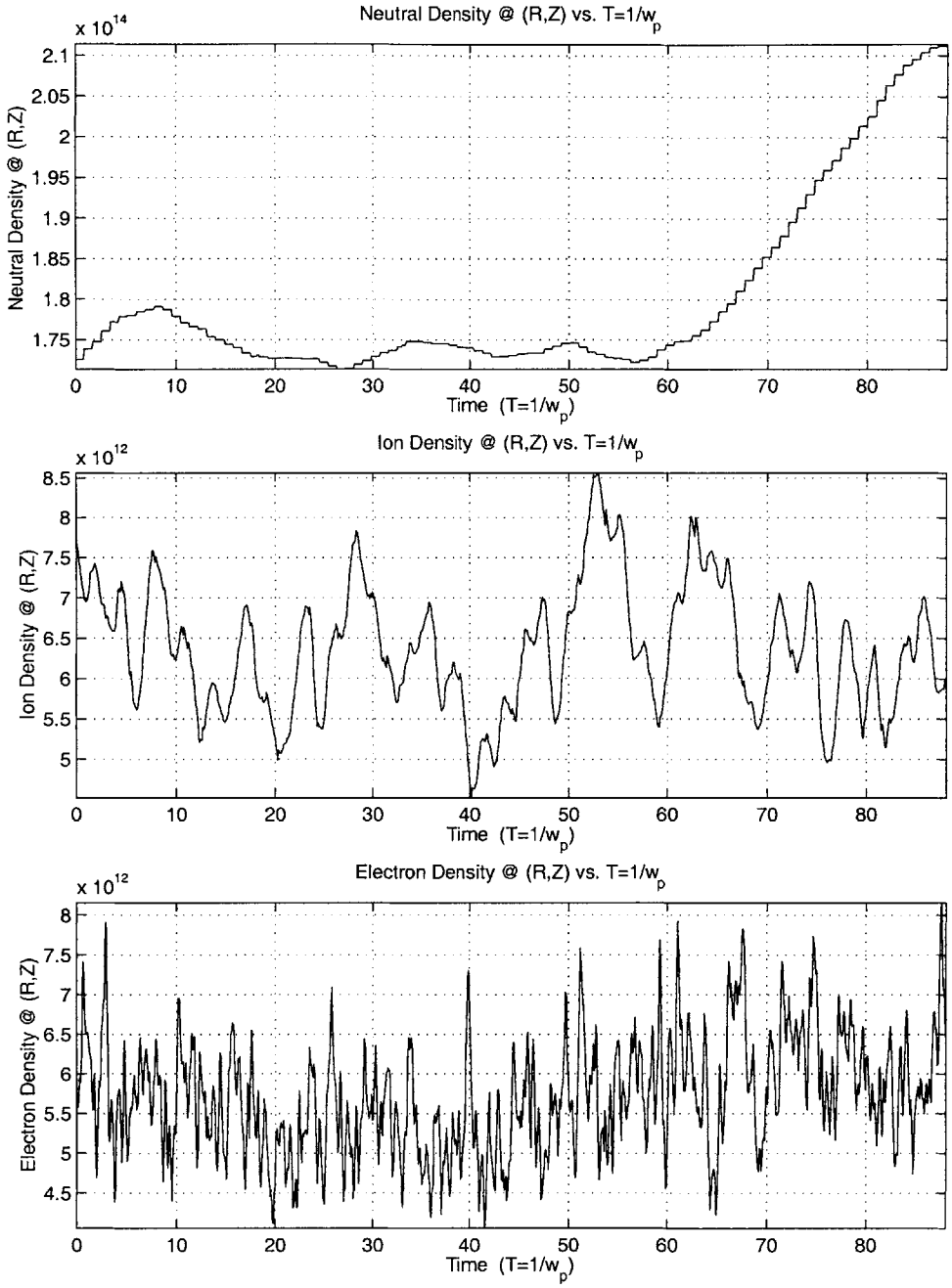

Figure 5-23: *Oscillations in* n_n, n_i, *and* n_e at point $(\xi, \eta) = (50, 65)$, just downstream from the anode. Large increase to the right of n_n plot is probably due to a large neutral super-particle; not all neutrals are the same size.

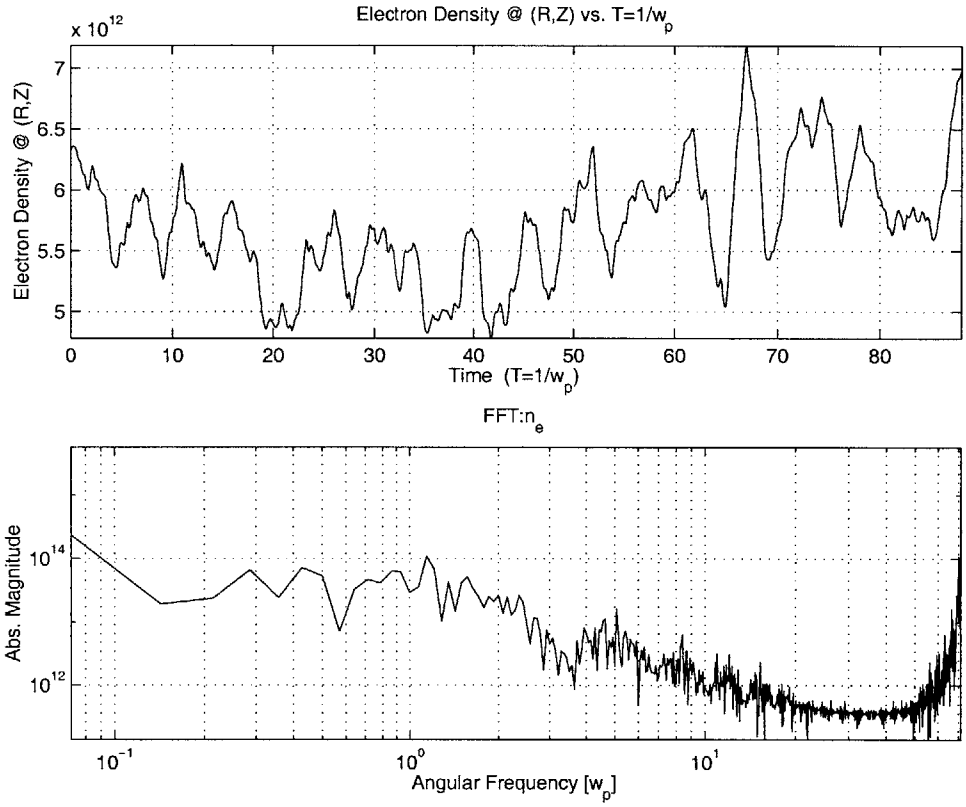

Figure 5-24: *Oscillations in* n_e at point $(\xi, \eta) = (50, 65)$, just downstream from the anode. Filter level of ± 5 time-steps is assumed. The almost sinusoidal portion at the right has a frequency of $\omega \approx 1.67$.

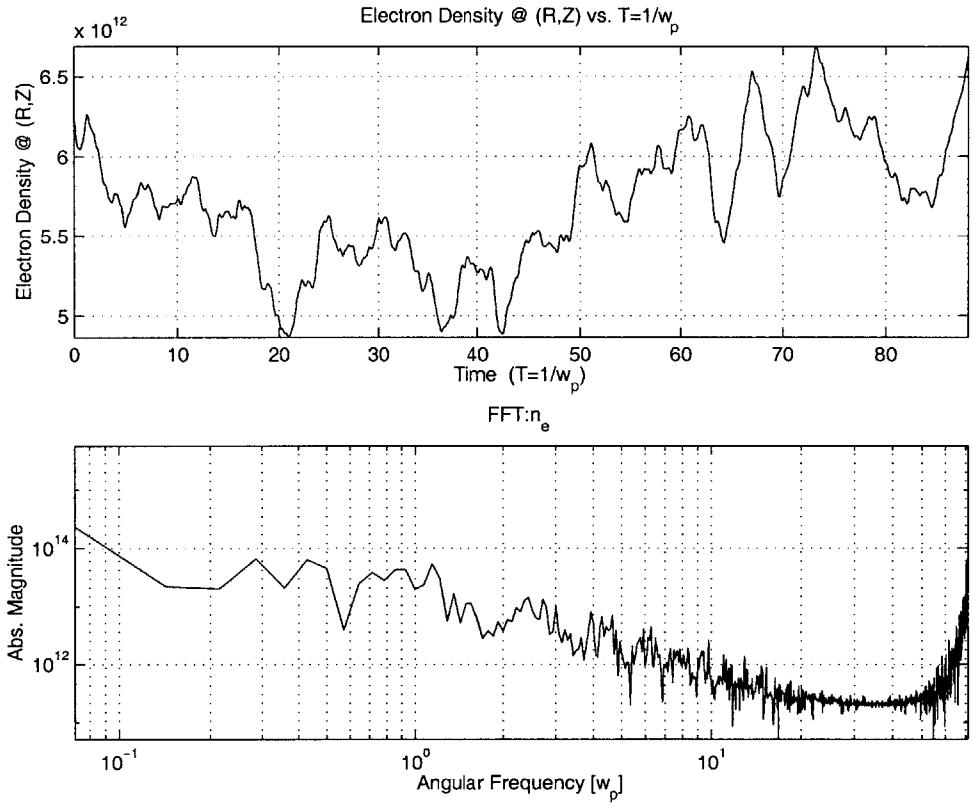

Figure 5-25: *Oscillations in* n_e at point $(\xi, \eta) = (50, 65)$, just downstream from the anode. Filter level of ± 10 time-steps is assumed. The broad peaks have a frequency of $\omega \approx .6$.

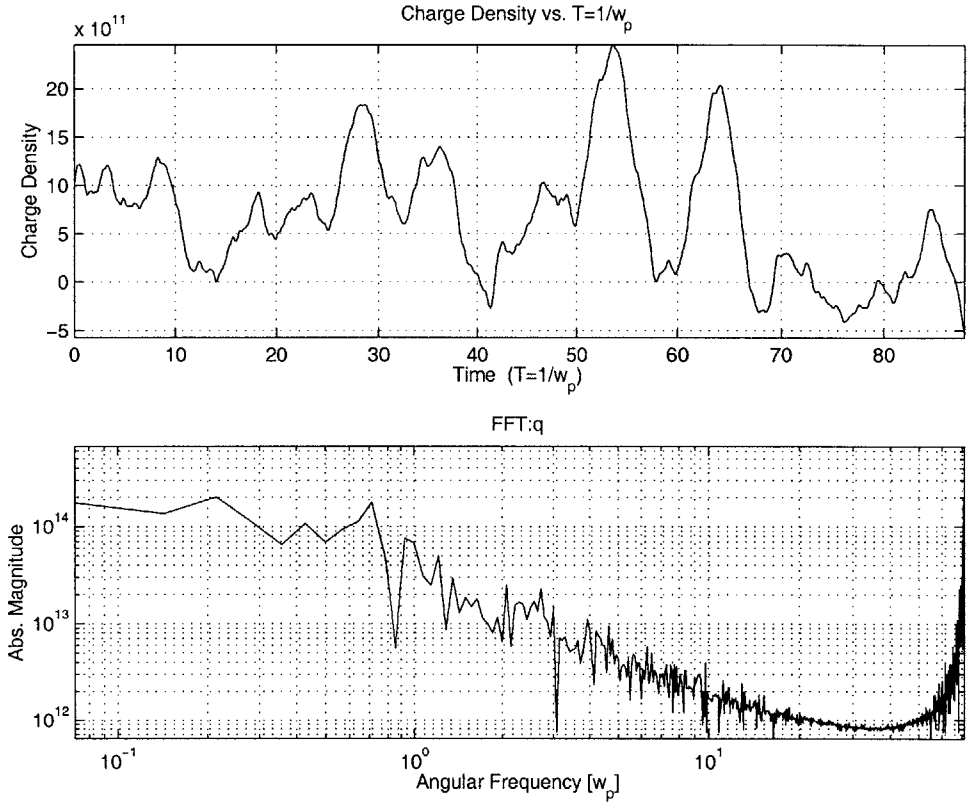

Figure 5-26: *Oscillations in the function* $q = n_i - n_e$ at point $(\xi, \eta) = (50, 65)$, just downstream from the anode. Filter level of ± 10 time-steps is assumed.

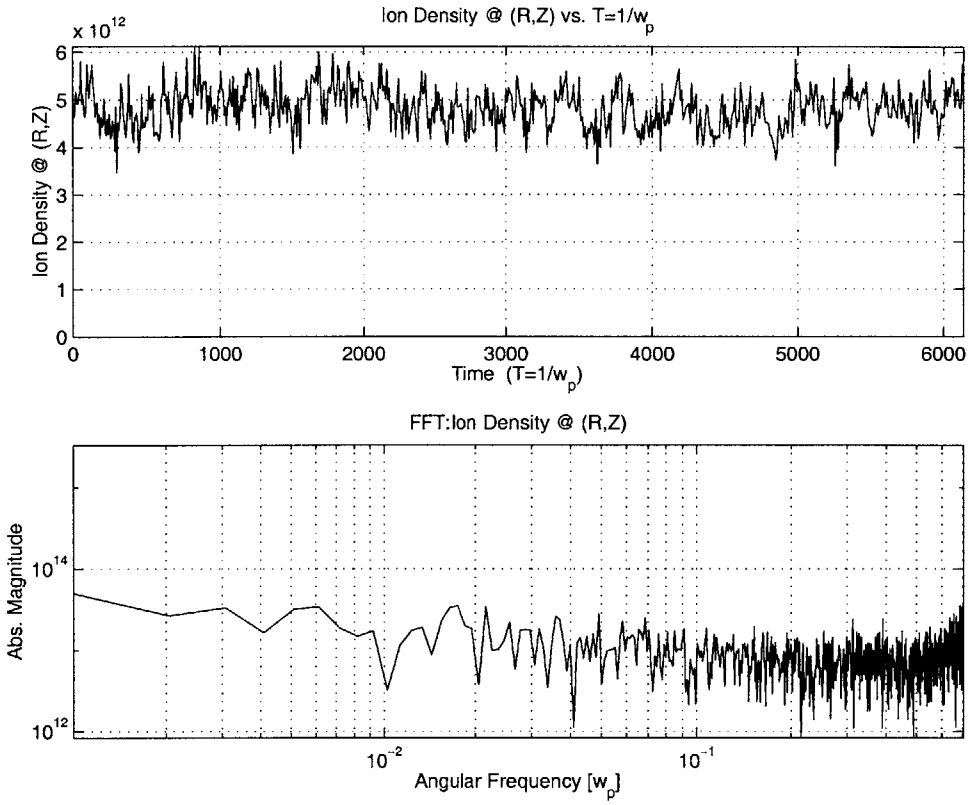

Figure 5-27: *Oscillations* n_i at point $(\xi, \eta) = (50, 65)$, just downstream from the anode. Plot shows density for the entire run plotted in Figure 4-23. No filter is used. Shallow peak near $\omega = .006$ may be ionization oscillation.

We can do a quick check to see if the observed Larmor radius seen in Figure 5-28 makes sense. If $E_\perp$ is the perpendicular energy of an electron in eV, $.5mv_\perp^2 = E_\perp$, and $v_\perp = \omega_c \times r_L$ defines the Larmor radius, then one can easily show that

$$r_L \approx 3.4 \frac{\sqrt{E_\perp}}{B} cm, \tag{5.13}$$

where B is the magnetic field strength in Gauss. For $B = 3000G$ and $E = 20$ eV, this formula yields $r_L = 5.07 \times 10^{-3}$ cm. To produce the trace shown in Figure 5-28, units were scaled by $[x] \approx .02$ cm. Therefore, we should see a radius of about $r \approx .005/.02[x] = .25$[x]. This is exactly what we see.

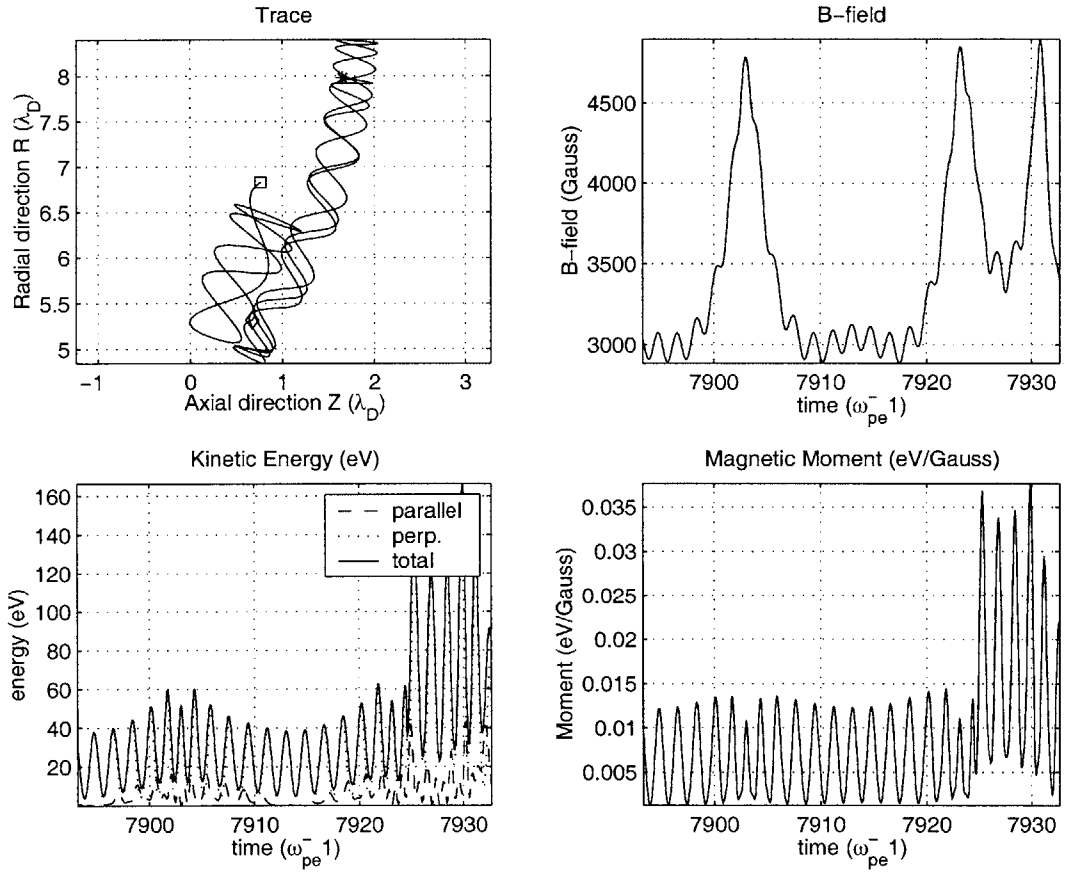

Figure 5-28: *A single electron diffusing across the magnetic field.* Particle begins at (*), undergoes a collision at diamond, and ends at square.

5.6.2 Anomalous Diffusion

In SPT type Hall thrusters, "anomalous" diffusion due to azimuthal oscillations and wall effects is thought to significantly increase electron transport. In TAL thrusters, such diffusion would rely upon azimuthal oscillations not captured by this simulation. However, "anomalous" diffusion may be introduced through an equivalent scattering frequency (see Section 2.10.5). The total electron collision frequency becomes, sans Coulomb collisions,

$$\nu_e = \nu_{en} + \nu_{Bohm}. \tag{5.14}$$

Bohm diffusion is typically assumed to be proportional to $\frac{1}{16B}$. In Hall thrusters, diffusion proportional to $\frac{1}{64B}$ is a better assumption; similar rates are required by many 1-D analytic models and by the 2-D Hybrid PIC code to match experimental measurements [52]. For diffusion proportional to $\frac{1}{64B}$, a frequency of $\nu_{Bohm} = \frac{1}{64}\omega_{ce}$ is appropriate. This means that the Hall parameter, $\beta = \omega_c/\nu_e$ is numerically limited to less than 64. To compensate for artificial mass ratios, ν_{Bohm} must be increased;

$$\nu'_{Bohm} = \nu_{Bohm}\sqrt{\frac{M_n}{M'_n}}. \tag{5.15}$$

A mass ratio of $M_n/m_e \approx 960$ requires $\sqrt{M_n/M'_n} \approx 16$ such that β' is numerically limited to about 4. This is sufficient to ensure that the electron diffusion rate across the field is still nearly proportional to the collision frequency.

The code was run both with and without anomalous diffusion. The control case is shown in Figure 4-22. This case assumed $\dot{m} = .1$ mg/s, $\gamma = 10$, and $M_n/m_e \approx 960$. Obviously, the simulation converges with only classical diffusion. The second case, which includes stochastic Bohm diffusion according to 1/64, is shown in Figure 5-29. Performance predictions for both cases are summarized in Table 5.7. Unfortunately, neither solution is fully converged (to the longest *neutral* time-scale) due to time constraints. Therefore, thrust efficiency and specific impulse in Table 5.7 are derived from ion thrust. This enables a more accurate comparison.

The most remarkable thing about Figure 5-29 is that it is, at first glance, almost indistinguishable from Figure 4-22. A closer look reveals that addition of stochastic anomalous diffusion changed performance predictions slightly. Table 5.7 shows that thrust and specific

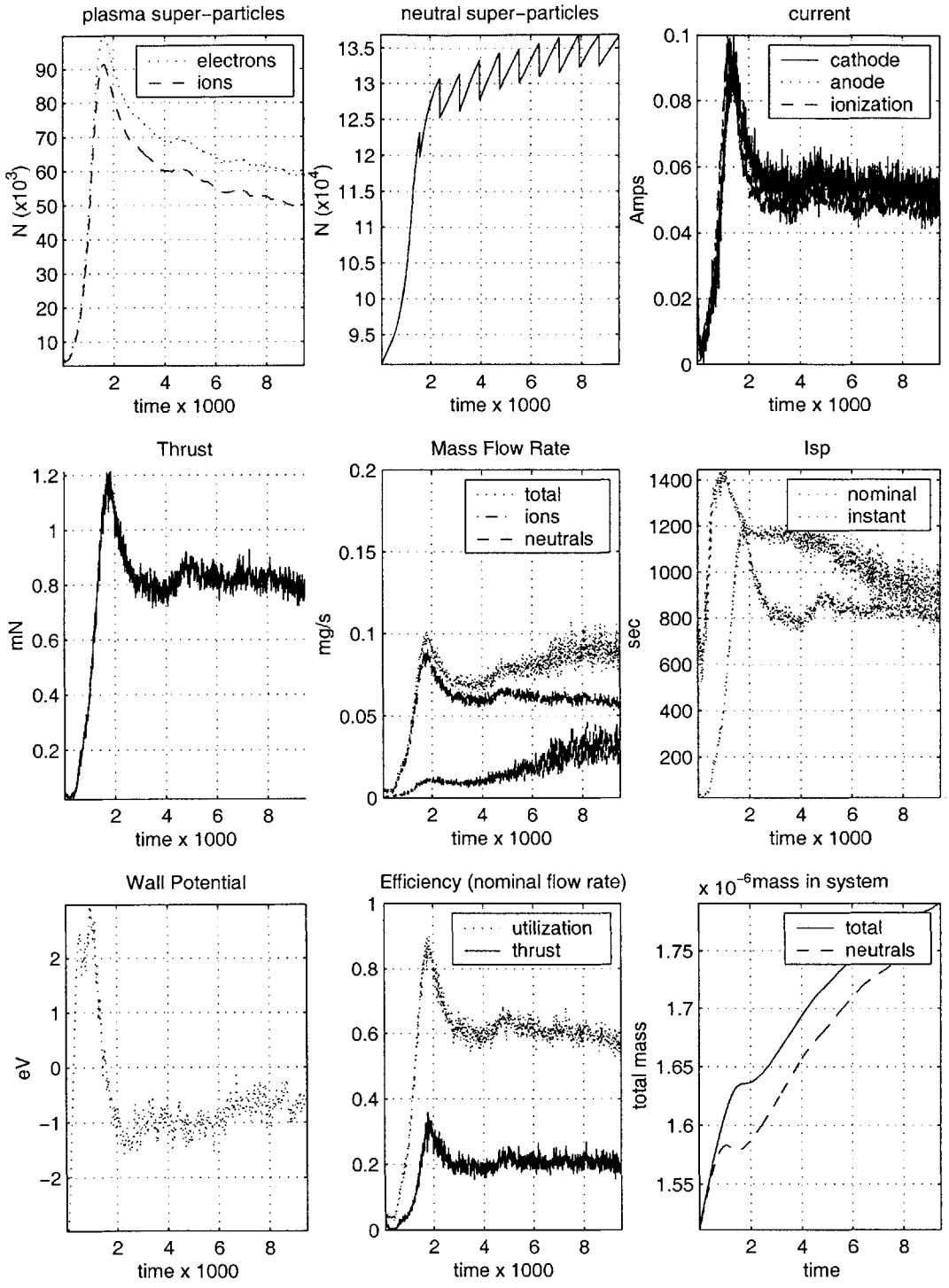

Figure 5-29: *Performance including Bohm type anomalous diffusion.* Performance for $\gamma = 10$, $M_n/M_n' = 250$, $s_o = 50$, $C = 1 \times 10^{-10}$. Quasineutral cathode electron injection assumed. MCCC Coulomb collisions only. $E_z = 0$ at RHS. Sheath calculated explicitly on upper right boundary. Solution is not fully converged. Compare to Figure 4-22, which assumed no anomalous diffusion.

impulse both increased by about ten percent. Wall potential seems to be slightly higher with Bohm diffusion, reflecting perhaps increased impedance in the direction parallel to the Magnetic field. The discharge current increases slightly, but because thrust increases, the thrust efficiency does not change much. The various currents are shown in Figure 5-30.

Coulomb Type	No Bohm	Bohm
I_{sp} (sec)	690	753
Ion Thrust (mN)	.68	.74
η_t	.17	.17
η_u	.53	.58
η_a	.37	.37

Table 5.7: Summary of Bohm diffusion results. All predictions assumed MCCC V1, $M/m \approx 960$,$\gamma = 10$, and $\dot{m} = .1$mg/s. Thrust efficiency and I_{sp} refer to ion thrust only, which enables us to more accurately compare solutions which have yet to converge on the longest neutral transit time scale.

Numerically, then, the addition of anomalous diffusion does not seem to change much. Performance increased a little, but not a lot. Of course, the mass flow rate and magnetic field strength are also factors contributing to electron transport. If the magnetic field were lower in magnitude, then D_B would be higher and hence the bulk transport rate due to Bohm diffusion would increase. Such may have been the case with Khayms thruster experimentally.

Numerical note: During write-up, a slight error was discovered in the anomalous diffusion algorithm: No electrons to the left of the anode face were being scattered. This should make very little real difference, since the point of adding anomalous diffusion was to increase transport across $\vec{B}$ *to* the anode.

5.6.3 Mach Number

The mach number of the plasma is of general interest. Let the local acoustic speed be $v_a = \sqrt{KT_e/M}$. The Mach number can then be defined

$$M = \frac{| < v_i > |}{v_a}, \tag{5.16}$$

where $| < v_i > |$ is the bulk speed of the ions. The Mach number for the parameters just presented, $M/m \approx 960$, $\gamma = 10$, with anomalous diffusion is plotted in Figure 5-31. The

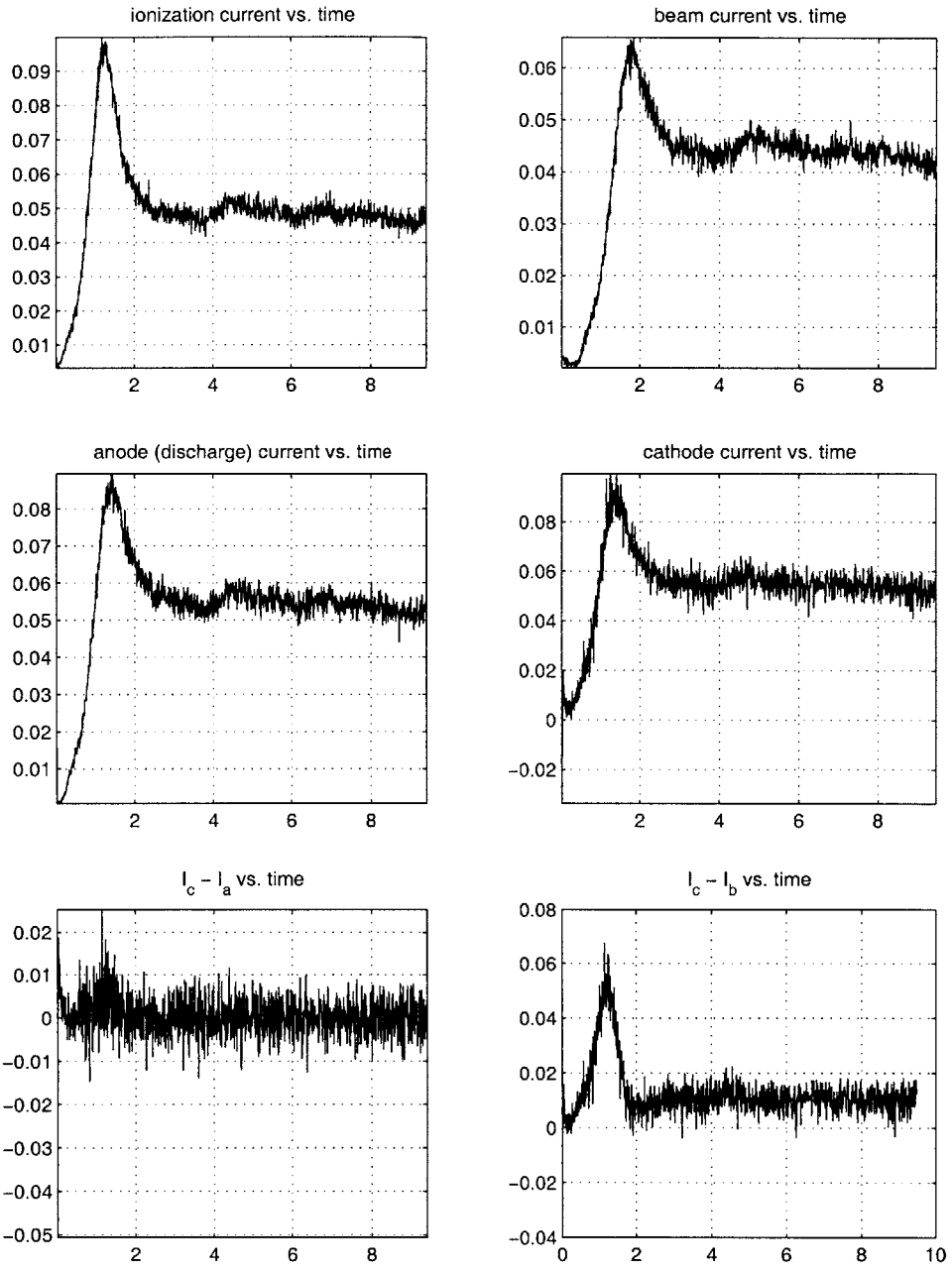

Figure 5-30: The simulation coming to equilibrium from $t = 0$ at $\dot{m} = .1$ mg/s, $M/m \approx 960$, $\gamma = 10$, *with Anomalous diffusion* and MCCC Version 1.0 Coulomb collisions.

electron temperature, T_e, was time averaged over 100 iterations, but v_i is instantaneous, the ion velocity at the end of the run. Also plotted is the instantaneous ion density, n_i, which shows the primary zone of ionization to be upstream of the $M = 1$ streamline.

If we define the ionization zone as being the region before the $M = 1$ contour, then the extent of the ionization zone is less than 5 [x]. Given (for $\gamma = 5$ and $T_e = 25$) the electron cyclotron radius is about .6[x], Thus, the extent of the zone of acceleration is 5-10 electron cyclotron radii from the anode. This is consistent with the estimate found in Section 2.11. For this reason, it is appropriate to term the mini-TAL an "anode layer thruster", as defined in the Russian literature [12].

5.7 Ion-Neutral Scattering Error

The method for scattering ions off neutrals was discussed in in Section 3.15.3. We conserved momentum in such collisions by increasing or decreasing the neutral bulk momentum. We conserved energy by increasing or decreasing the internal energy of the neutrals. We did so by multiplying neutral relative velocities by the scalar α, given by Equation 3.179. However, an error in the calculation was discovered after many of the results presented in this thesis were compiled. Instead of using $\alpha^2 = \frac{E_{bulk,o}+E_{internal,o}+\Delta E-E_{bulk,f}}{E_{internal,o}}$, the simulation was computing α according to $\alpha^2 = \frac{E_{bulk,o}+\Delta E-E_{bulk,f}}{E_{internal,o}}$. Thus, it was removing too much energy from the neutrals. To show that this makes little difference to the final results obtained, we ran the simulation with the error corrected. Results are shown in Figure 5-32. This Figure should be compared to Figure 4-22. The hoped for result is obtained; performance is nearly the same.

Numerical note: Simulations which are slightly tainted by the ion-neutral scattering error include all those presented in Chapter 4, as well as those which assumed $\gamma = 5$, with the exception of the high frequency oscillation plots. The anomalous diffusion simulation was also slightly tainted. Simulations without the error include all of the Coulomb collision tests, and the test of the new geometry.

Numerical note: After running the fixed simulation for about 130 thousand iterations, an error flag appeared indicating that $\alpha \leq 0$. This error occurs very infrequently; we ran the simulation for 1000 additional electron/ion time-steps in "debug" mode and failed to produce the flag. The cause is unknown at this date, but it may be due to $\alpha = 0$, which is not necessarily an incorrect result. In any case, it should not change the simulation results in any noticeable way.

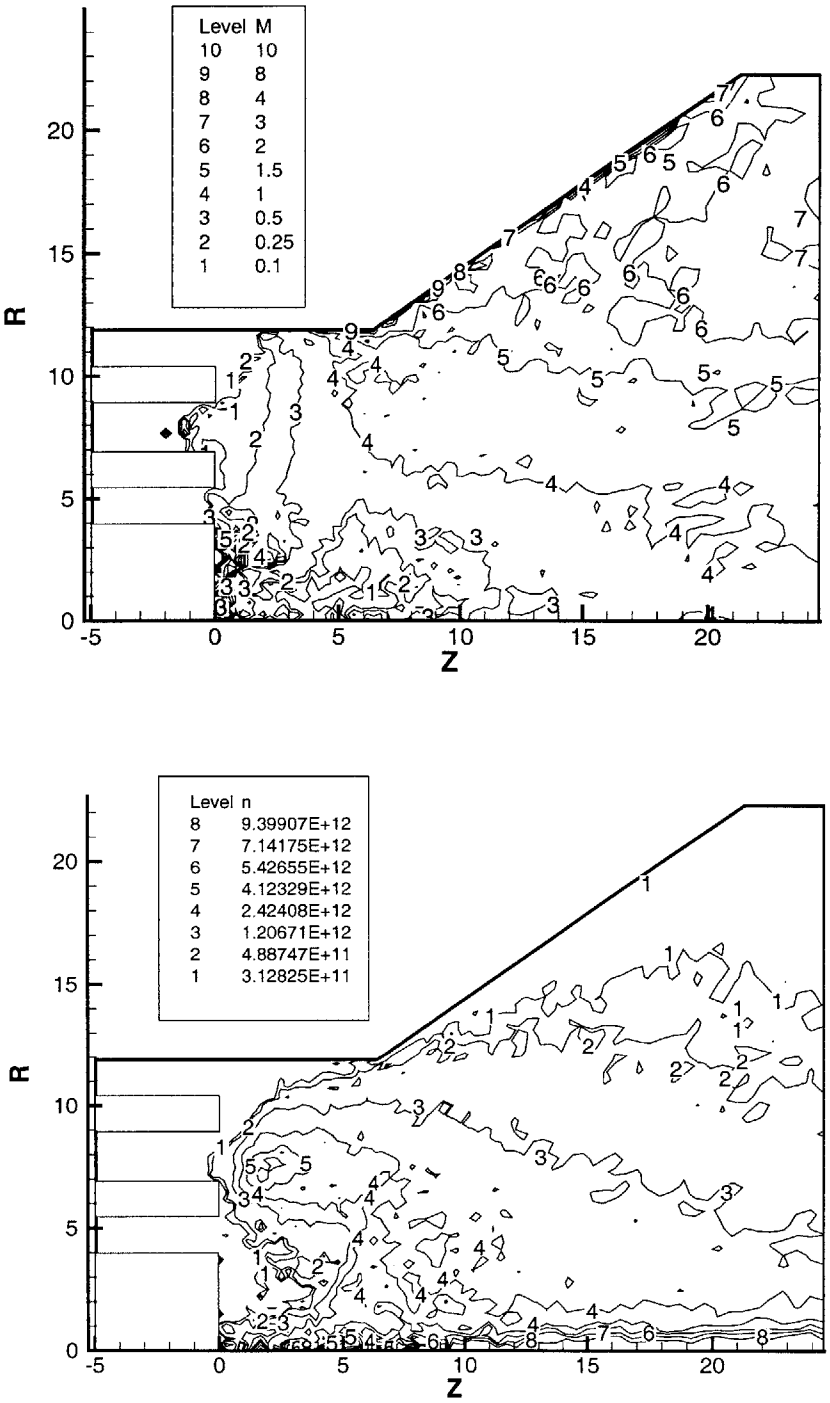

Figure 5-31: *Mach number* $M = | < v_i > |/v_a$ and ion density, for $\gamma = 10$, $M_n/M_n' = 250$. Conditions are taken from the end of the run shown in Figure 5-29. Anomalous diffusion is included.

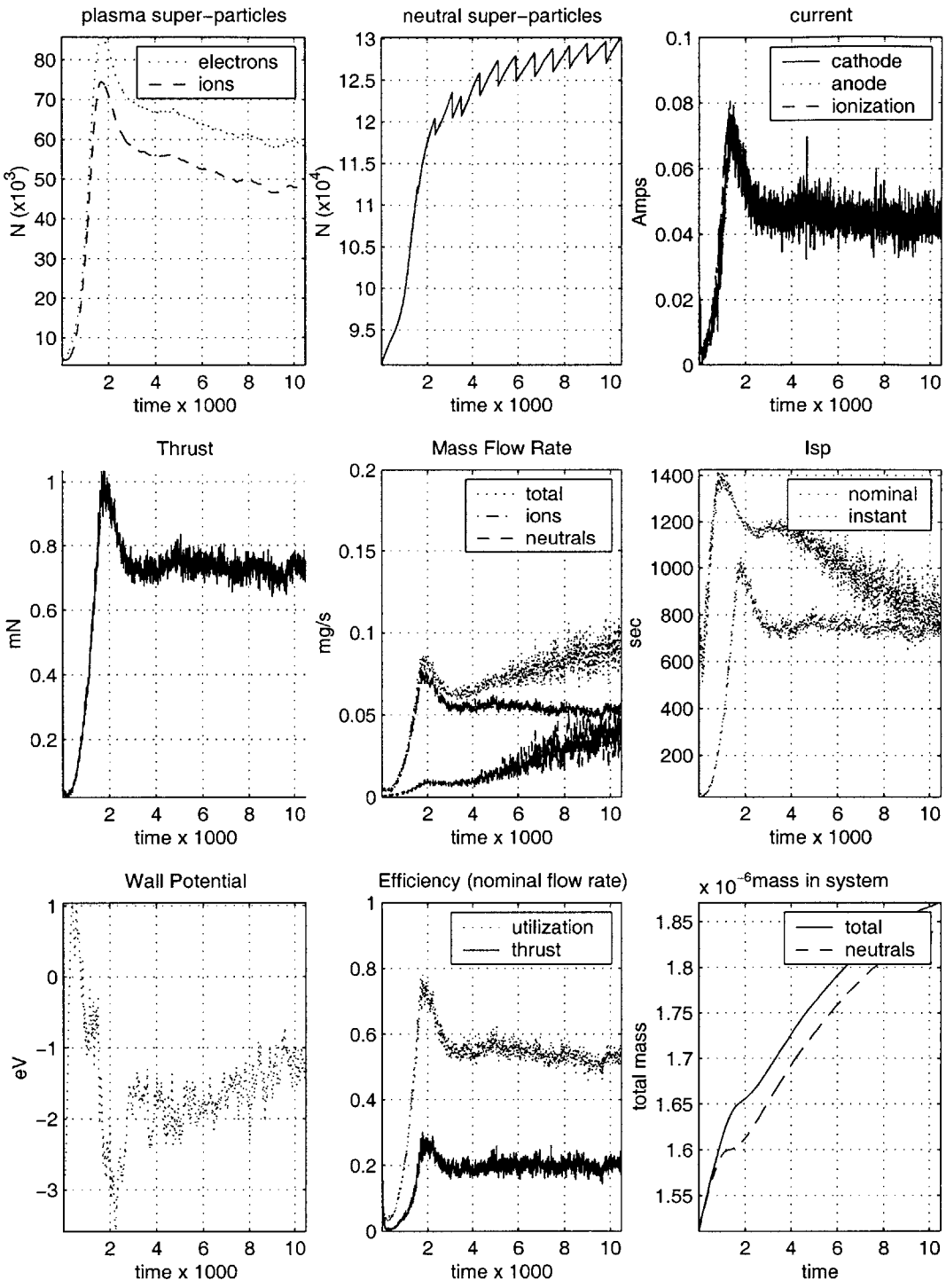

Figure 5-32: *Correct rate of neutral internal energy removal for ion-neutral scattering events.* Performance is extremely similar to that shown in Figure 4-22, which was obtained from a simulation which removed too much neutral internal energy. Performance for $\gamma = 10$, $M/m \approx 960$, $s_o = 50$, $C = 1 \times 10^{-10}$. MCCC Coulomb collisions Version 1.0. Solution is not fully converged. No anomalous diffusion.

5.8 Coulomb Collisions

Electron-electron and electron-ion Coulomb collisions are often considered to be unimportant in Hall thruster models. That assumption is tested parametrically by running the simulation with both Monte Carlo Coulomb Collision methods, the Langevin Coulomb collision method, and no Coulomb collisions whatsoever. For all these tests we use $\gamma = 10$ and a high mass ratio, $M/m \approx 960$. This mass ratio was used to ensure that results from the Monte-Carlo Coulomb Collision algorithms were not warped by loss of electron magnetization. Performance predictions for the various Coulomb collision algorithms are summarized in Table 5.8.

Coulomb Type	None	Langevin	MCCC V1	MCCC V2
I_{sp} (sec)	675	663	690	736
Ion Thrust (mN)	.66	.65	.68	.72
η_t	.17	.16	.17	.18
η_u	.52	.52	.53	.57
η_a	.37	.36	.37	.36
T_n/T	.08	.09	.08	.08

Table 5.8: Summary of Coulomb collision results. All predictions assumed $M/m \approx 960$,$\gamma = 10$, and $\dot{m} = .1$mg/s. Thrust efficiency and I_{sp} refer to ion thrust only, which enables us to more accurately compare solutions which have yet to converge on the longest neutral transit time scale. T_n/T is fraction of total thrust derived from neutrals, but is very approximate as simulations are not fully converged on neutral transit time-scales.

5.8.1 Rationale

Most Hall thruster PIC simulations ignore Coulomb collisions altogether. Indeed, the mean free path for these collisions should be long in the discharge, where electron temperatures are on the order of $10 - 30$ eV or more. However, the electron temperature is much lower outside the discharge. In areas where T_e is less than a few electron volts, the cross section for Coulomb collisions is actually quite large. Even in the discharge, these events influence the low energy population.

5.8.2 Monte Carlo Coulomb Collisions

The simulation was validated using a Monte Carlo Coulomb Collision (MCCC) model. Version 1.0 of this model (see Section 3.15.4) was used to generate the bulk of the results

presented in this Chapter. However, the model under-estimated transport by neglecting the Coulomb logarithm. Figure 5-32 shows results for this model, assuming $M/m = 960$. (It is most accurate to use a high mass ratio for this algorithm to keep highly collisional electrons magnetized). Specific impulse, ion thrust, utilization, acceleration efficiency, and thrust efficiency derived from ion thrust only are shown in Table 5.8. Instead of converging this run further, we used it as the starting point for several new runs. Thus, Table 5.8 also shows results from MCCC Version 2.0, as well as Langevin Coulomb collisions and no Coulomb collisions whatsoever. All predictions are time averaged over the last 10,000 iterations of the respective run.

First, we tested Version 2.0 of the MCCC model (see Section 3.15.4), which includes the Coulomb logarithm and revises the electron-electron cross section. Results from Version 2.0 are shown in Figure 5-33. The starting distributions were those at the end of Figure 5-32, at time $\hat{t} = 10,500$. Performance predictions are found in Table 5.8.

5.8.3 No Coulomb Collisions

Figure 5-35 shows both the initial run ($\hat{t} < 10,500$) and an additional 30,000 iterations *without any Coulomb collisions at all.* The various currents are shown in Figure 5-34. Performance predictions are found in Table 5.8. Without Coulomb collisions, performance drops but so does current such that thrust efficiency actually increases. Thrust and specific impulse have decreased, although efficiencies are largely unchanged.

5.8.4 Diffusive (Langevin) Coulomb Collisions

An alternative to MCC Coulomb collisions was devised and implemented. The algorithm, based on a Langevin formulation of the Fokker-Planck collision term, is described in Section 3.16. We also showed in Section 3.16 that this algorithm drives a single electron toward a Maxwellian at T^{β}, where β is the background species.

To see if this "more correct" way of modeling Coulomb collisions changes the results, we run a parametric test. Starting yet again from the distributions at the end of Figure 5-32, at time $\hat{t} = 10,500$, we ran the simulation fifty thousand iterations using the Langevin method to model both electron-electron and electron-ion collisions. Except for the substitution of the diffusive Coulomb collision algorithm for the old MCC algorithm, the simulations are identical. Charged particle transit times found in Section 2.7 are much shorter than $\Delta\hat{t}$;

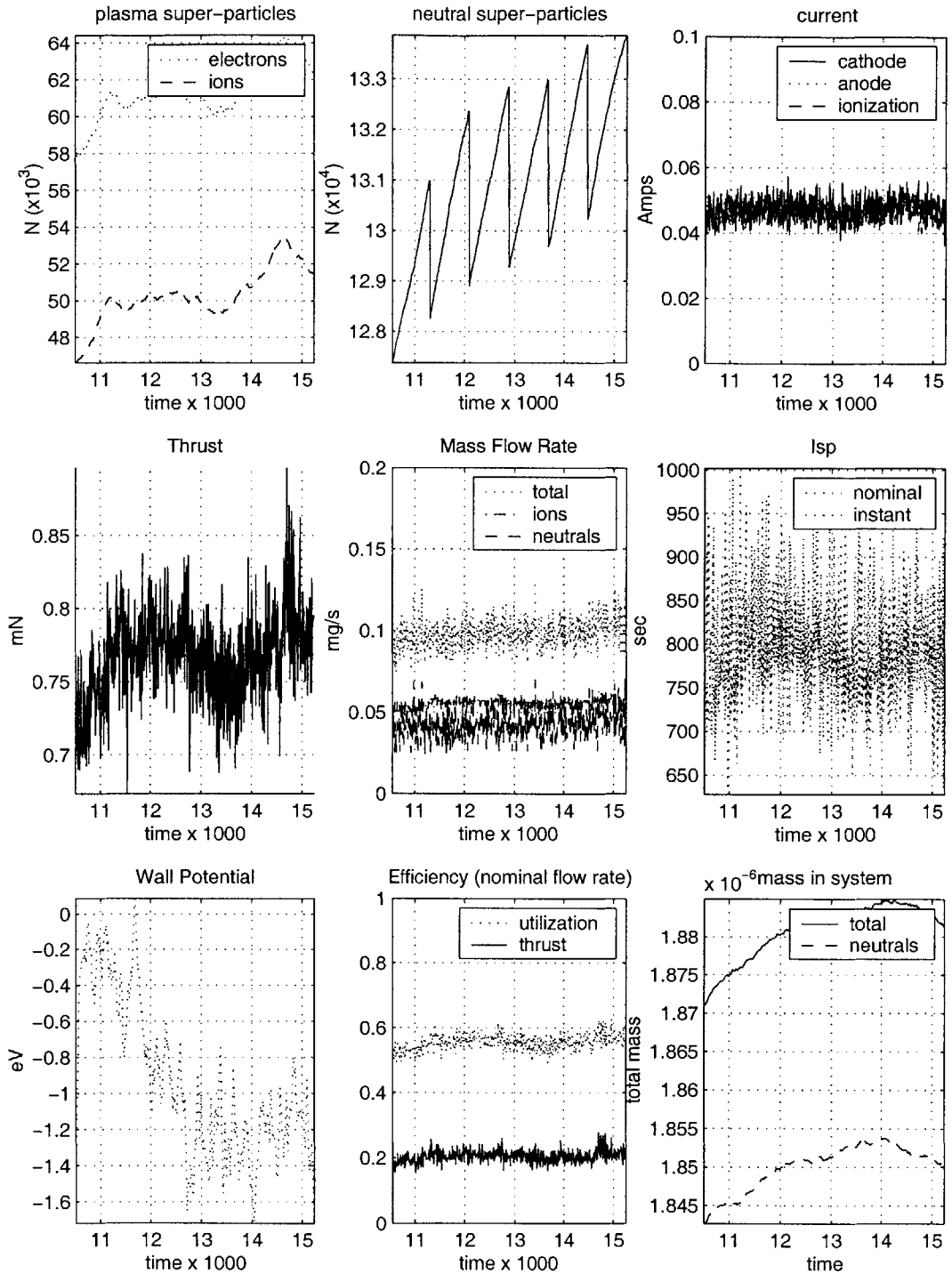

Figure 5-33: *Results from MCCC Version 2.0.* Performance for $\gamma = 10$, $M/m \approx 960$, $s_o = 50$, $C = 1 \times 10^{-10}$. Quasineutral cathode electron injection. Correct ion-neutral scattering. No anomalous diffusion. Not fully converged.

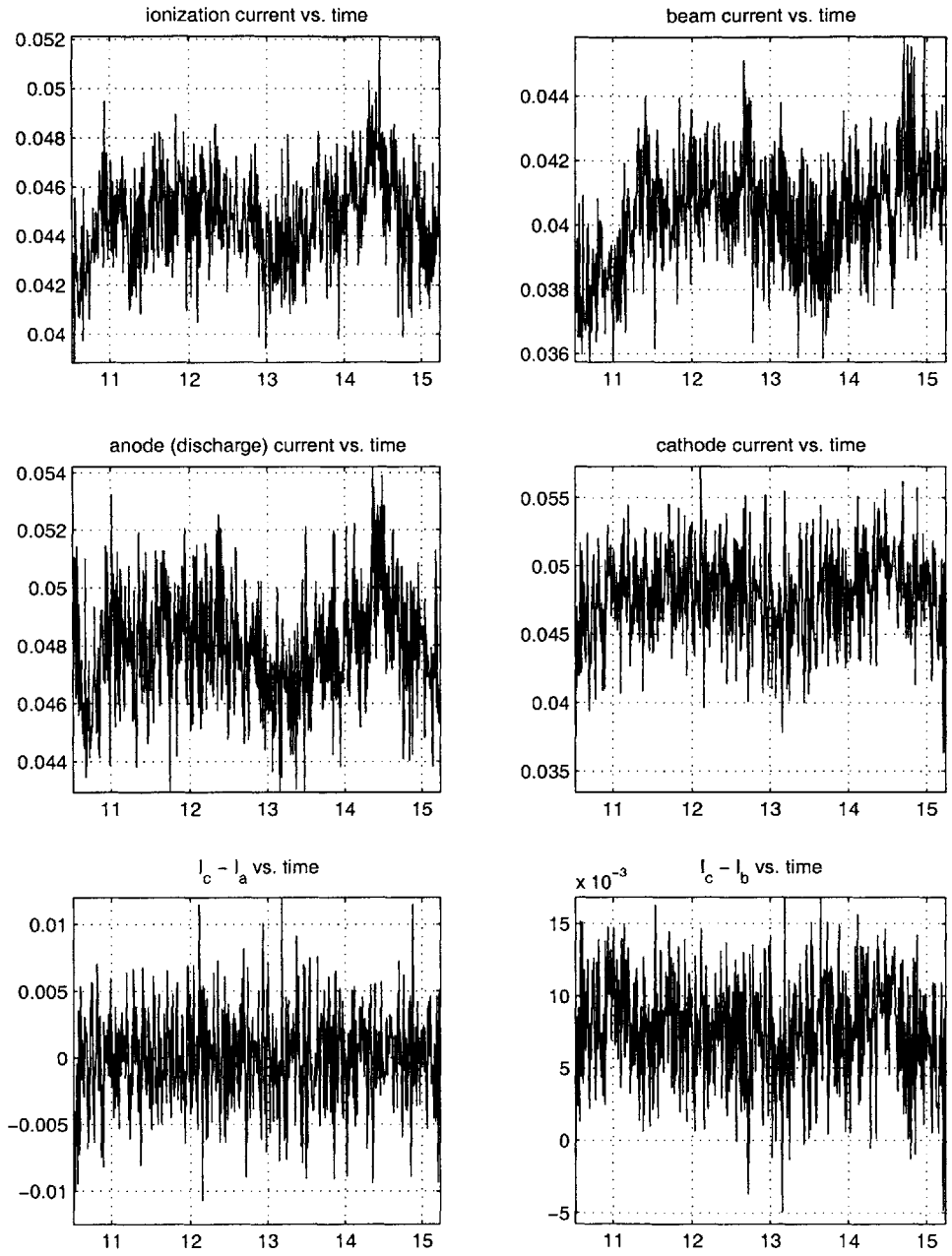

Figure 5-34: The simulation coming to equilibrium from $t = 10,500$ at $\dot{m} = .1$ mg/s, $M/m \approx 960$, $\gamma = 10$, *MCCC Version 2.0* (see Figure 5-33). Cathode, discharge, ionization currents higher than control case, period $t < 10,500$ in Figure 5-36.

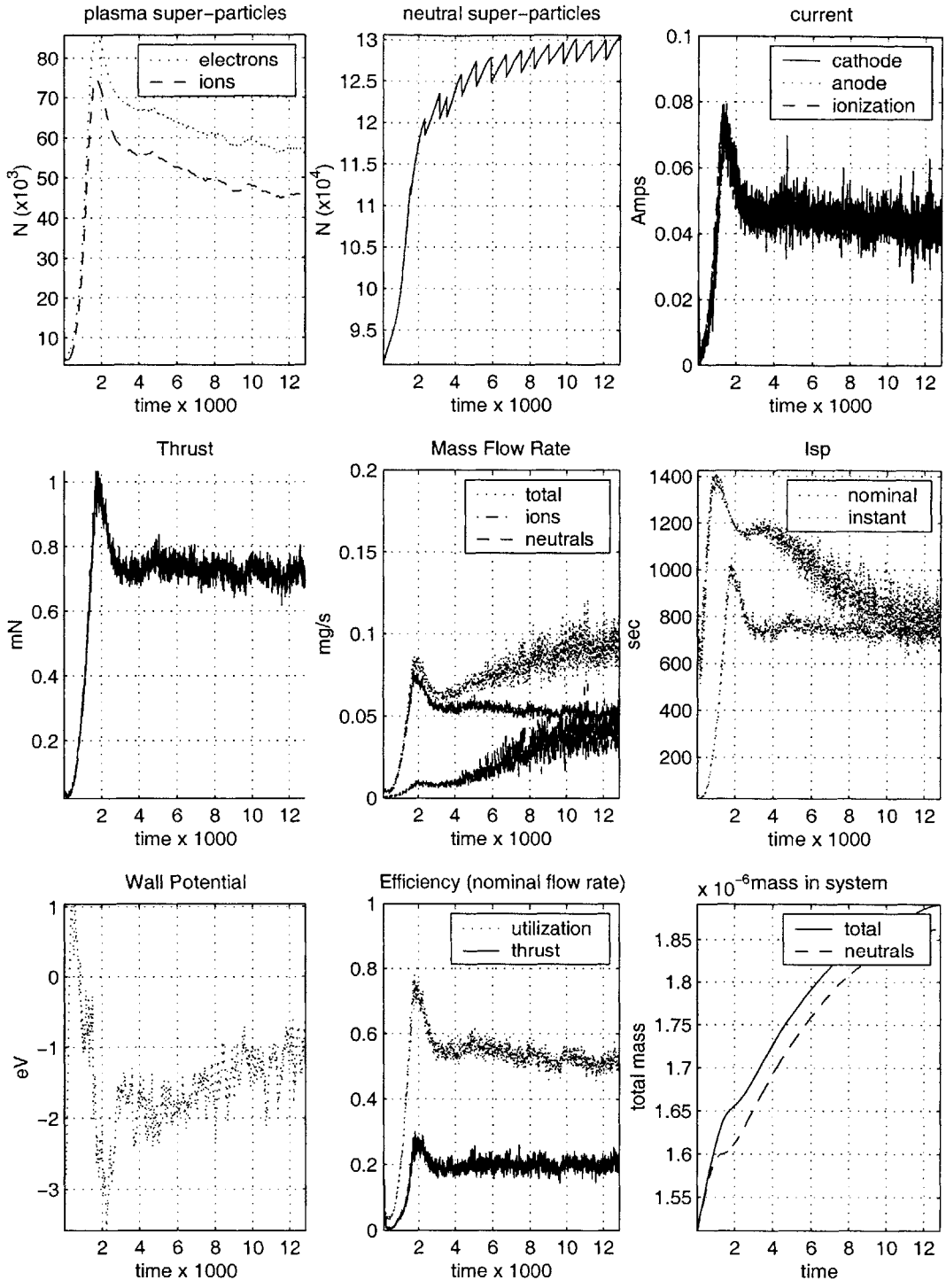

Figure 5-35: Performance for $\gamma = 10$, $M/m \approx 960$, $s_o = 50$, $C = 1 \times 10^{-10}$. Quasineutral cathode electron injection. "Corrected" ion-neutral scattering. No anomalous diffusion. Not fully converged. Two regimes are shown: $\hat{t} < 10,500$, *MCCC Version 1.0*; $\hat{t} > 10,500$. *No Coulomb collisions.*

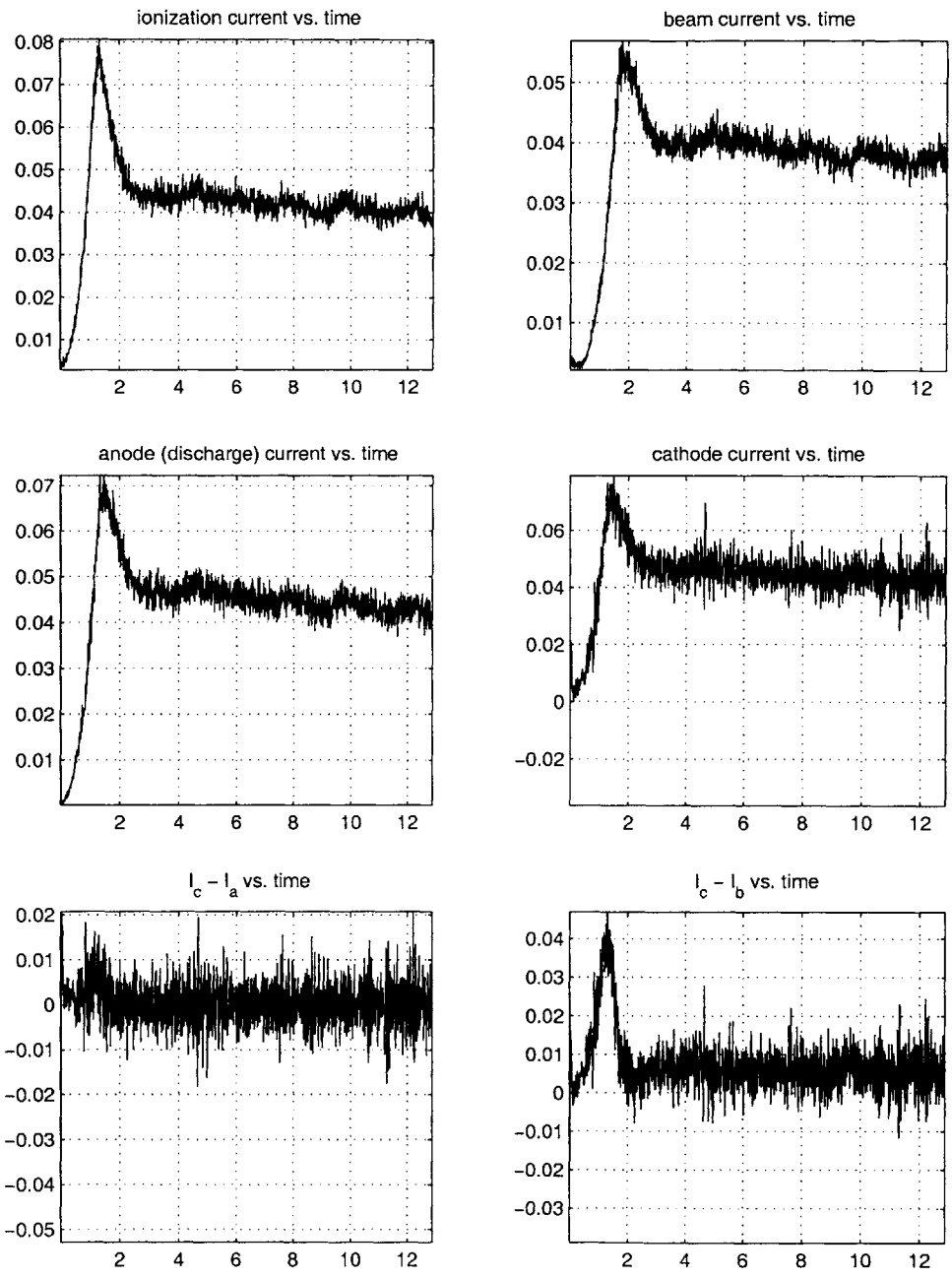

Figure 5-36: The simulation coming to equilibrium from $t = 0$ at $\dot{m} = .1$ mg/s, $M/m \approx 960$, $\gamma = 10$, no Anomalous diffusion (see Figure 5-35). Two regimes are shown: $\hat{t} < 10,500$, *MCCC Version 1.0*; $\hat{t} > 10,500$. *No Coulomb collisions.*

effects should be visible by the middle of this simulation. Neutral transit times are much longer; the discharge should be fully developed, but the far field neutral distribution is still a work in progress.

Performance results are shown in Figure 5-37. Performance predictions are summarized in Table 5.8. Currents are shown in Figure 5-38. While the particle count is closer to that obtained using MCCC Version 2.0, other performance parameters are more similar to those obtained without any form of Coulomb collisions whatsoever!

A comparison of results obtained with Langevin Coulomb collisions and no Coulomb collisions indicates that ion thrust and specific impulse changed by only about one percent. This is statistically insignificant.

5.8.5 Changes in Electrical and Beam Efficiencies

Let us consider the currents once again. In a steady state, $I_d = I_c = I_i \times I_b/I_i + (I_c - I_b)$. The quantity I_i is the amount of ions created, and the quantity $\eta_b = I_b/I_i$ is the percentage of ions created which actually enters the beam, the beam efficiency. Ions which do not enter the beam recombine at the walls somewhere. The last quantity, $I_c - I_b$, is the "leakage", the amount of additional electrons required to sustain the discharge. This determines the electrical efficiency, $\eta_e = I_b/I_d$.

Figures 5-34 and 5-36 show electrical efficiencies of between 82 and 88 percent and beam efficiencies of about 90 percent. Of course, we could calculate these numbers precisely by integrating over time (we do this in Section 5.10.3). Looking back at Figure 5-30, we see that adding Bohm diffusion did not have much effect on the beam efficiency, but increased leakage from about 10 percent before to about 18 percent after. This is why, though thrust and I_{sp} increased, the thrust efficiency did not.

5.8.6 Changes in Distribution Function

Figures 5-39, 5-40, and 5-41 show the perpendicular distribution function $g(\epsilon'_\perp)$ gathered on streamlines near the anode assuming $M/m = 960, \gamma = 10$. Figure 5-39 was obtained using no Coulomb collisions, 5-40 was obtained using MCCC V1, and 5-41 was obtained using Langevin Coulomb collisions. The first two plots are very similar to each other and to Figure 5-21, obtained with $M/m = 96, \gamma = 5$, and MCCC V1 collisions. All three show non-Maxwellian features. The Langevin plot, however seems to show a more Maxwellian

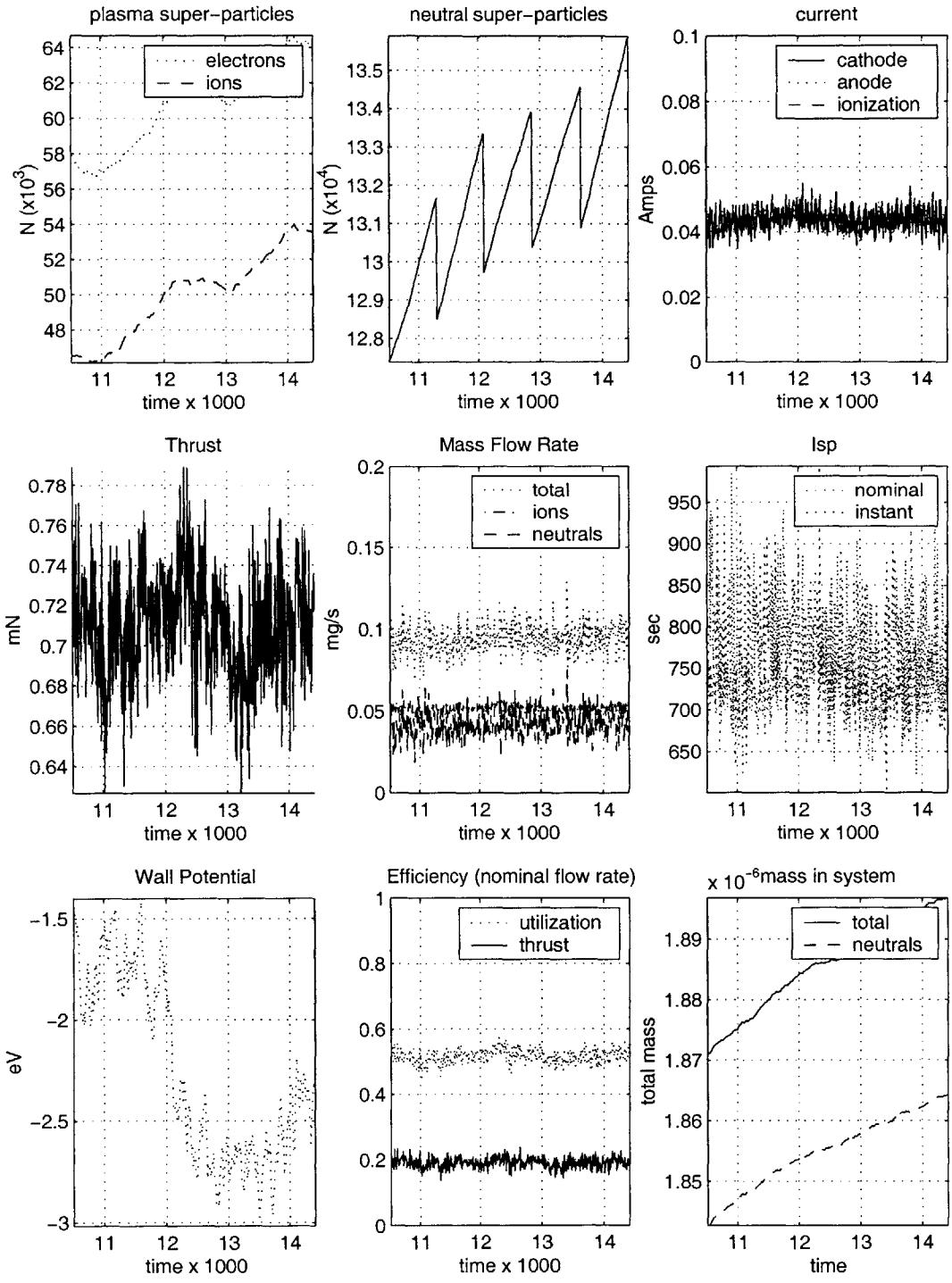

Figure 5-37: *Langevin Coulomb collisions.* Performance for $\gamma = 10$, $M/m \approx 960$, $s_o = 50$, $C = 1 \times 10^{-10}$. No anomalous diffusion.

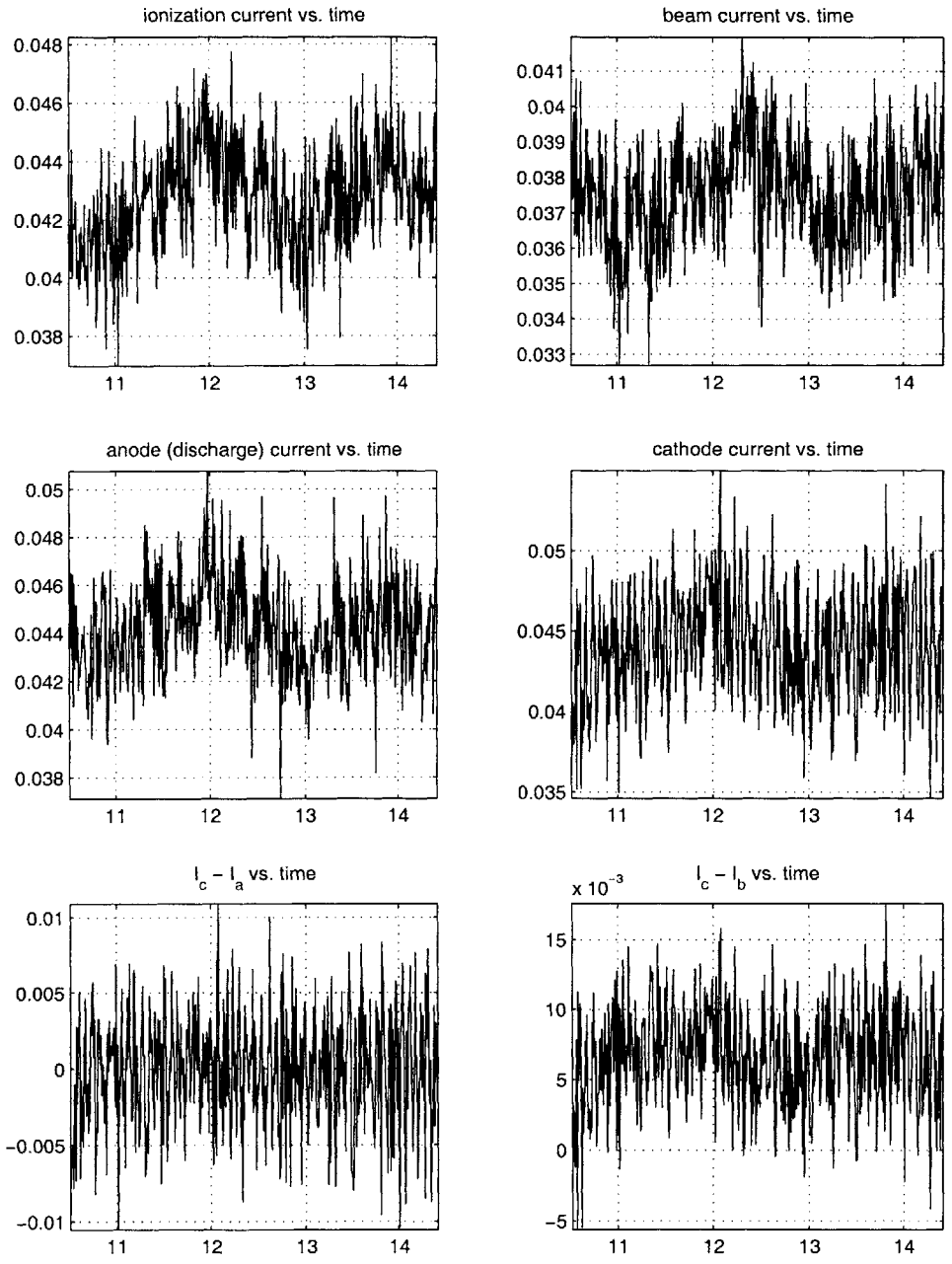

Figure 5-38: *Currents when Langevin Coulomb collisions are introduced.* Performance for this case is shown in Figure 5-37.

temperature distribution. This is, of course, expected.

5.8.7 Temperature Isotropy

With the introduction of Langevin collision, the electron temperature appeared to follow ψ more closely. Furthermore, anisotropy was less pronounced. Anisotropy assuming Langevin collisions is shown in Figure 5-42, which may be compared to Figure 5-11, which showed anisotropy for Monte Carlo Coulomb collisions, and to Figure 5-43, which shows anisotropy for no Coulomb collisions. Anisotropy changed the most downstream, where the electron temperature is low; before, we saw ratios $T_{\|}/T_{\perp}$ on the order of 2. Now, ratios downstream are generally between 1 and 1.25.

5.8.8 Recommendation

Because anisotropy and the shape of the distribution are important factors when it comes to interpreting measurements of the discharge, future versions of this simulation should use a Langevin formulation for Coulomb collisions.

5.9 Recommendation for Improving the mini-TAL

In a Hall thruster, the magnetic field controls the discharge. Thus, the mini-TAL can be improved by changing the field, or by changing the geometry of the thruster in relation to the field.

5.9.1 Magnetic Field and Utilization

The primary problem with the mini-TAL is its low propellant utilization. Khayms estimated utilization to be between twenty to thirty five percent for the flow rates modeled. Using modified acceleration efficiencies ($\eta_a \approx .5$), the experimental utilization was found to be closer to $\eta_u = .44$ at the lowest flow rate. But this is still poor. Utilization should be much higher.

How can utilization be increased? First, by extending the ionization zone. Second, by raising the amount of energy available to ionize. The two suggestions are inter-related and can both be accomplished by making the magnetic field more parallel to the anode. Figure 5-44 shows that some magnetic streamlines near the anode go from $\phi = 300$ all the way

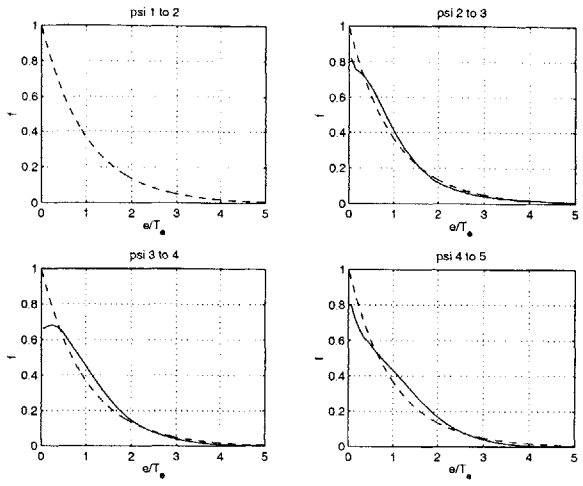

Figure 5-39: $g(\epsilon'_\perp)$ for streamlines. $M/m = 960, \gamma = 10$, no Coulomb collisions.

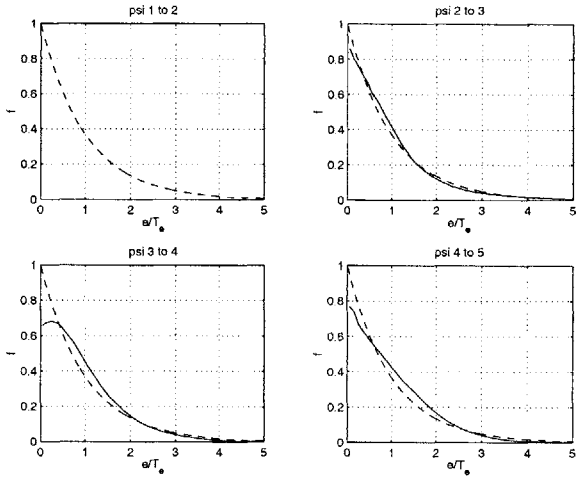

Figure 5-40: $g(\epsilon'_\perp)$ for streamlines. $M/m = 960, \gamma = 10$, MCCC V1 Coulomb collisions.

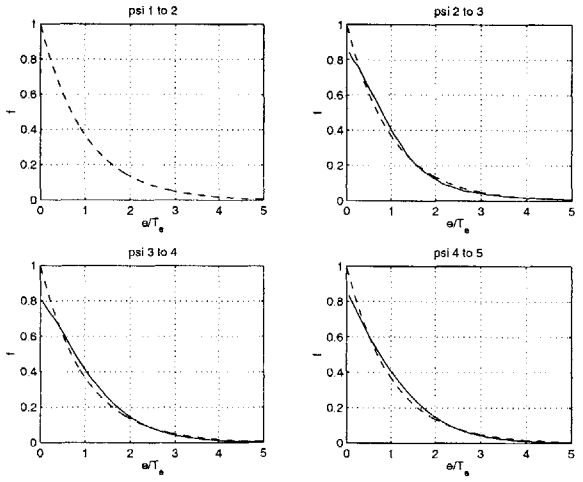

Figure 5-41: $g(\epsilon'_\perp)$ for streamlines. $M/m = 960, \gamma = 10$, Langevin Coulomb collisions.

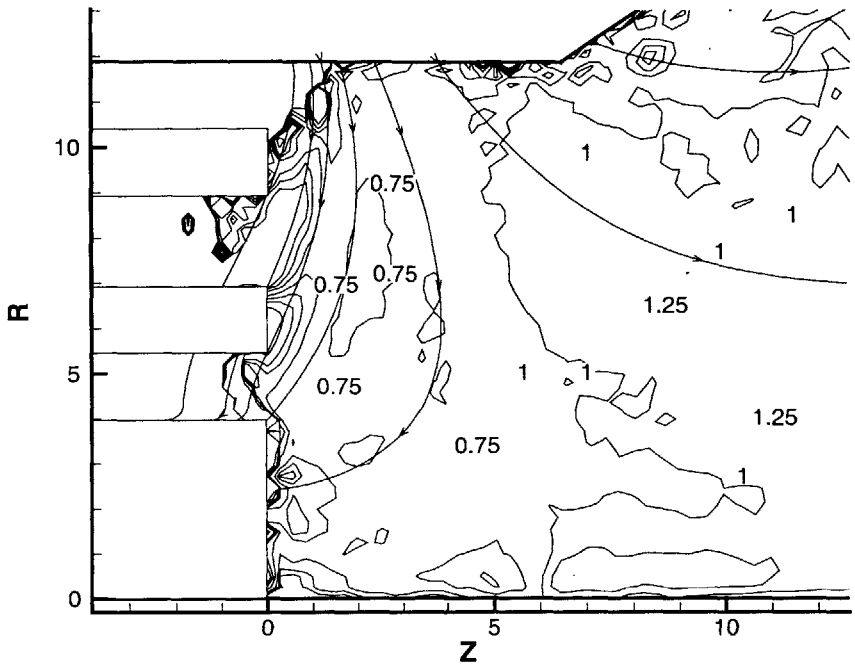

Figure 5-42: Anisotropy in electron temperature when *Langevin Coulomb collisions are modeled.* Shown is the ration $T_{\|}/T_{\perp}$ near the anode. $M/m = 960.\gamma = 10.$

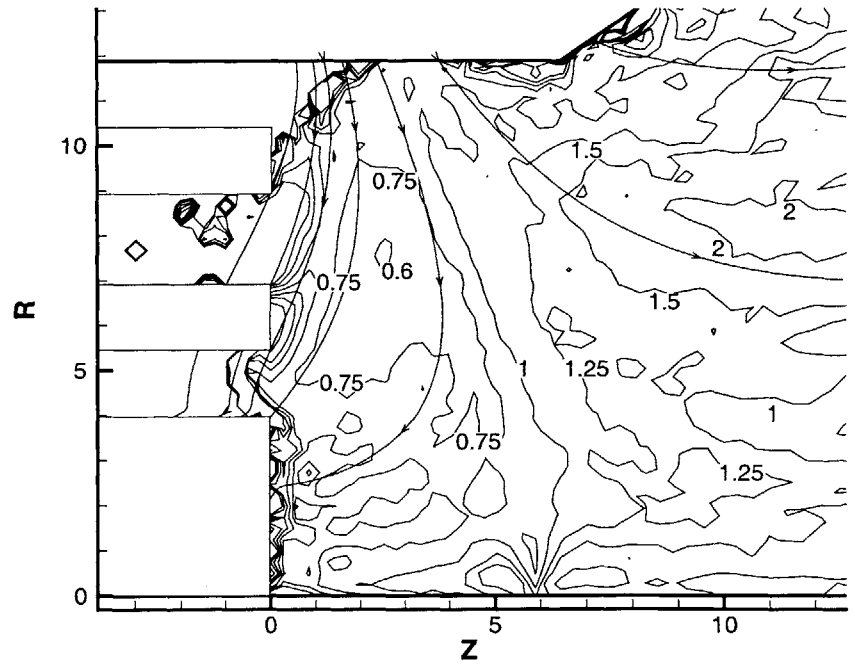

Figure 5-43: Anisotropy in electron temperature when *no Coulomb collisions are modeled.* Shown is the ration $T_{\|}/T_{\perp}$ near the anode. $M/m = 960,\gamma = 10.$

to $\phi \approx 0$. Furthermore, we notice from Figure 5-6 that the edge of the ionization zone lies along these same anode-intersecting streamlines. The key point is that electrons have a direct path from $\phi \approx 140$ eV, where they are produced through ionization, to the anode at 300 eV. This is most inefficient. Over 150 eV of energy goes straight to the anode instead of being transferred to the neutrals in the form of ionization and excitation. If this energy were transferred, the utilization might rise by 50 percent or more.

These same figures also help explain why the performance increases as M/m decreases. To compensate for the artificial M/m, we increased the collision frequency. This decreased the impedance perpendicular to the streamlines, but *increased* impedance parallel to the streamline. This should make little difference if the magnetic field is parallel to the anode, i.e. if the problem is 1-D. However, it is not. Because of the increased $\|$ impedance, some electrons have time to diffuse further inward toward the neutral source before they run down the streamlines to the anode. As a result, the predicted thrust, I_{sp}, and utilization all increase. Again, the shape of the magnetic field is the fundamental problem. It makes the simulation less linear.

In summary, making the magnetic field more parallel to the anode may improve both the physical performance of the thruster, and the code's ability to predict it. The most obvious way to do this is to move the center pole outward in the +Z (axial) direction. Another possibility is to move all or a portion of the anode inward. Numerical design tools can be used to re-design the circuit.

5.9.2 A Design Error

The magnetic field obtained from Dexter Magnetics was given in vector form, $\vec{B} = B_z\vec{i}_z + B_r\vec{i}_r$. This enabled us to construct the stream function $\psi = -rA_\theta$ (see Section 3.13), which is constant along magnetic streamlines. Figure 5-44 showed that the streamlines (the contours of ψ) are not purely radial near the anode at $z = 0$, as they should be for optimum performance.

Turning to Khayms Master's Thesis, however, we find a different magnetic field, one which is radial at $z = 0$. To find out why, we contacted Dexter Magnetics, who pointed out that the vector potential $\vec{A}$ is often used in early designs of magnetic circuits and that, in this case, it better matched the figure in Khayms thesis.

To resolve the issue, we constructed the magnetic vector potential, $A_\theta = -\psi/r$, setting

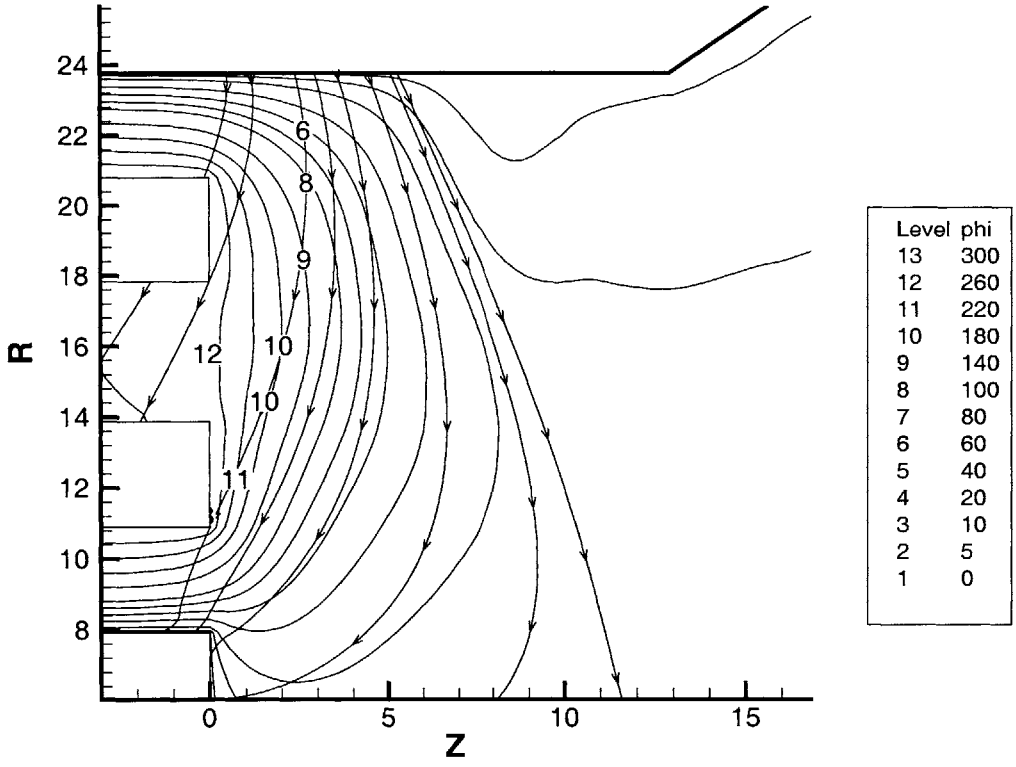

Figure 5-44: *Magnetic streamlines near the anode.* This figure ($\gamma = 5$, $M/m \approx 96$), shows that the magnetic streamlines (the arrowed lines) create a path for the electrons from $\phi = 140$ (the edge of the ionization zone) all the way to the anode.

it to zero on the axis. Figure 5-45 shows both ψ and A_θ. The plot of vector potential indeed matches the picture in Khayms thesis.

Khayms used the vector potential to design the magnetic circuit of the mini-TAL! He designed the circuit such that contours of the vector potential A_θ were radial at the anode exit. He should have designed the circuit such that $\psi = -rA_\theta$ was radial here. This simple mistake explains the poor utilization, thrust, and specific impulse of the mini-TAL.

5.10 Simulation of Modified Thruster Geometry

The power of this simulation is demonstrated by the numerical experiment described in this section. We re-designed the thruster and generated a new series of performance estimates.

5.10.1 Old Design

The old thruster geometry is shown in Figure 5-46. The streamlines were obtained (by Tecplot) from the original data supplied by Dexter Magnetics.

5.10.2 New Design

We re-designed the anode, moving the lower lip inward by .35 mm. This enabled us to retain the old magnetic field circuit. The re-designed geometry is shown in Figure 5-47 where the old geometry is again shown for comparison. Also shown are several magnetic streamlines, which are now nominally parallel to the anode surface. The magnetic streamlines compared to the initial potential difference (very low plasma density) are shown in Figure 5-48. To reach the anode, magnetized electrons must now (in theory) diffuse across an additional hundred to hundred and fifty Volts of potential difference. Ionization should begin at a higher potential, resulting in both faster ions and more ions overall. Thrust, I_{sp}, and utilization should all increase. On the negative side, one would expect that such a re-designed geometry would result in more erosion at the center pole. But our simulation predicts that the ion loss fraction to the walls does not change.

5.10.3 Performance Results of New Simulation

At a flow rate of $\dot{m} = .1mg/s$, the new performance is shown in Figure 5-49. MCCC Version 2.0 was used for Coulomb collisions.

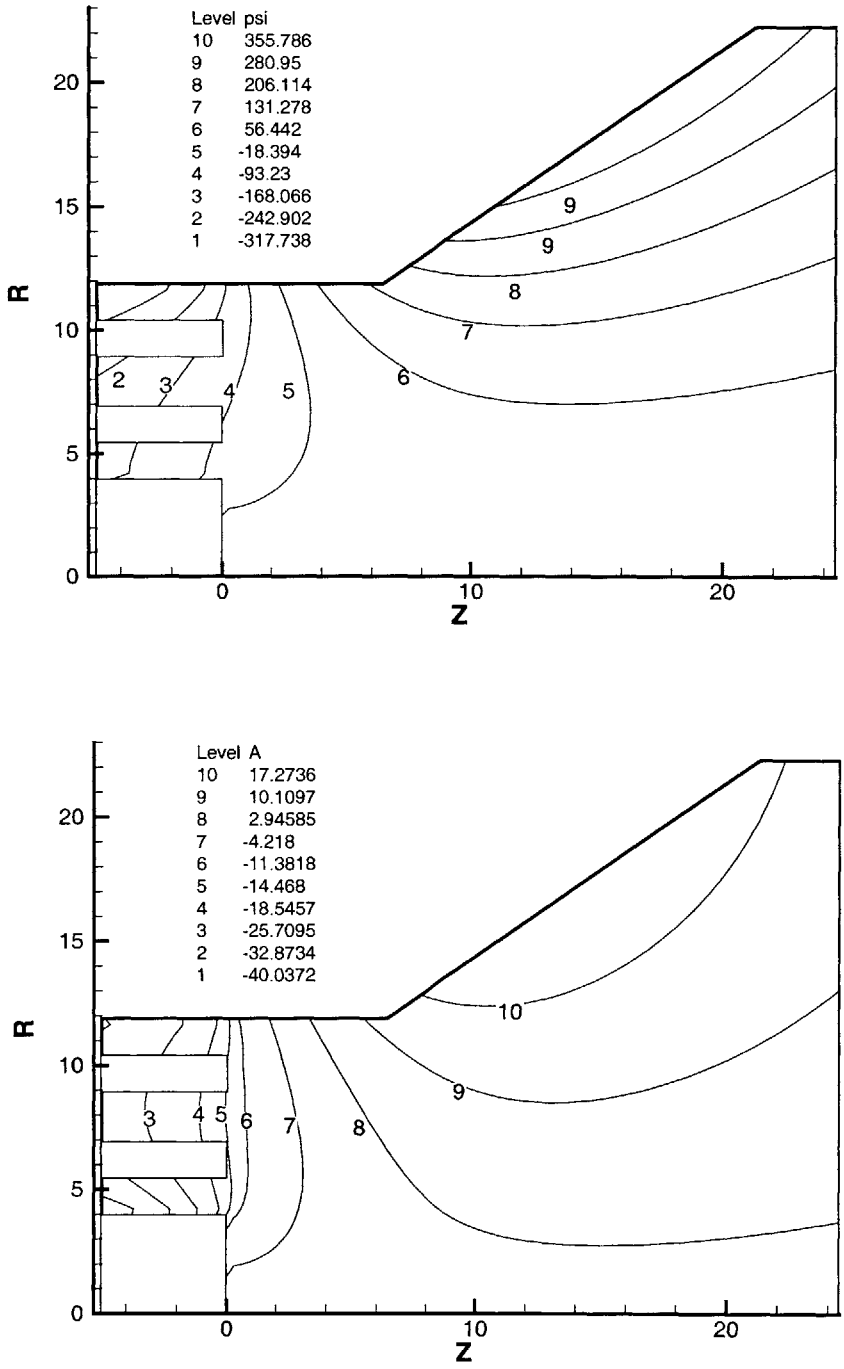

Figure 5-45: *Top*: Magnetic stream function ψ, which is parallel to the magnetic field. *Bottom*: Magnetic vector potential $A_\theta = -\psi/r$, where $A_\theta = 0$ on the axis. Units are normalized. The shape of the contours is the point of this figure.

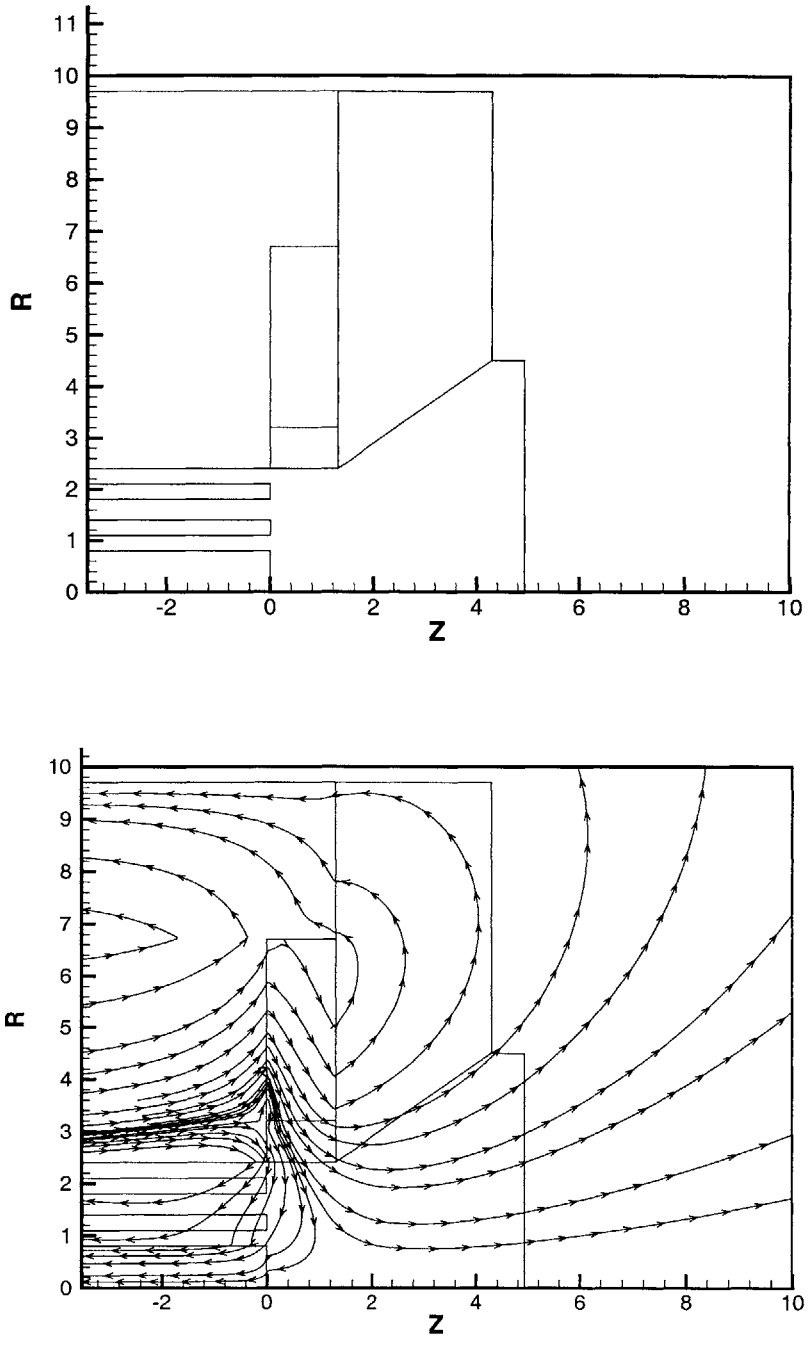

Figure 5-46: *Original design of thruster.* Top: Outline of the thruster body. Bottom: Overlay of magnetic streamlines.

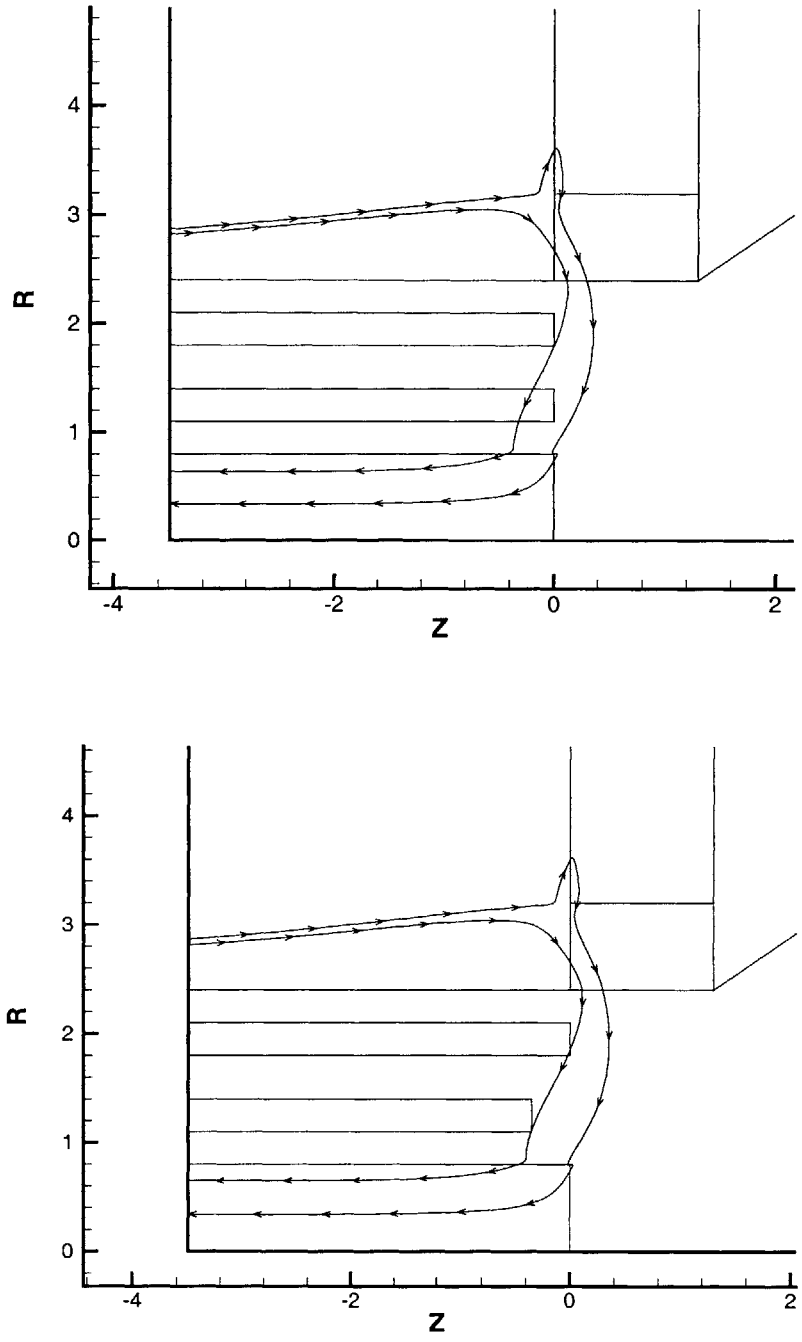

Figure 5-47: *Magnetic streamline positions relative to anode.* Top: Old thruster geometry. Bottom: New thruster geometry. The inner lip of the anode has been moved inward by .35 mm.

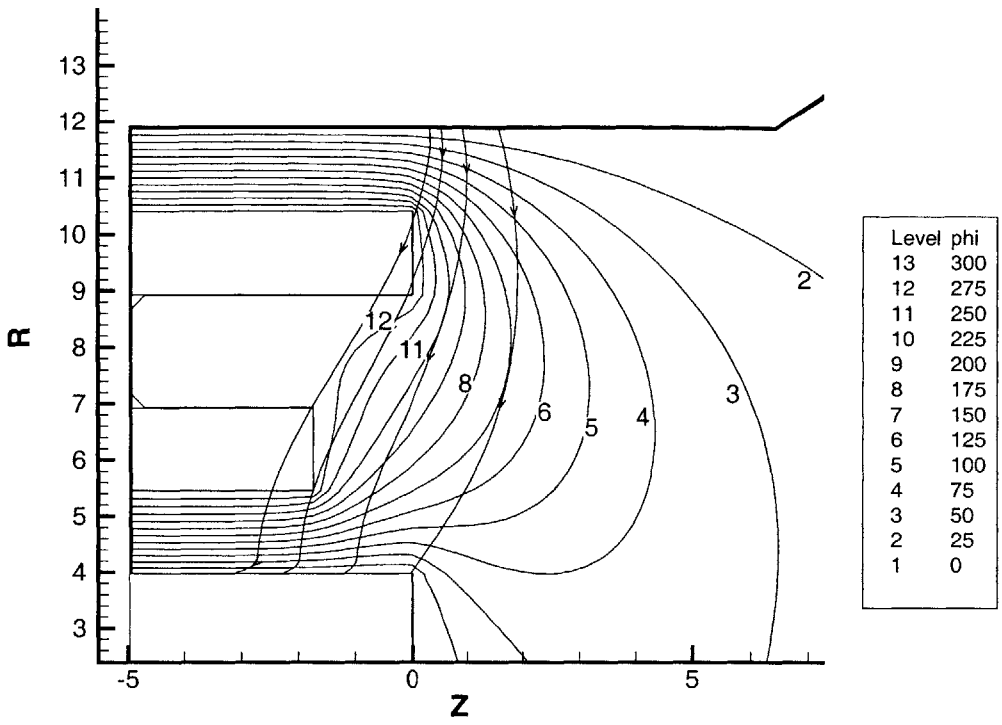

Figure 5-48: *Streamlines and potential contours near the anode for new geometry.* Electrons have no easy path to the anode anymore.

Old and new performance time averaged predictions are compared in Table 5.9. Clearly, the performance of the thruster increases dramatically. Thrust and specific impulse (calculated from ions only) increase by over sixty percent, and thrust efficiency from ions only increased by over ninety percent! But where did these gains come from?

First, recall that $\eta_t \approx \eta_e \eta_a \eta_u$, where $\eta_u = \eta_b \times \eta_i$. In English, thrust efficiency is the product of electrical efficiency, acceleration efficiency and utilization efficiency, which itself the product of beam efficiency and ionization efficiency.

Table 5.9 shows that the utilization efficiency rises by fifty percent, to about eighty five percent utilization. This seems to be the dominant improvement. The utilization improvement comes mostly from an improvement in ionization efficiency; the improvement in beam efficiency, or the fraction of ions which impacts the wall increases by just two percent. That beam efficiency does not decrease despite the new anode geometry is somewhat of a pleasant surprise. The increase in acceleration efficiency is the next largest contributor; η_a rises by almost twenty percent. This means the ions are produced at a higher potential; the discharge is less "short circuited" than before. The last contribution is electrical effi-

ciency. Because the discharge is more efficient, the fraction of current required to sustain the discharge decreases. All of the currents in Table 5.9 are plotted in Figures 5-51 and 5-38).

Still, this is only a beginning. By trial and error, we may arrive at a geometry geometry which results in even better performance.

[Caveat: The new estimates are based on a simulation which converged for one hundred thousand twenty thousand iterations, starting with a previous semi-converged solution for the old geometry. Because $Deltat\hat{}$ is less than the neutral end to end transit time, the neutral flow near the outer boundary is still high, i.e. many of the neutrals flowing through this boundary left the discharge region before the simulation began. Also, the old estimates were based on a simulation which only converged for sixty thousand iterations using MCCC V2. Further converging these solutions will change these results slightly.]

This test shows three things:

- The test validates Khayms theory of why the thruster performed poorly; the B-field is not shaped as he thought it was.
- The mini-TAL has more performance potential than was thought. A re-design and subsequent series of experimental measurements may be in order.
- This simulation, or one based on it, can be a powerful tool for Hall thruster design.

5.10.4 Moments of New Design

Numerical particle moments and other quantities of interest with the new anode design are shown in Figures 5-52, 5-53, 5-54, and 5-55. Figures 5-52 shows n_e and n_i. Electrons no longer congregate near the lower anode; in fact, they congregate near the upper anode, but in the middle of the neutral flow. Figure 5-53 shows ionization and excitation rates obtained by counting. The ionization zone covers the mouth of the anode. Figure 5-54 shows the total electron-neutral scattering rate and the numerically obtained hall parameter, β. The electrons should be fully magnetized. Figure 5-55 shows the electron temperature and electric potential. The electron temperature appears to track magnetic streamlines well in the central region.

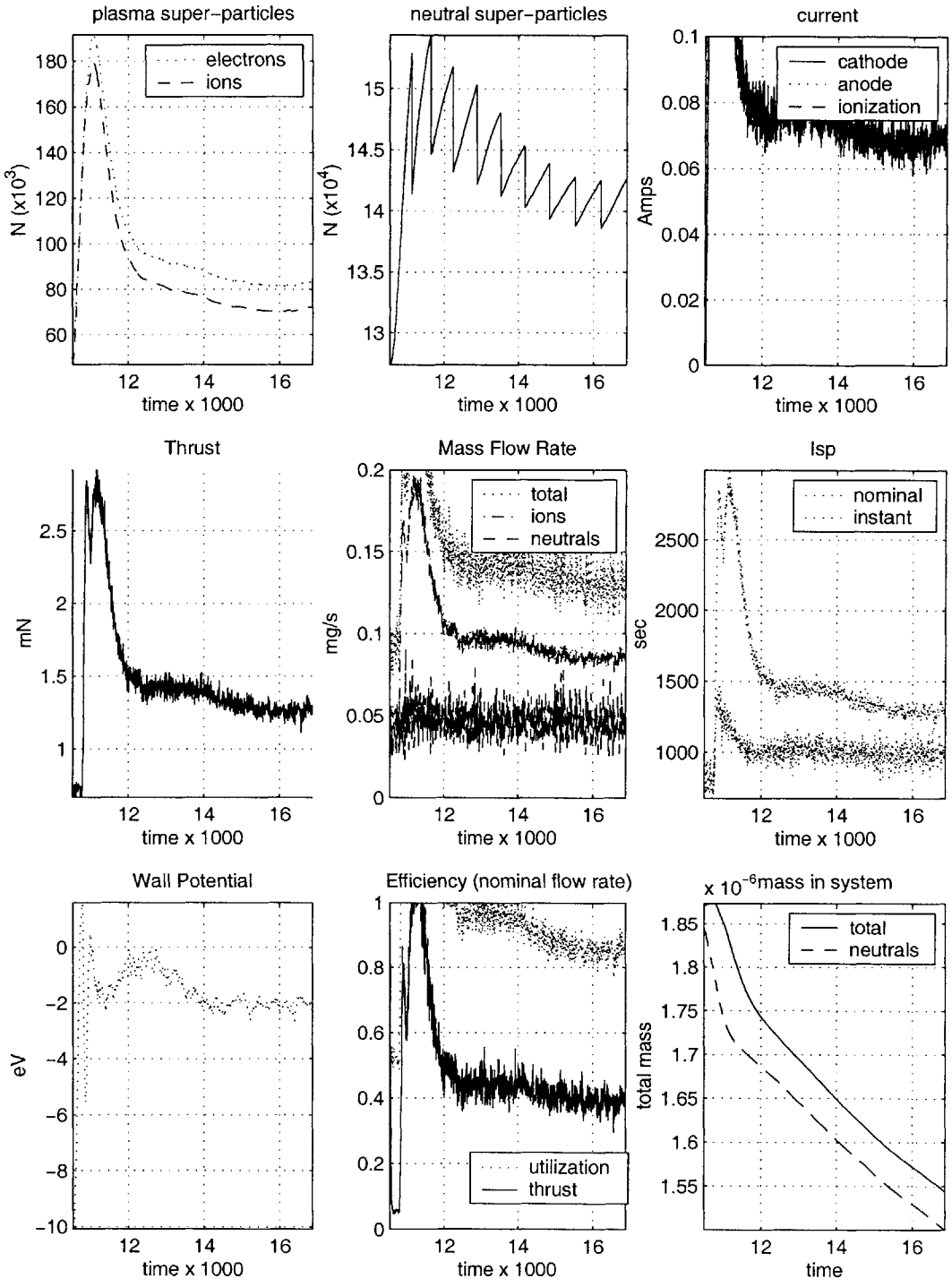

Figure 5-49: *Re-designed thruster performance* for $\gamma = 10$, $M/m \approx 960$, $s_o = 50$, $C = 1 \times 10^{-10}$. No anomalous diffusion. MCCC Version 2.0.

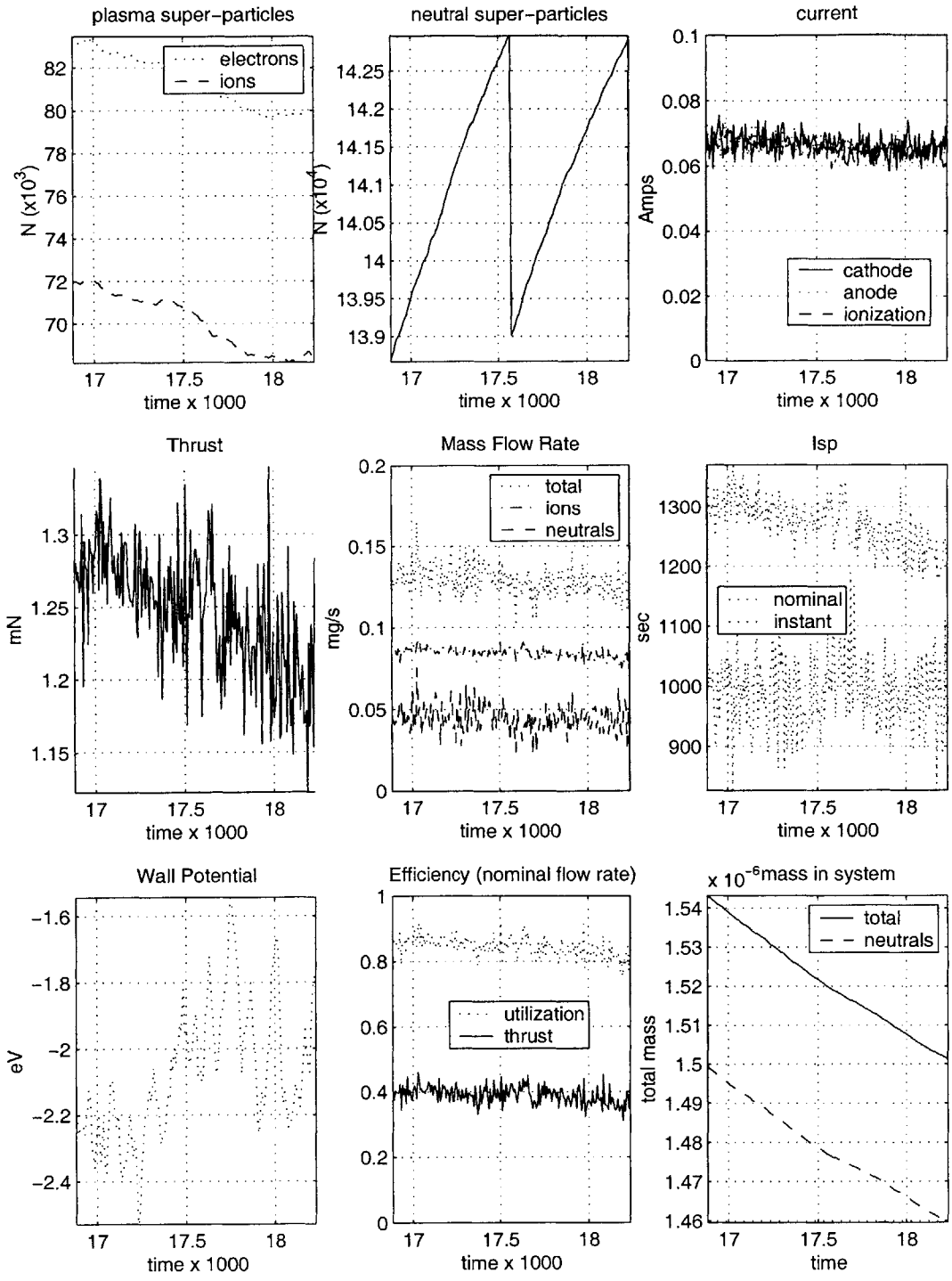

Figure 5-50: *Re-designed thruster performance* for $\gamma = 10$, $M/m \approx 960$, $s_o = 50$, $C = 1 \times 10^{-10}$. No anomalous diffusion. MCCC Version 2.0. Extension of Figure 5-49 for an additional 20K time-steps.

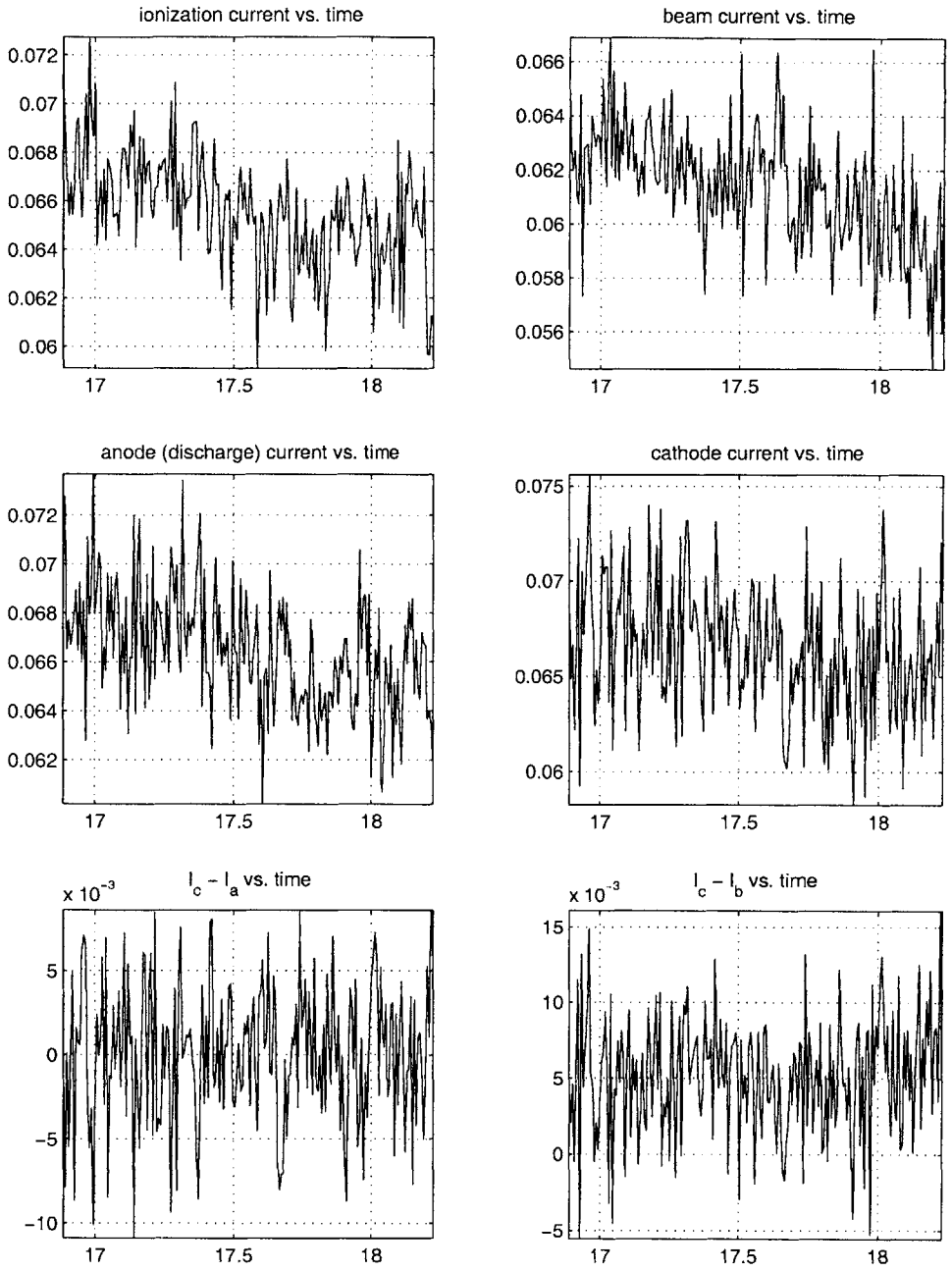

Figure 5-51: *Currents for the new geometry.* Performance for this case is shown in Figure 5-50.

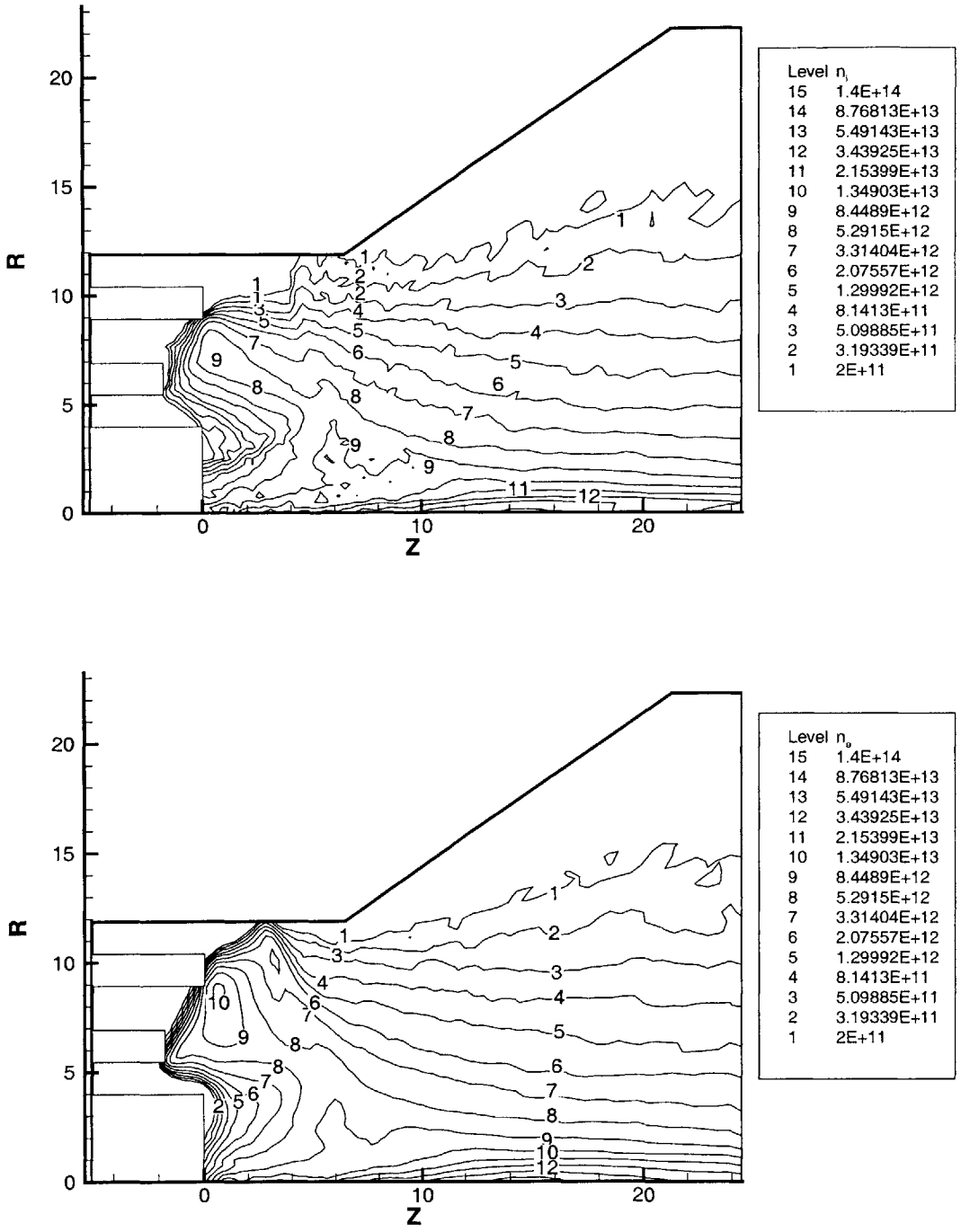

Figure 5-52: *Results for re-designed anode.* Top: Ion density. Bottom: Electron density. Units are CGS.

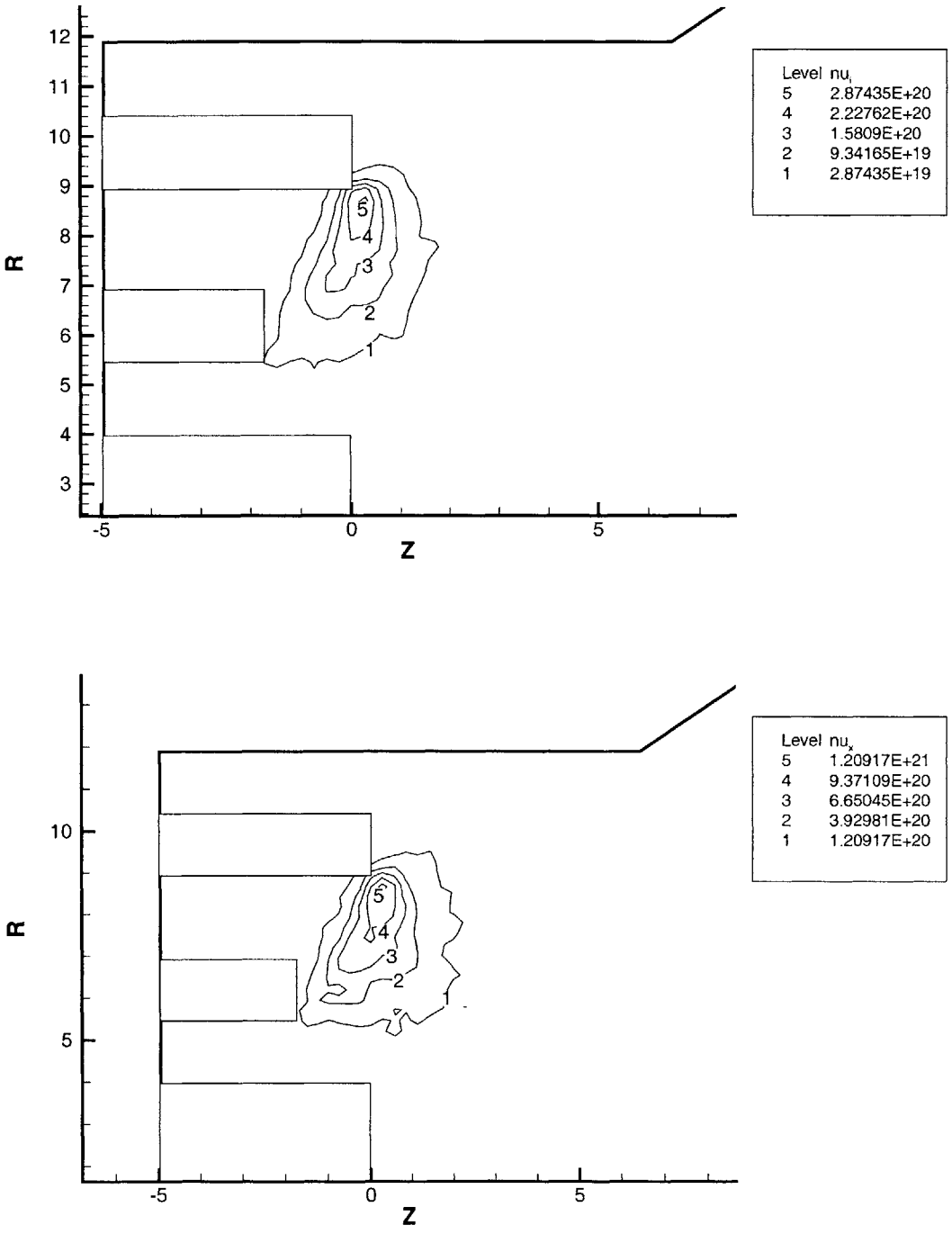

Figure 5-53: *Results for re-designed anode.* Top: Ionization rate, $1/cm^2/s$. Bottom: Excitation rate, $eV/cm^3/s$. A direct comparison requires dividing the excitation rate by 8.82 eV.

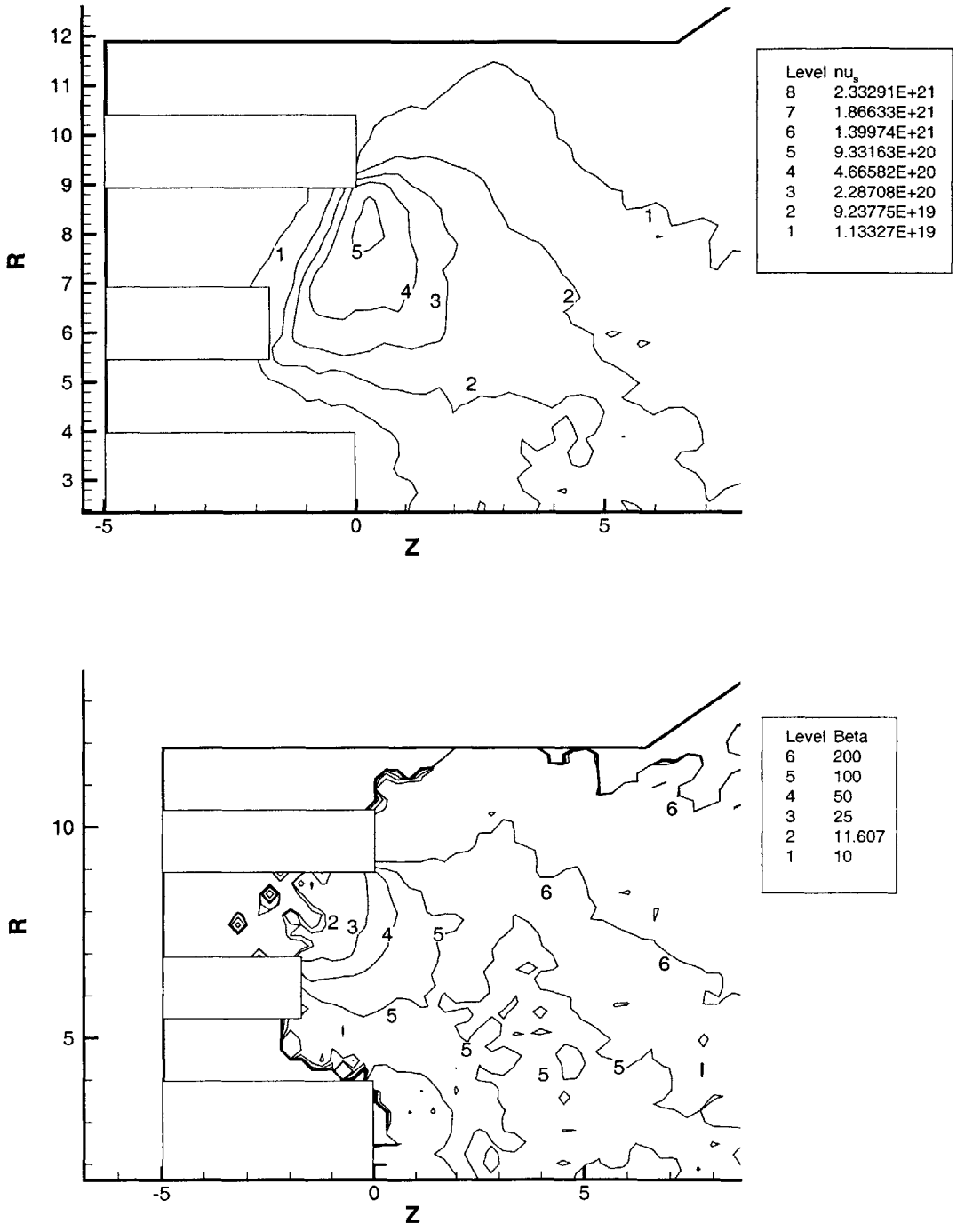

Figure 5-54: *Results for re-designed anode.* Top: The total scattering rate, $1/cm^2/s$. Bottom: The Hall parameter for electron-neutral scattering only.

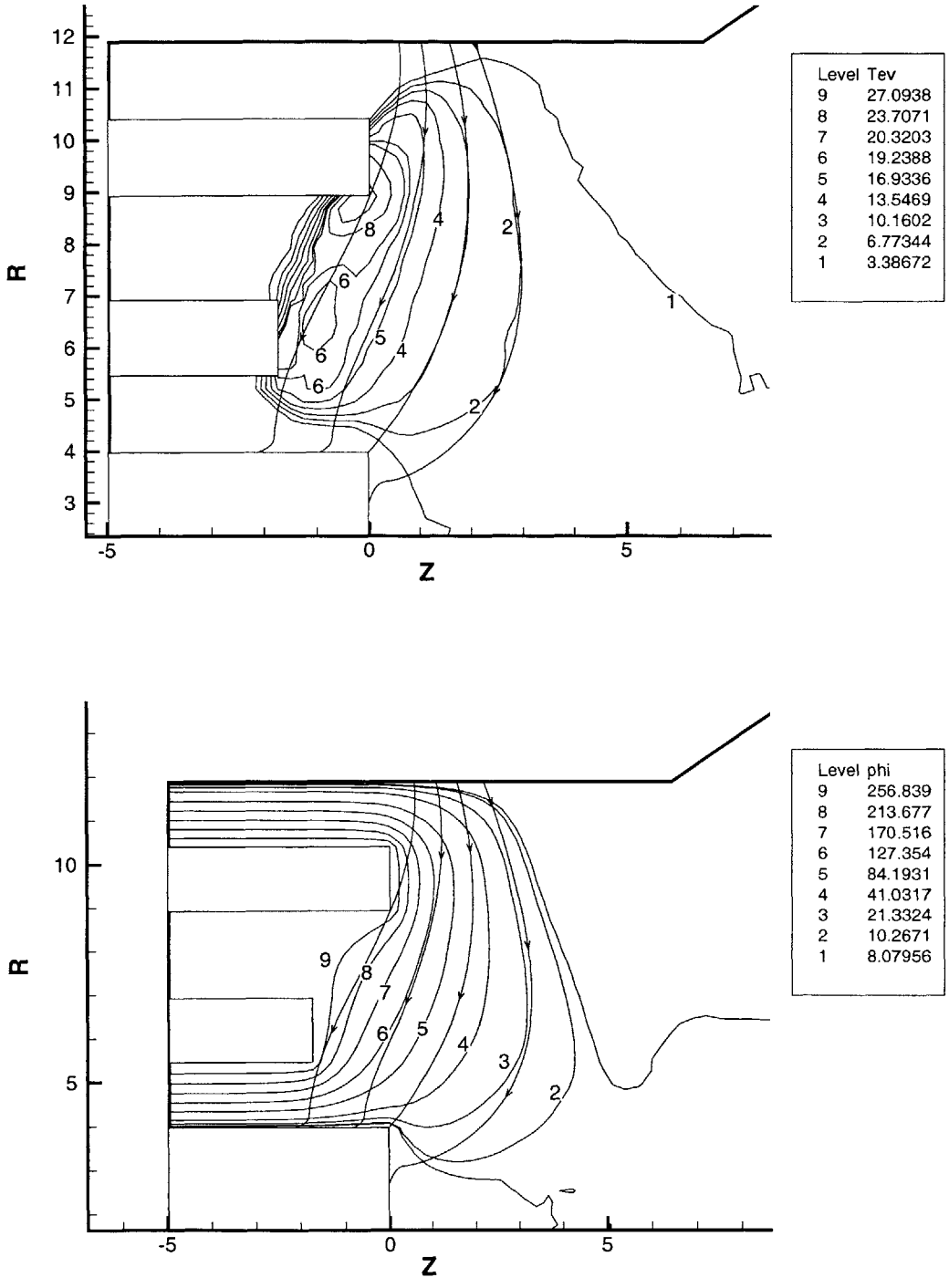

Figure 5-55: *Results for re-designed anode.* Top: The electron temperature in units of eV. Bottom: The electric potential in Volts. Also shown are magnetic streamlines.

	Old	New	Percent Increase
I_{sp} (sec)	740	1200	59
Ion Thrust (mN)	.72	1.15	59
cathode current, I_c(Amps)	.0445	.0655	47
anode current, I_a(Amps)	.0444	.0653	47
beam current, I_b(Amps)	.0378	.0605	60
ionization current, I_i(Amps)	.0434	.0643	48
η_t	.18	.34	92
η_e	.86	.92	9
η_a	.36	.43	19
η_u	.57	.83	46
η_i	.61	.88	43
η_b	.92	.94	2

Table 5.9: Numerical performance increase due to re-design of mini-Tal anode. All predictions assumed MCCC V2, $M/m \approx 960$,$\gamma = 10$, and $\dot{m} = .1$mg/s. Thrust efficiency and I_{sp} refer to ion thrust only, which enables us to more accurately compare solutions which have yet to converge on the longest neutral transit time scale; $\eta_t \approx \eta_e \eta_a \eta_u$. The neutral flow in Amps equivalent of $I_n = .0734$ is used to calculate ionization efficiency. Values are averaged from last 10,000 iterations.

Chapter 6

Conclusions

The Particle-in-Cell method is a powerful tool for modeling plasma thrusters. It lets us look inside the plasma to see its microscopic properties up close. The effects of many different mechanisms (such as scattering collisions, excitation collisions, anomalous diffusion, and wall effects, to name just a few) can be studied.

6.1 Summary of Method

The plasma inside a diminutive Hall thruster was simulated using a fully kinetic numerical model. This simulation differs significantly from previous full PIC Hall thruster simulations. Unique features include the following:

- The geometry is that of a real thruster, for which some experimental data is available.
- The numerical grid is non-orthogonal.
- A novel method for accelerating classical diffusion and retrieving physical results is implemented.
- The free space permittivity constant is changed to exaggerate sheaths and accelerate the simulation.
- Anomalous diffusion is included via an equivalent scattering frequency.
- Ion-neutral charge exchange and scattering collisions are modeled.
- The wall potential is allowed to float. It is computed self-consistently.

- Cathode electrons are injected at the rate required to preserve quasineutrality at the free-space (plume) boundary.

- Coulomb collisions are modeled as a diffusion process in velocity space.

After the code was validated, the thruster was simulated under various operating conditions and the results were examined. One such result, the ion density, is shown to approximate scale with the thruster in Figure 6-1.

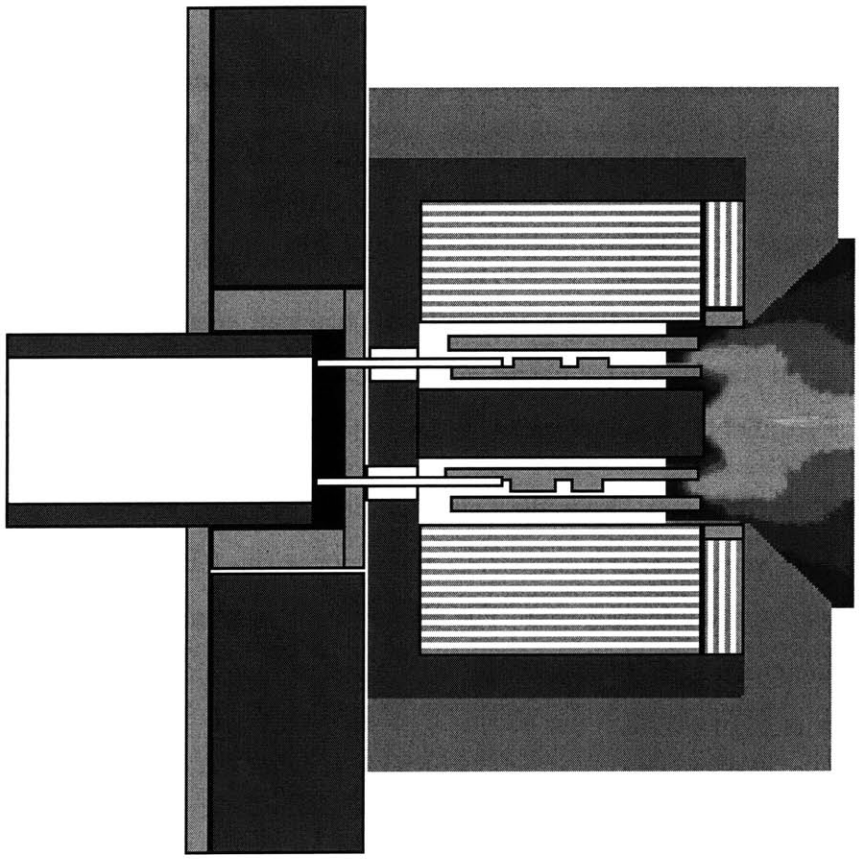

Figure 6-1: *The mini-TAL thruster along with numerically predicted ion densities* for $M/m = 960$, $\gamma = 5$, and $\dot{m} = .1mg/s$.

6.2 Summary of Results

New results from this fully kinetic simulation include the following:

- The magnetic field of the mini-TAL was designed incorrectly. In the near anode region,

we discovered an axial component which is probably responsible for the mini-TAL's poor thrust, specific impulse, and propellant utilization.

- The mini-TAL was re-designed numerically; the inner portion of the hollow anode was shortened by .35 mm. Propellant utilization increased by forty five percent, acceleration efficiency increased by nineteen percent, and thrust and specific impulse increased by about sixty percent. Thus, the thrust efficiency increased by about ninety percent. These results may be verified by re-constructing the thruster and measuring its performance.

- The mini-TAL thruster's published propellant utilization may be too low. The simulation predicted acceleration efficiencies of 36-47 percent. When used to re-evaluate Khayms data, utilization of $\approx$ 44 percent was predicted at both $\dot{m} = .1mg/s$ and $\dot{m} = .1676mg/s$ Previous estimates were 29 and 34 percent, respectively.

- The numerical model predicts a non-isotropic electron energy distribution function. In general, the distribution is better represented by a two-temperatures, one each for directions parallel ($T_{||}$) and perpendicular ($T_{\perp}$)to $\vec{B}$.

- The model predicts non-Maxwellian electron populations in the perpendicular direction near the anode (see Figure 5-17). We propose the following explanation. The following explanation is proposed: The electric field (nominally $\perp\vec{B}$) increases the $\perp$ energy preferentially. Electrons do not have time to fully thermalize, resulting in the shape seen in Figure 5-17.

Other interesting results include the following:

- Predicted performance was compared to experimental performance. The most physically realistic cases over-predicted thrust, specific impulse, and utilization by twenty five to thirty three percent. These cases included classical diffusion and Monte Carlo Coulomb collisions, but no anomalous diffusion.

- The introduction of anomalous Bohm type diffusion proportional to $\frac{1}{64B}$ increased thrust and specific impulse by about ten percent.

- Thrust, specific impulse, and propellant utilization increased with mass flow rate.

- The plasma was found to extend to the interior of the hollow anode under certain conditions, but this did not seem to be an essential feature of the flow for effective operation.
- The simulation predicts gradients in electron temperature along magnetic streamlines.
- Ionization oscillations were observed at higher mass flow rates.
- Oscillations in plasma density were observed, some of which correspond to theoretical modes.
- Coulomb collisions changed ion thrust propellant utilization, and specific impulse by less than ten percent.
- Langevin Coulomb collisions changed thrust and specific impulse by about one percent. This is statistically insignificant. However, the shape of the electron distribution near the anode was more Maxwellian.

In summary, we showed that the full-PIC Monte-Carlo method is a viable alternative for investigating small-scale plasma flows as present in Hall or Ion thrusters.

6.3 Recommended Work

Highly recommended follow-up work is discussed in this section.

6.3.1 Additions to Code

In constructing the numerical model, we attempted to capture all essential features of the plasma. However, some significant and interesting phenomena (e.g. multiply charged ions) were left out. We recommend adding some of these phenomena to the code and changing the way other phenomena are modeled. All of the improvements listed here would be easy to make.

Multiply Charged Ions

The simulation results presented in Chapters 4 and 5 included only one ion state, Xe^{1+}. However, populations of Xe^{2+} on the order of five to ten percent have been measured. Therefore, multiply charged Xenon ions should be added to the simulation. At a minimum,

Xe^{2+} produced through electron-neutral collisions and electron-ion collisions should be included. Both additions are almost trivial; much of the required coding is already in place.

Excitation Levels

Instead of using a single lumped excitation level, several levels of excitation should be included. Alternately, cross sections for various energy levels could be added and the effective level placed at single *intermediate* value. This would require a more detailed model of excitation, but the results would be enlightening.

High Energy Neutral Wall Accommodation

In the simulation as constructed, all neutrals experience full accommodation in energy and momentum when they hit boundaries. However, charge exchange neutrals have kinetic energies comparable with ion energies. Like ions, therefore, high energy neutrals should be only partially accommodated at the boundaries. This change would affect the neutral distribution slightly.

Coulomb Collisions

Electron-ion collisions as implemented in MCCC method Version 2.0 (see Section 3.15.4) should produce the correct amount of transport. It may be desirable to keep using this method. However, electron-electron collisions should be removed from the MCCC model and handled instead using the diffusive model described in Section 3.16.

Secondary Electron Emission

No secondary emission of any kind was included in the mini-TAL numerical model. However, as discussed in Section 2.12.5, secondary emission due to electron impact may be quantitatively significant. Secondary emission due to multiply charged Xenon ions may also be quantitatively significant.

We justified excluding secondary emission from ion impact by noting that we only model Xe^{+}, for which secondary yield is insignificant. We justified excluding emission from electron impact by arguing that most secondary electrons will fall back. In any case, secondary emission is thought to be important in moderating the temperature of the discharge in SPT

type Hall thrusters. The addition of secondary emission to this numerical model would allow it to be used for all types of Hall thrusters.

6.3.2 Errors in Leapfrog Scheme

The leapfrog scheme used in this simulation is very good at tracking electron motion in the electric and magnetic fields. However, small offset errors may occur when particles are initialized (see Section 3.14). The scheme should be modified slightly to correct these errors.

6.3.3 Static Magnetic Field

The static magnetic field produced by Dexter Magnetics has anomalous features; along the center pole boundary, $\nabla \cdot \vec{B} \neq 0$. A field with zero divergence should be obtained.

6.3.4 Thermal Effects

The temperatures of the anode and thruster walls are held constant in the simulation. However, these values could be easily changed to test the effects of wall temperature on performance. Furthermore, a thermal model could be developed to actually estimate the wall temperature.

6.3.5 Simulation Region

The simulation region could be expanded outward to encompass the cathode. This would probably double the number of grid cells required, slowing solution of Poisson's equation and many other aspects of the simulation. Still, the added CPU time would be well worth it.

6.3.6 Electron Injection

The logical electron injection method could be refined to consider local plasma conductivity. As already mentioned, however, the cathode should be placed inside the simulation region, which would improve statistics.

6.3.7 Experimental Measurements

A set of experimental measurements of the mini-TAL thruster in operation should be collected. Such measurements could be compared to numerical predictions. These measurements should include both $T_\perp$ and $T_{||}$. If further testing of the mini-TAL is infeasible, then the simulation should be re-constructed and applied to some well known device.

6.3.8 Modify mini-TAL Thruster

The anode in the mini-TAL should be re-designed such that $\vec{B}$ is nominally parallel to the anode face. Alternately, the magnetic field in the mini-TAL thruster could be re-designed, again, such that $\vec{B}$ is parallel to the anode face. New sets of thrust measurements could then be taken and compared to numerical predictions. This would be an excellent project for a Master's Degree student.

6.4 General Improvements

The numerical method can be improved in many ways. Here we discuss general improvements, beginning with the easiest and descending, in rough order, to the most difficult.

6.4.1 Particle Count

One of the easiest ways to improve the simulation is to increase the number of particles, which should improve statistical accuracy. Four hundred thousand particles of each species on a 100×180 grid (as per $\gamma = 5$) is quite possible. Unfortunately, computational time increases more or less linearly with particle count. The law of diminishing returns quickly takes effect. That is why the charged particle counts in the simulations presented in this thesis are usually less than one hundred thousand of each species.

6.4.2 Grid

A slightly finer grid is another easy way to improve the simulation at next to no cost. A finer grid would better capture fluctuations in electric field. Producing a finer grid requires simply adjusting a few constants in the header files and ensuring that the solution does not blow up. However, a finer grid by itself is not enough. The number of particles per cell

should stay the same. A much more difficult (but potentially rewarding) task would be to re-construct the simulation to work on an un-structured grid.

6.4.3 Time-step

Since ions already move much slower than electrons, it should be possible to run them on a different time-step. We already do this for neutrals. This would require only minor changes in the code, as it was written with this possibility in mind. Also, convergence might be accelerated by further de-coupling electrons and ions. We could "freeze" the electron distribution but step forward the heavy particle distribution for some period of time. This would require larger changes in the code than the previous suggestion.

6.4.4 Induced Magnetic Field

A first order model for induced magnetic field could be introduced. The induced field should be insignificant for the mini-TAL thruster, but may be more significant for larger thrusters. Observable electromagnetic waves may result from this addition.

6.4.5 Dimensions

The simulation should include 3 dimensions in space, including the complete $\Delta\Theta$ of 2π. This would be relatively easy to code, but computationally cumbersome. A more palatable alternative would be to model a "slice of pie", i.e. a grid which includes some fraction of 2π in the azimuthal direction. Periodic boundary conditions might make this possible. This would enable direct calculation of diffusion due to azimuthal oscillations, possibly explaining definitively the so-called anomalous diffusion.

6.4.6 Electric Potential Solution

The electric potential solver and the interpolation method associated with it are responsible for numerical heating of the plasma. However, higher order interpolation and finite differencing methods (or finite element methods) may be able to reduce heating by 1-2 orders of magnitude, increasing confidence in results obtained from very long runs such as would be required for $M_n/m_e = 10,000$. Such improvements on Cartesian grids are described in Ref. [19]. Also, stopping ϕ iterations at some intermediate accuracy level could cut in half computation time without affecting overall accuracy.

6.4.7 Energy Conservation vs. Momentum Conservation

Numerical schemes which conserve energy, but not momentum, have been developed. It is possible that such schemes might produce different electron energy distribution functions. This is related to the previous suggestion, improving the electric potential solver.

6.4.8 Physical Constants

An artificial mass ratio and free space permittivity constant were adopted purely for numerical reasons. There is no fundamental reason (aside from numerical heating) why this simulation cannot be run with both physical mass and permittivity. The price is computational time. A physical Xenon neutral would move 16 times slower than a neutral at $M/m = 960$, and the mini-TAL thruster would need a grid 5 times finer to resolve the Debye length everywhere. To maintain the same number of particles per cell, 25 times more particles would be needed. The result would be a simulation which runs hundreds of times slower. Today, this could only be performed on a super-computer. However, restraints are relaxing inexorably. Ever faster computers are evolving. Just as the human evolved from the anchovy, so will the computers of tomorrow evolve from today's desktops. Very soon, it will be possible to obtain results almost indistinguishable from the physical on a mere PC.

6.5 Last Word

In this thesis, we described the first complete, fully kinetic simulation of a Hall thruster. It is not perfect, but it is a good beginning.

Centuries ago, Laplace wrote that a mind of infinite intelligence could predict the future of the universe [27]. We cannot hope for such intelligence. But we can hope for a computer powerful enough to realistically simulate a small scale plasma flow.

Appendix A

Running the Simulation

The following is edited output from the simulation for the case where $\gamma = 5$ and $M_n/M_n' = 2500$ with $[T_e] = 50$ eV. Several extraneous lines have been edited.

```
Running PIC.C, Version 1.0, 2000
setting the dielectric constant...
Anode Potential: 300-V
Tev (nominal) of neutrals: 0.1-eV
Tev (nominal) of electrons: 50-eV
nominal neutral velocity: 1.90695e+006-cm/sec
nominal neutral velocity: 0.00646302-X/T (debye lengths/w_pe^-1)
neutral velocity to right: 0.00205725 -X/T
nominal ion acoustic speed: 3.03044e+007-cm/s
nominal ion acoustic speed: 0.10219-X/T
nominal electron thermal velocity: 4.19309e+008-cm/sec
nominal electron thermal velocity: 1.41395-X/T (debye lengths/w_pe^-1)
Nominal neutral density:  5.27464e+014 cm^-3
Nominal plasma density:  6.77565e+012 cm^-3
Nominal Debye length: 0.0100972 cm
Nominal plasma frequency: 2.93695e+010 sec^-1
Nominal gyro frequency: 1.40706e+011 rad/sec
Nominal gyro frequency: 4.79091 rad/T
Nominal gyro radius: 0.00298003 cm
```

```
Units of charge:  1 Q = 4.8032e-010 emu
Units of mass:  1 M = 9.1094e-028 gm
Units of distance:  1 X = 0.0100972 cm
Units of time:  1 T = 3.4049e-011 sec
Units of velocity:  1 V = 2.9655e+008 cm/sec
Units of B-field:  1 B = 1669.83 gauss
Units of E-field:  1 E = 16.5062 statvolts/cm (statcoul/cm^2)
Units of Potential: 1 Phi = 0.166667 statvolts = 50 volts
loading data from structured grid...
matching boundary nodes to geometry...
assigning boundary materials...
calculating 1st order differential grid constants...
getting gauss constants...
checking for consistency
Superparticle size for 150000 neutrals:  1.39707e+006
capacitance of thruster: 22368.2 super-particles/50-eV

 load old particle files? (y or n) y
loading sim data...
mass factor for previous run: 2500 current run 2500
epsilon factor for previous run: 5 current run 5
progress=1, wall_charge=1405 previous_its=84094 sim_time=7674.71, residue=0, re
idue_lhs=0,residue_top=0 leftover_xs 0

loading N_n_dot.dat
507 and 0 neutrals to be singly and doubly ionized, 41 charge exchange ions
loading neutrals
loading ions
loading electrons
START:  ions: 94469, neutrals: 395374, electrons: 99415

free space charge leftover=0 (int)=0 round_pn()=0
```

```
insulator charge leftover=0

finding initial densities...
Particle moments...

Getting the magnetic field
loading and interpolating master b_field from DEXTER
B_field loaded, 54471 nodes
adjusting anomalous B-field points
r: 70 16  hi -8377.23 low -18484.5
z: 70 16  hi -4275.06 low -10140.2
new -9837.35 r -10757.1
r: 70 48  hi -7195.52 low -6995.17
z: 70 48  hi 3177.32 low -1724.51
new 726.406 r -7095.34
making b zero at axis
interpolating B_field to our grid
zero is master node k=0 j=0 z -34.663 r 0
getting normalized B field...
getting magnetic stream function
maximum gyro frequency to be resolved is 12.626 / T

getting parallel and perpendicular electron moments
phi_wall 0.0628123

Initial Neutral moments...
neutral quick moments...
mass 6.27001e+006
mom.z 20271.5 mom.r 2751.73 mom.theta -18.2094
en.z 48.5526 en.r 5.16998 en.theta 1.17915 sum 54.9017
neutral_total 395374
Scrubbing neutrals:  Found 188859 of size 1
```

```
25253 Charge exchange neutrals to be excluded
worst cell to be cleaned has 103 XS neutrals size 1, requires 10.3 iterations
scrubbing 10 times
after scrubbing 10 times,  neutral total 393148
Still 186052 neutrals size 1
ke initial: 292.593 final 292.59
quick moments...
Neutral moments...
mass_total_o 6.27001e+006 mass_total_f 6.27001e+006
mass 6.27001e+006
mom.z 20271.8 mom.r 2751.93 mom.theta -18.0088
en.z 48.554 en.r 5.17006 en.theta 1.17897 sum 54.903

getting and saving eedf...
eedf_psi[0] lo=-255.004 hi=-202.025
eedf_psi[1] lo=-202.025 hi=-166.519
eedf_psi[2] lo=-166.519 hi=-112.71
eedf_psi[3] lo=-112.71 hi=-22.1339
eedf_psi[4] lo=-22.1339 hi=0
eedf_psi[5] lo=0 hi=15
eedf_psi[6] lo=15 hi=75
eedf_psi[7] lo=75 hi=200
eedf_psi[8] lo=200 hi=350
eedf_psi[9] lo=350 hi=481

enter number of iterations: 1000

delta_spots 6
spot 0 = 40 65 z 0 r 15.8459
spot 1 = 46 65 z 1.66097 r 15.9521
spot 2 = 52 65 z 3.32714 r 16.0804
spot 3 = 58 65 z 4.99776 r 16.2118
```

```
spot 4 = 64 65 z 6.67616 r 16.355
spot 5 = 70 65 z 8.36679 r 16.5199
spot 6 = 76 65 z 10.0758 r 16.7184
spot 7 = 82 65 z 11.8119 r 16.9673
spot 8 = 88 65 z 13.5878 r 17.2992
spot 9 = 94 65 z 15.4209 r 17.7664

It: 0, T: 7674.829,  ions: 94471, neutrals: 393152, electrons: 99409
It: 1, T: 7674.947,  ions: 94472, neutrals: 393156, electrons: 99406
It: 2, T: 7675.061,  ions: 94486, neutrals: 393160, electrons: 99415
It: 3, T: 7675.176,  ions: 94485, neutrals: 393164, electrons: 99392
It: 4, T: 7675.278,  ions: 94494, neutrals: 393173, electrons: 99389
It: 5, T: 7675.396,  ions: 94486, neutrals: 393183, electrons: 99379
\end{performance}
```

Several of the lines above deserve explanation.

- The normalization constants are re-calculated each time the simulation is initialized.
- The simulation asks the user whether old particle files should be loaded. If not, the simulation seeds the simulation region uniformly with a pre-set number of particles.
- At the beginning of each run, the neutral population is scrubbed for small neutrals is regions of high number density. Such neutrals are lumped together. The data-stream above seems to indicate that energy and momentum are not conserved in this operation. However, what are shown are only rough estimates. Energy and momentum are conserved exactly in this operation.

Appendix B

Cross Sections

The following functions (written in C) return some of the cross sections for electron-neutral scattering of a particle at relative energy E off a neutral background. Units of energy are in eV, while the cross sections themselves are in cm^2:

```
/* ------------------------------------------------------------------ */
/* The total electron-neutral scattering cross section, 3/7/00 */
/* ------------------------------------------------------------------ */
double sigma_total(double E){
double rootE;
double ans;

rootE=sqrt(E);

if (E<=.1592)
ans=1.699e-15;       /* not exact -- data is at 1.703,
  function evaluates to 1.695 */
else if (E<=2.8)
ans=
1.0e-13 *(
0.07588072747894*E*E
-0.34475940259139*E*rootE
+0.58473840309059*E
```

```
-0.42726069455393*rootE
+0.11430271021684);

else if (E<=24.7)
ans =
1.0e-13 *(
-0.00199145459640*E*E
+0.02974653588357*E*rootE
-0.16550787909579*E
+0.40171310068942*rootE
-0.31727871240879);

else if (E<=50)
ans =
1.0e-13 *(
-0.00217736834537*E*rootE
+0.04302155076778*E
-0.28567311384223*rootE
+0.65180228051047);

else if (E<=500)
ans =
1.0e-14 *(
-0.00002249610521*E*rootE
+ 0.00109930275788*E
-0.02071463195923*rootE
+ 0.22876772390428);
else
ans=
6.400000000000000e-16;

return ans;
```

```
}

/* ------------------------------------------------------------------ */
/* The total neutral to Xe+1 ionization x-section, 3/7/00 */
/* ------------------------------------------------------------------ */
double sigma_n1(double E){
double rootE;
double ans;

rootE=sqrt(E);

if (E<=12.1)
ans=0;

else if (E<=20)
ans =
1.0e-13 *(
0.00135612832973*E*E
-0.02258559839486*rootE*E
+ 0.14035004086532*E
-0.38335664819867*rootE
+0.38736677629904);

else if (E<=44)
ans =
1.0e-14 *(
-0.00061869954583*E*E
+0.01448501832638*E*rootE
-0.13321973517308*E
+0.57375481836921*rootE
-0.92720818547058);
```

```
else if (E<=360)
ans =
1.0e-15 *(
-0.00001627288393*E*E
+0.00103294012446*E*rootE
-0.02400846159171*E
+0.21746827014037*rootE
-0.18814292010734);
else
ans=2.440000000000000e-16;

return ans;
}

/* ------------------------------------------------------------------ */
/* The total neutral excitation x-section, 3/7/00 */
/* ------------------------------------------------------------------ */
double sigma_excite(double E){
double rootE;
double ans;

rootE=sqrt(E);

if (E<=E_EXCITE)
ans=0;

else if (E<=11)
ans =
1.0e-12 *(
0.00194724369808*E*E
-0.02261576374741*E*rootE
+0.09807793114366*E
```

```
-0.18808539260191*rootE
+0.13446494003922);

else if (E<=25)
ans =
1.0e-13 *(
0.00069390658261*E*E
-0.01241570210985*E*rootE
+0.08109737428153*E
-0.22730324307635*rootE
+0.23122639784590);

else if (E<=500)
ans =
1.0e-14 *(
0.00000121267639*E*E
-0.00008169557347*E*rootE
+0.00207211887803*E
-0.02409700583197*rootE
+0.11701534311188);

else
ans=3.950000000000000e-17;

return ans;
}
```

Appendix C

The Boltzmann Equation

The Particle-In-Cell (PIC) and Monte Carlo Collision (MCC) methodologies described in this thesis are fully kinetic. They produce, for each species, a particle distribution in phase space, $f(\vec{r},\vec{v},t)$, which changes over time. The total derivative of $f(\vec{r},\vec{v},t)$ with time is

$$\frac{df}{dt} = \frac{\partial f}{\partial t} + \frac{\partial f}{\partial x}\frac{dx}{dt} + \frac{\partial f}{\partial y}\frac{dy}{dt} + \frac{\partial f}{\partial z}\frac{dz}{dt} + \frac{\partial f}{\partial v_x}\frac{\partial}{dv_x} + \frac{\partial f}{\partial v_y}\frac{dv_y}{dt} + \frac{\partial f}{\partial v_z}\frac{dv_z}{dt} \tag{C.1}$$

or

$$\frac{df}{dt} = \frac{\partial f}{\partial t} + \vec{v}\cdot\nabla f + \dot{\vec{v}}\cdot\nabla_v f \tag{C.2}$$

This leads to a continuity equation, were we note that $m\dot{v} = \vec{F}$:

$$\frac{df}{dt} + \vec{v}\cdot\nabla f + \frac{\vec{F}}{m}\cdot\nabla_v f = 0 \tag{C.3}$$

This is just the Vlasov equation, which applies for a collisionless plasma. Adding in collisions, a source term S_a, and a sink term L_a, we reach the fundamental equation which a distribution $f(\vec{r},\vec{v},t)$ must satisfy, the Boltzmann equation:

$$\frac{\partial f}{\partial t} + \vec{v}\cdot\nabla f + \frac{\vec{F}}{m}\cdot\frac{\partial f}{\partial \vec{v}} = (\frac{\partial f}{\partial t})_c + S_a + L_a \tag{C.4}$$

Here, F is the force acting on the particles and $(\frac{\partial f}{\partial t})_c$ is the collision term. In a Hall thruster, collisions drive the discharge. Some collisions (e.g. ion-ion, neutral-neutral) are relatively infrequent and can be neglected. The most important are electron collisions which excite and ionize the neutrals, and those which significantly affect the electron energy distribution

function. Electrons collide with both neutrals and other charged particles; the collision term for electrons can be expressed,

$$(\frac{\partial f}{\partial t})_c = (\frac{\partial f}{\partial t})_N + (\frac{\partial f}{\partial t})_C. \tag{C.5}$$

Electron-neutral collisions can be treated as discrete events using a standard MCC method. Electron-ion and electron-electron collisions are better treated as a diffusion process in velocity space.

Charged particles are also subject (via the potential solver) to non-physical forces which lead to artificial heating of the plasma. This subject has been treated by Hockney [19] and is discussed in Chapter 4.

Appendix D

Maxwell's Equations in SI Units

This simulation uses the CGS formulation of Maxwell's equations. However, the SI formulation provides a clearer understanding for many engineers. In fact, it is needed to follow the changes in ϵ_o used to accelerate the simulation.

D.0.1 Maxwell's Equations in SI Units

We begin with Maxwell's equations:

$$\nabla \times \vec{E} = -\frac{\partial \vec{B}}{\partial t} \tag{D.1}$$

$$\nabla \times \vec{H} = \frac{\partial \vec{D}}{\partial t} + \vec{J} \tag{D.2}$$

$$\nabla \cdot \vec{D} = \rho_e \tag{D.3}$$

$$\nabla \cdot \vec{B} = 0 \tag{D.4}$$

$$\vec{D} = \epsilon \vec{E} \tag{D.5}$$

$$\vec{B} = \mu \vec{H} \tag{D.6}$$

In free space and in a plasma, $\mu \approx \mu_o$. In free space, the permittivity $\epsilon \approx \epsilon_o$. In a material $\vec{D} = \epsilon_o \vec{E} + \vec{P}$ where $\vec{P} = \epsilon_o \overleftrightarrow{\chi}\, \vec{E}$ is the polarization per unit volume (the sum over all the individual moments of the electric dipoles in the material), such that $\vec{D} = \epsilon_o(\overleftrightarrow{I} + \overleftrightarrow{\chi})\vec{E}$ where $\overleftrightarrow{\chi}$ is a non-dimensional tensor called the susceptibility.

In plasma physics, electron energies are temperatures are frequently expressed in electron-

Volts, or eV. If Boltzmann's constant, K, and electron charge, e, are in SI units, and temperature is given in Kelvin, then $KT_K = eT_{ev}$.

D.0.2 Plasma Formulation of Maxwell's Equations in SI Units

In plasma physics, we normally use the free space formulation of Maxwell's equations:

$$\nabla \times \vec{E} = -\frac{\partial \vec{B}}{\partial t} \tag{D.7}$$

$$\nabla \times \vec{H} = \epsilon_o \frac{\partial \vec{E}}{\partial t} + \vec{J} + \vec{J}_{ext} \tag{D.8}$$

$$\epsilon_o \nabla \cdot \vec{E} = \rho_e + \rho_{e,ext} \tag{D.9}$$

$$\nabla \cdot \vec{B} = 0 \tag{D.10}$$

where $\vec{J}_{ext}$ and $\rho_{e,ext}$ are external currents and charge densities, here assumed to be zero. In free space and in a plasma, $\mu \approx \mu_o$. In free space, $\epsilon = \epsilon_o$. For good measure, we include the Lorentz force equation:

$$\vec{F} = q(\vec{E} + v \times \vec{B}) \tag{D.11}$$

The internal current $\vec{J}$ and its transform define the tensor susceptibility, $\overleftrightarrow{\chi}$, of the plasma:

$$\vec{J} = \epsilon_o \overleftrightarrow{\chi} \cdot \frac{\partial \vec{E}}{\partial t} \tag{D.12}$$

$$\vec{J} = -i\omega\epsilon_o \overleftrightarrow{\chi} \cdot \vec{E} \tag{D.13}$$

(This may be likened to the polarization, $\vec{P}$, where we note that an actual polarization current can only arise if $\vec{E}$ is time varying.) The susceptibility determines the response of the plasma to the magnetic field and thus describes the physics of the problem. When the susceptibility is a function of ω, the plasma is said to be dispersive in time. When it is a function of wave number, the plasma is said to be dispersive in space. The dielectric tensor (permittivity tensor) $\overleftrightarrow{K}$ is defined by the identity and susceptibility tensors: $\overleftrightarrow{K} = \overleftrightarrow{I} + \overleftrightarrow{\chi}$. Thus, the transform of Ampere's Law (D.8) may, in the absence of external currents ($\vec{J}_{ext} = 0$), be written:

$$\nabla \times \vec{H} = -i\omega\epsilon_o \overleftrightarrow{K} \cdot \vec{E} \tag{D.14}$$

The transform of Faraday's Law (D.7) yields:

$$\nabla \times \vec{E} = i\omega\mu_o\vec{H} \tag{D.15}$$

Taking the curl of (D.15) and substituting for $\nabla \times \vec{H}$ with (D.14), we arrive at a wave equation for the electric field:

$$\nabla \times \nabla \times \vec{E} - \mu_o\epsilon_o\omega^2 \overleftrightarrow{K} \cdot \vec{E} = 0 \tag{D.16}$$

Noting that $\mu_o\epsilon_o = c^{-2}$, and defining $k_o = \frac{\omega^2}{c^2}$, we may rewrite this equation as follows:

$$\nabla \times \nabla \times \vec{E} - {k_o}^2 \overleftrightarrow{K} \cdot \vec{E} = 0 \tag{D.17}$$

Bibliography

[1] Batishchev, O. V. . Personal communication, 2000.

[2] Batishchev, O. V. and et. al. Kinetic Effects on Particle and Heat Fluxes in Detached Plasmas. *Phys. Plasmas 3*, 9, 1996.

[3] Beidler, P. Two Dimensional Particle-in-Cell Simulation Model for Hall Type Thrusters. Master's thesis, Massachusetts Institute of Technology, 1999.

[4] Bird, G.A. *Molecular Gas Dynamics and the Direct Simulation of Gas Flows.* Clarendon Press, Oxford, 1994.

[5] Birdsall, C.K and A.B Langdon. *Plasma Physics via Computer Simulation.* Institute of Physics Publishing, Bristol and Philadelphia, 1991.

[6] Chen, Francis F. *Introduction to Plasma Physics and Controlled Fusion;Volume 1: Plasma Physics.* Plenum Press, New York, 2nd edition, 1984.

[7] Press et. al. *Numerical Recipes in C.* Cambridge University Press, 1995.

[8] Fife, J. M. , M. Martinez-Sanchez, and J. J. Szabo. A Numerical Study of Low-Frequency Discharge Oscillations in Hall Thrusters. 33rd AIAA Joint Propulsion Conference, Seattle, WA, July 1997.

[9] Fife, J.M. Two-Dimensonal Hybrid Particle-In-Cell Modeling of Hall Thrusters. Master's thesis, Massachusetts Institute of Technology, 1995.

[10] Fife, J.M. *Hybrid-PIC Modeling and Electrostatic Probe Survey of Hall Thrusters.* PhD thesis, Massachusetts Institute of Technology, 1998.

[11] Gardiner, C.W. *Handbook of Stochastic Methods.* Springer-Verlag, Berlin, 1983.

[12] Grishin, S.D. and L.V. Leskov. Electrical Rocket Engines of Space Vehicles. Partially Edited Machine Translation of Russian original, USAF Foreign Technology Division, FTD-ID(RS)T-1261-89, 1990.

[13] Guerrini, G. and et. al. Characterization of Plasma Inside the SPT-50 Channel by Electrostatic Probes. IEPC-97-53, 25th International Electric Propulsion Conference, 1997.

[14] Hayashi, M. . Determination of Electron-Xenon Total Excitation Cross-Sections, From Threshold to 100-ev, from Experimental Values of Townsend's α. *J. Phys. D: Appl. Phys*, 16:581–589, 1983.

[15] Hirakawa, M. Electron Transport Mechanism in a Hall Thruster. IEPC-97-021, 25th International Electric Propulsion Conference, 1997.

[16] Hirakawa, M. and Y. Arakawa. Particle Simulation of Plasma Phenomena in Hall Thrusters. IEPC-95-164, 24th International Electric Propulsion Conference,Moscow, Russia, September 1995.

[17] Hirakawa, M. and Y. Arakawa. Numerical Simulation of Plasma Particle Behavior in a Hall Thruster. AIAA-96-3195, 32nd AIAA/ASME/SAE/ASEE Joint Propulsion Conference, Lake Buena Vista, FL, July 1996.

[18] Hirsch, C. *Numerical Computation of Internal and External Flows , Vol. 1.* John Wiley and Sons., New York, 1988.

[19] Hockney, R. W. and J. W. Eastwood. *Computer Simuation Using Particles.* Institute of Physics Publishing, Bristol and Philadelphia, 1988.

[20] Hodgman, M, editor. *Handbook of Chemistry and Physics.* Chemical Rubber Publishing Co., Cleveland, 1954.

[21] Hoffman, J. D. *Numerical Methods for Engineers and Scientists.* McGraw-Hill, New York, 1992.

[22] Hoffman, K. A. *Computational Fluid Dynamics for Engineers.* Engineering Education System (EES), Austin, TX, 1989.

[23] Houston, W. V. *Principles of Mathematical Physics.* McGraw-Hill, New York, 1948.

[24] Jahn, R. G. *Physics of Electric Propulsion.* McGraw-Hill Book Company, New York, 1968.

[25] Khayms, V. *Advanced Propulsion for Microsatellites.* PhD thesis, Massachusetts Institute of Technology, 2000.

[26] Khayms, V. and M. Martinez-Sanchez. Preliminary Experimental Evaluation of a Miniaturized Hall Thruster. IEPC-97-077, 25th International Electric Propulsion Conference, 1997.

[27] Laplace, Pierre Simon, Marquis de. *A Philosophical Essay on Probabilities.* John Wiley and Sons, Inc., New York, 1917.

[28] Lentz, C. A. Transient One Dimensional Numerical Simulation of Hall Thrusters. Master's thesis, Massachusetts Institute of Technology, 1993.

[29] Manheimer, W. M. , M. Lampe, and G. Joyce. Langevin Representation of Coulomb Collisions in Pic Simulations. *Journal of Computational Physics*, 138:563–584, 1997.

[30] McDaniel, E. *Collision Phenomena in Ionized Gases.* John Wiley and Sons, New York, 1964.

[31] Mitchner, M. and Charles H. Kruger, Jr. *Partially Ionized Gases.* John Wiley and Sons, Inc., New York, 1973. Reprints available from authors.

[32] Noguchi, R. , M. Martinez-Sanchez, and E. Ahedo. Linear 1-D Analysis of Oscillations in Hall Thrusters. IEPC-99-105, 26th International Electric Propulsion Conference, Kitakyushu, Japan, October 1999.

[33] Oh, D. *Computational Modeling of Expanding Plasma Plumes in Space using a PIC-DSMC Algorithm.* PhD thesis, Massachusetts Institute of Technology, Department of Aeronautics and Astronautics, 1997.

[34] Opal, C. B. , W. K. Peterson, and E. C. Beaty. Measurements of Secondary-Electron Spectra Produced by Electron Impact Ionizationof a Number of Simple Gases. *J. Chem. Phys*, 55(2):4100–4106, 1971.

[35] Piekos, E. DSMC Modeling of Micromechanical Devices. Master's thesis, Massachusetts Institute of Technology, 1995.

[36] Pierce, F. J. *Microscopic Thermodynamics.* International Textbook Company, Scranton, PA, 1968.

[37] Pollard, J.E. and S. Janson. *Spacecraft Electric Propulsion Applications.* The Aerospace Corporation, Report no. ATR-96(8201)-1, 1996.

[38] Ramsauer, C. . Ueber den Wirkungsquerschnitt der Gasmolekuele langsamen Elektronen. II. Fortsetzung and Schluss. *Ann. d. Physik*, 72:345, 1923.

[39] Ramsauer, C. and R. Kollath. Ueber den Wirkungsquerschnitt der Edelgasmolekuele gegenueber Elektronen unterhalb 1 Volt. *Ann. d. Physik*, 3:536, 1929.

[40] Rapp, D. and W. E. Francis. Charge Exchange Between Gaseous Ions and Atoms. *Journal of Chemical Physics*, 37(11):2631–2645, 1962.

[41] Rapp, D. and P. Englander-Golden. Total Cross Sections for Ionization and Attachment in Gases by Electron Impact. I. Positive Ionization. *Journal of Chemical Physics*, 43(5), 1965.

[42] Sakabe, S. and Y. Izawa. Cross Sections for Resonant Charge Transfer between Atoms and their Positive Ions: collision Velocity $\leq$ 1 a.u. *Atomic Data and Nuclear Data Tables*, 49:257–314, 1991.

[43] Samanta Roy, R. I. *Numerical Simulation of Ion Thruster Plume Backflow for Spacecraft Contamination Assessment.* PhD thesis, Massachusetts Institute of Technology, 1995.

[44] Seiler, H. *J Appl. Phys*, 54:R1, 1983.

[45] Seldner, D. and T. Westermann. Algorithms for Interpolation and Localization in Irregular 2D Meshes. *Journal of Computational Physics*, 79:1–11, 1988.

[46] Sheppard, E. *Ionizational Nonequilibrium and Ignition in Self-Field Magnetoplasmadynamic Thrusters.* PhD thesis, Massachusetts Institute of Technology, 1994.

[47] Shkarofsky, I. P., T. W. Johnston, and M. P. Bachynski. *The Particle Kinetics of Plasmas.* Addison-Wesley Publishing Company, Reading, Massachusetts, 1966.

[48] Steger, J. L. and R. L. Sorenson. Automatic Mesh-Point Clustering Near a Boundary in Grid generation with Elliptic Partial Differential Equations. *Journal of Computational Physics*, 33, 1979.

[49] Syage, J. A. Electron-impact Cross Sections for Multiple Ionization of Kr and Xe. *Physical Review A*, 46(9), 1992.

[50] Szabo, J. J, M. Martinez Sanchez, and O. Batishchev. Particle-in-Cell Modeling of Thruster with Anode Layer. IEPC 99-100, 26th International Electric Propulsion Conference, October 1999.

[51] Szabo, J. J, M. Martinez Sanchez, and O. Batishchev. Numerical Modeling of the Near Anode Region in a TAL Thruster. 36th AIAA/ASME/ASE/ASEE Joint Propulsion Conference, July 2000.

[52] Szabo, J. J, M. Martinez Sanchez, and J. Monheiser. Application of 2-D Hybrid Pic Code to Alternative Hall Thruster Geometries. AIAA-98-3795, 34th AIAA Joint Propulsion Conference, July 1998.

[53] Tajima, T. *Computational Plasma Physics: With Applications to Fusion and Astrophysics.* Addison-Wesley Publishing Company, Inc., Redwood City, CA, 1989.

[54] Thompson, W. B. *An Introduction to Plasma Physics.* Pergamon Press, Oxford, Great Britain, 1962.

[55] Trubnikov, B. A. Particle Interactions in a Fully Ionized Plasma. in Acad. M. A. Leontovich (ed) *Reviews of Plasma Physics: Volume 1*Consultants Bureau, New York, 1995.